UNCLASSIFIED

AD 284 280

Reproduced

by the

ARMED SERVICES TECHNICAL INFORMATION AGENCY
ARLINGTON HALL STATION
ARLINGTON 12, VIRGINIA

UNCLASSIFIED

NOTICE: When government or other drawings, specifications or other data are used for any purpose other than in connection with a definitely related government procurement operation, the U. S. Government thereby incurs no responsibility, nor any obligation whatsoever; and the fact that the Government may have formulated, furnished, or in any way supplied the said drawings, specifications, or other data is not to be regarded by implication or otherwise as in any manner licensing the holder or any other person or corporation, or conveying any rights or permission to manufacture, use or sell any patented invention that may in any way be related thereto.

DISCLAIMER NOTICE

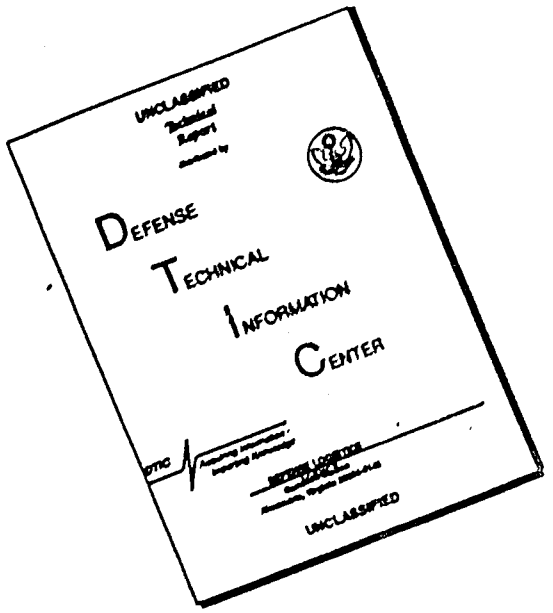

THIS DOCUMENT IS BEST QUALITY AVAILABLE. THE COPY FURNISHED TO DTIC CONTAINED A SIGNIFICANT NUMBER OF PAGES WHICH DO NOT REPRODUCE LEGIBLY.

284 280

Proceedings

of the

Fifth Symposium on Hypervelocity IMPACT

VOLUME I - PART 2
APRIL, 1962

Denver
October 30, 31,
November 1, 1961

TABLE OF CONTENTS

CONTENTS

CONTENTS

CONTENTS

SESSION IV

EXPERIMENTS

CHAIRMAN

F. E. HOWARD

EGLIN AIR FORCE BASE

CHAIRMAN'S REMARKS

Good afternoon, I am happy to be here this afternoon representing the active Air Force interest in hypervelocity impact, in company with Harry Davis of APGC, and a few in-house workers and contractors, some of whom are presenting papers. I only wish there were more of us trying to do some active work in some small portion of this field.

The introductory review paper in the field of experiments is by one of the more distinguished long-term workers in the field of hypervelocity impact and shaped charges, Dr. Robert Eichelberger of BRL.

INTRODUCTION -- EXPERIMENTAL STUDIES

R. J. Eichelberger

Ballistic Research Laboratories
Aberdeen Proving Ground, Maryland

Before presentation of papers representing the results of experimental studies in hypervelocity impact during the past eighteen months, it is appropriate to consider the state of knowledge immediately after the Fourth Symposium.

Experimental research generally falls into four -- not always readily distinguishable -- categories:

a. Exploration of newly discovered phenomena;

b. Procurement of qualitative observations for use in phenomenological or pseudo-theoretical mathematical description;

c. Testing of existing theory, qualitative or quantitative;

d. Accumulation of numerical data for engineering use.

Concerning each of these aspects of experimental research, the state of the art after the Fourth Symposium can be superficially summarized as follows:

1. Exploration of hypervelocity impact had long since been completed. A sufficiently clear and complete picture of the gross aspects of the problem had been presented at the Rand Symposium in 1955 to effectively end this stage.

2. The phenomenological approach had provided a fairly complete description of the ultimate effects of "hypervelocity" impact (in many cases a question arose as to whether truly hypervelocity conditions had been attained) on a variety of target materials; i.e., the form of the crater produced, including the effects of oblique incidence, the effects of fracture in brittle materials, and the other final and static manifestations of the impact. The transient aspects of crater formation had been subjected to observation by means of a variety of novel and potentially very useful techniques; although the experiments had not been sufficiently extensive nor thoroughly enough analyzed to provide detailed, quantitative information, they had yielded a physical model of the process that was accepted quite generally. More will be said of this model below.

3. The testing of theory had proceeded to the point of discouraging all the theoretical models that had been attempted prior to the Fourth Symposium.

The various assumptions and simplifications used to arrive at tractable mathematical forms had all been proven too unrealistic to be trustworthy. Only the theoretical approach of Bjork, which does not depend upon a priori assumptions, remained as a possibly acceptable treatment. With respect to Bjork's hydrodynamic calculations, the experiments were inconclusive. It had been amply demonstrated that, at the relatively modest velocities attainable in the laboratory, strength properties of the target material were not negligible, as implicitly assumed to be in the hydrodynamic approach. The velocities attainable had been well below the lower limit for which the theory was expected to be accurate, however, so that the results did not constitute a critical test. Attempts to verify or disprove the predictions of the theory with respect to influence of projectile density and target density had been entirely futile because of the disagreement among various experimenters as well as the inadequate velocity range.

4. The accumulation of engineering data had, of course, not even begun. In order to obtain such data, one must be able to accurately simulate conditions to be encountered in application, and the velocities attainable by known techniques were not nearly adequate. Only in "model" tests, with target materials having very low wave propagation velocities, had truly hypervelocity impact even been observed under controlled conditions.

In more specific terms, the state of agreement (or disagreement) among experimental workers, with respect to each of the primary physical variables, was:

a. Velocity - It was widely accepted that, neglecting low-velocity transition regions, crater volume (τ) is proportional to V^2 (V = impact velocity), although there were not infrequent "anomalies" presented, and there was considerable reluctance to extrapolate the relationship beyond the range of the data. The data had been extended to 10 km/sec by use of microparticle data, and the linear relation between volume and energy appeared to be still valid. It was also commonly agreed that craters in all ductile materials would be very nearly hemispherical at sufficiently high impact velocities, although a few workers held reservations about specific materials (not the same ones in all cases).

b. Mass - The validity of linear modelling laws was almost universally accepted, having been demonstrated with a fair degree of precision over eleven orders of magnitude (10^{-10}gm to 10 gm) in mass.

c. Shape - It was generally granted that projectile shape had no significant influence on crater form or dimensions neglecting, of course, the extremes of long rods or thin discs of very large diameter.

d. Density - The influence of density, of either the projectile or the target upon crater dimensions continued to be a subject of considerable controversy. Opinions ranged from quadratic relations (between crater volume and projectile density) to no effect. Unfortunately, none of the experimental observations were made at sufficiently high velocities to permit the "primary" penetration contribution to the crater to be neglected, and only rarely were the data analyzed with any attempt to remove the recognized influence of density upon the early stages of crater formation from the correlations.

E. Wave propagation velocity - With few exceptions, experimental investigators agreed that the wave propagation properties of the target (or the projectile) had no direct influenee upon crater formation, at least insofar as final dimensions were eoncerned.

f. Compressibility - No attempt had been made to eorrelate crater parameters with the Hugoniot properties of the projeetile or the target.

g. Strength - The strength of the projectile was generally held to have no measurable effect upon erater formation at velocities well above the transition values. The strength of the target material, as measured statically in terms of Brinell hardness number, ultimate tensile strength, or shear strength, had been shown to have a primary influence at velocities up to 10 km/sec. In addition to the more or less routine experiments, observing impacts on targets of various materials or varying strength by heat treatment, the effects of varying target temperature and of anisotropic properties of single crystals had also been clearly related to strength properties. It was commonly acceded that the energy required to produce unit crater volume (E/τ) is proportional to the Brinell hardness of the target material.

h. Obliquity - Although there were relatively few experiments reported on oblique impaet, the conclusions were in very close agreement. It was generally accepted that eraters formed at very oblique angles of incidence would have a degree of asymmetry dependent upon the impact velocity; at sufficiently high velocities, the craters would be very nearly hemispherical, however, even at very large angles of incidence. It was also widely agreed that the crater volume would decrease with increasing obliquity, although the precise relationship had not been well established.

All of the above remarks apply only tc impact upon targets of ductile materials and very large dimensions. Only very cursory observations had been made concerning impact on brittle (frangible) materials. Experiments with thin plate targets had also been mainly exploratory, there having been no systematic, quantitative results obtained. Observations of phenomena associated with crater formation, such as vaporization and ionization had been even more superficial.

It must, then, be concluded that the significant successes of the experimentalists lay almost exclusively in the realm of phenomological studies of the mechanism of crater formation. This type of work had demonstrated the inherent weaknesses in all of the simple models used for mathematical treatment and had yielded a fairly detailed qualitative description of the sequence of events as they actually occur. The attempts to develop empirical formulae have yielded no results that can be used with confidence because (a) they do not reach into the range of real hypervelocity for materials of interest; (b) there is no acceptable theory that will span the gap between the velocity range of the data and the hypervelocity regime (the hydrodynamic approach in its present form is clearly not valid at low velocity); and (c) the formulae are subject to so much controversy that they are certainly not satisfactory in themselves for extrapolation. The empirical work can be said to have provided only engineering data regarding impact at moderately high velocities and, possibly, a foundation for more useful experimental work or for testing a more complete theory if one becomes available.

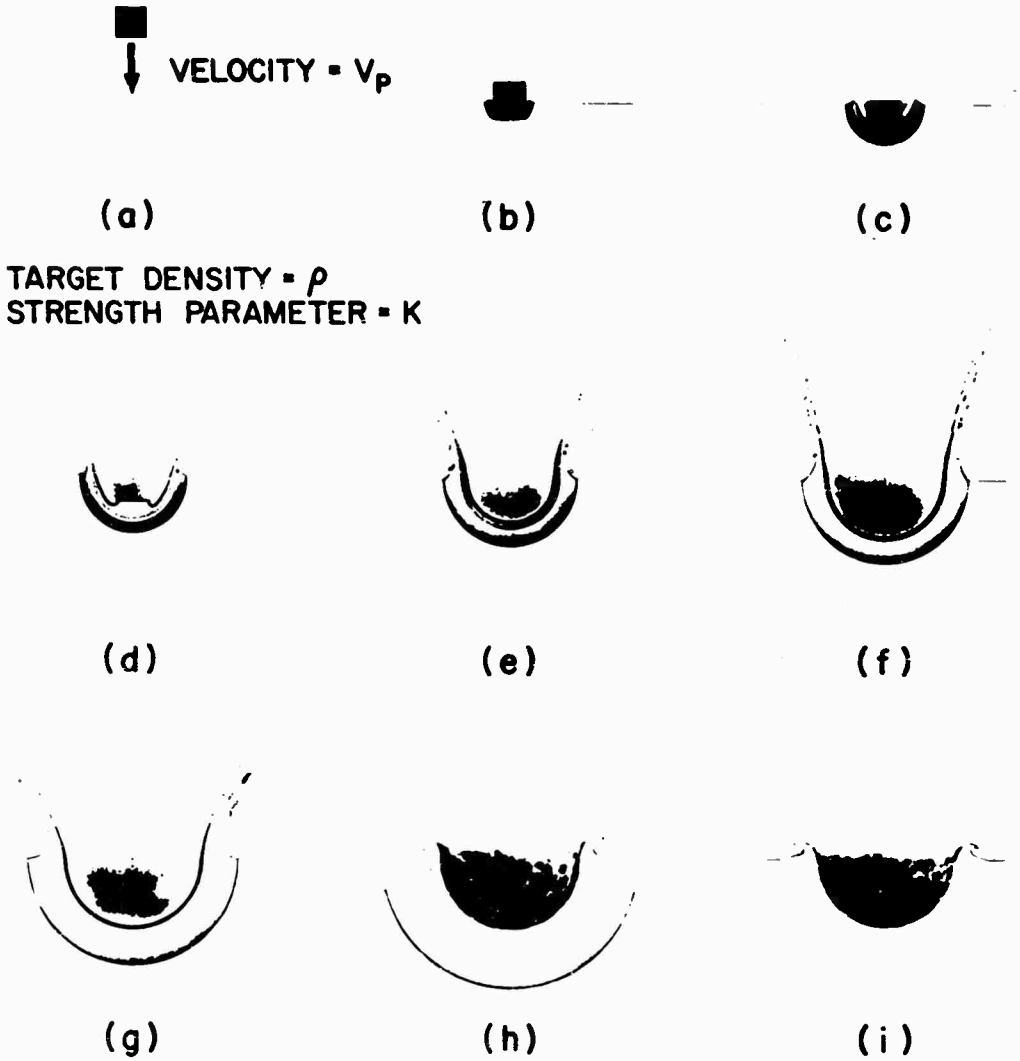

Figure 1. Schematic representation of phenomenological model of crater formation.

The phenomenological model of crater formation warrants a review, especially for those who are not particularly familiar with it. The essential features are illustrated in Figure 1. The first stages (b, c, d) consist of a primary penetration resembling very closely the shaped charge jet penetration process. In really hypervelocity impact, the penetration velocity during this stage will be supersonic with respect to the target material. The primary penetration is completed in a very short time and leaves only a very small crater, but it has resulted in the transfer of a great deal of energy to the target. The energy is initially confined to a very narrow shell adjacent to the crater surface

because; in typical cases, the early crater motion takes place at such a high velocity that the shock wave cannot increase the intervening distance. The effect of the high energy density and the concomitant high particle velocity is an extensive cavitation, which persists for a time orders of magnitude longer than the primary penetration and results in a many-fold enlargement of the crater. During the latter stages of cavitation, the energy density decreases and the motion of the crater surface becomes much slower; the shock wave will then pull away from the surface and dissipate its remaining energy in plastic and elastic deformation of the target material. Finally, the crater ceases to expand and undergoes a certain amount of contraction due to elastic recovery. If the material is brittle, the remaining compression shock and reflected tension and shear waves may produce extensive fracture that will partially or completely obscure the form of the crater itself.

During the primary and at least the early portion of the secondary (cavitation) portions of the process, a great deal of target material is ejected from the crater at moderately high velocities; extensive shear deformation obviously takes place near the expanding crater surface during this time. Later, apparently, radial deformation occurs together with shear.

It is also interesting to re-establish a reference by means of which one can judge whether experimental data are appropriate to hypervelocity impact. The magnitudes of "transitional velocities" quoted by Hopkins and Kolsky during the Fourth Symposium still comprise as useful a set of values as are available. Based upon theoretical considerations, the values given for several of the common metals are:

	Steel	Duralumin	Aluminum	Copper	Lead
V_1 (mm/μ sec)	0.046	0.065	0.013	0.008	0.002
V_2 (mm/μ sec)	0.36	0.43	0.19	0.13	0.04
V_3 (mm/μ sec)	4.6	5.3	5.3	3.75	2.1

According to Hopkins and Kolsky, velocities in excess of V_2 would correspond to a hydrodynamic regime, and might be considered marginally as belonging in the hypervelocity range. To be assured of having attained a high enough velocity, however, one would have to exceed V_3, entering a "sonic" regime; then, another transition to an "explosive" regime could still be anticipated for velocities above $3V_3$. It is interesting to compare the velocities attained in experiments with these values.

OBSERVATIONS OF CRATER FORMATION IN DUCTILE MATERIALS

John H. Kineke, Jr.

Ballistic Research Laboratories
Aberdeen Proving Ground, Maryland

INTRODUCTION

In the past several years a qualitative model of crater formation in ductile materials has evolved, primarily from the synthesis of basic experimental observations made at the Ballistic Research Laboratories and several other organizations. This model was described by Gehring at the Fourth Hypervelocity Impact Symposium (1a), and by Eichelberger and Gehring at the American Rocket Society (2). Basically, this model divides the crater formation process into four parts which can be characterized as the transient regime, the steady-state regime, the cavitation regime, and the recovery regime.

During the transient regime, immediately after the projectile contacts the target, the pressure at the interface is that which would occur under plane impact with no lateral flow. Lateral flow of both projectile and target is initiated by a release of pressure at the boundary of the projectile. At the same time shock waves are propagated into both the projectile and target from the contact surface. When the two shock waves become stationary with respect to the interface the steady-state regime commences. During the steady-state regime, which persists for times of the same order as the transient regime (less than one microsecond), the projectile and target are deformed hydrodynamically, in accordance with the theory developed to describe the penetration of shaped charge jets [3]. Because crater growth is proceeding at a rate in excess of the dilatational wave velocity of the target material the region of compressed material is confined to a thin shell adjacent to the crater surface.

The cavitation regime begins when the projectile has been completely deformed and is no longer supplying energy to the target. The crater continues to grow, but the shock wave detaches itself from the crater surface, because it decreases in velocity less rapidly than the free surface of the crater. During this regime the principal mode of deformation is shear, which occurs parallel to the walls of the expanding crater. The projectile and target material are both ejected from the crater at fairly considerable velocities, and a crater lip is formed in the more ductile target materials. Finally, the energy density in the region near the free surface of the crater becomes so low that the intrinsic resistance of the material to deformation cannot be overcome. At this point the crater ceases to increase in size. In the fourth regime the crater may shrink somewhat, due to plastic and elastic recovery.

TABLE I

Target Material	Velocity Range km/sec.	Dependent Variable	Weighted Least Squares Fit	$\sigma_{Residuals}$
Pb	2 - 12	$P_c/m_p^{1/3}$	$+ 0.399 + 0.700v_p^{2/3}$	0.114
Cu	2 - 12	$P_c/m_p^{1/3}$	$- 0.766 + 0.674v_p^{2/3}$	0.225
Cd	2 - 10	$P_c/m_p^{1/3}$	$+ 0.099 + 0.571v_p^{2/3}$	0.147
Zn	2 - 10	$P_c/m_p^{1/3}$	$- 0.472 + 0.679v_p^{2/3}$	0.111
Steel - 1020	2.5 - 5.5	$P_c/m_p^{1/3}$	$- 0.641 + 0.531v_p^{2/3}$	0.078
Al - 2S0	2.5 - 12	$P_c/m_p^{1/3}$	$- 0.696 + 1.128v_p^{2/3}$	0.417
Al - 2024	2.5 - 12	$P_c/m_p^{1/3}$	$- 0.605 + 0.729v_p^{2/3}$	0.165
Pb	2 - 12	$D_c/m_p^{1/3}$	$+ 0.891 + 1.358v_p^{2/3}$	0.213
Cu	2 - 12	$D_c/m_p^{1/3}$	$+ 0.331 + 0.890v_p^{2/3}$	0.040
Cd	2 - 10	$D_c/m_p^{1/3}$	$+ 0.285 + 1.136v_p^{2/3}$	0.156
Zn	2 - 10	$D_c/m_p^{1/3}$	$+ 0.420 + 0.866v_p^{2/3}$	0.030
Steel - 1020	2.5 - 5.5	$D_c/m_p^{1/3}$	$+ 0.418 + 0.665v_p^{2/3}$	0.049
Al - 2S0	2.5 - 12	$D_c/m_p^{1/3}$	$+ 0.513 + 1.088v_p^{2/3}$	0.131
Al - 2024	2.5 - 12	$D_c/m_p^{1/3}$	$+ 1.048 + 0.666v_p^{2/3}$	0.191
Pb	2 - 12	V_c/m_p	$+ 3.917 + 0.885v_p^{2}$	2.78
Cu	2 - 12	V_c/m_p	$- 0.481 + 0.223v_p^{2}$	0.34
Cd	2 - 5.5	V_c/m_p	$+ 0.024 + 0.454v_p^{2}$	0.59
Zn	2 - 5.5	V_c/m_p	$- 0.295 + 0.264v_p^{2}$	0.34
Steel - 1020	2.5 - 5.5	V_c/m_p	$- 0.193 + 0.092v_p^{2}$	0.18
Al - 2S0	2.5 - 5.5	V_c/m_p	$- 6.029 + 1.131v_p^{2}$	1.54
Al - 2024	2.5 - 5.5	V_c/m_p	$- 0.726 + 0.268v_p^{2}$	0.40

where : v_p is in units of km/sec., $P_c/m_p^{1/3}$ is in units of $10^{-1}m/kg^{1/3}$, $D_c/m_p^{1/3}$ is in units of $10^{-1}m/kg^{1/3}$, V_c/m_p is in units of $10^{-3}m^3/kg$.

Öpik (4) and Bjork (5a) in discussing crater formation, treated the early phases of the process. At the last Symposium a phenomenological model was presented by Hopkins and Kolsky (1b). They qualitatively discussed the entire process, proposing that it could be divided into five regimes, depending for their limits on the impact velocity and material properties. These regimes are characterized as elastic, plastic, hydrodynamic, compressible, and thermal, with progressively higher impact velocities required for each.

This paper describes a number of observations which have been performed within the framework of the model of Eichelberger and Gehring. These observations fall into three general categories: observations of the effect of target strength on final crater size; observations of the rate of crater formation; and observations of shock propagation and attenuation in targets after the impact of hypervelocity projectiles.

EXPERIMENTAL OBSERVATIONS

I. Observations of the Effect of Target Strength on Final Crater Size

a. Crater Size Observations in Seven Metallic Materials

At the Third and Fourth Hypervelocity Impact Symposia (1c) (5b) (5c), crater data in semi-infinite targets of a number of materials were reported by the Ballistic Research Laboratories. At the Fourth Symposium, data for steel projectiles with masses up to 10 grams and velocities up to 10 km/sec were presented. In the past year and one-half, additional data at impact velocities up to 12 km/sec have been collected. All BRL data accumulated to date are summarized in Figures 1-4 and Table I. The target materials investigated are 1100-0 aluminum, 2024 aluminum, cadmium, copper, lead, 1020 steel, and zinc. Crater depth (P_c) and crater diameter (D_c) have been normalized by dividing by the one-third power of the projectile mass. Least square fits have been made of these data to the two-thirds power of the impact velocity. Crater volume (V_c) has been normalized by dividing by the projectile mass; it has been fitted to the square of the impact velocity. Regressions and statistics are shown in Table I.

It should be noted that the regressions do not differ from those shown at the Fourth Symposium. Thus it can be concluded that the additional observations at 12 km/sec follow the same relation as those at lower velocities; the volume of the crater is proportional to the energy of the projectile. This is in agreement with the hypothesis that a large portion of the crater volume is formed by a shear process. The common fundamental property of these seven materials which can be used to correlate all of the data is now known, however, an empirical property, the Brinell hardness, has been used successfully as a gauge of the resistance of the targets to shear deformation. It has been found that the ratio of the volume of the crater to the energy of the impacting projectile varies as the reciprocal of the Brinell hardness of the target, independently of the mass of the projectile, and independently of the density of the projectile, for impact velocities greater than the dilatational wave velocity of the target material.

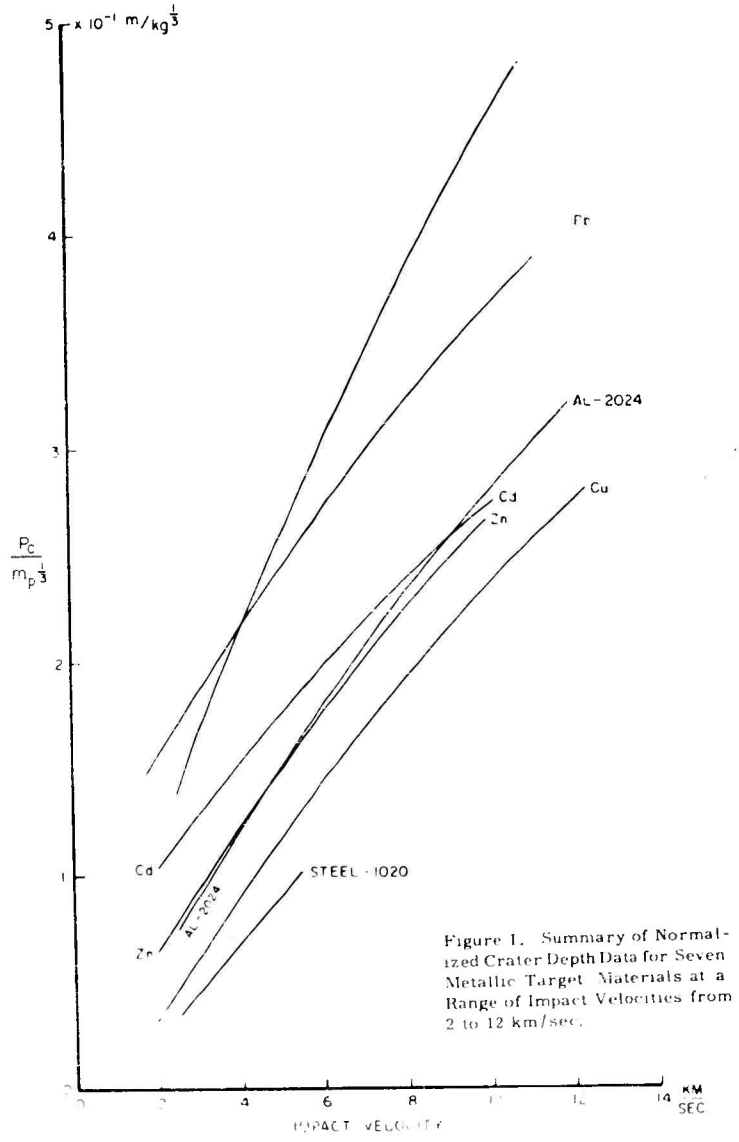

Figure 1. Summary of Normalized Crater Depth Data for Seven Metallic Target Materials at a Range of Impact Velocities from 2 to 12 km/sec.

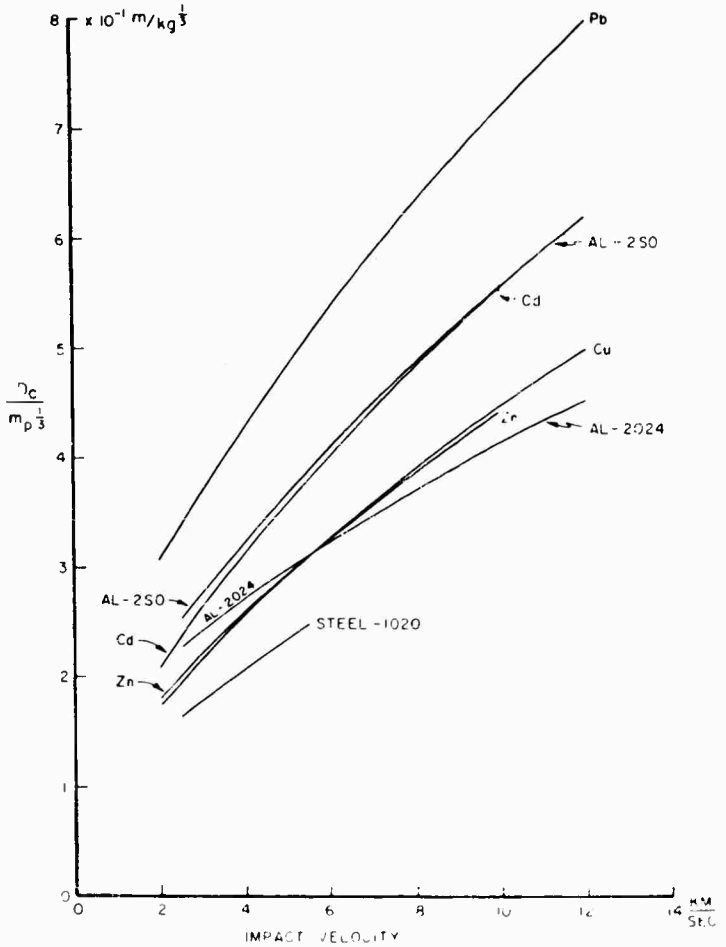

Figure 2. Summary of Normalized Crater Diameter Data for Seven Metallic Target Materials in a Range of Impact Velocities from 2 to 12 km/sec.

b. Effect of Ambient Target Temperature on Crater Size

At the Fourth Symposium, Allison, Becker, and Vitali (1d) reported observations of the effect of target temperature on craters in cadmium, copper, lead, and zinc. These observations were made in order to determine the effect on cratering of changes in the mechanical properties of the target. Recently, these observations have been extended to include 1100-0 aluminum and 2017-0 aluminum tested at temperatures in excess of 90 per cent of the melting point.

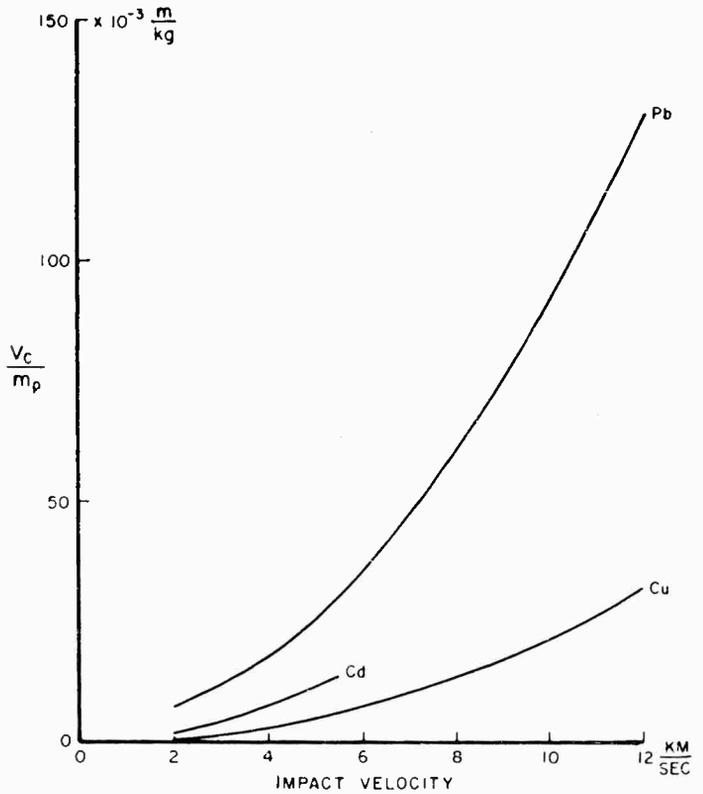

Figure 3. Summary of Normalized Crater Volume Data in Lead, Cadmium, and Copper in a Range of Impact Velocities from 2 to 12km/sec.

Steel pellets (mass: 0.18 grams, velocity: 5.01 km/sec) were fired into the targets at normal incidence and the volumes of the craters measured. The volumes were plotted as a function of the normalized target temperature, defined as the quotient of the target temperature at the time of impact (^{O}K) divided by the melting temperature of the target (^{O}K), these data are plotted in Figure 5.

For the 1100-0 aluminum, the crater volume is a continually increasing function of the target temperature over the entire temperature range. This behavior is very similar to that exhibited by lead, and since all the common elastic indices of pure aluminum are smoothly varying functions of temperatures, there is little hope of correlating these data with any single mechanical property.

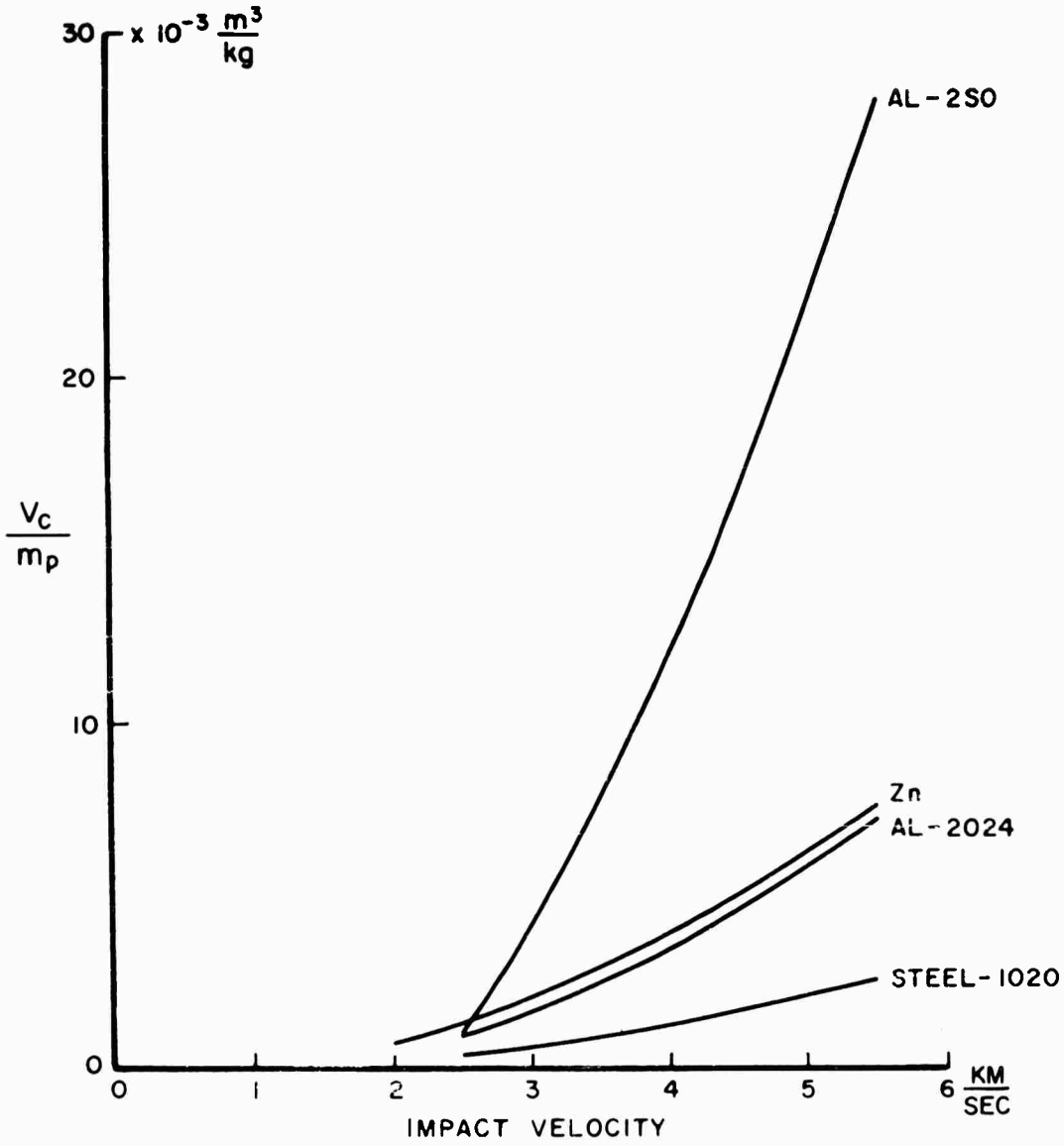

Figure 4. Summary of Normalized Crater Volume Data in 2SO Aluminum, 2024 Aluminum, 1020 Steel and Zinc in a Range of Impact Velocities from 2 to 5.5 km/sec.

The results obtained with the 2017-0 alloy show that the crater volume is an increasing function of temperature in the range from 0.1 (77°K) to 0.7 (550°K); above 550°K the crater volume is essentially independent of the target temperature, an effect which possibly may be correlated with the metallurgical behavior of 2017-0 aluminum at elevated temperatures.

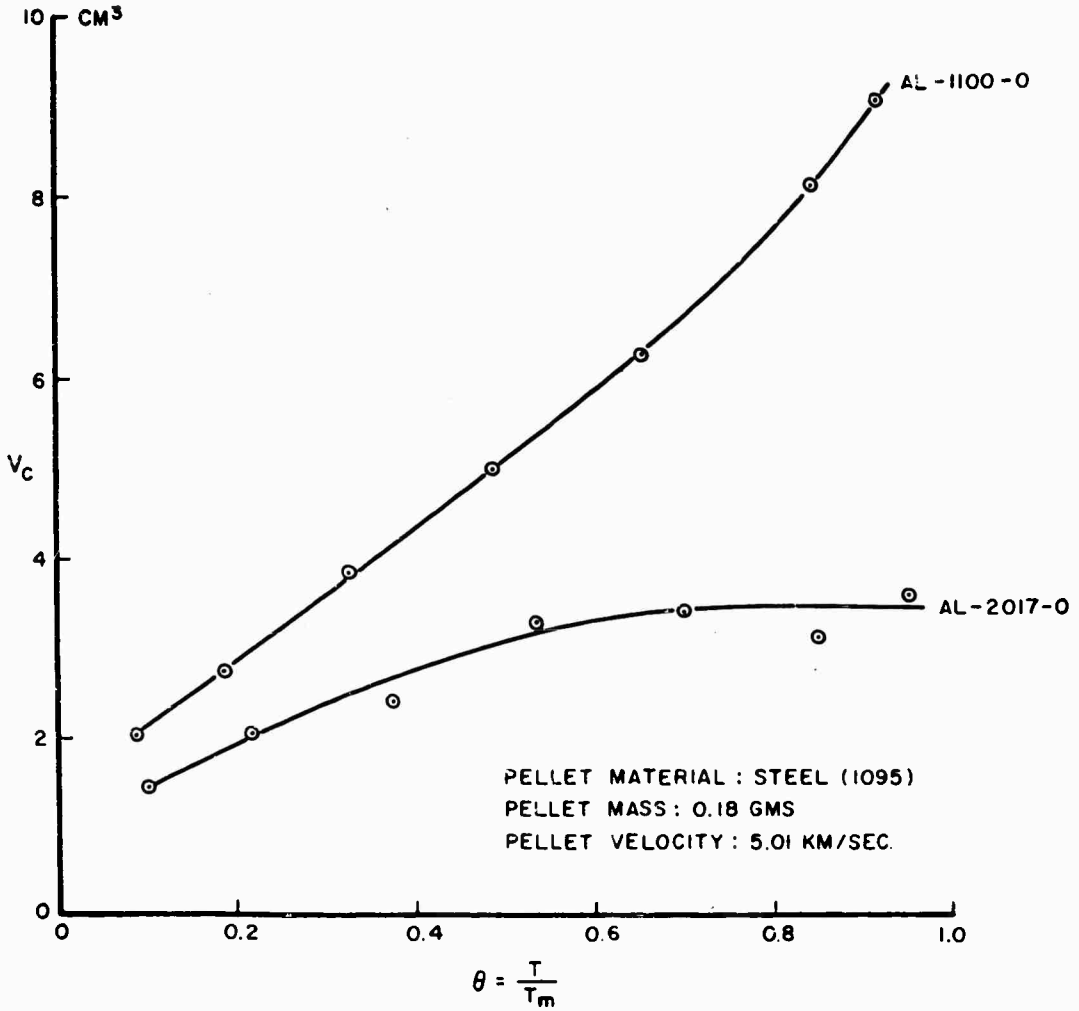

Figure 5. Effect of Target Temperature on Crater Volume in Targets of Two Aluminum Alloys.

II. Observations of the Rate of Crater Formation

a. Rate of Crater Formation in Lead

Crater formation in lead targets is illustrated in Figures 6a-6o. The pictures are a sequence of flash radiographs at the indicated time intervals after impact. These craters were made by 0.18 gram steel pellets striking at 5.01 km/sec. The radiographs show the impacted surfaces of essentially semi-infinite targets, and are intended to demonstrate the manner and extent of ejection of target material from the crater. The material flows along the surface of the expanding crater and is ejected at moderately high velocities. At high impact velocities the mass of material ejected in this manner is very considerable; the total

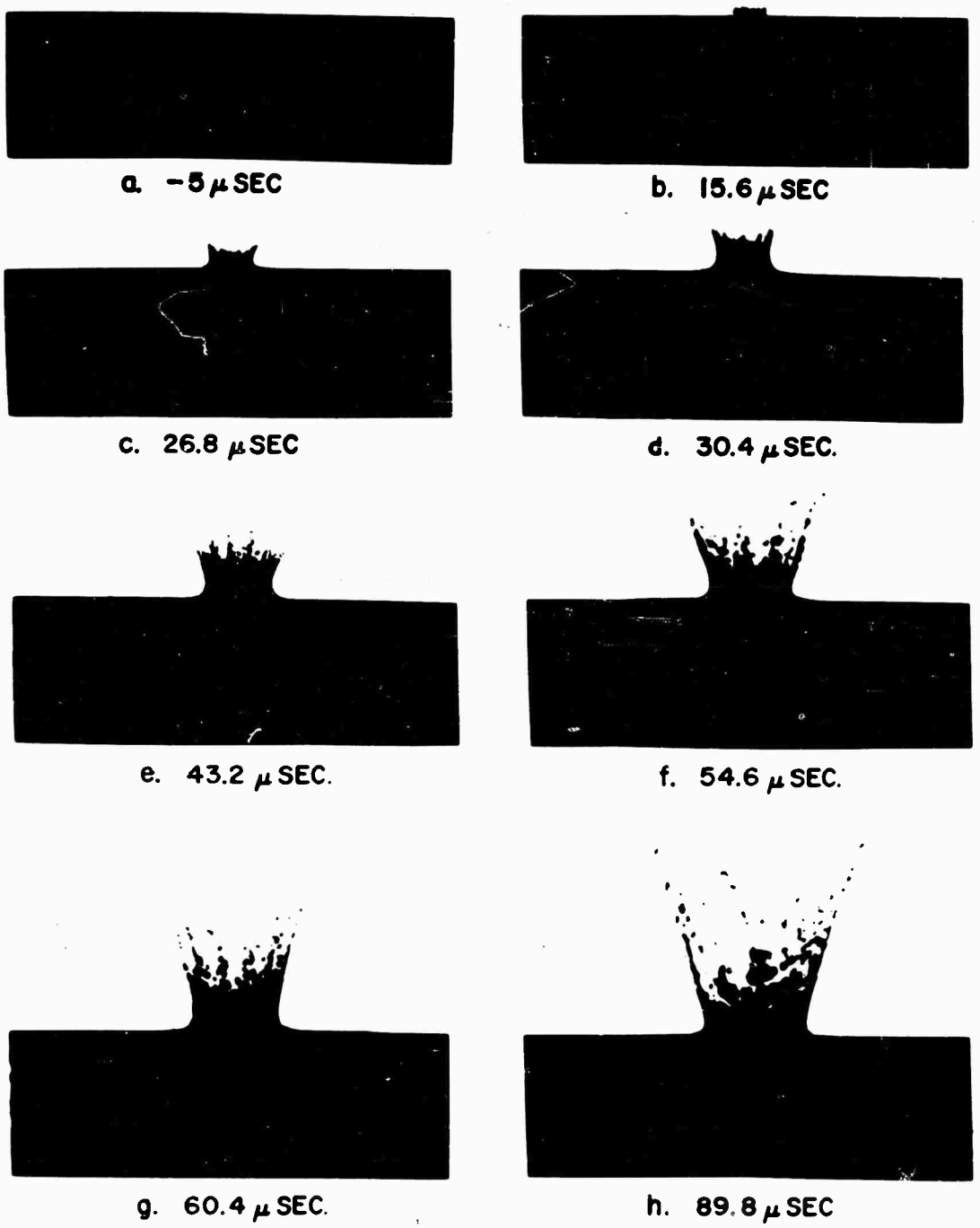

Figure 6. Surface Phenomena Associated with Crater Formation in a Lead Target.

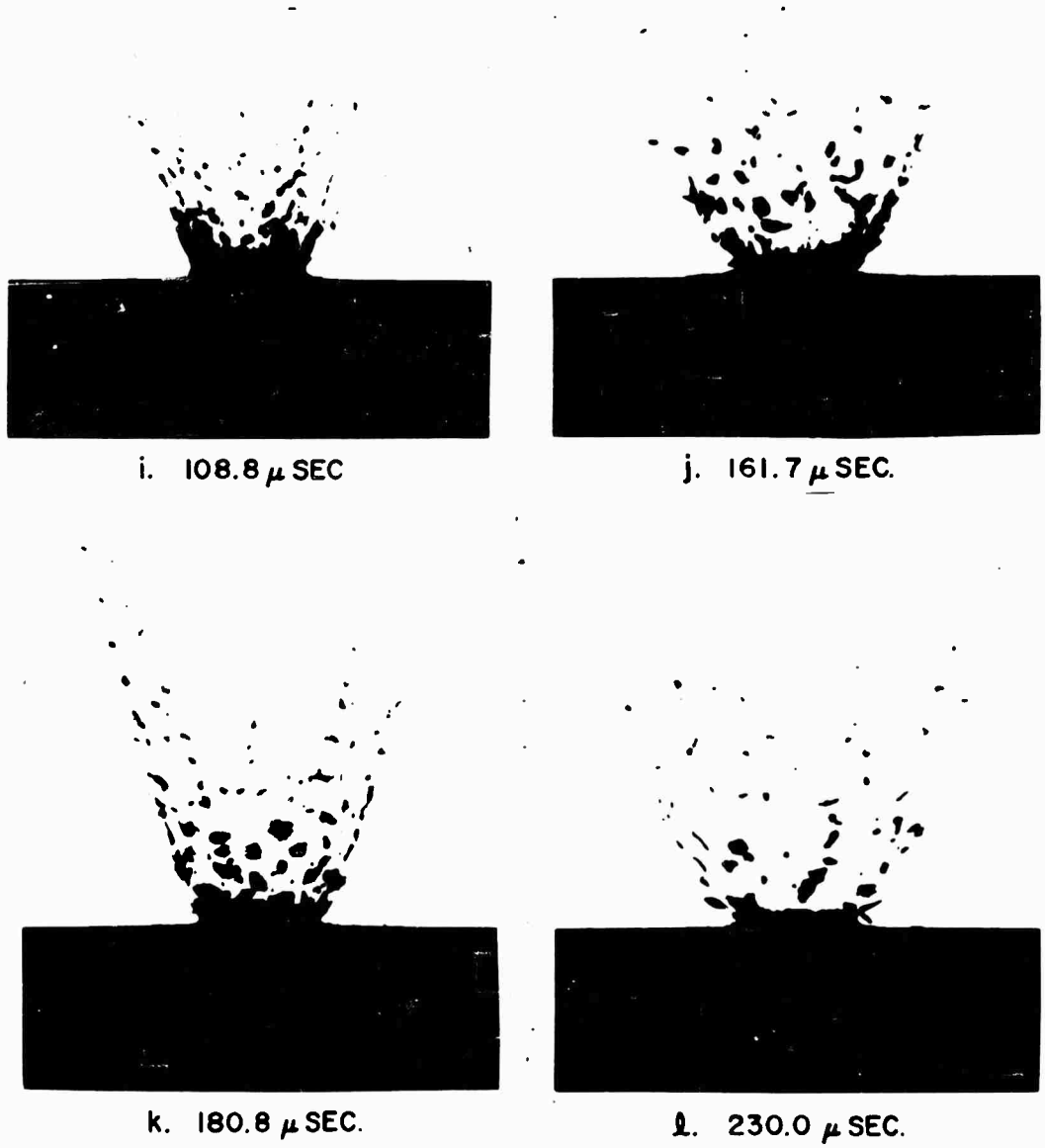

Figure 6 continued. Surface Phenomena Associated with Crater Formation in a Lead Target.

Pellet Material -- Steel - 1095

Pellet Mass -- 0.18 grams

Pellet Velocity -- 5.01 km/sec

m. 347.2 μSEC.

n. 413.6 μSEC.

Figure 6 continued. Surface Phenomena Associated with Crater Formation in a Lead Target

m. 347.2 μSEC.

n. 413.6 μSEC.

Figure 6 continued. Surface Phenomena Associated with Crater Formation in a Lead Target

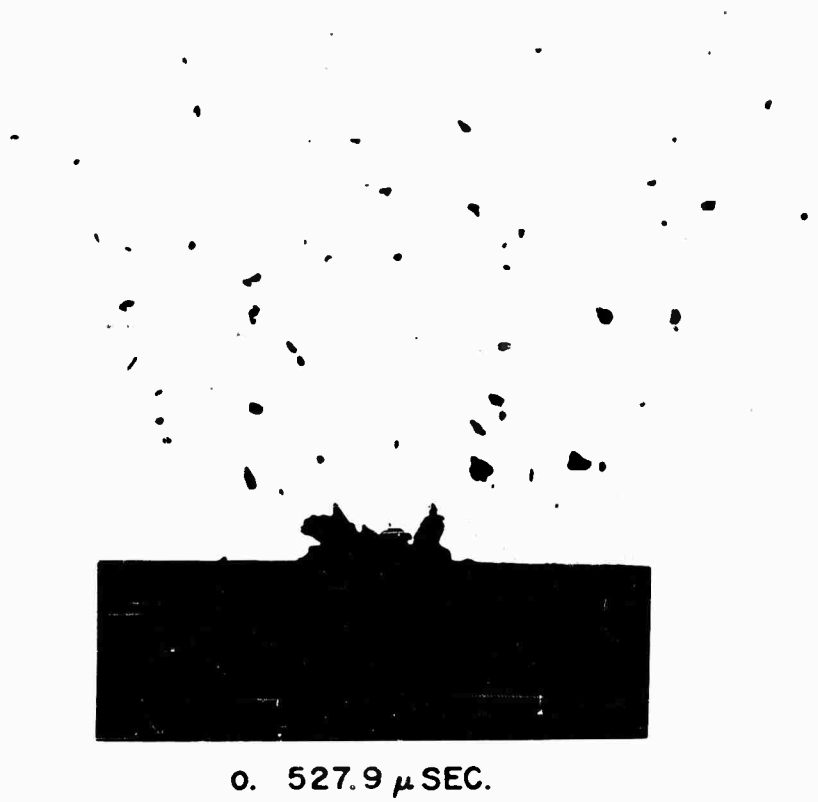

Figure 6 continued. Surface Phenomena Associated with Crater Formation in a Lead Target.

Pellet Material -- Steel - 1095

Pellet Mass -- 0.18 grams

Pellet Velocity -- 5.01 km/sec

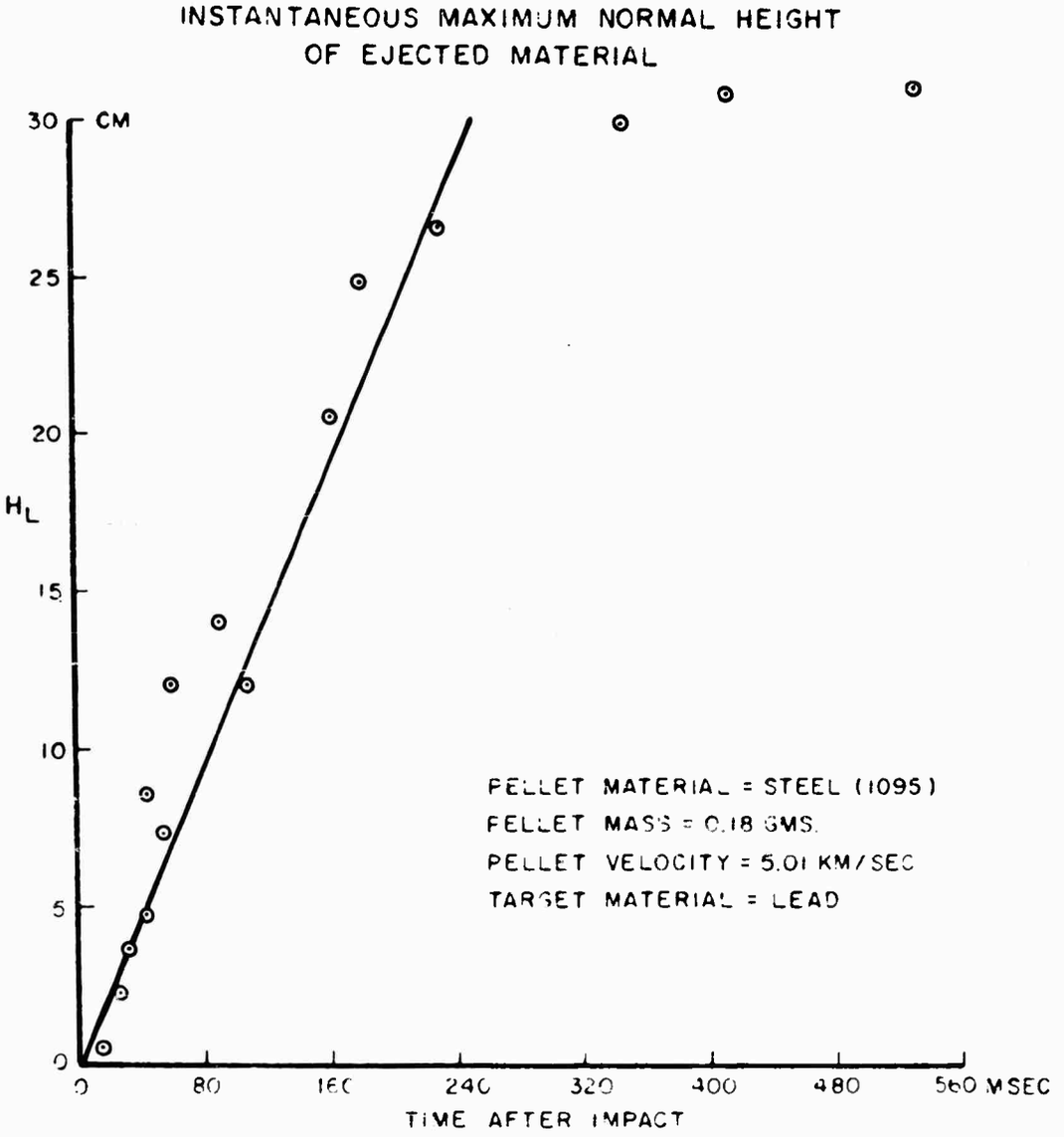

Figure 7. Maximum Normal Height of Material Ejected from Craters in Lead Targets.

momentum in the direction from which the pellet impacted associated with this ejecta is many times greater than the initial momentum, in the opposite direction, of the impacting projectile, so that the total forward momentum that must somehow be absorbed by the target material is also many times greater than that of the projectile.

The pieces of material ejected from the crater lip are not uniform in size. There is a definite trend toward larger pieces later in the process. These later pieces are ejected at continually lower velocities. The maximum normal height

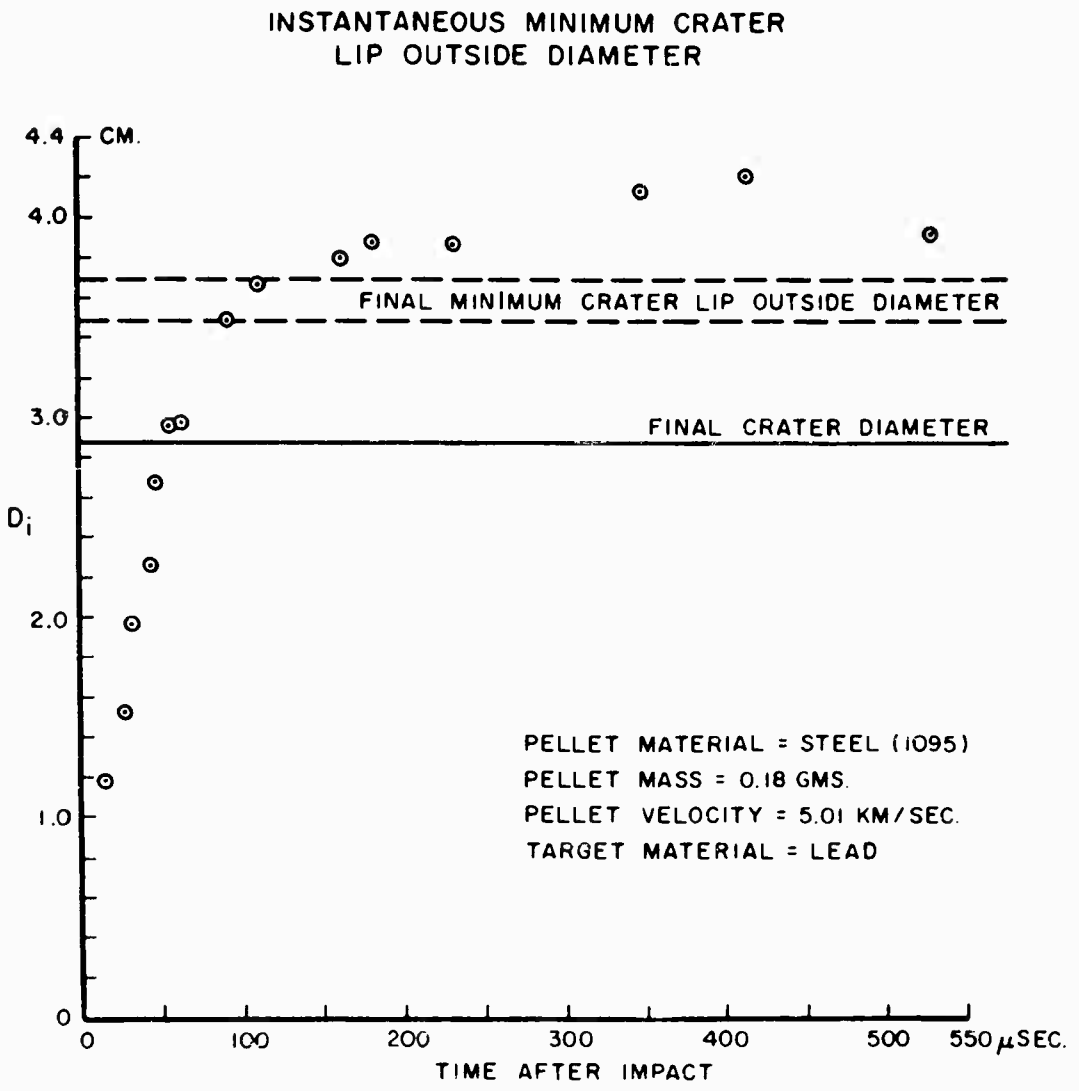

Figure 8. Minimum Outside Diameter of the Crater Lip in Lead Targets.

of ejected material is plotted as a function of time in Figure 7. The points at the latest times may be unrepresentatively low, because ejecta may have passed out of the field of the x-ray film. The data indicate a maximum velocity of 1 km/sec for the ejected material. Since measurements have not been made of the ejection velocity as a function of ejecta size, it is not possible to calculate the total momentum in the backward direction. It can be stated, however, from measurements of the mass of the target before and after impact, that fully one-half of the

displaced crater volume is ejected under these impact conditions, which yields a total ejected mass of about 35 grams, compared to the incident mass of 0.18 grams.

Since lead is quite opaque to x-rays it is not possible to obtain an actual time history of the crater depth and diameter, measured at the level of the impacted surface. However, it is possible to obtain an appreciation for the growth of the crater diameter. In Figure 8 the minimum outside diameter of the crater lip has been plotted as a function of time. This increases very rapidly for the first 100 microseconds, then rises more slowly, apparently reaching a peak about 400 microseconds after impact. Subsequently there is a decline in the crater lip diameter. The initial phase of the crater growth does not correspond to the duration of the transient and steady-state regimes in the model, these having been calculated to be about one microsecond for the projectile used in this series of observations. Rather, these observations fall in the cavitation regime, where the material is flowing without impetus from the impacting projectile, and where the resistance to flow is supplied principally by the dynamic shear strength. Gradually, as the energy density decreases in the vicinity of the crater, the shear strength becomes more effective and the rate of crater growth is slowed considerably. Finally, it is reversed, due to plastic and elastic recovery, eventually reaching its final value, shown as the region between the dashed lines on the graph. For comparison, the final value of the inside crater diameter is plotted as a solid line on the same graph.

b. Rate of Crater Formation in Aluminum and Lucite

The rates of crater growth in 1100-0 aluminum and in Lucite are shown in Figures 9-11. The measurements of crater size in aluminum were made from flash radiographs, while those in the Lucite were made from a streak camera record. In both cases the projectile was a 0.18 gram steel disc; the impact velocity into aluminum was 5.01 km/sec, while into Lucite it was 4.6 km/sec. Thus the impact conditions were almost identical with those in the crater rate study in lead described in Section II a. The final crater in Lucite, while difficult to measure because of local fracture around the crater, was 15 mm deep; thus the crater formation process in Lucite is essentially complete in about 10 microseconds. In aluminum, the duration of the crater formation process is about 60 microseconds, while the transient and steady-state phase should encompass about 0.5 microseconds for the impact in aluminum and 0.7 microseconds for the impact in Lucite, because of the differing densities of aluminum and Lucite. Thus, in Lucite the cavitation regime lasts about fifteen times longer than the transient and steady-state regimes, while in aluminum it lasts about 120 times longer than the transient and steady-state regimes. This difference is probably due to the difference in behavior of brittle and ductile materials at high rates of strain. The more ductile aluminum exhibits a reduced resistance to deformation at extreme rates; on the other hand, the less ductile Lucite exhibits an increased strength, over its static strength, at high strain rates. (See Section III.)

c. Rate of Crater Formation in Wax

Crater formation has been observed in nine-inch thick blocks of wax, transparent to 600 kilovolt x-rays. A sequence of these craters at the indicated times is shown in Figure 12a-12k. Gross differences in exposure, due to the large thickness of the target, made it necessary to use shielding in front of that part of the film which was directly exposed to the x-ray beam. This effectively cut down

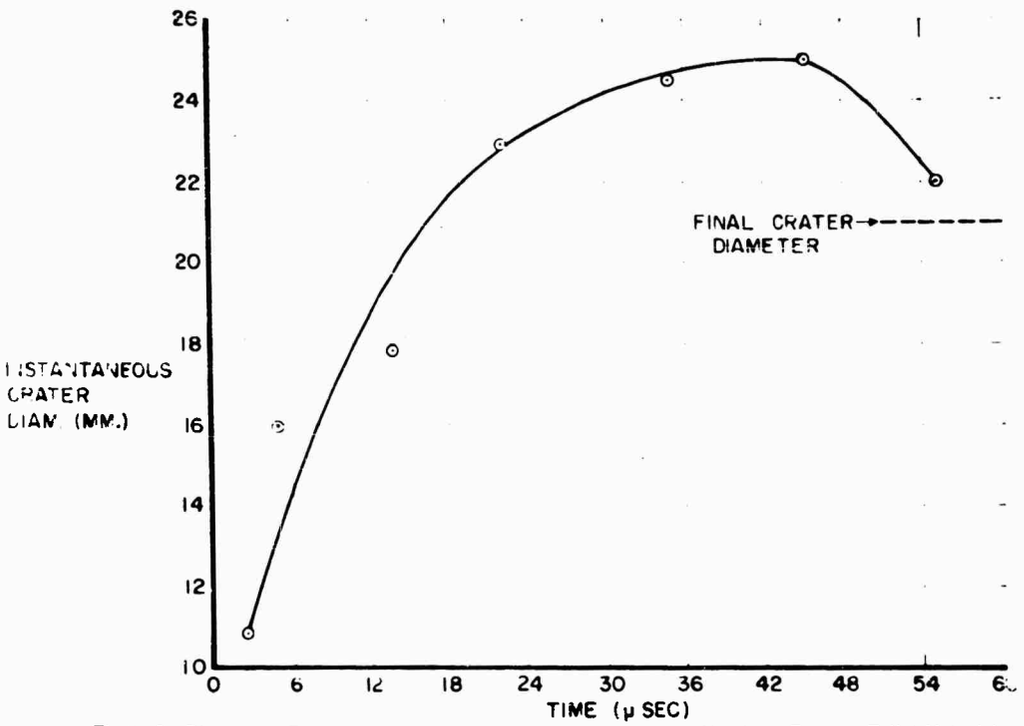

Figure 9. Diameter - Time History for a Crater Formed in an 1100-0 Aluminum Target. Pellet Material -- Steel 1095. Pellet Mass -- 0.18 grams. Pellet Velocity -- 5.01 km/sec.

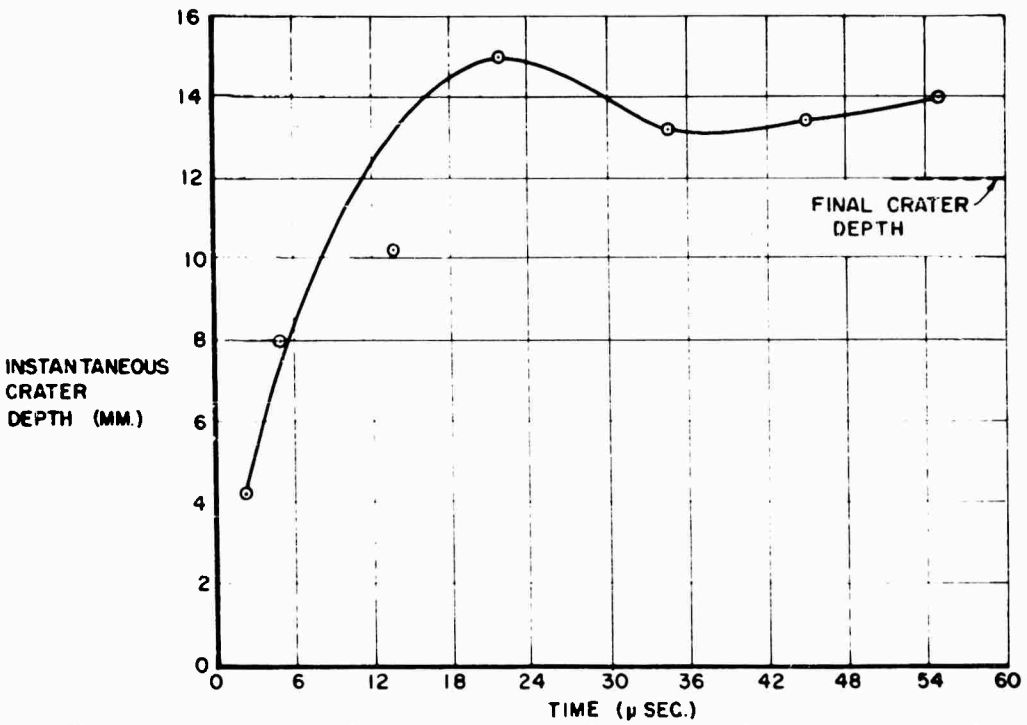

Figure 10. Penetration - Time History for a Crater Formed in an 1100-0 Aluminum Tartet. Pellet Material -- Steel 1095. Pellet Mass -- 0.18 grams. Pellet Velocity -- 5.01 km/sec.

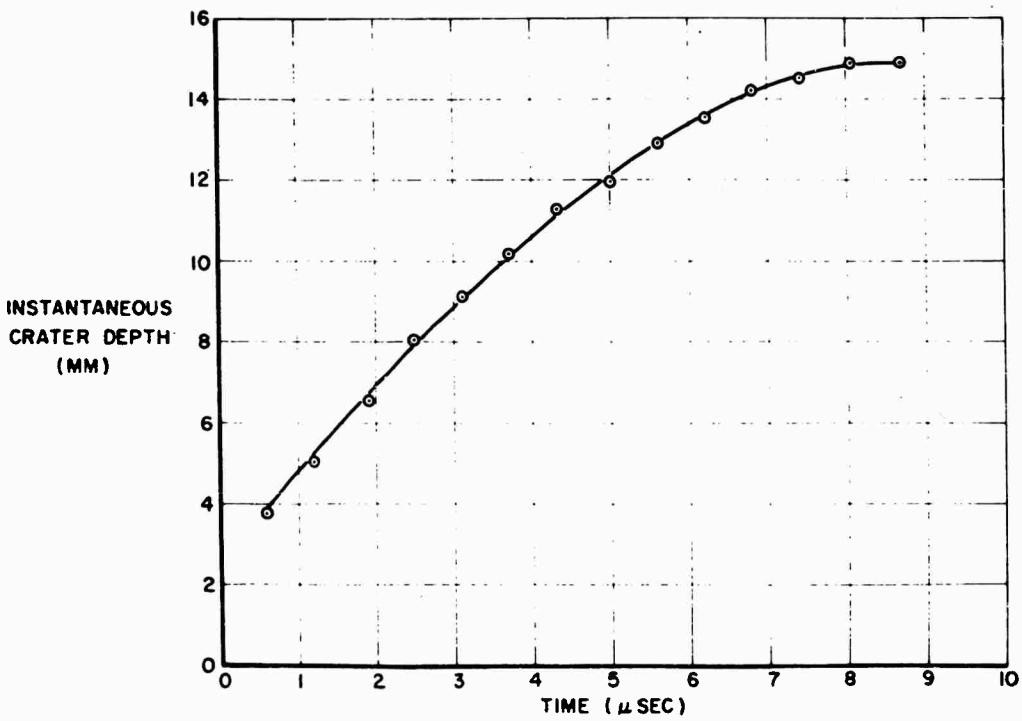

Figure 11. Penetration - Time History for a Crater Formed in a Lucite Target. Pellet Material -- Steel - 1095. Pellet Mass -- 0.18 grams. Pellet Velocity -- 4.6 km/sec.

the scattered radiation which otherwise would have obscured the image of the crater, but at the same time produced a loss of detail in the crater lip. The instantaneous crater diameter and crater depth, however, are clearly evident. It should be mentioned that this sequence is not at exactly the same magnification.

The first phase of the investigation with wax targets involved observation of craters produced by small explosive charges. The craters shown in Figure 12 were made by one-half inch diameter by one-half inch long tetryl pellets, detonated while in contact with the surface of the target. Subsequently, crater formation by other size explosive charges and various hypervelocity pellets will be studied.

The instantaneous crater diameter and crater depth are plotted in Figures 13 and 14 as functions of time after impact of the detonation front on the target surface. The crater diameter increases very rapidly in the first 100 microseconds, in the same manner as the minimum crater lip diameter does in the lead target; then, a further, much more slow, increase in diameter ensues, with rebound to the final value of the diameter commencing about 1000 microseconds after the crater started to form. The rebound in diameter observed is about ten per cent of the final diameter. The rebound is crater depth is much more pronounced. After the initial rapid rate of growth is completed the crater is forty per cent deeper than its final depth. During the following 900 microseconds the crater depth decays exponentially, and is still ten per cent greater than its final value when the last observation was made. The ratio of crater depth to crater diameter, or crater profile, plotted in Figure 15, reaches its final value about 400 microseconds after the process started. The final crater is not a hemisphere, as would be expected in the case of pellet impact; rather, it is somewhat shallower, because an explosive charge instead of a hypervelocity pellet was used. Not only is the intrinsic mechanism by which craters are formed by explosive charges different, because the energy is not all delivered in a direction normal to the surface of the target, but also the energy applied per unit area of the target surface is less than 5 per cent of that when a steel pellet impacts at 5 km/sec.

III. Shock Propagation and Attenuation

Details of shock propagation, and its attenuation, associated with the impact of a hypervelocity pellet are best illustrated by using transparent targets and optical photography. Figure 16 shows a selected frame in a sequence taken with a 1.2 million frame per second framing camera. The target is Lucite; the impact was produced by a 0.18 gram steel pellet, striking at 4.6 km/sec. Eleven microseconds after impact the shock envelope and the free surface of the crater behind it can be seen. For quantitative purposes, a streak camera provides better data than a framing camera. A rotating mirror camera picture of an impact similar to that in Figure 16 is shown in Figure 17, which constitutes a time-distance plot of events occurring in a plane that contains the trajectory of the impacting pellet. It shows: (1) the pellet before striking the target, (2) the shock wave in the target, (3) the surface of the expanding crater, and (4) the envelope of cracks propagating through the target. The propagation of fracture in the target prevented observation of the crater after it had attained its final depth. Representative data are shown in Figure 18. The intensity of the shock wave in Lucite is plotted as a function of distance from point of impact. The initial pressure is determined by the shock properties of the pellet and target materials

a. 10 μ SEC.

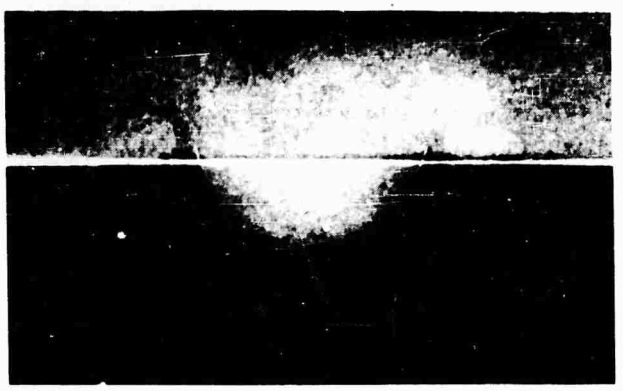

b. 20 μ SEC.

c. 40 μ SEC.

Figure 12. Time-sequence of a Crater Forming in a Wax Target After the Detonation of a Small Explosive Charge on the Surface.

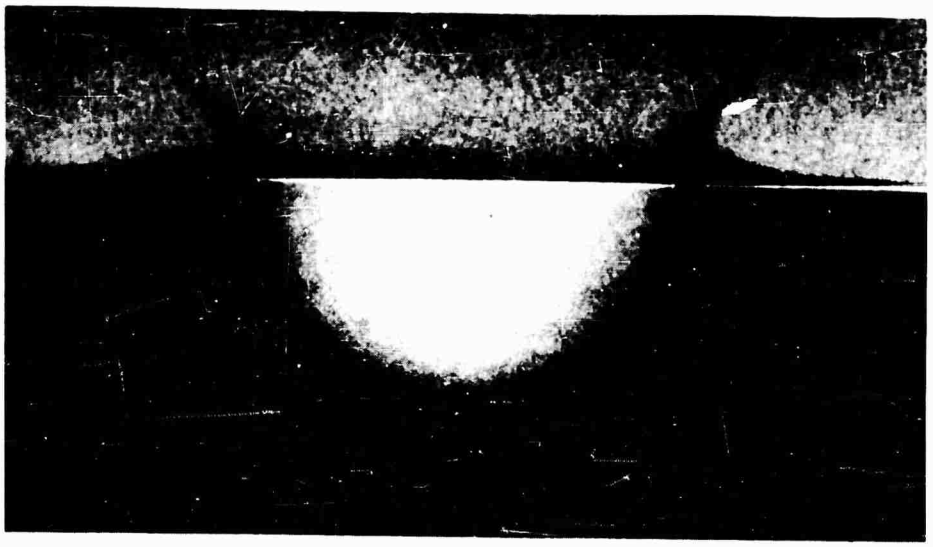

d. 80 μ SEC.

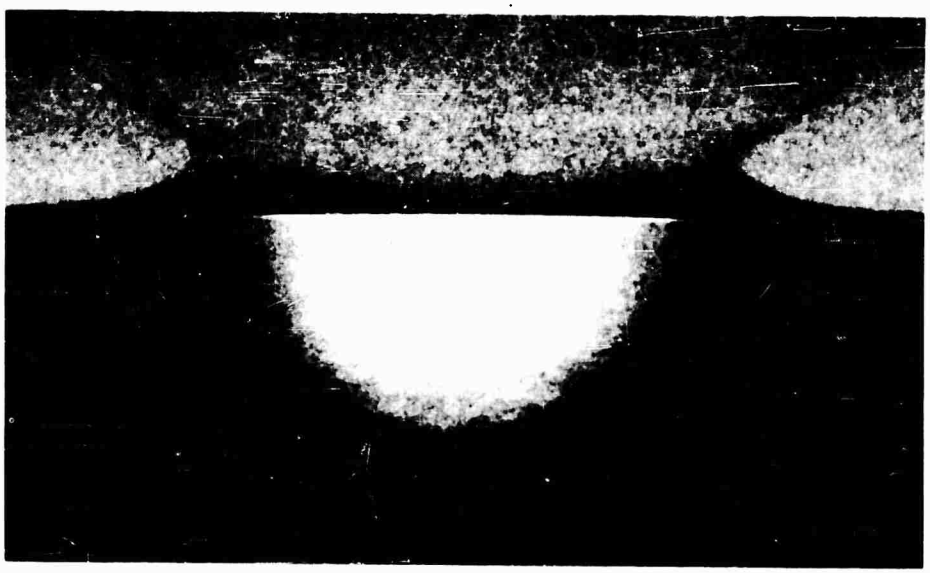

e. 120 μ SEC.

Figure 12 continued. Time-sequence of a Crater Forming in a Wax Target After the Detonation of a Small Explosive Charge on the Surface.

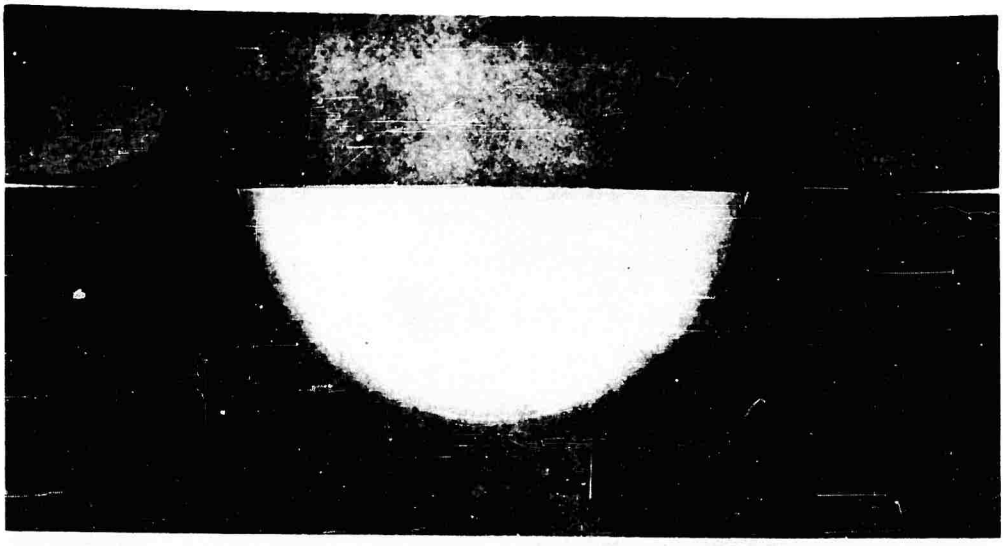

f. 240 μ SEC.

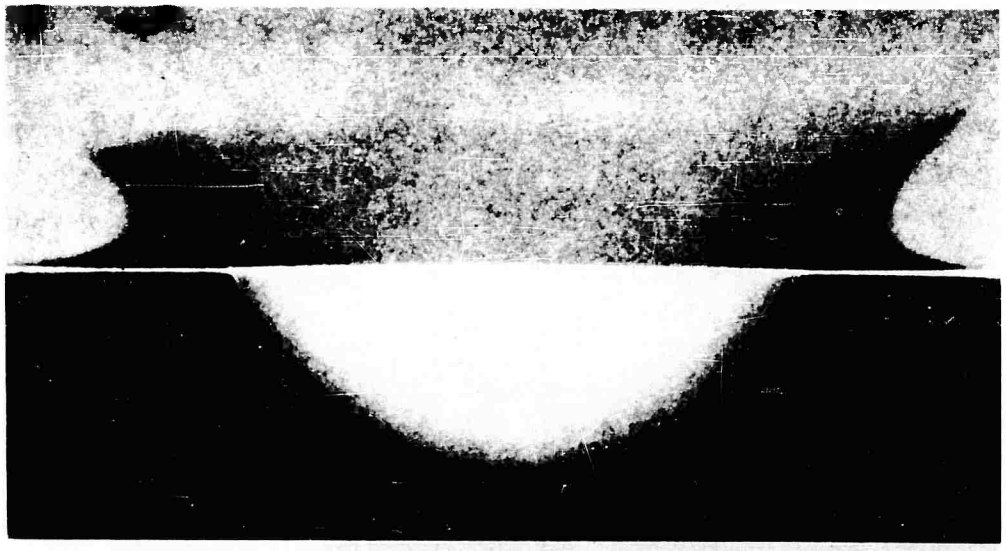

g. 440 μ SEC.

Figure 12 continued. Time-sequence of a Crater Forming in a Wax Target After the Detonation of a Small Explosive Charge on the Surface.

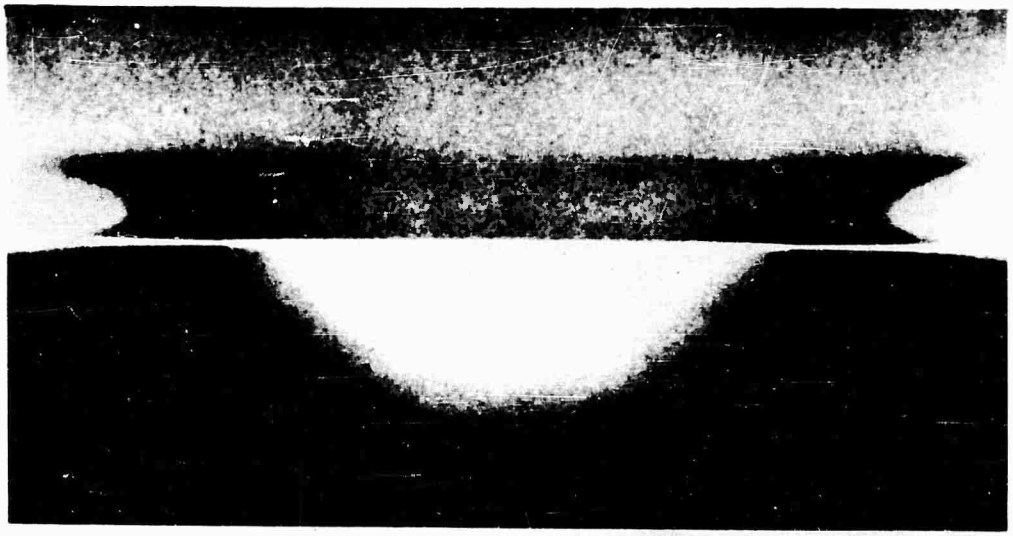

h. 640 μ SEC.

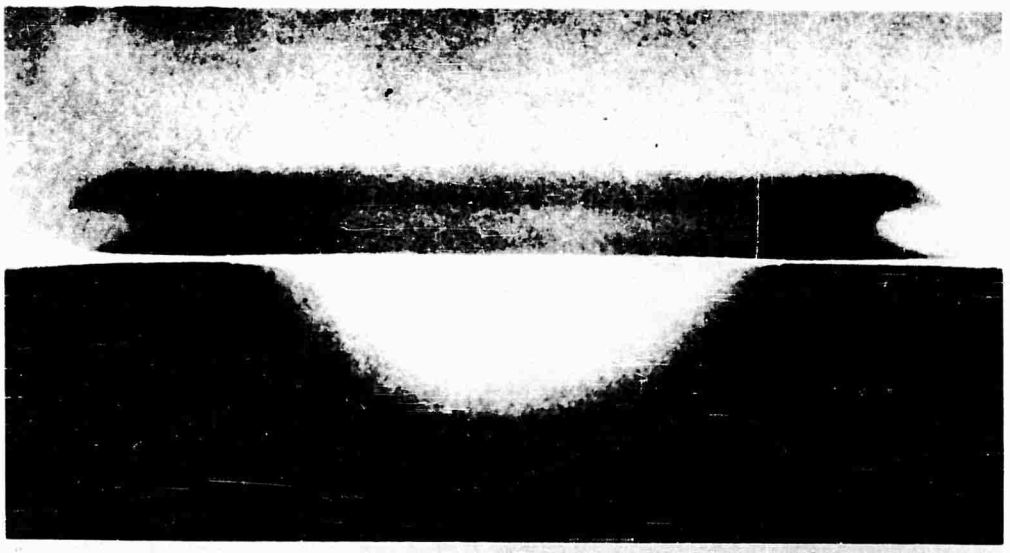

i. 840 μ SEC.

Figure 12 continued. Time-sequence of a Crater Forming in a Wax Target After the Detonation of a Small Explosive Charge on the Surface.

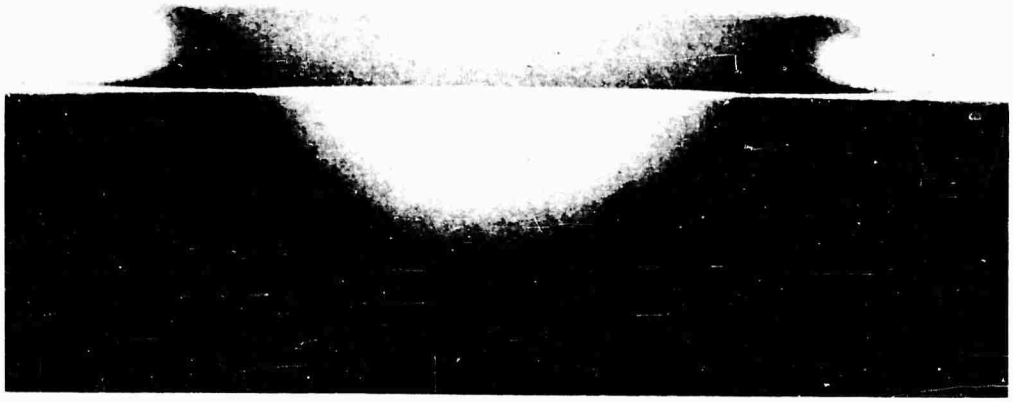

j. 1000 μ SEC.

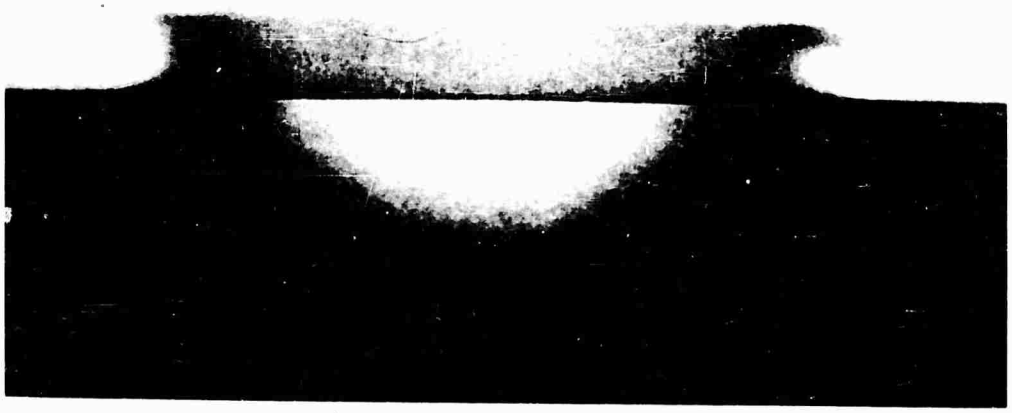

k. FINAL CRATER

Figure 12 continued. Time-sequence of a Crater Forming in a Wax Target After the Detonation of a Small Explosive Charge on the Surface.

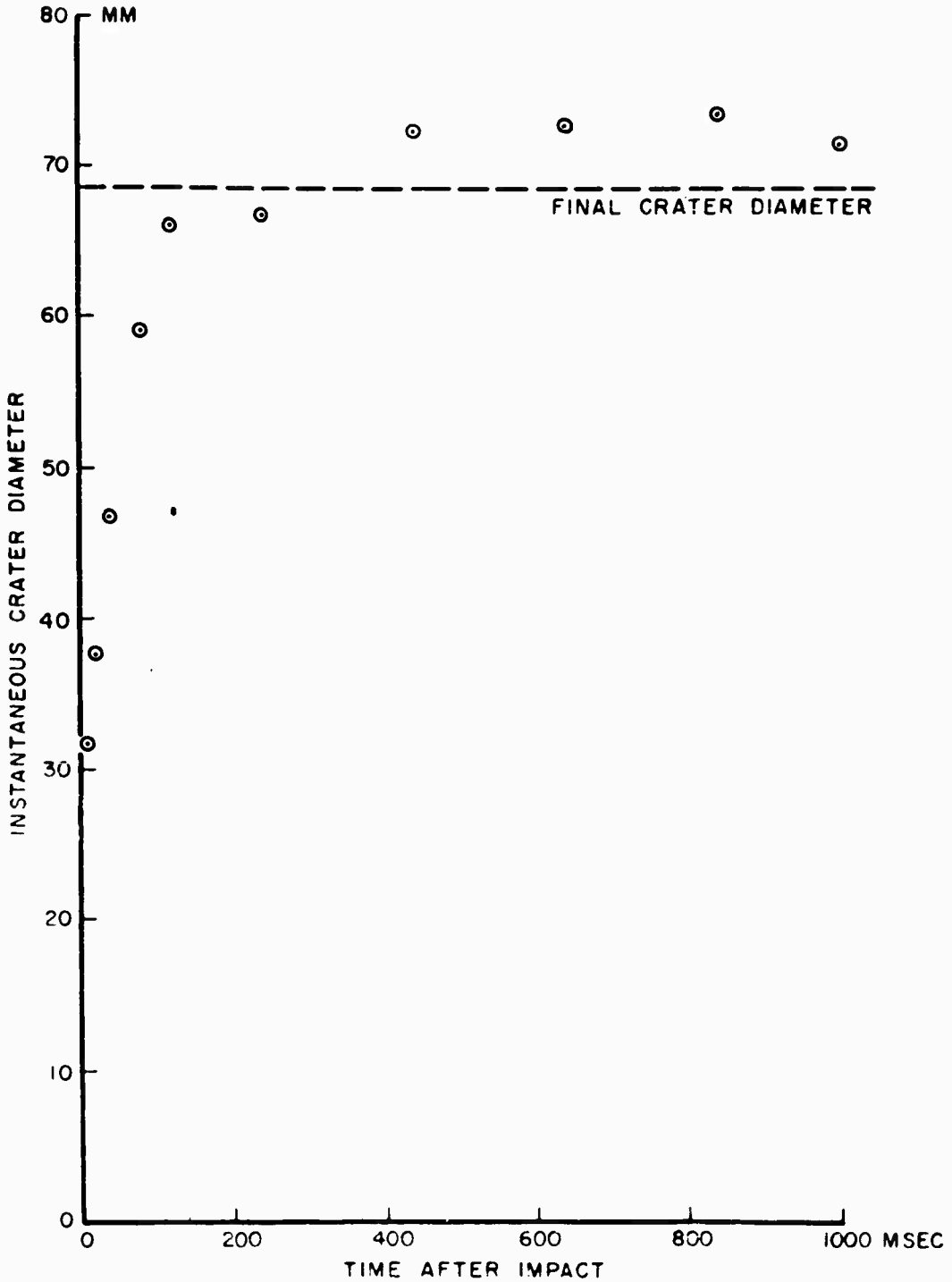

Figure 13. Diameter - Time History of a Crater Formed in a Wax Target by the Surface Detonation of a Small Explosive Charge.

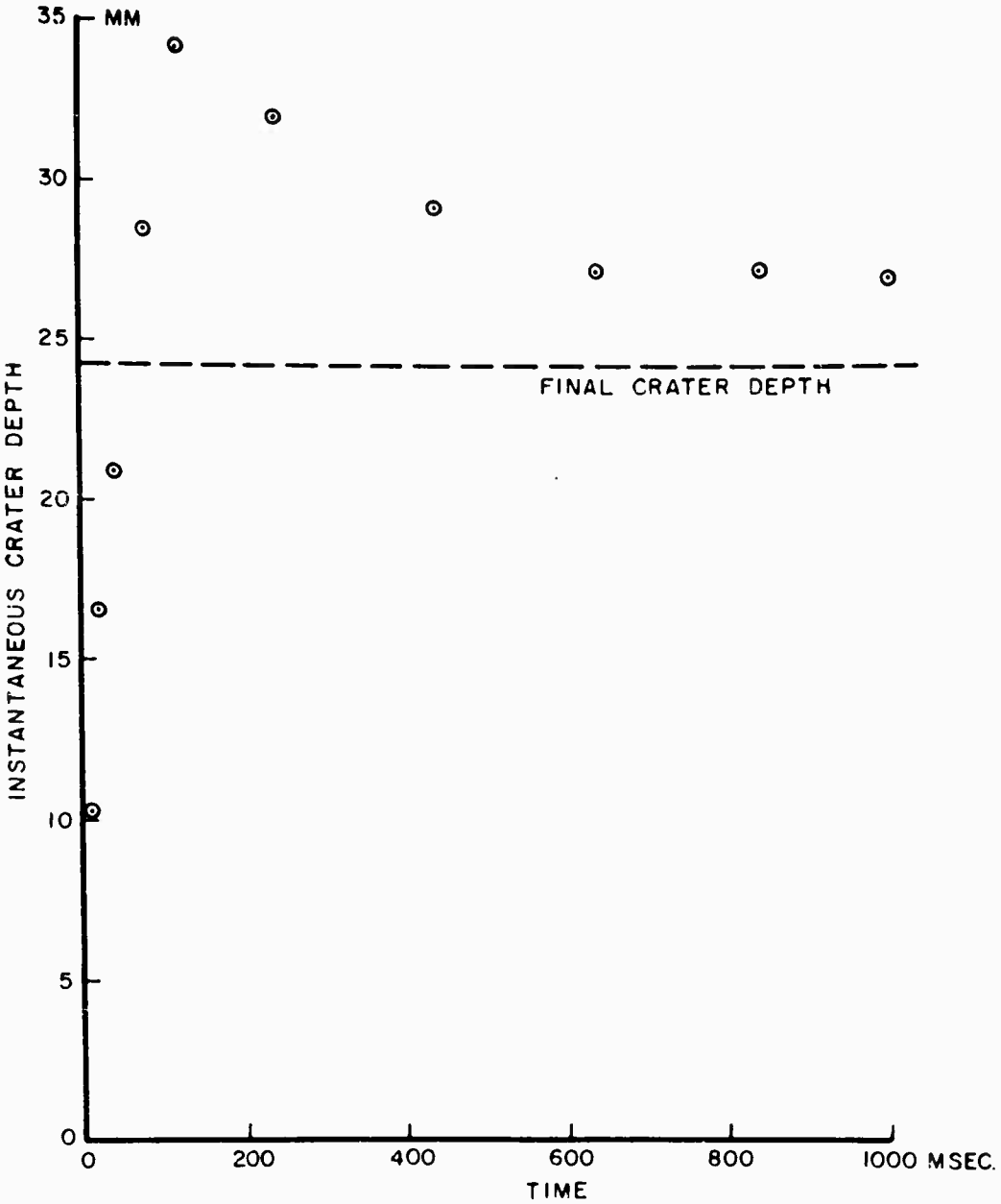

Figure 14. Penetration - Time History of a Crater Formed in a Wax Target by the Surface Detonation of a Small Explosive Charge.

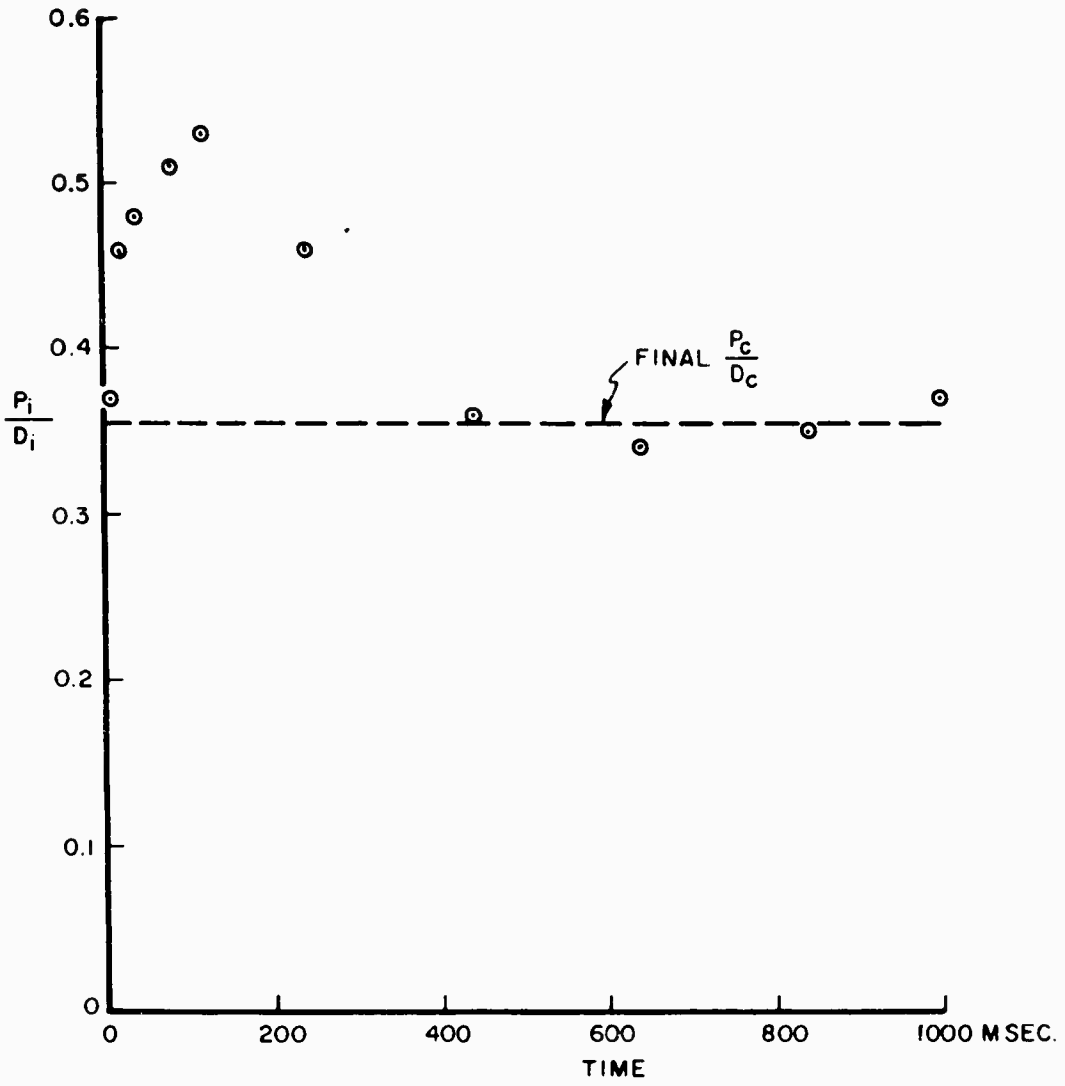

Figure 15. Variation of Shape with Time for a Crater Formed in a Wax Target by the Surface Detonation of a Small Explosive Charge.

Figure 16. Hypervelocity Impact in Lucite Eleven Microseconds After the Impact of a 0.18 gram Steel Pellet at 5.91 km/sec.

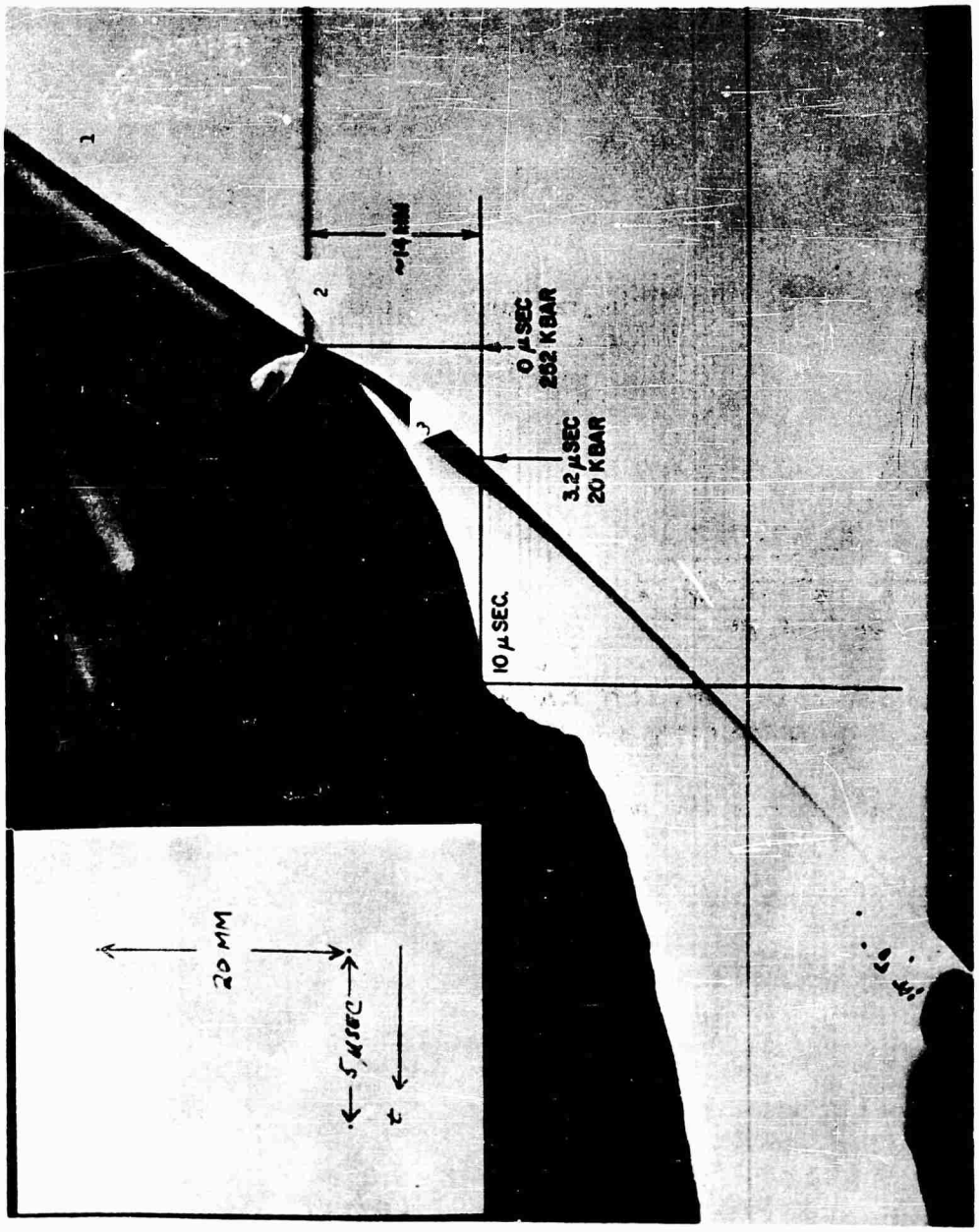

Figure 17. Streak Camera Record of Impact in Lucite Target. 1. Steel Pellet before Striking Target at 4.6 km/sec. 2. Shock Wave in the Target. 3. Surface of the Expanding Crater. 4. Envelope of Cracks Propagating Through the Target.

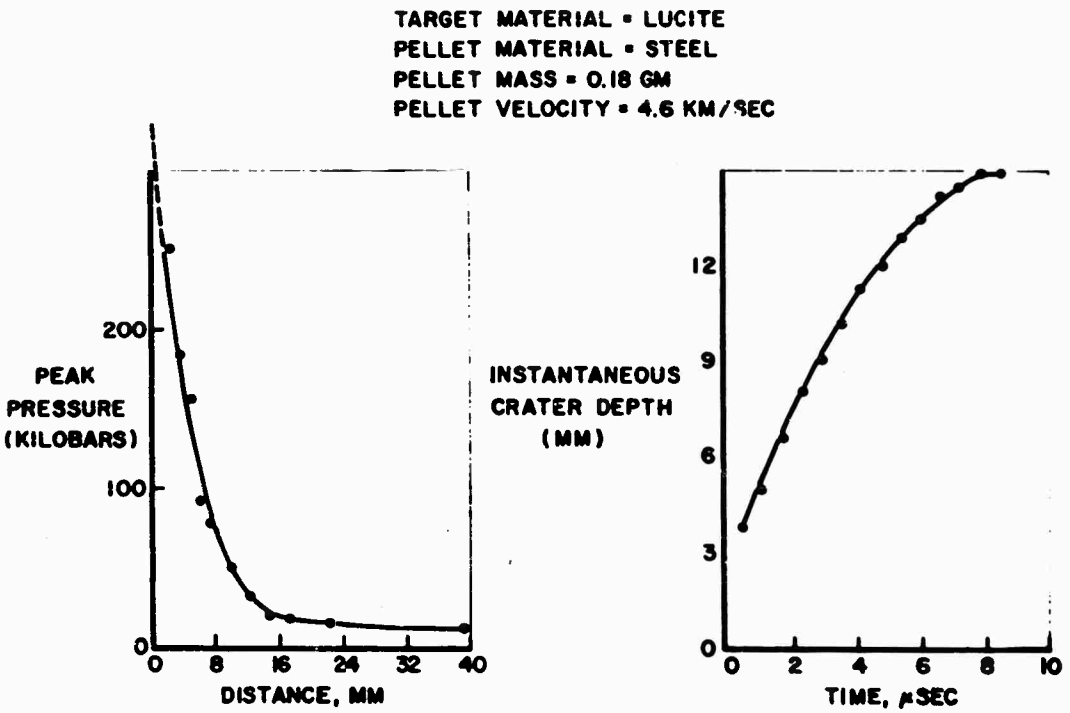

Figure 18. Shock Intensity and Rate of Crater Expansion in a Lucite Target

and the impact velocities; it corresponds to the theoretical prediction for a plane impact. The initial pressure falls off very rapidly, as the wave propagates into the material, even during the period in which the crater expands so rapidly that the shock wave cannot detach. This is consistent with the concept that, as soon as the deformation of the projectile and target begins, the pressure at the contact surface will fall to the Bernoulli value (for compressible materials). The magnitude of the pressures should be particularly noted, together with the fact that the pressure, for a given pair of materials, will increase with the square of the impact velocity. It can be seen that the original pressure on the target was nearly 300 kilobars; and, at the distance of 15 mm in the target, the pressure had fallen to approximately 20 kilobars, or approximately 300,000 psi. Note that the crater ceased to enlarge beyond 15 mm in depth, and that the Lucite was able to withstand flow under a compressive force of this magnitude, while the static tensile strength is of the order of 4,000-6,000 psi. This supports the conclusion that the dynamic strength of the more brittle materials, such as Lucite, increases with increasing strain rate.

CONCLUSIONS

The experimental observations all tend to support the model discussed in the Introduction.

1. The crater size observations at various impact velocities in a number of target materials, and the crater size observations in the two aluminum alloys at various temperatures indicate that the strength of the target material is the predominant factor in determining the final crater size in targets of ductile materials.

2. The investigation of shock propagation gives evidence that the dynamic strengths of materials under hypervelocity impact substantially exceed those under static loading conditions, in targets of brittle materials.

3. The observations of crater growth show that craters are formed in periods of time long compared with those for the completion of the transient and steady-state regimes. They also substantiate the existence of a rebound in the crater dimensions in the latest stages of its development.

ACKNOWLEDGMENTS

The author acknowledges the efforts of Mr. Richard Watson, Mr. Karl R. Becker, and Mr. Richard Vitali, all of the Carnegie Institute of Technology, in producing the data on temperature effects. He also thanks Mr. Vincent M. Boyle for making available his data on shock propagation, Mr. Boyd C. Taylor for his efforts in performing the observations in wax, and Mr. Lee S. Holloway for producing the series of observations in lead.

BIBLIOGRAPHY

1. Fourth Hypervelocity Impact Symposium, Eglin AFB, April 1960.
   a. J. Wm. Gehring, Jr., -- Observations of the phenomena of Hypervelocity Impact.
   b. H. G. Hopkins and H. Kolsky -- Mechanics of Hypervelocity Impact of Solids.
   c. John H. Kineke, Jr., -- An Experimental Study of Crater Formation in Metallic Targets.
   d. F. E. Allison, K. R. Becker, and R. Vitali -- Effects of Target Temperature on Hypervelocity Cratering.

2. R. J. Eichelberger and J. W. Gehring, -- Effects of Meteoroid Impacts on Space Vehicles. American Rocket Society Space Flight Report to the Nation, October 9-15, 1961.

3. R. J. Eichelberger, Experimental Test of the Theory of Penetration by Metallic Jets, Journal of Applied Physics, Vol. 27, No. 1, January 1956.

4. Ernst Öpik -- Researches on the Physical Theory of Meteor Phenomena. Acta Comment. Univ. Tartuensis, Tome XXVIII, No. 6, 1936. Also: Irish Astronomical Journal, Vol. 5, No. 1, March 1958.

5. Third Hypervelocity Impact Symposium, Armour Research Foundation, October 1958.
   a. R. L. Bjork -- Numerical Solution of the Axially Symmetric Hypervelocity Impact Process Involving Iron.
   b. J. W. Gehring, Jr., -- An Analysis of Microparticle Cratering in a Variety of Target Materials.
   c. John H. Kineke, Jr., -- An Experimental Study of Crater Formation in Lead.

HYPERVELOCITY IMPACT STUDIES IN WAX

J. T. Frasier

Brown University
Providence, Rhode Island

B. G. Karpov

Ballistics Research Laboratories
Aberdeen Proving Ground, Maryland

INTRODUCTION

The purpose of this paper is to present the techniques and results of an experimental program being conducted in the Exterior Ballistics Laboratory at Aberdeen Proving Ground for the investigation of hypervelocity impact. The intent of this program is to contribute to what are felt to be two basic needs for as complete an understanding as possible of the impact cratering process. The first of these needs is for quantitative experimental information defining the stress levels, deformation rates, and behavior of solids under the severe conditions of loading associated with the cratering mechanism. This information is necessary in the formulation of rational theoretical analyses describing the damage process. The second need is for means through which the validity of any particular theory can be evaluated. At present, little other than observation of the final geometry of an impact crater is possible. It would be desirable to have methods available through which more detailed evaluations of the predictions of theoretical analyses could be accomplished.

To fulfill the intent of the E. B. L. program, its major emphasis has been toward the development and use of experimental techniques capable of providing significant data concerning the transient response of targets to macro-particle impacts and the condition of targets subsequent to completion of the cratering process. To date, all experimentation has made use of wax targets. This material was selected because of several attractive features it possesses for investigations of the type desired. The most important of these is that it provides a means whereby target blocks can be internally instrumented with relative ease for the purpose of gathering transient data. Also, it has a relatively low dilatational wave velocity (approximately 1.85 km/sec) and, as a result, allows investigations of a fairly broad range of impact conditions as determined by the ratio (V/C) of impact velocity to dilatational wave velocity. These characteristics coupled with the fact that the conventional mechanical properties and impact behavior of wax are essentially those of a soft, ductile metal, makes it well suited for the purposes at hand. The specific material in use is Petroflex Plastic Wax*

*Manufactured by Petroflex Corp., now Beeline Refining Co., Salt Lake City, Utah.

(ρ = 0.91 gm/cm^3). This is a petrolatum and paraffin mixture which is crystalline in structure. Its impact craters are visually similar to those in metallic targets having well formed lips and minimal spalling, see Figure 1. It may be

Figure 1

cast into homogeneous blocks free of entrained gas pockets and other inclusions with little difficulty.

At present, significant information regarding the impact response of wax targets has been obtained from several types of tests. These are:

1) standard crater damage tests,
2) tests in which data have been collected for determining the velocity of propagation and pressures of the disturbance generated in target blocks by pellet impacts,
3) tests which provide data concerning the final deformation state and den ity distribution in damaged targets,
4) and investigation of the amount and condition of the material detached from the target blocks as a result of impact.

In the following presentation the techniques, results, and consequences of the above mentioned tests will be given. In all cases, the experiments were conducted

by firing 0.30 cal plastic (ethocel, ρ = 1.2 gm/cm^3) projectiles initially weighing approximately one-half gram into nine inch cube target blocks. An N. R. L. type light-gas gun was used as projectile launcher in conjunction with an evacuated range facility[1].

CRATERING EXPERIMENTS

Conventional cratering experiments were conducted on the wax target material for the purpose of obtaining a general knowledge of its impact behavior and to determine whether this behavior is similar to that exhibited by metals. These results have been reported elsewhere [2] and will only be summarized here to provide a brief demonstration of the cratering characteristics of the material. The data gathered in the course of the tests were the initial mass and impact velocity of the projectiles, and the depth, diameter, and volume of the craters formed in the target blocks. Crater dimensions were referenced to the undistrubed face of the blocks by removing the crater lips prior to making measurements. The range of impact velocities covered was 0.46 to 5.28 km/sec (V/C from 0.25 to 2.88).

Figures 2, 3, 4, and 5 present the data on cratering. As can be seen by comparing these results with similar data for metallic targets, the behavior demonstrated by these curves is qualitatively that of most metals. In particular, this is true for such materials as copper, zinc, cadmium, and lead for which data is available for a comparable range of the parameter V/C. (See, for instance, References 3, 4, and 5.) In the case of lead, considerable data are available for comparison and it is worthy of note that both this metal and wax demonstrate the dip in the normalized crater depth versus impact velocity curve in evidence in Figure 2. Also, the linear dependence of crater area on impact momentum shown in Figure 5 is common to both. Furthermore, wax, as lead, possesses a non-linear relation between crater volume and kinetic energy of impact projectile, Figure 3.

The general conclusion provided by the wax cratering data is that, where comparison is possible, this material's impact behavior is in no way qualitatively dissimilar to that of metals. The consequence of this similarity of behavior is that it implies more detailed observation of the response of wax to the impact process can yield pertinent information on the mechanics of impact damage in materials of more practical interest. On this basis, study of the transient response and the condition subsequent to crater formation of wax targets has been pursued.

THE TRANSIENT RESPONSE OF WAX TARGETS TO IMPACT

To obtain information concerning the transient behavior of targets under impact conditions, a technique has been developed which is capable of providing data concerning the propagation and particle velocities at the front of the disturbance generated in targets by an impacting pellet. The basis of this technique is the e. m. f. generated in a wire moving in a magnetic field. This is made use of by imbedding fine wires (0.003 in. Cu) at selected positions within the targets, placing the blocks in a strong magnetic field, and monitoring on oscilloscopes

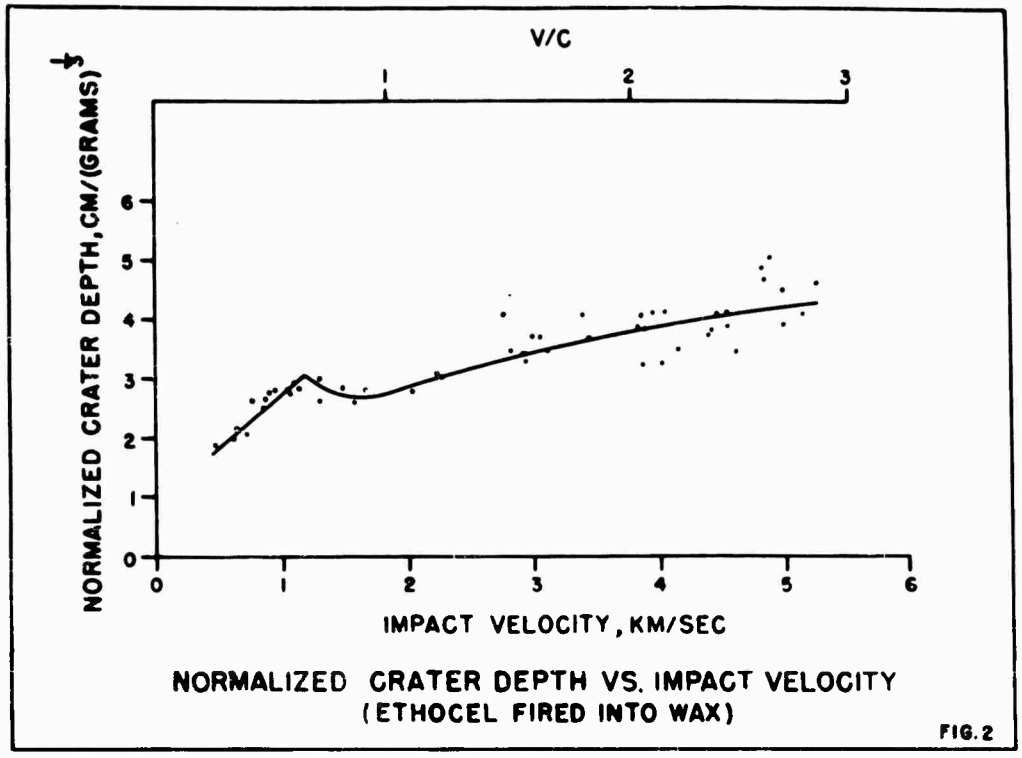

NORMALIZED CRATER DEPTH VS. IMPACT VELOCITY
(ETHOCEL FIRED INTO WAX)

FIG. 2

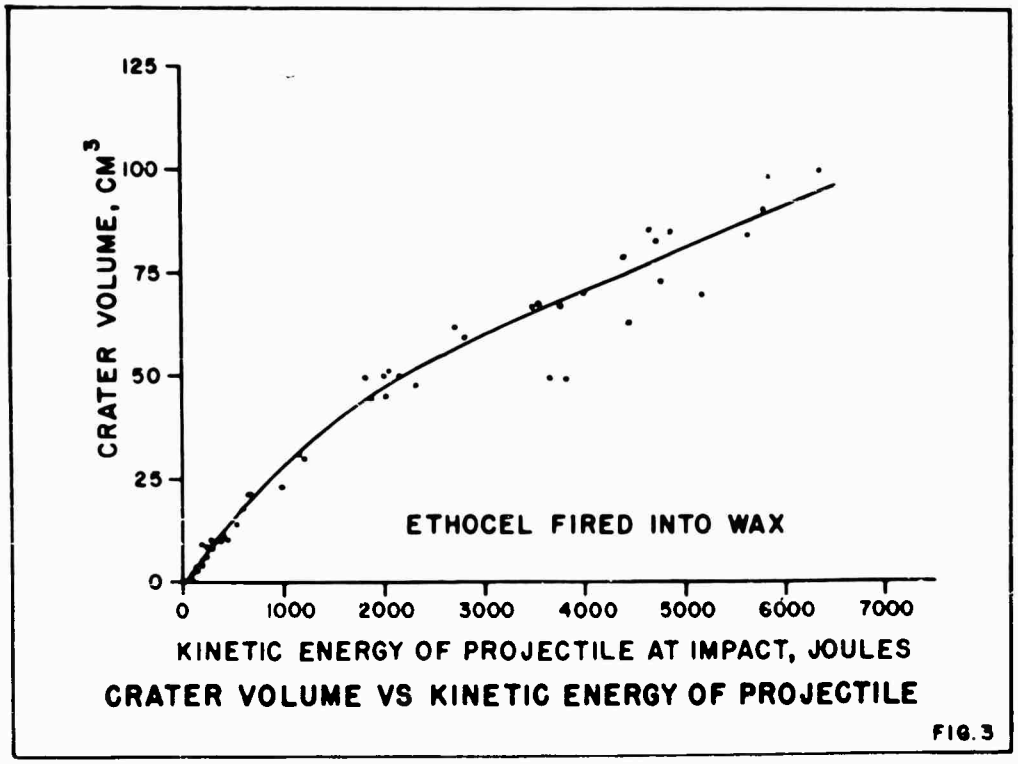

CRATER VOLUME VS KINETIC ENERGY OF PROJECTILE

FIG. 3

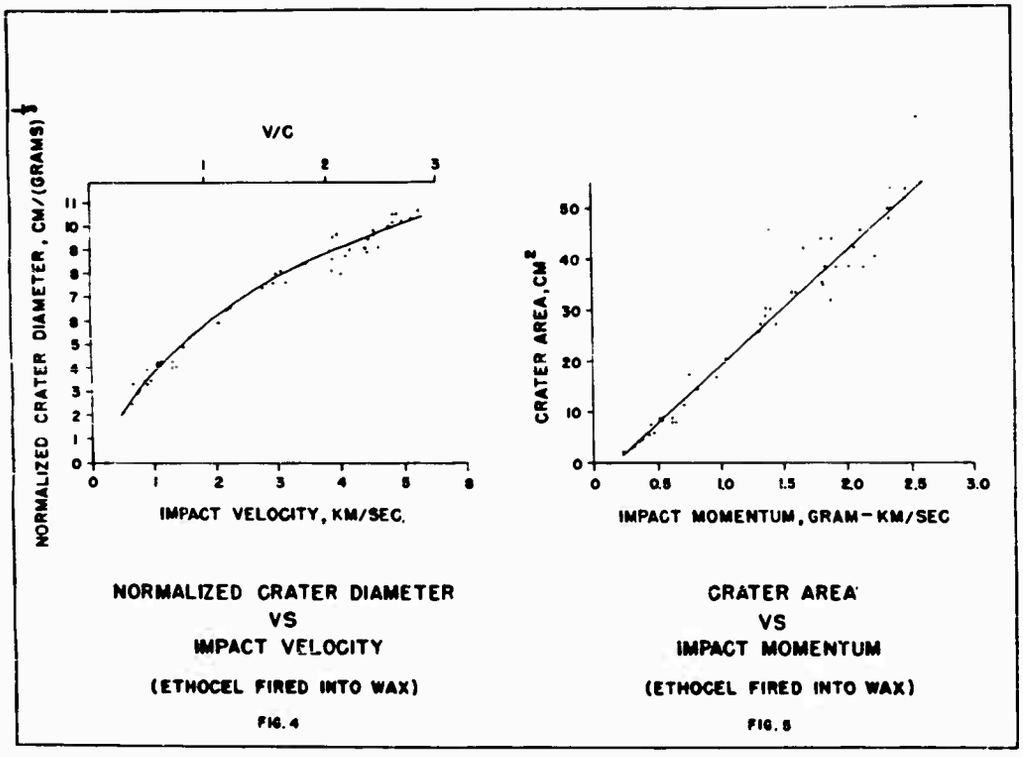

NORMALIZED CRATER DIAMETER
VS
IMPACT VELOCITY

(ETHOCEL FIRED INTO WAX)

FIG. 4

CRATER AREA
VS
IMPACT MOMENTUM

(ETHOCEL FIRED INTO WAX)

FIG. 5

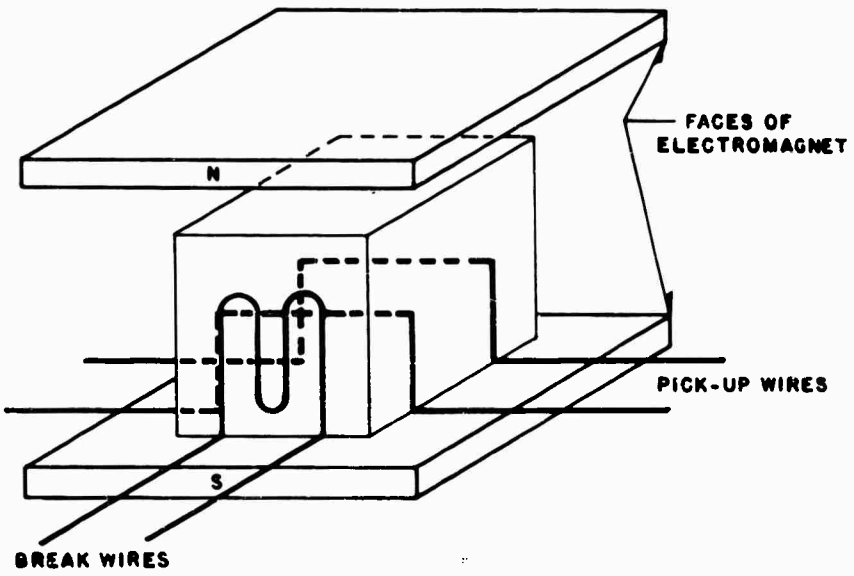

ARRANGEMENT OF PICK-UP WIRES
IN TARGET BLOCK AND ELECTROMAGNET

FIG. 6

TYPICAL OSCILLOSCOPE RECORDS

IMPACT VELOCITY APPROX. 4 Km/sec

LONG WIRE

WIRES AT 2" AND 3"

FIG 7A

SHORT WIRE

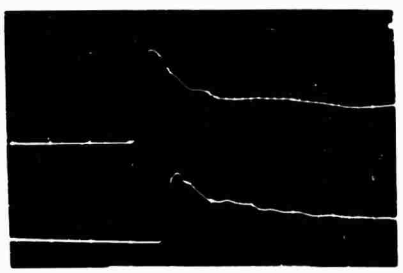

WIRES AT 2" AND $2\frac{1}{4}$"

FIG. 7B

SWEEP RATE 5 μsec/cm

the e. m. f. induced in the wires when they are set in motion by the particles surrounding them during the target deformation process. The monitored e. m. f. provides time of arrival data of the disturbance front at each wire station and the velocity history of each wire. With this information, it is possible to calculate the velocity of propagation of the front and the velocity of the particles behind it. Consequently, by use of the standard relations for conservation of mass and momentum through a shock, the pressure, p, (strictly, the compressive stress normal to the front), and the volume change through the front can be determined. These relations are:

$$p = \rho_o U v \tag{1}$$

$$\tau/\tau_o = (U - v)/U \tag{2}$$

where

ρ_o is the material density ahead of the front,
U is the velocity of propagation of the front,
v is the particle velocity directly behind the front, and
τ and τ_o are the volumes per unit mass directly behind and ahead of the front, respectively.

To date, two variations of the basic technique described above have been utilized. In the first, wires are placed through the entire width of the targets so that a nine inch length is normal to the trajectory of the pellet and transverse to the flux lines of the magnetic field surrounding the blocks, see Figure 6. The standard arrangement makes use of three pick-up wires monitored by two dual beam oscilloscopes. The intermediate pick-up wire is observed on each oscilloscope to provide reliable time of arrival data. Typical records from a firing using the set-up are shown in Figure 7A. The oscilloscopes are triggered by a break wire on the face of the targets.

The second variation of the pick-up wire technique is identical to that just described except that the wires are placed within the blocks with only one-half inch of their length transverse to the magnetic flux lines. This "short wire" arrangement provides data which can be more reliably interpreted in terms of the particle velocity history in the disturbed target than the first variation. This will be remarked upon in more detail later.

The initial tests which were conducted with the velocity pick-up wire technique made use of the first, "long wire," variation described above [2]. They provided a general survey of the pellet engendered disturbance as it traveled through the target blocks; gave an indication of the usefulness and reliability of the experimental technique; and served as a guide in planning further tests. A summary of the most significant results from these tests will be given here. The experiments were performed with wires placed either three and six inches; two, four, and six inches, or one, two, and three inches from the impacted target face. With these wire spacings, extensive firings in the low impact velocity range of 0.4 to 1.6 km/sec showed the propagation velocity of the disturbance to be constant at about 1.85 to 1.90 km/sec. This is the dilatational wave velocity of the target. To observe propagation velocities definitely in excess of this constant value, it was necessary to exceed an

impact velocity of 3.0 km/sec with wires placed one, two, and three inches from the point of impact. Results of such tests are shown in Figures 8A and 8B as plots of average wave velocity between wire stations versus impact velocity. The first plot shows a constant average velocity between wires two inches, four inches, and six inches from the face of the block for impact velocities up to 1.6 km/sec. The second plot indicates that the wave velocity increases linearly (wires at one, two, and three inches from face) with impact velocity. As a means of reference, it is worth noting here that the final crater depths associated with the impacts above 3.0 km/sec were greater than one inch, the location of the first wire station.

At impact velocities of 0.76 km/sec and 4.06 km/sec the long wire e.m.f. - time records provided by the oscilloscopes were used to evaluate the particle velocity directly behind the front of the disturbance traveling through the target blocks (see Reference 2 for the details of this analysis). With this data and the propagation velocities provided by Figure 8, the pressures and volume ratios, τ / τ_0, at the front were determined from Equations 1 and 2. The results of these calculations are shown in Figure 9 as plots of pressure versus distance from point of impact and, in Figure 12, as points for the Hugoniot curve of the target wax. To provide a reference scale for the data of Figure 9; the final crater depth, the tensile rupture strength (static), and strong shock threshold pressure of the targets have been indicated on the graphs. The latter pressure is that at which the propagation velocity first exceeds the dilatational value and is about 4×10^8 dynes/cm^2.

Two features of the data presented in Figures 8, 9, and 12 should be remarked upon here. The first is the rapid decay of both propagation velocity (when above 1.85 km/sec) and pressure as the wave front progresses through the targets. A more detailed knowledge of the character of the attenuation would be useful and naturally suggests the use of wire spacings appreciably smaller than the one inch of these data. Details of the manner in which the propagation velocity decreases as the wave front travels into the blocks are required to avoid introducing uncertainties in evaluation of p and τ / τ_0 from Equations 1 and 2. This difficulty arises when U exceeds 1.85 km/sec and use is made of an average velocity determined by widely separated timing stations.

The second significant feature of the data is the extremely good agreement between the experimentally determined low pressure portion of the Hugoniot and that predicted by the bulk modulus of the target material, i.e., $\frac{dp}{d(\tau/\tau_0)} = -K$. This provides an encouraging overall evaulation of the creditability of the pick-up wire technique.

In order to obtain more detailed information concerning pressure and velocity of propagation, tests are currently being conducted using a station-to-station spacing between wires of 1/4 inch. Also, the short-wire (1/2 inch transverse to magnetic field) variation of the basic wire technique is being utilized. This is done to avoid the somewhat tedious and uncertain analysis required to determine particle velocities from the long wire e.m.f.-time records. The difficulties are a result of the fact that the length of a long wire in motion continually increases as it is enveloped by the hemispherical wave front. However, a half-inch wire length is sufficiently short to be considered constant for practical purposes and its velocity and that of the particles surrounding it is given by:

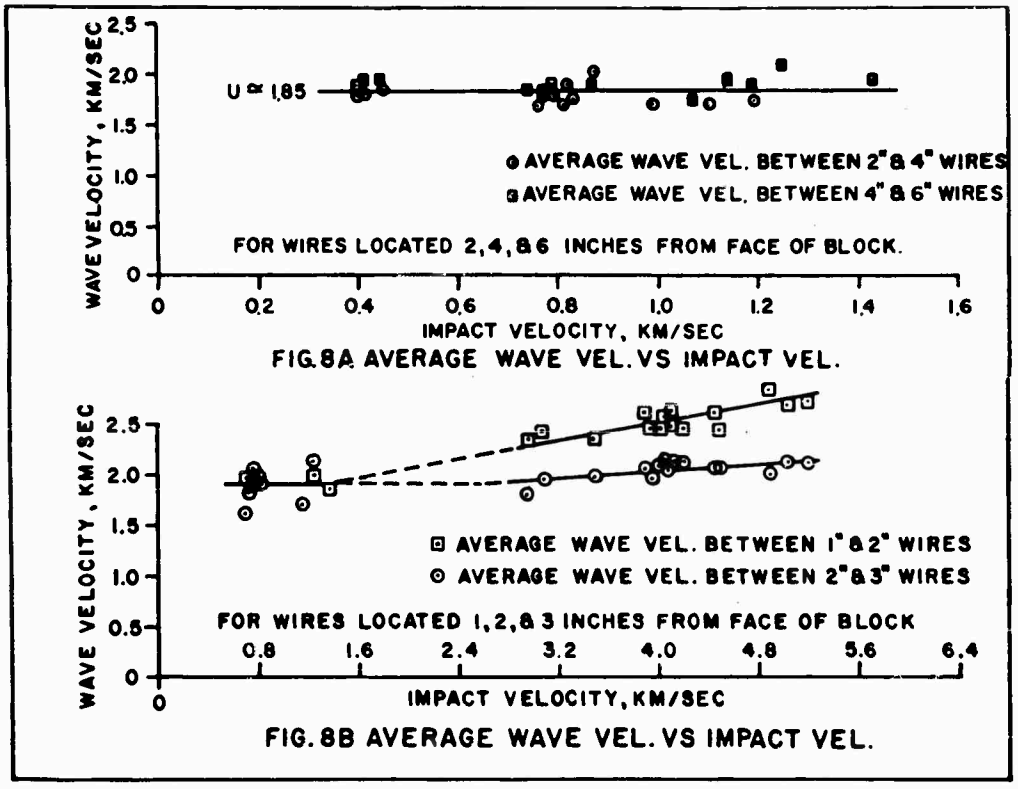
WAVE VELOCITY, KM/SEC
2.5
2.0
1.5
1.0
0.5
0
U ∝ 1.85
● AVERAGE WAVE VEL. BETWEEN 2" & 4" WIRES
⊡ AVERAGE WAVE VEL. BETWEEN 4" & 6" WIRES
FOR WIRES LOCATED 2, 4, & 6 INCHES FROM FACE OF BLOCK.
0
0.2
0.4
0.6
0.8
1.0
1.2
1.4
1.6
IMPACT VELOCITY, KM/SEC
FIG. 8A AVERAGE WAVE VEL. VS IMPACT VEL.
WAVE VELOCITY, KM/SEC
2.5
2.0
1.5
1.0
0.5
0
⊡ AVERAGE WAVE VEL. BETWEEN 1" & 2" WIRES
⊙ AVERAGE WAVE VEL. BETWEEN 2" & 3" WIRES
FOR WIRES LOCATED 1, 2, & 3 INCHES FROM FACE OF BLOCK
0.8
1.6
2.4
3.2
4.0
4.8
5.6
6.4
0
IMPACT VELOCITY, KM/SEC
FIG. 8B AVERAGE WAVE VEL. VS IMPACT VEL.

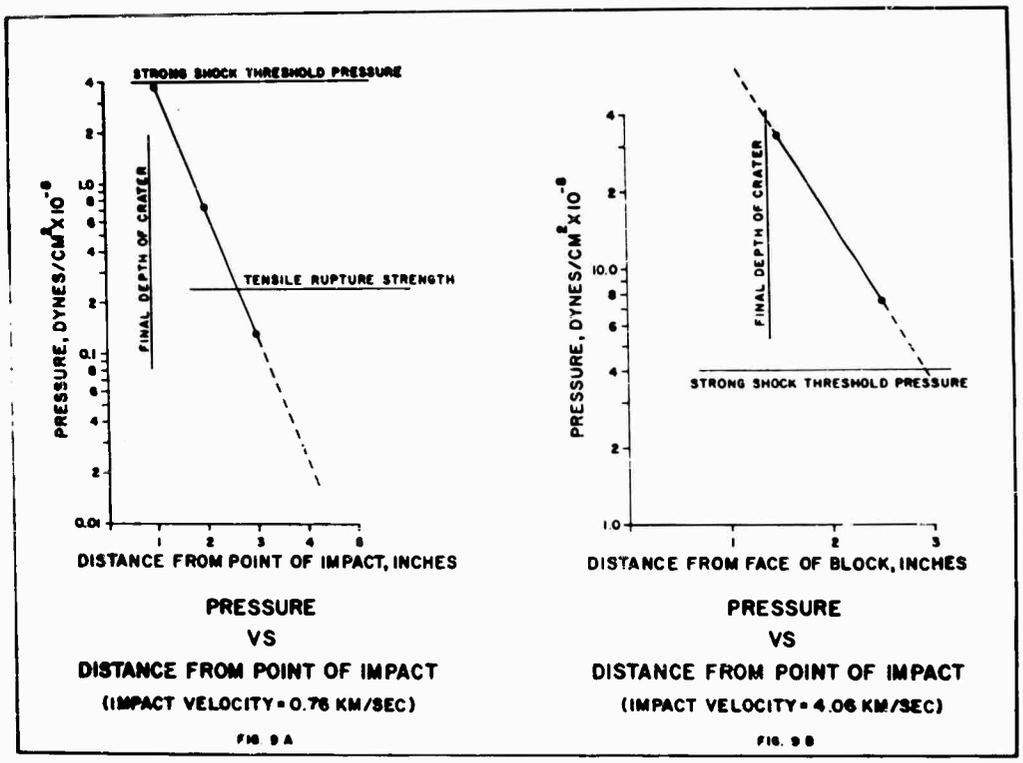
STRONG SHOCK THRESHOLD PRESSURE
TENSILE RUPTURE STRENGTH
FINAL DEPTH OF CRATER
PRESSURE, DYNES/CM² X 10⁻⁸
DISTANCE FROM POINT OF IMPACT, INCHES
PRESSURE
VS
DISTANCE FROM POINT OF IMPACT
(IMPACT VELOCITY = 0.76 KM/SEC)
FIG. 9A
FINAL DEPTH OF CRATER
STRONG SHOCK THRESHOLD PRESSURE
PRESSURE, DYNES/CM² X 10⁻⁸
DISTANCE FROM FACE OF BLOCK, INCHES
PRESSURE
VS
DISTANCE FROM POINT OF IMPACT
(IMPACT VELOCITY = 4.06 KM/SEC)
FIG. 9B

$$v = e/B\,\ell \qquad (3)$$

where e = observed e. m. f., abvolts,
B = magnetic flux density, lines /cm^2, and
ℓ = length of pick-up wire, cm.

At present, the most extensive data obtained from short-wire tests are for an impact velocity of 4.0 km/sec. In Figure 10, data of these experiments are given as a plot of average wave velocity between the 1/4-inch timing stations against distance from the impact face. These data show the history of the velocity of the front with considerable detail. Specifically, the rapidity and nonlinearity of the decay should be noted.

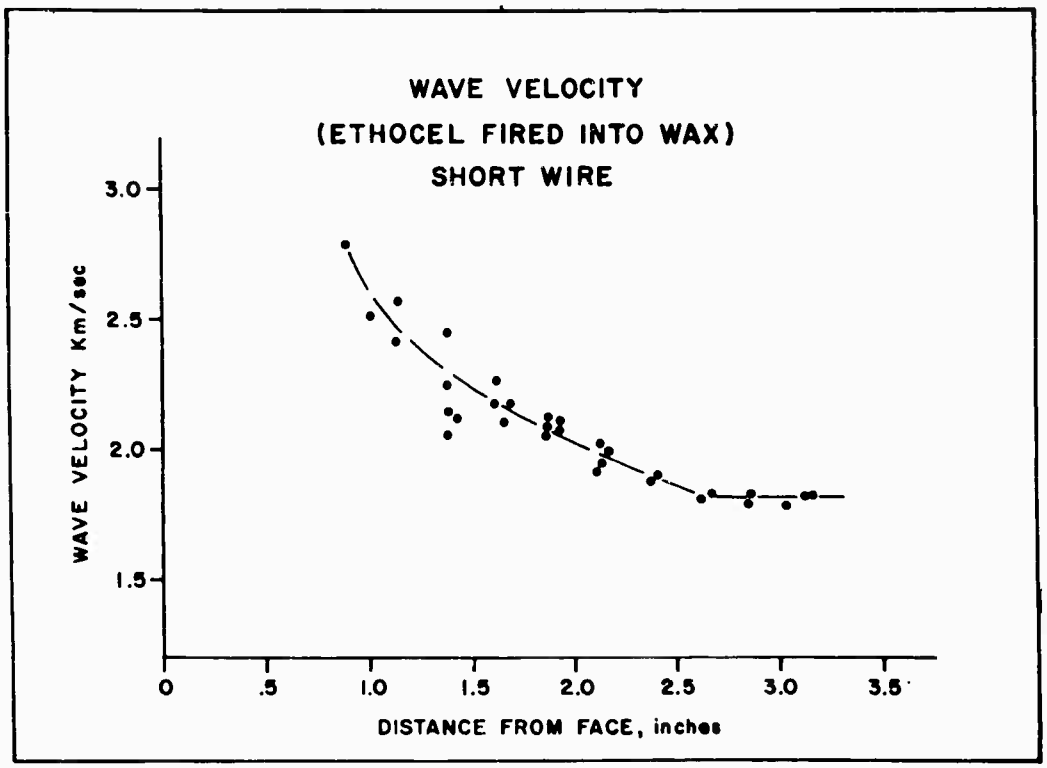

Figure 10

To determine the pressures at the front of the disturbance, the e. m. f. - time oscilloscope records were interpreted to evaluate the particle velocities directly behind the shock. Typical short-wire oscilloscope records are shown in Figure 7B. To evaluate the particle velocity, the peak e. m. f. of these records is read and used in Equation (3). Thus, with this data and the wave velocities provided by Figure 10, the pressures and volume ratios, v/v_o, may be calculated. In Figure 11, the averaged results of the pressure evaluations are shown on a semi-logarithmic plot of pressure against distance from the point of impact. The data indicate an exponential decay with distance. The rate of attenuation is of the order of 4 to 1 for each inch of travel. This is in substantial agreement with the data of Figure 9.

The magnitude of the pressures shown in Figure 11 should be pointed out. At a distance of one inch from the target face, the evaluated pressure is 56×10^8 dynes/cm^2. This is more than two orders-of-magnitude greater than the conventional static tensile rupture strength of the wax (0.24×10^8 dynes/cm^2). Also, it should be noted that the strong shock threshold pressure of about 4×10^8 dynes/cm^2 is an order-of-magnitude greater than the rupture strength. This latter pressure is reached at a distance of about 2 3/4 inches from the face of the target. Thus, it is seen that relatively intense pressures are present at the shock front for appreciable distances into the blocks.

The pressures set forth in Figure 11 and the corresponding values of τ / τ_o given by Equation (3) are shown in Figure 12 as points for the Hugoniot curve of the target wax. These data join well with those provided by the long wire tests at low pressure. The agreement at higher pressures (30×10^8 dynes/cm^2) is not as good, but this was to be expected due to the uncertainty in the long wire pressure evaluations when U exceeded 1.85 km/sec.

TERMINAL CHARACTERISTICS OF TARGET BLOCKS

In order to have definitive data regarding the condition of targets subsequent to completion of the cratering mechanism, methods are being developed for examining their final deformation state and for determining the condition and amount of material detached from them as a result of impact. Presently, the results of such experiments are only partially quantitative. However, they are informative and will be described here.

To examine the final deformation state within targets, they are cast in alternating layers of dyed and colorless wax, fired upon, and then sectioned through the center of the crater. The result of such a test at an impact velocity of 4.0 km/sec is shown in Figure 1. As demonstrated by the photograph, it has been possible to cast a portion of the target in firmly bound layers having distinct boundaries. The most interesting feature of this photograph is the overall view it gives of the final target deformation. In particular, it is worth noting that the entire lower portion of the crater is definitely lined with the wax of the first colored layer below the surface. The initial depth of the lower boundary of this layer was about 5/8 inches while the final crater depth was 1 1/2 inches. This indicates that all the material actually expelled from the target during crater formation is initially quite close to the target surface and that the majority of the crater formation simply consists of transport of material from one location in the target to another.

Another interesting feature of the final condition of wax target blocks is the character of the highly disturbed region in the vicinity of the crater. This region is very distinct in any sectioned target and can be seen in Figure 13. It seems to be analogous to that seen in sectioned and etched metallic targets where an area of definite change in crystal structure is present [6]. In the case of wax, it has been found that the density of this region is definitely less than that of the undisturbed material. Whether this is due to severe fracture or dilatation as a result of the pressure release wave is not known.

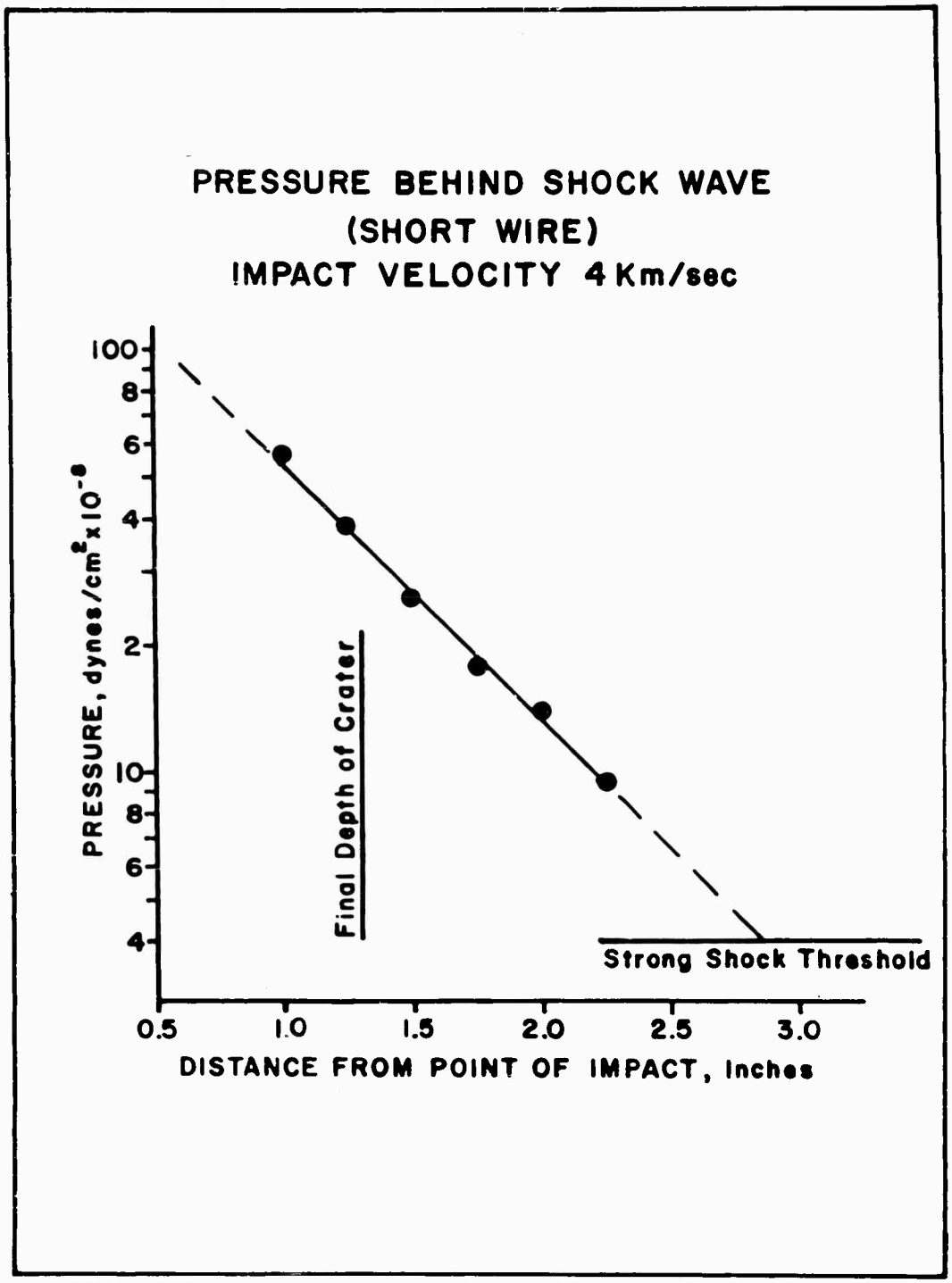
PRESSURE BEHIND SHOCK WAVE
(SHORT WIRE)
IMPACT VELOCITY 4 Km/sec
PRESSURE, dynes/cm²x10⁻⁸
100
8
6
4
2
10
8
6
4
Final Depth of Crater
Strong Shock Threshold
0.5
1.0
1.5
2.0
2.5
3.0
DISTANCE FROM POINT OF IMPACT, Inches

FIG. 11

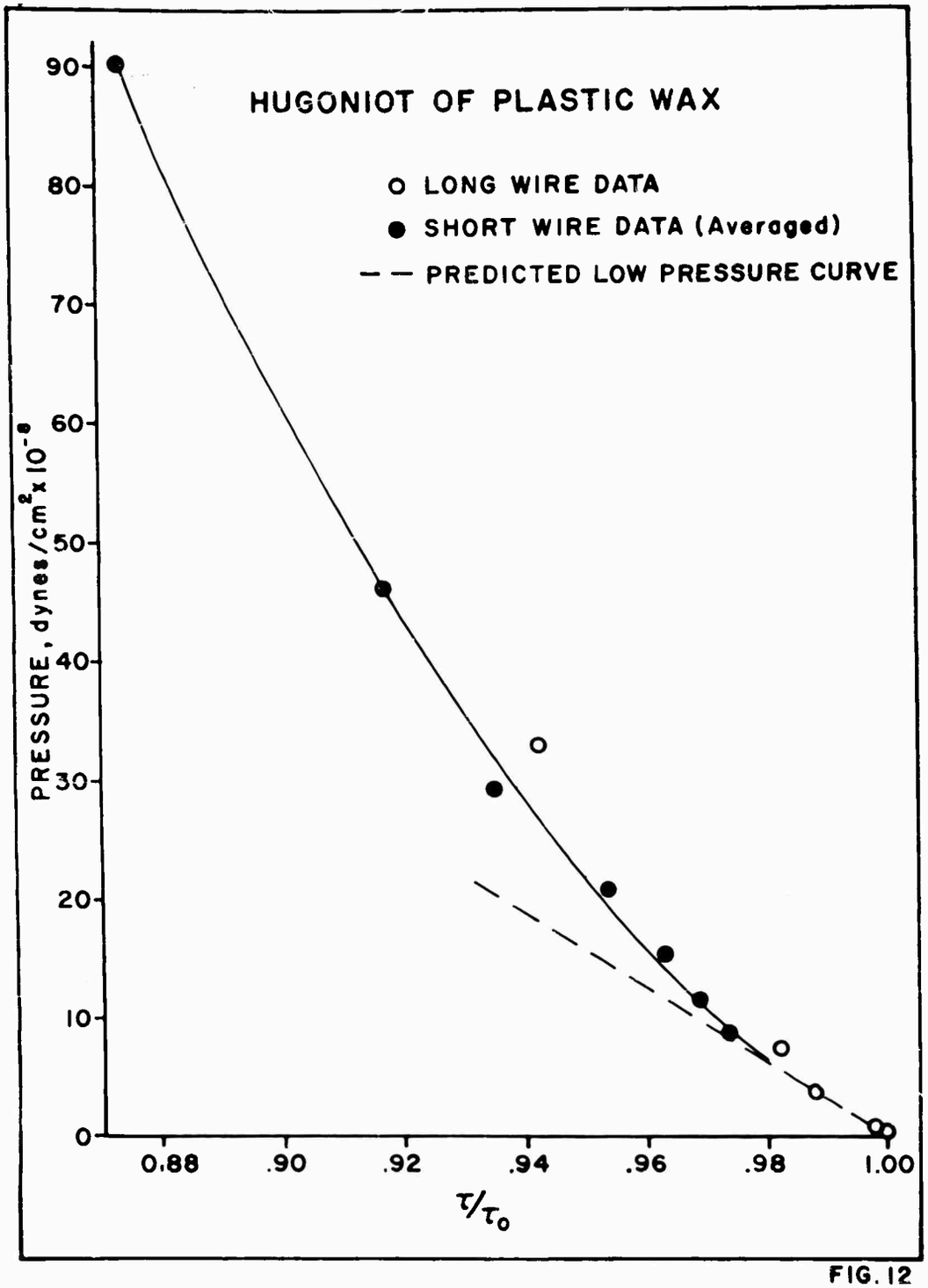
HUGONIOT OF PLASTIC WAX
LONG WIRE DATA
SHORT WIRE DATA (Averaged)
PREDICTED LOW PRESSURE CURVE
PRESSURE, dynes/cm² x 10⁻⁹
90
80
70
60
50
40
30
20
10
0
0.88
.90
.92
.94
.96
.98
1.00
τ/τ₀

FIG. 12

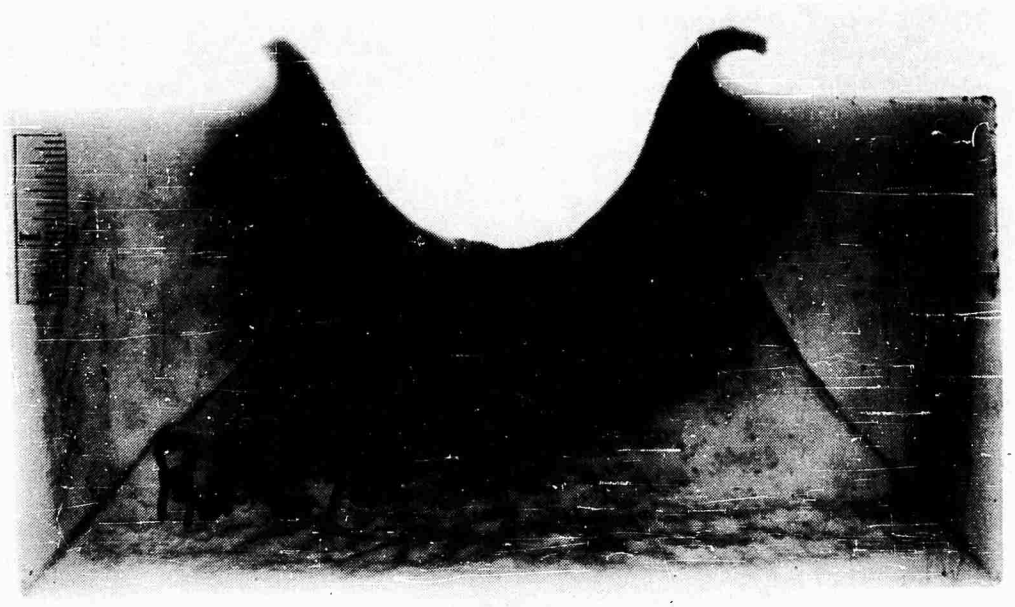

Figure 13

To investigate the amount and character of the material severed from damaged blocks, their mass loss has been determined by weighing targets before and after firings. Also, a collector has been employed to gather the expelled wax. For 4.0 km/sec impacts the mass of the detached material is approximately 30 percent of that required to fill the final volume of the crater. About two-thirds of this 30 percent consists of large spalls from the lips of the crater. The remaining third is in the form of small, uniform size particles which apparently are separated from the target during the early stages of contact between pellet and target. A further characteristic of the material expelled from targets is the presence of a very small amount of vaporization. This is indicated by deposition of a very thin wax film on the observation ports of the evacuated range during tests. No estimate of the mass of material vaporized has been possible. The presence of vaporization, of course, implies the existence of relatively high temperatures at the target surface during the very initial stages of crater formation, at least. Further evidence of high temperatures is given by the recovery of charred particles of the plastic projectiles in use.

DISCUSSION OF EXPERIMENTAL TECHNIQUE AND RESULTS

Comment is necessary on the accuracy of the pick-up wire technique used to evaluate wave velocities, particle velocities, and pressures. Based on the reliability of the times read from the oscilloscope records and the accuracy of wire placement, the expected maximum errors of individual average wave velocities determined in the long and short wire tests are $\pm$ 6 percent and $\pm$ 10 percent, respectively. Of course, the reliability of averaged data from a number of tests is better.

The adequacy of the method used to determine particle velocities is difficult to assess quantitatively. Basically, the usefulness of the technique depends upon whether the pick-up wires assume the motion of the particles surrounding them. As a result of examining sectioned targets subsequent to impact tests for evidence of relative motion between wires and the material round them, and by comparing oscilloscope records from pick-up wires of various densities; it appears an accurate description of the wax's motion is provided by the e. m. f. - time data. Furthermore, the overall accuracy of the entire method of data acquisition and reduction associated with determining particle velocities, pressures, and volume ratios can be examined through use of the Hugoniot. As noted earlier, the agreement of the experimentally determined low pressure portion of the curve with its predicted shape is very good. At higher pressures, comparison of the present results with extrapolated data (minimum pressure of 500×10^8 dynes/cm^2) of tests performed on a paraffin wax (ρ also 0.91 gm/cm^3) by investigators at Los Alamos [7] is also extremely good. In fact, the solid curve used to represent the data points of Figure 12 is that of the analytic fit of the Los Alamos data.

In view of the factors mentioned above, it does not seem unreasonable to assign arbitrarily an accuracy to the Hugoniot data of about $\pm$ 15 percent. Of course, this figure applies to the averaged data of a number of tests and not the results of a particular experiment. While greater accuracy is certainly desirable and is anticipated with refinement of techniques, that presently attainable is not particularly distressing in view of the severe lack of quantitative data of the type provided by these tests. In short, the test results are meaningful.

With the results presented in the preceding sections in mind, a brief partially quantitative, description of the transient response of wax targets to impact can be given. Attention must be focused on the 4.0 km/sec case (Figures 10, 11, and 12). However, this is totally representative, since it is well within the hypervelocity region of the target material, i.e., V/C = 2.16. The pressure initially generated at the target face by the pellet is very intense and may be roughly estimated by extrapolation of the curve of Figure 10. This gives a value of 230×10^8 dynes/cm^2, a pressure three orders-of-magnitude greater than the conventional mechanical strength of the material ($\simeq 0.24 \times 10^8$ dynes/cm^2). Associated with this intense pressure are temperatures sufficiently high to cause a very small amount of vaporization of the target. Subsequent to the initial contact of pellet and target; the pellet is rapidly expended (in the order of 10 μ sec), a relatively small amount of material is expelled from the block in the form of particles, and a hemispherical shock front starts to travel through the target. The velocity and pressure of this front attenuate fairly rapidly as it progresses. By the time it has reached the position of the final crater depth, its pressure has decreased to about 36×10^8 dynes/cm^2. With continued travel, the pressure decays to the strong shock threshold at a distance into the target about twice the final crater depth. The wave front then travels at the dilatational velocity with continued decay of pressure, see Figures 10 and 9A. As regards the final deformation of the target, reference to Figure 1 shows that very severe deformation of the target is confined to a region within about 1/4 inch of the crater surface. However, as indicated by Figure 13, the material is markedly disturbed to an appreciably greater depth.

As noted previously, the largest of the pressures represented by the results given here is several orders-of-magnitude greater than the conventional

mechanical strength of the target wax. This is the case in any material suffering a hypervelocity impact. The existence of such pressures at the front of the disturbance in the targets implies rather severe stress levels within the region undergoing deformation. As a result of these stresses, it is frequently assumed the strength of the target material may be neglected in describing the cratering mechanism; the customary basis of the assumption being that the mechanical strength is very small compared to the stresses. The process of crater formation, or at least portions of it, is then termed "fluid" or "hydrodynamic". The adequacy of this assumption is the subject of controversy and the usual justification for its use is certainly not tenable. Whether the fluid concept of the impact process is reasonable must be based on a comparison of stress gradients and material strength, and not on a comparison of stresses, per se, and material strength. Stated otherwise, the pertinent question is whether the strength of the material is small compared to the inertial forces present during the impact deformation process. Based on the criteria emphasized above, arguments too numerous to elaborate on here may be devised to substantiate or refute the hydrodynamic concept of impact damage. The authors' opinion is that it is an extreme simplification when applied to any stage of the cratering mechanism other than that when the project maintains a semblance of its integrity. However, arguments for or against the assumption are, in the main, of the plausibility variety.

Definitive quantitative experimental data is needed to settle questions concerning the impact process such as that mentioned in the preceding paragraph. Such information can only be obtained from experiments specifically designed to yield pertinent and reliable results about the transient and terminal characteristics of cratering. In this manner, appropriate concepts can be conceived and evaluated. The techniques and results presented in this paper show that the study of wax targets under impact conditions is a very useful means for obtaining the desired information. This is a result of the relative ease with which it can be instrumented and observed both during and subsequent to the cratering phenomenon. Further advantage will be taken of its usefulness through design and application of meaningful experimental methods.

REFERENCES

1. J. Frasier, "A Small Light-Gas Gun Range," BRL Memo Report No. 1290, July, 1960.

2. J. Frazier, "Hypervelocity Impact Experiments in Wax," BRL Report 1124, February 1961, Aberdeen Proving Ground, Maryland.

3. J. Kineke, "An Experimental Study of Crater Formation in Lead," Proc. 3rd Symposium of Hypervelocity Impact, Vol. I, p. 157, Chicago, Illinois, 1959.

4. H. B. Van Fleet, W. S. Partridge, and E. T. Conner, "The Anomalous Behavior of Lead-to-Lead Impact," Proc. 3rd Symposium of Hypervelocity Impact, Vol. I, p. 115, Chicago, Illinois, 1959.

5. J. Kineke, "An Experimental Study of Crater Formation in Metallic Targets," Proc. 4th Symposium of Hypervelocity Impact, Vol. I., Eglin AFB, Florida 1960.

6. C. H. Glass and Robert B. Pond, "A Metallurgical Approach to the Hypervelocity Problem," Proc. 4th Symposium of Hypervelocity Impact, Vol. III, Eglin AFB, Florida, April 1960.

7. Unpublished data.

CORRELATION OF HYPERVELOCITY IMPACT DATA

Walter Herrmann and Arfon H. Jones

Massachusetts Institute of Technology
Cambridge, Massachusetts

ABSTRACT

Published experimental data on cratering by high velocity projectiles in quasi-infinite metallic targets, comprising over 1,700 data points, generated at fifteen laboratories, were collected and analyzed statistically. The fit of the data to a simple power law was investigated, and it was found that the penetration depth in the high velocity region is best fitted by the non-dimensional equation

$$\frac{P}{d} = k K^{2/3} B^{1/3}$$

where P is the penetration, d the projectile dimension, $K = \rho_p / \rho_t$ the projectile to target density ratio, and $B = \rho_t V^2 / H_t$, where V is the projectile velocity and H_t the Brinell Hardness of the target, in appropriate units. The value of k is near 0.36 for most materials. It was found that the cratering efficiency could be approximately fitted by

$$\frac{E}{V_c} = k K^{-2/3} H_t$$

where E is the projectile kinetic energy and V_c the crater volume, with a value of k near 3.1 for most materials.

The experimental data were also compared with the theoretical prediction of Grimminger, Bohn and Fuchs, Bjork, Öpik, Whipple, Langton, and Grow, and hydrodynamic jet theory. Only the theory of Bohn and Fuchs showed reasonable agreement over most of the velocity range. Based on this observation, the fit of the data to an empirical expression of the type

$$\frac{P}{d} = k_1 K^{2/3} \log_e \left(1 + \frac{K^{2/3} B}{k_2} \right)$$

was investigated. This expression was found to fit the experimental data for ductile projectiles over the entire experimental velocity range. The constants k_1 and k_2 were found to be close to 0.6 and 4 respectively for most materials.

Validity of extrapolations of these expressions to higher velocities is discussed, and it is concluded that, because the expressions are not based on rational theoretical grounds, extrapolation either to higher velocities or other materials cannot be carried out with any confidence.

1. INTRODUCTION

Cratering and penetration of targets by projectiles traveling at velocities at which the projectile suffers severe deformation or breakup has recently received a great deal of attention, due to the importance of this phenomenon in the protection and lethality of space vehicles and ballistic missiles.

A great deal of experimental data has been published by a number of laboratories, and considerable theoretical work has appeared during the last few years. Limited comparisons of data from one laboratory with those from another, and of experimental data with theoretical predictions have shown some large discrepancies. Considerable confusion exists, because, except in a few instances, the data from one laboratory are not directly comparable with those from another, since identical materials, projectile shapes and velocity ranges were not used. Each laboratory has produced a different empirical expression which was found to fit the limited range in experimental parameters explored at that laboratory. The empirical expressions are more or less contradictory, and when extrapolated to velocities of interest in space applications, lead to large disagreements in predicted penetration.

Consequently a study of currently available impact data was carried out in an effort to clarify the situation. Insufficient data were available for projectile-target configurations, other than normal incidence on a quasi-infinite metallic target, to warrant extensive correlation, and this study was therefore restricted to the latter configuration.

2. EXPERIMENTAL DATA

During the data acquisition phase, thirty-nine groups active in high velocity impact were contacted. The work in progress at each laboratory is indicated in Table I. Data on penetration depths, diameters and volumes in quasi-infinite targets, released prior to April 1961, was gathered.

In many cases, the data was presented in non-dimensional graphical form. Actual tabulations of measured quantities were supplied in only a few instances. In most cases, additional information had to be requested, in order to extract measured quantities from data plots. In a few cases, some difficulty was experienced in extracting measured quantities from data plots, due to the fact that relevant information was not provided, or because only excessively small scale data plots were supplied, and as a consequence some uncertainty is associated with the corresponding data.

Considerable difficulty was experienced in obtaining reliable material property information. Material properties such as indentation hardness were measured on the actual target specimens in only a few instances. In many cases,

TABLE I ESTABLISHMENTS ACTIVE IN HIGH VELOCITY RESEARCH

LABORATORY	ACCELERATORS											TARGETS								PROJECTILES			
	SHAPED CHARGES	AIR CAVITY CHARGES	POWDER GUN	HIGH EXPLOSIVE GUN	EXPLODING WIRE	SHOCK TUBE	LIGHT GAS GUN	ELECTRICALLY HEATED GAS GUN	ELECTRO-MAGNETIC GUN	ELECTRO-STATIC ACCELERATOR	PROTON CHARGED PARTICLE ACCELERATOR	SEMI-INFINITE TARGETS	FINITE TARGETS	THIN TARGETS	SPACED THIN PLATE TARGETS	BUMPERS	HEATED TARGETS	NON METAL TARGETS	CELLULAR IMPACTS	DISC SPHERES CYLINDERS	MICROPARTICLES	RODS
AEROJET GENERAL CORPORATION	X	X					X	X						X					X	X		
A.R.D.E., FORT HALSTEAD, UNITED KINGDOM	X						X					X								X		
A.R.D. INCORPORATED			X				X	X														
ARMOUR RESEARCH FOUNDATION (CHICAGO)						X	X															
AVCO, WILMINGTON							X	X										X		X		
BALLISTIC RESEARCH LABORATORY	X	X					X					X		X				X	X	X	X	
C.A.R.D.E.							X					X	X					X		X		
CARNEGIE INSTITUTE OF TECHNOLOGY	X	X										X		X			X		X	X		
COLORADO SCHOOL OF MINES			X									X						X		X		
CONVAIR, SAN DIEGO		X					X								X					X		
DENVER RESEARCH INSTITUTE	X	X													X					X		
EGLIN A.F.B.							X					X	X				X	X		X		
FRANKFORD ARSENAL				X																		
GENERAL ELECTRIC COMPANY	X			X					X							X				X		
GRUMMAN AIRCRAFT											X										X	
LINCOLN LABORATORY, M.I.T.			X				X					X										X
M.I.T., A.S.N.L.			X									X				X				X		
N.A.S.A., AMES			X				X					X			X			X	X	X		X
N.A.S.A., LANGLEY			X				X					X				X	X	X		X		
NAVAL ORDNANCE TEST STATION			X				X						X							X		X
NAVAL RESEARCH LABORATORY			X				X	X				X	X		X			X		X		
NORTH AMERICAN					X																	
PICATINNY ARSENAL		X										X						X		X		
THOMPSON RAMO-WOOLDRIDGE CORPORATION										X		X		X							X	
RHODES AND BLOXSOM INCORPORATED								X				X						X		X		
S.R.I. POULTER LABORATORIES	X	X										X						X	X		X	
TECHNICAL OPERATIONS					X																	
UNIVERSITY OF UTAH	X	X	X				X		X			X		X			X	X		X		
UTAH RESEARCH AND DEVELOPMENT COMPANY INCORPORATED							X					X								X		
WATERTOWN ARSENAL			X				X					X								X		

material properties had to be taken from handbooks, (Ref. 1) corresponding to the material specification, with a consequent large uncertainty. In several instances, material specifications were so incomplete as to make it impossible to deduce even very approximate values for material properties, thus rendering the corresponding data valueless for the present correlation.

It is very strongly urged that experimenters publish tabulations of measured quantities in all future work, and determine actual material properties of the target and projectile materials, so that the experimental data will be more generally useful.

The extracted data has been tabulated in uniform units and format in Reference 2. Over 1,700 data points were obtained for normal impact on quasi-infinite metallic targets. Most of this data lay in the velocity range 1,500-10,000 ft/sec. Fifty-two projectile material-target material combinations are represented. These are shown in matrix form in Table II together with the velocity ranges covered by the data for each material combination.

For those material combinations for which a reasonably large number of experimental points existed, plots of penetration versus velocity were prepared. Since both spherical and cylindrical projectiles of different sizes were represented, the penetration arbitrarily was normalized by the equivalent sphere diameter defined as

$$d = \left(\frac{6}{\pi} \frac{m_s}{\rho_p} \right)^{1/3} \tag{1}$$

While data for a few material combinations from individual laboratories was very smooth and showed little scatter, most of the data showed scatter of the order of $\pm$ 0.05 in p/d, where p is the penetration depth. With the above definition of d, no shape or size effect could be detected within the scatter of the data. However, the scatter was in most cases such, that in comparing spheres and cylinder of unit length to diameter ratio, the cylinder length or diameter could be used directly as the equivalent sphere diameter without increasing the scatter significantly.

3. COMPARISON WITH PREVIOUS THEORIES

Predicted penetrations on the basis of the theories of Grimminger (Ref. 3), Bohn and Fuchs (Ref. 4), Öpik (Ref. 5), Whipple (Ref. 6), Langton (Ref. 7), Grow (Ref. 8), and shaped charge jet theory (Ref. 9, 10) were inserted on the individual data plots, covering twenty-four material combinations. In addition penetrations predicted by Bjork's theory (Ref. 11) were inserted on plots for aluminum projectiles striking aluminum targets, and steel projectiles striking steel targets. Examples are shown in Figures 1 through 6.

All of the theories were originally proposed for very high impact velocities, and would therefore not be expected to show good agreement in the experimental velocity range. Most of the theories not only showed little agreement with the experimental data, but also showed a different trend over the experimental velocity range. One exception is the theory of Bohn and Fuchs, which showed surprising agreement with the data at low velocities for quite a number of materials, but generally slightly overestimated penetration at higher velocities.

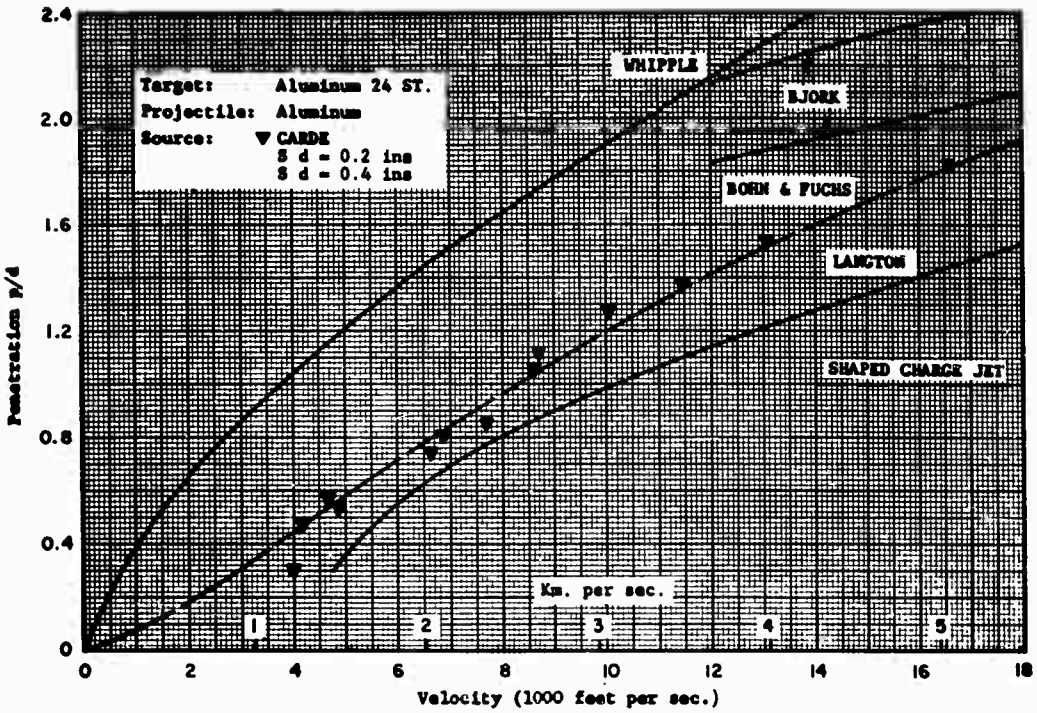

Fig. 1 The Penetration of Aluminum Spheres into 24 ST Aluminum Targets

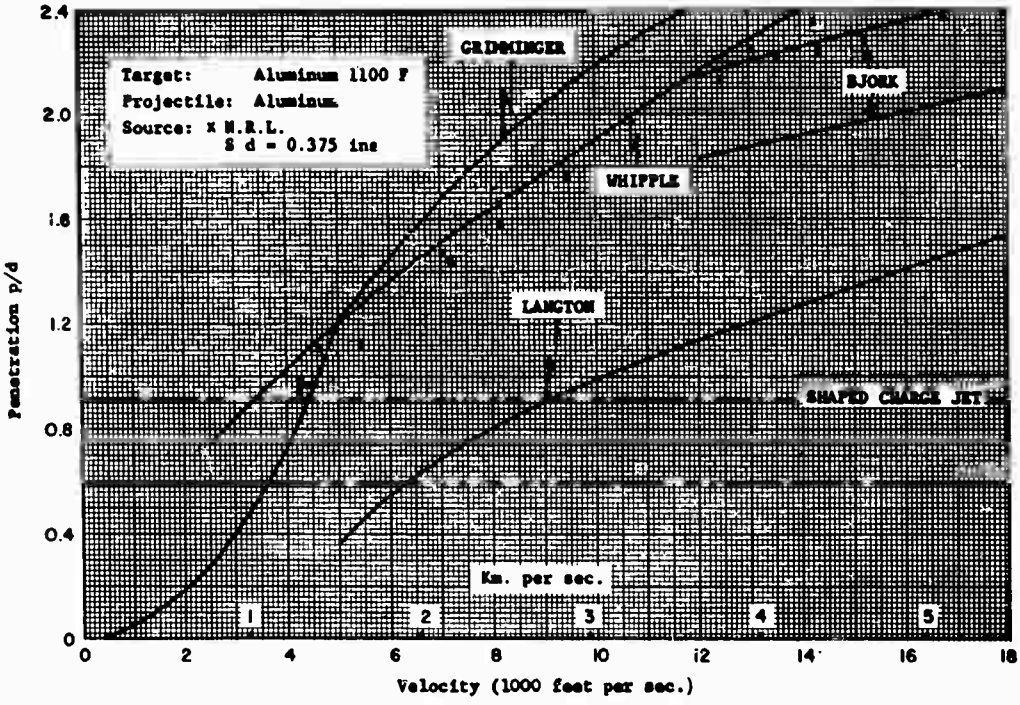

Fig. 2 The Penetration of Aluminum Spheres into 1100 F Aluminum Targets

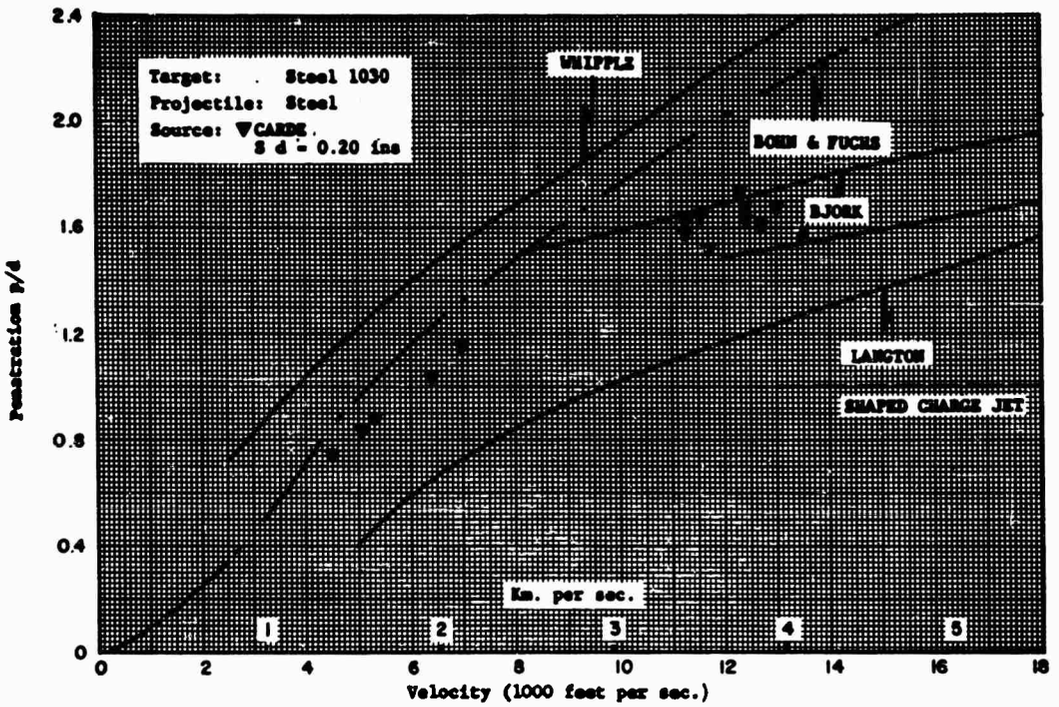

Fig. 3 The Penetration of Steel Projectiles into 1030 Steel Targets

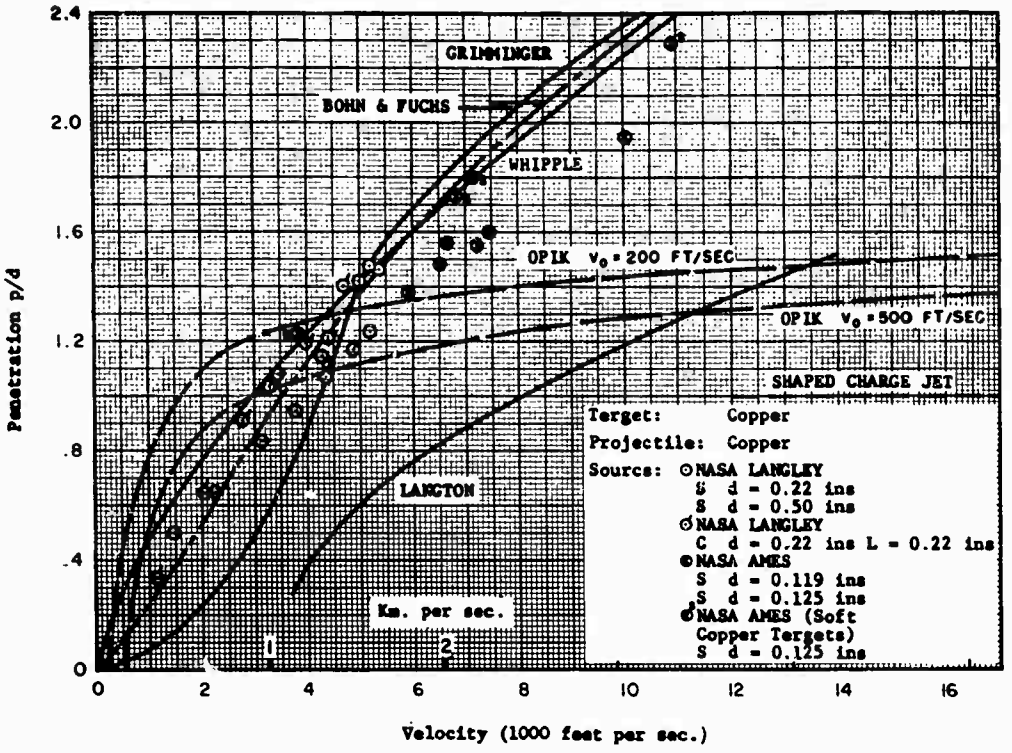

Fig. 4 Penetration of Copper Projectiles into Copper Targets

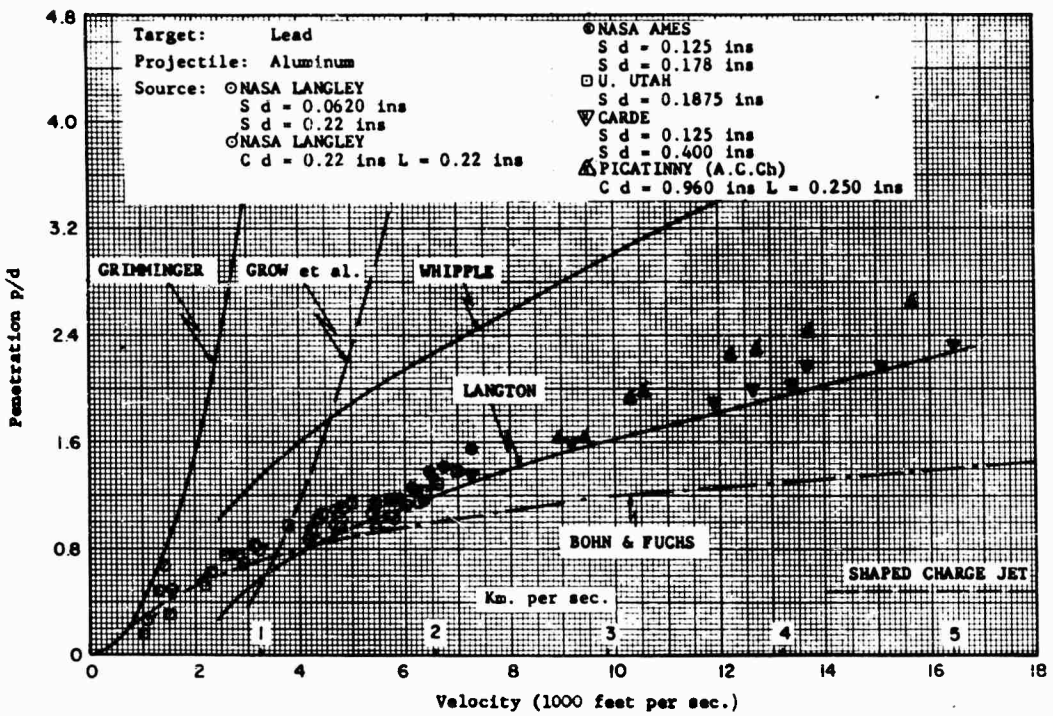

Fig. 5 The Penetration of Aluminum Projectiles into Lead Targets

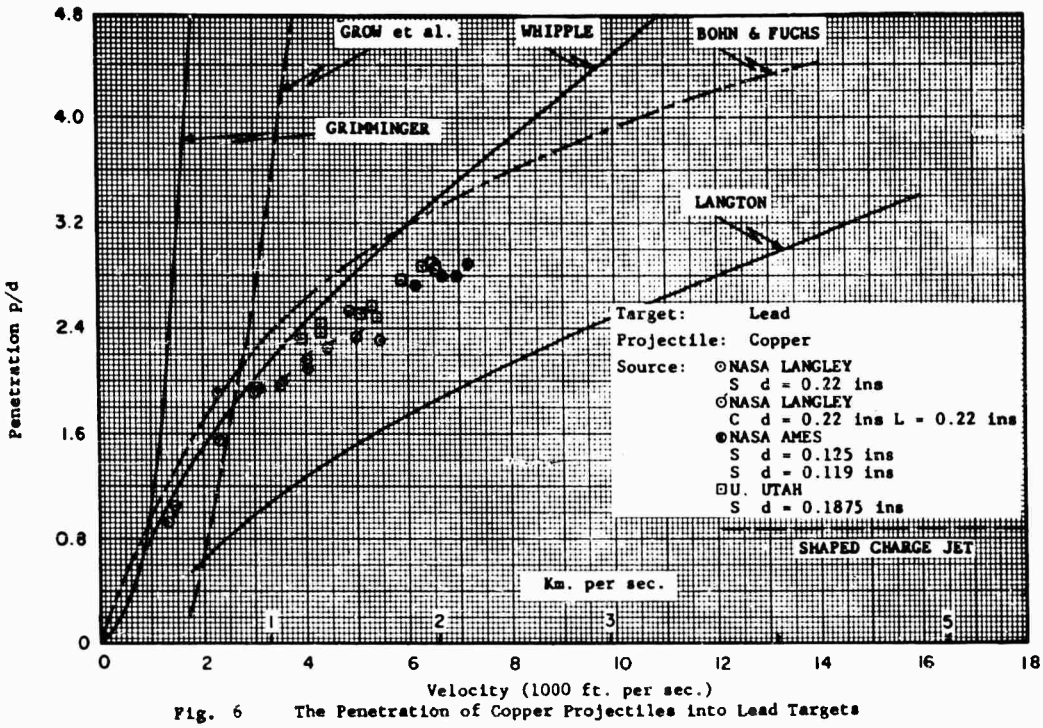

Fig. 6 The Penetration of Copper Projectiles into Lead Targets

Bohn and Fuchs assumed that the resistance to projectile penetration was a combination of a static part, proportional to the Brinell Hardness of the target, and a dynamic part proportional to the instantaneous projectile velocity squared. They therefore assumed that the force resisting penetration could be expressed as

$$F = \frac{\pi}{4} d^2 \left\{ H_t^{1/2} + \left(\frac{1}{2} f \rho_t v^2 \right)^{1/2} \right\}^2 \tag{2}$$

where H_t is the target Brinell Hardness (with dimensions of a stress in appropriate units), ρ_t the target density, v the instantaneous velocity, and f a shape factor defined by

$$f = \frac{1}{\pi/4\, d^2} \int \sin \phi \cdot dA \tag{3}$$

where dA is an element of the projectile area perpendicular to the direction of motion, and ϕ the inclination of that element to that direction. For spherical projectiles, the value $f = 2/3$ was given.

Integration of the equation of motion

$$-F\,dx = \frac{1}{2} m_p v\, dv \tag{4}$$

between the limits $x=0$, $v=V$; $x=p$, $v=0$, where V is the initial projectile velocity and p the final penetration depth, yields

$$\frac{p}{d} = \frac{4}{3f} K \left\{ \log_e \left[1 + \sqrt{\frac{1}{2} f B} \right] - \frac{\sqrt{\frac{1}{2} f B}}{1 + \sqrt{\frac{1}{2} f B}} \right\} \tag{5}$$

where $$K = \frac{\rho_p}{\rho_t}$$

and $$B = \left(\rho_t \frac{V^2}{H_t} \right)$$

Here, d is defined according to Eq. (1).

A slight increase in the value of f would have the effect of reducing the predicted penetration at higher velocities, thus leading to better agreement over the entire velocity range. The comparative success of Bohn and Fuchs' theory suggested that an expression of the general type Eq. (5) might prove useful as an empirical correlation expression.

4. CONSTRUCTION OF EMPIRICAL EXPRESSIONS

It is a great advantage to express empirical expressions in non-dimensional form. It is therefore convenient to enquire into convenient non-dimensional parameters formed from physical quantities entering into the cratering problem. The geometric quantities are straightforward; viz., characteristic projectile size d,

TABLE II
EXPERIMENTAL PROJECTILE – SEMI-INFINITE TARGET

Material Combinations for which Data are Available
(Velocity Ranges in feet per Second are Shown)

TARGETS → / PROJECTILES ↓	ALUMINUM	BERYLLIUM - COPPER	CADMIUM	COPPER	GRAPHITE	LEAD	LEAD - TIN ALLOYS	MAGNESIUM
ALUMINUM	CARDE 4,000-15,000 NASA LANGLEY 1000-15,000 G R L 4,000-14,000 WRDC 7,000-20,000	NASA LANGLEY 5,000-14,000		CARDE 4,000-15,000 NASA AMES 6,000	NASA LANGLEY 1,000-5,000	CARDE 1000-15,000 NASA AMES 5,000 7,000 NASA LANGLEY 1,000-6000 GRL 5,000-7,000 U UTAH 1,000-12000		
BRASS						U UTAH 1,000-7,000		
COPPER	NASA LANGLEY 1000-5,000 PHILCO 1,000-6,000	NASA LANGLEY 5,000-11,000		NASA AMES 4,000-15,000 NASA LANGLEY 1,000-5,000	NASA LANGLEY 2,000-7,000	NASA AMES 6,000-7,000 NASA LANGLEY 1,000-5,000 U UTAH 4,000-6,000		
DIAMOND						U UTAH 2,000-6000		
K-MONEL						U UTAH 1000-7000		
LEAD	NASA LANGLEY 1,000-5,000			NASA AMES 5,000-6,000 NASA LANGLEY 1000-4,000	NASA LANGLEY 1,000-4,000	NASA AMES 1000-7000 NASA LANGLEY 1,000-4,000 U UTAH 1,000-7000		
LEAD-TIN ALLOYS							U UTAH 5,000-7,000	
MAGNESIUM						U UTAH 5,000-6,000		
MAGNESIUM - LITHIUM						NASA AMES 5000-6,000		
MALLORY 1,000	PHILCO 1000-5,000							
NYLON	NASA LANGLEY 5,000-10,000	NASA LANGLEY 4,000-6,000				U UTAH 1,000-5,000		
PYREX GLASS						U UTAH 1000-2,000		
STEEL	GRL 5,000-8,000 NASA LANGLEY 1000-8,000 PHILCO 1000-5,000 U UTAH 400-5,000 POULTER LAB 5,000	NASA LANGLEY 4,000-8,000	G R L 5,000-15,000	G R L 5,000-15,000 NASA AMES 5,000 NASA LANGLEY 1,000-5,000 U UTAH 1,000-5,000 POULTER LAB 2,000-6,000	NASA LANGLEY 1,000-7,000	GRL 5,000-10,000 NASA AMES 6,000-10,000 NASA LANGLEY 1,000-4,000 U UTAH 1,000-7,000 POULTER LAB 5,000		U UTAH 1,000-5,000 POULTER LAB 5,000-7,000
TIN								
TIN-LEAD ALLOYS								
TUNGSTEN				NASA AMES 5,000-7,000		NASA AMES 5,000-7,000 U UTAH 2,000-5,000		
TUNGSTEN CARBIDE	G R L 500-5,000			G R L 1,000-4,000		G R L 500 - 5,000		
URANIUM	PHILCO 1,000-4,000							
OAK								

TABLE II (Continued)
EXPERIMENTAL PROJECTILE – SEMI-INFINITE TARGET

Material Combinations for which Data are Available
(Velocity Ranges in feet per second are Shown)

NICKEL	NYLON	SILVER	STEEL	TIN	TIN - LEAD ALLOYS	WAX	ZINC
			CARDE 1,250-11,000 NASA LANGLEY 500- 12,500 WATERTOWN 5000- 11,500				
			NASA LANGLEY 700 - 2,500				
			NASA LANGLEY 1,000- 4,000				
			CARDE 5,000-10,000				
POULTER LAB 2200 - 5,250	NASA LANGLEY 1,200-11,000	U UTAH 1,250- 5,250	CARDE 4,800 <5,000 NASA LANGLEY 1,000- 5,000 U UTAH 1,250 - 7,500 WATERTOWN 2,500-7,500 POULTER LAB 7,200-8,500				B R L 4,500-10,000 U UTAH 1,000- 5,000
				U UTAH 2,250- 7,000			
					U UTAH 1,000- 7,000		
			B R L 500-11,000				
						U UTAH 900-4250	

crater size P and projectile velocity V. Not so obvious are the material properties important to the problem. Drawing on static material properties quantities which might be considered to be relevant are the densities ρ_p, ρ_t, of projectile and target respectively, the sonic velocity c, relevant elastic modulus G, yield stress Y, the indentation hardness H, and the energy necessary to heat, melt or vapourise unit mass of material Q. In addition, since the problem is dynamic in character, parameters to characterise strain rate effects, and change of compressibility with pressure may be relevant. Such quantities have, however, not been satisfactorily defined at the present time.

Not all of the material properties are independent. For example $c^2 = G/\rho$. There is an approximate dependence of indentation hardness on yield stress, as may be seen in Figure 7. The Brinell Hardness is defined as the load applied to a spherical stylus divided by the area of the resultant depression, and thus has dimensions of a stress with conventional units kilogrammes per square millimeter. Expressing Y and H in identical units, the relation is approximately

$$H \approx 3.6Y \tag{6}$$

Drawing on these elementary material properties considered relevant in the cratering problem, one might form the following convenient non-dimensional parameters.

p/d	Penetration Ratio
$K = \rho_p/\rho_t$	Density Ratio
$M = V/c$	Mach Number
$T = V^2/Q$	Thermal Parameter
$B = \rho V^2/H$	Best Number

The last parameter appears so frequently in both empirical expressions and simplified theoretical expressions, that it seems appropriate to give it a name. Following a suggestion of Dr. John S. Rinehart *, it is proposed that this parameter be termed the Best Number in honour of the early French ballistician Best who carried out cratering experiments between 1835 and 1845.

It is likely therefore that the penetration may be expressed as a function of the above parameters, i. e.,

$$\frac{p}{d} = f(K, M, B, T) \tag{7}$$

Many different empirical expressions have been used to correlate penetration data at various laboratories. Some of these are tabulated in Table III

* Proceedings of the Third Hypervelocity Impact Symposium, Vol. 1, p. 187, February 1959.

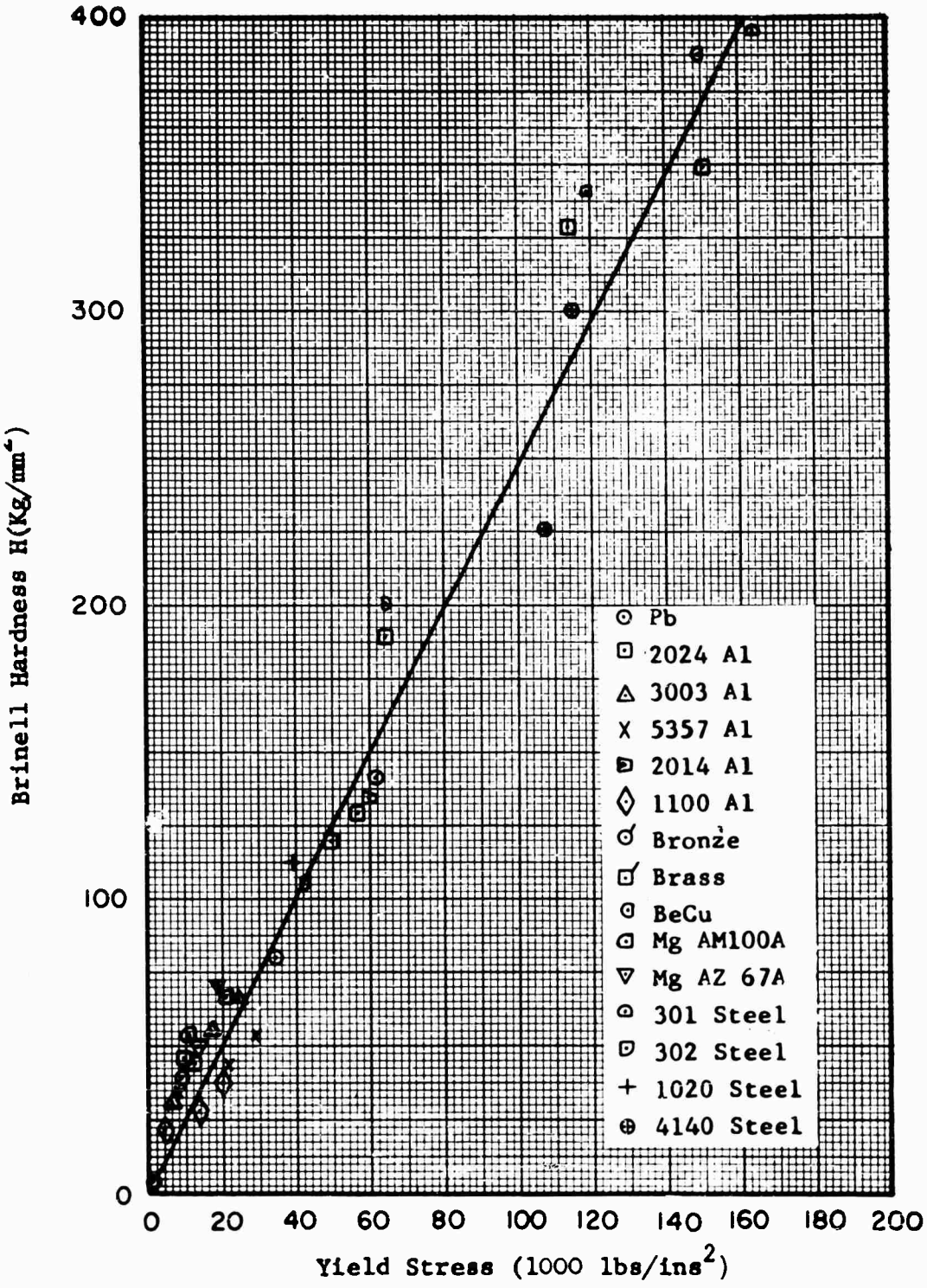

Fig. 7 Brinell Hardness versus Yield Strength for a Number of Representative Target Materials

TABLE III POSTULATED EMPIRICAL EQUATIONS

PENETRATION LAW	TARGET	PROJECTILE	SHAPE	SIZE	VELOCITY	INVESTIGATOR
$T = \left(\frac{3K_1K_2}{2\nu}\right) v_p^{1/3} \left(\frac{\rho_p}{\rho_t}\right)^{1/3} \left(\frac{V}{c_t}\right) \frac{1}{(3-K_2 V/c_t)}$	ALUMINUM WAX (10°C) BRASS LEAD MAGNESIUM STEEL ZINC	ALUMINUM BRASS LEAD MAGNESIUM STEEL ZINC	SPHERES	$\frac{1}{8}$"	$\frac{V}{c_t} \ll 1$	VAN VALKENBURG et al
$\frac{P}{d} = 2.5 \left(\frac{V}{c_t}\right)^{1.4}$	ALUMINUM BRASS LEAD MAGNESIUM MAGNESIUM - LITHIUM LEAD	ALUMINUM BRASS LEAD MAGNESIUM MAGNESIUM - LITHIUM LEAD	SPHERES CYLINDERS	$\frac{1}{8}$"	$0.1 \leq \frac{V}{c_t} \leq 1.0$	HUTH et al
$p = 1.25 \frac{m_p^{1/3} v^{1/3}}{\rho_t^{1/3} H^{1/4}}$	ALUMINUM BRASS BRONZE COPPER MALLORY STEEL TITANIUM	———	JET	———	10,540 f.p.s.	PUSH AND FICHELBERGER
	LEAD	STEEL	DISC	———	1300 to 8400 f.p.s.	RINEHR
$\bar{p} = \frac{V_p (1 - e^{-K_0 E})}{K_1 K_2 (2 m_p E)^{1/2} + K_0}$	LEAD	LEAD	SPHERES	$\frac{1}{8}$" $\frac{3}{16}$" $\frac{3}{8}$"	< 9800 f.p.s	VANFLEET et al
$\bar{p} = K m_p^{1/3} \frac{(V - V_0)}{c_t}$ $\frac{V_0}{c_t} < \frac{V}{c_t} < 2$	WAX (23°C)	WAX (4°C)	SKHERES CYLINDERS	0.177 ins d=0.22 ins L=0.33 ins d=0.22 ins L=0.388 ins	$0.5 < \frac{V}{c_t} < 2.2$	PARTRIDGE AND CLAY
$\frac{P}{d} = K \left(\frac{V}{c_p}\right)^{c_p/c_p}$	ALUMINUM COPPER LEAD STEEL TIN	ALUMINUM COPPER MALLORY 1000 STEEL	FRAGMENTS	———	1000 to 6000 f.p.s	McKERRIE et al
$\frac{P}{d} = \frac{7.2 c_p \rho_p}{c_t \rho_t + c_p \rho_p} \left(\frac{V}{c_p}\right)$ $\frac{-136.8 V_t \rho_p^{1/3}}{c_t \rho_t^{1/3}}$ 1.5 d≤ target thickness≤ 5d	ALUMINUM 1100 ALUMINUM 2024-0 COPPER LEAD STEEL ALUMINUM 2024-0 COPPER LEAD ALUMINUM COPPER IRON LEAD ZINC	MERCURY WATER ALUMINUM COPPER IRON LEAD ZINC	SPHERES	———	< 6500 f.p.s	ZABEL
$\frac{P}{d} = 2.28 \left(\frac{\rho_p}{\rho_t}\right)^{2/3} \left(\frac{V}{c_t}\right)^{2/3}$	COPPER LEAD	ALUMINUM COPPER LEAD MAGNESIUM - LITHIUM STEEL TUNGSTEN	SKHERES	0.125", 0.178" 0.125", 0.119" 0.125", 0.109" 0.125", 0.218" 0.125", 0.125" 0.125", 0.098"	$\leq 11,000$ f.p.s	CHARTERS AND LOCKE
	ALUMINUM MAGNESIUM NICKEL POLYETHYLENE STAINLESS - STEEL	STAINLESS STEEL	MICROPARTICLES	100Å AND 190μ	2,500 - 15,000 f.p.s	SHOEMAKER
$\frac{K}{d} = 1.8 \left(\frac{\rho_p}{\rho_t}\right) \left(\frac{V}{c_t}\right)$	ALUMINUM STEEL STEEL	ALUMINUM MAGNESIUM	SKHERES	0.2", 0.4"	$\leq 17,700$ f.p.s	BAUER et al
$\frac{P}{d} = 2 \left(\frac{V}{c_t}\right)^{2/3}$	STEEL	STEEL	SPHERES	0.2"		
$\frac{P}{d} = 2.8 \left(\frac{\rho_p}{\rho_t}\right)^{0.6} \left(\frac{V}{c_t}\right)^{0.7}$	COPPER LEAD	ALUMINUM	SPHERES	0.2", 0.4"		
$p = \frac{308.8 (\rho_p V L \cdot K)}{(A_p)^{0.875} (c_t + 2.8 \times 10^5)^{0.75}}$	ALUMINUM COPPER LEAD STEEL	ALUMINUM COPPER LEAD STEEL	SPHERES CYLINDER L/d=11	0.0580" 0.232" 0.580" 0.232" 0.580"	≤ 13000 f.p.s	COLLINS AND KINARD
$p = \frac{K}{2} m_p^{1/3} v^{2/3}$	CADMIUM COPPER LEAD ZINC	———	———	———	———	A K L
$K = \left(\frac{3}{4\pi\alpha}\right)^{1/3} \frac{\alpha_K^{1/3} v^{2/3}}{H^{1/3}}$	ALUMINUM COPPER STEEL	———	———	———	———	H K L

together with materials and velocity ranges for which they have been used.

Those expressions which are dimensionally correct are mostly in the form of a simple power law

$$\frac{p}{d} = k K^i M^j B^k \tag{8}$$

where k is a constant.

In particular, the expression introduced by Charters and Locke [12]

$$\frac{p}{d} = k K^{2/3} M^{2/3} \tag{9}$$

and that in use at the Naval Research Laboratory [13], which is in effect

$$\frac{p}{d} = k K^{1/3} B^{1/3} \tag{10}$$

have been used extensively.

A simple power law such as Eq. (9) or (10) which has the general form

$$\frac{p}{d} = k V^m \tag{11}$$

may be derived by assuming that the resistance force on the projectile is of form

$$F \propto x^n \tag{12}$$

where x is the instantaneous distance of the projectile below the target surface. By inserting Eq. (12) into the equation of motion Eq. (4) and integrating, it may be verified that the result is equivalent to Eq. (11) with $n = (2/m - 1)$.

Early empirical fits to armor penetration data at very low velocities were found to have a velocity exponent m in Eq. (11) near 2. Thus $n = 0$, and the resistance force is in effect assumed to be independent of depth. Later work at higher velocities indicated that penetration was proportional to $V^{4/3}$ or $n = 1/2$. High velocity experiments can be fitted by a velocity exponent of 2/3, implying $n = 2$. Now in actual fact, the projectile is known to deform at high striking velocities, in effect increasing its presented area as the penetration proceeds. This effect is neglected in the simple reasoning used above. Thus it seems that the effect of projectile deformation appears as an increase in exponent n in Eq. (12).

At the highest experimental velocities, the projectile in fact appears to flow very much like a liquid over the surface of the crater, which is observed to be nearly hemispherical. Assuming the projectile to be an incompressible liquid, and crater expansion to be hemispherical, leads, on assuming the pressure between

the projectile and target to be a constant k, to an approximate expression for the force resisting motion

$$F = k\, 2\pi x^2$$

which on integration leads to an exponent $m = 2/3$ in Eq. (11).

The assumption that the pressure between the projectile and target is constant during the motion is hardly justified, since the projectile decelerates, eventually coming to rest, at which time the retardation force may be expected to be zero. Thus, an assumption which may be made is that the force resisting motion depends on the instantaneous projectile velocity v.

$$F = k_1\, \rho_t\, v^2 \tag{13}$$

A force of this type would be encountered by a rigid projectile moving through a non-viscous liquid of density ρ_t. Integration of the equation of motion Eq. (4) between limits $x=0$, $v=V$; $x=p$, $v=0$ then leads to an expression of the form

$$\frac{p}{d} = k\, K \log_e V \tag{14}$$

A logarithmic function has the interesting property that it may be approximated by functions of the form of Eq. (11) over limited ranges of the variable V, the exponent of m decreasing as V increases. One might therefore suppose that a suitable logarithmic expression might prove useful for empirical fits to penetration data over a wider range in velocity than may be fitted by a simple power law.

When the velocity of the projectile becomes very low, the resistance force does not become vanishingly small since the material is a solid. This may be introduced in a number of different ways. Following shaped charge jet theory, the limits of integration of the equation of motion may be altered to $x=0$, $v=V$; $x=p$, $v=v_o$ where v_o is the velocity below which no target deformation will be produced. The corresponding stress $(1/2\, \rho_t v_o^2)$ may be assumed to be proportional to the yield strength of the target, or by Eq. (6) to the Brinell Hardness, i.e.,

$$\rho_t v^2 = k_2 H_t$$

This then leads to a penetration law of the form

$$\frac{p}{d} = k_1 K \log_e \left(\frac{B}{k_2}\right)^{1/2} \tag{15}$$

Alternatively, this effect may be accounted for as follows. Under static deformation, the resistance force may be assumed to be related to the Brinell Hardness of the target. Thus the resistance force may be approximated by

$$F = \pi/4 \; d^2 \, k_1 (\rho_1 v^2 + k_2 H_1) \tag{16}$$

which on integration of the equation of motion Eq. (4) leads to a penetration law

$$\frac{p}{d} = \frac{1}{6k_1} \mathbb{K} \log_e \left\{ 1 + \frac{B}{k_2} \right\} \tag{17}$$

Bohn and Fuchs used a slight modification of Eq. (16) to obtain their equation (Eq 5).

The behaviour of Eq. (15), (17), and (5) may be graphically illustrated by plotting the corresponding functions

$$\frac{p}{d} = k \log_e \xi \tag{18}$$

$$\frac{p}{d} = k \log_e (1 + \xi^2) \tag{19}$$

$$\frac{p}{d} = k \left\{ \log_e (1 + \xi) + \frac{\xi}{1 + \xi} \right\} \tag{20}$$

using logarithmic coordinates. (Fig. 8) Straight lines on this plot then represent an equation

$$\frac{p}{d} = k \xi^m \tag{21}$$

with the slope of the line corresponding to the exponent m. The functions can be made to coincide over a wide range in variable x by suitable adjustment of the constants k in Eq. (18) through (20) above. In particular Eq. (19) and (20) may be made to almost coincide over a range over which the curves can be approximated by Eq. (21) with m from 2 to about 2/3. Thus, they may be equally suitable for empirical correlation purposes. Equation (17), corresponding to Eq. (19) was somewhat arbitrarily chosen for use in the present study.

Actually Eq. (17) must at this point be considered simply as a convenient two-parameter empirical expression, since clearly neither realistic compressibilities of the materials involved, nor realistic flow geometries, have been introduced into its derivation. The same must be said of Eq. (11).

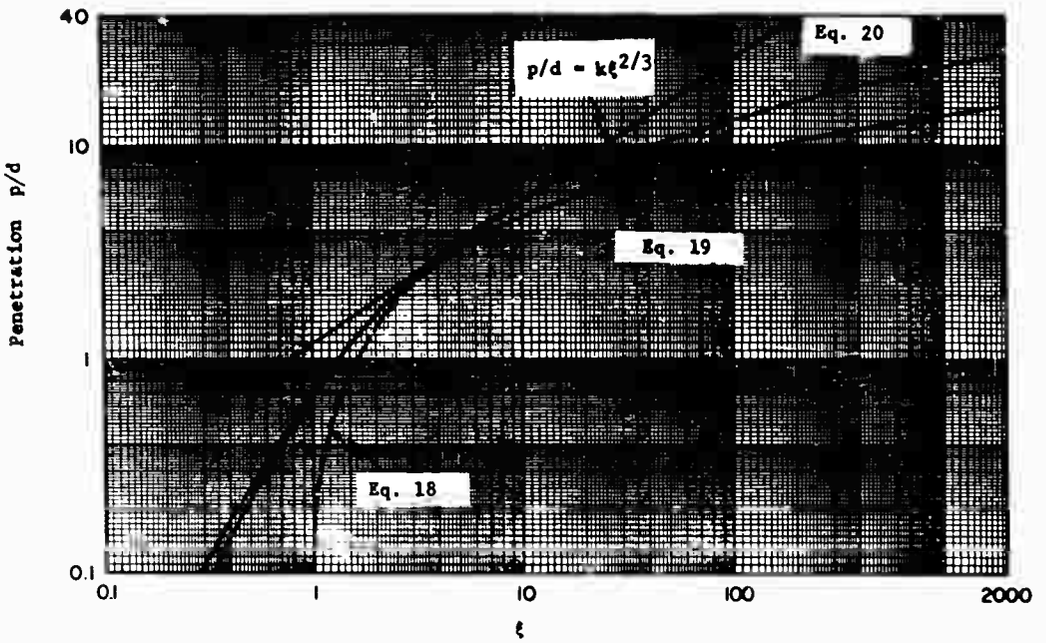

Fig. 8 Behaviour of Logarithmic Penetration Laws

The fit of the data to empirical expressions of the form Eq. (11) and (19) are investigated in the following.

5. EMPIRICAL POWER LAW

The dependence of penetration on velocity is best illustrated by log-log plots. Figure 9 illustrates the behaviour for copper targets struck by ductile projectiles. The penetration may be seen to be approximately proportional to $V^{4/3}$ at low velocities, and $V^{2/3}$ at high velocities, with a smooth transition between these regions. The region in which the penetration is nearly proportional to $V^{4/3}$ will be here arbitrarily defined as the low velocity region. Within this region, projectiles generally suffer relatively minor deformation, and craters are generally observed to be almost cylindrical or conical, without excessive inertial expansion of the sides of the crater. The region in which the penetration is nearly proportional to $V^{2/3}$ will be here arbitrarily defined as the high velocity region. Within this region the projectile suffers major deformation, and the crater is observed to expand laterally to a nearly hemispherical shape. The intermediate region will be referred to as the transition region, within which the flow changes character from low velocity behaviour to high velocity behaviour.

Figure 10 illustrates the behaviour for copper targets struck by brittle, high-strength projectiles. The low velocity region is extended to higher velocities than in the previous case. At the onset of the transition region the projectile is observed to fragment into several pieces, which separate during the penetration to effectively increase the presented area of the projectile. This generally results in an abrupt reduction in penetration. At higher velocities, the projectile is observed to fragment into many small pieces, and the flow approximates normal ductile projectile transition behaviour. The high velocity region is similar to that for ductile projectiles.

It was desired to investigate the fit of Eq. (11) to data in the high velocity region, and in particular to investigate the dependence of the proportionality constant on material properties. Sufficient data existed so that the dependence of the constant on each parameter could be investigated separately.

In particular, numerous sets of firings were reported in which closely similar target materials were used, but different projectile materials were used. In particular three studies were reported in which steel projectiles heat treated to different hardnesses were employed with identical target materials. Maiden (Ref. 14) reported penetration in 1030 steel targets by steel spheres heat treated to a Brinell Hardness of 210, 290 and 580. The data was in the high velocity region, and no effect due to projectile strength was apparent. Blake, Grow and Palmer (Ref. 15) report penetration by two types of stainless steel spheres in lead targets with Brinell Hardness of 155 and about 400 (handbook values) respectively in lead targets. While large differences are evident in the transition region, no effect due to projectile strength may be seen in the high velocity region. Abbot (Ref. 16) has reported penetration in hard 30 RC steel targets by steel projectiles heat treated to a Brinell Hardness of 140 and 705 respectively. Small differences appear in the penetration by the two types of projectile up to the highest velocity explored, but all of the data lie in the transition region. While the above evidence is hardly conclusive, these firings would seem to represent extreme cases of

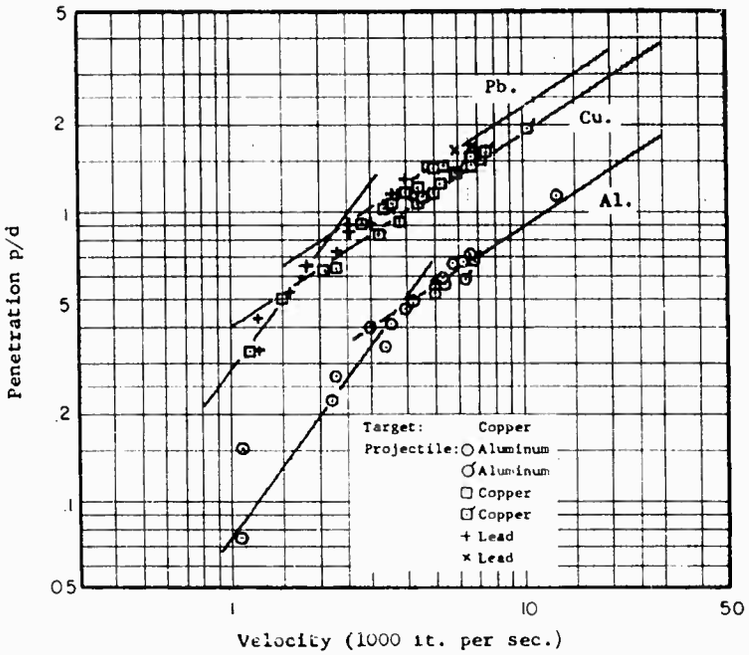

Fig. 9 Penetration in Copper Targets

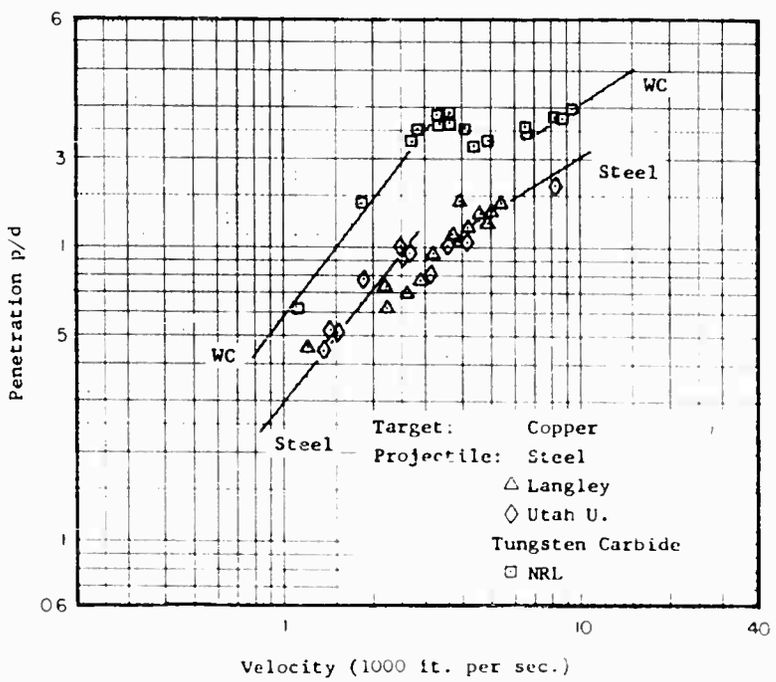

Fig. 10 Penetration in Copper Targets

projectile strength variation, and it might be assumed that projectile strength does not affect the data in the high velocity region.

The only other parameter to account for variation of penetration by different projectiles is the projectile density. By fitting straight lines to the high velocity data on log-log plots of the type of Figures 9 and 10, for numerous target materials struck by a large number of different projectile materials, it was found that the proportionality constant for each target material was very nearly proportional to the projectile density to the 2/3 power, a fact first observed by Charters and Locke (Ref. 12).

In order to confirm the penetration dependence on $(\rho_p V)^{2/3}$ in the high velocity region, and to obtain reliable values of the proportionality constants for each target material, the following procedure was adopted. Linear large scale plots of

$$\pi = \frac{(p/d)}{(\rho_p V)^{2/3}}$$

versus velocity were prepared. If the expression

$$\frac{p}{d} = k_1 \rho_p^{2/3} V^{2/3} \tag{22}$$

fitted the data, then the resultant points should form a straight line as in Figure 11(a). Actually, since a different velocity exponent fitted the data in the low velocity and transition region, the plots would be expected to appear as in Figure 11(b), and the proportionality constant should be obtainable from the straight line portion of the curve. The velocity at which the curve became horizontal would represent the lower limit of the high velocity region, for that material combination. If a density exponent other than 2/3 fitted the data, the curves for different projectile materials should separate, as in Figure 11(c).

Examples of actual data plots for 2024-T3 aluminum, half hard copper, and lead targets are shown in Figures 12, 13 and 14. While the data points in the horizontal portions of the curve largely represent firings with aluminum projectiles, the curves for other projectile materials do converge to the same value of k_1, confirming the dependence of penetration on $\rho_p^{2/3}$. Only very rough values of limiting velocities could be obtained, but the value of k_1 corresponding to the horizontal portions of the curves could be obtained quite accurately for several target materials. Least squares fits of the values of k_1, together with standard mean deviations, were obtained, using experimental points for velocities above the estimated limiting velocity for each material combination. These are listed in Table IV.

The effects of target strength could be determined separately, since values of k_1 could be determined for several types of aluminum, copper and steel targets, which varied in hardness, but had closely similar densities and sonic velocities. Values of k_1 found above were plotted versus the target hardness H_t on log-log paper, Figure 15. The uncertainty flags represent standard mean deviations in k_1 and uncertainties in H_t. It may be seen that the points for each target material may be approximately fitted with a line of slope -1/3, within the uncertainty in the data, indicating a dependence of the form

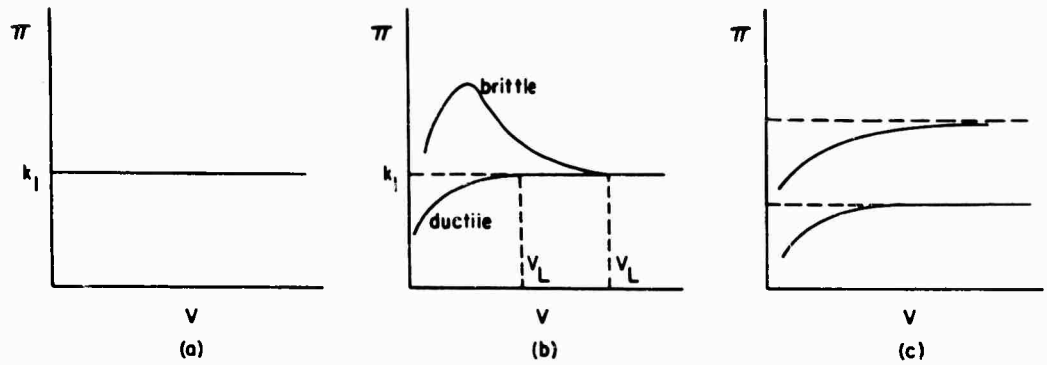

Fig.11 Description of Projectile Behavior

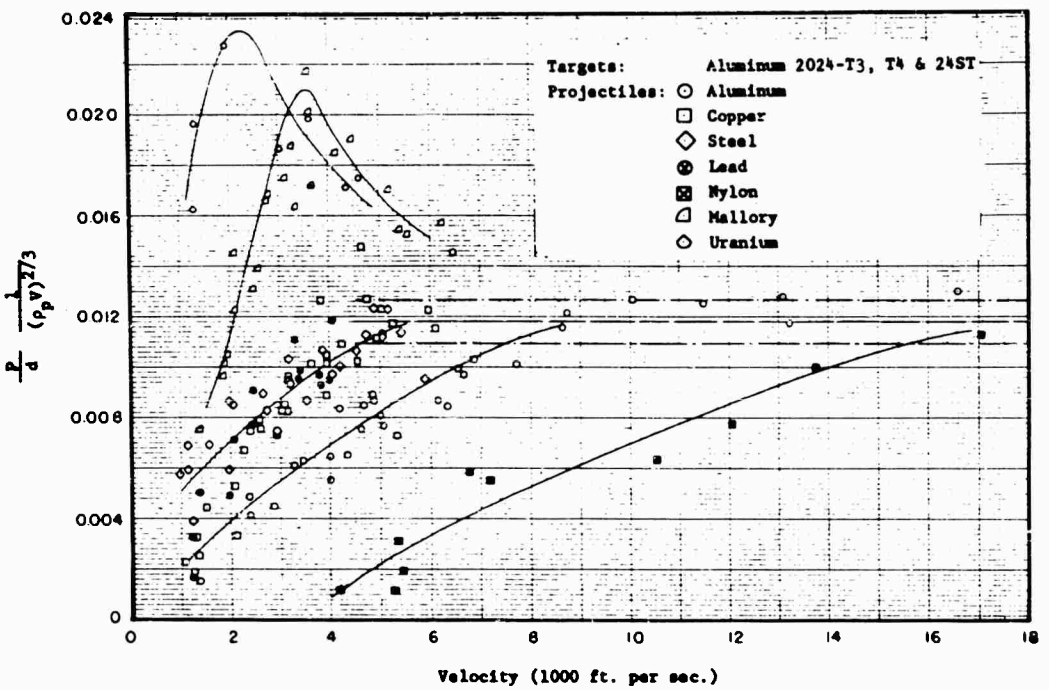

Fig. 12 Penetration Ratio in Aluminum Targets

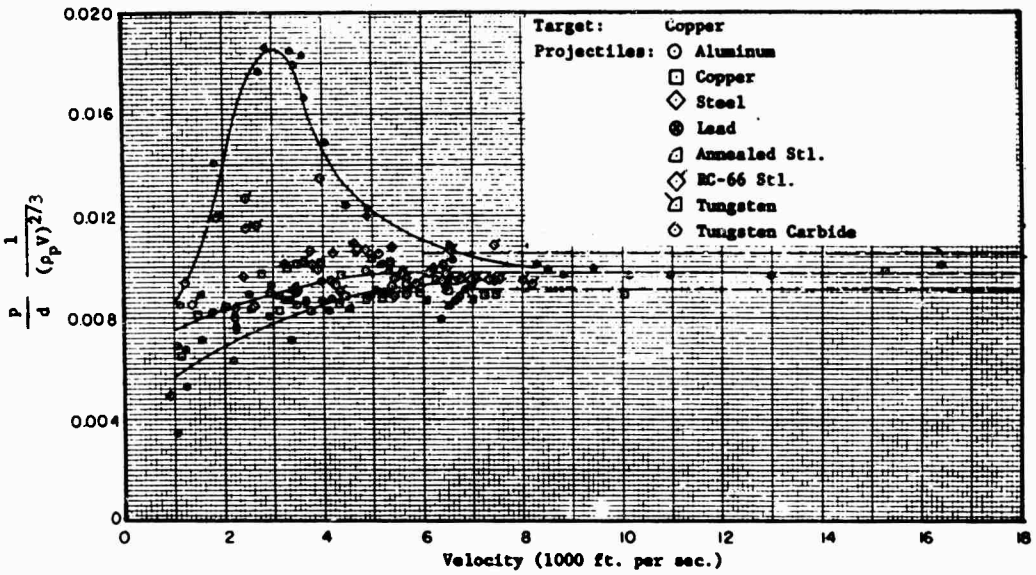

Fig. 13 Penetration Ratio in Copper Targets

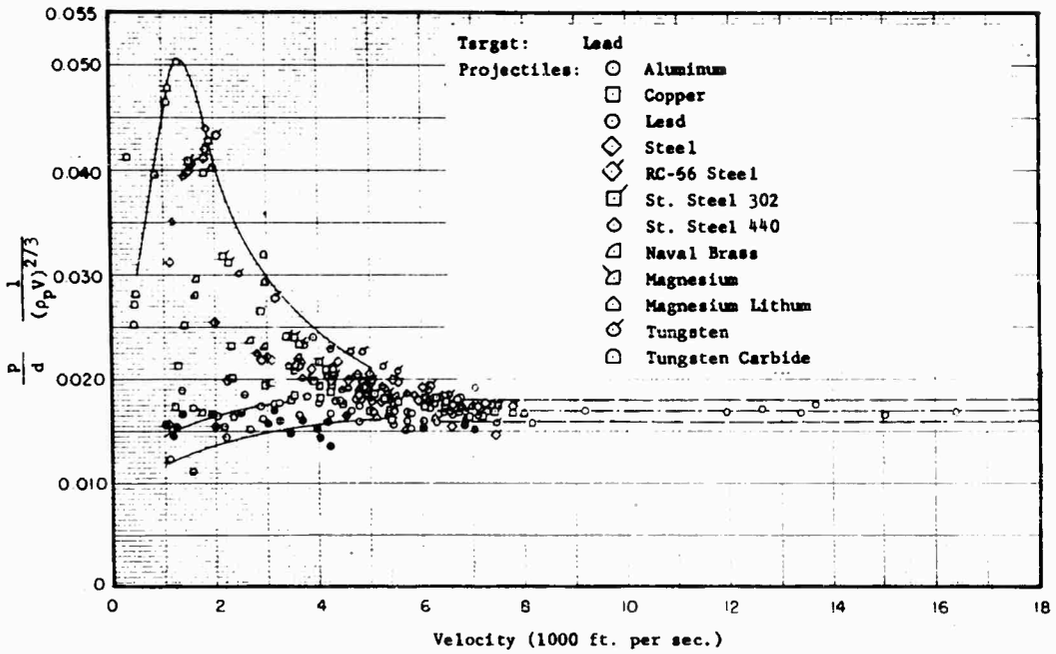

Fig. 14 : Penetration Ratio in Lead Targets

TABLE IV

EMPIRICAL FITS TO THE PENETRATION LAW

$$\frac{p}{d} = k \left(\frac{\rho_p}{\rho_t}\right)^{2/3} \left(\frac{\rho_t V^2}{H_t}\right)^{1/3}$$

Target	ρ_t (gm/cc)	H_t (kg/mm^2)	Max. Vel. (km/sec)	$k = \left(\frac{\rho_t}{\rho_p}\right)^{2/3} \left(\frac{H_t}{\rho_t V^2}\right)^{1/3} \left(\frac{p}{d}\right)$
Al. 1100F	2.79	*	4.37	
Al. 2024 & 24ST	2.68	114-120	3.98	0.413 ± 0.007
Cu. (36)	8.88	36	3.33	0.366 ± 0.009
Cu. (65)	8.88	65	5.27	0.419 ± 0.031
Pb.	11.34	4	5.00	0.312 ± 0.020
Stl. 1020	7.69	111	3.95	0.378 ± 0.010
Stl. 1030	7.69	123	3.96	0.371 ± 0.012
Stl. 30 RC	7.74	302	3.52	0.279 ± 0.004
Cd.	8.66	23	5.01	0.309 ± 0.046
Ag.	10.45	*	2.54	*
Zn.	7.13	45	2.51	0.371 ± 0.014

*H_t for these materials is unknown. The values of $k/H_t^{1/3}$ for these are: (i) 1100F Al. target, $(0.257 \pm 0.008) \times 10^{-3}$ cm/dyne$^{1/3}$, and (ii) Ag. target $(0.277 \pm 0.024) \times 10^{-3}$ cm/dyne$^{1/3}$.

Fig. 15 Penetration Dependence on Target Hardness

$$\frac{p}{d} = k_2 \frac{\rho^{2/3} V^{2/3}}{H_t^{1/3}} \tag{23}$$

Values of k_2 were computed from values of k_1 listed in Table IV by $k_2 = H_t^{1/3} k_1$, uncertainty intervals in k_2 being obtained from a combination of standard mean deviations in k_1 and uncertainties in H_t.

No correlation of k_2 with sonic velocities could be found. However k_2 could be approximately correlated with target density. From Figure 16, the slope of the logarithmic plot of k_2 versus ρ_t is seen to be close to $-1/3$, leading to an approximate empirical penetration law

$$\frac{p}{d} = (0.36 \pm 0.06) K^{2/3} B^{1/3} \tag{24}$$

The maximum and minimum values of the proportionality constant above correspond to the two extreme lines drawn on Figure 16. The correlation is clearly not very exact. The uncertainty indicated in Eq. (24) above would seem reasonable, but some material combinations may deviate from the mean value by as much as 25 percent.

Some interesting trends appear from plots such as Figures 12, 13, and 14. The lower velocity limit of the high velocity region is dependent on both projectile and target material. For example, the points for nylon projectiles striking aluminum targets in Figure 12 indicate that the high velocity region is not attained until a velocity of at least 17,000 ft/sec is approached.

The stresses induced in the target are a function of projectile velocity. A convenient measure of the magnitude of the average stress is the initial stress induced on first contact of the projectile on the target.

The initial maximum pressure, generated on first contact of the projectile and target, may be estimated quite accurately from one-dimensional shock theory. Based on the experimental observation that the shock velocity U and material velocity V^* behind the shock are very nearly related linearly

$$U = c + SV^* \tag{25}$$

the shock relation

$$P^* = \rho V^* U \tag{26}$$

where P^* is the pressure behind the shock, may be applied to the shock proceeding into the target and the shock receding back into the projectile, to provide two simultaneous equations for P^* and V^*

$$P^* = \rho_t V^* (c_t + S_t V^*)$$
$$P^* = \rho_p (V - V^*) \left[c_p + S_p (V - V^*) \right] \tag{27}$$

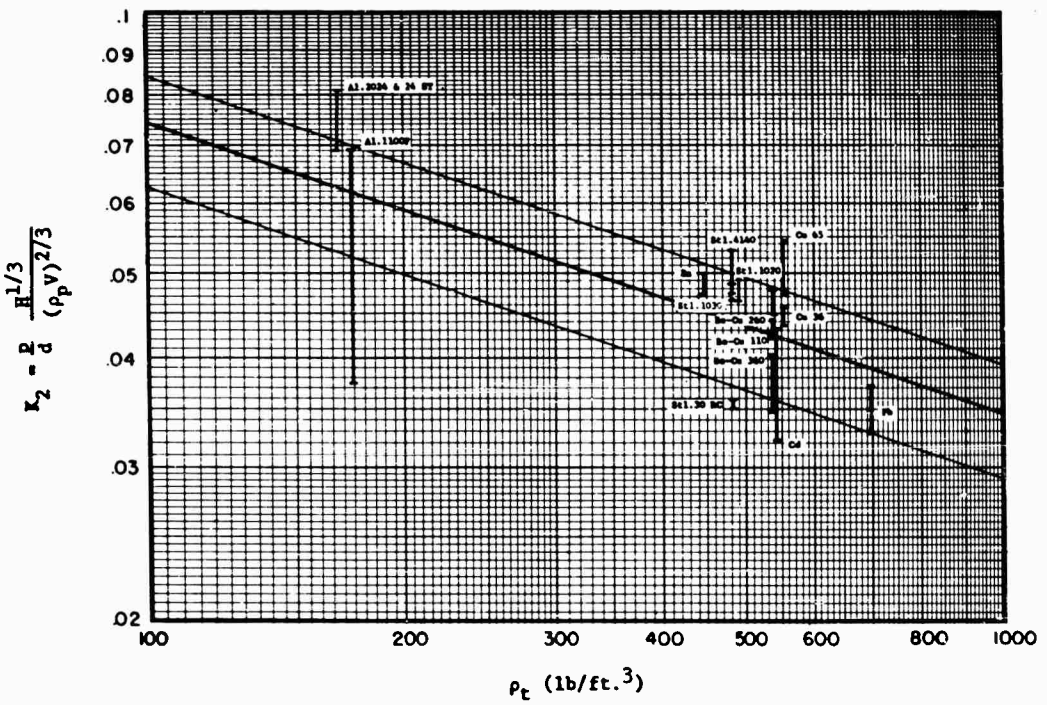

Fig. 16 Penetration Dependence on Target Density

where V is the initial projectile velocity. Analytical solution is diffieult, but a simple graphical method may be used for rapidly finding P^* and V^*. However, it has been observed that for velocities above 10,000 ft/sec, V^* is very nearly a linear function of V, and may be approximated by

$$V^* \approx 1/2\ K^{1/3} V \tag{28}$$

leading to an expression for the initial maximum pressure generated by the impact

$$P^* \approx 1/2\ K^{1/3} \rho_t c_t V + 1/4\ S_t K^{2/3} \rho_t V^2 \tag{29}$$

The maximum error involved in this approximation is about 20 percent.

At low velocities, the initial pressure will be comparable to the yield strength of the material. Thus the target material strength, which tends to inhibit the penetration, becomes relatively more important at lower velocities, until at some very low velocity, the initial stress will be less than the yield strength of the target material, and no permanent deformation will result. This effect reduces the penetration predicted by Eq. (24), at low velocities.

Equation (24) shows that the initial induced pressure is a function of the density ratio. Thus, the maximum pressure induced in the target by a low density projectile is much less than that induced by a high density projectile at the same velocity. In the transition region therefore, at a particular projectile velocity, one might expect that the effects of material strength in inhibiting the crater formation will be much greater in the case of low density projectiles, thus leading to the type of behaviour observed in Figures 12, 13 and 14.

Howevcr, at the same time, there will be an effect on the projectile. In the transition region, the shock in the projectile generally rises above the level of the original target surface. Since the sides of the shocked zone are unsupported, the projectile material will be forced to flow laterally, this motion being inhibited by the material strength. In the case of a nylon projectile, although the initial pressure induced by the impact is relatively low, the material has very low strength, and considerable lateral flow of the projectile may be expected, with consequent increase in presented area and decrease in penetration. On the other hand, although the initial pressure induced by a uranium or tungsten projectile will be very much higher at the same velocity, these materials have relatively high strength, and not too much lateral flow may be expected.

These transition region strength effects may be expected to become unimportant when the initial induced pressure is very much higher than the yield stress of the material. By examining the lower limiting velocities of the high velocity region, estimated from plots such as Figures 12, 13 and 14, it was found that the limit $P^* > 100 Y_t$, where Y_t is the static yield strength of the target, seemed to be reasonable. Making use of Eq. (6), the lower limit of the high velocity region is then approximately

$$\frac{P^*}{H_t} > 30 \tag{30}$$

For high strength projectiles showing "brittle" projectile behaviour, the limit Eq (30) was found to be too low. Unfortunately strengths of projectiles have almost never been reported. One piece of information due to Blake, Grow and Palmer (Ref. 15), for stainless steel projectiles shot into lead targets, indicates that an extension of Eq. (30) may be adequate,

$$\frac{P^*}{H_p} > 30 \qquad (31)$$

The lower limit then corresponds to the maximum of the two velocities given by Eq. (30) and (31).

Nothing can be said at this point about the upper velocity limit of the high velocity region, the highest velocity data considered in the study showing a penetration dependence on $V^{2/3}$, and speculation on this matter will be deferred to a later section.

Crater diameters, measured in the plane of the original target surface, have been reported for a large number of experiments. The ratio p/D_c, which may be regarded as a crater shape parameter, was plotted versus velocity, in order to determine crater shapes in the high velocity region. Examples are shown in Figures 17 and 18 for copper and lead targets respectively. Numerous authors have noted the trend for the shape parameter to tend to 1/2 in the high velocity region, indicating that the crater had become nearly hemispherical.

However, it is apparent from Figures 17 and 18 that this is not true of all material combinations. Craters formed by low density projectiles such as aluminum and magnesium were found to tend to a ratio p/D_c of about 0.4 in the high velocity region, indicating a crater somewhat shallower than hemispherical. In many target materials, it was also observed that tungsten and tungsten carbide projectiles lead to values of p/D_c of 0.6 or greater in the high velocity region, indicating craters deeper than hemispherical.

Measured crater volumes have also been reported for many of the experimental firings. Many authors have noted a tendency for the ratio of the projectile kinetic energy to the volume of the crater E/V_c to become approximately constant in the high velocity region. Plots of E/V_c versus velocity were prepared for each target material for which data existed. Examples are shown in Figures 19 and 20. While measurements were generally restricted to velocities bordering on the high velocity region, the trend for E/V_c to become a constant in the high velocity region did seem to be confirmed for those few material combinations for which high velocity data existed. Also evident was a trend for the asymptotic values of E/V_c to depend on projectile density, a fact first noted by Summers, (Ref. 17). This is clearly illustrated in Figure 20. Asymptotic values of E/V_c in the high velocity region were estimated from the data plots.

The dependence on projectile density could be estimated separately, since values of E/V_c could be estimated for several projectile materials in lead, copper, aluminum and steel targets. Values of E/V_c were plotted versus K on log-log paper (Fig. 21) from which it appeared that E/V_c was proportional to $K^{-2/3}$. Computed values of $EK^{2/3}/V_c$ were then plotted versus H_f (Fig. 22, note linear scale). The points indicated a rough proportionality with target

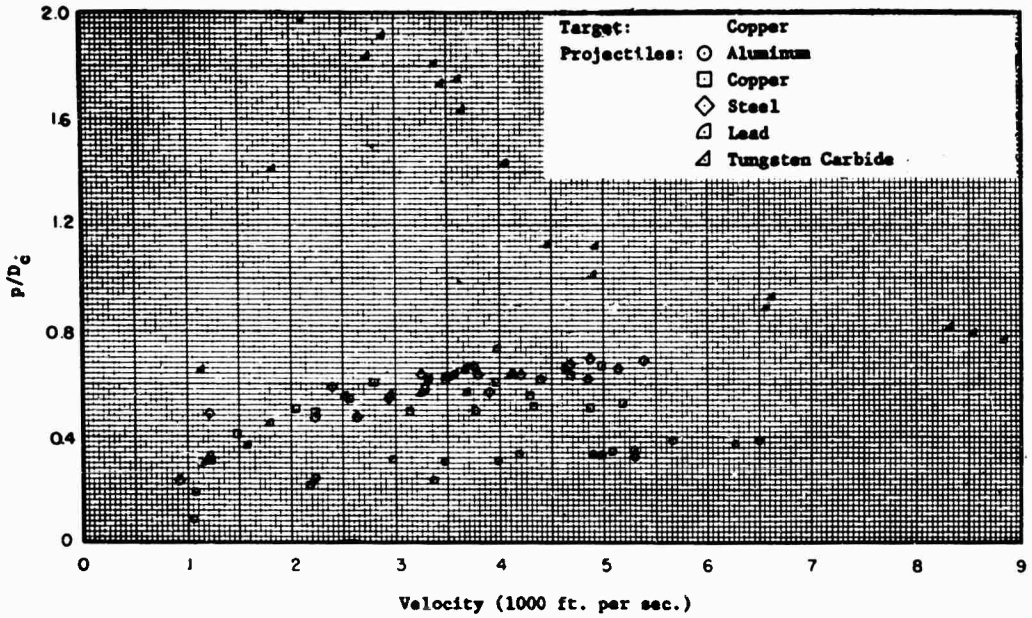

Fig. 17 Depth-Diameter Ratios for Craters in Copper Targets

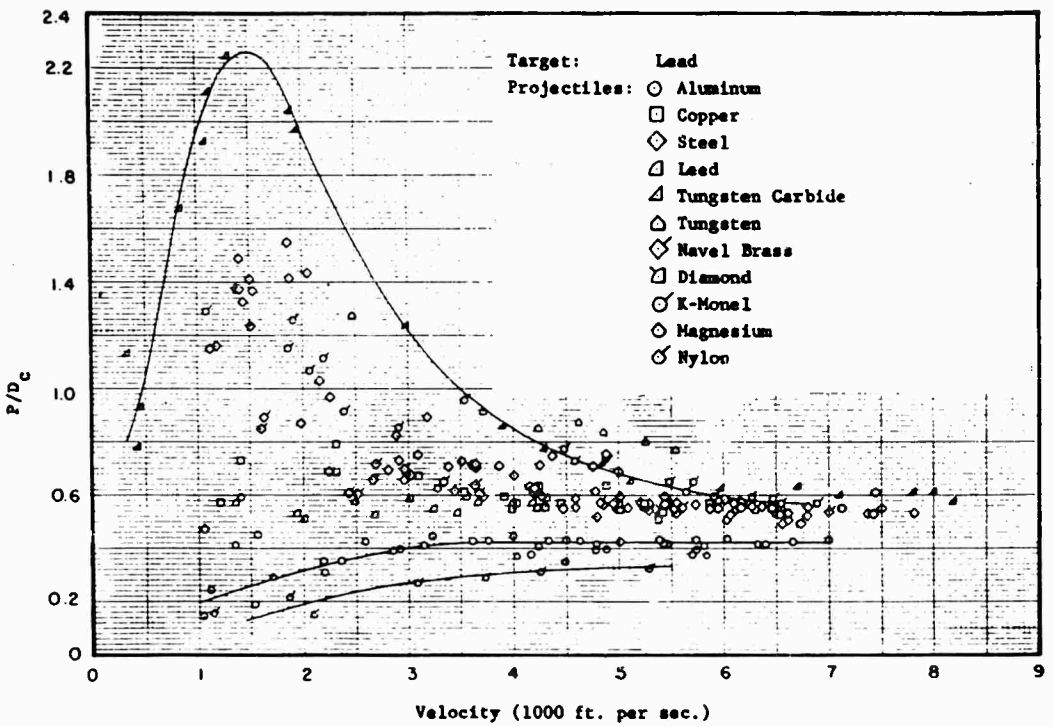

Fig. 18 Depth-Diameter Ratios for Craters in Lead Targets

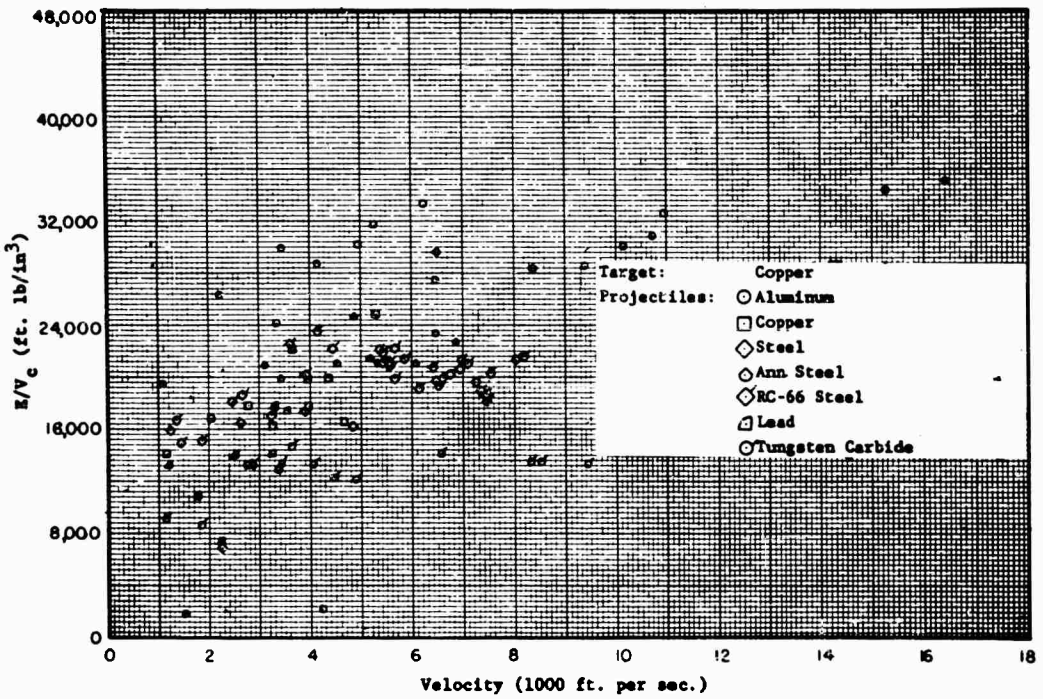

Fig. 19 Energy-Volume Ratios for Copper Targets

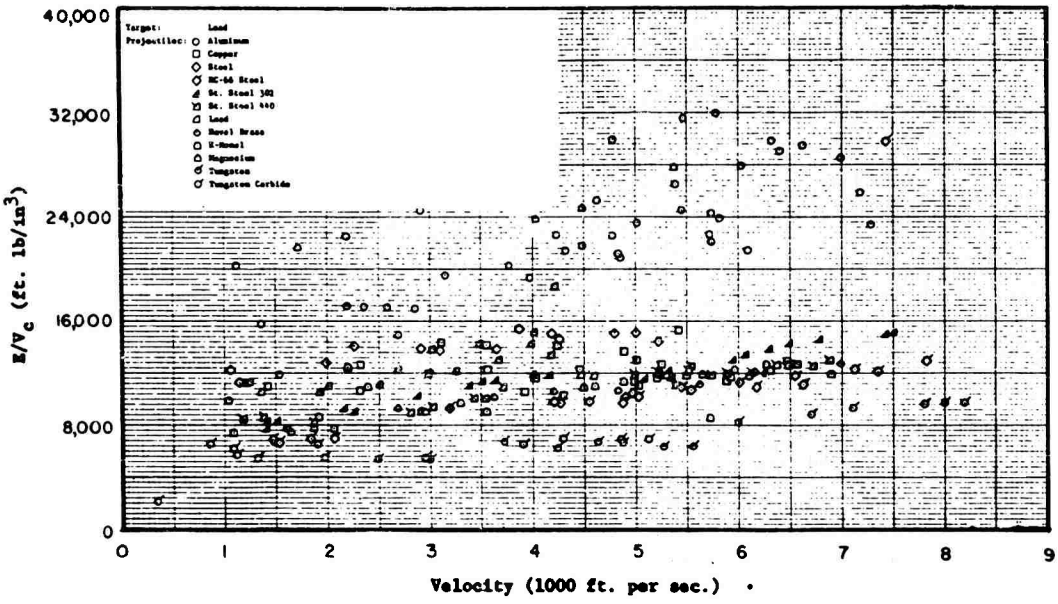

Fig. 20 Energy—Volume Ratios for Lead Targets

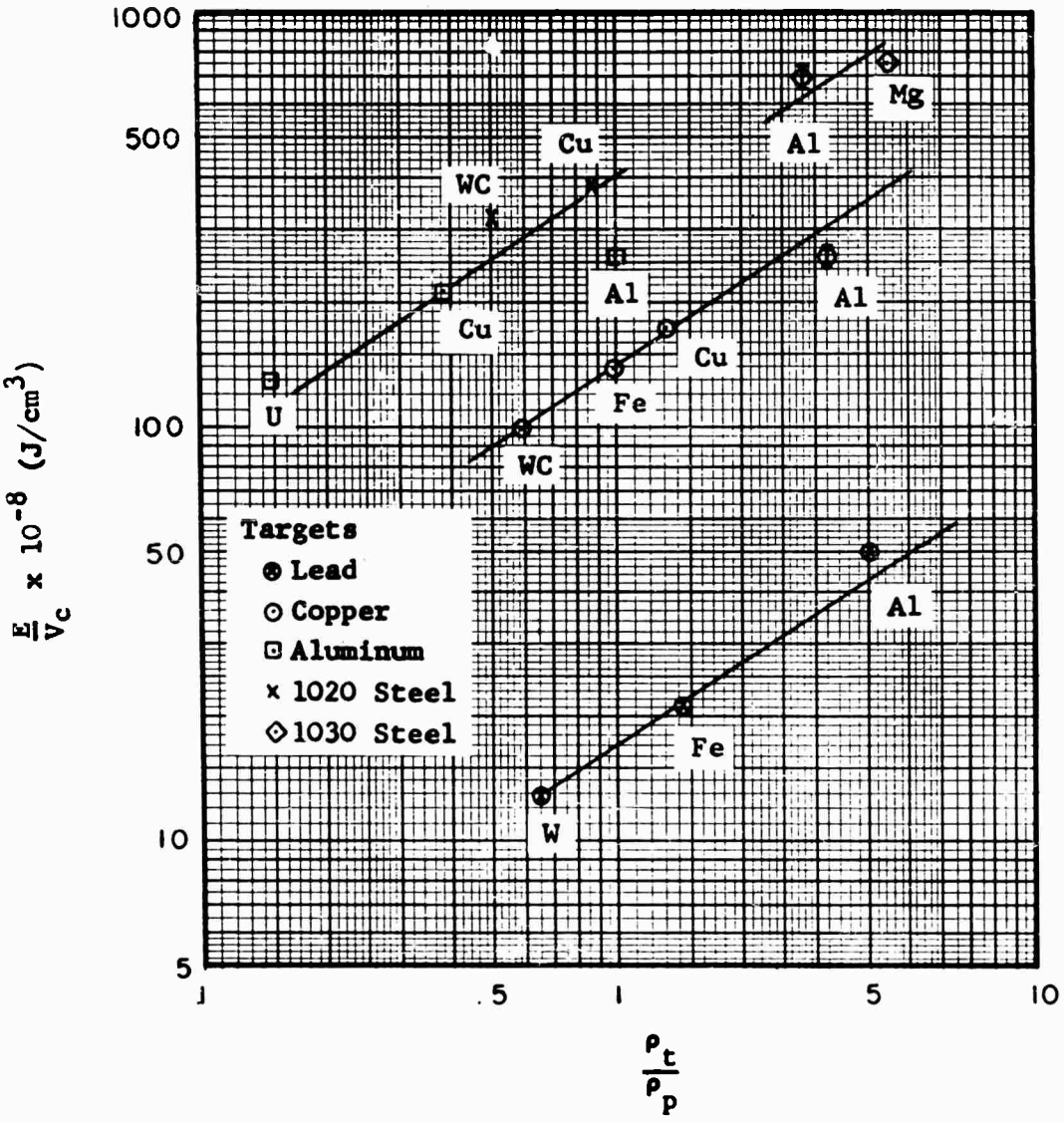

Fig. 21 **Energy-Volume Ratio Dependence on Density Ratio**

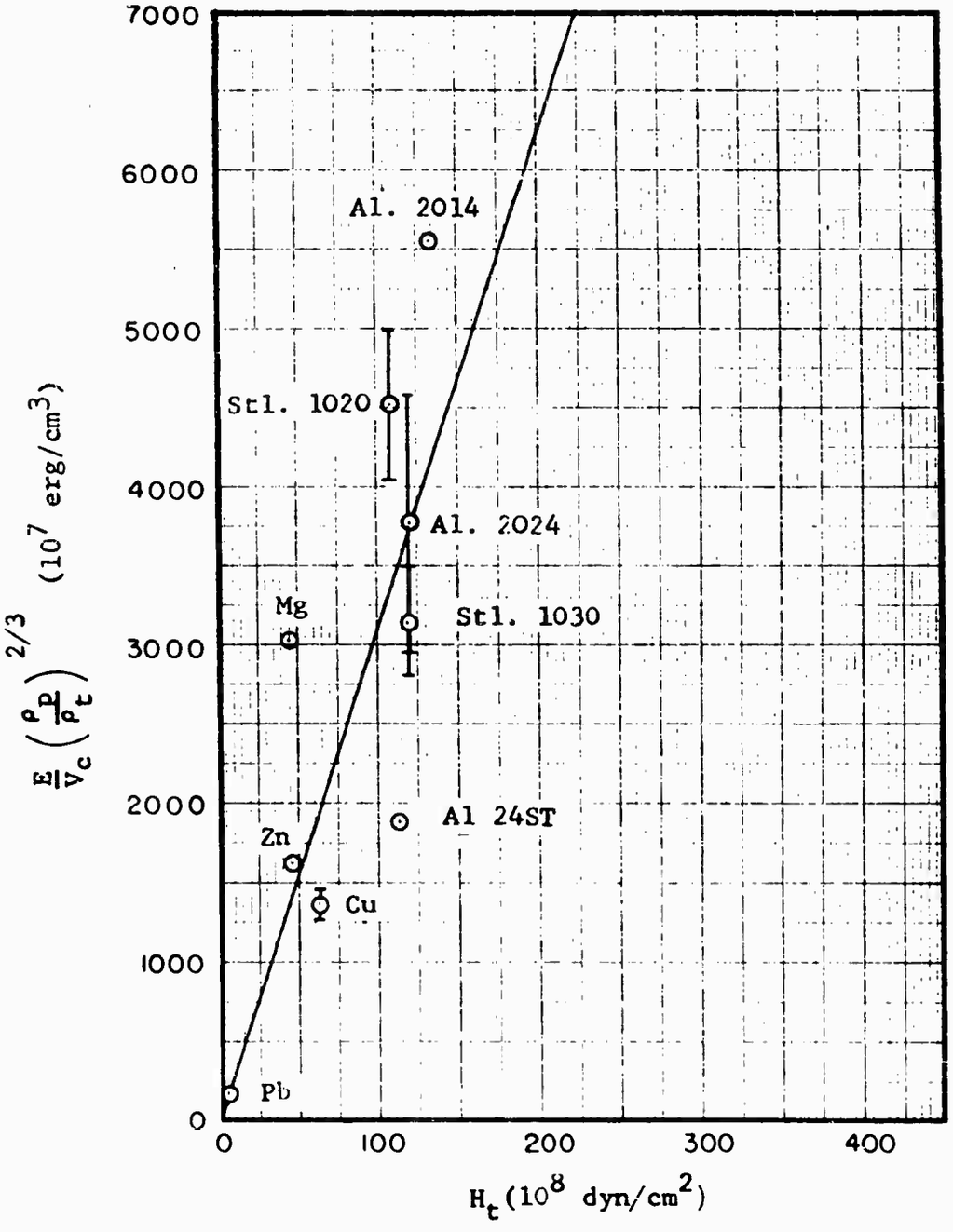

Fig. 22 Energy-Volume Ratio Dependence on Target

hardness, leading to a very rough correlation of the form

$$\frac{E}{V_c} = 3.1\, K^{-2/3} H_t \tag{32}$$

Some of the material combinations may show a deviation of as much as 50 percent from this law, but results for most of the material combinations may be expected to lie within $\pm$ 30 percent.

It is interesting to note that if craters are assumed to be hemispherical in the high velocity region, a law of the type Eq. (32) may be derived directly from Eq. (24) by noting that

$$E = \frac{1}{2}\,\frac{\pi}{6}\, d^3 \rho_p V^2$$

$$V_c = \frac{1}{2}\,\frac{4}{3}\,\pi\, \rho^3$$

resulting in an expression

$$\frac{E}{V_c} = 2.9\, K^{-1} H_t \tag{33}$$

This differs slightly from Eq. (32) in both constant and exponent in density ratio. The correlation of E / V_c with density ratio is quite good (Fig. 21). The fact, noted above, that craters formed by low density projectiles are shallower than hemispheres, and craters formed by high density projectiles are deeper than hemispheres, leads to the discrepancy. Thus the volume of craters formed by low density projectiles is underestimated by Eq. (33). It may be seen from Figure 21 that a reduced volume for a low density projectile and an increased volume for a high density projectile would lead to a higher negative exponent in K, as in Eq. (33).

The correlation equations Eq. (24) and Eq. (33) may be compared with previously published correlation expressions. Several empirical expressions in Table III are based on a penetration dependence on velocity to an exponent greater than 2/3. It may be concluded that these fits apply to data in the transition region. The fact that even approximate correlations could be obtained with elementary material properties must be attributed to the small range in materials considered in derivation of these expressions.

Attempts to fit the present data by expressions of the form Eq. (9) were unsuccessful. No provision for target strength variation is made in expressions of this type. The assumption that the effects of material strength are negligible in the high velocity region, has been shown to be erroneous. The fact that data for lead and half-hard copper targets could be correlated on the basis of Eq. (9) with identical constants must be considered fortuitous. Data for copper targets of much less or much greater hardness could not be correlated by Eq. (9) with the same value of the constant.

The expression Eq. (10) differs from Eq. (24) only in the value of the constant, and in exponent of the density ratio. Equation (10) was derived, on the

assumption that craters are hemispherical in the high velocity region, from the expression of Feldman (Ref. 18)

$$\frac{E}{V_c} = 2.65\, H_t \tag{34}$$

which may be compared to Eq. (32) derived here.

These also differ only in the value of the constant and in exponent of the density ratio. Attempts to fit the present data by Eq. (34) led to considerably increased scatter, indicating that Eq. (32) is preferable.

It is thus not surprising that Eq. (24) and Eq. (10) do not correspond. Attempts to fit the high velocity data by Eq. (10) by a method of least squares led to a considerably larger standard mean deviation than when Eq. (24) was used, indicating that the latter is preferable.

6. EMPIRICAL LOGARITHMIC LAW

Individual least squares fits were obtained to the experimental data for each projectile-target material combination, fitting k_1 and k_2 in the equation

$$\frac{p}{d} = k_1 \log_e\left\{1 + \frac{B}{k_2}\right\} \tag{35}$$

by using a standard iteration method on a high speed digital computer. Only materials exhibiting "ductile" behaviour were included, since for "brittle" projectile behaviour, the penetration is not a monotonic function of velocity, and thus could not be fitted by an equation of the type Eq. (35).

Results are tabulated in Table V. Individual fits are very good, mean deviations being no larger than the scatter in the data. However, values of k_1 and k_2 varied with material combination. Attempts were made to find correlations of k_1 and k_2 with elementary material properties. No correlation was found with c_t or H_t, and the best correlations obtained are shown in Figures 23 and 24 respectively on the basis of density ratio, leading to approximate values of k_1 and K_2 :

$$k_1 \approx (0.6 \pm 0.2) K^{2/3}$$

$$k_2 \approx (4 \pm 2) K^{-2/3} \tag{36}$$

for most materials, although some "anomalous" material combinations lie outside the indicated ranges.

It has been shown that a logarithmic function of form Eq. (19) can be approximated by a power law of form Eq. (21) with exponent $m = 2/3$ over a range $2.7 < \xi < 6$ i.e., Eq. (36) may be approximated by

TABLE V

EMPIRICAL FITS TO THE LOGARITHMIC PENETRATION LAW

$$\frac{p}{d} = k_1 \log \left\{ 1 + \frac{\rho_t V^2}{k_2 H_t} \right\}$$

Proj.	Target	H_t	ρ_p/ρ_t	Max. Impact Vel. (km/sec)	k_1	k_2	Deviation (p/d)
Al.	1100F Al.	*	1.0	4.37	0.603	*	0.043
Al.	2024 Al.	120	1.0	2.00	0.602	3.815	0.091
Al.	24ST Al.	114	1.0	3.98	0.694	4.863	0.049
Fe.	2024 Al.	120	2.93	1.65	0.672	0.765	0.099
Cu.	2024 Al.	120	3.32	1.86	1.096	1.649	0.146
Sn.	Sn.	5.3	1.0	2.27	0.421	9.261	0.102
Al.	1020 Stl.	111	0.342	2.19	0.182	6.089	0.040
Fe.	1020 Stl.	111	1.0	1.71	0.521	4.305	0.106
Cu.	1020 Stl.	111	1.13	1.64	0.550	4.874	0.067
Pb.	1020 Stl.	111	1.46	1.29	1.116	11.639	0.049
Mg.	1030 Stl.	123	0.226	3.70	0.270	17.795	0.032
Al	1030 Stl.	123	0.360	4.00	0.287	4.181	0.028
Fe.	1030 Stl.	123	1.0	3.96	0.501	3.416	0.043
Fe.	4140 Stl.	245	1.0	2.30	0.359	1.137	0.062
Fe.	30RC Stl.	302	1.0	2.26	0.632	3.730	0.020
Cu.	Cu.	36	1.0	3.33	0.535	4.145	0.029
Al.	Cu.	65	0.301	5.27	0.427	14.695	0.058
Cu.	Cu.	65	1.0	3.06	0.421	1.555	0.080
Al.	Pb.	4	0.237	5.00	0.454	63.909	0.108
Cu.	Pb.	4	0.786	2.19	0.539	6.847	0.102

* H_t for this material is unknown. The value of $(k_2 H_t)$ from the least squares fit is 122.5×10^8 dynes/cm^2.

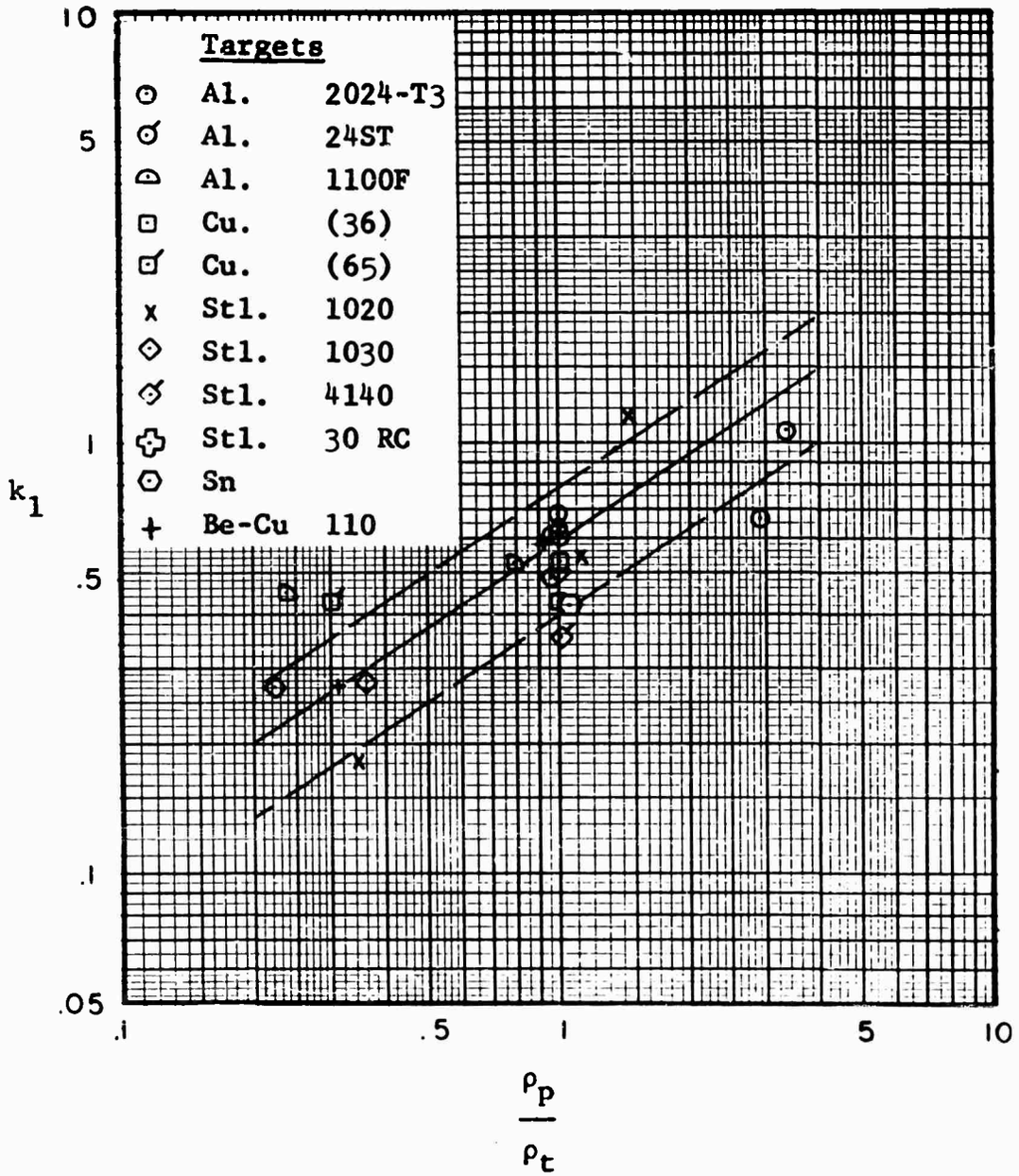

Fig. 23 Correlation of Logarithmic Penetration

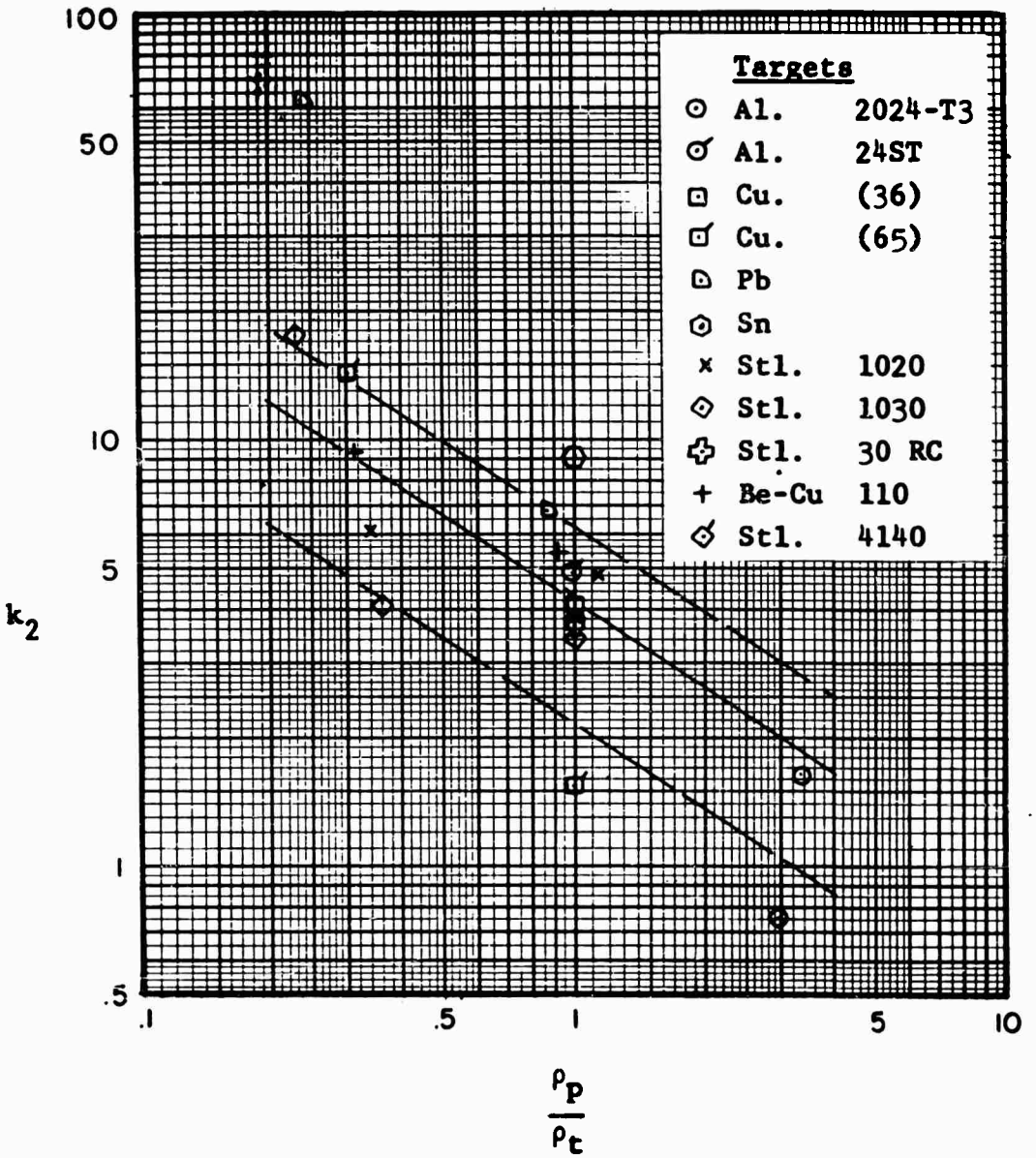

Fig. 24 Correlation of Logarithmic Penetration Law Parameters with Density Ratio

$$\frac{p}{d} = 0.6\, K^{2/3}\left[\frac{1}{4} K^{2/3} B\right]^{1/3}$$

or

$$\frac{p}{d} \approx 0.4\, K^{0.97} B^{1/3} \tag{37}$$

which may be compared to Eq. (24).

7. DISCUSSION

Although the empirical expressions are not based on physically realistic concepts, and there is therefore no sound basis for expecting extrapolations to be valid, it is nevertheless interesting to investigate the consequences of extrapolations to higher velocities.

Figure 25 shows experimental data points and penetration predicted by Eq. (22) and (35) with appropriate constants from Tables IV and V for 1020, 1030 and 30 RC steel targets struck by steel projectiles. Also shown are the three theoretical points computed by Bjork (Ref. 11) for iron targets struck by iron projectiles. A logarithmic scale has been used to accommodate a wide velocity variation.

The theoretical points of Bjork are based on numerical integration of the conservation equations with a realistic equation of state for the solid materials at high pressures neglecting shear strength. Thus the theoretical points would be expected to provide a rational upper limit for the penetration in the absence of shear strength. The steel targets used all have rather high strengths, and it might be expected that the actual penetration would be somewhat below that computed by Bjork, at least at the lower velocity (5.5 km/sec).

The experimental data for all three targets lay in the transition region, the highest velocity points bordering on the high velocity region. Thus the logarithmic fits are strongly influenced by the transition strength effects, discussed in Section 5. The effect of the transition region strength in reducing penetration is more marked at low velocity. Thus the effect is to increase the initial slope and increase the curvature of the two-parameter fit. These two effects partially offset one another, as may be seen from Figure 25, so that the extrapolations agree fairly well with Bjork's point at 72 km/sec. However, the extrapolation may be expected to overestimate the actual penetration at lower velocities.

A similar plot for 24ST and 1100F aluminum targets is shown in Figure 26. In this case, the 1100F material was very soft, and almost all of the experimental points used in the data fit lay in the high velocity region. Thus, transition strength effects have only a weak influence on the fit.

In view of the very limited physical significance of the logarithmic fit, the remarkable agreement of the logarithmic fit with Bjork's theoretical points must be considered somewhat fortuitous. It may be pointed out that the logarithmic expression fits the theoretical points of Bjork considerably better than a law of the type $p/d = kV^{1/3}$.

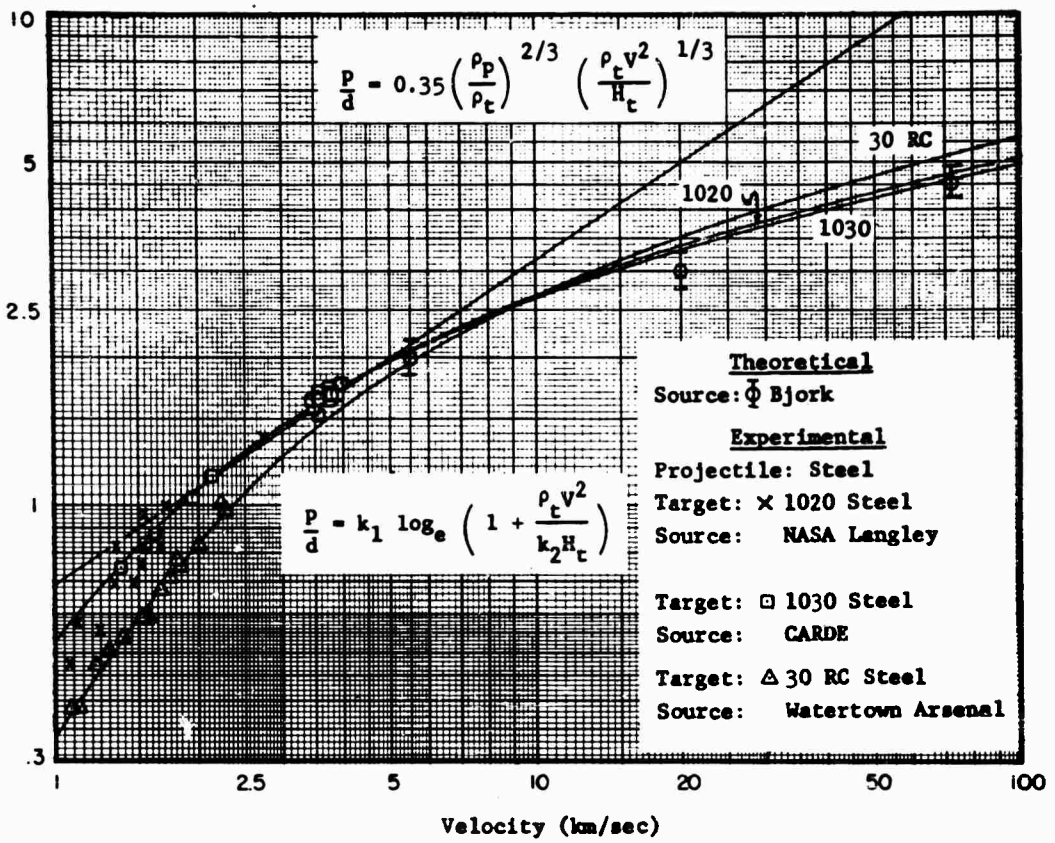

Fig. 25 Extrapolation of Empirical Penetration Laws for Steel Projectiles and Targets

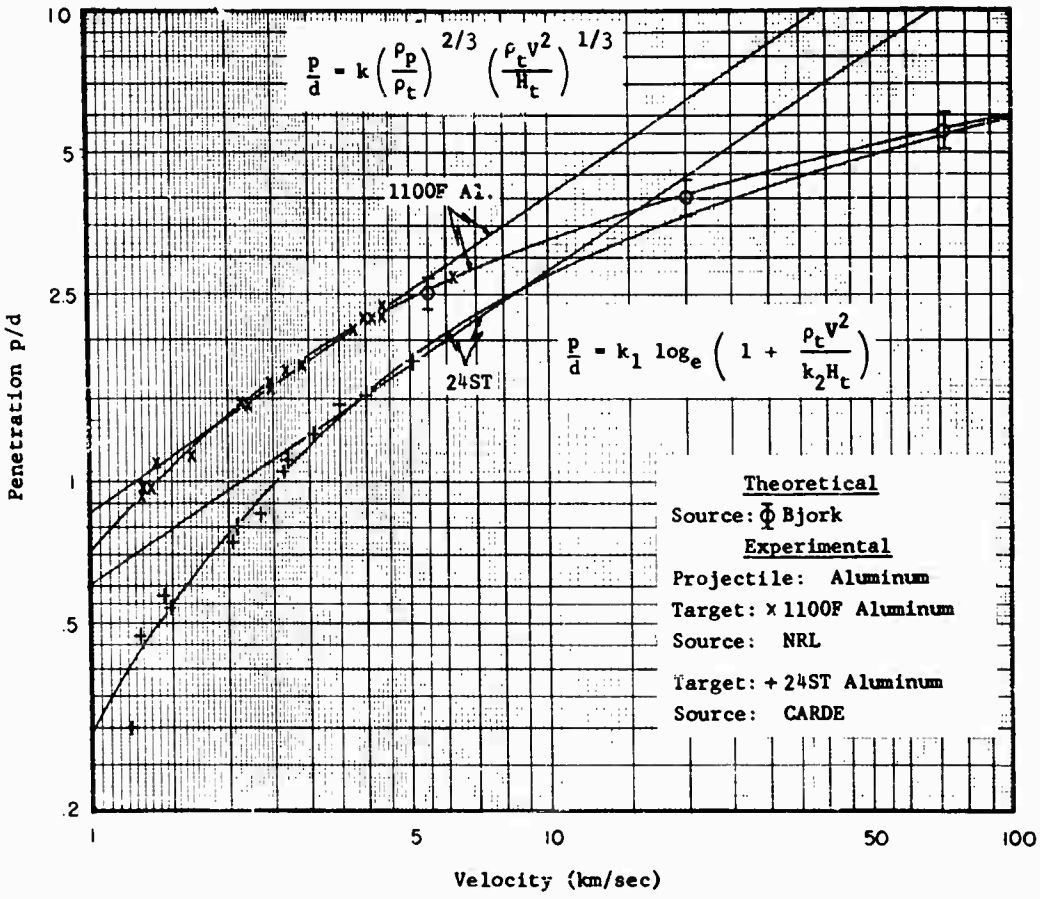

Fig. 76 Extrapolation of Empirical Penetration Laws for Aluminum Projectiles and Targets

For the 24ST material, the transition region extended to about 2.5 km/sec, so that transition strength effects have a somewhat greater influence on the logarithmic fit. Nevertheless the extrapolation shows just the type of behaviour which might be expected. The penetration is less than that predicted by Bjork neglecting strength effects, the offset being reduced as the velocity increases (this is still true on a linear scale).

It must be pointed out that transition strength effects may be such that extrapolations of the logarithmic penetration law for material combinations other than the five considered here (Figs. 25, 26) may be quite unrealistic. The power law extrapolations in each case, of course, lead to much larger predicted penetrations than computed by Bjork. Based on the assumption that Bjork's calculations provide a reasonable upper limit, it may be concluded that extrapolations of the power law are unrealistic.

Based on the previous discussion, it may be speculated that there will be another region of impact in which the penetration will be proportional to $V^{1/3}$. It is to be expected that target material strength effects will in fact be negligible, and craters will be hemispherical, in this region. It would be appropriate to reserve the name hypervelocity for this region.

The lower velocity limit of this region will clearly be a function for target strength, as it may be theorized that, based on the logarithmic penetration law, the limit will be given roughly by

$$\frac{B}{k_2} > 36 \tag{38}$$

with k_2 supplied from Table V. However, since the slope and curvature of the logarithmic fit are strongly influenced by the transition strength effects, it is clear that the limit Eq. (38) cannot be expected to be too accurate. As data become available at higher velocities, definition of the limit can be refined.

The lower limit of the hypervelocity region, predicted by Eq. (38), is 11.4 km/sec for aluminum striking 24ST aluminum targets, 5.3 km/sec for aluminum striking 1100F aluminum targets, 8.2 km/sec for aluminum projectiles striking half hard copper targets, and 2 km/sec for lead projectiles striking lead targets.

An additional effect may enter in the hypervelocity region. Since the compression of the material is by a shock process and expansion is adiabatic, the material is left at a higher temperature than ambient on release of pressure. While little effect may be expected during the high pressure phase of the motion, material strength may be drastically reduced during the later stages of the motion, particularly for low melting point alloys, leading to increased penetration. It is possible that this effect may be operative in lead at velocities near 2 km/sec, and thus mask a change in penetration law from $V^{2/3}$ to $V^{1/3}$.

It may be noted that the Best Number has the significance of the ratio of a pressure ($\rho_t V^2$) to the strength of the material. Somewhat greater physical significance may be introduced by assuming that the instantaneous interface pressure is related to the instantaneous velocity by the shock relation Eq. (29).

Integration of the equation of motion Eq. (4) with

$$F = k_1' \frac{\pi}{4} d^2 (P^* + k_2 H_t) \tag{39}$$

then leads to

$$\frac{p}{d} = k_1 K \log_e \left\{ 1 + \frac{P^*}{k_2 H_t} \right\} - R \tag{40}$$

where R may be shown to vary with velocity but become a small constant at high velocities. It is interesting to note that when $V \gg c_t$ the first term in the expression for P^* Eq. (29), is negligible compared to the second. Noting that S_t is nearly 1.5 for all of the materials considered here, it appears that Eq. (36) is an approximation for Eq. (40) at very high velocities. This suggests that a correlation of the type Eq. (40) may be feasible. In fact, some of the scatter in the constants of Eq. (36) may be due to the poor approximation for the interface pressure in Eq. (36).

8. CONCLUSIONS

Two empirical fits to the experimental data have been found. When used with constants given in Tables IV and V for the particular material combinations which have been investigated experimentally, these expressions are useful for interpolation purposes within the velocity ranges covered by the data.

It has been shown that material strength influences penetration in the high velocity region, defined as the region in which the penetration is approximately proportional to the two-thirds power in velocity. Craters in this region are not necessarily hemispheres. The effects of target strength are expected to be non-negligible throughout the high velocity region. A hypervelocity region is postulated, in which target strength will in fact be negligible, but it is likely that penetration will be approximately proportional to the one-third power in velocity.

Only very rough correlations of the constants in the empirical expressions with simple functions of elementary material properties can be found. That some correlation exists at all must be ascribed to the fact that there is some correlation between dynamic compressibility and strength properties, and elementary static properties.

While the existence of a dependence of the constants in the correlation expressions on more complex functions of elementary material properties cannot be ruled out, it appears to be a hopeless task to deduce such a functional relationship from the data alone. This is partially due to the low precision in many of the measurements, and partially due to the fact that only very few material combinations have been investigated in the high velocity region, so that insufficient information exists to untangle the separate effects of the many complex phenomena occurring during the crater formation process.

The simple correlation expressions used here were derived on the basis of quite unrealistic physical models of the cratering process. Therefore, they

cannot be expected to contain much physical significance, nor to provide a rational basis for extrapolation. Before much further progress can be made it would seem necessary to carry out further theoretical work on the cratering problem, in order to be able to deduce a more physically realistic functional relation. Such a theory must necessarily contain realistic compressibility, geometrical and strength effects. This involves integration of the strongly nonlinear differential equations of motion and equation of state.

While numerical integration will not lead to a functional relationship such as that sought, an extension of Bjork's analysis to include shear strength should be attempted, if only to gain deeper insight into the magnitude of the varied strength effects occurring during the cratering process. Such insight may then aid in deducing the required relationships.

It may be concluded that the present empirical relations have very limited physical significance or value for extrapolation purposes, a property generally common to empirical expressions. Without a rational theory, no information can be gained, other than that contained in the experimental data. However, a good understanding of the physical phenomena accompanying the cratering problem has been gained. Further work should therefore be directed towards formulating a rational theory.

The help of personnel from most of the laboratories listed in Table I both in making data and other information available, and in discussion is gratefully acknowledged. Without the patience and understanding of Miss Helen Petrides, who programmed the least squares fits, and organised the data on punched cards, and of Mrs. Marion Andrews of the Lincoln Computation Centre, and Miss Maxine Weiner who typed the manuscript, this study could not have been carried out.

REFERENCES

1. Metals Handbook, Vol. 1, 8th Edition 1961, American Society for Metals.

2. Herrmann, W., and Jones, A. H., Survey of Hypervelocity Impact Information: Aeroelastic and Structures Research Lab. Report, M. I. T., September 1961.

3. Grimminger, G., Probability that a Meteorite Will Hit or Penetrate a Body Situated in the Vicinity of the Earth: J. of Applied Physics, Vol. 19, 1948, p. 947.

4. Bohn, J. L., and Fuchs, O. P., High Velocity Impact Studies Directed Towards the Determination of the Spatial Density, Mass and Velocity of Micrometeorites at High Altitudes: Contract AF 19(604)-1894, Scientific Report No. 1, ASTIA AD 243 106.

5. Öpik, E., Researches on the Physical Theory of Meteor Phenomena: I Theory of the Formation of Meteor Craters: Acta et Comm. Univ. Tartuensis 1936.

6. Whipple, F. L., Vistas in Astronautics 1958: The Meteoric Risk to Space Vehicles: pp. 115-124, Pergamon Press, N. Y., 1958.

7. Langton, N. H., The Thermal Dissipation of Meteorites by a Bumper Screen: Bericht Uber den V. Internationalen Astronautischen Kongres, August 1954.

8. McDermott, C. E., Cannon, E. T., and Grow, R. W., Temperature Studies and Effects in Perforation of Thin Aluminum Targets: Tech. Rept. UU-3, Univ. of Utah, May 1959.

9. Pack, D. C., and Evans, W. M., Penetration by High Velocity ('Munroe') Jets. I: Proc. of the Physical Society, London, Vol. B 64, 1951.

10. Rostoker, N., The Formation of Craters by High Speed Particles: Meteoritics, Vol. 1, 1953, p. 11.

11. Bjork, R. L., Effect of Meteoroid Impact on Steel and Aluminum in Space: Rand Paper No. P-1662, also the 10th International Astronautical Congress, London, England, August 1959.

12. Charters, A. C., and Locke, G. S., Jr., A Preliminary Investigation of High-Speed Impact: The Penetration of Small Spheres into Thick Copper Targets: NACA RM A 58 B 26, May 1958, Declassified December 1958.

13. Atkins, W. W., and Swift, H. F., Hypervelocity Capability and Impact Research: ARPA Order 70-59, NRL Memo. Rept. 1115 December 1960.

14. Maiden, C. J., Charest, J., and Tardif, H. P., An Investigation of Spalling and Crater Formation by Hypervelocity Projectiles: Fourth Hypervelocity Impact Symposium, Vol. 3, April 1960, also CARDE Tech. Memo. AB 62, May 1960.

15. Turner, G. H., Palmer, E. P., and Grow, R. W., Projectile Effects and Subsurface Disturbance in High-Velocity-Impact Cratering In Lead: Tech. Rept. No. UU-5, Contract AF 04(647)-176, August 1960.

16. Abbot, K. H., Metallurgical Observations of High Speed Impact: Fourth Hypervelocity Impact Symposium, Vol. 2, April 1960.

17. Summers, J. L., Investigation of High Speed Impact: Regions of Impact and Impact at Oblique Angles: NASA TN D-94, October 1959.

18. Feldman, J. B., Jr., Volume-Energy Relation from Shaped Charge Jet Penetrations: Fourth Hypervelocity Impact Symposium, Vol. 2, April 1960.

REVIEW AND ANALYSIS OF HIGH VELOCITY IMPACT DATA

E. P. Bruce

General Electric Company
Philadelphia, Pennsylvania

ABSTRACT

A thorough review has been made of existing experimental data applicable to the impact of high velocity projectiles with semi-infinite metal targets. Empirical equations relating depth of penetration and crater volume to properties of the projectile and target have been derived based upon the assumptions that:

1) projectile shape does not affect crater shape for projectiles which range from spheres to cylinders up to one caliber in length, and

2) craters are hemispherical.

Both of these assumptions are supported by the available data. Additional data and/or a rigorous theoretical treatment of the problem are required to evaluate the utility of the equations at higher impact velocities.

SYMBOLS

P_C - depth of penetration, measured from the plane of the undamaged target surface to the deepest point in the crater.

D_C - crater diameter, measured in the plane of the undamaged target surface.

$D_{C_{MAJ.}}$ - crater diameter, used only in describing craters formed under oblique impact, measured in the plane of the undamaged target surface and in-line with the projectile trajectory.

$D_{C_{MIN.}}$ - crater diameter, used only in describing craters formed under oblique impact, measured in the plane of the undamaged target surface and normal to the projectile trajectory.

V_C - crater volume, measured to the plane of the undamaged target surface.

V_P - projectile volume.

ρ_P - projectile mass density

ρ_T - target mass density

v - impact velocity, measured normal to the target surface for impact at either normal or oblique incidence.

c - velocity of propagation of a plane longitudinal wave in a slender rod.

D - diameter of a cylindrical projectile

L - length or height of cylindrical projectile

D_S - diameter of a spherical projectile or diameter of a sphere having the same mass as a cylindrical projectile.

θ - incidence angle in oblique impact, measured from the normal to the target surface to the projectile trajectory.

INTRODUCTION

Early in 1960, a review of existing single particle metal-to-metal impact data was initiated at the General Electric Missile and Space Vehicle Department. The reasons for this review were three-fold. First, the available data and analysis indicated that a uniform crater shape, that of a hemisphere, was approached as the impact velocity increased; second, the available, general, empirical relations for depth of penetration and crater volume were based on only a small portion of the existing data; and third, the existing relations for depth of penetration and crater volume, while based on separate analyses of penetration and volume data, did not yield a compatible set of equations. Specific reference is made to the following equations [1]

$$P_C/D_S = 2.28\,(\rho_P/\rho_T)^{2/3}\,(v/c)^{2/3} \tag{1}$$

$$V_C/V_P = 34\,(\rho_P/\rho_T)^{3/2}\,(v/c)^{2} \tag{2}$$

which were, at the time this study was initiated, the latest and most generally applicable relations in the field. If the assumption is made that for sufficiently high impact velocities only hemispherical craters will appear, then the penetration parameter (P_C/D_S) and the crater volume parameter (V_C/V_P) are related, from geometrical considerations alone, by

$$V_C/V_P = 4\,(P_C/D_S)^3 \tag{3}$$

REVIEW AND ANALYSIS OF DATA

Examination of Equations 1 and 2 shows that they disagree with the requirements of Equation 3 both in the value of the numerical constants and in the exponents to which the quantity (ρ_P/ρ_T) is raised. Consequently, the available data were examined to determine the projectile-target systems for which hemispherical craters had been observed. A $\pm$ 20 percent limitation on (P_C/D_C) was selected, that is, only penetration and volume data in the velocity range where (P_C/D_C) had reached and remained within the limits $0.4 \leq (P_C/D_C) \leq 0.6$ as the impact velocity was increased were considered. For these selected cases, a method of analysis similar to that used by Huth, et al.,[2] Charters and Locke[3], and Summers[1] was utilized. Specifically, the penetration and crater volume data were examined to ascertain whether equations of the same form as Equation 1 and 2 would result which would, at the same time, satisfy Equation 3. In order to incorporate data obtained as a result of impact investigations in which non-spherical projectiles were used, the diameter of a sphere having the same mass as the non-spherical projectile was calculated for these data and used in determining the penetration parameter (P_C/D_S). Kineke's investigations with cylindrical projectiles of varying fineness ratio[4] form the basis for this step. Midway through this analysis, the data presented at the 1960 Hypervelocity Impact Symposium by Kineke[5], Atkins[6], and Maiden[7] were included in this review. These data represent a large percentage of the available high velocity data.

IMPACT AT NORMAL INCIDENCE

The sections that follow are devoted to the presentation and analysis of impact data. Detailed information describing projectile material, size, and shape; target material; projectile and target material properties; and parameters of interest with respect to the projectile-target system are presented in Table I. Material properties have been taken from handbooks in all cases where they were not presented in the data source.

Crater Profile

Data illustrating the variation of (P_C/D_C), the ratio of crater depth to crater diameter, with impact velocity are shown in Figures 1-7 for projectile-target systems in which projectiles of various materials have been impacted against targets of aluminum alloy, zinc, tin, steel, cadmium, copper, and lead. The low velocity peaks in the parameter (P_C/D_C), which occur only in certain systems, are associated with undeformed projectile penetration. The higher velocities required to produce projectile shatter also produce increasing degrees of flow in the target with the net result that even though penetration is increasing (cases have been observed where penetration initially drops off with the onset of projectile shatter[1]) a larger increase in crater diameter is taking place due to the dissipation of momentum in the target. Examination of the lead target data indicates that both the presence and amplitude of the low velocity peak depends upon some function of the relative projectile-target densities and strengths. The tungsten carbide-lead system exhibits the highest peak -- tungsten carbide is

TABLE I SUMMARY OF PROJECTILE, TARGET, AND PROJECTILE-TARGET SYSTEM PROPERTIES

PROJECTILE			TARGET			SYSTEM				
SIZE & SHAPE	MATERIAL	ρ_P gm./cm^3	MATERIAL	ρ_T gm./cm^3	c km./sec	ρ_P/ρ_T	K_1	K_2	REFERENCE	SYMBOL ON FIGURES 26 & 27
3/8-in dia sphere	Aluminum	2 81	1100 F Aluminum	2 71	5 041	1 037	3 55	37 94	6	○
6, 3 & 6 4-in dia sphere, 0 0620 & 0 22-in. dia sphere & 0. 33 & 0 55-in dia (L/D) = 1 cylinders	2034-T4 Aluminum, 2024-T3 Aluminum	2 77	Same as projectile	2 77	5 105	1	1 71	18 12	7, 13	○
3/16-in dia sphere	Zinc	7.13	Same as projectile	7 13	3 670	1	1 81	25 02	17	□
6 375, 0. 500, 6 625, 6 1 000-in dia (L/D) = 0 267. 0. 06 & 0. 14, 0. 72, & 0. 064 & 0. 10 cylinders.	Steel	7. 83	Zinc	7 13	3 670	1. 068	1. 96	27 43	5	□
3/16-in. dia. sphere	Tin	7 30	Same as projectile	7 30	2 643	1	2. 17	33 63	14	◇
6. 3-in dia sphere, 0 0620, 0 50, & 0 22-in. dia spheres & 0 22-in dia (L/D) = 1 cylinder	AISI 1030 steel, cold rolled steel having a carbon range from 0 12 to 0 30 and a manganese range from 0 30 to 0. 60	7 83	Same as projectile	7 83	5 126	1	1. 94	30 41	7; 13	△
1/8 & 3/16-in. dia spheres	Iron	7 87	Same as projectile	7 87	5 196	1	--	26. 22	17	--
6 375, 0. 500, 0 625, 6 1 000 in dia (L/D) = 6 267, 0 08 & 0 14, 0 72, & 6 064 & 0 10 cylinders	Steel	7 83	Cadmium	8 65	2 307	0. 905	1. 74	18 44	5	◺
6 125 & 0 4-in dia spheres, 0 0620 & 0 22-in. dia spheres & 0 22 & 0 50-in dia (L/D) = 1 cylinders	2024-T6 Aluminum, 2024-T3 Aluminum	2 77	Copper	8 86	3 557	0 309	1 12	8 22	7, 13	□
6 375, 0 500, 0 625, 6 1 000-in dia (L/D) = 0 267, 0 08 & 0 14, 0 72, & 0 064 & 6 10 cylinders, 0 0620 & 0 22-in dia spheres & 0 22 & 0 50 in dia (L/D) = 1 cylinders	Steel, cold rolled steel having a carbon range from 0 12 to 0 30 and a manganese range from 0 30 to 0 60	7 83	Copper	8 96	3 557	0 874	1 82	24 88	5, 13	□
1/8 & 3/16-in dia spheres, spheres, 6 22 & 6 50-in dia spheres & 0 22 & 6 50-in dia (L/D) = 1 cylinders	Copper	8 96	Same as projectile	8 96	3 557	1	3 03	31 50	17, 1, 13	□
6 125 & 6 4-in dia spheres, 0 0620 & 6 22-in dia spheres & 0 22-in dia (L/D) = 1 cylinder; 1/8-in dia spheres	2024-T4 Aluminum, 2024-T3 Aluminum, Aluminum	2 77	Lead	11 34	1 227	0 244	0 55	3 72	7, 13, 6	□
6 375, 6 500, 0 625, 6 1 000-in dia (L/D) = 6 267, 0 08 & 0 14, 0. 72, & 6 064 & 6 10 cylinders, 0. 0620 & 0. 23-in dia spheres & 0 22-in dia (L/D) = 1 cylinder	Steel, cold rolled steel having a carbon range from 0 12 to 0 30 and a manganese range from 0 30 to 0 80	7 83	Lead	11 34	1 227	0 690	1 81	14 88	5, 13	□
6 22 & 6 50-in dia spheres & 0 22-in dia (L/D) = 1 cylinders	Copper	8 88	Lead	11 34	1 227	0 790	1 96	22 97	13	□
Spheres & 22-in dia spheres & 0 22-in dia (L/D) = 1 cylinders 3/16-in dia spheres	Lead	11 34	Same as projectile	11 34	1 227	1	2 29	36 31	1, 13, 14	□

VARIATION OF CRATER PROFILE PARAMETER WITH IMPACT VELOCITY FOR VARIOUS PROJECTILE MATERIALS AND ALUMINUM TARGETS

FIGURE-1

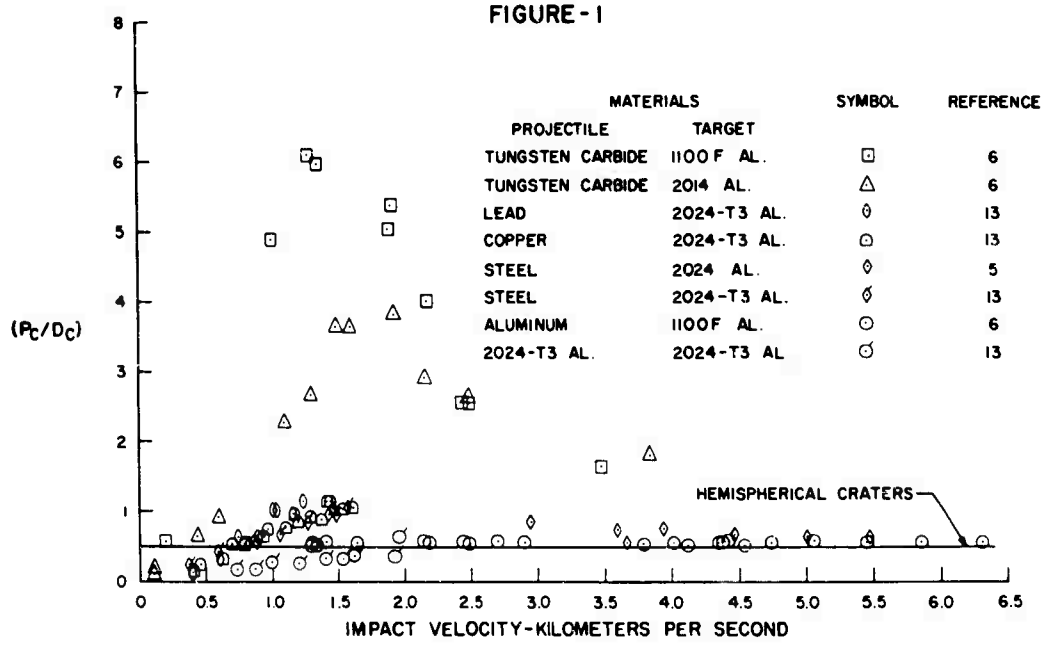

VARIATION OF CRATER PROFILE PARAMETER WITH IMPACT VELOCITY FOR STEEL PROJECTILES AND ZINC TARGETS

FIGURE-2

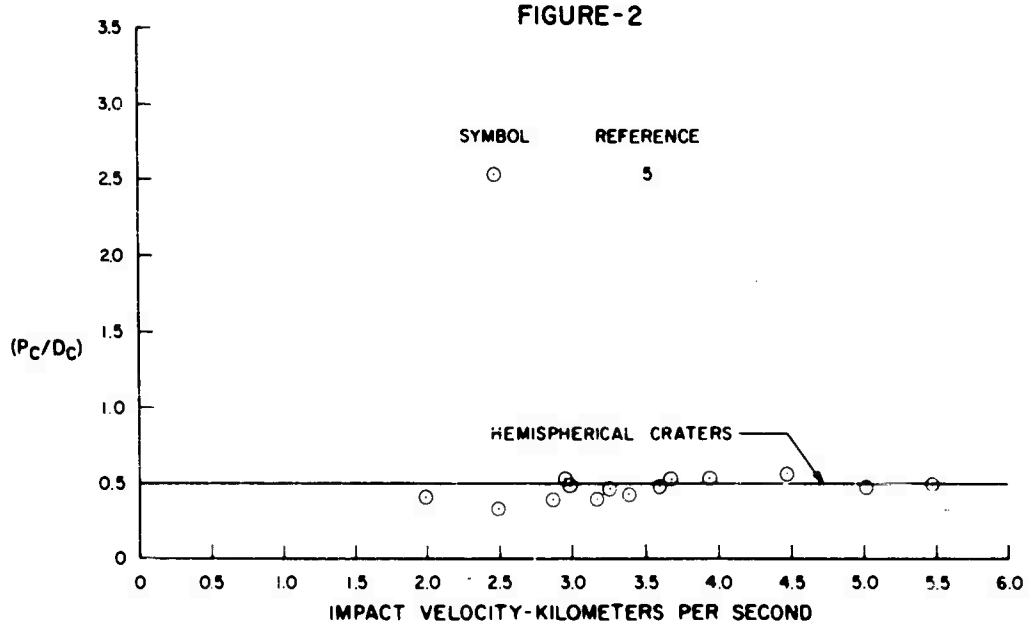

VARIATION OF CRATER PROFILE PARAMETER WITH IMPACT VELOCITY FOR TIN PROJECTILES AND TIN TARGETS

FIGURE-3

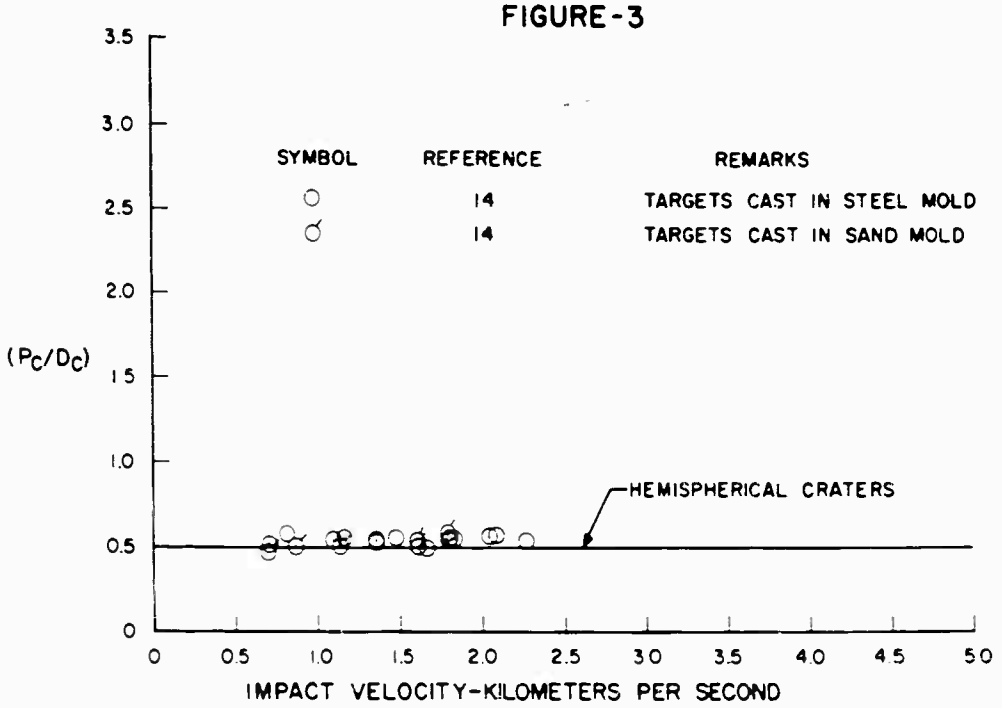

VARIATION OF CRATER PROFILE PARAMETER WITH IMPACT VELOCITY FOR VARIOUS PROJECTILE MATERIALS AND STEEL TARGETS

FIGURE-4

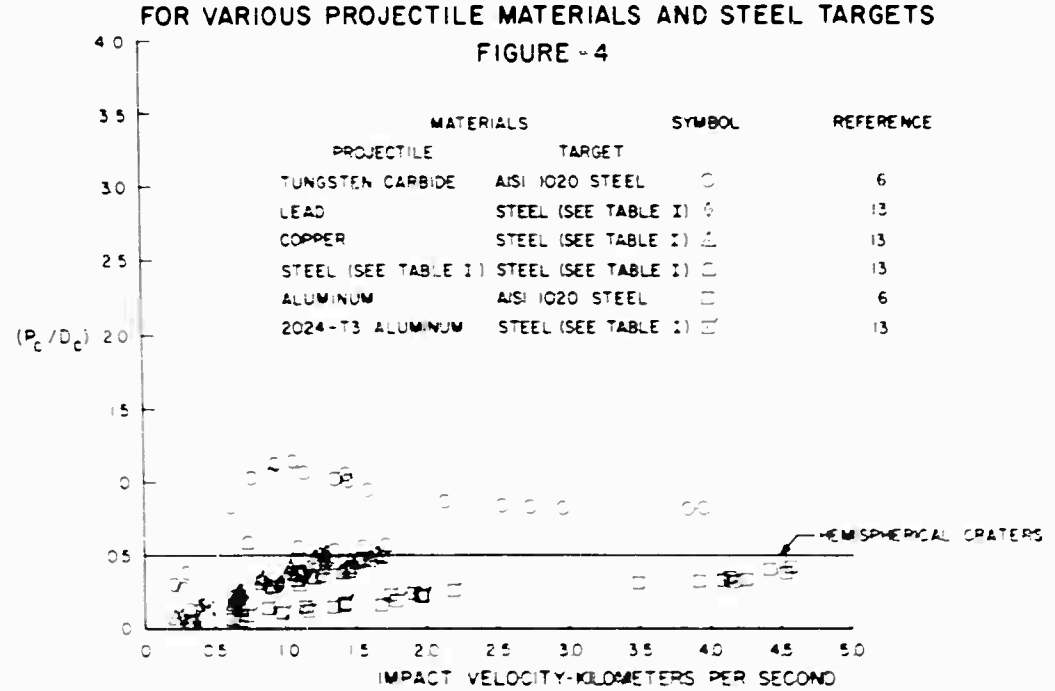

VARIATION OF CRATER PROFILE PARAMETER WITH IMPACT VELOCITY FOR STEEL PROJECTILES AND CADMIUM TARGETS

FIGURE -5

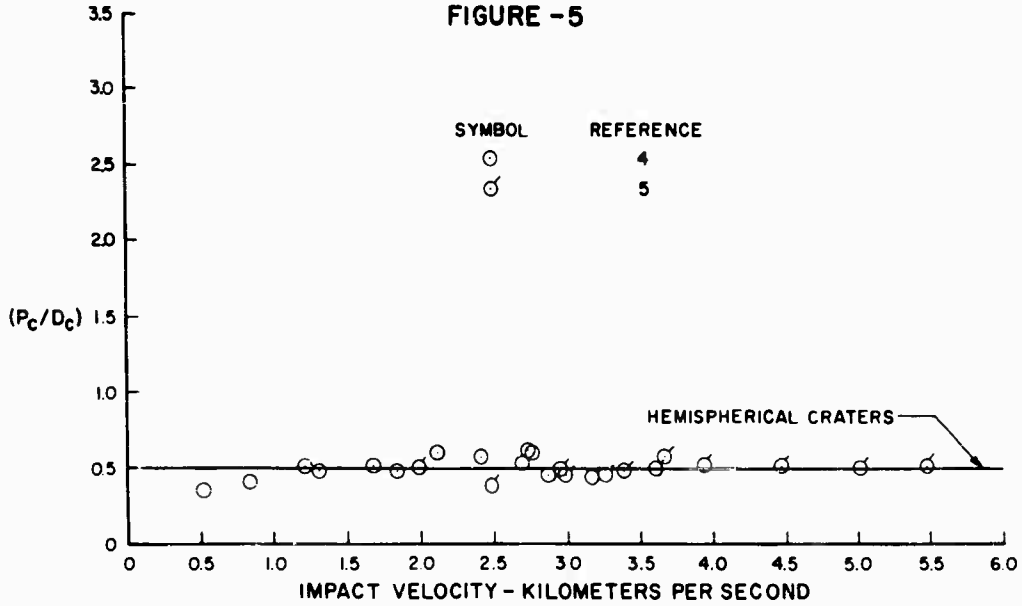

VARIATION OF CRATER PROFILE PARAMETER WITH IMPACT VELOCITY FOR VARIOUS PROJECTILE MATERIALS AND COPPER TARGETS

FIGURE -6

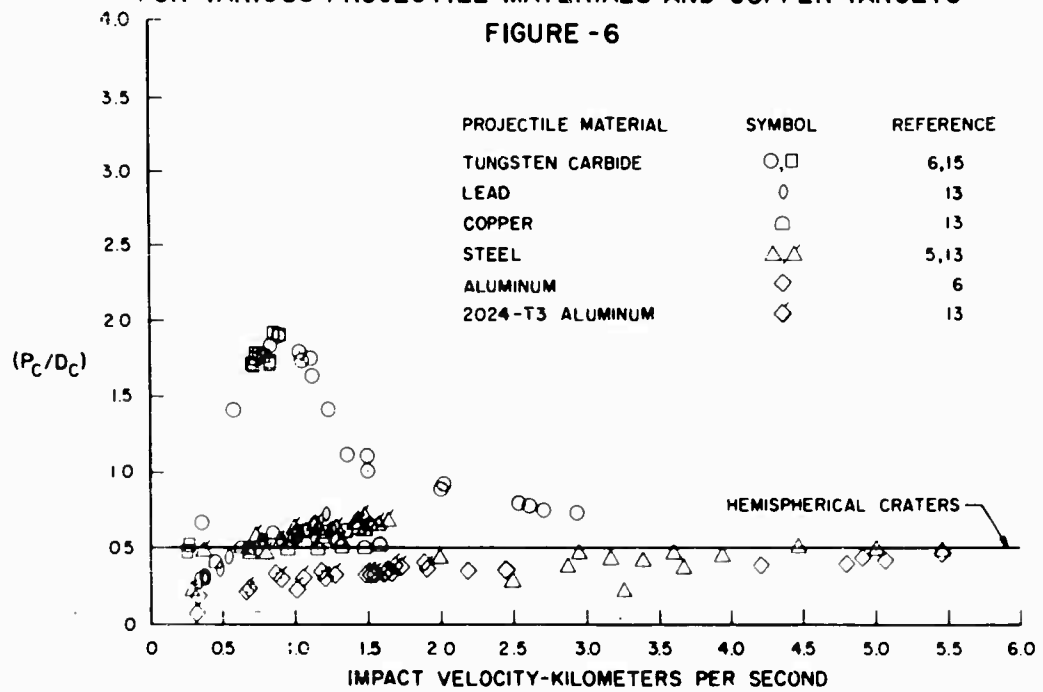

both stronger and more dense than lead. However, both steel and copper exhibit peaks while 2024 - T3 aluminum does not -- all are less dense and stronger than lead.

The data show, however, that as the impact velocity increases, the crater profile parameter (P_C/D_C) approaches 0.5, the value corresponding to hemispherical craters. The velocity at which this level is reached can be quite high, particularly for cases in which either strong heavy or strong light projectiles impact against a strong target as illustrated by the data for tungsten carbide and 2024 - T3 aluminum impacting steel (Fig. 4). It is of interest to note that the $(P_C/D_C) = 0.5$ level is, in general, reached at a relatively low velocity for systems in which the projectile and target are of identical materials. The data for the aluminum projectile - 1100F aluminum target system (Fig. 1) also indicate that small differences in material densities do not alter this observation.

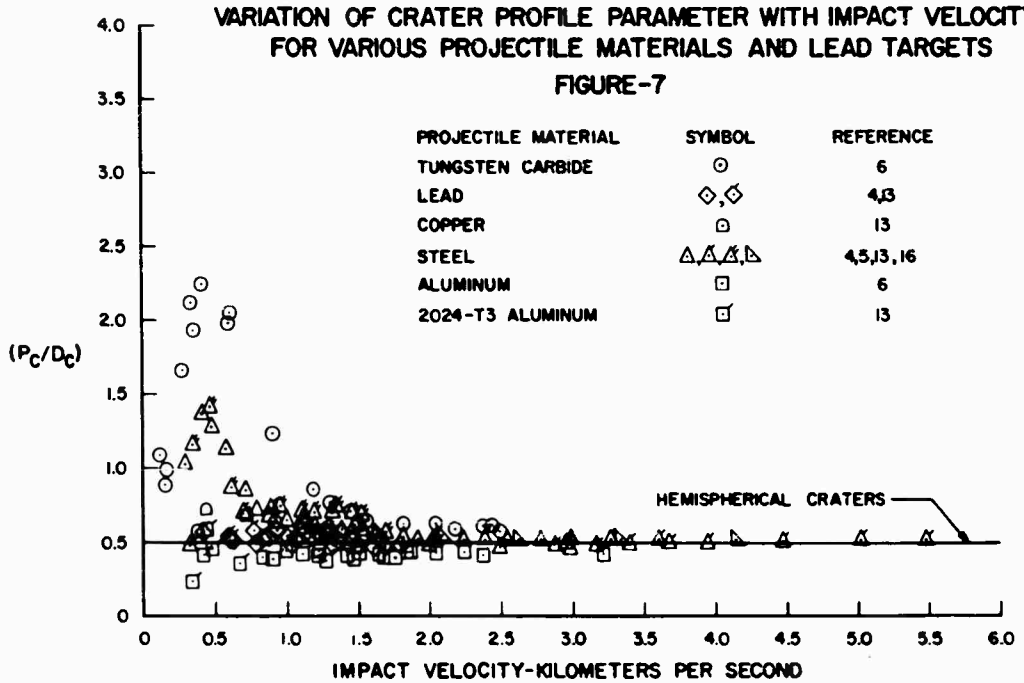

Depth of Penetration

The penetration data for all projectile-target systems which have reached and maintained a value of (P_C/D_C) within the established $\pm$ 20 percent tolerance are shown in Figures 8-14. These data, as presented, describe the variation of penetration in sphere diameters with the non-dimensional velocity parameter (v/c). The data have been arranged in the order of increasing target density and subdivided to reflect effects due to increases in projectile density for constant target density. The vertical line shown on each figure separates the data for which (P_C/D_C) is within $\pm$ 20 percent of 0.5 from the lower velocity data --

only data to the right of this line have been used in this analysis. These data have been analyzed, by a modified least squares technique, to determine the constant K_1 in the following relation:

$$P_C/D_S = K_1 (v/c)^{2/3} \quad (4)$$

Normal least squares fitting procedures would result in determination of both the constant K_1 and the exponent; however, the exponent was fixed in this analysis since it had been established in a number of separate investigations [1, 5, 6]. The values of K_1 thus determined are presented in Table I.

The penetration data for the 2024 - T3 and T4 aluminum, steel, and copper systems in which the projectile and target materials were identical (Figs. 8b, 11, and 13c respectively) and for the 2024 - T3 and T4 aluminum projectile-copper target system (Fig. 13a) illustrate systems in which the (P_C/D_C) = 0.5 level is reached either at relatively low velocities and maintained throughout the velocity range or by a build-up from values less than 0.5. For these systems, the variation with $(v/c)^{2/3}$ is reached by a smooth transition after a higher power dependence. The penetration data for the following systems illustrate cases in which the (P_C/D_C) = 0.5 level is reached following low velocity undeformed projectile penetration in which much higher values of (P_C/D_C) are attained; steel projectiles-copper targets (Fig. 14b), and copper projectiles-lead targets (Fig. 14c). For these cases the variation of (P_C/D_S) with $(v/c)^{2/3}$ is reached after a similar higher power dependence followed by a region in which penetration decreases and then increases. No effort has been expended in trying to define a minimum velocity at which $(v/c)^{2/3}$ dependence will appear for a given system. The two types of build up to this dependence are of primary interest in low velocity applications, however, the rather complete picture thus afforded illustrates that, for many systems, the highest velocities recorded were barely sufficient to yield impacts that produced the characteristic high velocity crater shape.

Crater Volume

The crater volume data, presented and ordered in a manner similar to that used with the penetration data, are shown in Figures 15-21. These data have also been analyzed by the modified least square technique to determine the constant K_2 in the relation

$$V_C/V_P = K_2 (v/c)^2 \quad (5)$$

The exponent was fixed as shown in Equation 5 based upon the results of a number of independent investigations, [1, 5, 6, 7] many of which included portions of the total body of data included in this analysis. The values thus obtained for K_2 are tabulated in Table I.

VARIATION OF PENETRATION PARAMETER WITH IMPACT VELOCITY PARAMETER FOR ALUMINUM PROJECTILES AND ALUMINUM ALLOY TARGETS

FIGURE-8a

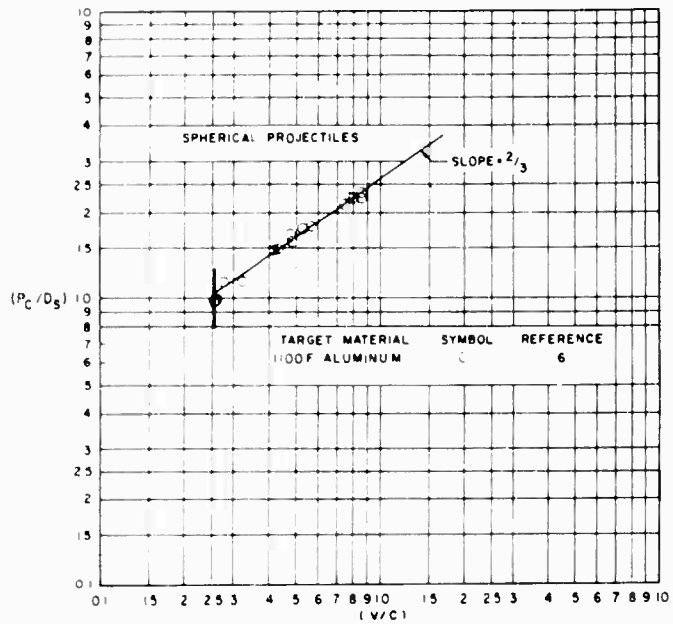

VARIATION OF PENETRATION PARAMETER WITH IMPACT VELOCITY PARAMETER FOR ALUMINUM ALLOY PROJECTILES AND TARGETS

FIGURE-8b

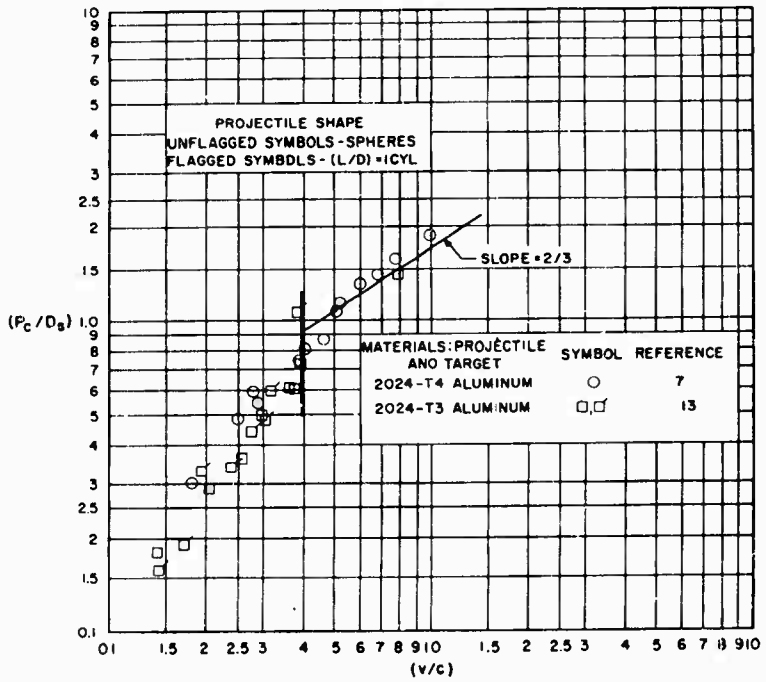

VARIATION OF PENETRATION PARAMETER WITH IMPACT VELOCITY PARAMETER FOR ZINC PROJECTILES AND TARGETS

FIGURE–9a

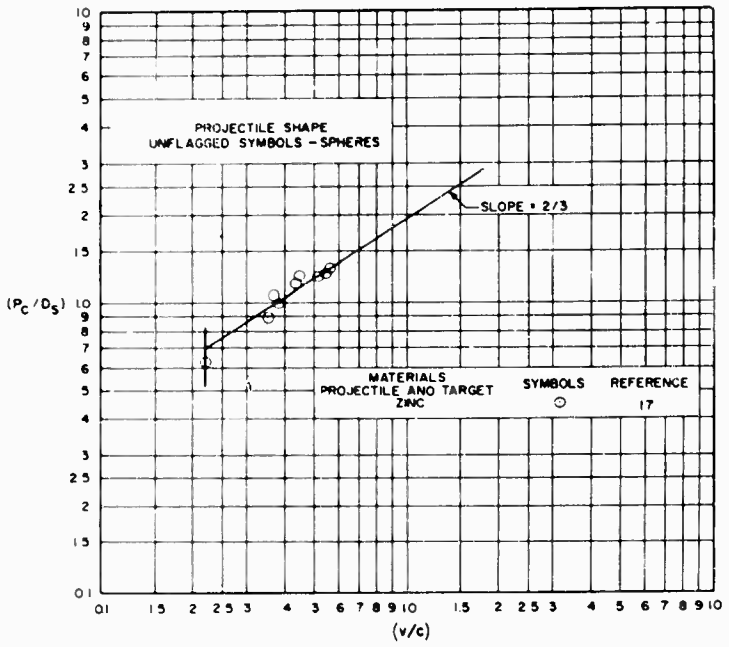

VARIATION OF PENETRATION PARAMETER WITH IMPACT VELOCITY PARAMETER FOR STEEL PROJECTILES AND ZINC TARGETS

FIGURE-9b

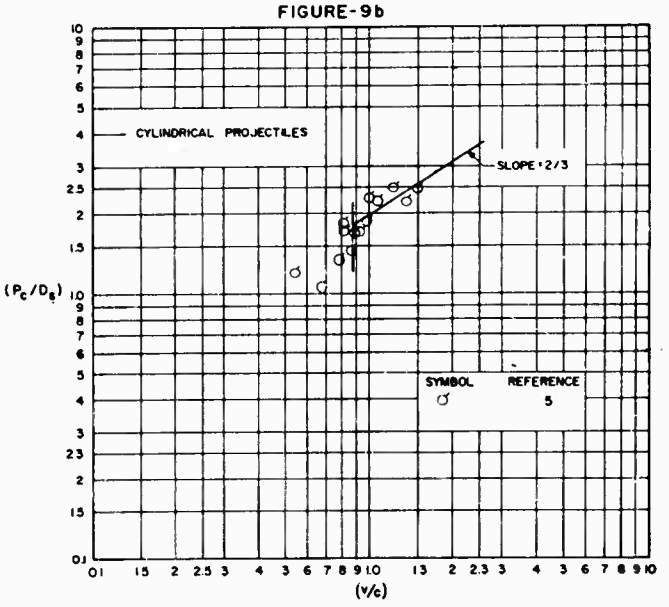

VARIATION OF PENETRATION PARAMETER WITH IMPACT VELOCITY PARAMETER FOR TIN PROJECTILES AND TARGETS

FIGURE-10

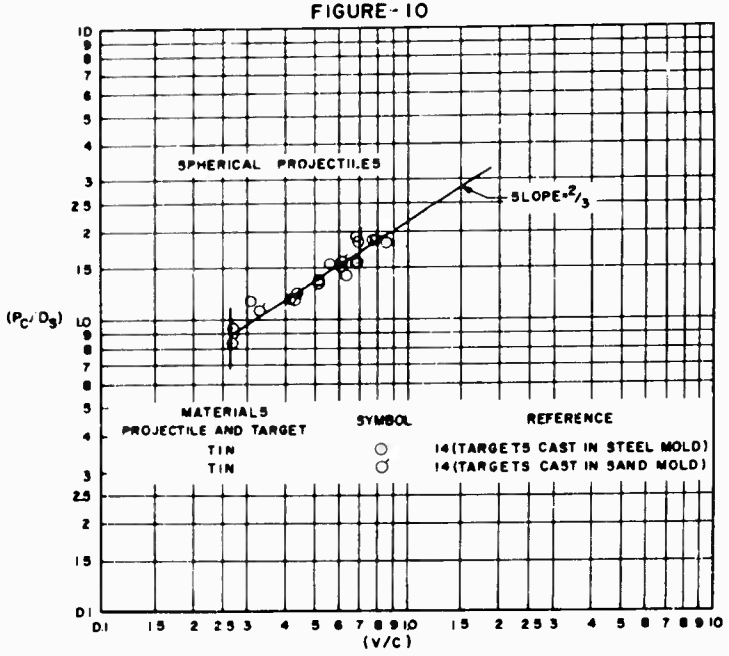

VARIATION OF PENETRATION PARAMETER WITH IMPACT VELOCITY PARAMETER FOR STEEL PROJECTILES AND TARGETS

FIGURE-11

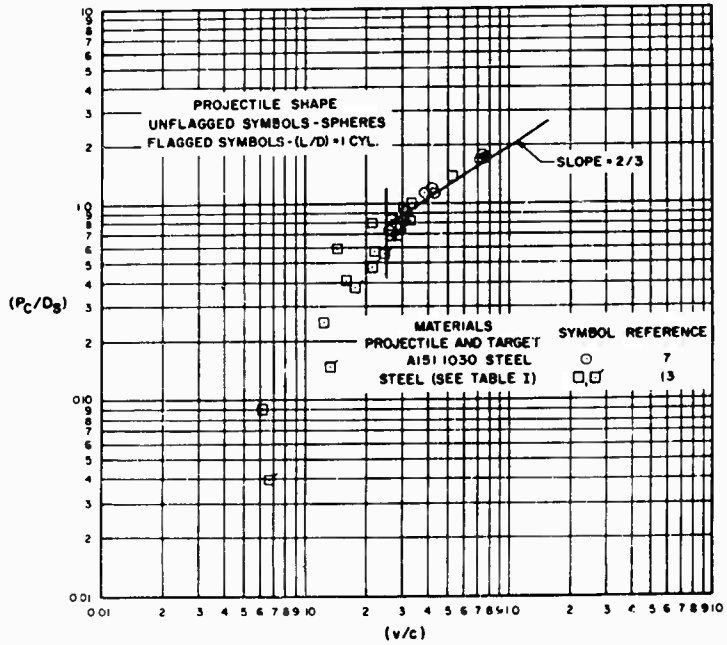

VARIATION OF PENETRATION PARAMETER WITH IMPACT VELOCITY PARAMETER FOR STEEL PROJECTILES AND CADMIUM TARGETS

FIGURE-12

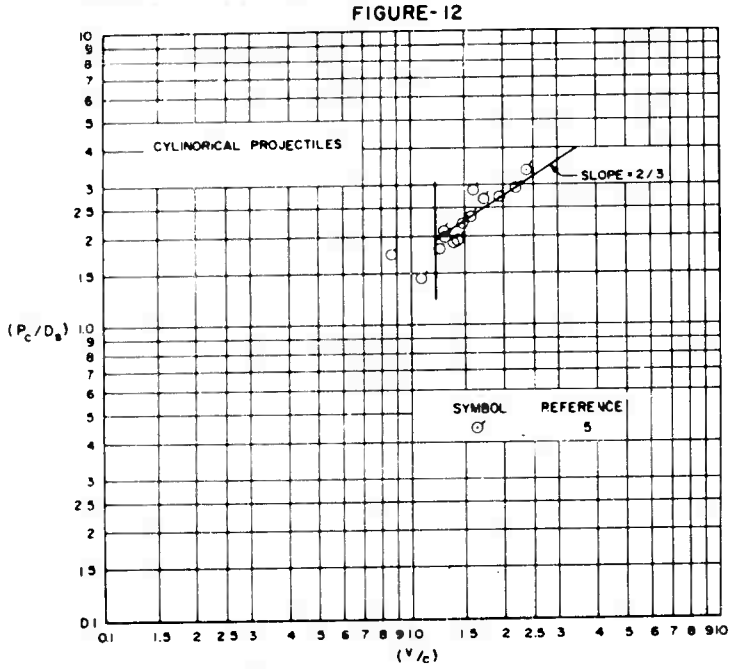

VARIATION OF PENETRATION PARAMETER WITH IMPACT VELOCITY PARAMETER FOR ALUMINUM ALLOY PROJECTILES AND COPPER TARGETS

FIGURE-13a

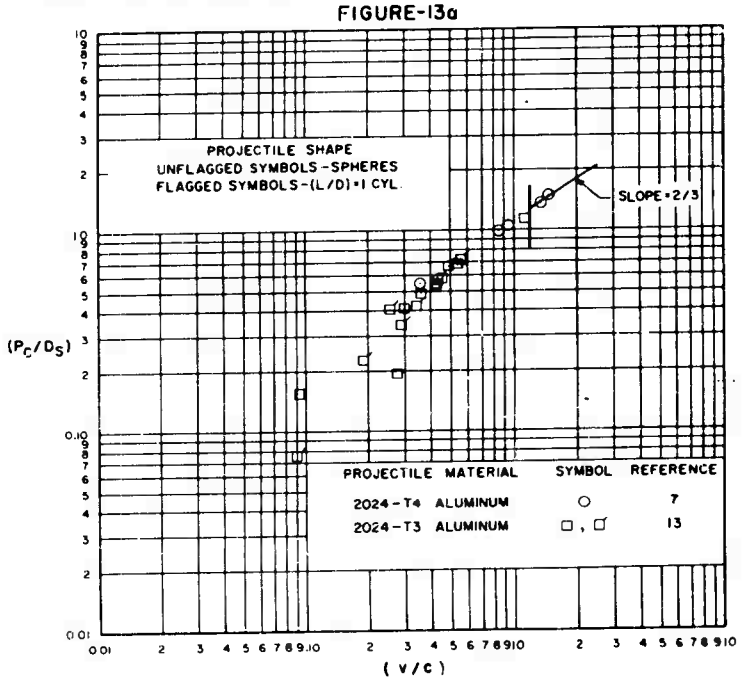

VARIATION OF PENETRATION PARAMETER WITH IMPACT VELOCITY PARAMETER FOR STEEL PROJECTILES AND COPPER TARGETS

FIGURE-13b

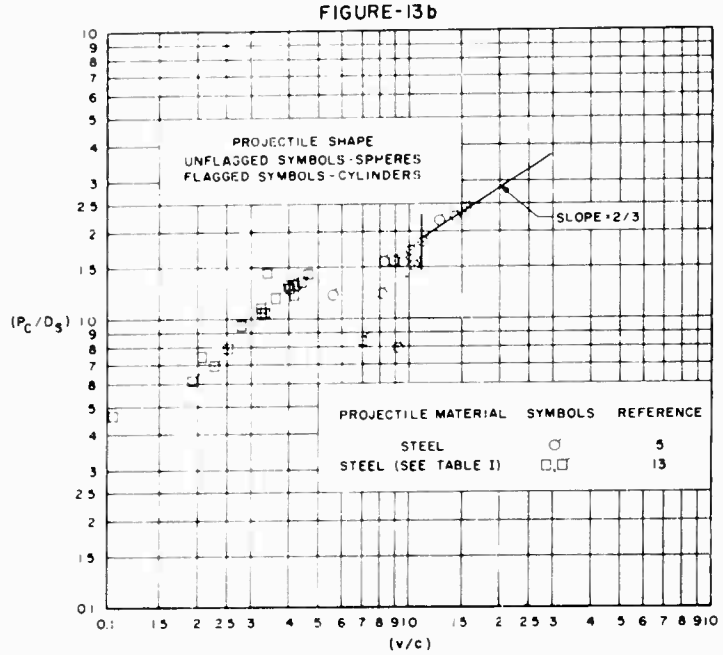

VARIATION OF PENETRATION PARAMETER WITH IMPACT VELOCITY PARAMETER FOR COPPER PROJECTILES AND TARGETS

FIGURE-13c

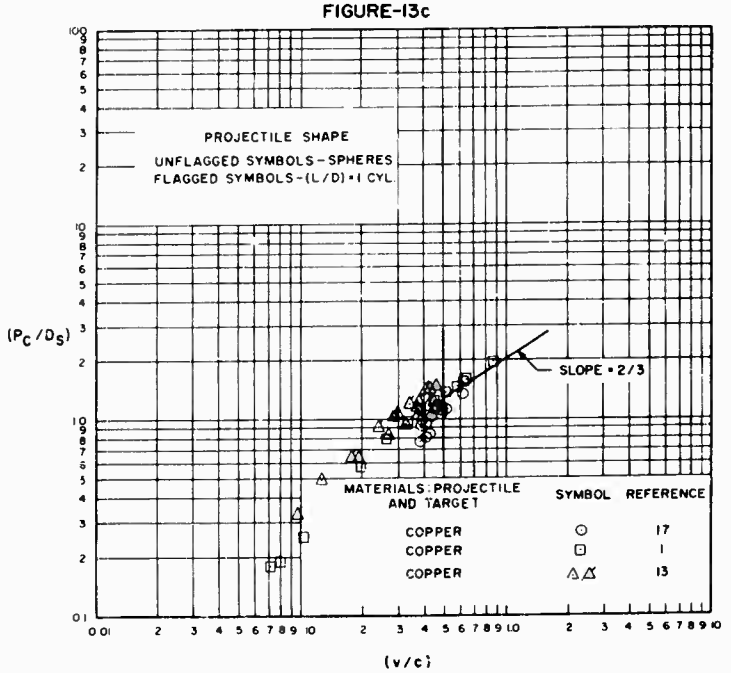

VARIATION OF PENETRATION PARAMETER WITH IMPACT VELOCITY PARAMETER FOR ALUMINUM ALLOY PROJECTILES AND LEAD TARGETS

FIGURE-14a

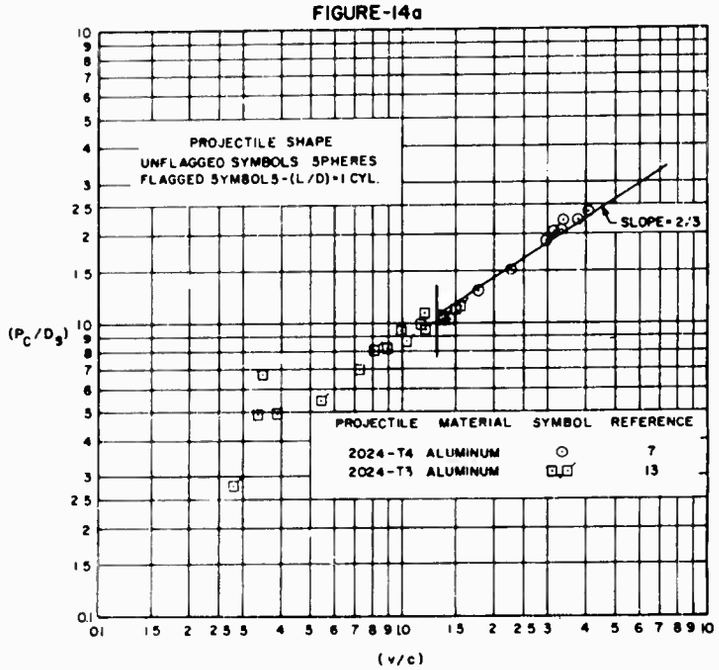

VARIATION OF PENETRATION PARAMETER WITH IMPACT VELOCITY PARAMETER FOR STEEL PROJECTILES AND LEAD TARGETS

FIGURE-14b

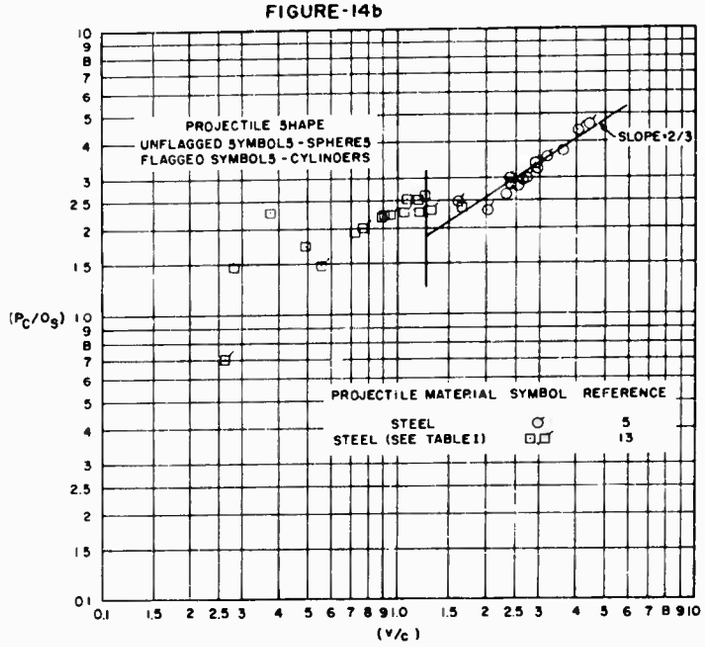

VARIATION OF PENETRATION PARAMETER WITH IMPACT VELOCITY PARAMETER FOR COPPER PROJECTILES AND LEAD TARGETS

FIGURE-14c

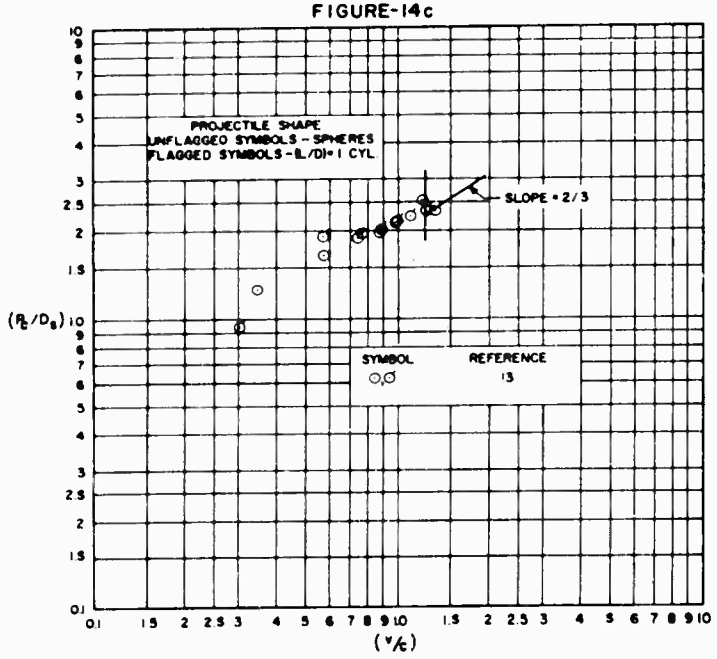

VARIATION OF PENETRATION PARAMETER WITH IMPACT VELOCITY PARAMETEP FOR LEAD PROJECTILES AND TARGETS

FIGURE-14d

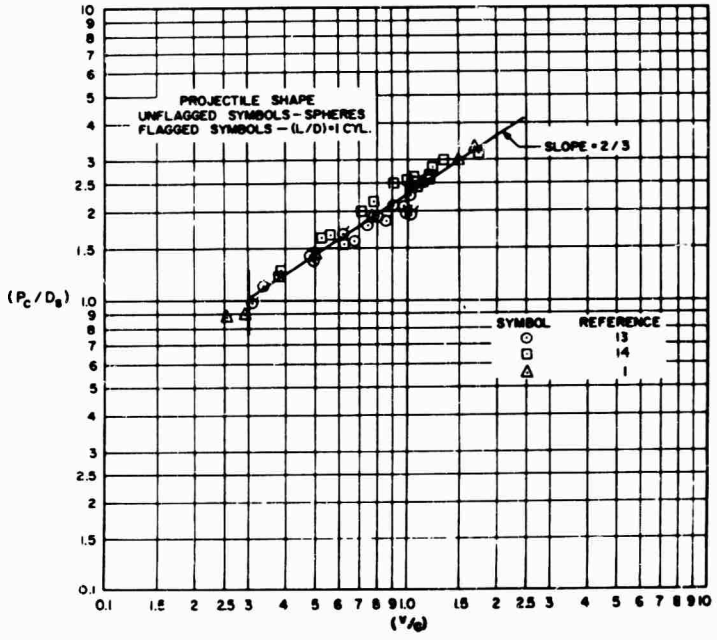

The volume data do not reflect the changing nature of the parameter (P_C/D_C) as strongly as do the penetration data. The crater volume data at low velocities in systems that reach the $(P_C/D_C) = 0.5$ level either at relatively low velocities and maintain it throughout the velocity range or by a build-up from values less than 0.5 (Figs. 15, 17-19, 20a, 20c, 21a, and 21d) show very slight, if any, deviations from the established high velocity variation. However, for every system in which (P_C/D_C) has peaked at a value above 0.5 at low velocities and has reached 0.5 from above at higher velocities, a definite shift is present in the volume data that is associated with the transition to high velocity cratering after projectile shatter occurs. In every case the shift is toward lower high velocity values of (V_C/V_P) than would be estimated based upon an extrapolation of low velocity data. This characteristic behavior is illustrated by the following projectile-target systems: steel-copper (Fig. 20b), steel-lead (Fig. 21b), and copper-lead (Fig. 21c).

Effect of Projectile and Target Density

The penetration and crater volume data for systems in which zinc, copper, and lead were used as targets indicate, by increases in K_1 and K_2 which correspond to increases in projectile density (see Table I) that penetration and crater volume are functions of projectile density. The data also indicate, for systems in which aluminum, steel and copper were used as projectiles, that penetration and crater volume are also functions of target density. The crater volume (K_2) data have been plotted versus target density (for constant projectile density families) and versus projectile density (for constant target density families), as shown in Figures 22 and 23. The results of previous investigations[1,7] indicate that K_2 should be proportional to $(\rho_T)^{3/2}$ and to $(\rho_P)^{3/2}$. Accordingly, lines representing this variation have been drawn through the data for each family in Figures 22 and 23. The data exhibit some scatter, but in general, they substantiate the previous results. The penetration data (K_1) permit an independent check on these observations, since, if these data satisfy Equation 3, then K_1 should be proportional to $(\rho_T)^{-1/2}$ and to $(\rho_P)^{1/2}$. The penetration data are presented in Figures 24 and 25, along with lines which describe the above variation for each family. The proposed variation adequately describes the actual variation, indicating compatibility between the penetration and crater volume data as required by Equation 3.

Correlation of All Data

The step remaining in the establishment of general penetration and crater volume equations requires a determination of the constants of proportionality in the relations

$$P_C/D_S = K_3 (\rho_P/\rho_T)^{1/2} (v/c)^{2/3} \qquad (6)$$

and

$$V_C/V_P = K_4 (\rho_P/\rho_T)^{3/2} (v/c)^2 \quad (7)$$

Equation 3 again provides a check between the two sets of data, since it requires that $K_4 = 4 (K_3)^3$. The values of K_3 and K_4 determined by averaging over the complete body of data, thereby giving the data from each projectile-target system equal weight, are: $K_3 = 2.01$, and $K_4 = 30.25$. The agreement between the sets of data is again satisfactory, since $\sqrt[3]{\frac{K_4}{4}} = 1.96$. The following general equations, which satisfy Equation 3, thus result for high velocity cratering in semi-infinite, ductile metal targets:

$$P_C/D_S = 1.96 (\rho_P/\rho_T)^{1/2} (v/c)^{2/3} \quad (8)$$

$$V_C/V_P = 30.25 (\rho_P/\rho_T)^{3/2} (v/c)^2 \quad (9)$$

It should be noted that these equations are based on the limited amount of data presently available and that the objective of this stydy was to develop equations suitable for engineering estimates of impact effects. Consequently, extrapolations to higher impact velocities are, as yet, largely unsupported by experimental data. However, micro-particle data[8] at an impact velocity of 10 km/sec for steel projectiles impacting both copper and lead targets supports both the dependence of penetration on the two-thirds power of the impact velocity and the observation that high velocity impact craters (for particles larger than the material grain size) are hemispherical.

In order to illustrate the accuracy of Equations 8 and 9 and to compare them with Equations 1 and 2, the predicted values of (P_C/D_S) and (V_C/V_P), evaluated at $(v/c) = 1$, given by each expression have been plotted for each projectile-target system versus either K_1 or K_2. The results are shown in Figures 26 and 27. Dashed lines representing $\pm$ 10 percent error limits have been drawn on each curve. These curves illustrate the following:

1) that Equation 8 generally predicts depth of penetration more accurately than does Equation 1,

2) that the crater volume data are not accurately predicted by either of the equations, with Equation 9 possibly more accurate than Equation 2.

3) that the data in which aluminum alloys were used as targets are poorly predicted in all cases, and

4) that for systems in which the projectile and target materials were

VARIATION OF CRATER VOLUME PARAMETER WITH IMPACT VELOCITY PARAMETER FOR ALUMINUM PROJECTILES AND ALUMINUM ALLOY TARGETS

FIGURE-15a

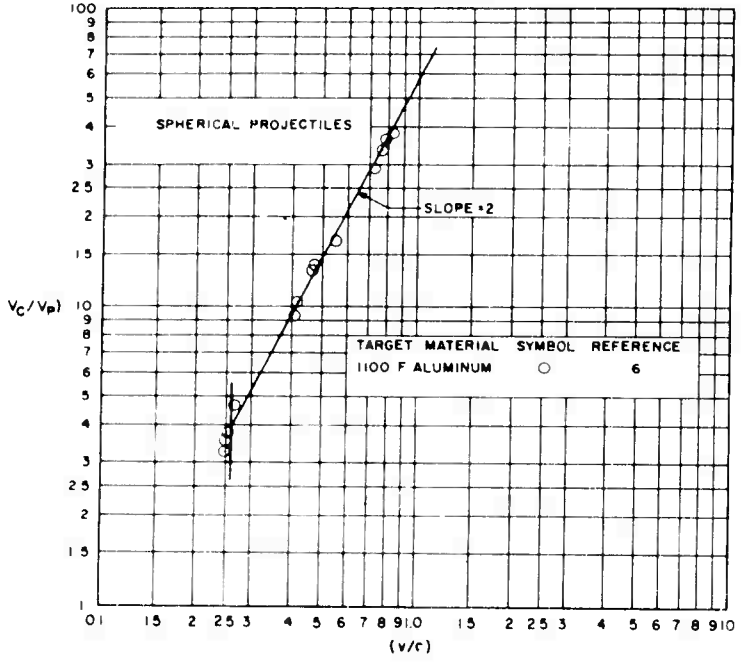

VARIATION OF CRATER VOLUME PARAMETER WITH IMPACT VELOCITY PARAMETER FOR ALUMINUM ALLOY PROJECTILES AND TARGETS

FIGURE - 15b

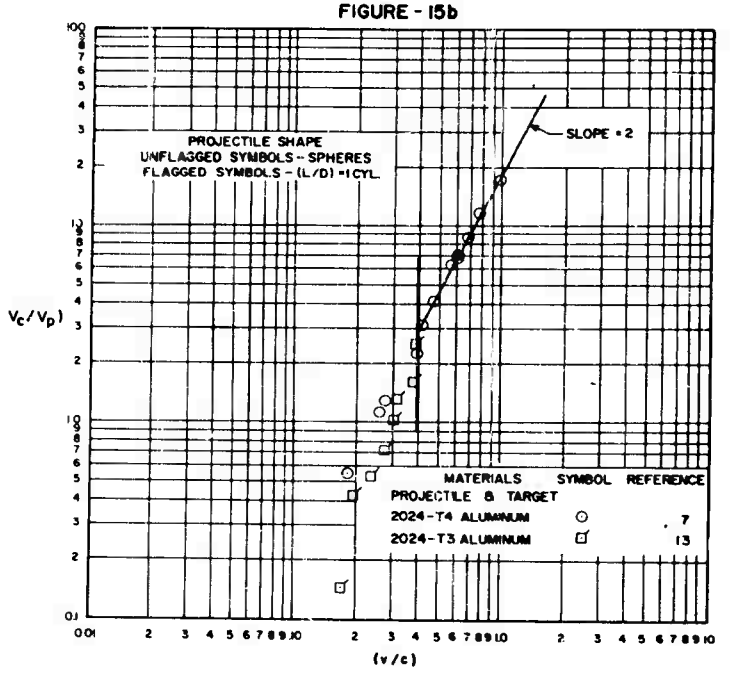

VARIATION OF CRATER VOLUME PARAMETER WITH IMPACT VELOCITY PARAMETER FOR ZINC PROJECTILES AND TARGETS

FIGURE - 16a

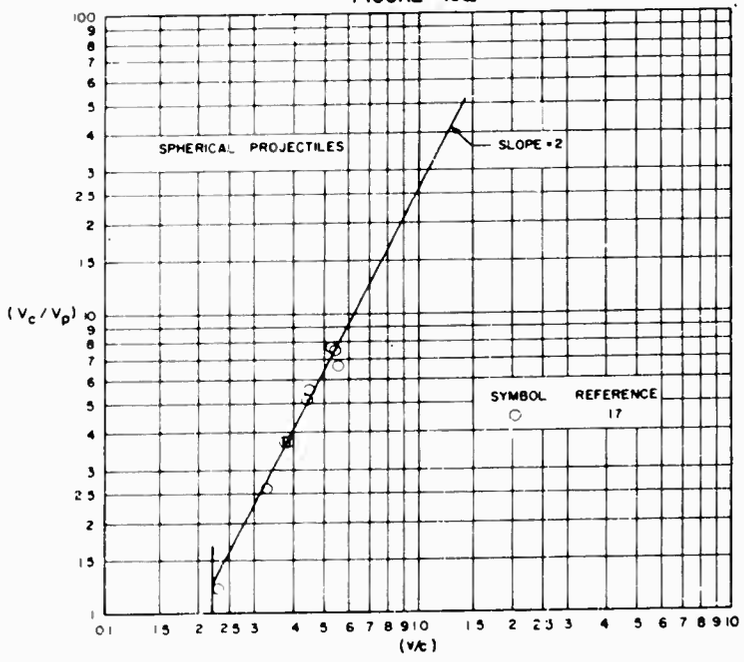

VARIATION OF CRATER VOLUME PARAMETER WITH IMPACT VELOCITY PARAMETER FOR STEEL PROJECTILES AND ZINC TARGETS

FIGURE-16b

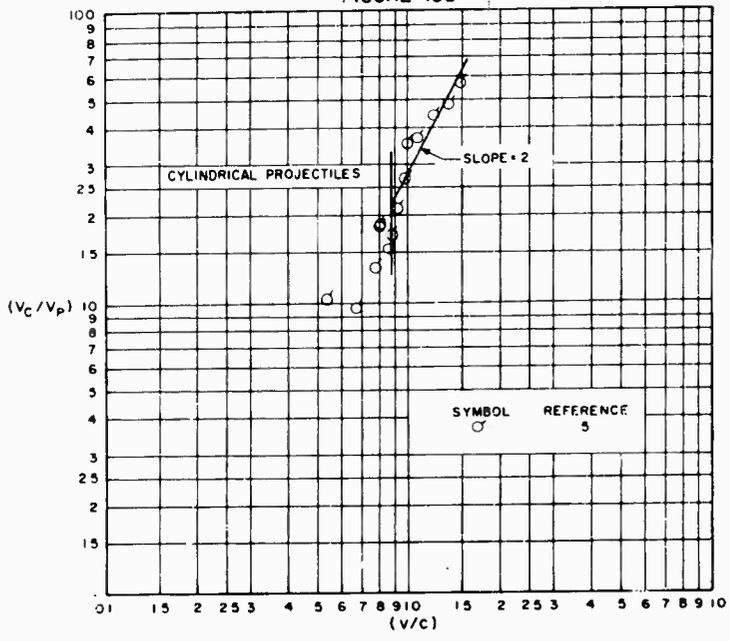

VARIATION OF CRATER VOLUME PARAMETER WITH IMPACT VELOCITY PARAMETER FOR TIN PROJECTILES AND TARGETS

FIGURE - 17

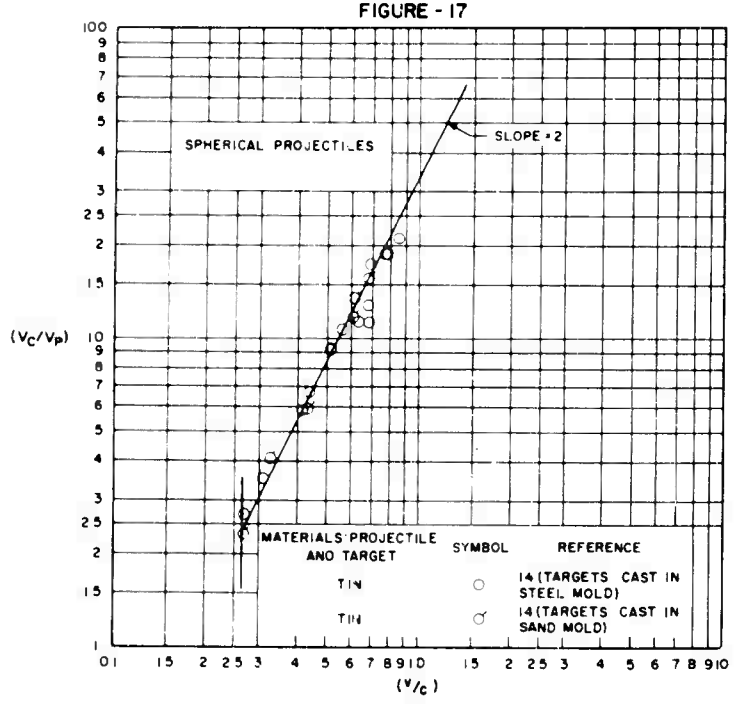

VARIATION OF CRATER VOLUME PARAMETER WITH IMPACT VELOCITY PARAMETER FOR STEEL PROJECTILES AND TARGETS

FIGURE - 18

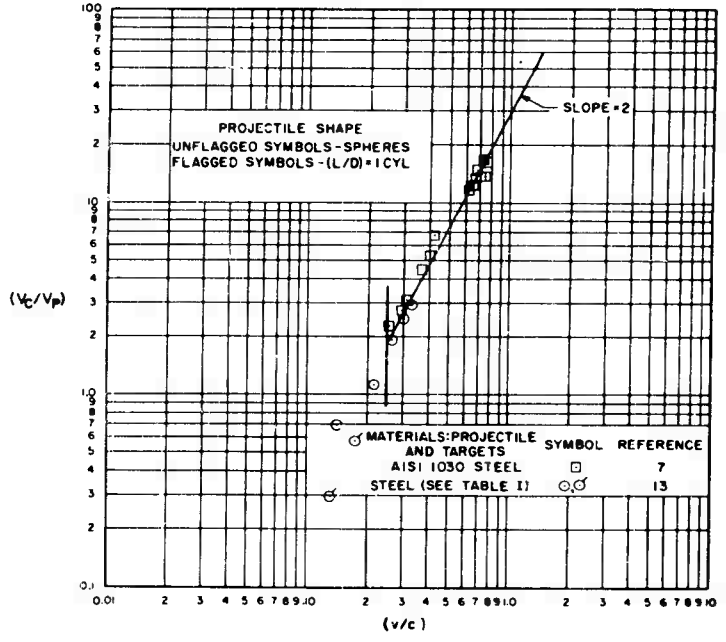

VARIATION OF CRATER VOLUME PARAMETER WITH IMPACT VELOCITY PARAMETER FOR STEEL PROJECTILES AND CADMIUM TARGETS

FIGURE-19

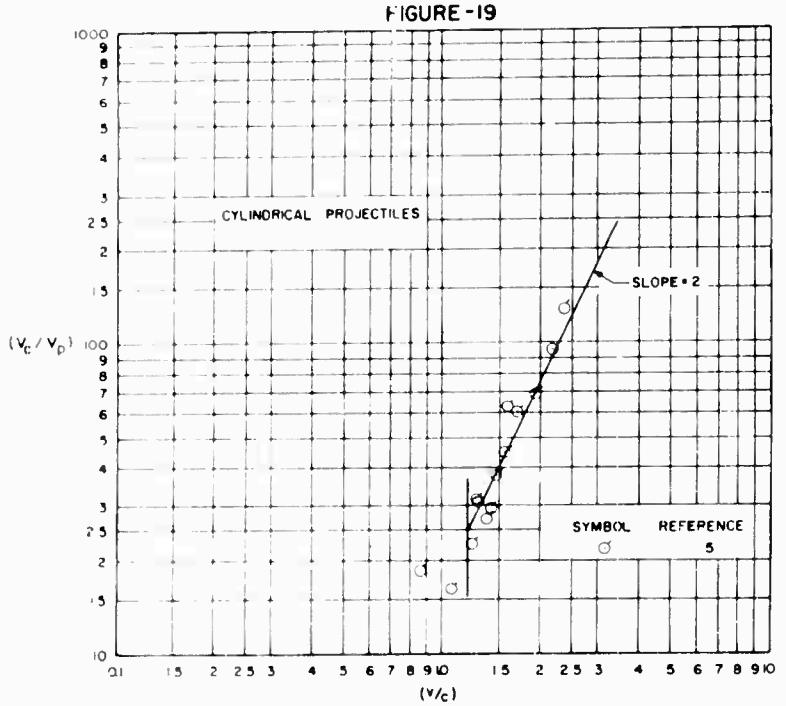

VARIATION OF CRATER VOLUME PARAMETER WITH IMPACT VELOCITY PARAMETER FOR ALUMINUM ALLOY PROJECTILES AND COPPER TARGETS

FIGURE-20a

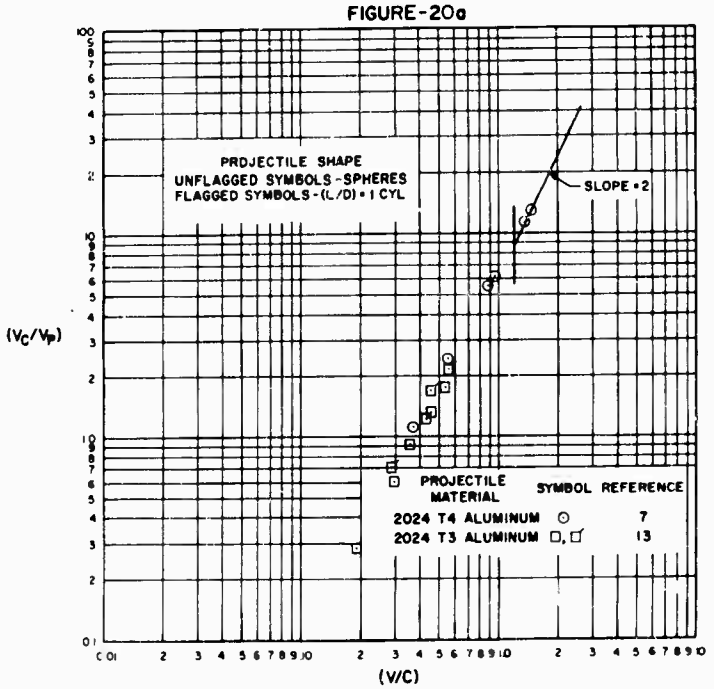

VARIATION OF CRATER VOLUME PARAMETER WITH IMPACT VELOCITY PARAMETER FOR STEEL PROJECTILES AND COPPER TARGETS

FIGURE - 20b

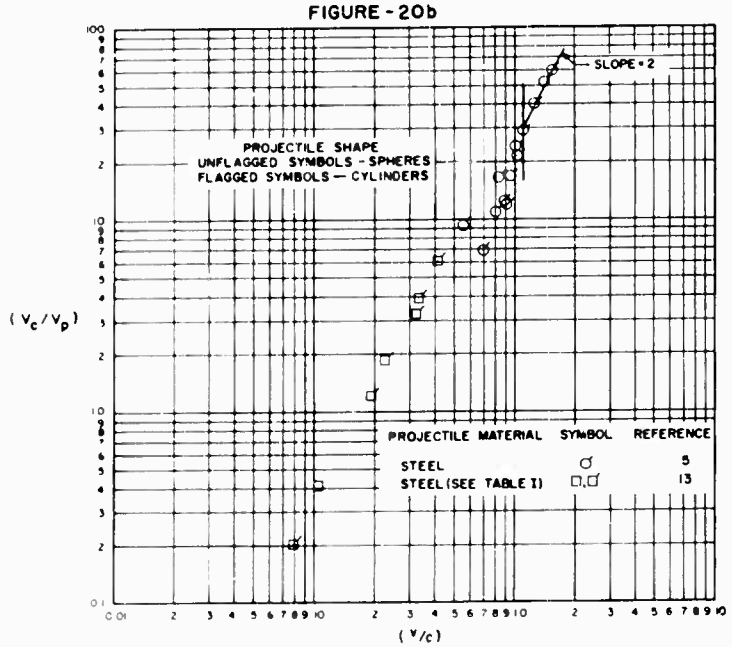

VARIATION OF CRATER VOLUME PARAMETER WITH IMPACT VELOCITY PARAMETER FOR COPPER PROJECTILES AND TARGETS

FIGURE - 20c

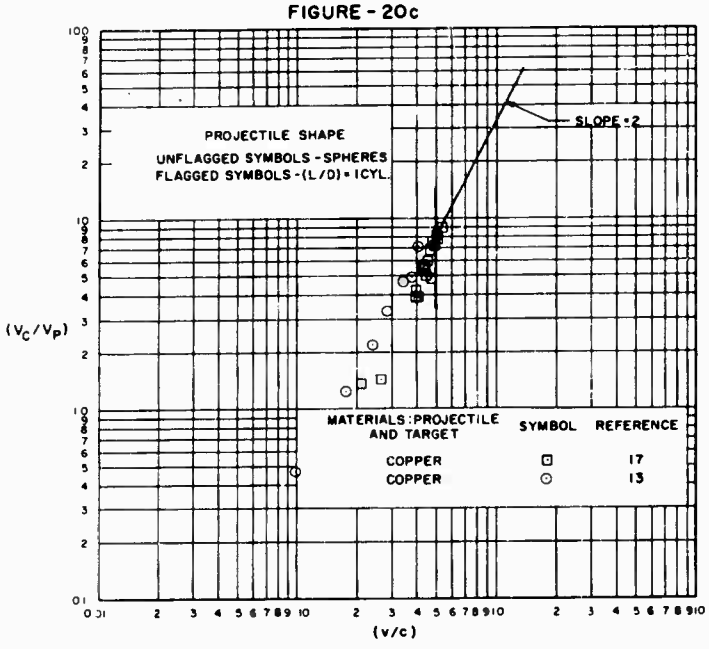

VARIATION OF CRATER VOLUME PARAMETER WITH IMPACT VELOCITY PARAMETER FOR ALUMINUM ALLOY PROJECTILES AND LEAD TARGETS

FIGURE-21a

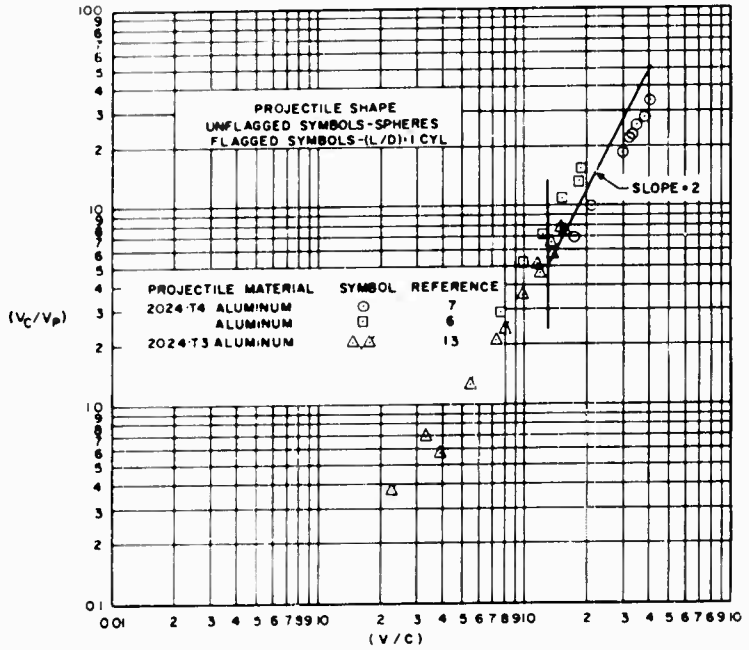

VARIATION OF CRATER VOLUME PARAMETER WITH IMPACT VELOCITY PARAMETER FOR STEEL PROJECTILES AND LEAD TARGETS

FIGURE - 21b

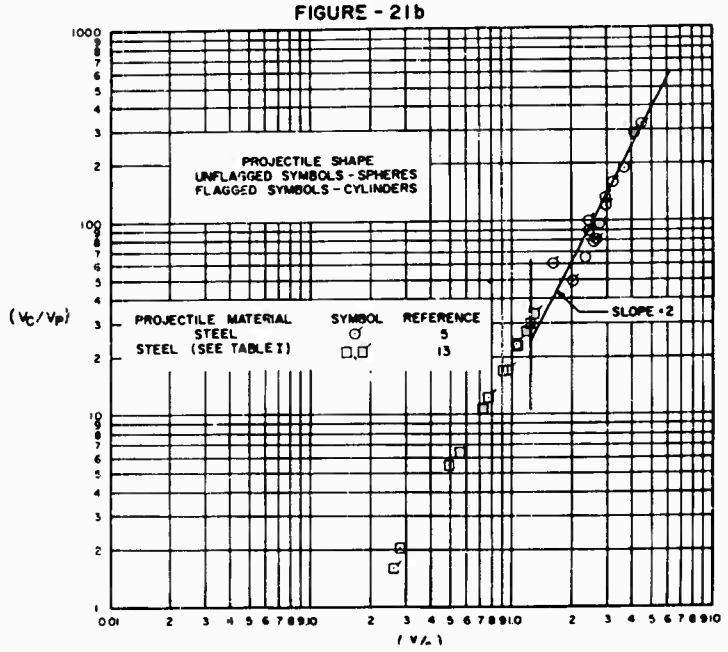

VARIATION OF CRATER VOLUME PARAMETER WITH IMPACT VELOCITY PARAMETER FOR COPPER PROJECTILES AND LEAD TARGETS

FIGURE - 21c

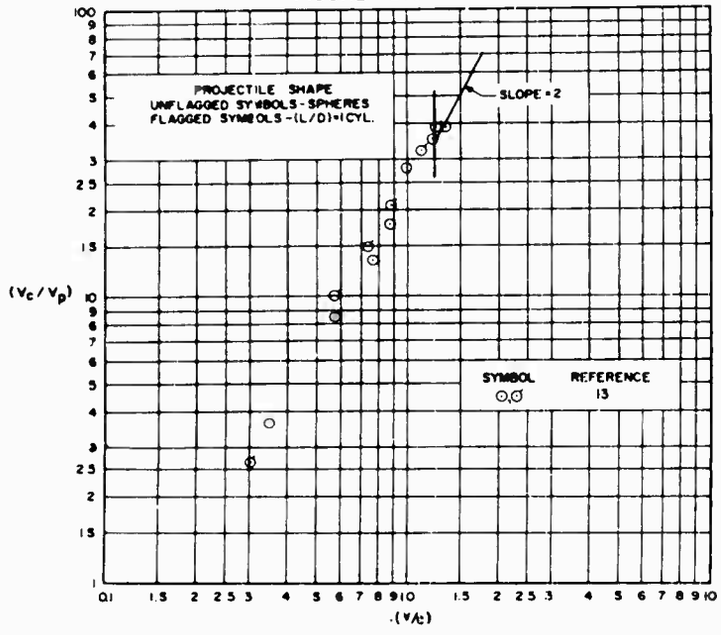

VARIATION OF CRATER VOLUME PARAMETER WITH IMPACT VELOCITY PARAMETER FOR LEAD PROJECTILES AND TARGETS

FIGURE - 21d

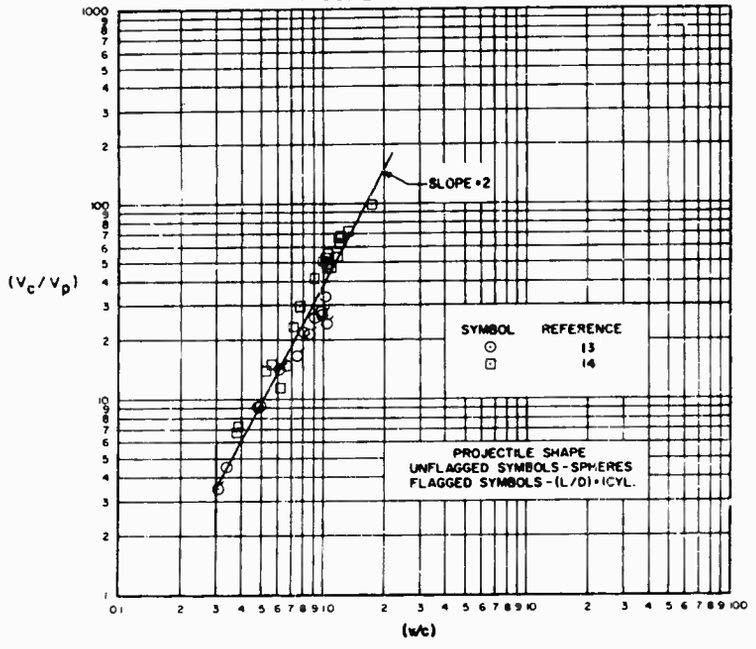

EFFECT OF PROJECTILE DENSITY ON CRATER VOLUME
FIGURE-23

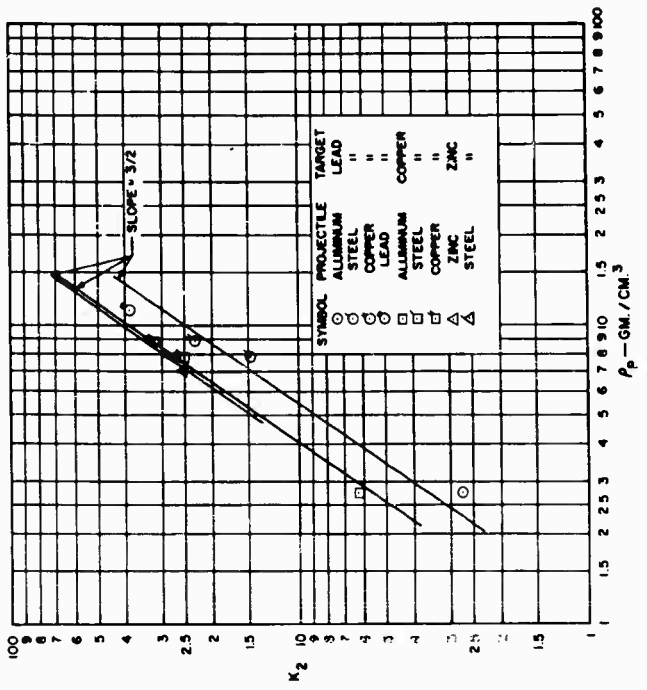

EFFECT OF TARGET DENSITY ON CRATER VOLUME
FIGURE-22

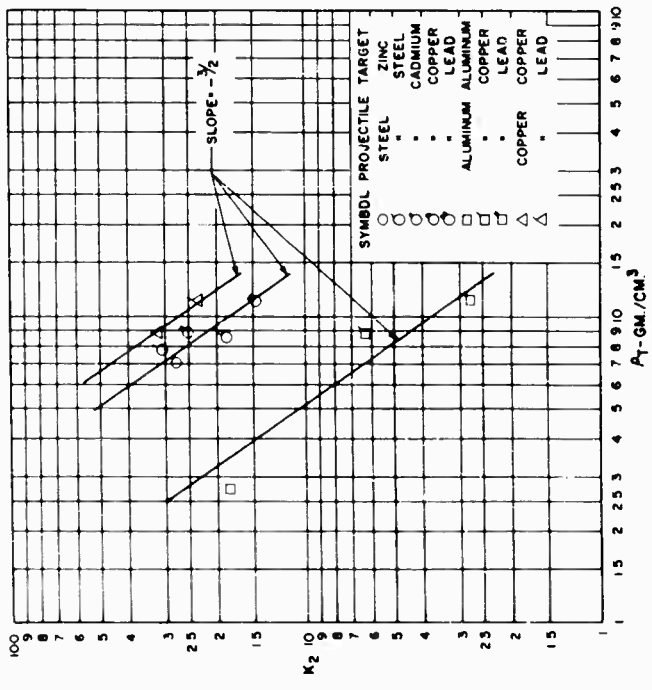

EFFECT OF PROJECTILE DENSITY ON PENETRATION
FIGURE-25

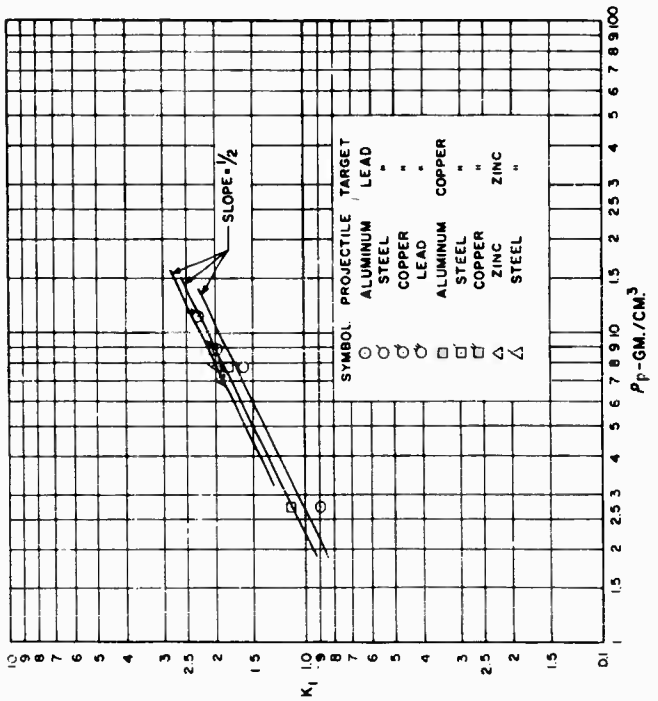

EFFECT OF TARGET DENSITY ON PENETRATION
FIGURE - 24

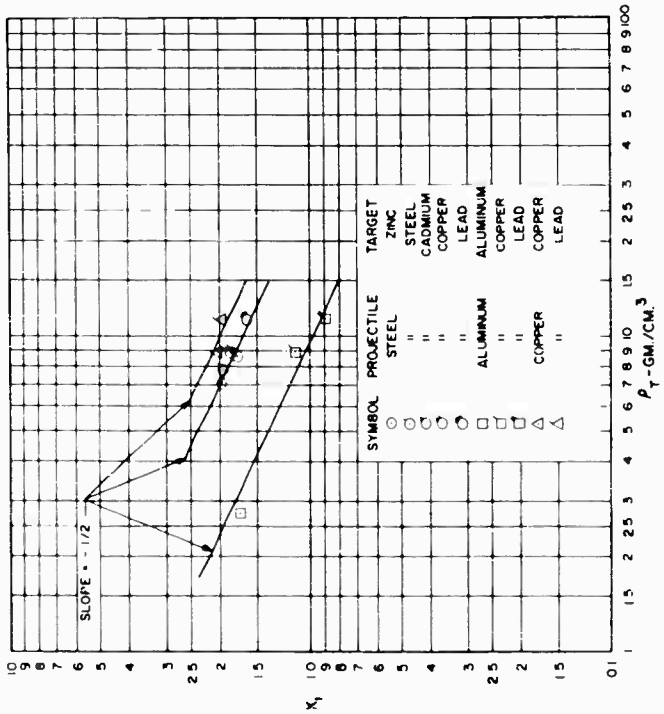

COMPARISON OF PREDICTED PENETRATION WITH TEST DATA

FIGURE - 26a

$$\left[P_C / D_S\right]_{(\frac{v}{c})=1} = K_1$$

TEST DATA

$$\left[P_C / D_S\right]_{(\frac{v}{c})=1} = 1.96\,(\rho_P/\rho_T)^{1/2}$$

EQN. 8

SEE TABLE I FOR KEY TO SYMBOLS

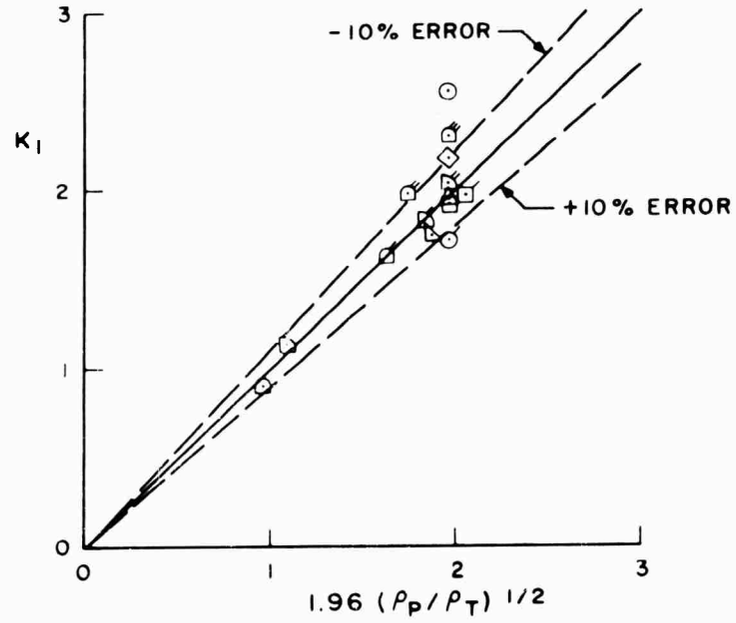

FIGURE - 26b

$$\left[P_C/D_S\right]_{(\frac{v}{c})=1} = K_1$$

TEST DATA

$$\left[P_C/D_S\right]_{(\frac{v}{c})=1} = 2.28\,(\rho_P/\rho_T)^{2/3}$$

EQN. 1

SEE TABLE I FOR KEY TO SYMBOLS

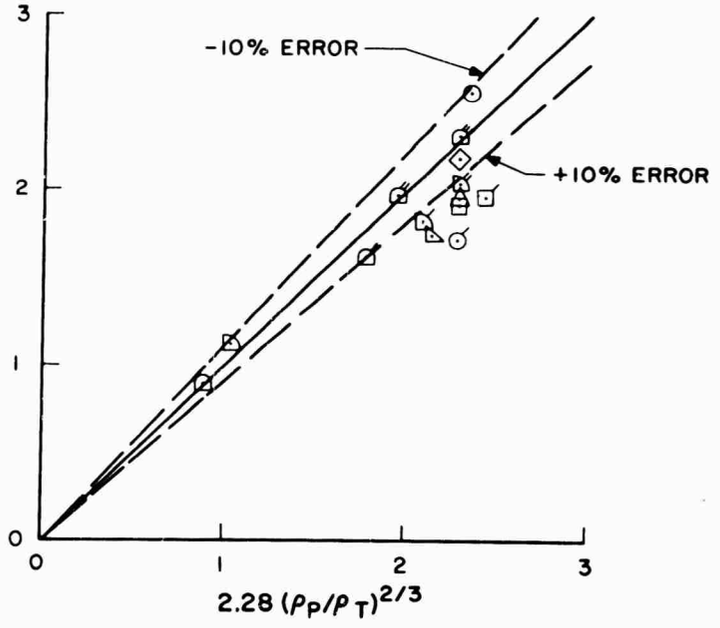

COMPARISON OF PREDICTED CRATER VOLUME WITH TEST DATA

FIGURE-27a

$\left[V_C/V_P\right]\left(\frac{v}{c}\right)_{=1} = K_2$

TEST DATA

$\left[V_C/V_P\right]\left(\frac{v}{c}\right)_{=1} = 30.25\,(\rho_P/\rho_T)^{3/2}$

EQN. 9

SEE TABLE I FOR KEY TO SYMBOLS

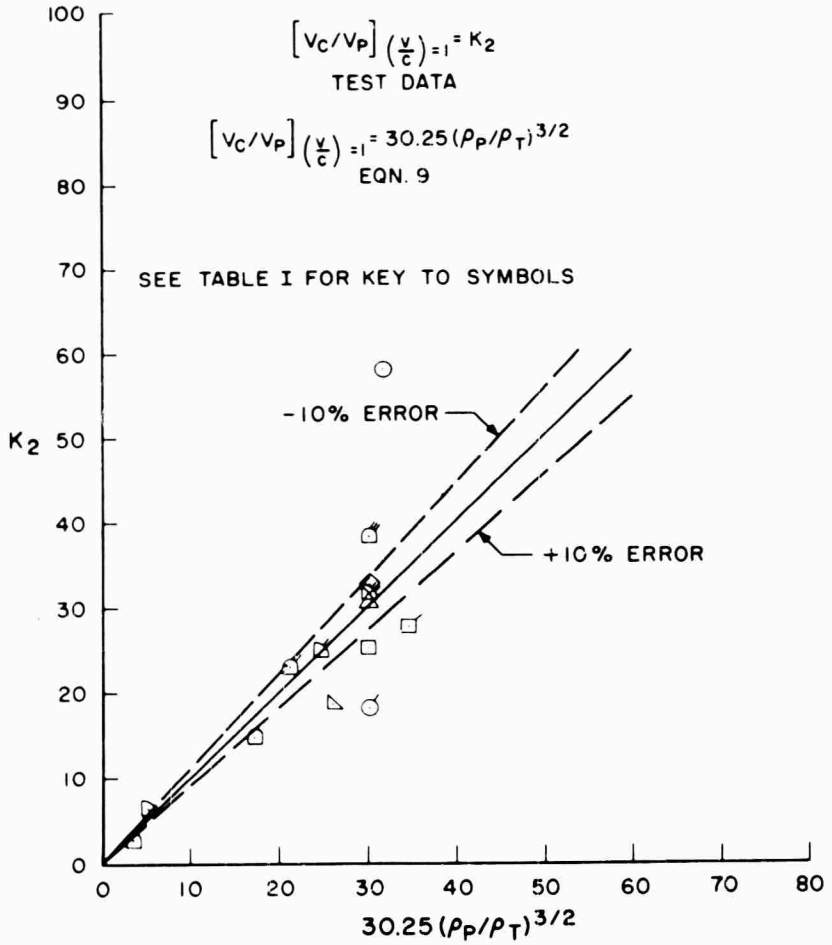

FIGURE - 27b

$\left[V_C/V_P\right]_{\frac{v}{c}=1} = K_2$

TEST DATA

$\left[V_C/V_P\right]_{\frac{v}{c}=1} = 34\,(\rho_P/\rho_T)^{3/2}$

EQN. 2

SEE TABLE I FOR KEY TO SYMBOLS

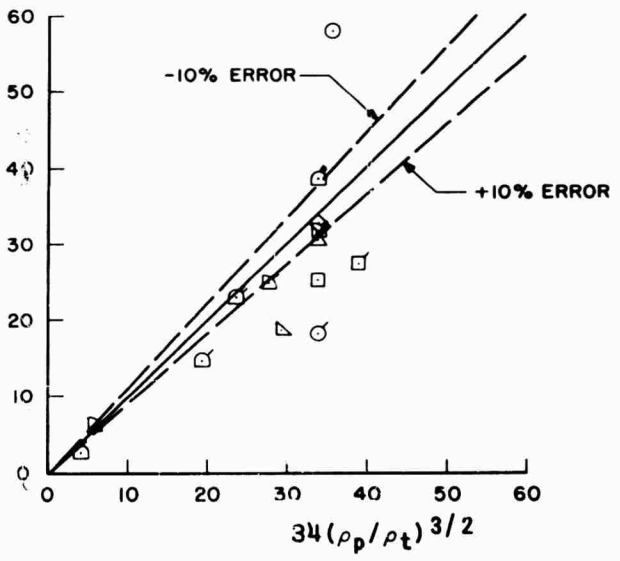

identical, both the penetration (K_1) and crater volume (K_2) data decrease in a manner that corresponds to increasing material strength or hardness properties.

The inability to predict cratering effects in the aluminum alloy targets could be due to a number of things. First, the data cover a range of impact velocities which does not extent to the value of the rod sound velocity (c) in these materials. Kineke[5] has established the following conditions for a truly hypervelocity impact:

1) the crater must be hemispherical in shape, and

2) the component of the impact velocity normal to the target surface must be greater than the velocity of a plastic (dilatational) wave in the target.

The dilatational wave velocity for the aluminum alloys (approximately 6.2 km/sec) exceeds the rod sound velocity -- consequently, even though these data fall within the (P_C/D_C) limits established for this investigation the maximum impact velocity falls far short of the dilatational velocity. Second, the properties (shear strength, hardness, etc.) of aluminum alloys vary over a wide range. While no strong effect at high velocities due to material strength or hardness has been indicated by the remainder of the data, the aluminum alloy target data combine a relatively low maximum test velocity (when compared with the dilatational wave velocity) with relatively high strength target materials, possibly resulting in a strong low velocity-material strength effect. Additional, higher velocity data for these alloys are required to clarify this issue.

The variation in K_1 and K_2 for the identical projectile-target material systems indicates that penetration and crater volume are also dependent upon a weak function of the target material properties. Several authors have suggested, based upon either experimental results or theoretical considerations, that impact cratering is dependent upon various mechanical or physical properties of the target material. Rinehart and Pearson[9], and Palmer[10], et al., have found that target shear strength is an important parameter. Allison[11], Summers[1], and Feldman[12] have shown effects due to variation in target Brinell hardness. Within the limitations of the present study, however, these parameters do not appear to have a strong effect. As in the case of the aluminum alloy data, additional higher velocity data are needed before a definite conclusion can be reached.

IMPACT AT OBLIQUE INCIDENCE

The preceding section was limited to an analysis of the case in which the projectile approaches the target along the normal to the target surface. This section is devoted to an examination of the data which apply to the related problem of impact at angles of incidence other than normal.

Crater Profile

The limited amount of data illustrating the variation of (P_C/D_C) with impact velocity at oblique angles of incidence are presented in Figure 28. The

erater profiles produced when steel projectiles impact against lead targets at both normal and oblique angles of ineidenee are compared at equal values of normal impact veloeity. The oblique impact data represent a series of tests at 60° incidenee in which both the mass and total velocity of the projeetile were varied and a series of tests in which angle of incidence was varied while projeetile mass and total velocity were held constant. It is apparent from these data that the eharaeteristie high veloeity crater shape is realized in oblique impact at roughly the same value of normal impact velo'ity as is requi'ed in normal impaet. It is also evident that the low velocity peak in (P_C/D_C) observed under normal impact is not present for low values of normal velocity under oblique impaet conditions. In oblique impact, low normal velocities are associated either with very high total velocity - high angle of obliquity impact or with low total velocity - low angle of obliquity impaet.

Further evidenee that the charaeteristie high veloeity erater shape is reaehed in oblique impact at high values of normal impaet velocity is presented in Figure 29. A eomparison of the ratio of the diameter of the erater mouth that is in line with the projectile trajeetory $(D_{C_{MAJ}})$ to the diameter at right angles to the projeetile trajeetory $(D_{C_{MIN}})$, both measured in the plane of the undamaged target surfaee, indicates that the craters produeed are eireular at high values of normal impact veloeity.

Depth of Penetration

Data illustrating the variation of the penetration parameter, (P_C/D_S), with the impact veloeity parameter, (v/c), for oblique angles of incidenee are presented in Figures 30 and 31. Here data obtained by impaeting eopper spheres with copper targets and by impaeting steel into lead at both normal and oblique angles of incidence are compared at equal values of normal impact veloeity. The data indieate that under high velocity conditions, projeetiles of equal mass impaeting at either normal or oblique incidenee penetrate to the same depth provided they have the same veloeity normal to the surface. In the ease of steel impacting into lead at oblique incidence, the typical transition region between undeformed projeetile penetration and high velocity penetration is not presenl. This supports the earlier observation that the low velocity (P_C/D_C) overshoot does not oeeur in oblique impact.

The combined crater profilc and penetration data indicate that, under high velocity impact conditions, it is impossible to determine either causitivc particle mass or vclocity by examination of a crater. Consequently, to the extent that the surface of the Earth and Moon react as ductile metals under high velocity impact conditions, these data invalidate calculations of the mass and velocity of the meteorites responsiblc for terrestrial or lunar craters that are based only on observations of the craters.

VARIATION OF CRATER PROFILE PARAMETER WITH IMPACT VELOCITY
FOR NORMAL AND OBLIQUE INCIDENCE
STEEL PROJECTILES AND LEAD TARGETS

FIGURE-28

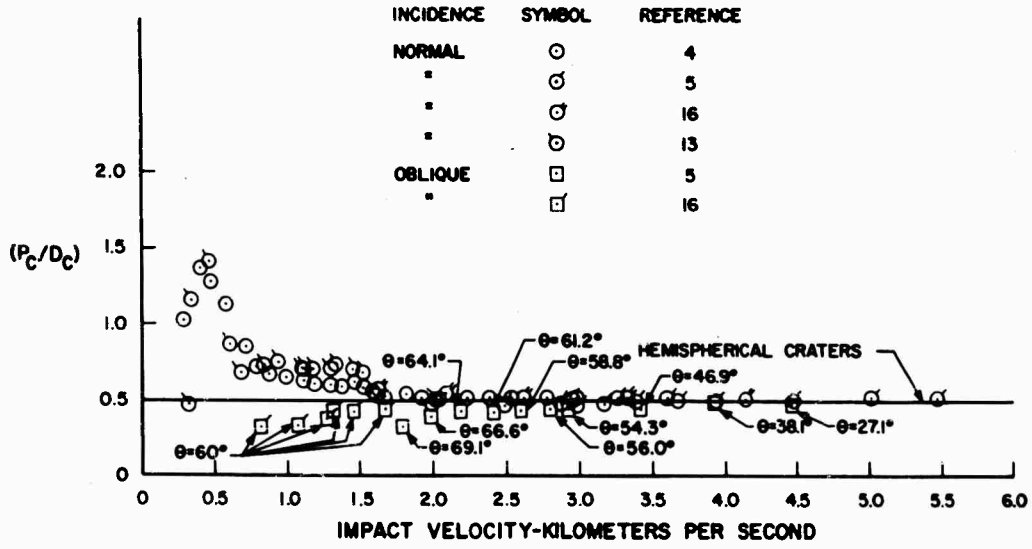

VARIATION OF CRATER SHAPE PARAMETER WITH IMPACT VELOCITY
FOR OBLIQUE INCIDENCE
STEEL PROJECTILES AND LEAD TARGETS

FIGURE-29

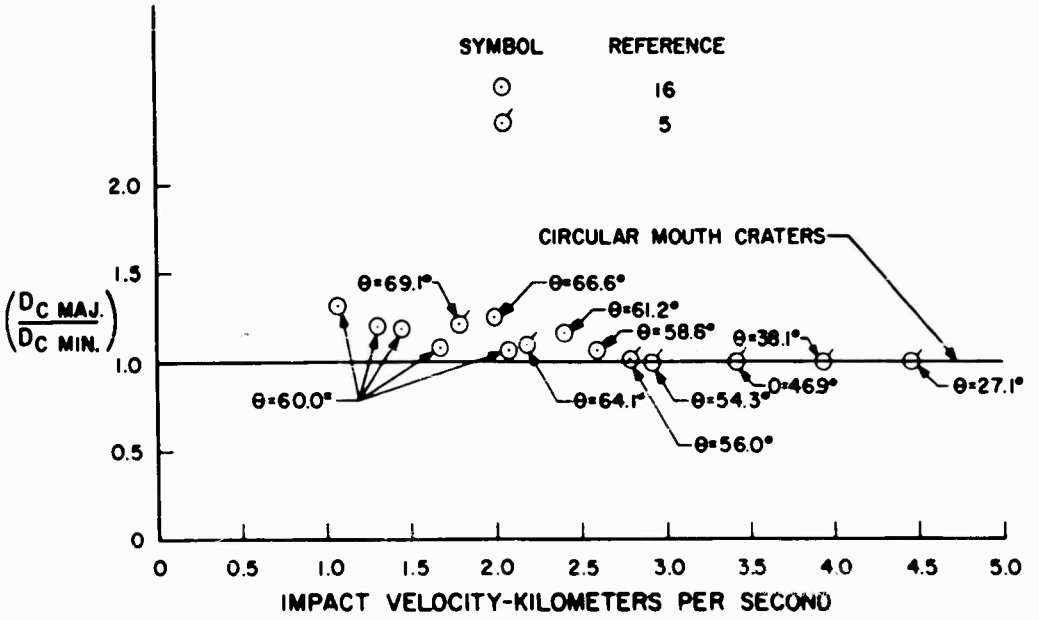

VARIATION OF PENETRATION PARAMETER WITH IMPACT VELOCITY PARAMETER FOR NORMAL AND OBLIQUE INCIDENCE-COPPER PROJECTILES AND TARGETS

FIGURE-30

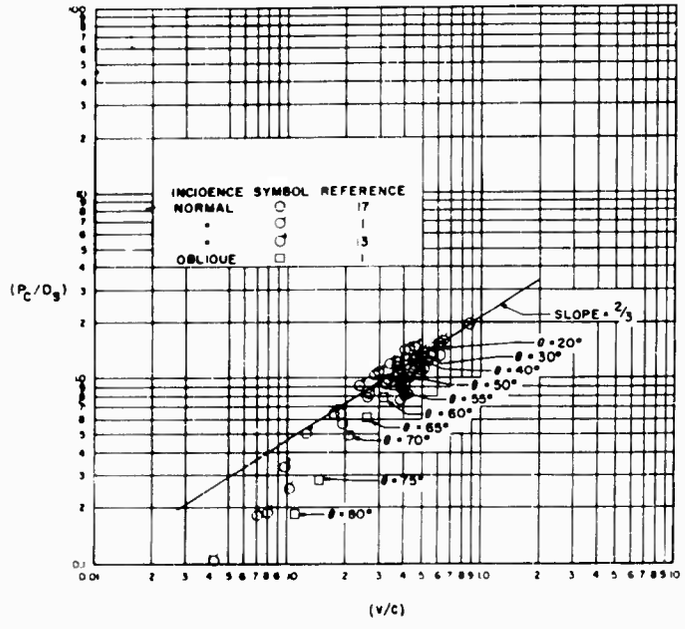

VARIATION OF PENETRATION PARAMETER WITH IMPACT VELOCITY PARAMETER FOR NORMAL AND OBLIQUE INCIDENCE-STEEL PROJECTILES AND LEAD TARGETS

FIGURE 31

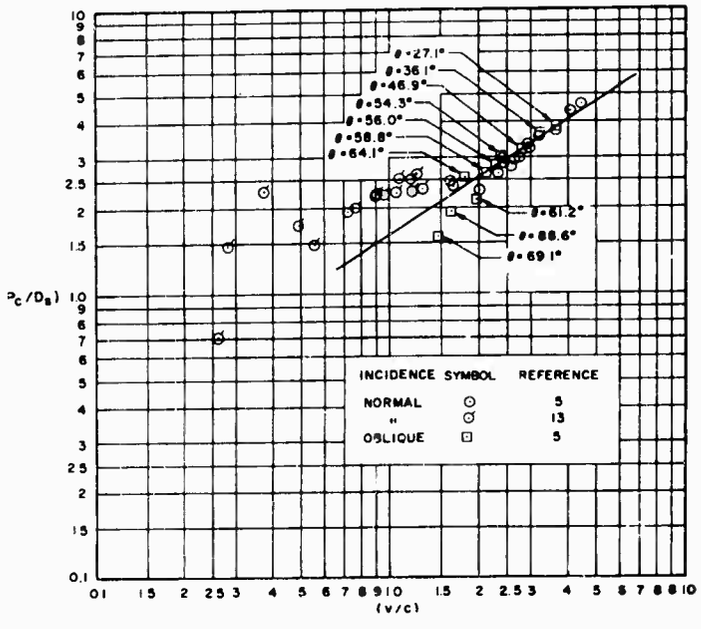

CONCLUSIONS

A thorough review has been made of existing experimental data applicable to the impact of individual high velocity metal projectiles with semi-infinite metal targets. The following empirical relations,

$$P_C/D_S = 1.96\ (\rho_P/\rho_T)^{1/2}\ (v/c)^{2/3}$$

and

$$V_C/V_P = 30.25\ (\rho_P/\rho_T)^{3/2}\ (v/c)^{2}$$

relating depth of penetration and crater volume to properties of the projectile and target have been derived based upon the following assumptions:

1) projectile shape and orientation do not affect crater size or shape, and

2) high velocity craters are hemispherical in shape.

Both of these assumptions are supported by experimental results; however, the first must be qualified slightly to apply only to either spherical projectiles or to cylindrical projectiles up to one caliber in length.

It should be noted that the objective of this study was to determine whether an analysis of the total body of impact data would result in a compatible set of equations of sufficient accuracy for engineering design purposes. The extension of the results to conditions not covered by the available data involves certain elements of uncertainty; however, some evidence is available which indicates that the trends established by these data appear at velocities of 10 km/sec.

Evidence has also been presented which indicates that, under high velocity conditions, particles of identical material and mass impacting at either normal or oblique incidence produce identical craters providing they have the same velocity normal to the surface.

ACKNOWLEDGMENT

The author wishes to take this opportunity to thank Mr. John H. Kineke, Jr., of BRL, Mr. Walter W. Atkins of NRL, and Dr. C. J. Maiden formerly of CARDE for their cooperation in making their data available for this study.

REFERENCES

1. Summers, J. L., October, 1959, Investigation of high speed impact: regions of impact and impact at oblique angles: NASA, TN D-94.

2. Huth, J. H., Thompson, J. S., and Van Valkenburg, M. E., 1957, Some new data on high speed impact phenomena: Jour. Appl. Mech., volume 24, March, p. 65.

3. Charters, A. C., and Locke, G. S., Jr., May 28, 1958, A preliminary investigation of high speed impact: the penetration of small spheres into thick copper targets: NASA, RM A58B26.

4. Kineke, J. H., Jr., 1959, An experimental study of crater formation in lead: Proceedings of the Third Symposium on Hypervelocity Impact, volume 1, February, p. 157.

5. Kineke, J. H., Jr., 1960, An experimental study of crater formation in metallic targets: Hypervelocity Impact, Fourth Symposium, volume 1, September, p. 10.

6. Atkins, W. W., 1960, Hypervelocity penetration study: Hypervelocity Impact, Fourth Symposium, volume 1, September, p. 11.

7. Maiden, C. J., Tardif, H. P., and Charest, J., 1960, An investigation of spalling and crater formation by hypervelocity particles: Hypervelocity Impact, Fourth Symposium, volume III, September, p. 38.

8. Gehring, J. H., Jr., and Richards, L. G., 1960, Further studies of micro-particle cratering in a variety of target materials: Hypervelocity Impact, Fourth Symposium, volume III, September, p. 34.

9. Rinehart, J. S., and Pearson, J., 1954, Behavior of metals under impulsive loads: Cleveland, Ohio, American Society for Metals.

10. Palmer, E. P., Grow, R. W., Johnson, D. K., and Turner, G. H., 1960, Cratering; experiment and theory: Hypervelocity Impact, Fourth Symposium, volume 1, September, p. 13.

11. Allison, F. E., 1959, A review of the theories concerning crater formation by hypervelocity impact: Proceedings of the Third Symposium on Hypervelocity Impact, volume 1, February, p. 287.

12. Feldman, J. B., Jr., 1960, Volume - energy relation from shaped charge jet penetrations: Hypervelocity Impact, Fourth Symposium, volume II, September, p. 26.

13. Collins, R. D., Jr., and Kinard, W. H., May, 1960, The dependency of penetration on the momentum per unit area of the impact projectile and the resistance of materials to penetration: NASA, TN D-238.

14. Van Fleet, H. B., Whited, C. R., and Partridge, W. S., January, 1958, High velocity impact craters in lead-tin alloys: University of Utah, Technical Report No. OSR-13.

15. Ferguson, W. J., and McKinney, K. R., November 19, 1959, The influence of temperature elevation on the penetration of missiles into copper targets: NRL Report 5407.

16. Culp, F. L., 1959, Volume - energy relation for craters formed by high velocity projectiles: Proceedings of the Third Symposium on Hypervelocity Impact, volume 1, February, p. 141.

17. Partridge, W. S., 1957, High velocity impact studies at the University of Utah: Proceedings of the Second Hypervelocity and Impact Effects Symposium, volume 1, December, p. 93.

HYPERVELOCITY LAUNCHERS AND HYPERVELOCITY IMPACT EXPERIMENTS AT ARDE, FORT HALSTEAD

F. Smith, W. A. Clayden, C. R. Wall, and D. F. T. Winter

Armament Research and Development Establishment
Fort Halstead, Kent, England

SUMMARY

This paper outlines the development of hypervelocity launchers at ARDE using fairly conventional techniques. Velocities up to 25,000 ft/sec have so far been attained.

The paper also summarises a series of impact studies on solid targets and thin plates inclined to the direction of motion. Future tests are discussed.

PART I - THE DEVELOPMENT OF HYPERVELOCITY LAUNCHERS

1. Introduction

In 1956 we at ARDE embarked on the development of hypersonic facilities. Our first step was the development of the light gas gun tunnel (Ref. 1) in which a light gas at high pressure accelerated a light piston in a gun barrel compressing and heating a working fluid, usually air. The working fluid was then allowed to expand through a throat to a working section giving a running time measured in fractions of a second.

The success of this technique led us to consider the possibility of adapting it to the design of a launcher for hypervelocity projectiles. Calculations were made (Ref. 2) on the basis of a light gas, hydrogen, driving a light piston to compress helium which in turn was the driver gas for the model. We were particularly attracted to the use of compressed gas at room temperature rather than techniques then starting in U. S. and Canada involving propellants, explosives and gas combustion. Subsequently, for safety reasons, we substituted helium for hydrogen.

2. Theory

A series of calculations were made using the now familiar non-dimensional variables $\bar{s}$, $\bar{t}$, $\bar{u}$ based on the simplified layout shown in Figure 2. It is not intended here to examine the theory in detail, but merely to point out a few conclusions.

The first point which is often not sufficiently stressed is the importance of high speed of sound in the launcher gas (Fig. 3). At high model velocities an increase in speed of sound is much more important than an increase in pressure, and this led us to think of multiple shock heating ahead of the piston. In practice, however, it is difficult to achieve this and at the same time have a piston heavy enough to maintain peak conditions for sufficient time. However, we believe that the piston should be light rather than heavy.

Secondly, the non-dimensional curves of Figure 4 show that for infinite chamber volume, the chamber should be large in diameter relative to the launcher barrel (curves 2 and 3). If, alternatively, we postulate that the piston moves forward to maintain constant pressure and speed of sound there is little gain with large chamber diameter (curves 3 and 5) but a large gain with a chamber of equal cross-section to that of the barrel (curves 2 and 4). This led us to think that piston extrusion to give constant peak conditions is a desirable feature. However, when we look at a typical case (Fig. 5) it is obvious that the gain is only achieved when the piston face is nearly equal in area to the launcher barrel and moving at very high velocity. If the piston fails to extrude at the required velocity then there will be a marked loss in performance. If it succeeds in attaining this high velocity, it is extremely difficult to prevent the piston following the model down the launcher barrel and range.

In some circumstances, however, this may not be an embarrassment and there may be other reasons why piston extrusion is desirable. Charters (Ref. 5) gives an example where a fragile model is limited in the peak accelerations it can stand, although here of course there must be a loss of performance when compared with a model without this limitation.

The conclusion here is that the launcher should be tailored to suit the required conditions and fortunately the calculations for the design are easy to make and are a reliable indication of performance. In our attempt to attain maximum velocity we have found that barrel strain and gas wash rather than, as might be supposed, our use of the relatively simple techniques using cold compressed helium as a driver gas have set the practical limits. This is not to say that with careful design and better barrel materials the more sophisicated systems currently in use in North America might not yield better model velocities, but at present we have achieved velocities of 25,000 ft/sec with a 0.15-gm, 0.25-inch calibre, model which is not dissimilar to the results obtained in North America.

As we said before the main gain in performance if gas wash is not a serious limitation would be by gain of temperature, i.e., speed of sound in the gas. Shock heating as we have mentioned is one way, preheating of the driver gas is another way if it can be achieved without contamination. Use of propellants to preheat tends tooffset the gain in temperature by an increase in molecular weight of the gas and some form of electrical heating seems desirable. Because of the reduction in $\bar{s}$ when speed of sound is increased, a longer launcher barrel may then be desirable.

Experiments at ARDE have shown that whilst at 10,000 ft/sec a 100 calibre long barrel is adequate, at 25,000 ft/sec 200 calibres length is necessary to achieve full performance. Higher velocities will probably require a still longer barrel.

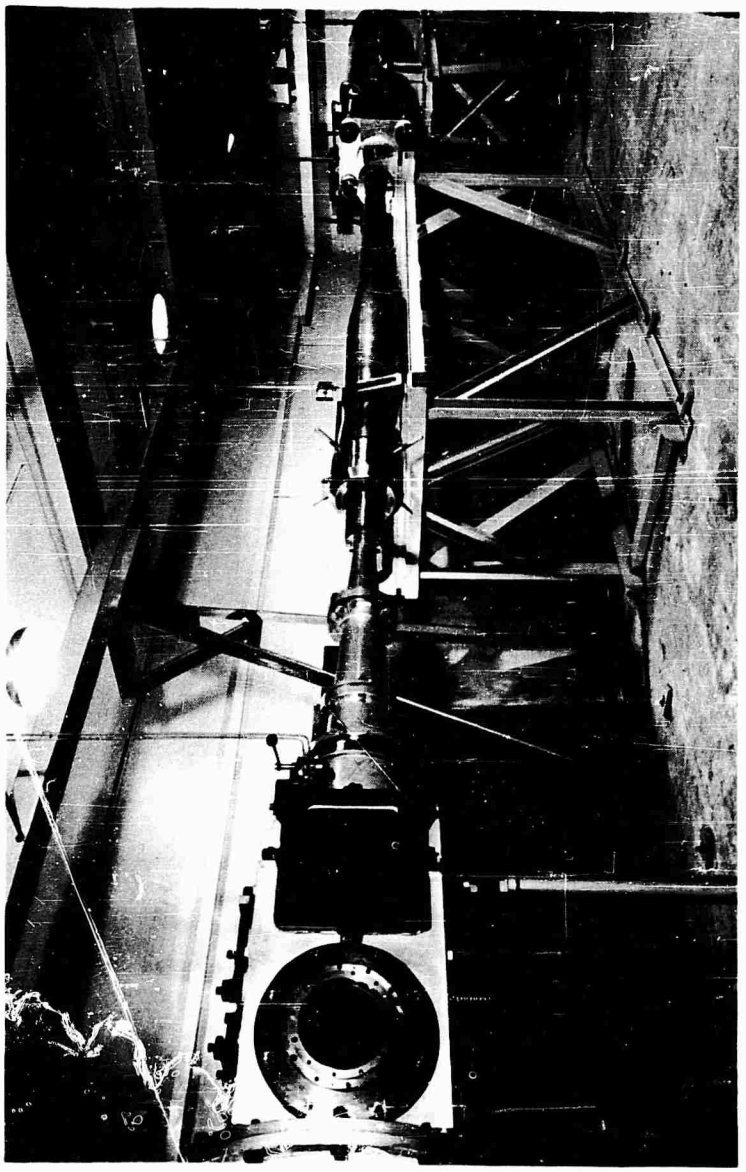

Figure 1. Light Gas Gun Tunnel

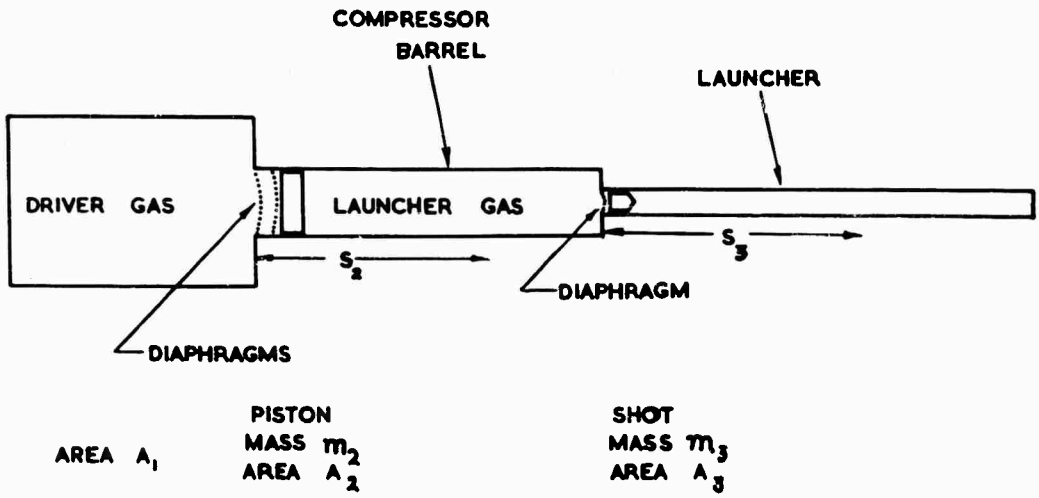

FIG 2 DIAGRAM OF HIGH VELOCITY LAUNCHER

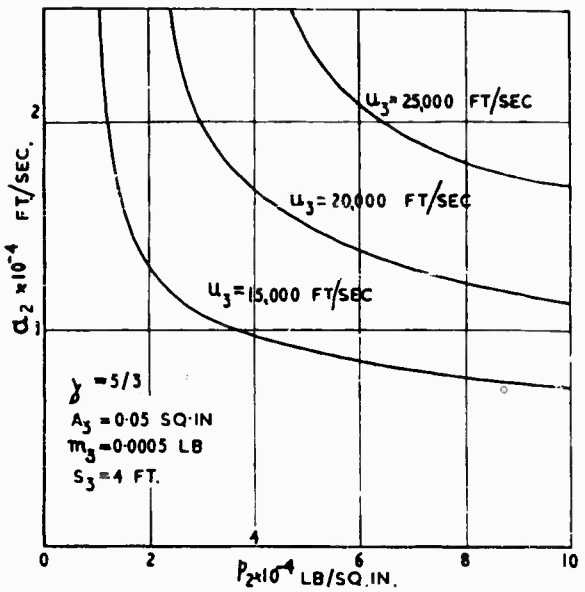

FIG 3 EFFECT OF a_2, P_2 ON MODEL VELOCITY

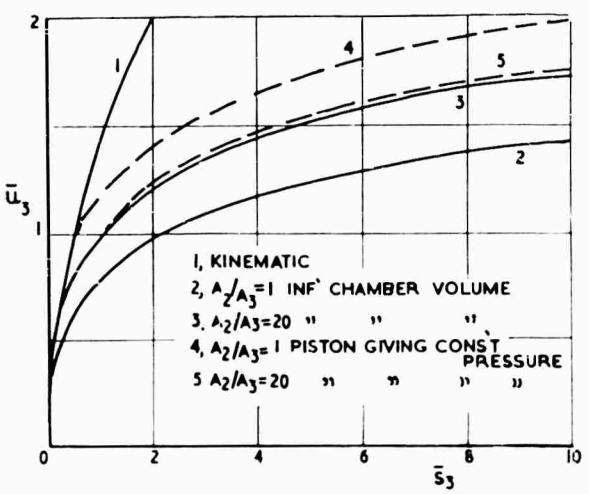

FIG 4 MODEL VELOCITY - DISTANCE CURVES

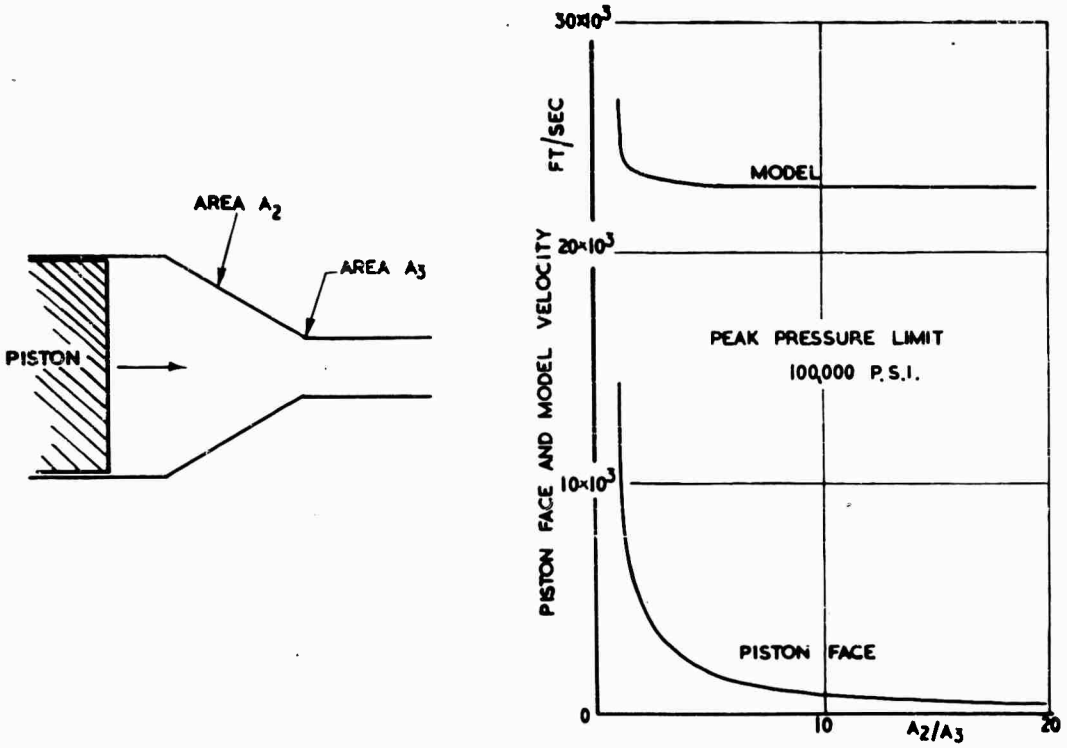

FIG 5 PISTON EXTRUSION TO GIVE CONSTANT PEAK PRESSURE IN THE BARREL

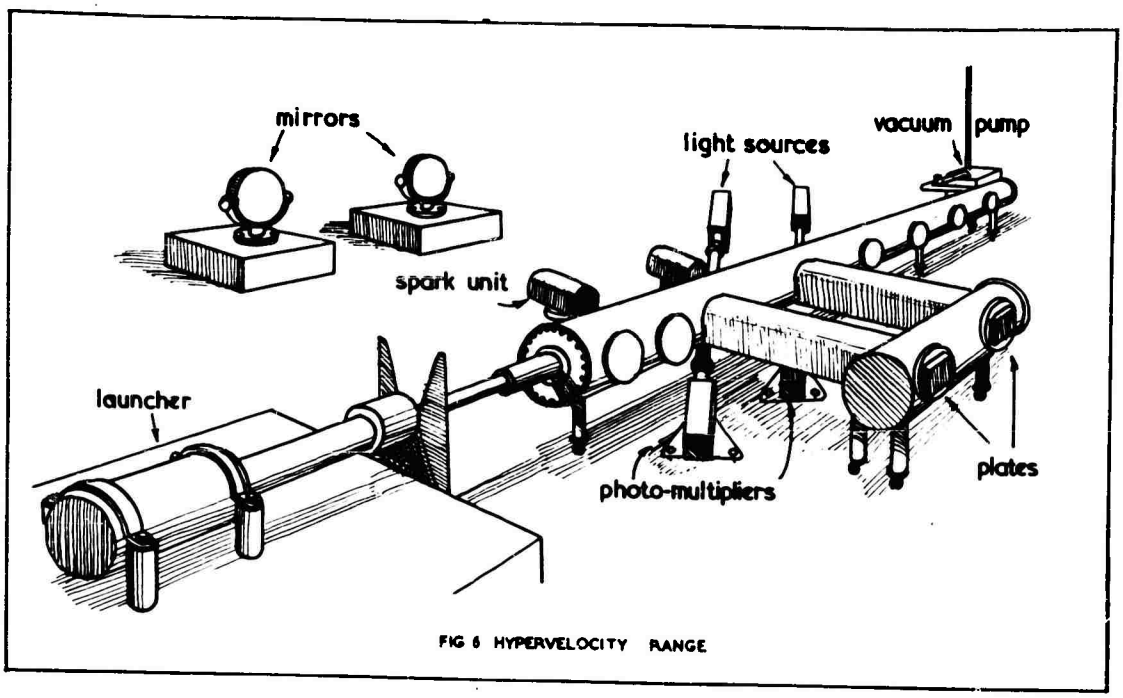

FIG 6 HYPERVELOCITY RANGE

3. Development of the No. 1 Launcher

Following the theoretical examination of the design of a hypervelocity launcher, a small launcher was built, primarily as a prototype of a larger launcher. The No. 1 launcher is shown in Figure 6. The launcher barrel is 1/4 inch calibre, 4 feet long. The compressor barrel is of 1 inch calibre and 5 feet long separated from the chamber 3.7 inches diameter, 3 feet long, by a double diaphragm. An intermediate pressure between the two diaphragms, each insufficient to hold the full pressure, is reduced when a firing is required causing first one and then the other diaphragm to burst.

During the period 1958-59 the driving pressure was limited to 4,000 psi due to a lack of suitable pumps and the impact tests described in Part II were made during this period. A maximum velocity of 12,000 ft/sec was achieved in this condition and the effects of piston mass, compressed barrel pressure and secondary diaphragm thickness were investigated. In 1960 the driving pressure was raised to 10,000 psi and a peak velocity of 24,800 ft/sec was obtained. Barrel wear was excessive at these velocities and experiments were made to improve the compressor barrel-launcher barrel joint. Leaks at this point caused a marked reduction in launcher velocity.

Experiments with piston mass and material resulted in the use of a simple cylinder of polythene weighing 45 gm. A lighter piston is just as effective but the tendency for the whole piston to extrude down the launcher barrel is greater for the lighter piston.

The range on the No. 1 launcher is simple and consists of five sections 12 inches diameter 4 feet long each with 3 pairs of observation windows. Timing is by interruption or reflection of a light beam. The range pressure is from 10 atmospheres down to 1 mm Hg; the launcher barrel is evacuated in all tests. The effect of muzzle flash was reduced by a dump chamber with baffles and by setting back the photographic equipment normal to the line of flight.

Barrels of 1/8 inch and 1/2 inch calibre have also been tested on this launcher. The 1/2 inch calibre gave an expected reduction in velocity to 15,000 ft/sec although the kinetic energy is greater than for the 1/4 inch barrel. The performance of the 1/8 inch barrel was poorer than expected possibly due to the effect of boundary layer on such a small diameter.

4. No. 2 Launcher

The No. 2 launcher is approximately 5 times larger than the No. 1 having a compressor barrel 5 inches diameter and 21 feet length. Launcher barrels available are 1/2 inch, 1 inch, and 1.8 inches calibre which it is anticipated will give velocities of 25,000 ft/sec (1/2 inch 0.8 gm, 1 inch 8 gm) and 20,000 ft/sec (1.8 inches, 45 gm). Doubling the model mass will reduce the velocity by approximately 10 percent. Installation is now proceeding and preliminary firings at 4,000 psi driving pressure have yielded results similar to those obtained with the No. 1 launcher. The range is at present limited to 50 feet in length but it is hoped to double this in the near future. Provision is made for velocity measurements and photography in two directions at right angles every 4 feet along the range. Hypervelocity impact studies can be made.

5. Other Developments

A third launcher similar to the No. 1 launcher will be used with an ionized range section to study ionospheric problems. A number of ionizing techniques are being examined and R. F. generation seems the most promising at the moment. Similar work is already in hand on a plasma-heated low density tunnel and the range will be used to study plasma effects in the presence of a magnetic field stationary with respect to the gas.

We also have under development a passive telemetry system to give model attitude on the range. The model contains a tuned circuit (of the order of 3 megacycles/sec) and passes through a long coil tuned to the same frequency. The two coils behave like a transformer, the impedance of the fixed coil being a function of the attitude of the secondary coil (Fig. 8). Preliminary firings with a 1/2-inch calibre model up to $1/4\ 10^6$ g acceleration are very promising. It is proposed to modify the system at a later date to a semi-passive system giving direct information from the model. In this respect it will be similar to developments at AEDC, CARDE, G. M. research laboratories (Ref. 5) and elsewhere.

In the passive role, measurement of model attitude might eventually lead to a considerable reduction in photographic recording and subsequent computation. A paper will be published shortly on this work.

PART II - SOME EXPERIMENTS ON HYPERVELOCITY IMPACT

1. Introduction

Impact phenomena at high speeds have recently become important because of the desire to obtain some understanding of the damage which will be sustained by the skin of a missile or space vehicle when struck by fragments of meteorites. More basic information on the behaviour of materials when subjected to very high loads may also be obtained.

The general problem of the damage sustained by a plate when struck by a fragment at high velocity contains a number of parameters and there does not yet appear to be an adequate theory or even a complete understanding of the physical processes. The comparatively simple case of a crater formed in a semi-infinite target when struck by a sphere at normal incidence has been studied experimentally by a number of workers and several empirical laws relating the penetration to the impact Mach number (ratio of the velocity of the projectile relative to the target/speed of sound in the target given by $\sqrt{E_t/\rho_t}$) have been proposed. This work has been extended at ARDE and some experiments were undertaken during the latter part of 1959 to show the general trend of damage which might result as the shape of the fragment, the angle of impact and the thickness of the target were varied; most of the results are given in this paper.

2. Results

The ARDE No. 1 light gas gun described in Part 1 of this paper was used to fire 1/4-inch projectiles into targets which were 4 inches in diameter, gas pressure was 4,000 psi limiting the projectile velocity to a maximum of 12,000

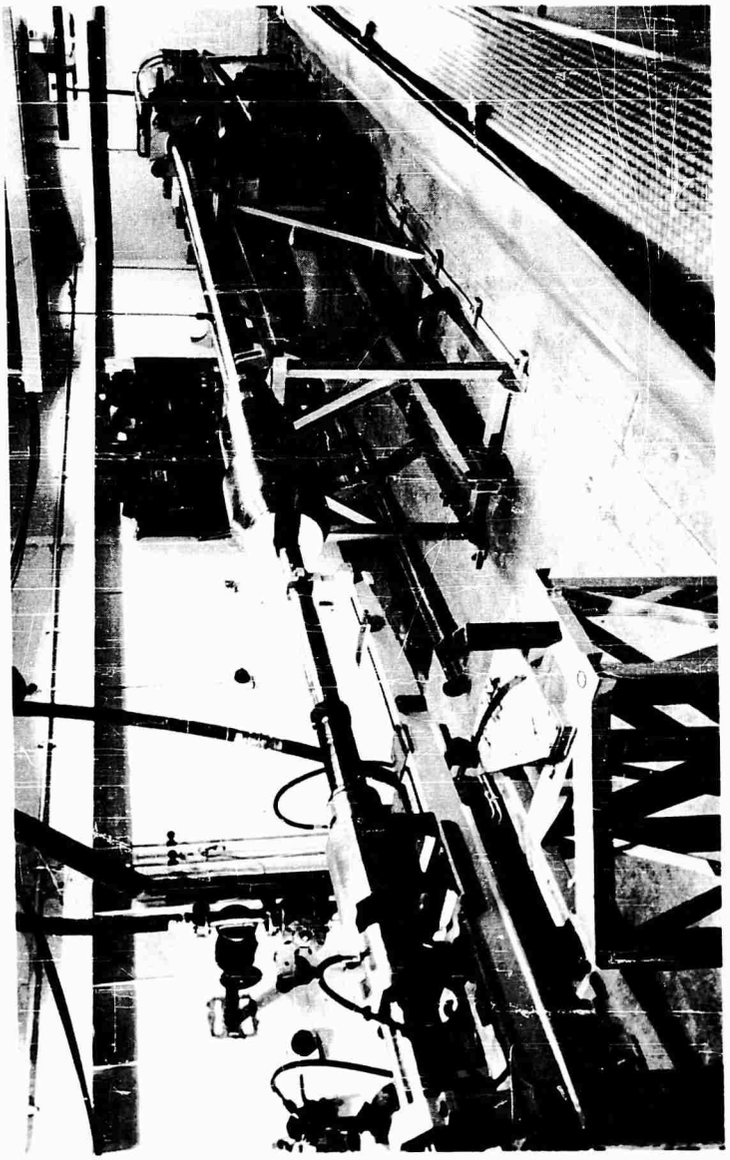

Figure 7. Hypervelocity Launcher

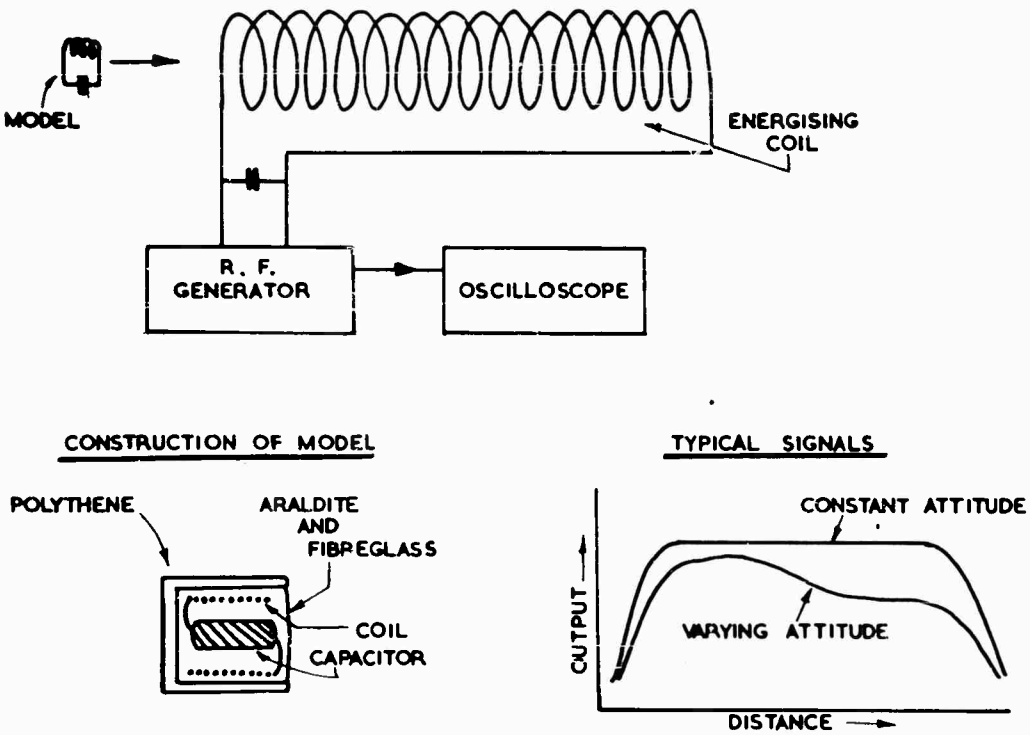

FIG 8 PASSIVE TELEMETRY SYSTEM

ft/sec. Consequently most of the tests described here were made at velocities of 10,000 ft/sec.

2.1 Impact of spheres into semi-infinite targets at normal incidence

No adequate underlying theory exists for impact at speeds of the order of 10,000 ft/sec but several workers (e.g., Refs. 7 and8) have attempted to relate the penetration of spheres to the velocity of impact and the target properties with a simple expirical formula of the form

$$\frac{P}{d}=k\left(\frac{U}{c_t}\right)^n\left(\frac{\rho_p}{\rho_t}\right)^m \qquad (1)$$

where P is the penetration, d is the diameter of the projectile, k, n, and m, are constants U is the velocity of impact, c_t is the speed of sound in the target given by $\sqrt{E_t/\rho_p}$ and ρ_t , ρ_p are the densities of the projectile and target respectively.

The penetration results of a systematic series of firings in which spherical projectiles were fired into various targets are plotted against $\left[\rho_p/\rho_t\right]\left[U/c_t\right]$ in Figure 9 and compared with previous results. These results which were obtained for 8 widely differing combinations of projectile and target material do not deviate by more than 30 percent from a mean line given by

$$\frac{P}{d}=2{\cdot}0\left(\frac{\rho_p}{\rho_t}\right)^{\frac{2}{3}}\left(\frac{U}{c_t}\right)^{\frac{2}{3}} \qquad (2)$$

and apart from a constant of 2 instead of 2.28 this is similar to the relationship obtained by Charters and Locke; in fact our results for aluminium and lead targets are fitted slightly better by the Charters and Locke formulae. A deviation of as much as 30 percent however is considerably more than would be expected by experimental error alone and it now seems likely from the growing volume of experimental data that whilst the correlation given by Equation (2) may be sufficient for engineering purposes for a limited range of velocities and materials it does not completely explain all the phenomena. When the depth of penetration is compared on the basis of Equation (2) there does not appear to be any marked difference between the ductile materials such as aluminium and copper and the brittle materials such as cast iron and titanium, nevertheless, the craters are completely different. Figure 10 illustrates typical craters formed in various materials ranging from very ductile aluminium to brittle perspex. It may be seen that in the case of the aluminium target the target has undergone considerable plastic deformation but has lost very little material, whereas, in the case of the cast iron target there is little plastic flow and most of the material from the crater has been lost. This is because in a brittle material the dynamic hoop stress produced by the impact causes extensive cracking and small fragments fall away from the target. It appears therefore, that when considering the damage to brittle materials the size of the crater is probably unimportant and the extent of the cracking should

be taken into account, this is particularly well illustrated in Figure 10e, where the radius of damage in the perspex target is about six times that of the crater. The elektron target shows that it is possible to have considerable plastic deformation and cracking together. The reason for the conical crater in titanium (this effect is repeatable) is not obvious but an examination of an etched specimen shows that the region of deformation and cracking is roughly hemispherical.

The magnitude and direction of the plastic deformation of the aluminium target was obtained and it appeared that the deformation was roughly spherically symmetrical with a centre in the middle of the crater. Taking this point as an origin the deformations, δx and δy, and strains, ϵ_x and ϵ_y, in the horizontal and vertical planes respectively have been plotted in Figure 11, as a function of x and y. These curves show that below a horizontal plane through the origin the target deformation is spherically symmetrical. Qualitatively it appears that the top part of the material from the crater has gone into the 'splash' and in deforming the free surface whilst the bottom part has deformed the whole target in a similar manner to a spherical expansion. By considering conservation of mass across a spherical surface centred at the origin the deformation of the target δr may be expressed in terms of the radius r and the volume of the lower part of the crater δV, thus

$$\delta V = \frac{2}{3}\pi\left\{(r+\delta r)^3 - r^3\right\}$$

which may be written as

$$(\delta r)^3 + 3r(\delta r)^2 + 3r^2(\delta r) - \frac{3\delta V}{2\pi} = 0. \qquad (3)$$

This curve has been fitted to the experimental points in Figure 11 and it may be seen that the fit is good. The ratio of the volume of the lower part of the crater δV to the total volume of the crater V is about one third for this target. At large distances from the crater the deformation is given approximately by

$$\delta r = \frac{\delta V}{2\pi r^2}. \qquad (4)$$

The strain may be obtained from (4) by writing

$$\epsilon = \frac{d(\delta r)}{dr}$$

and this curve has been drawn through the experimental points in Figure 11 and again the fit is good. At large distances from the crater the strain is given approximately by

$$\epsilon = \frac{-\delta V}{\pi r^3}. \qquad (5)$$

Applying (5) to the aluminium target and taking the limit of plastic flow to be given by $\epsilon = 0.001$, plastic flow will have extended to over 2 in from the centre of the crater. The analysis given above does not appear to be applicable to targets which

$\frac{P}{d} = 2{\cdot}28\left(\frac{\rho_p}{\rho_t}\right)^{0{\cdot}69}\left(\frac{U}{C_t}\right)^{0{\cdot}69}$ ---------- CHARTERS AND LOCKE

$\frac{P}{d} = 2{\cdot}18\left(\frac{\rho_p}{\rho_t}\right)\left(\frac{U}{C_t}\right)$ ——x——x——x— KINARD AND LAMBERT

$\frac{P}{d} = 2{\cdot}5\left(\frac{U}{C_t}\right)^{1{\cdot}4}$ — — — — — HUTH

$\frac{P}{d} = 2{\cdot}38\left(\frac{\rho_p}{\rho_t}\right)^{\frac{1}{3}}\left(\frac{\frac{U}{C_t}}{3-1{\cdot}66\ \frac{U}{C_t}}\right)^{\frac{1}{3}}$ — — — — — VAN VALKENBURG

$\frac{P}{d} = 2{\cdot}0\left(\frac{\rho_p}{\rho_t}\right)^{\frac{2}{3}}\left(\frac{U}{C_t}\right)^{\frac{2}{3}}$ ——————— A.R.D.E.

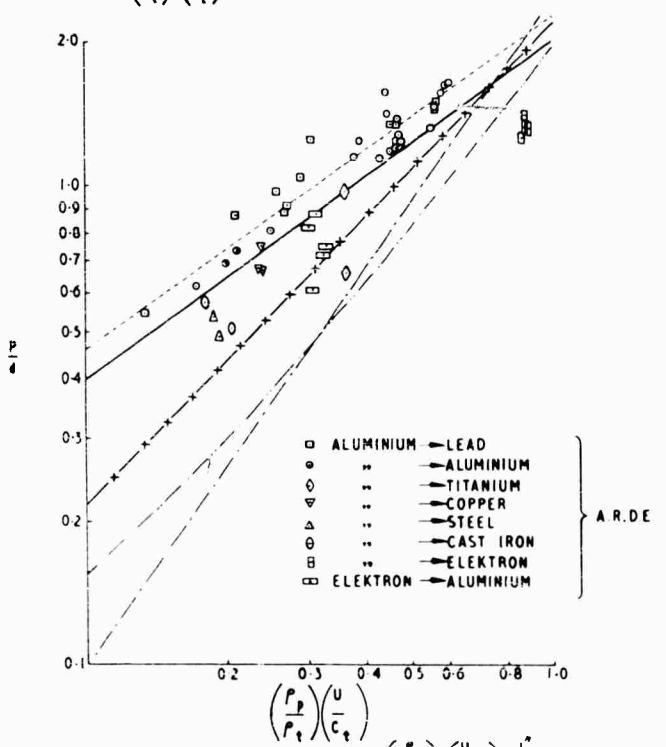

FIG 9 PENETRATION AS A FUNCTION OF $\left(\frac{\rho_p}{\rho_t}\right)\left(\frac{U}{C_t}\right)$ $\frac{1}{4}$" SPHERES INTO TARGETS AT NORMAL INCIDENCE

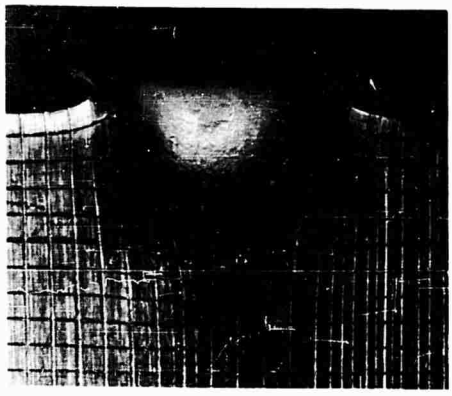

(a) Aluminum

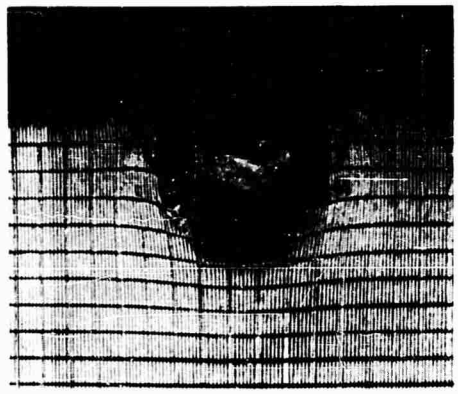

(b) Elektron

(c) Cast Iron

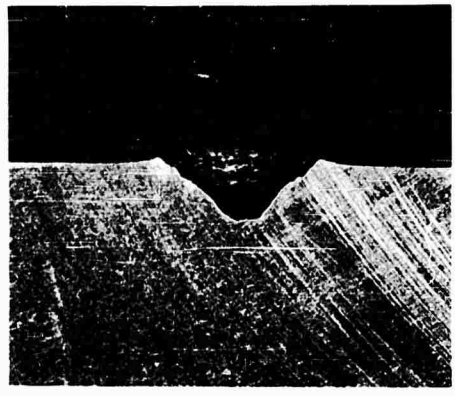

(d) Titanium

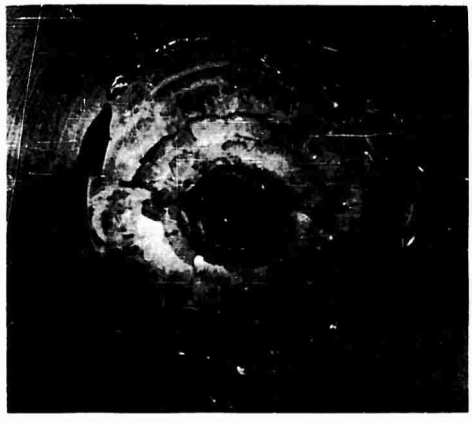

End View

Side View

(e) Perspex

Figure 10. Typical Craters Formed in Various Targets When Attacked by 1/4 inch Diameter Aluminum Spheres at 10,000 Ft/Sec.

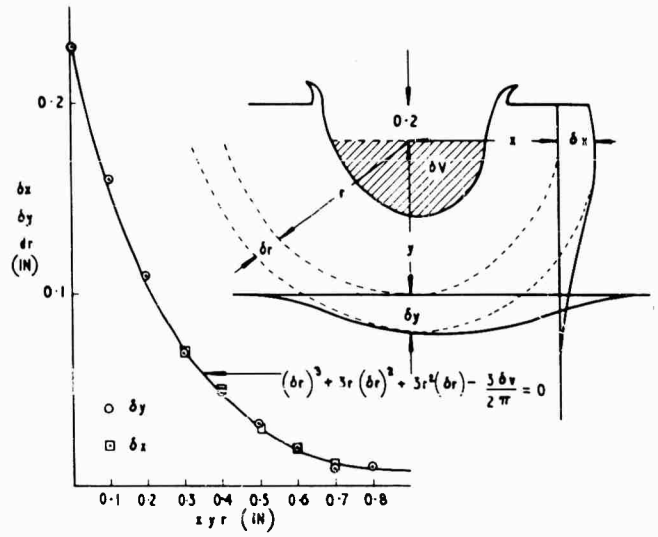

FIG 11a DEFORMATION

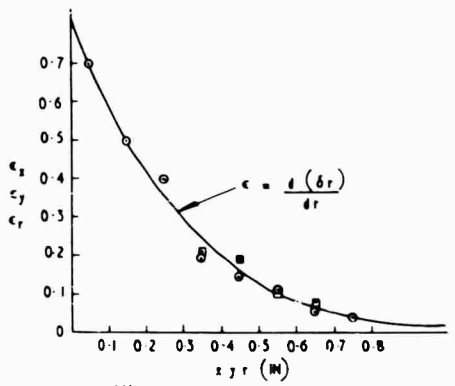

FIG 11b STRAIN

FIG 11 DEFORMATION AND STRAIN IN AN ALUMINIUM TARGET AT NORMAL INCIDENCE AFTER ATTACK WITH A 1/4" ALUMINIUM SPHERE AT 10,000 FT/SEC.

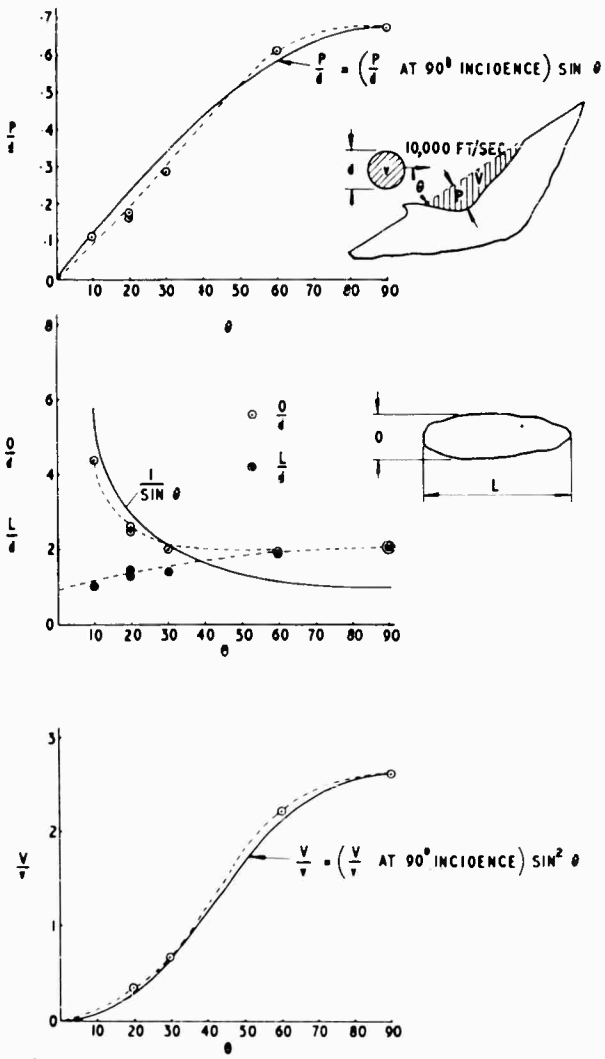

FIG 12 CRATER DIMENSIONS AS A FUNCTION OF INCIDENCE $\frac{1}{4}$" ALUMINIUM SPHERES INTO INCLINED COPPER TARGETS AT 10,000 FT/SEC

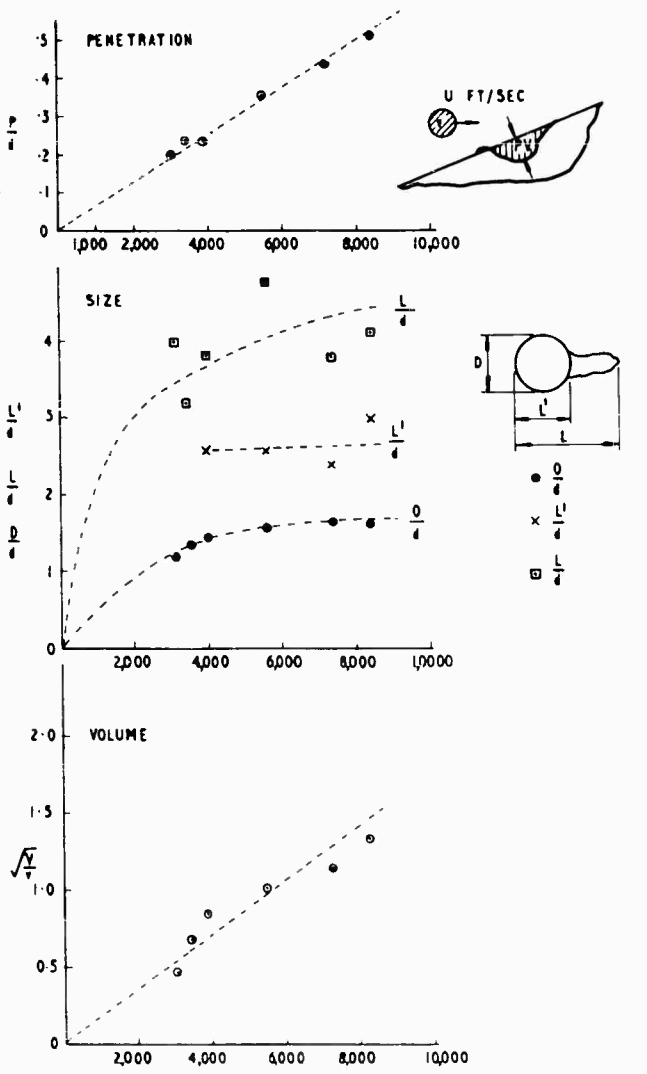

FIG 13 CRATER DIMENSIONS AS A FUNCTION OF IMPACT VELOCITY
1/4" ALUMINIUM SPHERES INTO LEAD TARGETS INCLINED AT 20°

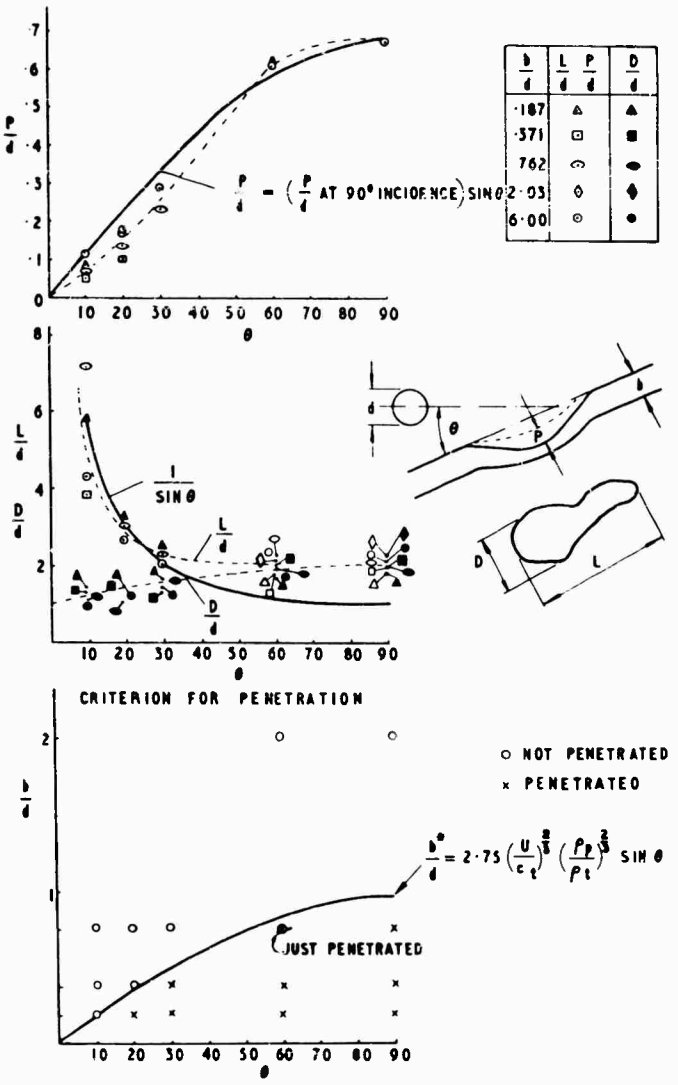

FIG 14 CRATER DIMENSIONS AS A FUNCTION OF INCIDENCE
¼" ALUMINIUM SPHERES INTO INCLINED THIN COPPER TARGETS AT 10,000 FT/SEC

lack symmetry such as Elektron and cast iron. The relationship given by Equation (5) may be used to obtain an estimate of the size of a target which is required before it may be considered semi-infinite and for this purpose δV may be replaced by an estimated V.

2.2 Impact of spheres into semi-infinite targets at varying angles of incidence

Figure 12 illustrates the results of firing 1/4 inch spherical aluminium projectiles at impact speeds of 10,000 ft/sec into 'semi-infinite' copper targets with the surface inclined at angles between 10° and 90° to the line of flight of the projectile. The results show that the penetration is approximately proportional to the sine of the angle of incidence for engineering purposes the results may be fitted quite well by

$$\frac{P}{d} = \left(\frac{P}{d} \text{ at } 90^\circ \text{ incidence}\right) \sin \theta \ .$$

The volume may be fitted by

$$\left[\frac{V}{v} = \left(\frac{V}{v} \text{ at } 90^\circ \text{incidence}\right) \sin^2 \theta \ .\right]$$

At small angles of incidence the crater consists of one main cavity and a series of subsidiary cavities as though the projectile had formed several small drops soon after impact each of which had gone on to form a cavity. At small angles of incidence also the length of these chains of craters tends to become equal to the length of the diameter of the projectile projected on to the target surface. This might be expected since the projectile tends to simply smear itself along the surface leaving only a very small impression. At small angles of incidence the crater is by no means well defined.

At normal angles of impact there is evidence to show that the crater dimensions can be correlated on a bssis of impact Mach number and hence to simulate very high speed impact the above series was repeated using lead targets. Somewhat similar results are obtained but in this case the crater is not dependent upon the angle of impact in the range 60° to 90° and at small angles of incidence a well-defined crater is formed with a lip on one side.

A third series of tests was performed in which the impact angle was held constant at 20° and the projectile velocity varied from 3,000 to 10,000 ft/sec and the results are shown in Figure 13. As the impact speed increases the crater changes shape from a shallow smear to become almost axisymmetric with only a small "splash" on one side to indicate that the projectile has not entered at normal incidence; further, at all speeds the deepest part of the cavity is towards the launcher. Under these conditions, it is interesting to note that the penetration is proportional to the impact velocity and the crater volume is proportional to the energy as in the case of normal incidence impact at low speeds.

2.3 Impact of spheres into thin targets at incidence

Figure 14 shows the results of firing 1/4 inch spherical aluminium projectiles at impact speeds of 10,000 ft/sec into thin copper targets with the surface inclined at various angles between 10° and 90° to the line of flight of the projectile. The results show that the depth of penetration when defined as shown in Figure 14 is slightly less than in a semi-infinite target presumably because some of the energy of the projectile has gone into bending the plate. These tests were repeated

for a series of thin lead plates and the results showed a similar trend.

The results in section 2.1 show that the depth of penetration of spheres into semi-infinite targets at normal incidence is proportional to the velocity raised to the power of two-thirds, so far consistency with this relationship, a criterion for penetration of thin inclined plates might be expected to be of the form

$$\frac{b^*}{d} = k\left(\frac{U}{c_t}\right)^{2/3}\left(\frac{\rho_p}{\rho_t}\right)^{2/3}\sin\theta, \qquad (6)$$

where b^* is the minimum thickness that will not be penetrated. The best results obtained for copper and lead targets is obtained with $k = 2.75$ and this relationship is shown in Figure 14. It must be admitted, however, that the two-thirds power in (6) cannot be justified from the results into inclined plates, as these were all performed at one velocity.

3. Conclusions

Crater dimensions have been obtained in various metal targets when attacked by 1/4 inch diameter spheres with velocities up to 10,000 ft/sec and the penetration correlated approximately with the relationship

$$\frac{P}{d} = 2.0\left(\frac{\rho_p}{\rho_t}\right)^{2/3}\left(\frac{U}{c_t}\right)^{2/3}$$

which is in reasonable agreement with much of the existing work. The deviation of the experimental points from this empirical relationship is more than can be attributed to experimental error and whilst it may be adequate for the practical problem of damage assessment within a limited range of velocities and materials it is not adequate to explain the whole phenomena of impact. The penetration of brittle targets may be estimated with the above formula but this is of little use in assessing damage since a region of severe cracking may surround the crater. The deformation surrounding the crater in a ductile aluminium target was spherically symmetrical about a point below the target surface apart for a small region extending to half the depth of the crater just below the surface. This fact enables the extent of plastic flow in a ductile target to be readily determined and hence the size of target required for a particular experiment may be estimated.

When 1/4 inch aluminium spheres were fired into inclined lead and copper targets at 10,000 ft/sec the depth of penetration was roughly proportional to the sine of the angle of incidence and the volume was proportional to the square of the sine of the angle of incidence. When lead targets were attacked at a constant angle of incidence of 20° with 1/4 inch aluminium spheres the crater tended to become axially symmetric as the impact speed increased to 12,000 ft/sec, indicating that if a crater was caused by a meteorite moving at speeds of several times this value, it would in all probability be completely symmetrical for all but very small angles of incidence. Even though the angle of incidence was 20° the penetration was proportional to the impact velocity and the crater volume proportional to the kinetic energy.

Thin lead and copper targets were attacked by 1/4-inch aluminium spheres at

10,000 ft. sec at normal incidence and it was found that the crater diameter increased with the target thickness and in some circumstances became greater than in a semi-infinite target. Projectiles completely penetrated targets whose thickness was significantly greater than the depth of penetration of a similar projectile in a semi-infinite target; this was partly due to the phenomenon of scabbing whereby the compression wave from the impact is reflected from the back of the target as a tension wave and the back of the target then fails under tension. This effect was much more pronounced with the lead targets as lead is weak in tension. Craters (complete perforations) in thin targets (thickness less than half the depth of penetration in a semi-infinite target) were caused by loss of material rather than any significant plastic flow. When these targets were attacked at incidence the crater dimensions were similar to those obtained for semi-infinite targets provided the target was not penetrated. A minimum thickness of target for non-penetration, b^*, is given by the following empirical relationship.

$$\frac{b^*}{d} = 2.75\left(\frac{U}{c_t}\right)^{2/3}\left(\frac{\rho_p}{\rho_t}\right)^{2/3}\sin\theta\,.$$

4. Further Developments

Consideration is being given to a basic research programme, aimed at a better understanding of the process of crater formation and plastic flow, in the target material.

REFERENCES

1. Cox and Winter, "The light gas hypersonic gun tunnel at ARDE, Fort Halstead," AGARD Rep. 139, 1957.

2. Smith, Unpublished Ministry of Supply Report, 1958.

3. Charters, Denardo, Rossow, "Development of a piston-compressor light gas gun for the launching of free-flight models at high velocity," NACA TN4143, November 1957.

4. Stephenson, "Theoretical light-gas gun performance," AEDC-TR-61-1, May 1961.

5. Charters, "The free-flight range: a tool for research in the physics of high-speed flight," paper given at the Int. Hypersonics Conf. of the Am. Rocket Soc. at M. I. T, August 1961.

6. Van Valkenburg, Clay, Huth, "Impact phenomena at high speeds," Jour. Appl. Physics, Volume 27, No. 10, October 1956.

7. Summers, Charters, "High speed impact of metal projectiles in targets of various materials," Third Symposium on Hypervelocity Impact Proceedings, October 1958.

Photographs by permission of the Controller, Her Britannic Majesty's Stationery Office.

OBSERVATIONS OF HYPERVELOCITY IMPACT

S. M. Halperson and W. W. Atkins

U. S. Naval Research Laboratory
Washington 25, D. C.

INTRODUCTION

Since the Fourth Hypervelocity Impact Symposium work has continued at NRL to increase the amount of experimental data available to all investigators of hypervelocity phenomena. Particular attention has been given to impact studies of both hard and soft aluminum, 2014 and 1100F, and two types of steel, 1020 and hardened 4340 steel. Spheres of aluminum and nylon (3/8-in. diameter) were the principal penetrators for these studies. The highest velocities attained were 6.03 km/sec with an aluminum sphere and 5.64 im/sec with a nylon sphere. Aluminum spheres of 1/4-inch diameter were also fired; maximum velocity was 6.27 km/sec.

EXPERIMENTAL TECHNIQUES

Cratering of quasi-infinite metallic targets has continued, with prime interest in aluminum and steel. There were two species of each material studied; 1020 steel (BHN 131) and hardened 4340 steel (BHN 280), and 1100F aluminum (BHN 25) and 2014 aluminum (BHN 119). The Brinell hardness numbers were obtained by measuring machined samples taken from targets.

A light-gas gun consisting of a 40-mm compression section, expendable middle breech, and 50-cal launch tube was the accelerator for the majority of the results reported. Other experimental information was obtained with a projector using a standard gun powder as the propellant. Light-gas-gun firings were conducted in a ballistics range usually having an ambient pressure of 1/4 atmosphere, since this pressure was found necessary to eliminate the sabot. Photographic records of each shot were examined for evidence of ablation. There usually were no signs of burning, and when burning was seen it was negligible.

A series of tests was conducted in which 3/8-inch diameter aluminum spheres were dropped from various heights onto 1100F aluminum, and the penetration measured. Since the force accelerating the sphere was only gravity; and since the sphere (BHN 125) was harder than the target, it was assumed that the sphere acted as a perfectly inelastic penetrator and that the resulting crater was a spherical segment. Experiments were conducted in open air, and an appropriate drag correction was applied to the calculated velocity. The minimum velocity was 1.77×10^{-3} km/sec.

CRATER SHAPE

Craters in the 1100F targets were all approximately hemispherical and well formed. With the more brittle 2014 aluminum, aluminum pellets produced nearly hemispherical cavities; however, this was not true after nylon impact. The ratio of penetration to crater diameter was about 0.2. Neither species of steel exhibited crater hemisphericity for either aluminum or nylon projectiles; ratios of penetration to crater diameter were approximately 0.3 and 0.2 respectively.

VOLUME-ENERGY RELATIONSHIPS

Graphs have been made of the crater volume-impact energy data for the various combinations (Figs. 1-4). The velocity ranges shown on the figures accentuate the differences in impact energies for the two projectiles, since the velocities are nearly the same but the mass ratio is 2.5 to 1. As would be expected the aluminum sphere is a much more efficient projectile than the nylon sphere, since for each material shown a nylon penetrator requires more energy to displace a unit volume of target material. Ultimately the values of energy per unit volume for the nylon spheres may be changed when more data are available at higher velocities, since it is felt that at true hypervelocity conditions the energy-per-unit volume parameter should be independent of projectile properties. This, however, should not be implied about target properties.

The cavitation of 1100F aluminum is of special interest, because of the wide range of available data. A spectrum of energy with 0.2×10^{-2} joule as a minimum and 23×10^{3} joules as a maximum is shown in Figure 5 on a log-log plot with crater volume in cubic centimeters as the ordinate. Results were obtained with the light-gas and powder guns, and from the drop tests. A straight line was drawn through the data with the equation $V = 3.05 \times 10^{-3} E^{0.92}$, where E is the impact energy in kilojoules. Hence, it can be said that for the given projectile-target system the volume is approximately proportional to the energy through the various phases of cratering; very low velocity, tunneling, transition and hypervelocity. A factor of $E^{0.08}$ is unaccounted for and could be due to heat, deformation of the projectile (at high velocities), and/or experimental scatter. Calculations made with this relationship show a maximum deviation of 5 percent over all zones of penetration. Figure 6 shows the higher-velocity regime, shown in Figure 5 as the zone bounded by the 1-km/sec and 6-km/sec points, plotted on rectangular coordinate paper; crater volume V is the ordinate and impact energy E the abscissa. A linear relationship is plotted, as is the experimentally determined curve. These curves fit the experimental points quite well.

Figure 7 shows the results of projecting saboted aluminum cylinders, 1.27 grams. Also shown are previously reported cylinder data (1) obtained from tests with the unsaboted, or shear-type cylinders. The linear relationship is also shown. The saboted projectile points agree quite well with the sphere results, whereas the unsaboted data show excessive scatter. This scatter is caused by an inaccurate mass figure in the energy expression. This tends to confirm the hypothesis that variation of impact mass is a major obstacle to the attainment of meaningful terminal ballistic data with unsaboted aluminum cylinders. The exact nature of the variation is unknown, it could be due to irregular shearing of the shear plug or

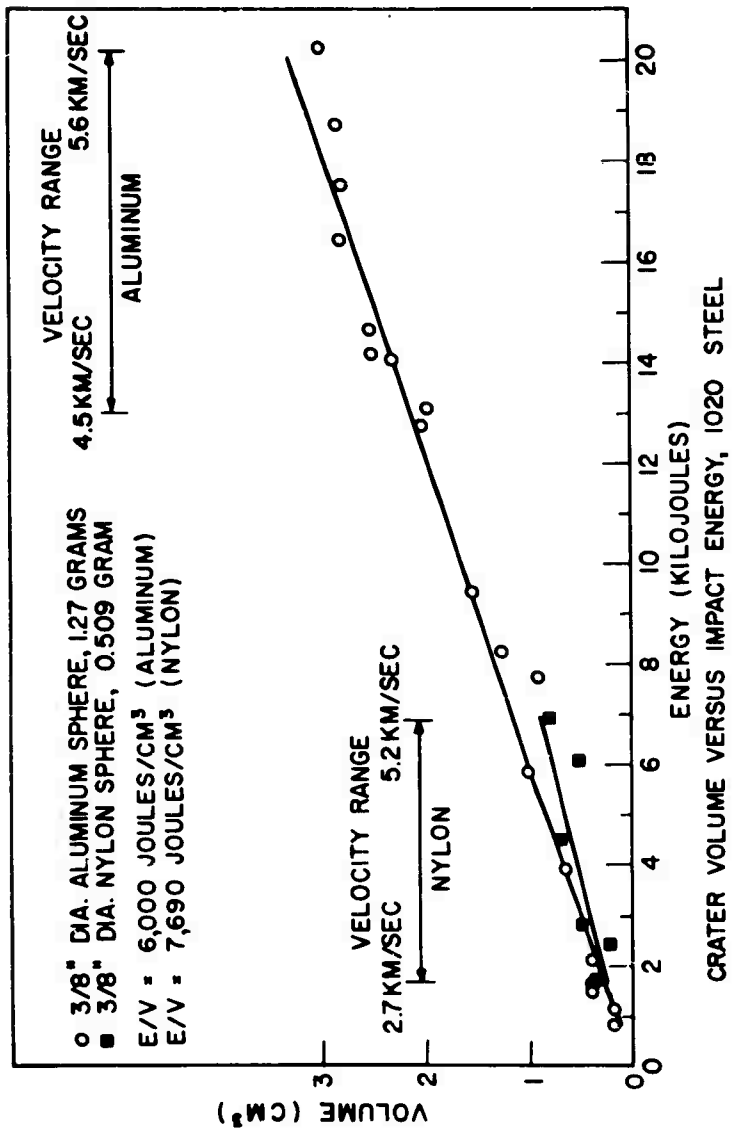
o 3/8" DIA. ALUMINUM SPHERE, 1.27 GRAMS
■ 3/8" DIA. NYLON SPHERE, 0.509 GRAM
E/V = 6,000 JOULES/CM³ (ALUMINUM)
E/V = 7,690 JOULES/CM³ (NYLON)
VELOCITY RANGE
4.5 KM/SEC
5.6 KM/SEC
ALUMINUM
VELOCITY RANGE
2.7 KM/SEC
5.2 KM/SEC
NYLON
VOLUME (CM³)
ENERGY (KILOJOULES)
CRATER VOLUME VERSUS IMPACT ENERGY, 1020 STEEL

Figure 1

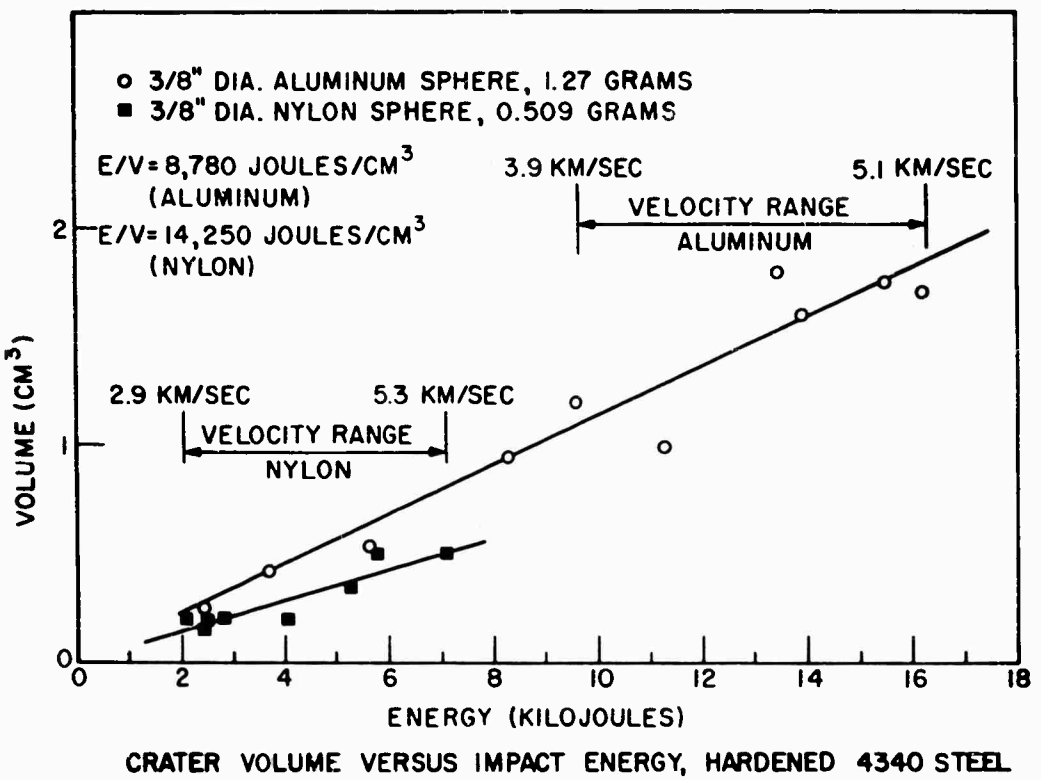

CRATER VOLUME VERSUS IMPACT ENERGY, HARDENED 4340 STEEL

Figure 2

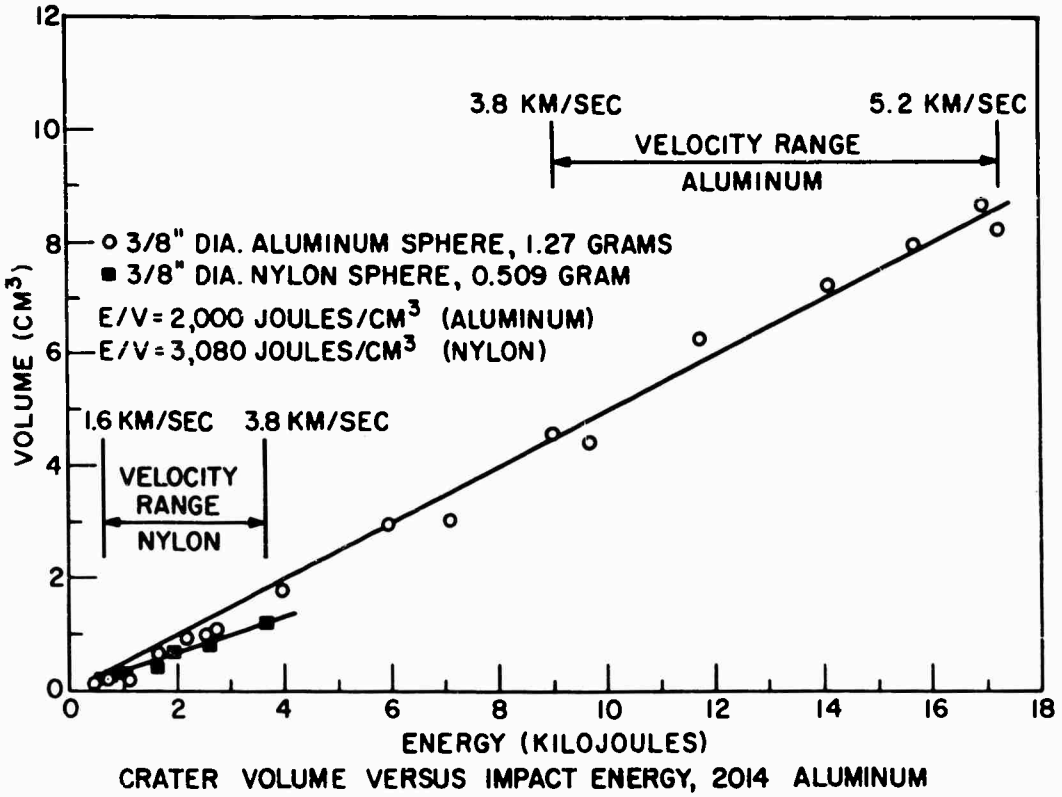

CRATER VOLUME VERSUS IMPACT ENERGY, 2014 ALUMINUM

Figure 3

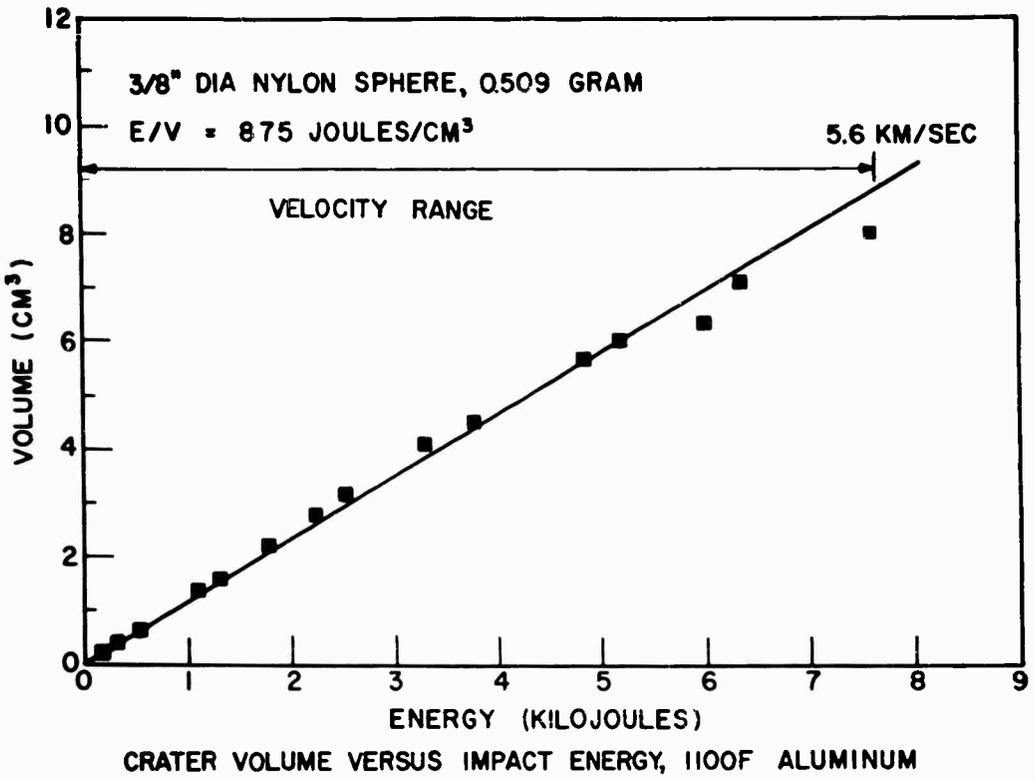

CRATER VOLUME VERSUS IMPACT ENERGY, 1100F ALUMINUM

Figure 4

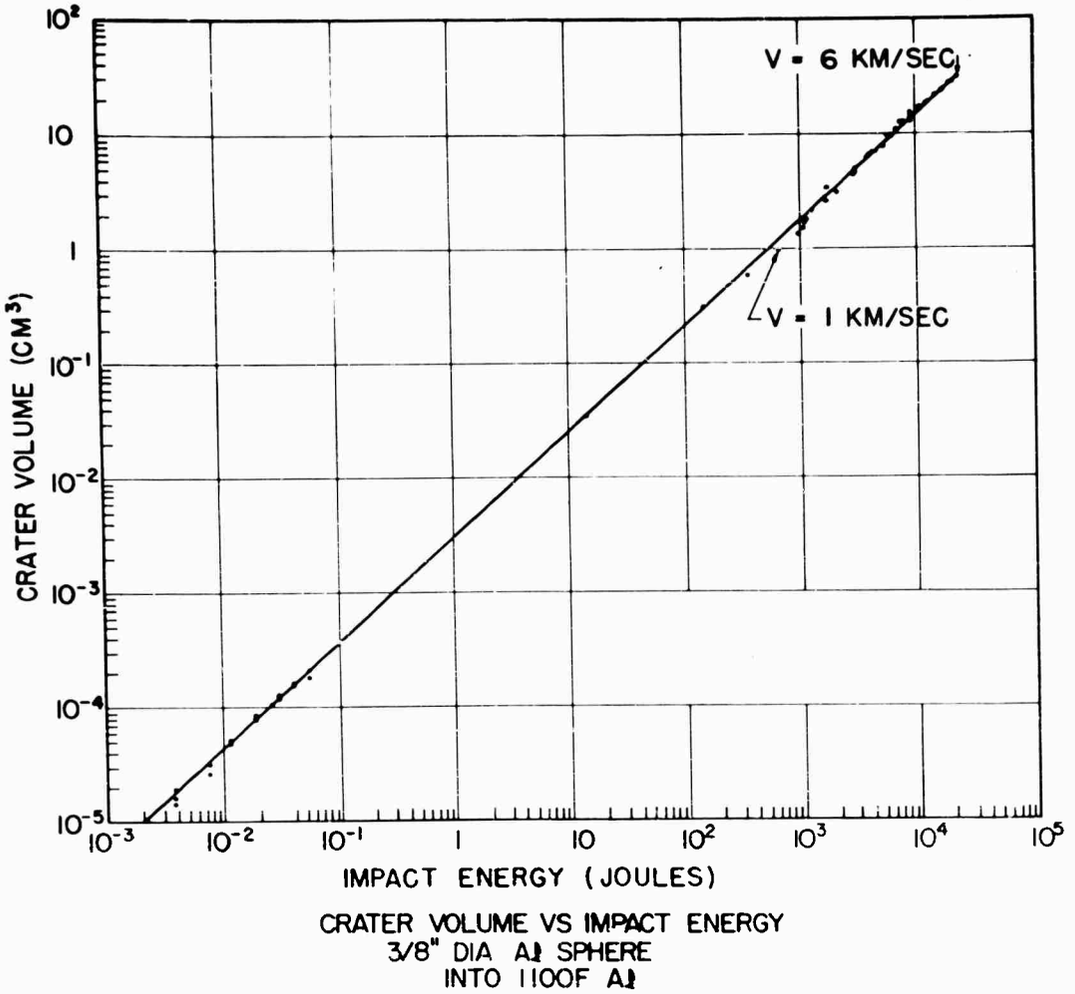

Figure 5

erosion in the barrel. Since the successful saboting of penetrators is by no means a well-defined technique, the evaluation of the mass loss of a cylindrical projectile is a topic which merits further study. Such methods as flash radiographs and high-speed photographs of small, high-velocity fragments are not yet developed to the extent that precise mass determination can be accomplished.

PENETRATION OF ALUMINUM TARGETS

The analysis of penetration of thick targets is of interest for several reasons. The question of whether the process is due to momentum or energy exchange has not yet been answered. Also the effect of target material properties has not been evaluated. There is conjecture that at very high velocities the impact pressure far exceeds the material tensile strength so that strength can be neglected.

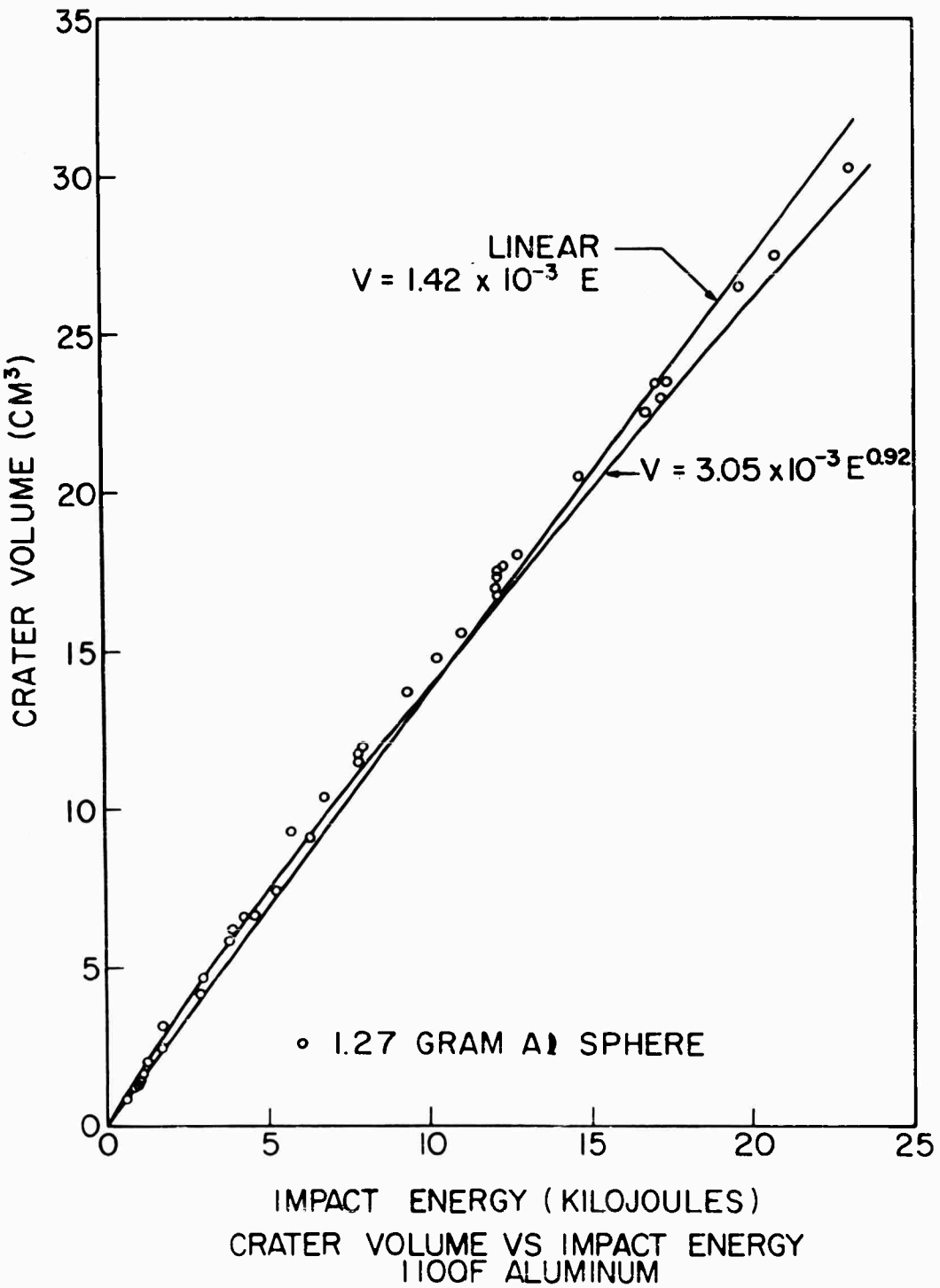
35
30
25
20
15
10
5
0
0
5
10
15
20
25
CRATER VOLUME (CM³)
IMPACT ENERGY (KILOJOULES)
LINEAR
V = 1.42 x 10⁻³ E
V = 3.05 x10⁻³ E^0.92
o 1.27 GRAM Al SPHERE
CRATER VOLUME VS IMPACT ENERGY
1100F ALUMINUM

Figure 6

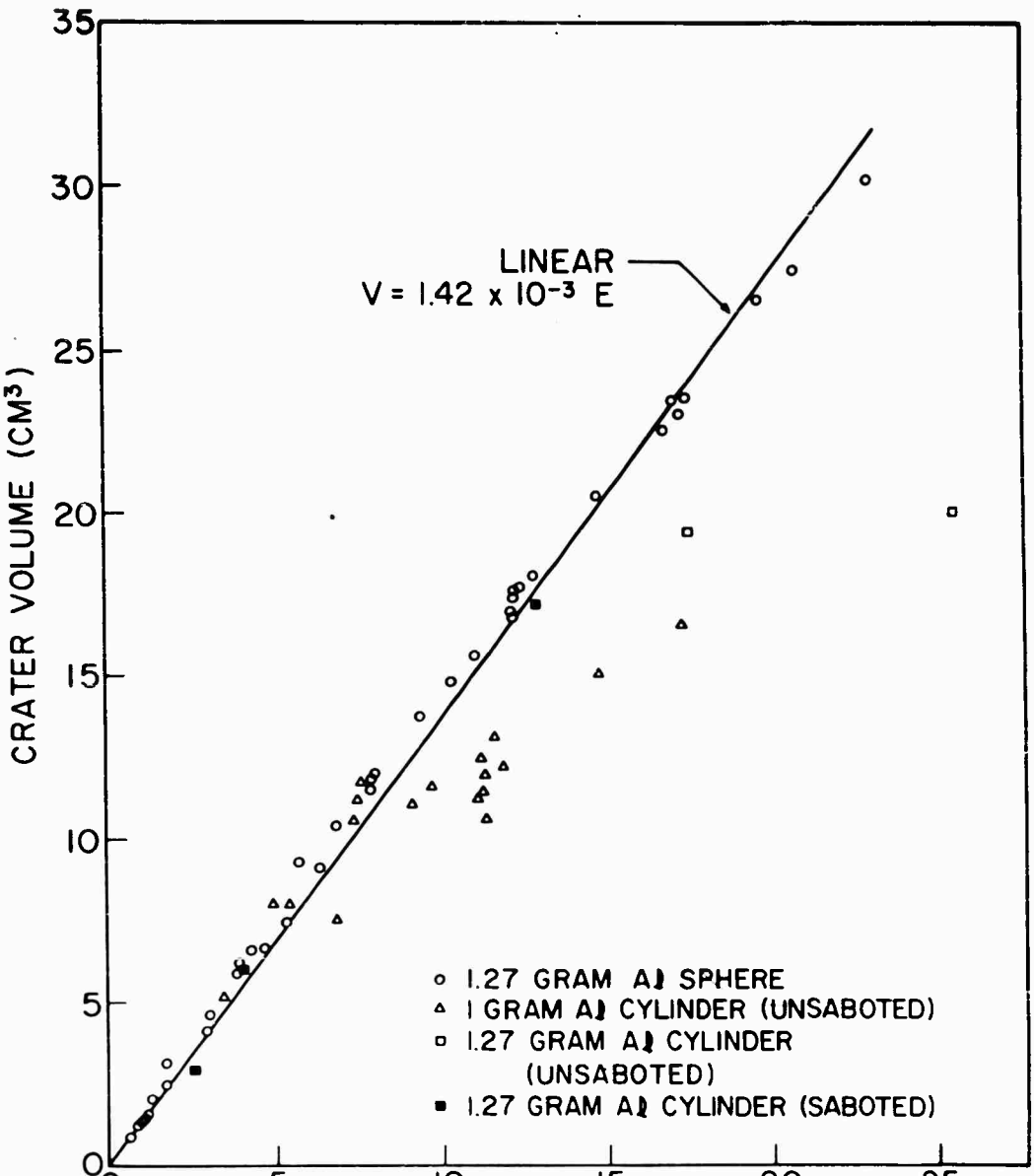

CRATER VOLUME VS IMPACT ENERGY
1100F ALUMINUM

Figure 7

An energy exchange or 2/3 power law states that crater volume is proportional to the impact energy, and a momentum exchange or 1/3 power law states that crater volume is proportional to the impact momentum. A graph of normalized penetration, penetration P divided by sphere diameter D_s versus the cube root of velocity is shown in Figure 8 for the two types of aluminum. The curves are linear and an expression of the form $P/D_s = K_1 V^{1/3} + K_2$ is obtained where K_1, and K_2 are empirical constants. For the 2/3 power law, values of energy per unit crater volume K_3 for the 1100F and 2014 aluminum, were substituted in the semi-empirical penetration relationship. $P = \left(\frac{3m}{4\pi K_3}\right)^{1/3} V^{2/3}$; where m is the impact mass and V is the impact velocity. This equation was derived assuming hemisphericity of the cavity.

Figure 9 shows the four equations in graphical form; also shown are the experimental data. The data agree favorably with both laws in the velocity regime thus far attainable. For both aluminums it appears that velocities in excess of 10 km/sec are needed to fully resolve the V exponent question.

R. L. Bjork, using a hydrodynamic model, has propounded a theory which culminates with the conclusion that crater volume is proportional to impact momentum. He feels that at high enough velocities target strength does not affect penetration; and this is shown in Figure 8 by the bounded region, where the penetration characteristics of both types of aluminum should merge (2, 3). Examining the available information, it is seen that the 1100F points are in the region and the 2014 points are approaching it. It is possible that both materials will pass through the region and not merge. Substantially more data at higher velocities are needed for verification of these statements.

CONCLUSIONS

Although much new information has been obtained about hypervelocity impact phenomena, still more data at higher velocities are needed before several pertinent questions can be answered. The effect of target strength is not yet resolved, although it appears from the E/V values for the different grades of aluminum and steel that at the velocities attained physical properties are important.

Another point of conjecture is the exponent of the velocity term, whether it should be 1/3 as for a momentum transfer or 2/3 as for an energy transfer. Extrapolation of the aluminum sphere-soft aluminum target data for another cycle of impact energy would probably not be out of order, since one would not expect deviation from a linear relationship after eight cycles, Figure 5. The volume-energy curves for each pellet-target combination are linear and do not show any tendency to curve over. On the penetration curve, both 1/3-power and 2/3-power laws look quite reasonable.

The validity of unsaboted aluminum cylinder data is questionable. Because of the loss of mass, the volume-energy curves using these data are not considered reliable. Results obtained with saboted aluminum cylinders show excellent agreement with the sphere data, unfortunately saboting increases the accelerated mass and lowers attainable velocities.

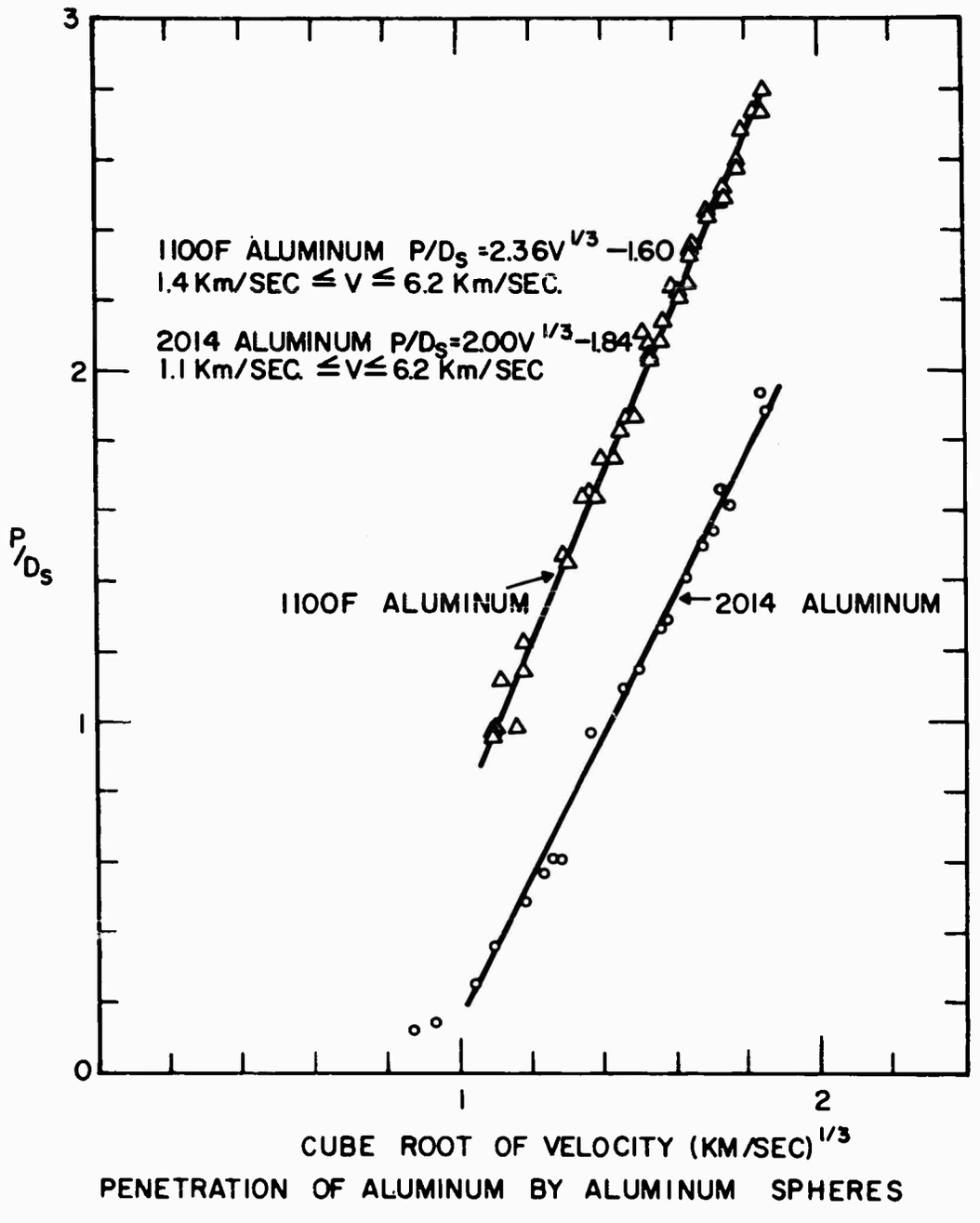
1100F ALUMINUM P/Ds =2.36V^1/3 −1.60
1.4 Km/SEC ≤ V ≤ 6.2 Km/SEC.
2014 ALUMINUM P/Ds=2.00V^1/3−1.84
1.1 Km/SEC. ≤V≤ 6.2 Km/SEC
P/Ds
1100F ALUMINUM
2014 ALUMINUM
0
1
2
3
1
2
CUBE ROOT OF VELOCITY (KM/SEC)^1/3
PENETRATION OF ALUMINUM BY ALUMINUM SPHERES

Figure 8

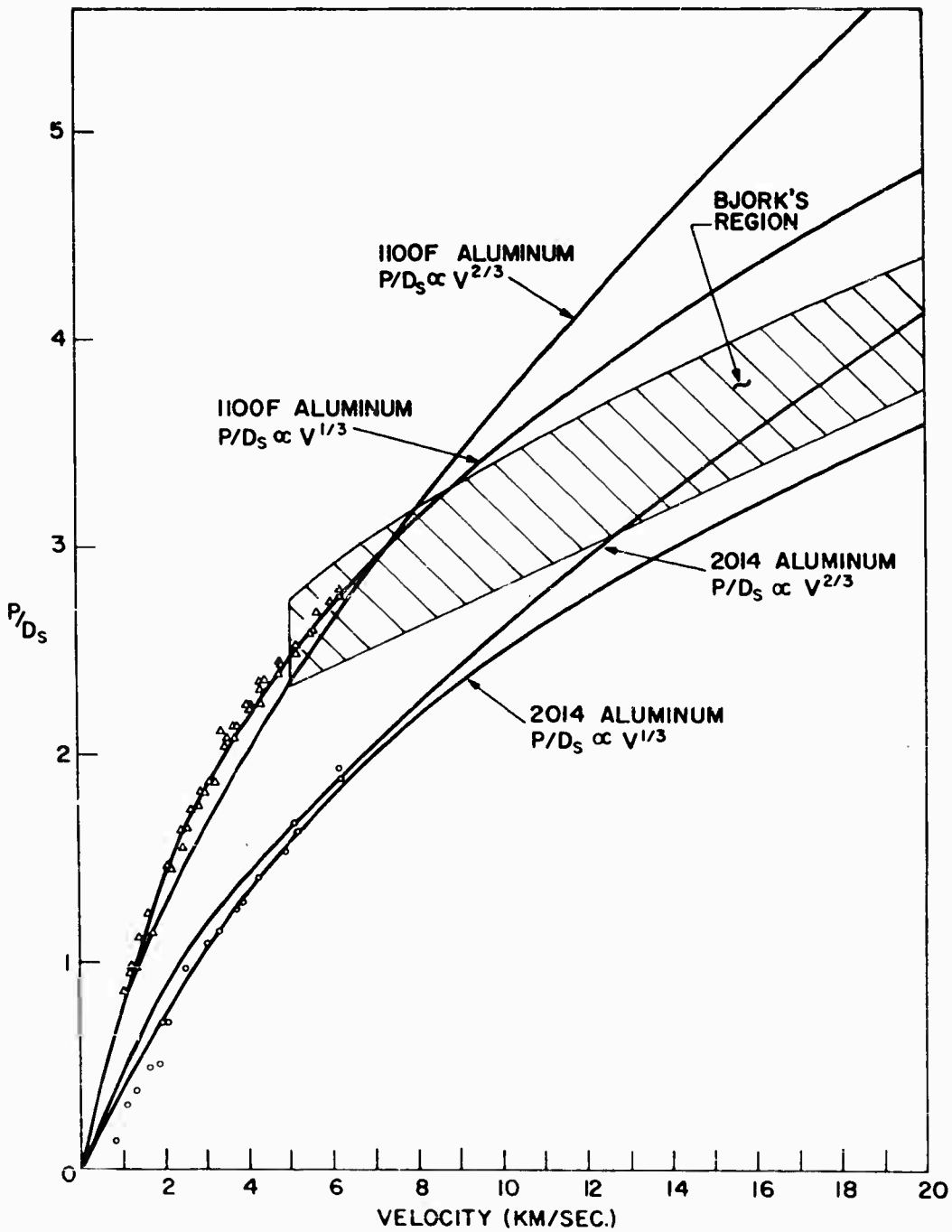

PENETRATION OF TWO TYPES OF ALUMINUM BY SPHERES

Figure 9

ACKNOWLEDGMENTS

The author is indebted to Jay R. Baker for his assistance in the preparation of this paper. The author is also indebted to the technicians of the Dynamics Branch for their cooperation in the experimental phase of this work.

REFERENCES

1. Atkins, W. W., and Halperson, S. M., "Hypervelocity Projection Techniques and Impact Studies - January 1959 - June 1960," NRL Memorandum Report 1116, November 1960.

2. Bjork, R. L., Personal Communication.

3. Roney, P. L., "Review of Hypervelocity Impact Theories" (U), CARDE Technical Memorandum 623/61, August 61.

OBLIQUE IMPACT OF HIGH VELOCITY STEEL PELLETS ON LEAD TARGETS

George M. Bryan

Carnegie Institute of Technology
Pittsburgh, Pennsylvania

INTRODUCTION

The formation of craters on solid surfaces by the impact of material bodies traveling at high speeds has been of great interest, for some time, in the fields of astronomy and geology. This interest arose in connection with the origin of lunar craters and the recognition of meteor craters on the earth. More recently the need for information regarding meteoritic damage to space vehicles has created new interest in impact cratering, particularly on metal surfaces. At the same time development of laboratory methods for shooting metal projectiles against metal surfaces at near-meteoric velocities has made it possible to study craters resulting from projectiles whose mass, velocity, and angle of incidence are known. Knowledge gained in such studies can in turn be applied to the older problems of lunar and terrestrial craters, where such information is not available. The status of these two problems can be summarized very briefly.

The origin of lunar craters. -- Although some half dozen or so separate hypotheses have been proposed to explain lunar craters since their discovery by Galileo in 1610, present-day controversy is limited almost entirely to choosing between meteoritic impact and some sort of volcanic action. Largely as the result of an exhaustive discussion by Baldwin [1], the impact theory is probably the more widely accepted at present. The main objections to this theory have been based on the fact that all the craters appear to be almost perfectly circular, while one would expect that meteor falls over the years would involve a large range of angles of incidence. Against the volcanic hypothesis, on the other hand, are the very large sizes of many of the craters and their general shape as compared to terrestrial volcanoes.

Meteor craters on the earth. -- It was not until the twentieth century that any terrestrial craters were recognized as arising from the impact of meteors. As late as 1953 some geologists did not accept the large crater in Arizona as a meteorite crater. At the present time there is disagreement concerning the origin of other craters on the earth, notably the Chubb crater in New Quebec, Canada, and the Crater Elegante of Sonora, Mexico. Here again

one would expect random angles of incidence, yet most of the dozen or so well-attested meteorite craters on the earth are roughly circular.

The high degree of circular symmetry found in both lunar and terrestrial craters was a serious stumbling block until 1924 when Gifford [2] discussed in some detail the similarity to be expected between high velocity impact and explosion. In fact, he called the crater forming process following impact an explosion process as opposed to simple mechanical indentation. By this he meant that the very large amount of kinetic energy possessed by the meteorite as it reaches the surface is quite suddenly made available to a small region of the target in the form of greatly increased molecular motion of a small amount of target material. Meteorite and target material are quickly vaporized and the resulting high pressure produces an explosion in the same way that a quantity of chemical explosive would. The crater produced would be circular even though the path of the meteorite were not normal to the target surface. A typical meteorite has far greater energy per unit mass by virtue of its impact velocity than does the most powerful chemical explosive.

More recently Baldwin [1] has pursued these ideas in a strong argument for the impact theory of lunar craters. In order to give additional credence to the explosion hypothesis he sought similarities in the geometrical aspects of lunar craters and craters from chemical explosions on the earth. In particular he considers the relationship between depth and diameter and claims that when one is plotted against the other the data fall on a single smooth curve from the largest lunar craters to the smallest shell holes. Because the largest chemical explosion pits are considerably smaller than the smallest lunar craters, it was necessary to include several large terrestrial meteorite craters to bridge the gap and thus make the curve at all convincing. That it is convincing is attested to by the many references to it in the literature as proof of the explosion hypothesis [3]. Nevertheless, La Paz [4] casts considerable doubt on the validity of the curve just at its most crucial point when he questions the figure used by Baldwin for the original depth of the Arizona crater. In any case the significance of the correlation has probably been overemphasized and, as a result, the concept of rapid vaporization of meteorite and target material in a relatively small region followed by explosive release of the concomitant high pressure has become widely accepted.

In an alternative approach to the problem of cratering by meteorites Öpik [5], and also Rostoker [6], treated meteorite and target as perfect fluids under the extremely high pressures involved. As in Pugh's theory [7] of penetration by high velocity metallic jets, the fluid was considered to be incompressible. Thus the process was viewed primarily as a mechanical splashing out of the material from the crater. As might be expected, these assumptions led to a relatively tractable mathematical model in contrast to the largely qualitative descriptions of the explosion model. However, only normal incidence was considered so that nothing could be said about the shape of the crater for oblique impact. Of course the perfect fluid treatment is applicable only for the short time that the pressure is large compared to the strengths of meteorite and target materials so it was necessary to include some sort of resistance to plastic flow or rupture, which could assert itself as the pressure dropped off, in order to obtain a realistic prediction of the final crater volume.

Gifford and Baldwin lay considerable stress on the idea that the meteorite, and some target material along with it, are actually vaporized and that this vapori-

ization is the source of the explosion. Furthermore they consider the explosion as quite separate from the initial impact and penetration; the meteorite hits, buries itself beneath the surface, and then explodes. Incompressible fluid models look upon crater formation as the result of hydrodynamic flow of both meteorite and target from the moment of contact until the pressures fall to the order of the material strengths. These two theories should be looked upon as representing particular aspects of the complete cratering process which includes elastic and plastic behavior, incompressible and compressible fluid flow, and vaporization (see, for example, Hopkins and Kolsky [8]). Thus the problem is extremely complex.

The difficulties encountered in obtaining a quantitative theory of cratering on the basis of the meager data available were equalled by the experimental difficulties entailed in simulating the phenomenon under controlled conditions in the laboratory. Muzzle velocities of conventional guns are not high enough to produce anything beyond ordinary plastic flow, and early work consisted mainly in attempting to achieve higher velocities by various means. As technique developed, data became available on the sizes and shapes of craters formed on various metal surfaces by projectiles whose mass and velocity were presumably known. The lack of a suitable theory led to many attempts to correlate the data with various physical properties of the target and projectile. Most of these empirical correlations tend to indicate that crater volume is directly proportional to the kinetic energy of the incident projectile, the proportionality constant being a function of parameters depending on the projectile and target materials [9-13]. However, this proportionality holds only over rather restricted ranges of incident energy and conflicting conclusions are drawn with regard to the way in which the results deviate from the linear relation. In most cases, particularly at the higher velocities, the scatter in the data is probably too large to establish the uniqueness of such correlations.

Such efforts are often hampered by uncertainty in the impact velocity and in the mass of the projectile actually reaching the target. Thus while the major effort has been directed toward raising projectile velocities to the meteoric range, there is considerable need for carefully controlled experiments at somewhat lower velocities where the state of the projectile as it reaches the target is accurately known.

The present work is an investigation of both the volume and the shape of the crater formed in massive lead targets by a steel projectile of fixed energy as a function of the angle of incidence. Lead was chosen in order to minimize effects due to the mechanical strength of the target material since such effects, even in much harder materials, probably play a relatively small role in impact phenomena at meteoric velocities.

PROJECTOR SYSTEM

A projector system is required which can accelerate a metal pellet to a very high velocity with negligible loss of mass (or at least with known loss of mass) and aim it accurately at a target. The obvious answer for sufficiently low velocities is the conventional gun in which chemical propellants expand in a confined chamber and force the projectile down the barrel like a piston. In such a system,

the projectile velocity is limited by the fact that the large mass of propellant gas must be accelerated along with the projectile. Beyond about 1500 meters per second further increase in the powder charge, loading density, and barrel length is reflected primarily in greatly increased pressure gradient in the column of propellant gases with relatively little increase in pressure immediately behind the projectile and consequently little improvement in muzzle velocity.

Attempts to increase pellet velocities have usually followed one of two alternatives. The first is the so-called light gas gun [14] in which the expansion of the chemical propellant is used to compress a much lighter gas such as helium or even hydrogen, which in turn expands and accelerates the projectile. The use of a high energy propellant in the first stage in combination with a very light gas in the second makes possible a substantial increase in final pellet velocity.

The second approach, which is the one adopted here, attempts to replace the conventional propellant with a high explosive. This obviates the need for a barrel since all of the acceleration is achieved by impulsive loading in times of the order of a microsecond. The acceleration of metal fragments by means of high explosives is of course nothing new; it is the basis of all fragmentation type bombs and warheads. The present problem is chiefly one of keeping the pellet intact and aiming it accurately. The technique has been developed over the past decade or so to a point where it now constitutes a relatively simple, inexpensive and convenient means of achieving useful pellet velocities. It is possible to obtain 5 kilometers per second with a single solid projectile of fairly well known mass, and up to 10 kilometers per second or more in shaped-charge jets. This is only an order of magnitude or so below naturally occurring meteoric velocities. There are difficulties, however, in connection with projectile mass and shape. In the single projectile type the highest velocities have been obtained only for relatively flat disks and with considerable loss of mass, the amount of which is not accurately known. In the shaped-charge jet a velocity gradient exists which causes it to stretch stretch and eventually break up into fragments traveling at different velocities. It would be necessary to isolate one fragment and determine its mass as well as its velocity.

In the design of a projector system for this experiment, emphasis was placed on delivering an accurately known mass and on maintaining approximately unit aspect ratio (ratio of length to diameter) at some expense to velocity.

When a flat steel disk is accelerated from one end of a cylindrical charge by a detonation wave initiated at the other end it is found that fracture occurs primarily near the periphery of the disk since the free boundary permits the compressed metal to unload radially as well as axially near the edge. If this radial component is large enough to overcome the strength of the steel the edges will spall off. Near the axis all the unloading occurs axially before a rarefaction wave can sweep in from the edge to permit radial motion. Thus if the required pellet is a relatively small disk surrounded by a tightly fitting washer-shaped ring of the same material, it will stay intact while the ring breaks up. The difficulty with this scheme is that fragments from the ring follow essentially the same path as the pellet, striking the target at the same point, and thus obscuring the results due to the pellet itself. In the past this difficulty has been minimized by making the surrounding ring out of lead or Wood's metal so that it is largely dispersed by the time it reaches the target surface. There is of course some slip

mismatching at the boundary between pellet and ring but the system is found to work fairly well in keeping the pellet intact and, against relatively hard targets like steel, contributes little damage to the surface.

On the other hand the damage caused by Wood's metal surrounds on lead targets was too great to be tolerated and an alternative system had to be found for the present work. As a first attempt, the end of the charge and the surrounding Wood's metal ring were made conical as shown in Figure 1. This gives a radial component to the motion of all the Wood's metal, so that if the angle θ is large enough the extraneous target damage will lie outside the region of interest. However, as θ increases from zero the pellet receives less and less support against radial unloading and begins to break up. It was found that for Wood's metal surrounds no value of θ would give both sufficient support of the pellet and sufficient dispersal of the surround at the target. The Wood's metal was then replaced by steel and it was found that for a steel pellet 1/16 inch in diameter and 1/16 inch thick an angle of $2\text{-}1/2^{\circ}$ gave ample dispersal, while the greater strength of the steel surround retarded the radial expansion at the pellet boundary long enough for the pellet to unload axially.

The final charge design, which yields a pellet velocity just over 3 km/sec, is shown in Figure 1. Since there is no barrel to guide the pellet after it begins to move, accurate aiming depends entirely on holding very close tolerances with regard to cylindrical symmetry. The main charge is Composition B (60% RDX and 40 % TNT) 5 inches long and 1-5/8 inches in diameter. This is initiated by a No. 8 detonator in conjunction with a pressed tetryl booster charge 1/2 inch thick and 1-5/8 inches in diameter. The Composition B is cast over the metal components, which are aligned accurately in a 1-5/8 inch diameter cylindrical charge mold. In order to maintain good contact between the explosive and the metal components a ring of shellac is smeared on the surround, near its outer edge, before the explosive is poured. The pellet is a press fit in the surround.

MEASUREMENT OF PROJECTILE CHARACTERISTICS

Projectile velocity.-- The velocity of the projectile was determined by timing its flight over fixed distances. A model 7270 Beckman-Berkeley Time Interval Meter with a ten-megacycle time base was used to record the time. The timer was started and stopped by pulses from charged condensers which are suddenly discharged by shorting switches at the beginning and end of the flight. The starting switch consisted of a pair of No. 28 Nylclad copper wires twisted together and taped to the side of the charge at the boundary between the charge and the steel surround. The stopping switch consisted of two sheets of lead foil about 5 mils thick separated by a sheet of paper about 1 mil thick.

Average velocities were measured over several path lengths in order to detect any acceleration or any systematic error arising from time lags in the pulsing systems. Distance-time data are plotted in Figure 2, together with a least-squares linear fit of the data. The velocity is seen to be constant over the range checked and has the value

$$v = (0.3186 \pm 0.0015) \times 10^{6} \text{ cm/sec.}$$

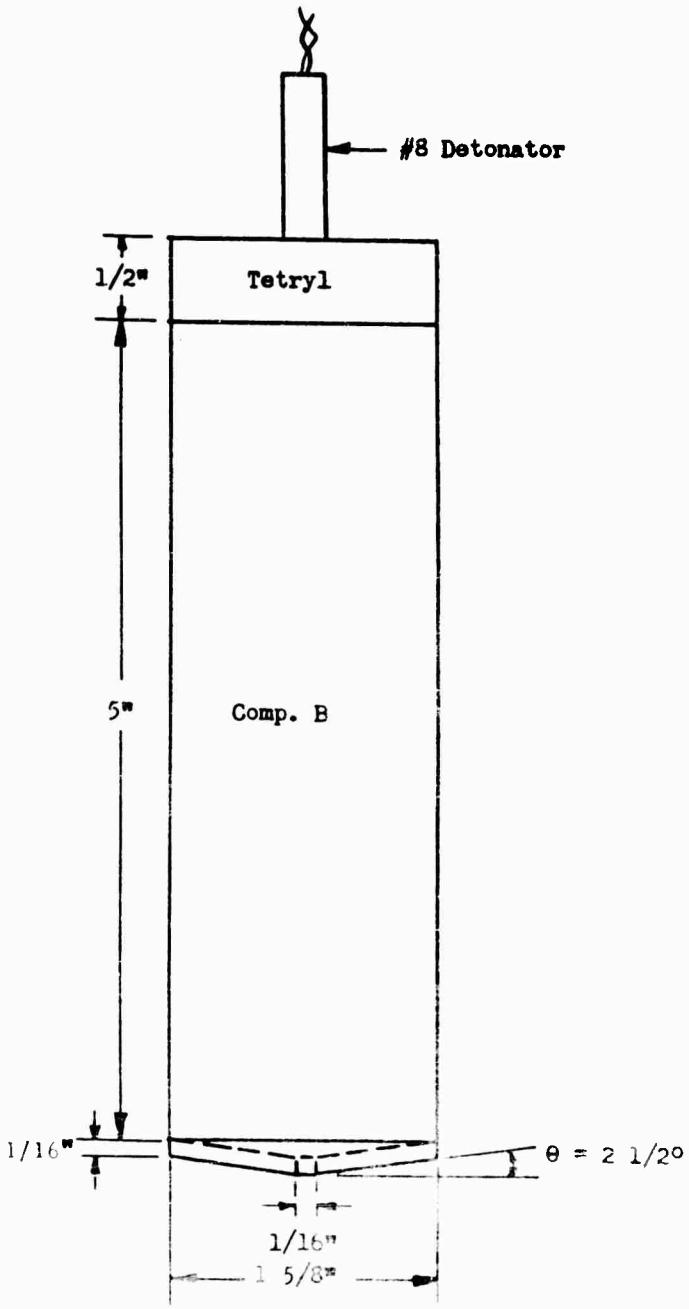

Fig. 1 Charge design for 3 km/sec projector system.

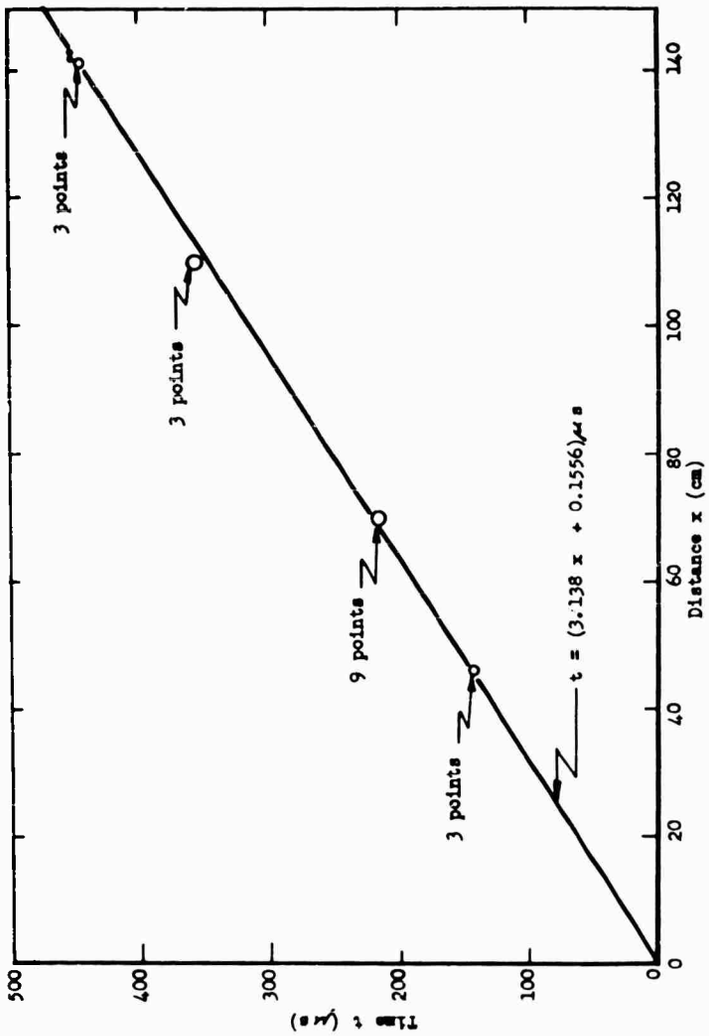

Fig. 2 Distance-time data for projectile flight, with least squares linear fit. Spreads of groups lie within circles shown.

Projectile mass. -- Several charges were fired into stacks of 1/2 inch Celotex sheets and the projectiles recovered intact after passing through three or four inches of Celotex. The distance between the charge and the Celotex was about 70 cm. The projectiles were weighed to a tenth of a milligram before and after firing. A one or two percent loss in mass was found. Since a good fraction of this loss probably occurred in the Celotex, it is a safe estimate that the mass lost in air is of the order of a percent or less.

The pellets were nominally 1/16 inch lengths. The important quantity is the mass. The average mass of the pellets used was

$$m = (0.0234 \pm 0.0001) \text{ grams}$$

where the limits represent an approximate standard deviation of the mean for a ten-shot sample. Based on a density of 7.81 g/cm^3, this figure corresponds to an actual volume about 5% less than the nominal volume.

CRATERING EXPERIMENT AT VARIOUS ANGLES

With the mass and velocity of the incident pellet accurately known there remained the problem of aligning the charge axis with the target surface at the desired angle. The method adopted is shown in Figures 3(a) and 3 (b). A 1-5/8 inch steel rod about 18 inches long was rigidly attached at one end to the roof of the firing chamber. An 18-inch length of wood molding of right angle cross section was taped to the lower end of the rod, and extended about 14 inches beyond it. After alignment of the target the charge was taped to the molding with the pellet aiming down and with the charge extending about an inch beyond the molding. The target was mounted on an adjustable frame placed on the floor of the chamber below a 1-inch thick baffle plate. The pellet was fired through a 3/4-inch hole in the baffle.

The target was aligned before the charge was mounted. This was done conveniently by the simple optical method indicated in Figure 3(a). First, the desired angle of incidence is set roughly on the adjustable target stand. On the target surface is placed a machinist's combination square and protractor set accurately to the desired angle of incidence. A mirror is fixed to the surface of the square. When the target angle is equal to the angle set on the protractor the mirror is then perpendicular to the charge axis, as determined by the piece of molding. This adjustment is made with the help of a telescope taped to the molding in the position to be occupied by the charge. The telescope is focused on its own image in the mirror and the target stand adjusted by means of its leveling screws until the image of the front end of the telescope is centered on cross hairs in the focal plane. Two pieces of white tape about 1/8 inch wide, placed across the objective of the telescope at right angles to each other, define the center of the image.

With this adjustment completed the mirror-protractor assembly is removed and the telescope focused on the target surface which is then marked at the point covered by the cross hairs. The diameter of the telescope body was equal to the charge diameter so the pellet should strike at this point. Deviation of the actual crater from this point then represents deviation of the pellet path from the charge

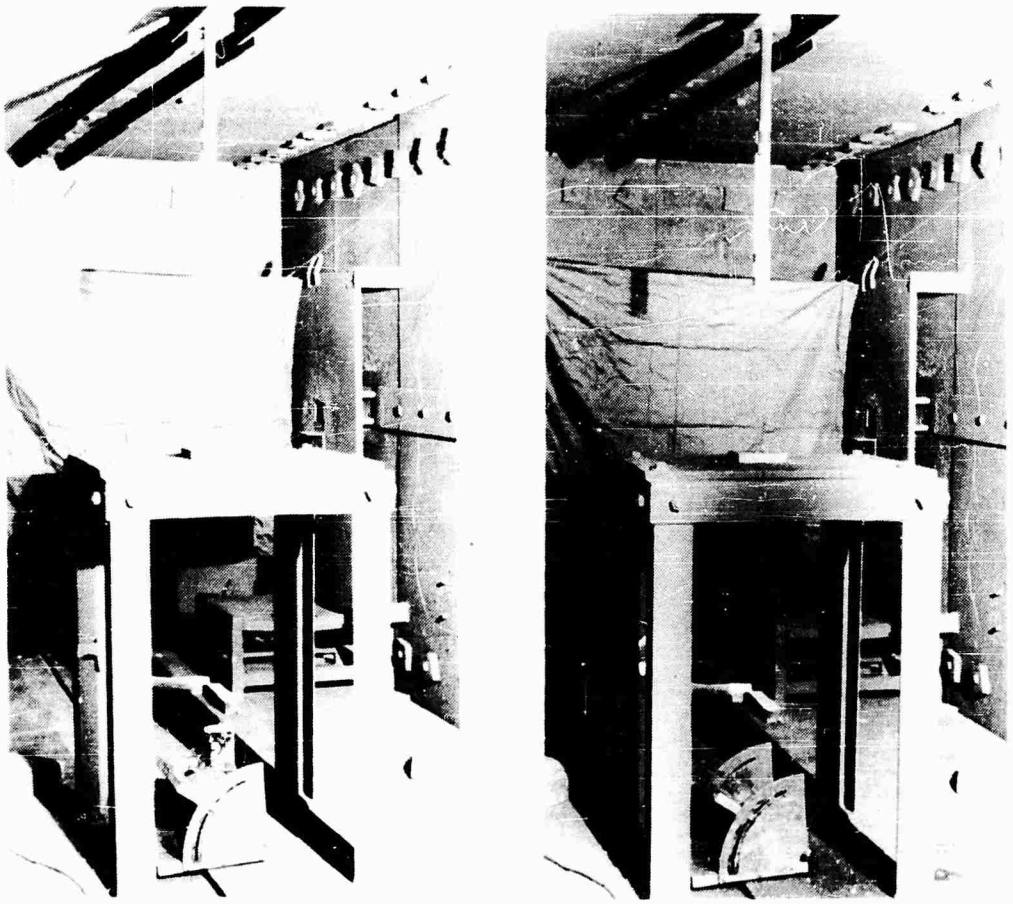

(a) (b)

Fig. 3 Experimental arrangement for oblique angle cratering. (a) Optical system for aligning target. (b) Charge and target ready for firing. Baffle plate is in place on large stand.

axis and corrections to the incident angle can be taken into account where necessary. The telescope is then removed and the charge mounted in its place.

Ten shots were fired at each of the following angles of incidence (measured from the normal); 0, 20, 30, 35, 40, 45, 50, 55, 60, 65, and 70 degrees. The targets were lead plates approximately 6 inches x 6 inches x 1 inch. The upper surfaces were machined flat on a shaper. The target was approximately 140 cm from the charge, but this distance varied a few centimeters depending on the angle setting. The baffle plate was about 40 cm from the charge.

Typical craters are shown in Figure 4. A good idea of the accuracy of the system can be obtained from the plan views by comparing the positions of the craters with the intersections of the scribed lines on the target surface. (A second set of marks, scribed after the shot, define the longitudinal and transverse lines along which subsequent measurements were made.) The maximum difference is of the order of one or two centimeters, corresponding to less than a degree of angular error. This error is in addition to the unknown, but presumably much smaller, error in the initial alignment of the target with the telescope axis. The actual uncertainty in the angle of incidence is considered to be of the order of one degree.

MEASUREMENT OF THE CRATER CHARACTERISTICS

Both the volume and the shape of the craters are of interest. For normal incidence at these velocities the craters are almost perfectly hemispherical regardless of the shape of the projectile, as long as its aspect ratio is not too different from unity. This characteristic has been widely used as the criterion for the hypervelocity regime of impact. It is usual, therefore, to measure depth and diameter as well as volume. In the case of oblique impact it is of interest to examine the deviation from the hemispherical shape as the angle of incidence is increased. Diameters were therefore measured in both the transverse and longitudinal directions. These measurements as well as the depth, were made with a low-power traveling microscope. As shown in Figure 4, diameters were measured at the level of the undisturbed surface, and depths were measured down from this surface.

A diameter was measured by first focusing the microscope on the undisturbed surface, then moving it across the rim until the wall came into focus at the cross hairs. The position of the microscope was recorded and it was then moved across the crater until the wall again came into focus, when the position was again recorded. The microscope was then moved across the rim to the undisturbed surface on the far side, where the focus was rechecked. In the course of making depth measurements, complete vertical profiles were obtained along the line of symmetry in the longitudinal direction by measuring the depth at 1 mm intervals. This procedure made it possible to ascertain the maximum depth with considerable assurance regardless of the degree of asymmetry and in fact gave a graphic picture of the asymmetric shape of the crater.

Crater volume was taken to be the volume below the original surface of the material. To determine this the crater rims were machined down to the undisturbed surface. The crater was then filled with modelling clay of known

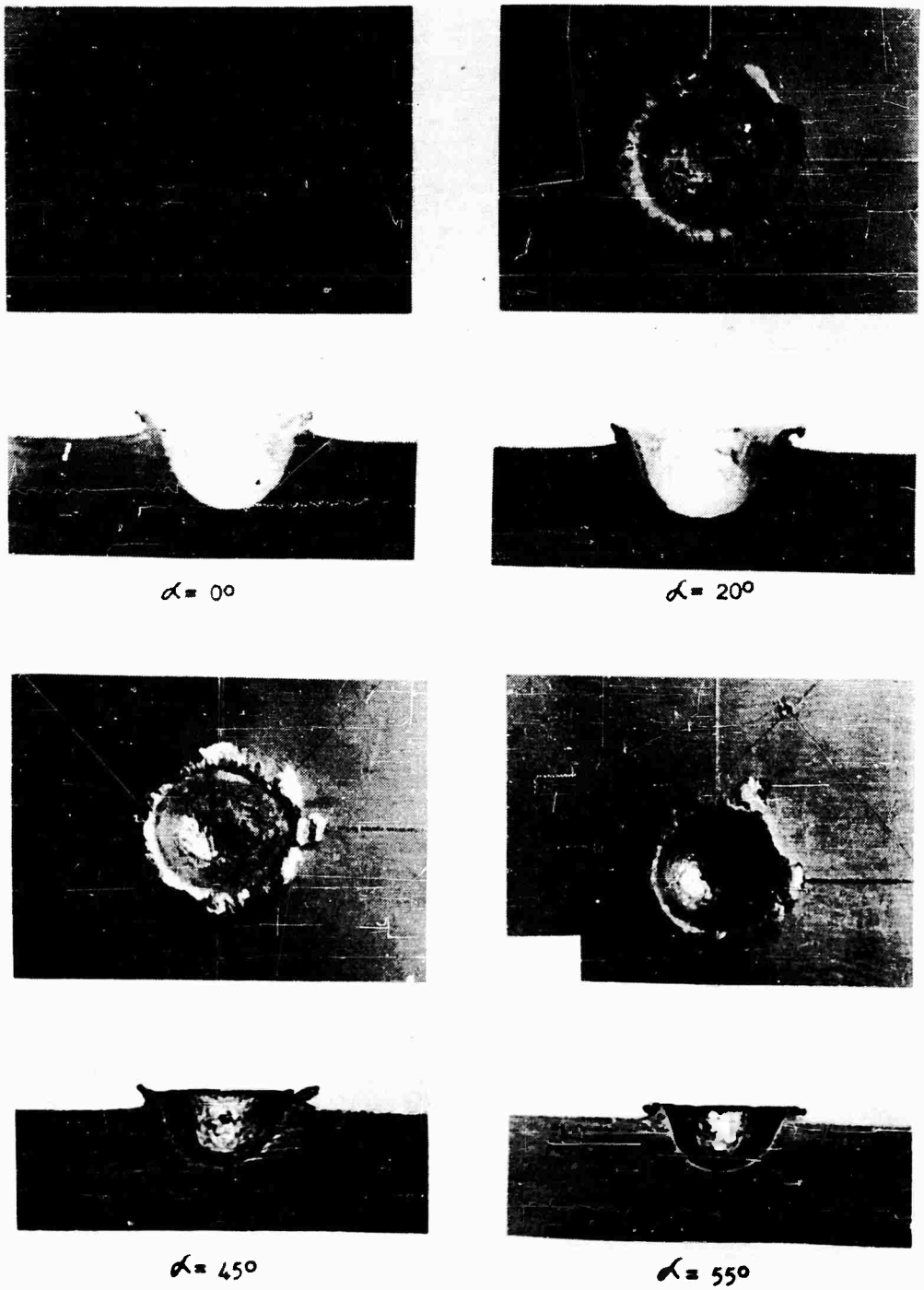

Fig. 4. Typical craters from impact on lead at 3.2 km/sec. Pellet came from the left in these photographs. Magnification is approximately 2:1.

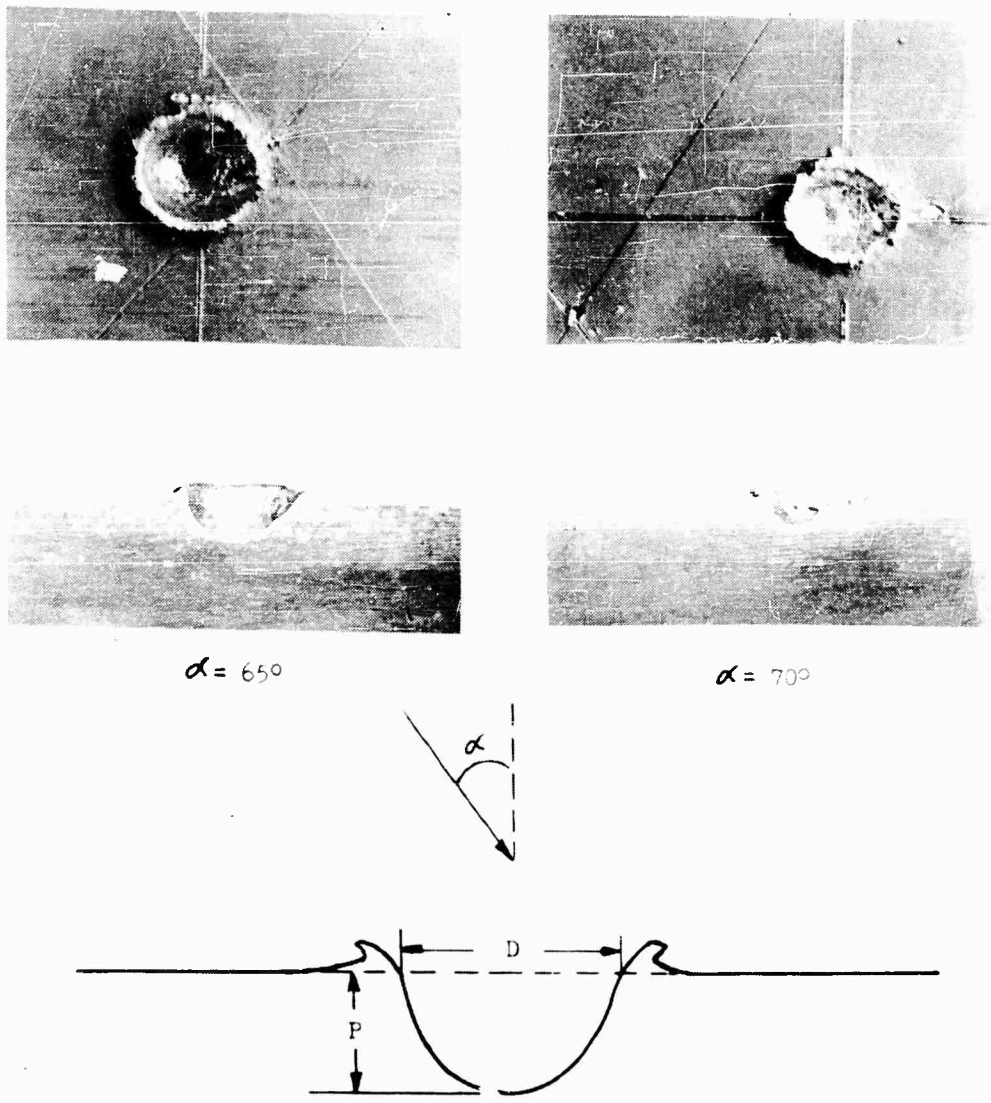

Fig. 4 (Continued). Typical craters from impact on lead at 3.2 km/sec. Pellet came from the left in these photographs. Magnification is approximately 2:1.

density. The excess clay was carefully shaved off with a razor blade. The remaining clay was removed and weighed.

RESULTS

The results of the crater measurements are summarized in Table I and plotted against the angle of incidence α in Figure 5. The depth measurements P have been doubled in Figure 5 to permit direct comparison with the transverse and longitudinal diameters D_t and D_ℓ. For hemispherical craters we have $D_t = D_\ell = 2P$. The results show that at normal incidence the crater is not quite hemispherical; 2P is greater than the diameter. Casual inspection of the plan views in Figure 4 leaves the impression that the craters are circular out to rather large angles; however, careful measurement shows that elongation begins to occur as soon as α deviates from zero.

Crater volume is shown as a function of cos α in Figure 6. The relation is quite linear except at the extremities of the curve. This suggests that the volume is linear in the component of velocity or momentum of the fragment normal to the target surface. However, when these results are combined with a similar set of data obtained by Kineke[15] for a .18 gram pellet with a velocity of 5 km/sec it is found (Fig. 7) that the ratio of crater volume to fragment energy is a linear function of cos α which is independent of the energy (at least approximately). In other words, at any angle of incidence the volume appears to be proportional to the incident kinetic energy and the proportionality constant is a linear function of the cosine of the angle of incidence.

DISCUSSION OF RESULTS

A detailed theory of cratering is out of the question at the present time. It is a problem involving three-dimensional time-dependent fluid flow, which also must include plastic and elastic behavior as the initial high pressures fall to values comparable to the strengths of materials involved. Even the related but much simpler problem of a steady state, perfect fluid jet impinging on a perfect fluid surface has been solved only in two dimensions where the methods of complex variable are applicable. The many attempts to solve this relatively simple problem in three dimensions have failed. Any interpretation of the experimental results described above must therefore rely primarily on plausibility arguments based on conservation of energy and momentum.

It is known that a considerable amount of material is splashed out of the crater, carrying with it a large fraction of the total energy initially available. It can be assumed that the final crater volume V is a function of the difference between the total initial energy E_p and the kinetic energy E_s carried away in this fashion. Furthermore the simplest possible form for this function will be assumed, namely that the volume is directly proportional to the energy difference. That is

$$V = K\,(E_p - E_s)$$

or

$$\frac{V}{E_p} = K\left(1 - \frac{E_s}{E_p}\right)$$

Table I. Results of crater measurements. Projectile mass = 0.024 g. Projectile velocity = 0.319 cm/μ sec.

α (°)	V (cm^3)	σ_m (cm^3)	P (cm)	σ_m (cm)	D_t (cm)	σ_m (cm)	D_ℓ (cm)	σ_m (cm)
0	.3054	.0102	.578	.007	1.063	.007	1.069	.012
20	.2971	.0073	.557	.002	1.027	.004	1.055	.007
30	.2710	.0068	.542	.004	0.995	.004	1.018	.007
35	.2458	.0035	.507	.005	0.986	.006	1.001	.005
40	.2182	.0069	.482	.008	0.954	.007	0.990	.008
45	.1980	.0081	.470	.007	0.923	.004	0.956	.014
50	.1715	.0069	.445	.007	0.873	.010	0.925	.005
55	.1405	.0076	.400	.006	0.831	.004	0.887	.012
60	.1039	.0076	.349	.006	0.746	.017	0.829	.010
65	.0714	.0048	.300	.006	0.652	.012	0.755	.013
70	.0242	.0058	.249	.013	0.563	.013	0.695	.015

α = angle of incidence, measured from the normal
V = crater volume
P = crater depth
D_t = transverse diameter
D_ℓ = longitudinal diameter
σ_m = standard deviation of the mean for 10-shot samples (8-shot samples in the case of V)

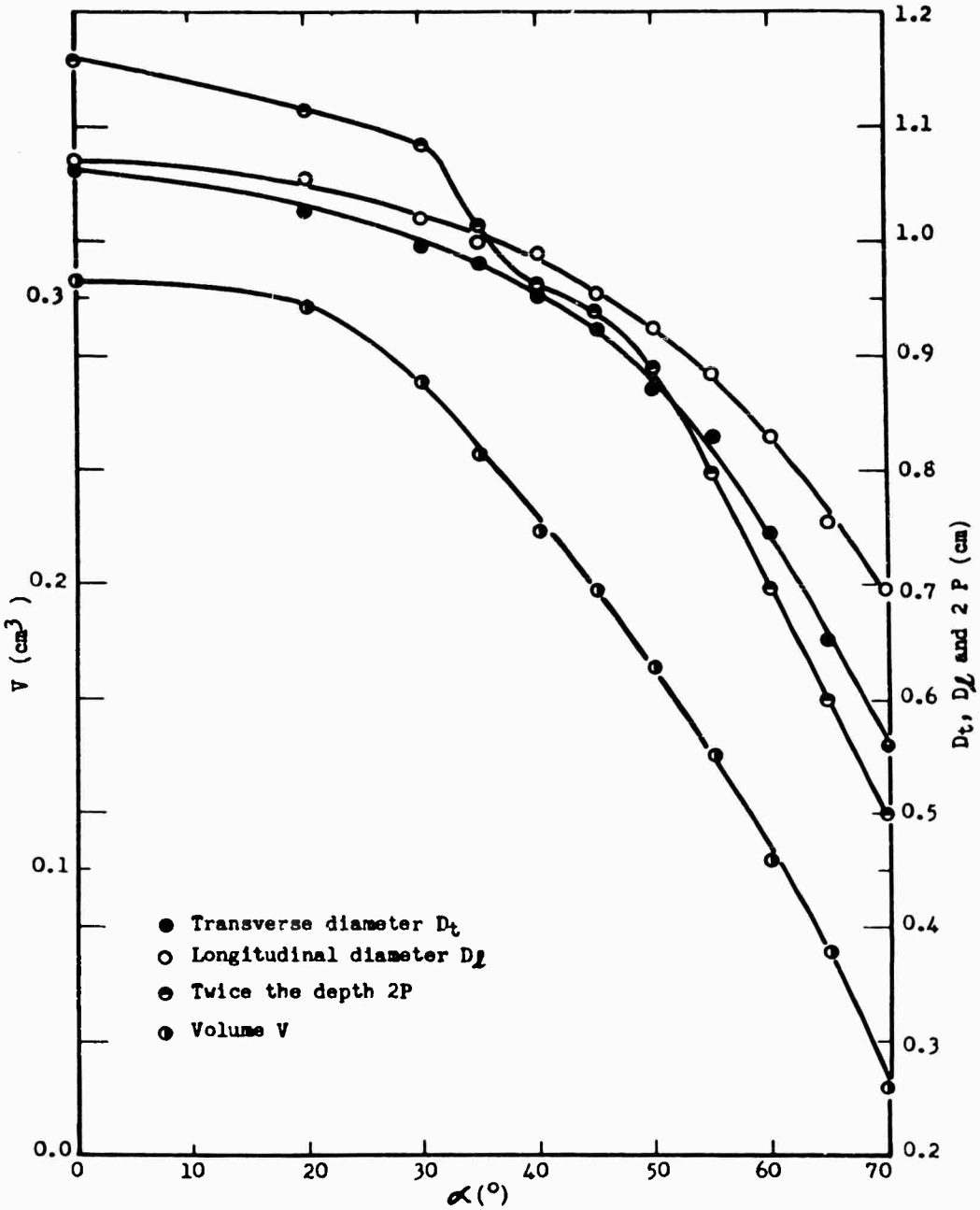

Fig. 5 Crater dimensions vs. impact angle α.

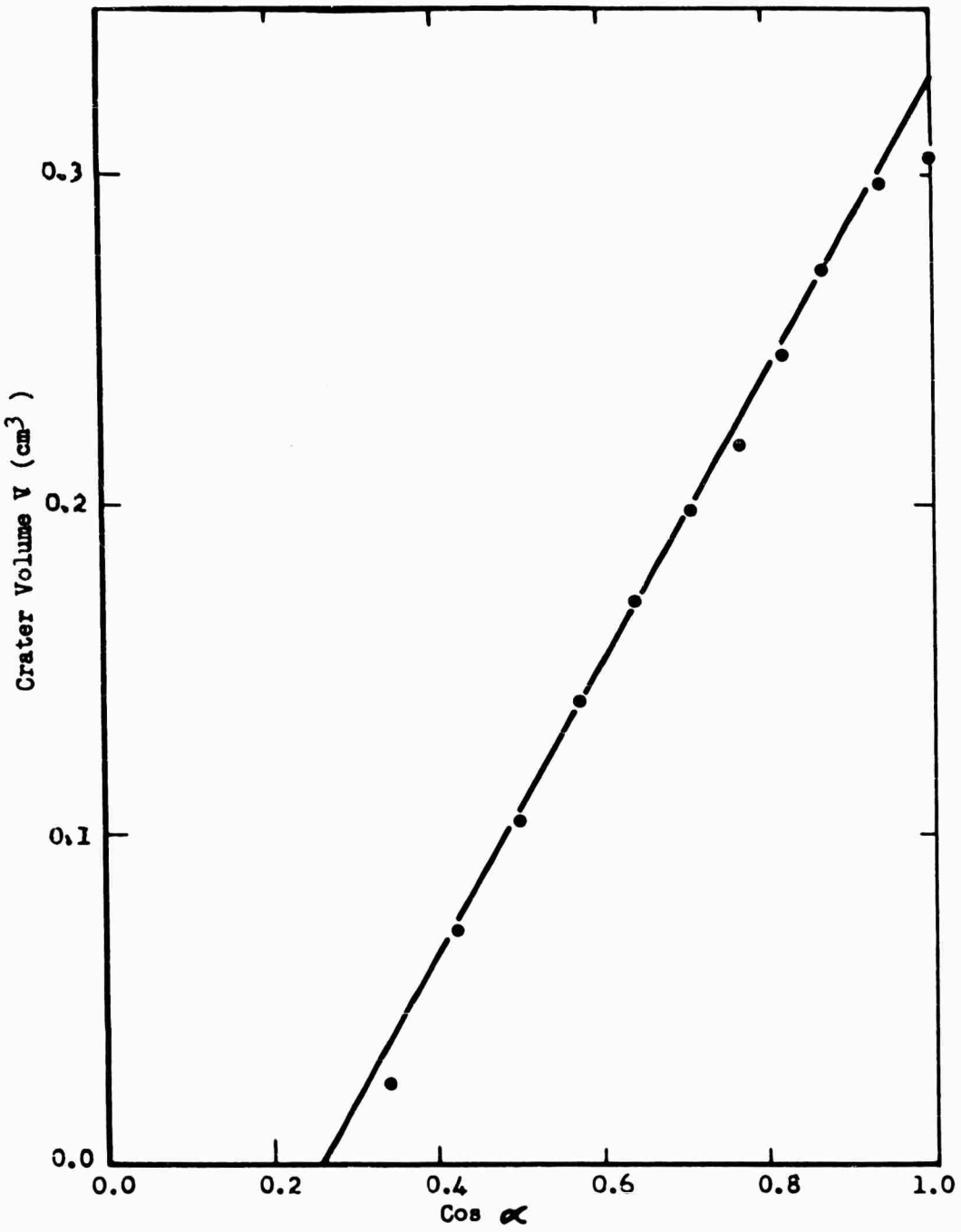

Fig. 6 Crater volume vs. cosine of the impact angle.

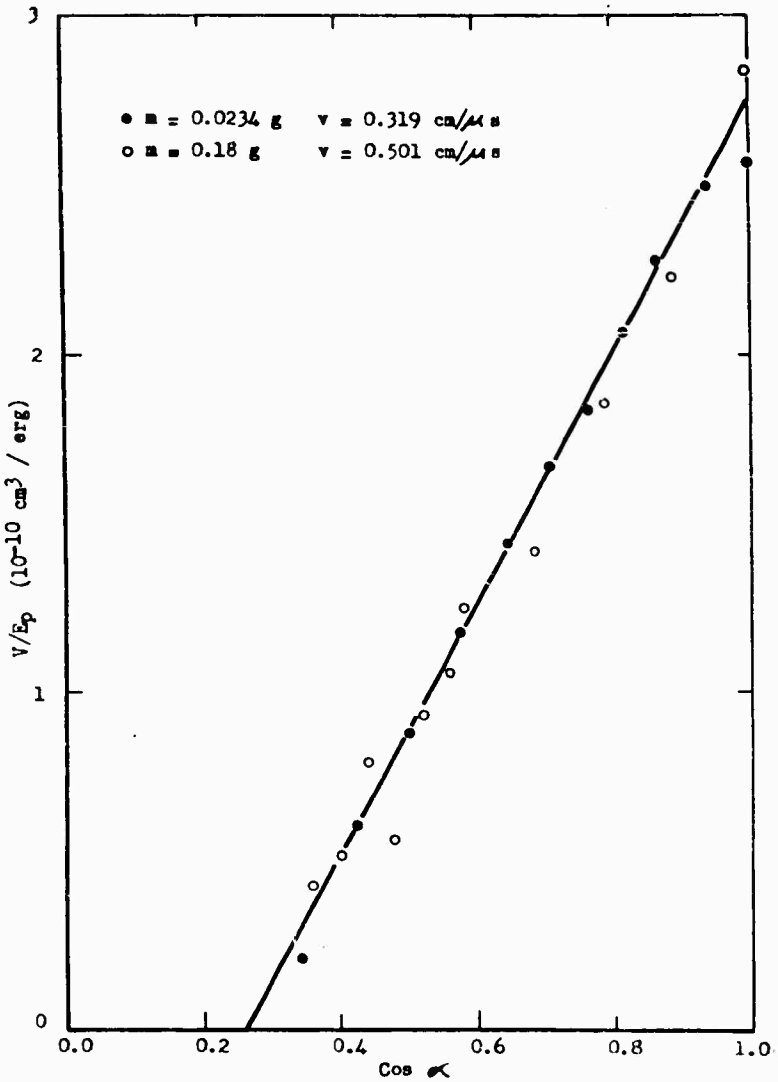

Fig. 7 Crater volume per unit projectile energy vs. cosine of the impact angle.

where $E = \frac{1}{2} mv^2$ is the kinetic energy of the pellet. In order to make use of the conservation of momentum we write E_s as the sum of the kinetic energy E_{cm} of the center of mass of the material splashed out and the energy E_r relative to the center of mass. Thus

$$\frac{E_s}{E_p} = \frac{E_{cm} + E_r}{E_p} = \frac{\frac{1}{2} m'v'^2}{\frac{1}{2} mv^2} + \frac{E_r}{E_p}$$

Put

$$\mu = \frac{m'}{m} , \quad \lambda = \frac{v'}{v} , \quad e = \frac{E_r}{E_p} :$$

$$\frac{E_s}{E_p} = \mu\lambda^2 + e$$

In the case of normal incidence the law of conservation of momentum gives

$$mv - (-m'v') = mv\ (1 + \mu\lambda) = \int F\, dt = I,$$

where I is the total impulse delivered to the target. Solving for λ we obtain

$$\lambda = \frac{1}{\mu} \left(\frac{I}{mv} - 1 \right) .$$

Then $$\frac{E_s}{E_p} = \mu \frac{1}{\mu^2} \left(\frac{I}{mv} - 1 \right)^2 + e = \frac{1}{\mu} \left(\frac{I}{mv} - 1 \right)^2 + e$$

or $$\frac{V}{E_p} = K \left[1 - \frac{1}{\mu} \left(\frac{I}{mv} - 1 \right)^2 - e \right].$$

Note that if volume is proportional to energy, as indicated by most experimental results, then the quantity in brackets must be constant. It is not unreasonable that this be approximately constant over limited ranges of v.

For the arbitrary angle α we consider normal and tangential components of momentum:

$$mv_n - (-m'v_n') = mv_n\ (1 + \mu\lambda_n) = I_n$$

$$mv_t - m'v_t' = mv_t\ (1 - \mu\lambda_t) = I_t$$

where $\lambda_n = \frac{v_n'}{v_n}$, $\lambda_t = \frac{v_t'}{v_t}$. Putting $v_n = v \cos \alpha$, $v_t = v \sin \alpha$ gives

$$\lambda_n = \frac{1}{\mu} \left(\frac{I_n}{mv \cos \alpha} - 1 \right) , \quad -\lambda_t = \frac{1}{\mu} \left(\frac{I_t}{mv \sin \alpha} - 1 \right) .$$

Then $$\frac{E_s}{E_p} = \frac{\frac{1}{2} m' (\lambda_n^2 v^2 \cos^2 \alpha + \lambda_t^2 v^2 \sin^2 \alpha)}{\frac{1}{2} mv^2} + e$$

$$= \mu (\lambda_n^2 \cos^2 \alpha + \lambda_t^2 \sin^2 \alpha) + e$$

$$= \frac{1}{\mu} \left\{ \left(\frac{I_n}{mv} - \cos \alpha \right)^2 + \left(\frac{I_t}{mv} - \sin \alpha \right)^2 \right\} + e.$$

The tangential forces are primarily viscous and should be much smaller than the normal pressures developed upon impact (except perhaps at very high values of α).

Setting $I_t = 0$ gives $\left(\text{with } i_n = \frac{I_n}{mv} \right)$

$$\frac{E_s}{E_p} = \frac{1}{\mu} \left\{ i_n^2 - 2 i_n \cos \alpha + 1 \right\} + e$$

or $$\frac{V}{E_p} = K \frac{2}{\mu} i_n \cos \alpha - K \left\{ \frac{1}{\mu} i_n^2 + \frac{1}{\mu} + e - 1 \right\} .$$

The experimental results then imply that the quantities

$$K \frac{2}{\mu} i_n = a$$

and

$$K \left\{ \frac{1}{\mu} i_n^2 + \frac{1}{\mu} + e - 1 \right\} = b$$

are independent of v and α . Solving for i_n and μ yields

$$i_n = \frac{K}{a} \left(1 + \frac{b}{K} - e \right) + \sqrt{\frac{K^2}{a^2} \left(1 + \frac{b}{K} - e \right)^2 - 1}$$

$$\mu = 2 \frac{K}{a} i_n .$$

Thus i_n and μ may still depend on v and α but only through e. However, the ratio i_n / μ is constant. a and b are the slope and intercept of the line in Figure 7. The quantity e is unknown but should be small compared to unity and can be neglected in making a rough calculation. K can be related to the shear strength of the target in accordance with the following rather crude picture:

The energy difference $E_p - E_s$ can be looked upon as the energy available to open the crater against whatever forces tend to prevent it -- predominantly the critical shear stress σ_c . The work done by this energy in forming a crater of volume V is then approximately given by

$$E_p - E_s = \int_0^V \sigma_c \, dV' = \sigma_c V$$

from which $K_2 = 1 / \sigma_c$. Under normal rates of loading σ_c is of the order of 10^8 dynes/cm^2. Using this value, with $a = 3.7 \times 10^{-10}$ cm^3/erg and $b = 1.0 \times 10^{-10}$ cm^3/erg, we obtain $i_n \cong 54$, $\mu \cong 2900$. Since the entire mass represented by the crater volume divided by the mass of the pellet is only 150, this

figure is much too large. At the very high rates of loading which occur in cratering σ_c will be higher than the usual handbook values and may even approach its theoretical value of 10^9 dynes/cm^2 or so. A value of 10^9 dynes/cm^2 gives $i_n \cong 6$, $\mu' \cong 31$. This value of μ seems to be about the right order of magnitude as estimated from the flash radiographs in Figure 8. If these arguments are valid, σ_c must be closer to the theoretical than to the statically measured value at these rates of loading. For normal incidence $\lambda_n \cong .15$ and the fraction of the initial energy which is carried away is $E_s/E_p \cong \mu \lambda_n^2 \cong 74\%$.

A relation between crater depth and crater diameter can be derived on the assumption that the cratering process consists of a primary penetration, in which the projectile is eroded away, followed by a so-called "afterflow" of the target material which is the result of the high pressures developed in the primary penetration and which continues after the projectile is used up until the pressure has fallen to the order of the material strength of the target. This is essentially the model used to explain penetration by shaped-charge jets [7]. In that case, however, the penetrator is a very long thin jet so that the primary penetration dominates the process; the afterflow concept merely explains, in a qualitative way, the fact that the hole is much wider than the jet and, in soft materials, slightly deeper than the primary penetration theory predicts. In cratering at hypervelocities the reverse is true. The projectile can be looked upon, approximately, as a very short jet, and the resulting primary penetration, which depends only on the length of the jet and not on the velocity, will therefore be small. The afterflow, which depends on the initial pressure, will increase with increasing velocity. The afterflow has approximate spherical symmetry so that when it is large enough to dominate the primary penetration the crater approaches a hemisphere, regardless of the geometry of the primary penetration.

According to this model, at normal incidence a crater would be approximately hemispherical if the primary penetration p_o were just half the projectile diameter d (see Fig. 9). But jet penetration theory gives

$$p_o = \ell \sqrt{\rho_p/\rho_t}$$

where ℓ is the length of the penetrator, ρ_p its density, and ρ_t the density of the target. The vertical elongation of the crater $P - \frac{1}{2} D$ will be given by

$$P - \frac{1}{2} D = p_o - \frac{1}{2} d = \ell \sqrt{\rho_p/\rho_t} - \frac{1}{2} d$$

or for unit aspect ratio ($\ell = d$):

$$P - \frac{1}{2} D = \ell \left(\sqrt{\rho_p/\rho_t} - \frac{1}{2} \right) .$$

For an angle of incidence α the primary penetration reaches a depth below the target surface given by

$$p = p_o \cos \alpha = \ell \sqrt{\rho_p/\rho_t} \cos \alpha$$

Fig. 8 Flash radiographs of typical impacts on lead. α is the angle of incidence measured from the normal. T is the approximate time after impact. The direction of incidence is indicated by arrows.

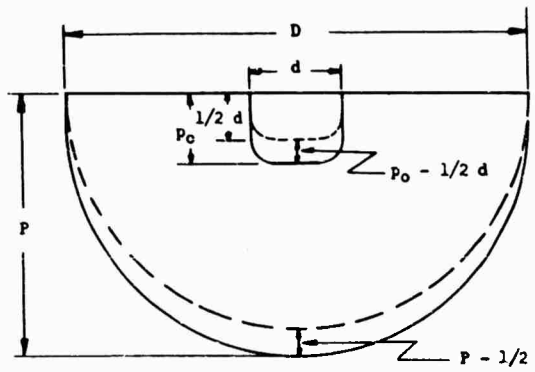

Fig. 9 Idealized representation of vertical elongation.

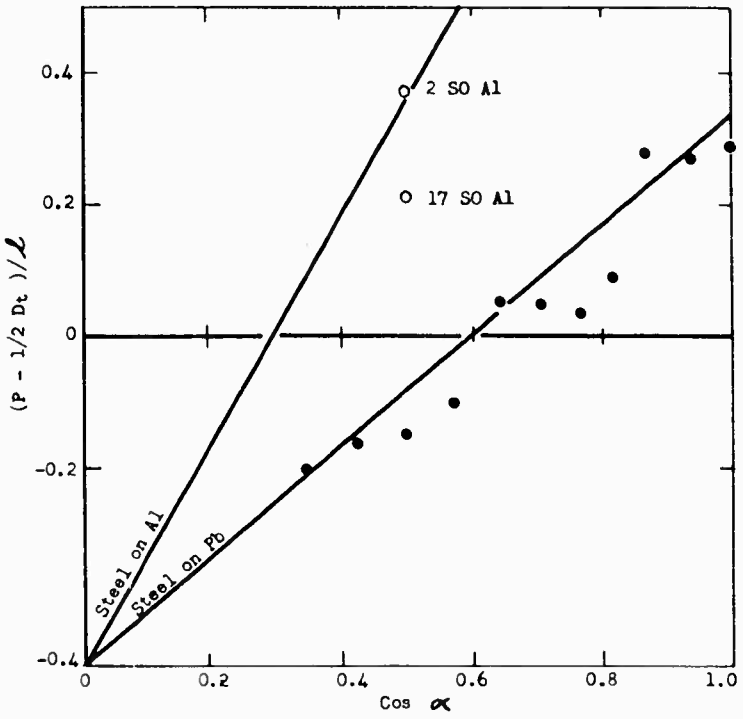

Fig. 10 Vertical elongation of the crater vs. cosine of the impact angle.

and the vertical elongation becomes

$$P - \frac{1}{2} D = \ell \left(\sqrt{\rho_p / \rho_t} \cos \alpha - \frac{1}{2} \right) .$$

In Figure 10 the quantity $\left(P - \frac{1}{2} D\right) / \ell$ is plotted against cos α for the lead data, together with the line predicted by this equation for a steel pellet (ρ_p = 7.81 g/cm^3) on a lead target (ρ_t = 11.35 g/cm^3). A small amount of aluminum data at 60^o obliquity is also shown. On the whole the agreement is good enough to indicate that the concept of primary penetration followed by afterflow comprises an adequate description of cratering in lead at 3 km/sec. As the pellet velocity is increased P and D increase while ℓ remains the same so that the relative asymmetry decreases and the crater appears more and more hemispherical. There would seem to be no necessity for introducing any sort of vaporization or other explosion mechanism to explain hemispherical craters, even at oblique angles of impact.

The tendency for the lead data to fall off in a stepwise fashion with decreasing cos α may be connected with the transient nature of the primary penetration of a short pellet. There is not sufficient time for the formation of a true steady-state penetration process as visualized by the jet theory. Nonsteady shocks and rarefaction waves undoubtedly complicate the picture. The fact that 17SO aluminum falls below 2SO aluminum is an indication that the strength of the target, which is neglected in the simple jet theory, does in fact play a role.

SUMMARY

It has been shown that for any given angle of incidence the ratio of crater volume to projectile energy is approximately the same for projectile velocities of 3 and 5 km/sec. This is in agreement with the general trend of results at normal incidence which indicates that volume is proportional to the projectile energy. In addition, this ratio is found to be a linear function of the cosine of the angle of incidence. Interpretation of this in terms of the requirements of conservation of energy and momentum provides sufficient information to estimate the fraction of energy which is carried away by the ejected material, provided the dynamic critical shear stress is known.

The relation between crater depth and crater diameter as a function of impact angle indicates that the cratering mechanism can be adequately described as a process of hydrodynamic penetration followed by a radial flow, resulting from a residual momentum and kinetic energy of target material produced by the initial high pressures. This flow continues until the dynamic pressure falls below the strength of the target.

REFERENCES

1. R. B. Baldwin, "The Face of the Moon," (University of Chicago Press, Chicago, 1949).

2. A. C. Gifford, New Zealand Jour. Sci. Tech. 7, p. 129, 1924; 11, p. 319, 1930.

3. H. C. Urey, "The Planets," Yale University Press, New Haven, 1952.

4. L. La Paz, Adv. in Geophysics, 4, p. 217, 1958.

5. E. Öpik, Acta et Comm. Univ. Tartu., A30, 1936; Irish Astronomical Journal 5, p. 14, 1958.

6. N. Rostoker, Meteoritics, 1, p. 11, 1953.

7. E. M. Pugh, Jour. Appl. Phys., 19, p. 563, 1948.

8. H. G. Hopkins and H. Kolsky, Proc. Fourth Symp. on Hypervelocity Impact, Eglin AFB, Florida, 1960, Volume 1.

9. M. E. Van Valkenburg, W. G. Clay, and J. H. Huth, Jour. Appl. Phys. 27, p. 1123, 1956.

10. W. A. Partridge, H. B. Van Fleet and C. R. Whited, Jour. Appl. Phys. 29, 1332, 1958.

11. J. L. Summers and A. C. Charters, Proc. Third Symp. on Hypervelocity Impact, Armour Research Foundation, Chicago, 1959, Volume 1.

12. E. P. Palmer, R. W. Grow, D. K. Johnson and G. K. Turner, Proc. Fourth Symp. on Hypervelocity Impact, Eglin AFB, Florida, 1960, Volume 1.

13. W. W. Atkins, Ibid., Volume 1.

14. W. D. Crozier and W. Hume, Jour. Appl. Phys. 28, p. 892, 1957.

15. J. H. Kineke, Proc. Fourth Symp. on Hypervelocity Impact, Eglin AFB, Florida, 1960, Volume 1.

HYPERVELOCITY IMPACT OF HEATED COPPER

Murray Rockowitz
Charles A. Carey
John F. Dignam

Avco Research and Advanced Development Division
Wilmington, Massachusetts

ABSTRACT

Hypervelocity impact of semi-infinite blocks of heated OFHC type copper has been made with aluminum, chrome alloy steel and tungsten carbide projectiles of 1/4 gram mass at velocities up to 6.5 km/sec. The target temperature varied between room temperature and 1600°F. All impacts were made normal to the target surface.

An investigation is made to determine how the importance of target temperature and mechanical properties vary with increasing projectile velocity. Also a correlation of the variation of energy/volume and target tensile strength is made.

INTRODUCTION

The impact of copper targets has been studied [1, 2, 7] extensively up to velocities of 2 km/sec. Atkins [4] summarizes the penetration data obtained for aluminum, and tungsten carbide projectiles into copper targets. There have been several studies [5, 6] performed on heated targets. Ferguson [5] presented the results of impacting copper targets with tungsten carbide projectiles at target temperatures of 75° and 800°F. Allison [3] impacted targets with steel projectiles at a velocity of 5 km/sec, varying the target temperature between room temperature and 1100° F. He showed a correlation between the volume of material removed and such mechanical properties of the target as the brittle to ductile transition in cadmium and zinc, and the annealing inflection in the tensile strength of worked copper. To a good approximation it has been shown [8] that the ratio of projectile energy/volume removed is directly proportional to the Brinnel hardness of the target, and penetration is proportional to the cube root of Brinnel hardness [9] of the target.

This paper is an attempt to do the following:

1) extend the existing data of impacts into heated copper to velocities up to 6 km/sec,

2) correlate the variation of energy/volume and tensile strength with target temperature,

3) investigate how the importance of target temperature and mechanical properties vary with increasing impact velocity.

The work presented in this paper was performed under contract to the ARPA (ARPA 149-60).

EXPERIMENTAL CONDITIONS

The projectiles used were aluminum 7075-T6 (density 2.78 gms/cc), chrome alloy steel (density 7.8 gms/cc), and tungsten carbide (density 14.9 gms/cc) spheres and cylinders of about 1/4 gram mass. The dimensions of the projectiles were 1/8" dia. tungsten spheres, 5/32" dia. steel spheres, and bore-size (0.22" dia.) aluminum spheres, cylinders (0.220" dia. x 0.165" long) and sphere-cone cylinders.

The targets used were semi-infinite (6" x6" x 3") blocks of Oxygen Free High Conductivity (OFHC) type copper. Because of the importance of target properties in the cratering process, a determination of tensile strength, Young's Modulus and grain size at temperature was made. The results are shown in Table 1 and 2. Brinnel hardness measurements across sectioned blocks in the direction of impact were made, and the average reading was 72.

The impacts were made at the Avco RAD Ballistics Range Facility. The 0.22 caliber light gas gun was used to launch projectiles at velocities up to 6500 m/sec. A description of the Ballistics Range, 0.22 caliber light gas gun, and method used to launch bore-size projectiles has been presented in a previous paper [10]. A sabot was developed for the 0.22 caliber gun in order to launch the higher density projectiles at velocities up to 4800 m/sec. The sabot was constructed of aluminum and consists of five pieces. Four accurately machined quarters of a cylindrical section are locked together by the spherical projectile. The fifth part is a disk with a conical back surface which acts as a driver that pushes evenly on the sectioned cylinder.

Two Kerr cell shadowgraph stations were used to obtain velocity measurements. The velocity obtained by measuring the time of flight over a measured distance between the photographic stations was corrected for drag to obtain the actual impact velocity.

The targets were heated along two edges and one face by means of nichrome wire heating elements located in an insulating box. The power supply consisted of a 110 volt 60 cycle line. The targets were heated to the desired temperature and then immediately impacted. A chromel-alumel thermocouple imbedded at the top of the block was used to determine target temperature. Calibration checks were made to determine if temperature gradients existed within the target. The measured gradients were found to be negligible.

The heating apparatus was mounted on a table top and the entire configuration placed at the end of the range. A mylar window was used at the end of the range to allow a vacuum to be maintained in the range. The target was positioned

TABLE 1

TENSILE PROPERTIES OF TARGET MATERIALS

Temperature (^{o}F)	Tensile Strength (psi x 10^{-3})	Modulus of Elasticity (psi x 10^{-6})
75	29.2	16.3
700	14.4	11.7
900	11.4	10.2
1200	3.75	3.7

TABLE 2

ASTM GRAIN SIZE AFTER COOLING

Target Temperature (^{o}F)	Grain Size Near Crater (mm)	Grain Size Base Material (mm)
1560	0.120 to 0.150	0.200 to 0.250
1560	0.120 to 0.150	0.150 to 0.200
1560	0.120 to 0.150	0.200 to 0.250
800	0.010 to 0.015	0.120 to 0.150
800	0.010 to 0.025	0.150 to 0.200
800	0.035 to 0.040	0.150 to 0.200

approximately seven inches from the mylar window when impact occurred.

Measurements of penetration depth, crater diameter and volume were made following impact. A micrometer depth gage (accuracy $\pm$ 0.005 cm) was used to determine penetration depth below the original surface of the target, and a vernier caliper (accuracy $\pm$ 0.01 cm) was used to measure the crater diameter at the original surface level. Volume measurements (accuracy $\pm$ 0.05cc) were made using a glycerine solution. The following sections describe the results obtained.

RESULTS

The results of the study are shown in Figures 1 through 12. Some of the plots denote points as being calculated. Some of the saboted impacts revealed parts of the driver disk in the crater. Where it appeared as if the crater diameter was undisturbed, the diameter was recorded. In an effort to make use of the data obtained on targets where sabot fragments were observed, a linear fit was made to the square of the center diameter and the crater volume. The results are shown in Figure 7. The data points marked calculated refers to points obtained in this manner.

1. Nature of Craters

The craters observed were characterized by a layer of projectile material covering the target material, the extent of which varied for the three pellet materials. The aluminum results showed a thin layer of aluminum plating the copper up to and including the lip of the crater, indicating the viscous fluid flow of the projectile. At the high temperature, (1600°F) and high velocity, (4000 to 6000 m/sec) cases, a film of brass was noticeable covering the aluminum film. The brass is formed due to the presence of 0.1 percent zinc in the aluminum (7075-T6) projectile. For steel and tungsten carbide impacts, the appearance of the projectile residue was that of both a thin layer concentrated on the bottom and fine particles found higher on the crater walls. Some of the steel impacts resulted in a small cone of steel (about 1/16" diameter and 1/16" high) located at the bottom of the crater, indicating that in these cases the projectile did not completely disintegrate. The steel impacts that did not exhibit this small cone showed a hole in the steel lining of the crater about the diameter of the cone. The presence or absence of this cone obviously affects the depth measurements but has negligible effect on the volumes measured. There were no noticeable changes in crater profile except for dimensional ones at the high target temperatures, for the steel and tungsten carbide impacts.

The shape of the craters varied with projectile material. The aluminum and steel craters have depth to diameter ratios of approximately 0.4 and 0.5, respectively, at the high end of the velocity scale, whereas the tungsten carbide results show craters which are somewhat deeper in penetration, having a depth to diameter ratio approaching 0.7 from above, at the upper limit of the velocities considered. The criteria that the depth to diameter ratio of 0.5 is a necessary condition for hypervelocity region, indicates that the tungsten carbide impacts are not in the hypervelocity region.

2. Volume Energy Relationships

Figures 4-6 show the variation of volume of material removed as a function of projectile energy for different target temperatures. For a given target temperature, the volume increases with increasing projectile energy in a non-linear manner. Atkins[4] and others have suggested that a linear volume-energy relationship is a characteristic of hypervelocity impact. This implies that energy dissipated per unit crater volume, $\frac{E}{V}$, is a constant over that velocity region for a given projectile-target combination. Bjork's[11] theory on the other hand predicts that volume is proportional to projectile momentum at high velocities, implying $\frac{E}{V}$ is a linear function of velocity in the hypervelocity region. The plots of

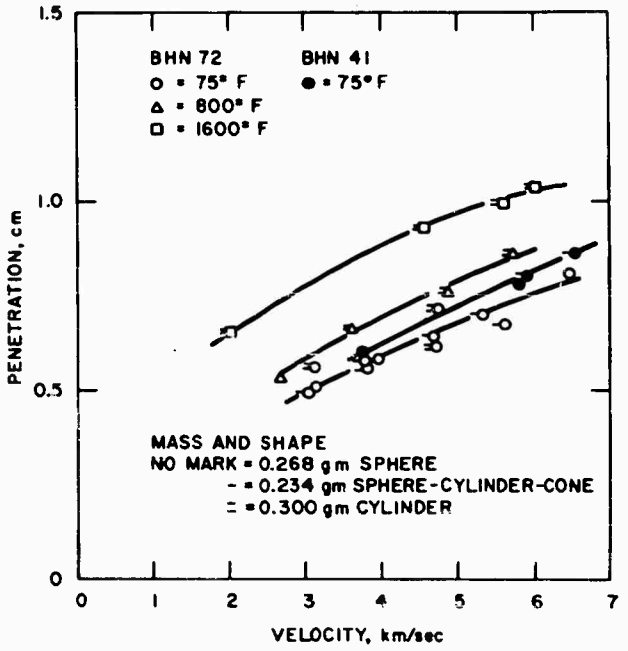

Figure 1. Penetration versus Velocity
Aluminum-Copper

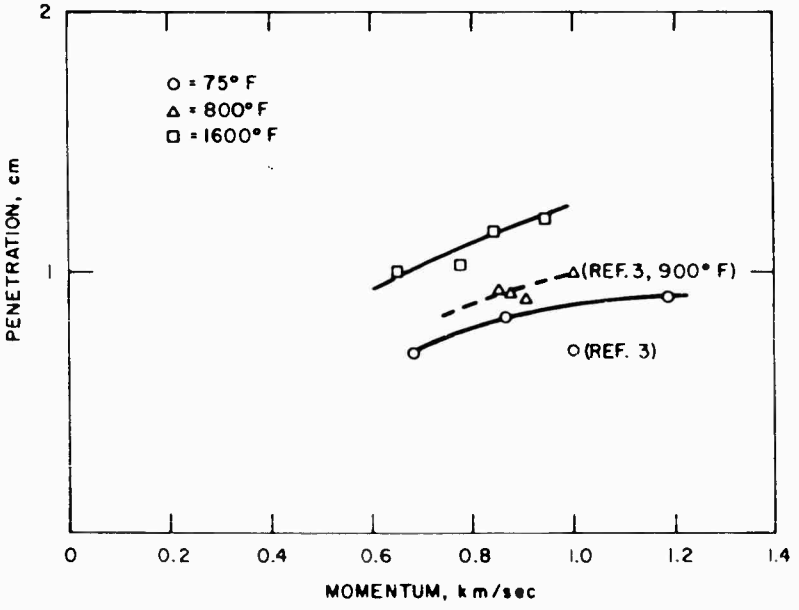

Figure 2. Penetration versus Momentum
Chrome Alloy Steel-Copper

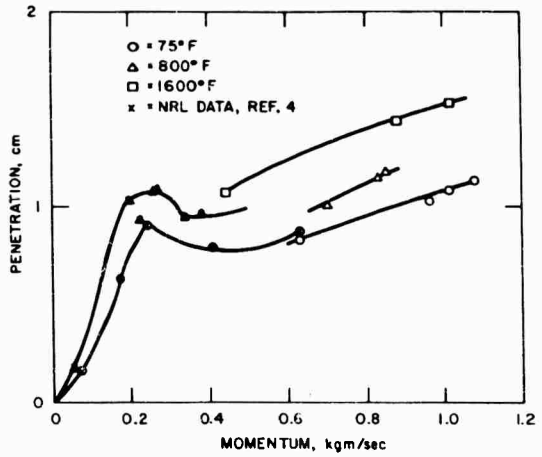

Figure 3. Penetration versus Momentum
Tungsten Carbide-Copper

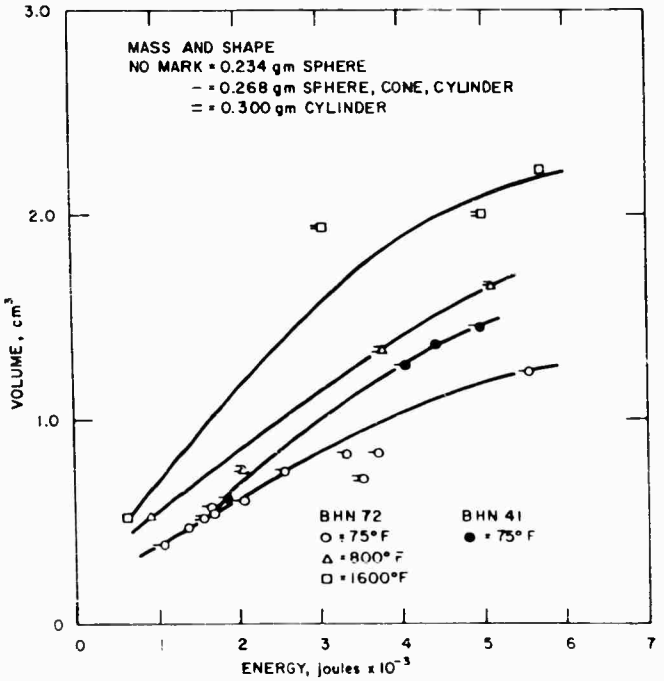

Figure 4. Volume versus Energy
Aluminum-Copper

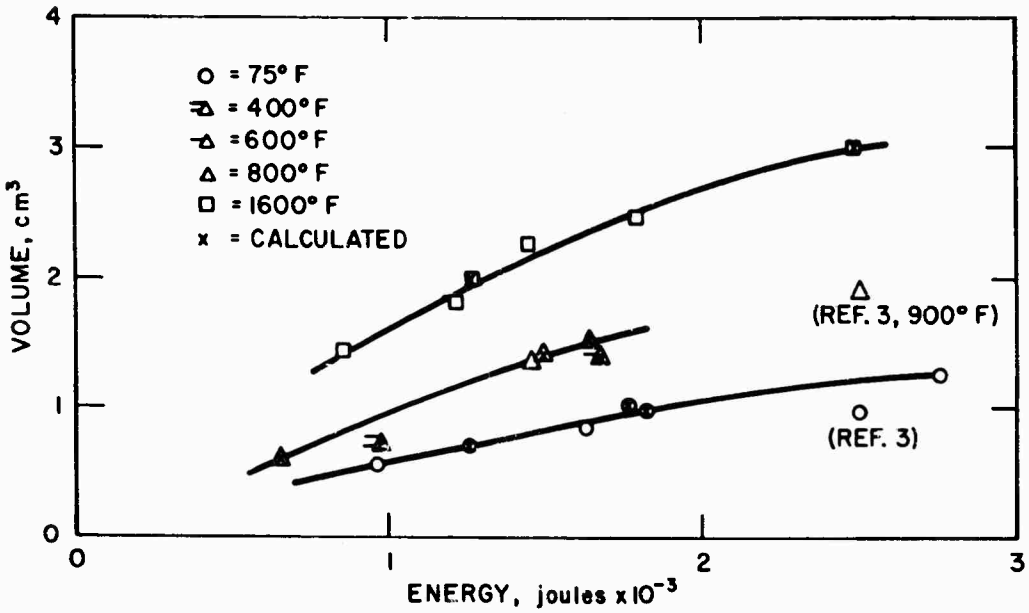

Figure 5. Volume versus Energy -- Chrome Alloy Steel-Copper

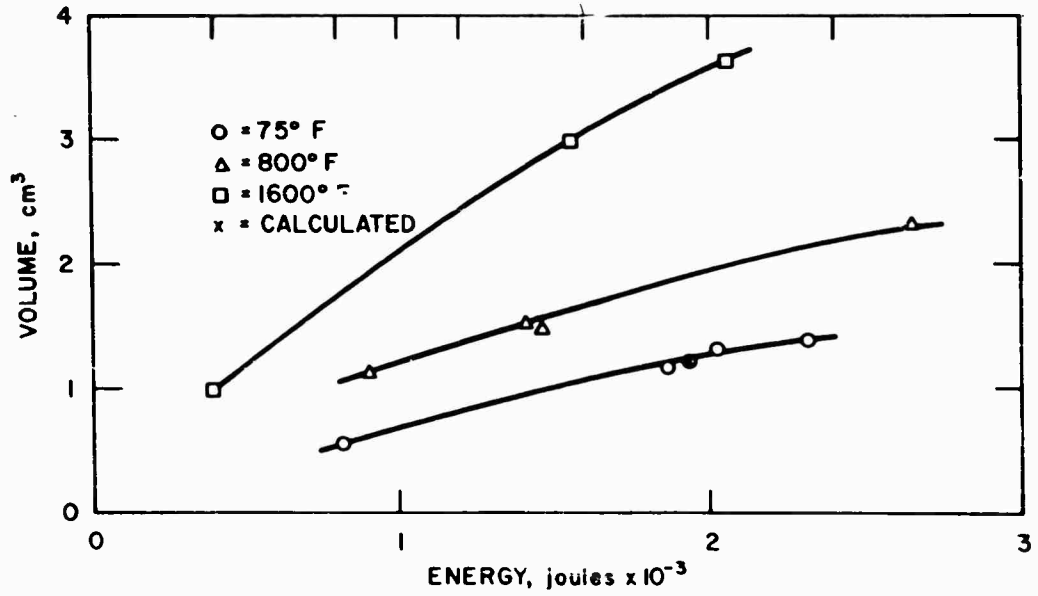

Figure 6. Volume versus Energy -- Tungsten Carbide-Copper

$\frac{E}{V}$ versus velocity, Figures 8-10, show that $\frac{E}{V}$ increases linearly with velocity.

Atkins[4] and others[12] have noted that for several projectile target combinations the energy per unit volume can be expressed as a linear function of the target Brinnel hardness. Hardness readings at temperature were not available for the copper used, but since the variation of tensile strength with temperature is quite similar[13, 14] to the hardness temperature profile, $\frac{E}{V}$ was correlated with the measured tensile values. Figure 11 is a plot of $\frac{E}{V}$ versus tensile strength for the different projectile materials considered. The curves are shown for several projectile velocities. A linear relationship exists of the form:

$$\frac{E}{V} = cU + d \tag{1}$$

where U is the tensile strength of the material
c, d, constants which depend on projectile velocity.

The intercept values, which have been determined by extrapolation, represent the energy/volume values near the melting point of copper, and the difference between this value and the energy/volume at a tensile value of 29,000 psi (target at room temperature) represent the change in $\frac{E}{V}$ due to the influence of target temperature. If one normalizes this difference by dividing it by $\frac{E}{V}$ (29 x 10^3 psi), a comparison of relative contribution of temperature effects on $\frac{E}{V}$ for different projectile velocities can be made. The results show in general that the extent of influence of target temperature on the cratering efficiency does not change with increasing projectile velocity over the range of velocities considered. This implies that we are impacting at velocities where the strength properties are important considerations.

Bjork's analysis was made ignoring the strength properties of the target material.

If one combines the linearity conditions of $\frac{E}{V}$ with velocity and target tensile strength, one can write the following general expression:

$$\frac{E}{V} = aU + bv + cUv + d \tag{2}$$

Where U = target tensile strength
v = projectile velocity
a, b, c, d constants
which can be rewritten

$$V = \frac{E}{aU + bv + cUv + d} \tag{3}$$

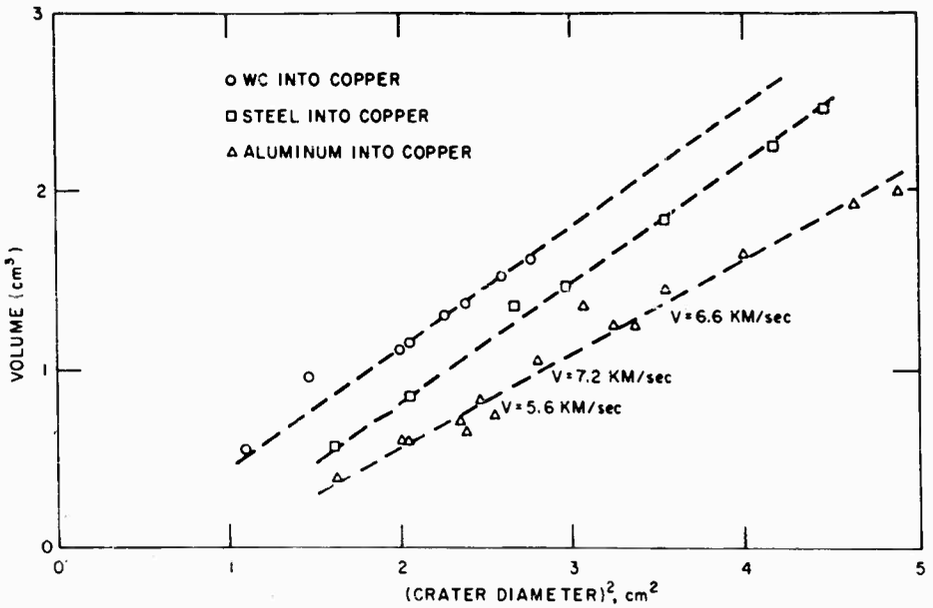

Figure 7. Crater Volume versus the Square of Crater Diameter

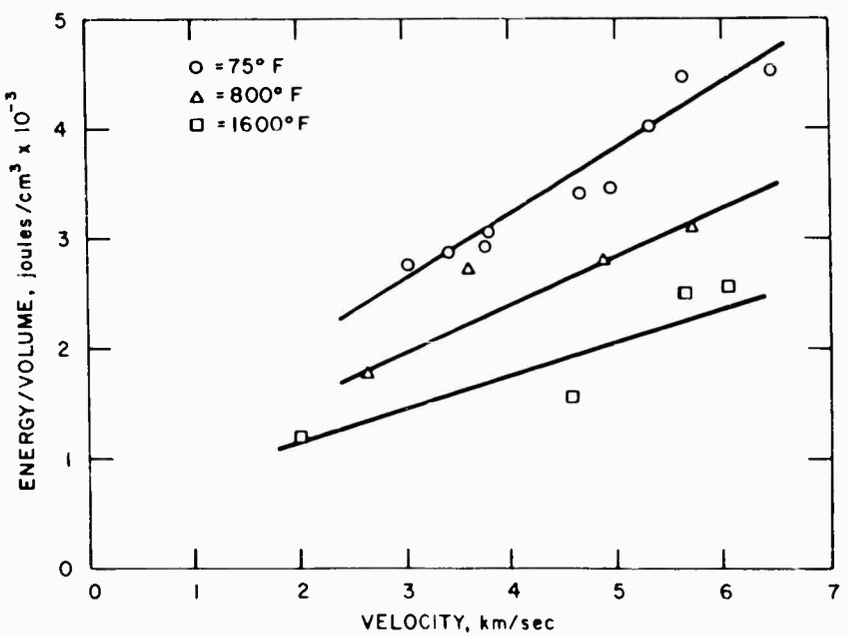

Figure 8. Energy/Volume versus Velocity Aluminum-Copper

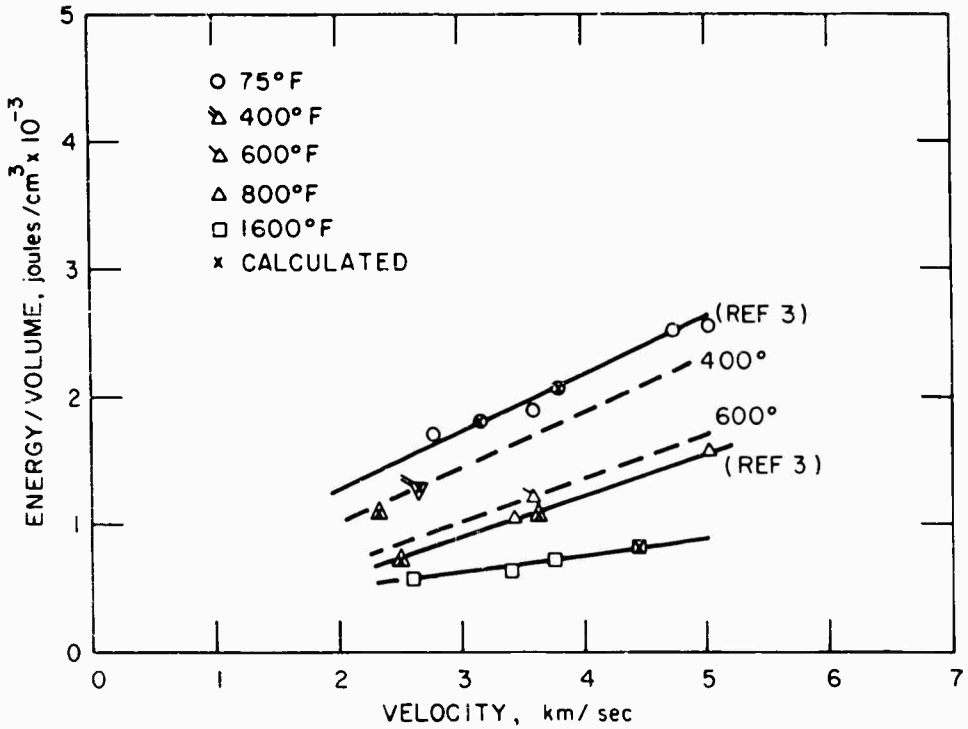

Figure 9. Energy/Volume versus Velocity Chrome Alloy Steel-Copper

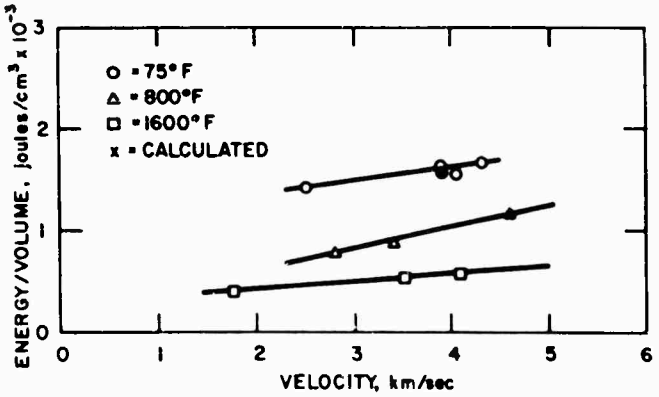

Figure 10. Energy/Volume versus Velocity
Tungsten Carbide-Copper

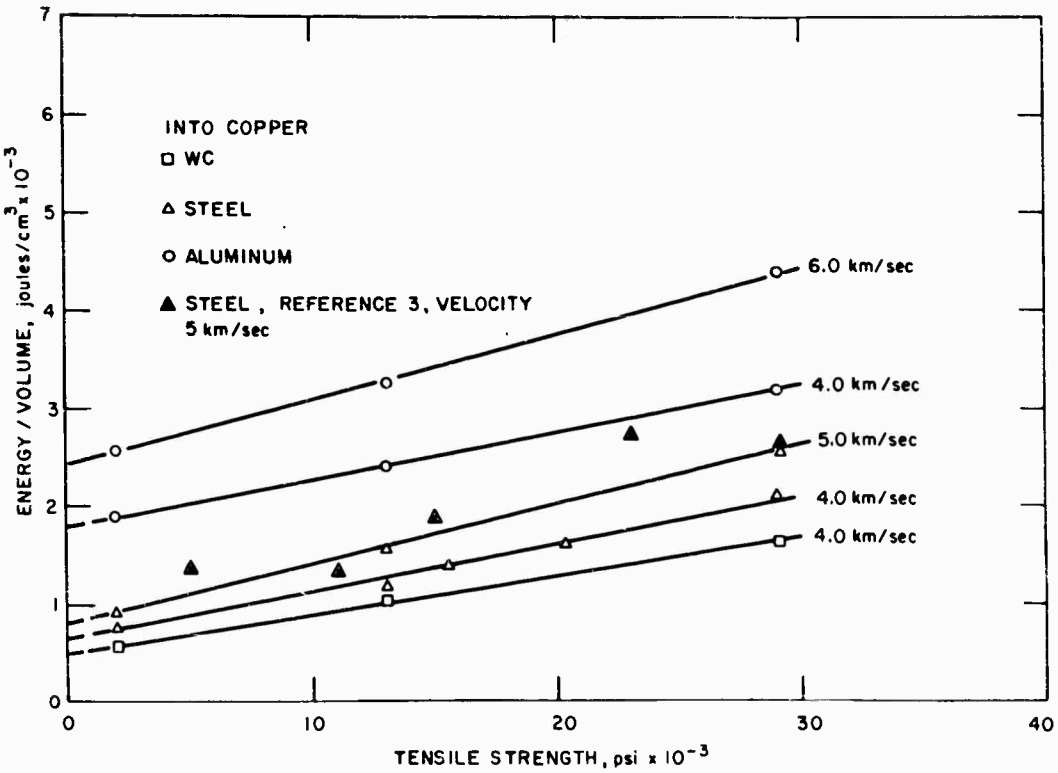

Figure 11. Energy/Volume versus Tensile Strength

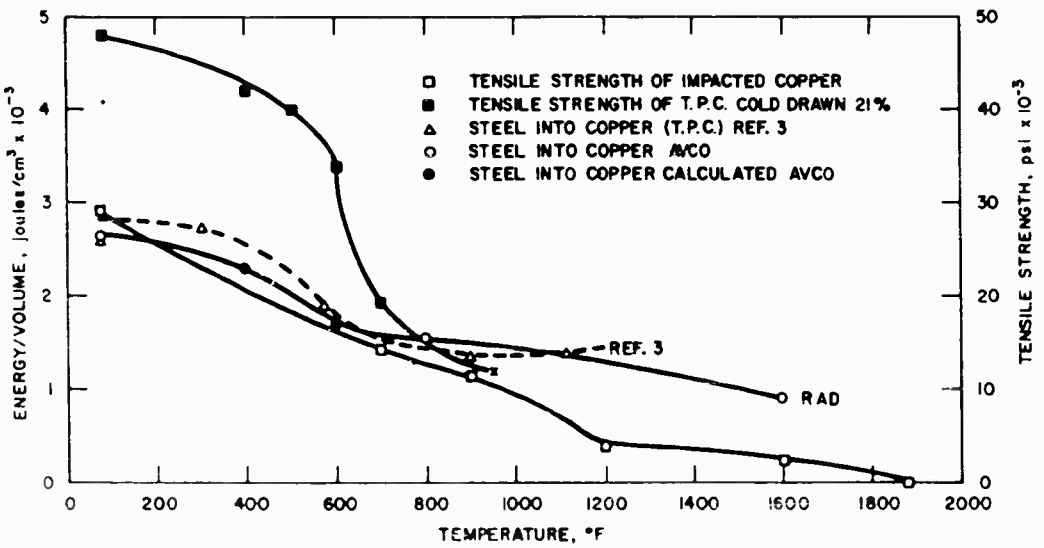

Figure 12. Comparison of Energy/Volume and Tensile Strength with Temperature

Dividing both numerator and denominator by projectile velocity, letting v get very large and holding U constant, one obtains:

$$V = k m v$$

which is valid at velocities where the strength properties of the target are small enough to be ignored. This conclusion is in agreement with Bjork's assumption.

Other investigators have noted a correlation between the volume of material removed during impact and the annealing region for copper. Allison in Reference 3 showed a large increase (about 100 percent) in volume occurring around the annealing region (500° F to 800° F) for steel impacting electrolytic tough pitch copper. The tensile strength of the copper used by Allison showed a decrease of 75 percent over that temperature region. The copper used in this study (OFHC 1/4 hard) had a tensile-temperature profile which was considerably different from that used by Allison, and the results obtained show a smoother volume-temperature variation over a similar temperature range. Figure 12 summarizes the above statements by comparing graphically the dependence of $\frac{E}{V}$ and tensile strength on temperature for both the results obtained by Allison and the authors. The conclusion that one can make from a comparison of this sort is that the response of the target material to particle impact is strongly dependent on the way the target material is worked prior to impact.

3. Penetration

Figures 1-3 are plots of the depth of penetration as a function of projectile momentum at target temperatures of 75°, 800° amd 1600° F. In general, the results show that at a given target temperature, the penetration increases with increasing projectile momentum or velocity. Also, the depth of penetration increases with increasing projectile density.

The aluminum data represents impacts made with the projectile of varying shape, over a small range of masses (0.20 to 0.30 gm). Cylinders, spheres and sphere-cylinder-cones were fired to investigate the effect of projectile shape or orientation on the subsequent damage. The results do not indicate any significant changes in the crater geometry occurring with the different shapes.

Figure 3 is a plot of the tungsten carbide data, including results obtained by Ferguson of the Naval Research Laboratory (reference 5). The targets used in the NRL study were annealed blocks having an average Brinnel Hardness of 48.0 for the as received blocks. The NRL studies indicate that the transition velocity for tungsten carbide into copper occurs approximately at 1 km/sec, at a target temperature of 75° F, and does not change in value when the target is impacted at 800° F. The results of the NRL study, if extrapolated into the velocity region reached in this study, show slightly higher values of penetration depth occurring at the same projectile velocity. This can probably be attributed to the difference in Brinnel Hardness of the two target materials considered, since there is evidence from the aluminum data (see Fig. 1) that the penetration into an annealed target (BHN 41) is somewhat greater than that into the (1/4 hard OFHC) (BHN 72).

CONCLUSIONS

The impact of semi-infinite blocks of heated OFHC copper with aluminum, steel and tungsten carbide projectiles of 1/4 gram mass at velocities up to 6.5 km/sec yielded craters whose dimensions increase with increasing target temperature. Both the depth of penetration and volume increased with increasing projectile density.

The results show that the ratio of (projectile energy/volume of material removed) varied linearly with both the projectile velocity and the target tensile strength. Combining these two results it was shown that the crater volume will be proportional to the projectile momentum at velocities high enough so that one can neglect the strength properties of the target. These velocities exist beyond the range considered in this study, since the results showed that the strength properties of the material are still significant at these velocities.

ACKNOWLEDGMENTS

The authors wish to express their appreciation to Messrs. J. A. Hull, R. N. Schweiger, Dr. J. Eckerman, Messrs. W. L. McKay, W. F. Keene, D. DeChristoforo, and many others of the Engineering Physics Section for their advice and co-operation during this study. Also, we would like to thank Messrs. J. Richards and R. Gardner of the Materials Section for their contribution to this study.

REFERENCES

1. Collins, L. D., and Kinard, W., The Dependency of Penetration on the Momentum per Unit Area of Impacting Projectile and Resistance of Materials to Penetration, NASA TNO-238, May 1960.

2. Charters, A. C., and Locke, G. S., A Preliminary Investigation of High Speed Impact: The Penetration of Small Spheres Into Thick Copper Targets, NACA RM A58326, 1958.

3. Allison, F. E., Becker, K. R., Effects of Target Temperature on Hypervelocity Cratering, Fourth Hypervelocity Impact Symposium Proc., Vol. I, 1960.

4. Atkins, W. W., Hypervelocity Penetration Studies, Fourth Hypervelootty Impact Symposium Proc., Vol. I, 1960.

5. Ferguson, W. J., and McKinney, K. R., The Influence of Temperature Elevation on the Penetration of Missiles Into Copper Targets, NRL Report 5407, 1959.

6. Kinard, W. H., and Lambert, C. H., An Investigation of the Effect of Target Temperature on Projectile Penetration and Cratering, NACA Research Memo RM L 58E14, 1958 (Confidential).

7. Summers, J. L., Investigation of High Speed Impact: Regions of Impact and Impact at Oblique Angles, NASA TN - D-94, 1959.

8. Atkins, W. W., and Persechino, M. A., Hypervelocity Impact, Proc. of AMRAC Vol. III, Nov. 1960, Secret.

9. Comeau, L. A., and Dignam, J. A., Empirical Hypervelocity Penetration Formula, Avco Technical Release, July 1961.

10. Carnevale, E. H., Hull, J. A., and McKay, W. L., Hypervelocity Impact Effects on Ablative Nose Cone Materials, Presented at BMD Symposium, L. A., 1960.

11. Bjork, R. L., Numerical Solutions to the Axially Symmetric Hypervelocity Impact Process Involving Iron, Rand Corp., 3rd Hypervelocity Impact Symposium Proc., Vol. II, 1958, Secret.

12. Feldman, James G., Volume-Energy Relations from Shaped Charge Jet Penetrations, 4th Hypervelocity Impact Symposium Proc., Vol. II, 1960.

13. Garofalo, F., Malenock, P. R., and Smith, G. V., Trans. ASM, 45, 1953, 377.

14. Westbrook, J. H., Temperature Dependence of the Hardness of Pure Metals, Trans. ASM 45, 1953, 221.

SPRAY PARTICLE TECHNIQUE

FOR STUDYING HYPERVELOCITY IMPACT

Thomas Lee, William Clark and Emerson Cannon

Utah Research and Development Company
Salt Lake City, Utah

INTRODUCTION

The problem of accelerating large masses to high velocities is one which is formidable. Accelerating a small mas (less than 10^{-3} gram) to a high velocity is not so difficult and has been done with some degree of success. The method used at Utah Research and Development Company is one which utilizes spray particles. The discovery of spray particles and the subsequent recognition of them as a tool for studying hypervelocity particle behavior and hypervelocity impact was made by the authors and others at the University of Utah High Velocity Laboratory. It was noted while studying the spectral characteristics of the impact flash that the light from the impact flash was mainly concentrated in some rather long streamers extending out from the point of impact. Open-shutter photographs of the impact flash (Fig. 1) show these streams of light clearly. Further investigation showed that when an obstacle is in the path of one of these streamers a secondary impact flash is produced. The existence of the secondary impact flash indicates the presence of spray particles producing the secondary flash. R. E. Blake [1] made a rather detailed study of the velocity and size distribution of spray particles. Clark, Kadesch and Grow [2] described the behavior of spray particles in terms of meteorite theory and suggested experimental techniques for studying single spray particles.

The striking similarity between the micro-craters made by impacting spray particles and the normal macro-craters was noted while looking at a spray impact area on steel shim stock through a microscope. As is seen in Figure 2, the micro-craters have all of the characteristics of the normal craters in aluminum. They have the same symmetrical pattern, the raised lip and the delicate petals.

Experimental work in the research facility of Utah Research and Development Company has been aimed at obtaining a single spray particle whose velocity may be measured accurately and whose diameter and mass may be determined. The experimental method of doing this is simple and straightforward in outline, but considerably less simple in practice.

The ability to obtain data which is of value from small particle impact

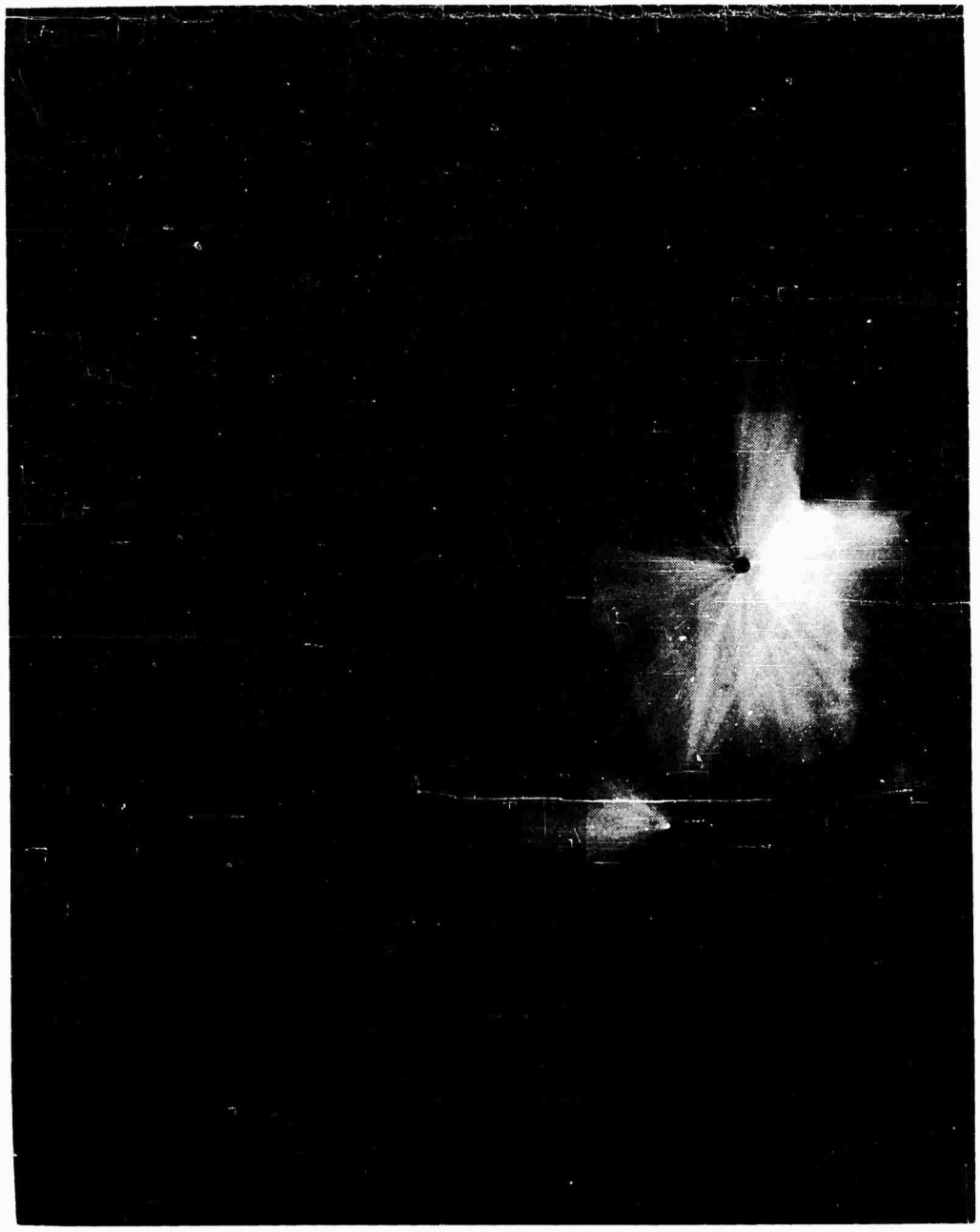

Figure 1

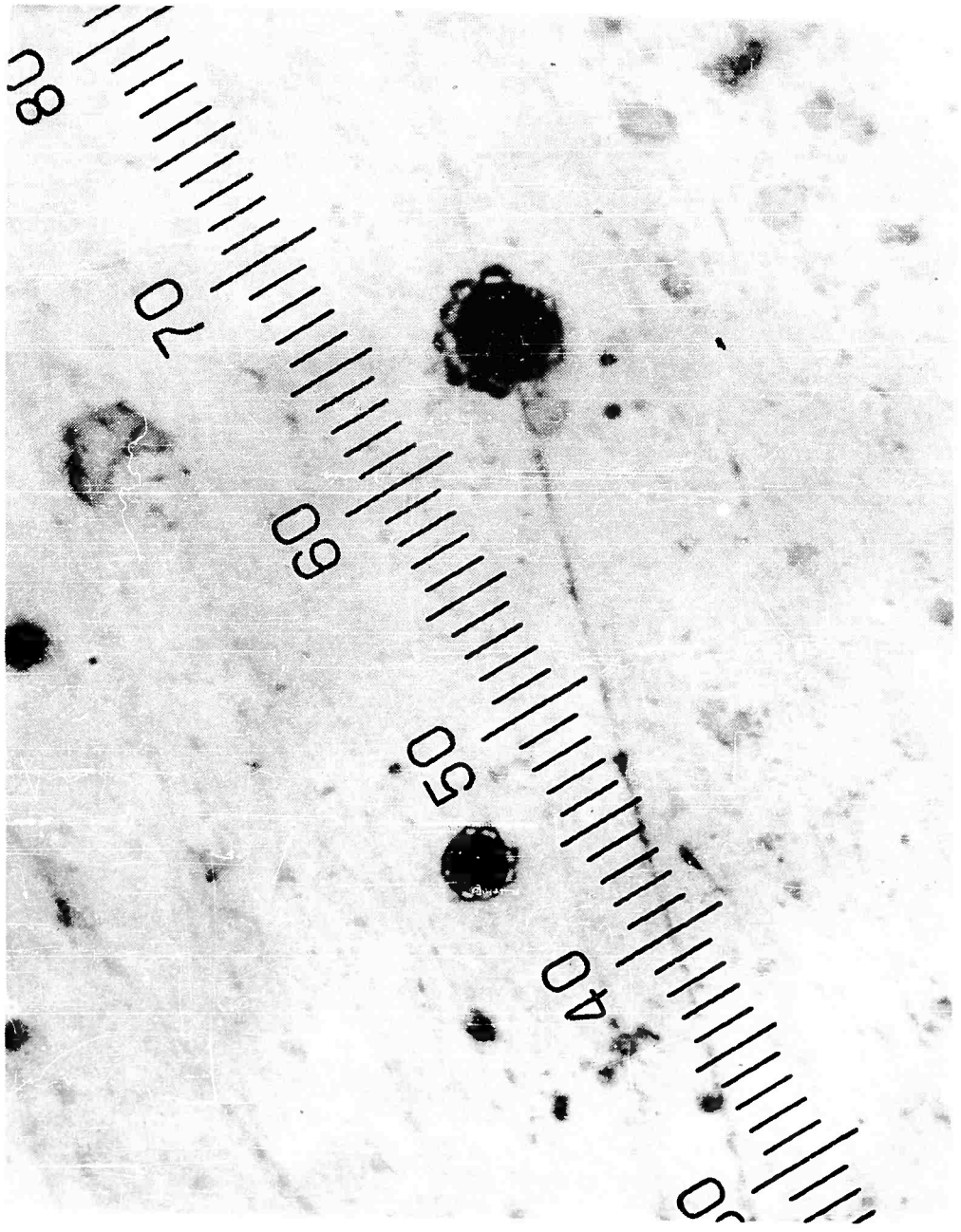

Figure 2

depends to a large degree on the validity of scaling laws employed. When the hydrodynamic model of impact damage is employed, (as has been done by most theorists) it is necessary to assume either that viscosity is of negligible importance or that it plays a large role. The validity of the assumption made determines, to a large extent, the ability of a given scaling law to represent the facts as will be discussed. It is possible to determine the effect of viscosity on the process of crater formation by varying the size of the impending projectiles over several orders of magnitude while maintaining a relatively constant velocity. The experiments which are reported in this paper are ideally suited for this purpose and have been used to determine the effect of viscosity on the cratering mechanism. This paper also indicates some scaling phenomena of importance in predicting damage due to projectiles of large mass at high velocity.

TECHNIQUES

Presently, the gun being used at URDC is a 25 caliber, smooth-bore, experimental gun that is well known to many of the readers. A picture of the gun mounted to the vacuum tank is seen in Figure 3. This gun is chambered for a 243 swift cartridge. The cartridge is loaded with a standard load and the one-quarter-inch steel sphere is forced into the mouth. The gun is fired into a vacuum range whose pressure measures 6 mm in mercury. The target assembly is seen in Figure 4. The primary target -- the target into which the steel sphere impacts -- is seen at the bottom of the assembly. Above the primary target is a steel box. Within the box are windows through which the photomultipliers observe the trails of the spray particles and the secondary target onto which the spray particles impact.

The relative positions of various components of the target assembly can more readily be seen in Figure 5. The leading edge of the primary target is lined up directly below the aperture into the box. A few experimental shots at URDC, correlated by the work of the High Velocity Laboratory, showed that the smallest spray and the fastest spray was ejected at nearly right angles to the line of travel of the primary particles. Figure 6 shows the distribution of the spray. The microparticles are exclusive in the first five degrees of arc as measured out from the face of the target. To take advantage of the highest velocity particle it was necessary to take care to be in the five degree region. The spray from the primary impact must then pass through the tiny aperture and in front of the photomultiplier slits before striking the secondary target.

For the most reliable measurements exactly one spray particle should be admitted to the velocity and diameter measuring system. This is obtained by adjusting the entrance aperture by trial and error. The most recent, and apparently satisfactory, entrance aperture is 0.1 millimeter by 0.1 millimeter. Spray particles enter every shot and occasionally only single or separable doubles pass.

The secondary target is presently 24ST aluminum. The surface is polished on the buffing wheel with 600 grit silicon carbide. A higher polish is, of course, possible, but experience has shown that the extra effort is not worth the results on this grade aluminum. The target is mounted in a target holder (Fig. 7) which can be accurately returned to the same spot for each successive shot. This facilitates the locating of the spray particle impact area under the microscope.

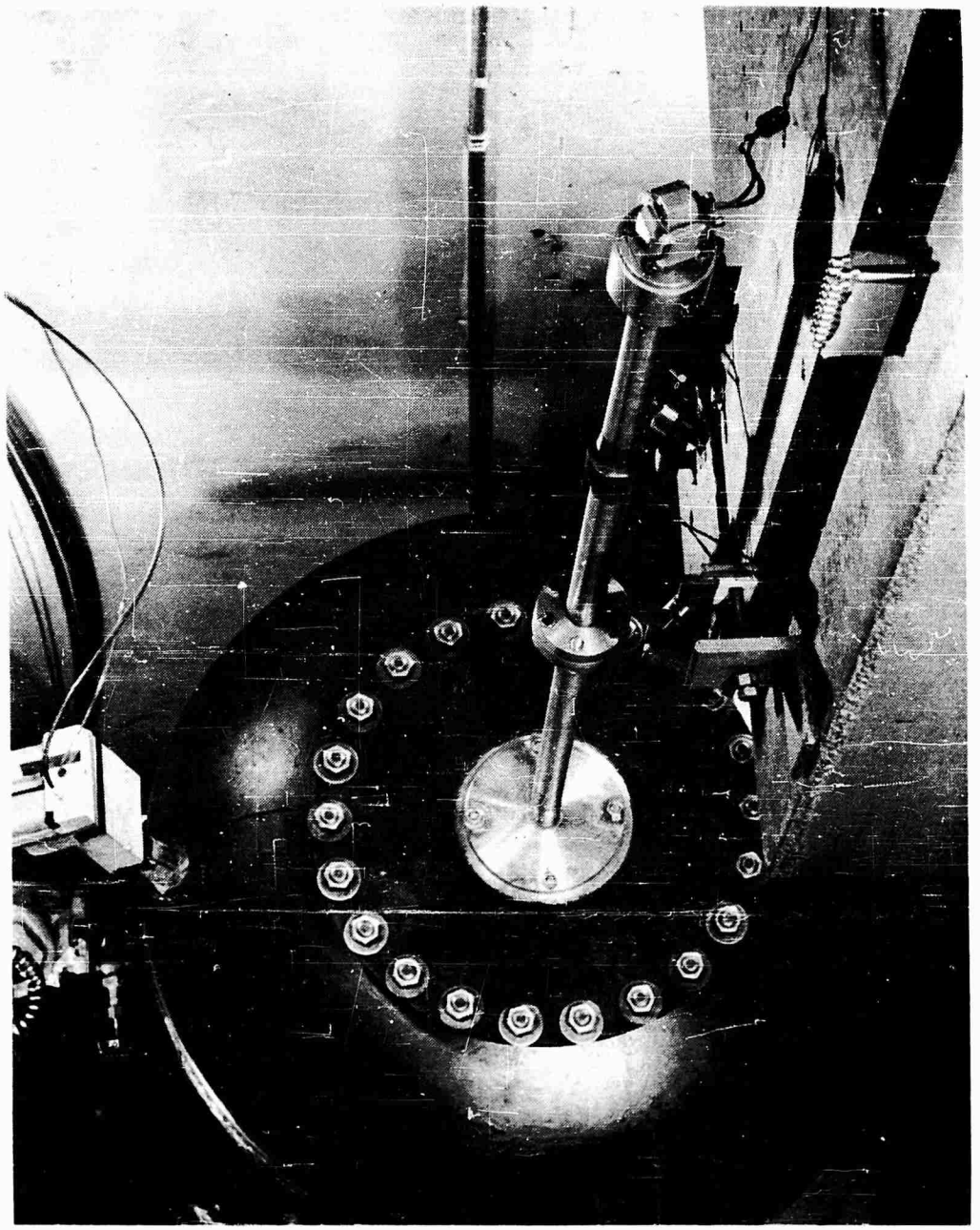

Figure 3

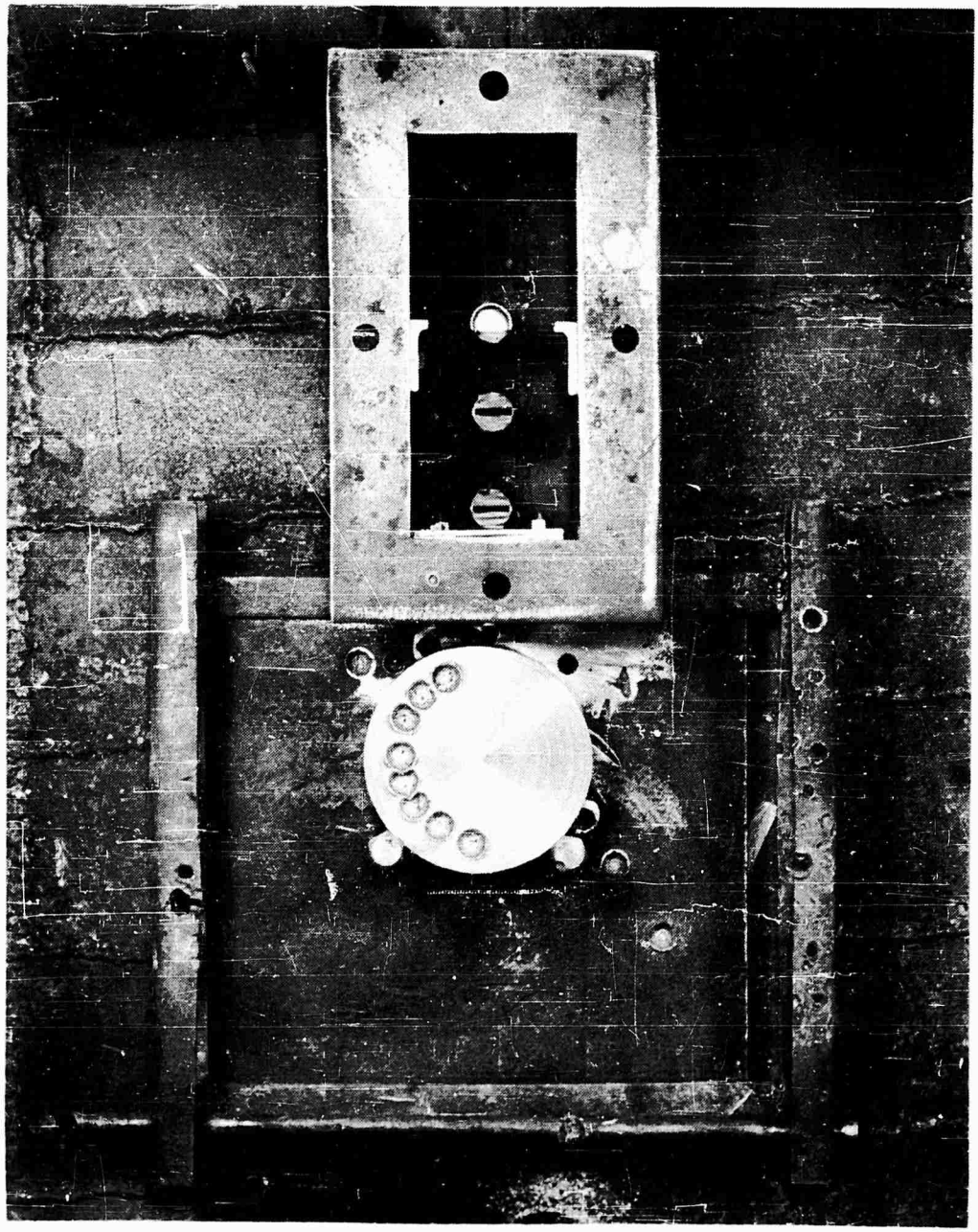

Figure 4

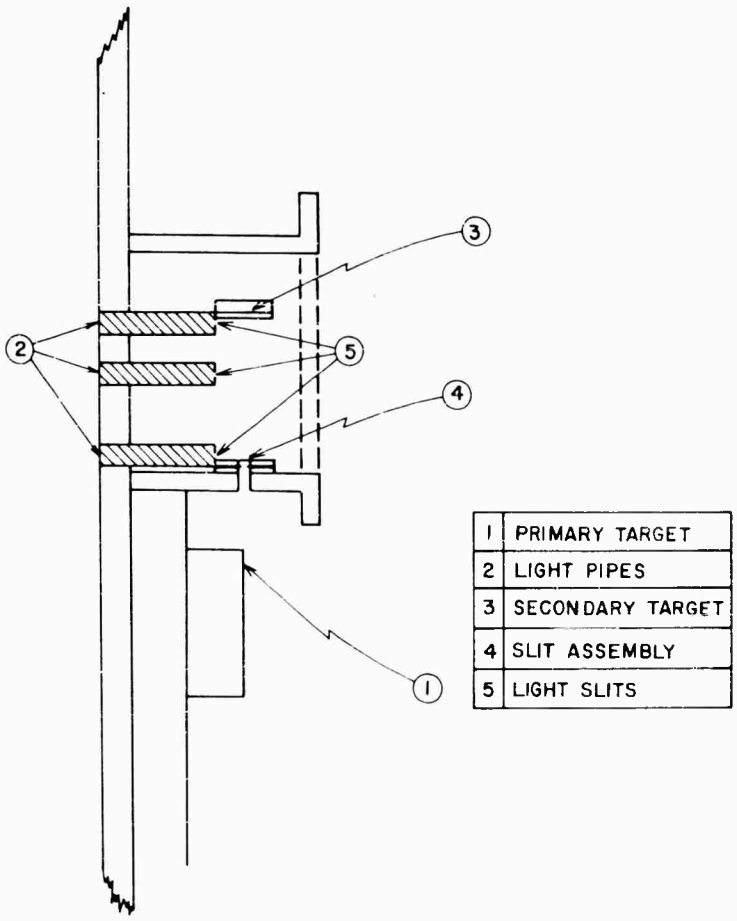
3
2
5
4
1
1 PRIMARY TARGET
2 LIGHT PIPES
3 SECONDARY TARGET
4 SLIT ASSEMBLY
5 LIGHT SLITS

Figure 5

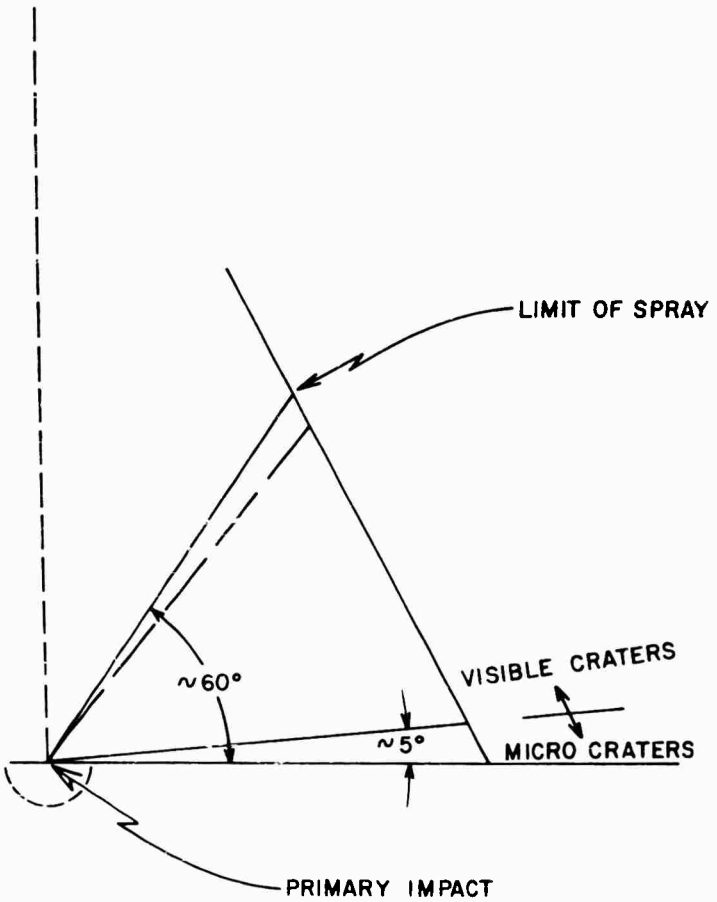
LIMIT OF SPRAY
~60°
VISIBLE CRATERS
~5°
MICRO CRATERS
PRIMARY IMPACT

Figure 6

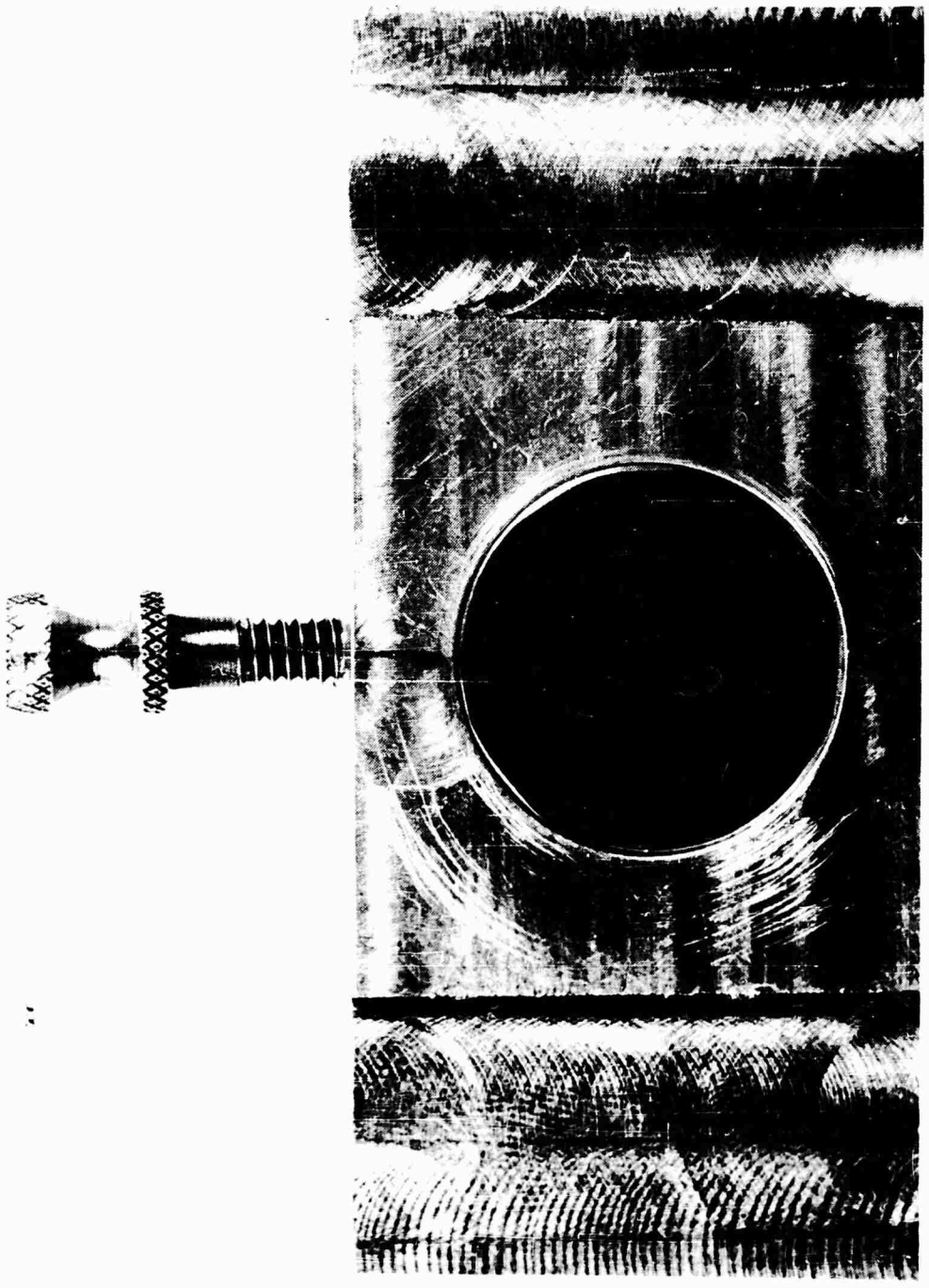

Figure 7

SPRAY PARTICLE TECHNIQUE

The microscope used to study and measure the spray particle craters is a Unitron, Model BU-11 metallograph microscope. Although the microscope itself has provision for taking photographs it was found more convenient to photograph the craters through the eye-piece. The scale on all pictures shown is 2.5 microns/scale division.

Two velocity measuring systems are required. The first measures the time of flight of the primary (steel sphere) pellet from the gun muzzle to the impact on the primary target. The photomultiplier which sees the impact sends a signal which both marks the arrival on the primary velocity oscilloscope and triggers the sweep for the spray velocity oscilloscope. The photomultipliers see the spray particle as it successively passes in front of each slit and strikes the secondary target. The signal from each cell is recorded on the scope trace and photographed. The oscilloscopes are calibrated for sweep synchronization with a Tektronix time mark generator.

Drag Theory:

In this work the particle diameters have been determined from the rate at which particles lose velocity. The smaller the spray particle the more rapidly it will slow down from friction with the atmosphere. Air molecule collisions with fast metal objects are not perfectly elastic. Some energy appears as heat in the metal. The size of this fraction is of some interest but is not at present accurately known. Rough calculations indicate that spray particles having an initial velocity around 10 km/sec are melted quickly but evaporation does not change their diameters seriously while they traverse the apparatus. Liquid drops are accurately spherical under the conditions of interest, surface tension forces greatly exceeding the drag forces. Spray particles are normally much smaller than the mean free path of molecules in the gas through which they are passing. The spray particle velocity is high compared to the random molecular motion. Drag on the spray particles is then due to repeated collisions with stationary gas molecules. It can be reliably computed and for a sphere is equal to the cross-sectional area times ρv^2 where ρ is the density of the gas and v the spray particle velocity.

In differential equations the rate at which the spray particle decelerates is

$$d^2x/dt^2 = k(dx/dt)^2$$

then upon integrating

$$x = (1/k)\ell n\ (1 + kV_0 t)$$

Three (x, t) points furnish sufficient information to calculate the initial velocity V_0 and the deceleration factor, k. From k and the free molecule drag theory the particle diameter can be calculated.

Inertia forces, equation state pressures, and material strength forces scale linearly, that is, crater formation is influenced by these forces only. The ratio of crater dimension to pellet dimension is independent of pellet size. On the other hand, viscous forces scale in such a way that their influence increases for

smaller apparata. Consider a sphere moving through a viscous fluid, by Stokes law the drag force on it is

$$\text{Drag force} = 6\pi r \eta V$$

r = sphere radius
η = fluid viscosity
V = sphere velocity

Dividing by the sphere mass, $4/3\pi r^3 \rho$, the deceleration is

$$\frac{dV}{dt} = -\frac{9}{2}\frac{\eta V}{\rho r^2}$$

integrating it is found that the range of the sphere is

$$\text{range} = \frac{2Vo\,\rho r^2}{9\eta}$$

It follows that the ratio of the range to the sphere radius is directly proportional to the radius. The impact case of a deformable pellet penetrating metal is more complicated than that of a sphere of constant dimensions penetrating a viscous fluid, but in a general way the same scaling laws should apply. If a centimeter-size pellet is stopped by viscous forces in about 10 radii, a micron-size pellet should be stopped in 10^{-3} radii leaving practically no crater at all. Put another way, if viscous forces are significant for an impact of an ordinary centimeter-size pellet they should be overwhelmingly dominant in the micron-size range.

Data and Conclusions:

The data plotted in Figure 8 was taken from steel-aluminum data by Johnson (3) and others at the High Velocity Laboratory and from the Kineke[4] data as reported at the Fourth Hypervelocity Symposium. Johnson and company were firing 3/16-inch steel spheres into aluminum while Kineke fired flat steel discs off the face of explosives into aluminum. The Kineke data was modified by assuming the discs to be spheres of equivalent mass.

The diameter of the crater in the data reported from URDC is subject to possible error. It is often difficult to determine the diameter at the surface of the original metal because the lips rise so much higher and the crater sides are almost vertical at "ground" level. Crater diameters were measured from "blown-up" photographs as shown in Figure 2. It is possible that more care should be taken in the future to photograph the crater while focusing the microscope at "ground" level rather than on the very photogenic lips.

The ratio D/d is the ratio of the crater diameter to the impacting sphere diameter. It should be noted that if the Kineke projectiles hit in such a way that they presented a diameter to the target that was smaller than the equivalent sphere diameter the points would move upward on the graph.

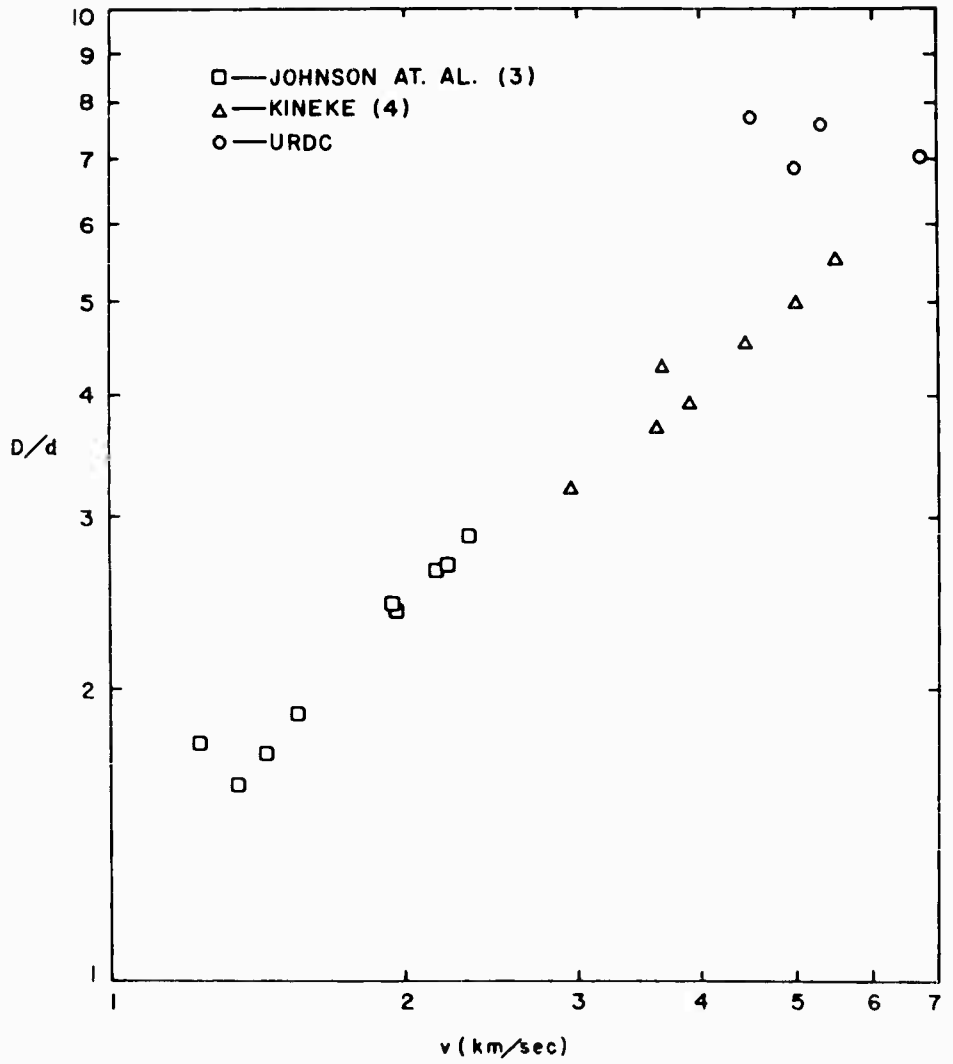

Figure 8

These data (Fig. 8) indicate the ratio of crater diameter to pellet diameter is about the same for a given velocity for pellets in the centimeter and micron-size ranges. The crater shapes are not conspicuously different. We conclude that the effect of viscous forces is small in the micron-size ranges. Due to the scaling laws, the effect of viscous forces must then be completely negligible for pellets in the centimeter-size range and the neglect of viscous forces in the Bjork[5] cratering theory is justified. We further conclude that damage to a space vehicle due to projectiles of large mass at high velocity may be predicted by scaling linearly from phenomena observed in spray particle impact.

BIBLIOGRAPHY

1. R. E. Blake, R. W. Grow, and E. P. Palmer, "Velocity and Size Distribution of Impact Spray Particles," University of Utah High Velocity Laboratory Technical Report No. OSR-19, May 1960.

2. W. H. Clark, R. R. Kadesch, and R. W. Grow, "Hypervelocity Impact Spray Particles," University of Utah High Velocity Laboratory Technical Report No. OSR-18.

3. D. K. Johnson, E. T. Cannon, E. P. Palmer and R. W. Grow, "Cratering Produced in Metals by High-Velocity Impact," University of Utah High Velocity Laboratory Technical Report UU-4, July 1959.

4. John H. Kineke, Jr., "An Experimental Study of Crater Formation in Metallic Targets," Procedures of Fourth Symposium on Hypervelocity Impact, APGC, Eglin Air Force Base, Florida, Vol. I, Paper 10, April 1960.

5. R. L. Bjork, "Effects of a Meteoroid Impact on Steel and Aluminum in Space," Rand Corporation Report, P-1662, December 1959.

SESSION V

EXPERIMENTS
(continued)

CHAIRMAN

MAURICE DUBIN

NATIONAL AERONAUTICS AND SPACE
ADMINISTRATION

CHAIRMAN'S REMARKS

I would like to address my opening remarks to this Experimental Session from the standpoint of the organization for which I work, the National Aeronautics and Space Administration. In the space program, there are a variety of areas where the hypervelocity field is of fundamental interest. These include: hypervelocity interactions of a projectile with gas; hypervelocity impacts on surfaces as the moon and space vehicles; the meteoritic environment for reliability in space missions; and some fundamental aspects of the scientific exploration of the solar system, particularly the nature of matter in the interplanetary space.

Although the re-entry problem for ICBM development has been solved, an extension of this problem area is required for entry into planetary atmospheres at velocities greater than escape velocity. The interaction of a probe upon entry into the atmospheres of Mars and Venus must be understood in order to obtain measurements of these planetary atmospheres and to land instrumentation on the planetary surfaces.

In the lunar program, it is expected that within the next two or three years instrumentation will be soft-landed on a lunar surface, and within the decade, it may be possible to send men to the moon and return them to the earth. The lunar surface represents a unique sample of material exposed to the space environment and unaffected by the telluric erosion processes from an atmosphere and water. The surface has been bombarded by meteoroids for millions of years and the signature of the craters thus formed may soon be examined in detail. We would like to know the effects of the meteoroid bombardment on the lunar surface, the degree of formation of dust, the effects of spallation, the crater shapes at impact velocities up to 70 km per/sec, and whether a meteoritic material may be recovered from the lunar surface. For such an investigation, extended theories and experiments on hypervelocity cratering is important in order to delineate the evolutionary variations of the lunar surface and its geological history.

The meteorite environment is also of importance for space missions particularly for manned space flight and for missions to the planets. There is concern about the reliability of storage of liquid fuels for extended flights; concern for the design parameters of radiators of large areas to be used in conjunction with nuclear power sources for propulsion, and, concern for the safety of a crew on extended flights. Based on available information of the meteoritic environment, the data on hand is presently insufficient for proper evaluation of design parameters. Not only is the knowledge of cratering effects at impact velocities up to 70 km of limited value, but also the knowledge of damage to thin targets and the effects of cratering by cometary particles of low density (0.1 grams per cc) not well known.

Hypervelocity impact studies are important also in the scientific exploration of the solar system, particularly with the study of interplanetary matter by direct measurements, i. e., cosmic dust, meteoroids, asteroids, and comets. In these direct measurements, the interaction of the particles with the sensors again occur at velocities up to 80 km per/sec. The physics of the impact effects, particularly in translating any measurements from the sensors to the understanding of the particle mass, velocity, and structure, is exclusively tied to our knowledge of the hypervelocity-impact physics. The astrophysical significance of such studies is apparent as a basis for understanding the origin of comets and stellar bodies. The value of such measurements is therefore related to the understanding of hypervelocity impact phenomena.

Thus, for a number of space-age problems, the study of hypervelocity effects indicated that theoretical and experimental work for the exploration of the solar system should be extended to velocities ranging close to 100 km per/sec. The studies of space environment are of immediate interest and should be continued to delineate the probability of impact and the hypervelocity studies are important in determining the methods of designing space vehicles for this environment.

AN EXPERIMENTAL INVESTIGATION OF SINGLE ALUMINUM "METEOR BUMPERS"

Don Humes, R. N. Hopko, and William H. Kinard

NASA Langley Research Center
Langley Air Force Base, Virginia

INTRODUCTION

Man and machine are now traveling in a new environment -- space. Meteoroids are part of this environment and thus pose a potential hazard to the space traveler. Considerable research effort is being directed to define this hazard. If it is discovered that meteoroids pose a serious hazard to space vehicles, means of reducing the hazard must be found. Several fabrication techniques to reduce the damage from meteoroid impacts are presently being studied. This report describes an investigation of one fabrication technique which utilizes a "Meteor Bumper", first proposed by Fred Whipple as a means of reducing impact damage. Figure 1 illustrates the meteor bumper which is simply a thin shield placed a short distance in front of the main structural wall. It is envisioned that meteoroids would be fragmented and/or vaporized upon impacting the bumper and the resulting debris dispersed over a large area of the main wall.

SCOPE OF THE PRESENT INVESTIGATION

In this investigation, the bumper shield thickness and the spacing between the bumper shield and the main structural wall have been varied. The bumper shields were 2024-T3 aluminum alloy and varied in thickness from 0.016 to 4.0 projectile diameters. The main walls were all 2024-T4 aluminum alloy.

In order to efficiently study the effectiveness of the various bumper shields, the main structural walls were all thick enough to be considered quasi-infinite.

The spacing between the bumper shield and the main walls varied from zero to 96 projectile diameters. The projectiles used in obtaining penetration data were 0.0625-inch-diameter copper spheres and were saboted during firings from both powder guns and light gas guns. Several 0.220-inch-diameter aluminum spheres were fired to obtain photographic data. The bumper targets impacted by projectiles fired from the light gas guns were contained in an evacuated test chamber while impacted. The targets impacted by projectiles fired from the powder guns were mounted in an open range. Instrumentation was employed to measure the

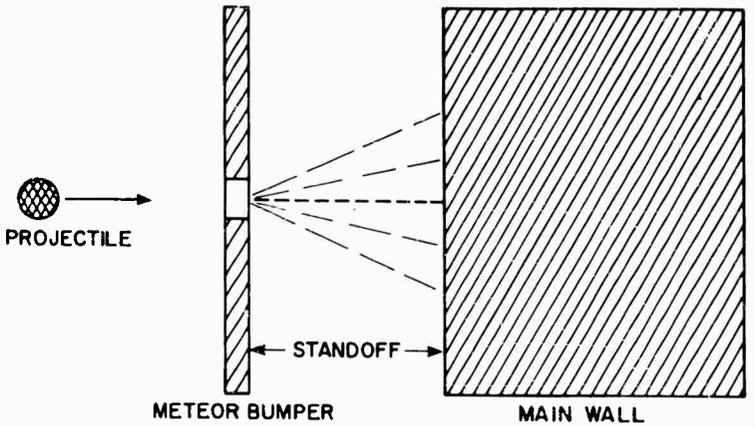

Figure 1. Sketch of meteor bumper configuration.

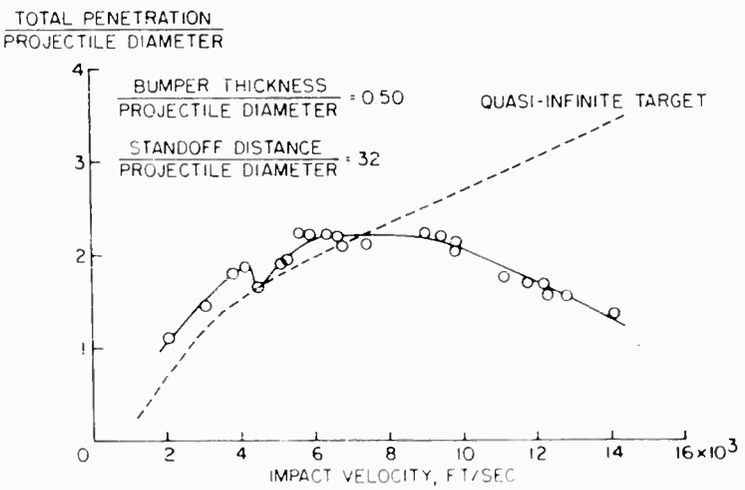

Figure 3. Variation of total penetration with impact velocity in a bumper protected target.

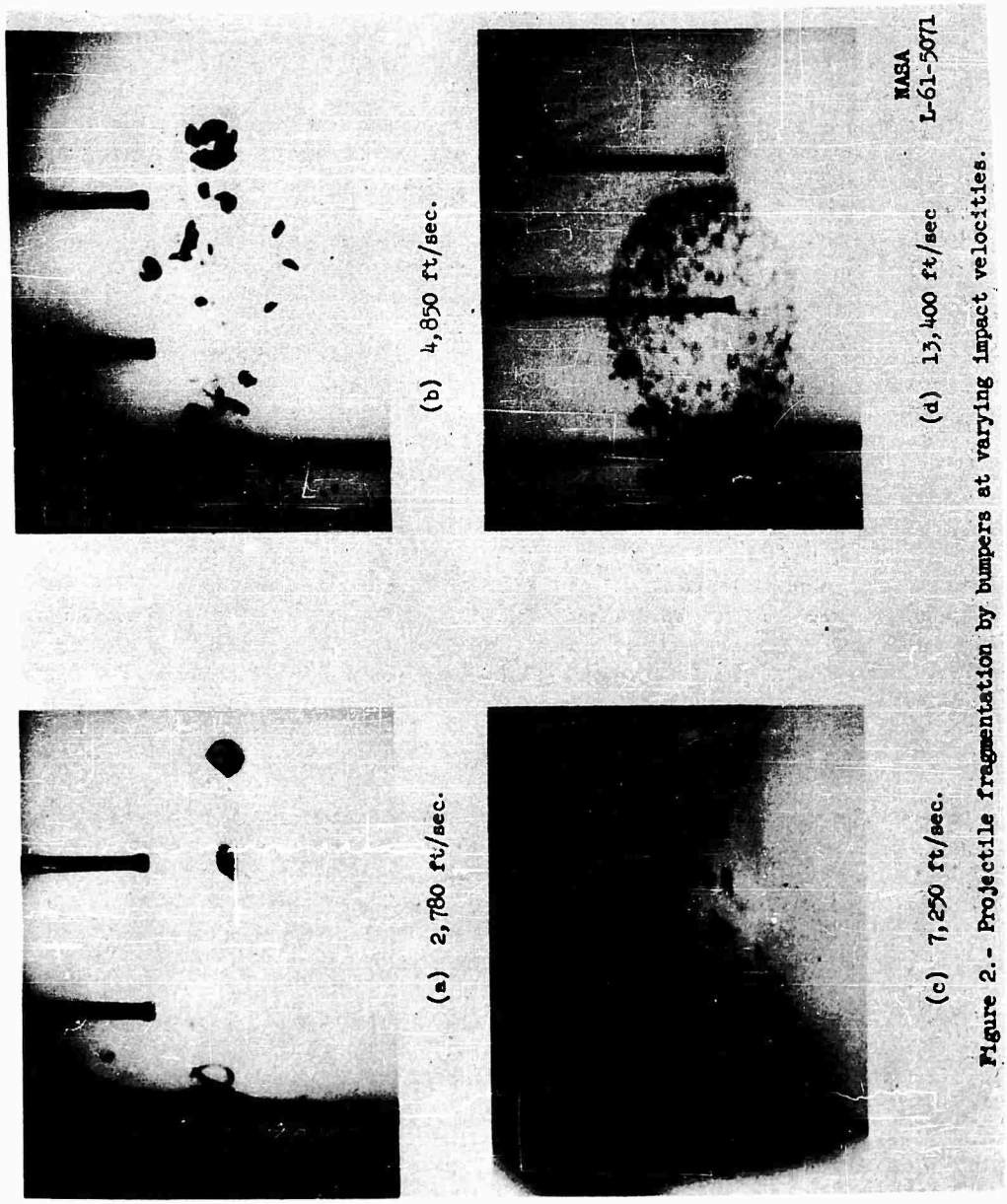

Figure 2.- Projectile fragmentation by bumpers at varying impact velocities.

velocity of the projectiles and to establish that the projectiles were launched undamaged and separated from the sabots before impacting the targets.

DISCUSSION OF THE RESULTS

Effect of impact velocity. The effect of projectiles impacting bumper shields at various impact velocities is shown in Figure 2. This figure shows photographs of 0.22-inch-diameter aluminum spheres after penetrating 1/8-inch-thick aluminum bumpers at impact velocities of 2,700, 4,600, 7,300, and 13,400 feet per second. At the impact velocity of 2,780 ft/sec the projectile which probably is the leading large fragment is essentially intact suffering only a slight deformation. One plug punched from the bumper can be seen following the projectile and a small ring of metal is visible just being spalled away from the bumper. When the impact velocity was increased to 4,800 ft/sec the projectile appears to be fractured in several large fragments which are remaining close together in a roughly small spherical pattern. Behind the projectile fragments can be seen a cone of bumper fragments. When the impact velocity was further increased to 7,250 ft/sec the projectile fragmented into smaller fragments which spread out such that they are indistinguishable from the fragments from the bumper. At the highest impact velocity of 13,400 ft/sec an expanding elliptical cloud of very small fragments was found.

The total measured penetration observed in a bumper protected wall combination at varying impact velocities is illustrated in Figure 3. The total penetration which is the bumper thickness penetrated plus the penetration in the main target is plotted on the ordinate with the impact velocity plotted on the abscissa. Plotted for comparison purposes are the penetrations achieved at identical impact velocities in quasi-infinite targets with no bumper shields. The thickness of the bumper shields used were all one-half the diameter of the impacting projectiles.

It can be noted that the penetration into the unprotected quasi-infinite targets increased with increasing impact velocities for the entire velocity range observed. In the low velocity range, the penetration into the bumper protected targets also increased with increasing impact velocities up to a velocity of about 6,000 ft/sec. At this velocity the penetration appears to reach a maximum value and as the impact velocities are further increased the penetration decreases.

Examination of the data shown in Figure 3 in the low velocity range shows that at these impact velocities the bumper shields were ineffective in reducing the penetration. In fact the projectiles penetrated deeper in the bumper protected targets than in the unprotected targets. This greater penetration in the bumper targets was due to the fact that less projectile momentum or energy was required to penetrate the bumper shield than was required to penetrate an equal depth in the quasi-infinite targets. This fact has been shown in Reference 1. In the low velocity range the copper projectiles were intact and essentially undeformed after penetrating the bumper shield as was the low velocity aluminum projectile shown in Figure 2.

Penetration data of Figure 3 at impact velocities above 9,000 ft/sec shows that the bumpers were effective in reducing the total penetration below that obtained in the unprotected targets. The copper projectiles were observed to begin fragmenting during the penetration of the bumpers at impact velocity above 9,000 ft/sec, almost twice the velocity required to begin fragmenting the larger aluminum projectiles illustrated in Figure 2.

The fragmentation of the higher velocity projectiles as they penetrated the bumper and the dispersion of the fragments over a large area of the main target accounts for the ability of the bumper shield at the higher impact velocities to reduce the penetration.

In hypervelocity impacts the crater volumes are observed to be a function of the kinetic energy of the impacting projectiles. In a bumper target system the energy is spread over a large area of the main target due to the projectile fragmentation and the dispersion of the fragments and there is a tendency to produce a very large diameter shallow crater rather than the usual hemispherical craters observed in unshielded targets. If the distance between the bumper and the main target is sufficient, many small individual craters are produced. The small crater having the deepest penetration will be that one produced by the fragment having the greatest energy.

The decrease in penetrations with increasing impact velocities shown in the high velocity range of Figure 3 results from an increase in the degree of projectile fragmentation which occurred at higher and higher impact velocities.

The velocities of the particles resulting from the penetration of a bumper shield vary widely. The measured velocities of the fastest fragments observed always increased with increasing impact velocities as shown in Figure 4. The increased rate of projectile fragmentation with increasing impact velocities shown in Figure 2, however, overshadowed the effects of the increasing fragment velocities and caused the penetration to decrease.

If the fragment sizes and the fragment velocities continue to change at velocities above 16,000 ft/sec as they have in the 9,000- to 16,000-ft/sec range then it is possible that the penetration depths in bumper protected targets may decrease and approach being equal only to the bumper thickness. If this trend be correct then it appears that possibly the maximum impact penetration damage to a shield protected wall may result from particles impacting at rather low velocities.

Effect of bumper spacing. The effects of the spacing between the bumper shield and the main wall are illustrated in Figure 5. This figure is a plot of the total penetration as a function of shield standoff.

It can be seen that at impact velocities up to about 9,000 ft/sec the penetrations were not affected by standoff. In this velocity range as has been mentioned the projectiles remained intact after penetrating the bumper. At impact velocities above 9,000 ft/sec in which cases the projectiles were fragmented by the bumper the penetrations were observed to decrease with increasing standoff up to a point beyond which additional increases in the standoff had no further effect. The decrease in the penetration observed as the standoff distance was increased up to about 40 times the projectile diameter occurred as the result of the greater dispersion of the fragments and consequently the reduced number of compound craters formed. The compound craters are those craters formed by two or more fragments impacting on or near the same location and consequently influencing the penetration depth of each other.

A typical dispersion pattern of fragments is illustrated in Figure 6 which

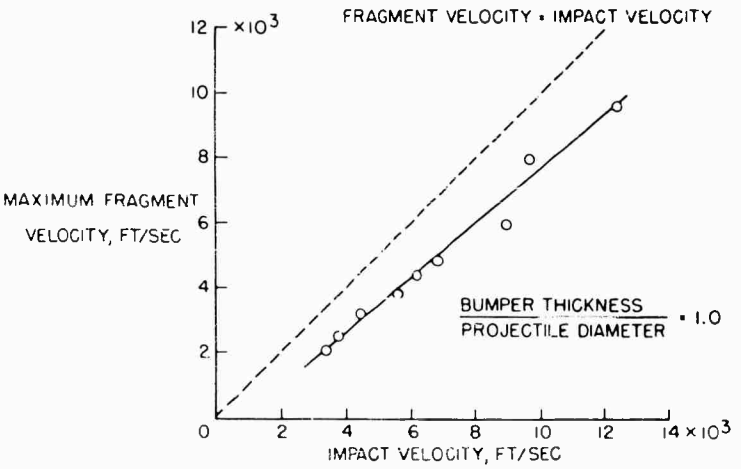

Figure 4. Maximum fragment velocities observed at varying projectile impact velocities.

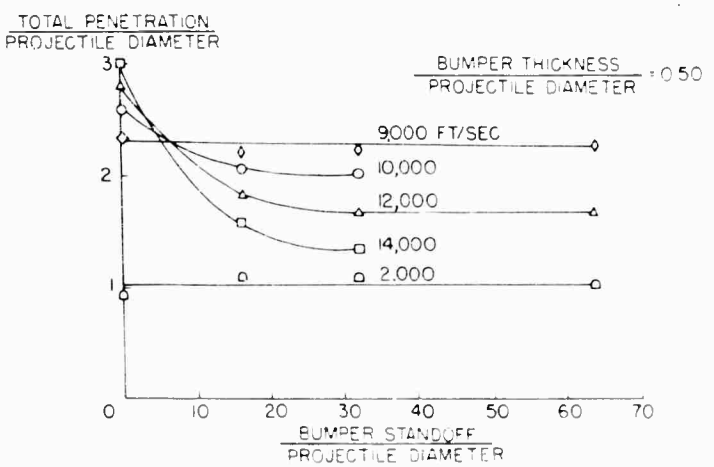

Figure 5. Effect of bumper standoff distance on penetration at varying impact velocities.

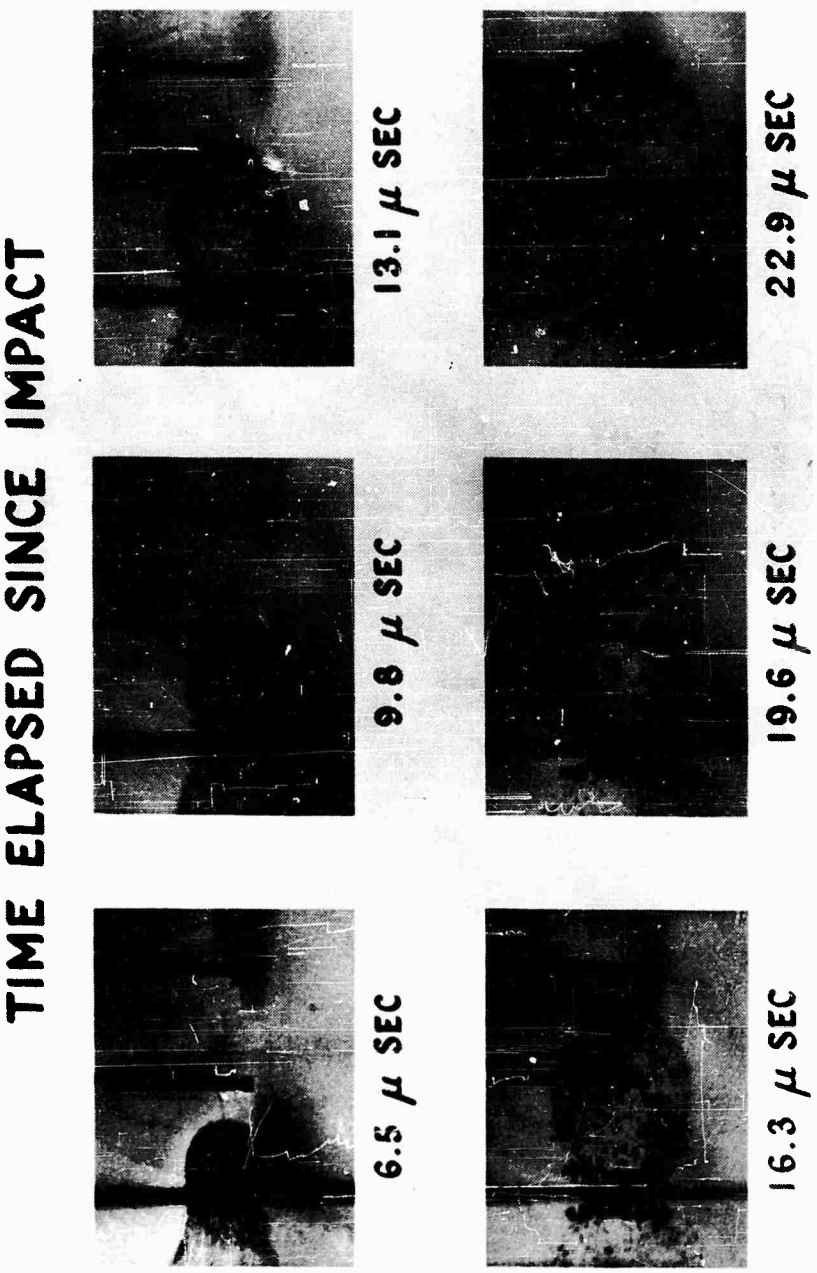

Figure 6. Effect of Bumper Standoff Distance on Penetration at Varying Impact Velocities.

shows a series of sequence photographs at varying times of a 0.22-inch-diameter aluminum sphere after penetrating a 1/8-inch-thick aluminum bumper. The impact velocity in this case was 13,400 ft/sec. The two vertical lines visible in the photographs behind the bumper are reference marks and are out of the plane of the projectile track. Once the standoff was sufficient to essentially eliminate any compound cratering, further increases in the standoff had no effect on the penetration.

Also indicated in Figure 5 is the apparent necessity for the bumper standoff to be at least eight times the diameter of the impacting projectiles for a maximum penetration depth to be obtained such as observed in Figure 1. At standoff distances below about 8 projectile diameters the penetration appears to always increase with increasing the impact velocity. When the standoff distance was greater than about 8 projectile diameters the maximum penetration was obtained at an impact velocity of 9,000 ft/sec and this maximum penetration was not influenced by the exact standoff distance. This fact may indicate that relatively short standoff distances will be sufficient to limit meteoroid penetrations of spacecraft. However, there are other factors to consider which may govern the required spacings between bumpers and main structural walls. Two such factors are the possibility of the total pressure pulse generated by the impact of a cluster of bumper and impacting particle fragments being sufficient to bend the main wall and produce a crack or to produce a spall from the back surface of the main wall. To reduce these types of damage considerably greater spacings may be required than those just sufficient to limit the penetration.

The effect of bumper shield thickness. Figure 7 shows the variations of penetration with impact velocity into six target arrangements that varied only in bumper thickness. The bumper thicknesses in curves (a) through (f) of Figure 6 were 0.16, 0.25, 0.50, 1.0, 2.0, and 4.0 projectile diameters, respectively. In curve (a) the penetration increased throughout most of the velocity range of the data reaching a penetration depth of about three projectile diameters at an impact velocity of 11,000 ft/sec. The very thin bumper shields used in these targets were unable, in the velocity range investigated, to fragment the projectiles sufficiently to reduce the penetration depths.

In the (b) curve of Figure 7 the penetration increased to an observed maximum of slightly less than three projectile diameters at a velocity of 10,000 ft/sec then decreased with additional increases in velocity until a velocity of about 12,000 ft/sec was reached at which point the penetrations again began to increase with still further velocity increases. The fastest impact velocity on these bumper shields which was in excess of 15,000 ft/sec still failed to fragment the projectiles to the degree necessary to cause the penetration depths to diminish with increasing impact velocities. The dip occurring at impact velocities slightly greater than 10,000 ft/sec results from the start of fragmentation. In curves (c) and (d) the bumper thickness was sufficient to permit extreme fragmentation of the projectiles within the velocity range investigated. Both of these curves follow the same general trends observed in Figure 3 with an apparent maximum penetration of about 2-1/4 projectile diameters being obtained at an impact velocity of about 8,000 ft/sec.

In curve (e) the largest portion of the total penetration observed from each impact was in the bumper shield due to its thickness. At velocities above 10,000

ft/sec the penetrations observed appear to be remaining very nearly constant with further velocity increases at a maximum value of 2.75 projectile diameters.

In curve (f) the impact velocities investigated were not sufficient to permit the complete penetration of the bumper shields. The penetration depth in the bumper shields increased with increasing impact velocities reaching a value of about 3.75 projectile diameters at the maximum impact velocity obtained.

By observing the maximum penetrations obtained with the varying bumper shield thicknesses shown in Figure 7, an indication of the most effective bumper thickness can be obtained. Figure 8 is a plot of the maximum penetrations observed in Figure 7 as a function of the thickness of the bumper shields. The maximum penetrations taken from curves (c), (d), and (e) of Figure 7 are felt to be probably the maximum penetration that can be obtained with the respective target arrangements used; in curves (a), (b), and (f) the maximum penetrations were not established. It was established, however, that these maximum values will be at least equal to or greater than the maximum penetrations obtained during these tests.

The bumper shield thickness investigated which provided the greatest protection appears to be about one-half the projectile diameter.

As mentioned before, all of the back main walls of the target arrangements used in this investigation were thick enough to be considered quasi-infinite. Designers of spacecraft are interested in the minimum finite thickness of material required to defeat impacting projectiles or meteoroids. Calculations were made to determine the total finite thickness of material required in a bumper and main back wall structure to just defeat the projectiles used in this investigation. The results of Reference 1 were used in making these calculations which indicated that finite plates 1.5 times the penetration depths observed in quasi-infinite targets are required to just defeat the projectiles. The results of these calculations are shown in Figure 9 which is a plot of the total thickness of material required to defeat the impacting projectiles on the ordinate and the bumper thickness plotted on the abscissa. It can be seen that the minimum thickness of material required to defeat the projectiles is about three projectile diameters with the bumper shield thickness equal to the projectile diameter. This means the main wall thickness must be twice the projectile diameter in order for the total of the bumper and the wall thickness to be equal to the value of three projectile diameters. It also should be noted in Figure 9 that varying the bumper thickness by plus or minus a factor of two produces results which are almost equally effective.

The curves shown in Figures 8 and 9 are for the particular materials used in this investigation. It is, however, felt that the trends observed will also be observed for the cases of meteoroid impacts against any materials used in bumper and main walls of spacecraft. It is therefore felt that they can be extremely useful as a guide in designing space structures for penetration protection.

Concluding remarks. Results of this "Meteor Bumper" investigation have indicated that impact damage from high velocity particles can be greatly reduced by using a properly selected bumper shield. With such properly selected shields the penetration damage on bumper protected wall combinations was observed to be limited to a maximum value which occurred at relatively low impact velocities.

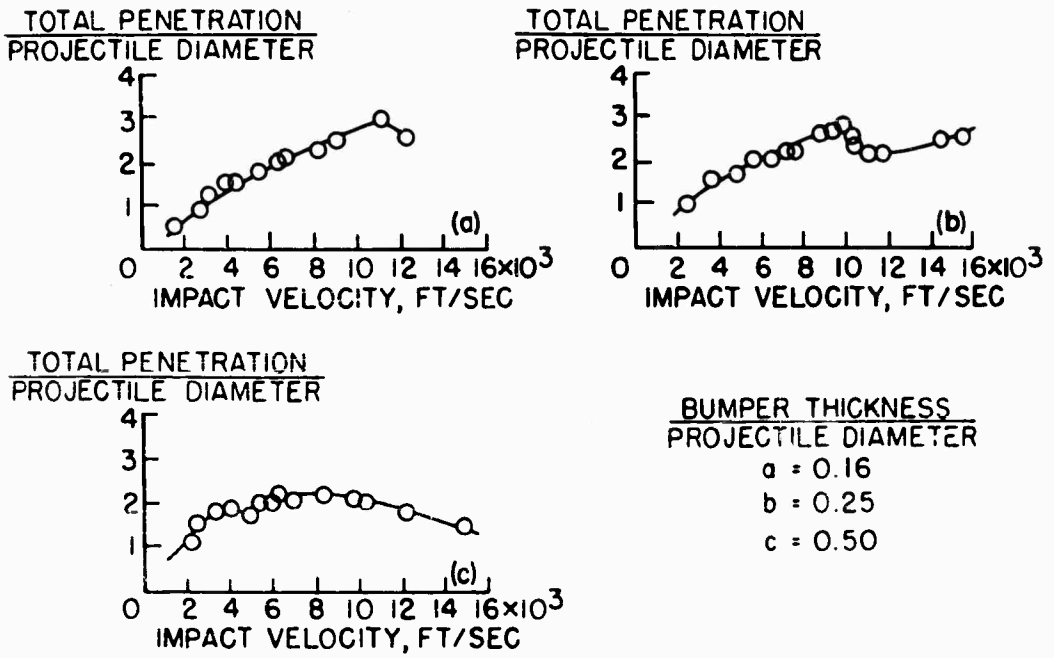

NAS

Figure 7.- Effect of bumper thickness on the variation of total penetration with impact velocity

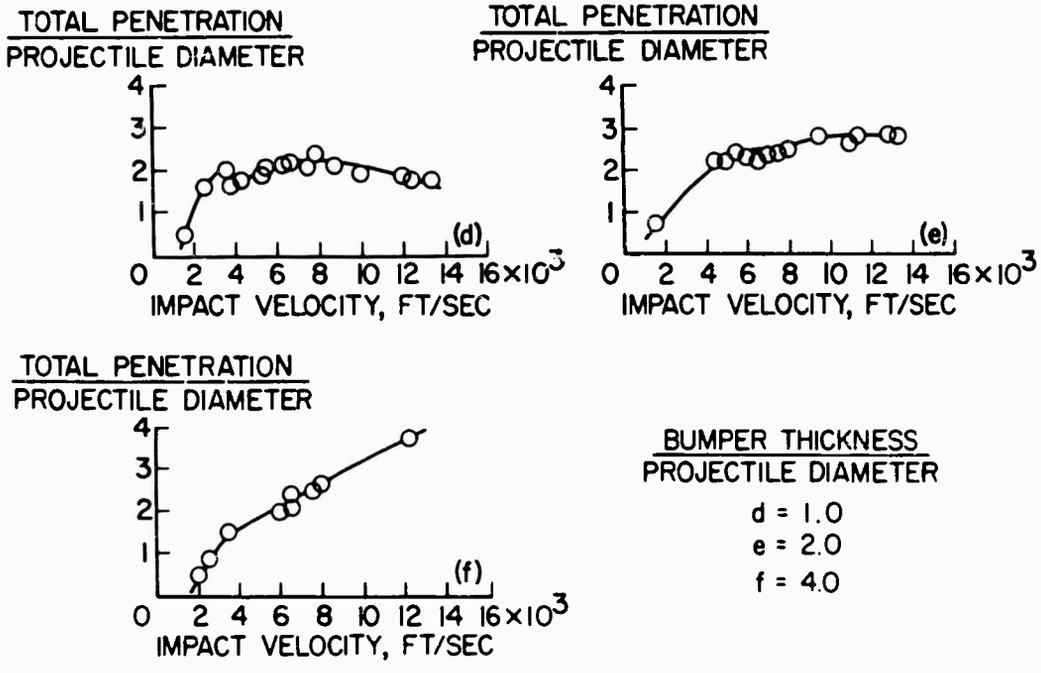

Figure 7 continued. Effect of bumper thickness on the variation of total penetration with impact velocity.

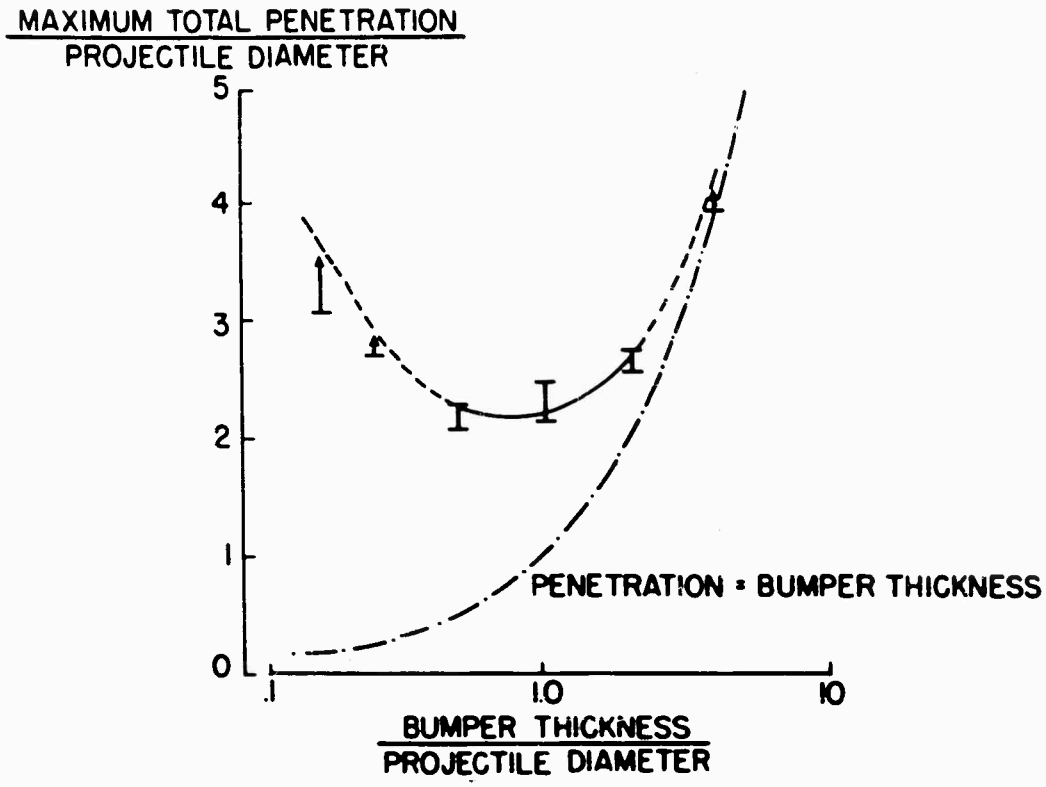

Figure 8. Effect of bumper thickness on maximum penetration.

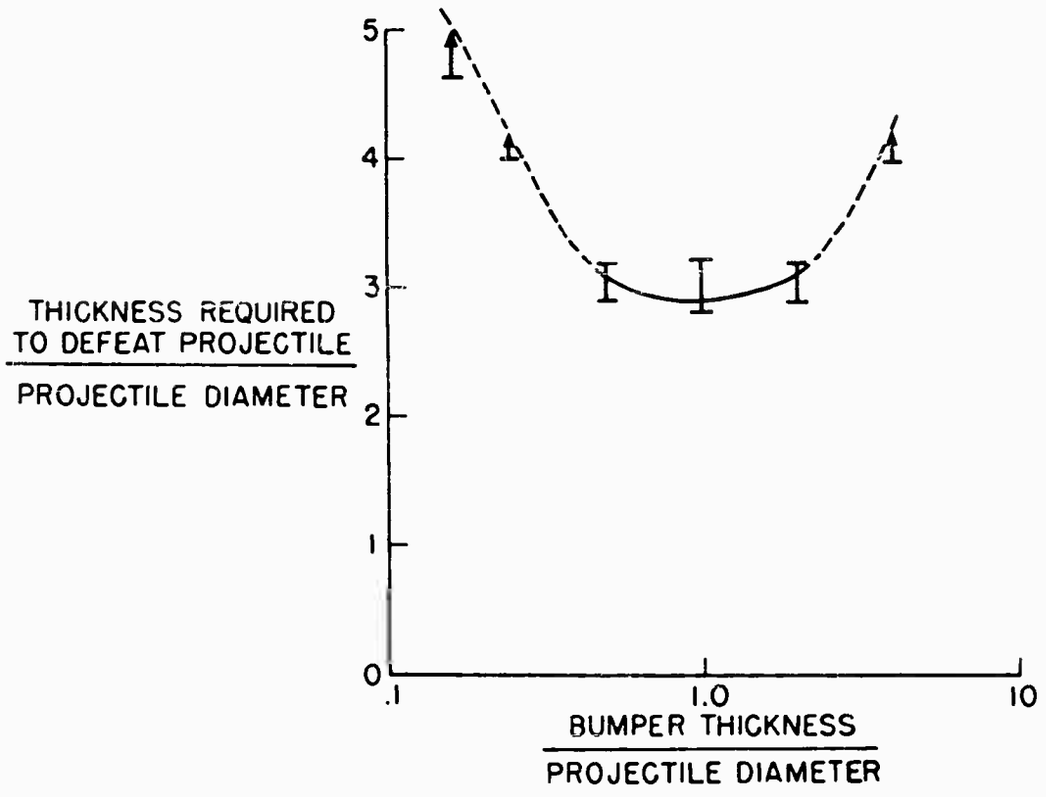

Figure 9. Effect of bumper thickness on the minimum material required to defeat projectile.

The bumpers were observed to be effective only if they are spaced greater than 8 projectile diameters in front of the back wall. Standoff distances greater than this may be necessary to limit bending or spalling of the back wall; however, they will not reduce the maximum penetration that can be achieved in the bumper protected wall.

The optimum design for the conditions of this investigation to defeat the projectiles used was found to be a bumper shield equal to the diameter of the impacting projectiles, a standoff of 8 projectile diameters or greater, and a back main wall equal to twice the diameter of the impacting projectiles and also equal to twice the thickness of the bumper shield.

REFERENCES

1. Kinard, William H., Lamber, C. H., Jr., Schryer, David R., and Casey, Francis W., Jr.: Effect of Target Thickness on Cratering and Penetration of Projectiles Impacting at Velocities to 13,000 Feet per Second, NASA Memo, 10-18-58L, 1958.

THE PERFORATION OF THIN PLATES BY HIGH VELOCITY FRAGMENTS

R. W. Watson

Carnegie Institute of Technology
Pittsburgh, Pennsylvania

INTRODUCTION

Since its inception, the major effort in the hypervelocity research field has been directed toward the solution of the problem of cratering in semi-infinite targets. However, the impact failure of thin targets, particularly the light structural alloys, has become an increasingly urgent problem. For the past year and a half our research group has been engaged in an extensive experimental program to determine the parameters governing the failure of thin plates under the impact of high velocity fragments. A wide variety of experiments have been completed. The results of several of these investigations have led to the formulation of a simple model that adequately describes certain aspects of the perforation phenomena. It is the purpose of this paper to describe these experiments and to discuss this theoretical model.

EXPERIMENTAL STUDIES

Fragment Projector

A precision fragment projector is essential in any hypervelocity study. Variations in striking velocity and delivered mass complicate the analysis of the experimental data obtained in impact tests. For this reason a serious developmental effort was made to obtain a high quality fragment projector. The final design, which yields a fragment having a velocity in excess of 3 km/sec, is shown in Figure 1. The charge is Composition B (60 % RDX and 40 % TNT), 5 inches long and 1-5/8 inches in diameter. It is initiated by a 1 5/8-inch-diameter by 1/2-inch-thick tetryl booster used in conjunction with a No. 8 electric detonator. The charge is cast directly on the steel surround containing the fragment, a Ketos steel cylinder 1/16 inch in diameter and 1/16 inch long. This compact fragment geometry was selected to minimize the effects of fragment tumbling on the outcome of impact experiments.

In experimental tests the fragment is usually projected through a 1-inch-thick baffle plate containing a 1-inch diameter hole. Experience has shown that a 6-inch standoff is adequate for dispersion of the tapered steel surround. Extensive velocity measurements and recovery experiments showed that the projector produced single fragments having an average velocity of 3170 ± 20 m/sec

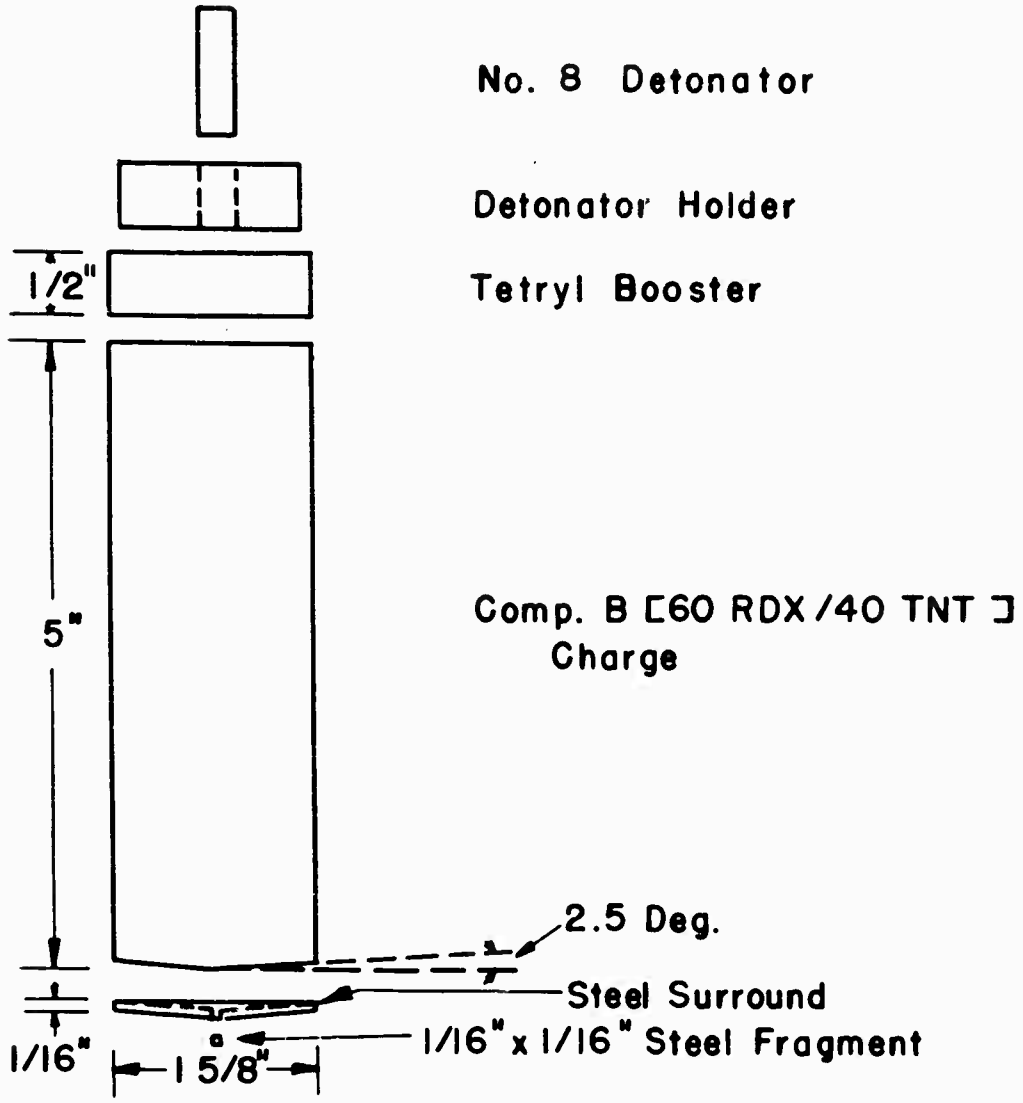

Fig. 1 Pertinent features of the fragment projector used in perforation studies with aluminum and magnesium alloys.

and a delivered mass of 0.0230 ± 0.0005 grams; the original fragment mass was 0.0234 ± 0.0002 grams. Close range flash radiographic studies indicated that the fragment was not appreciably deformed during the acceleration period.

Recovery Experiments

An experimental study was made to determine the composition of the material ejected from the back surface of thin plates during the perforation process. For this purpose various thicknesses of aluminum and magnesium alloys were securely attached to a water collection pot and impacted with 3170 m/sec fragments. Care was taken to assure that only the material projected through or spalled from the back surface of the plate was collected. The collected material was then chemically analyzed for steel content. The result of these tests, shown in Figure 2, show that within experimental error, all of the impacting fragment mass is projected through the target whenever complete perforation takes place.

Residual Velocity Measurements

Visual inspection of the material collected in the recovery experiments indicated that the fragment perforated the thinner targets (1/16 inch) without undergoing serious deformation. As a result of this observation an extensive flash radiographic program aimed at determining emerging fragment velocity as a function of target thickness was initiated. The experimental arrangement used in this investigation is depicted in Figure 3. The two delay networks are adjusted in a manner that allows the fragment to be viewed at a sufficient distance behind the perforated plate to permit accurate distance measurements. Time measurements were accomplished by recording the interval between the luminous flash occurring at impact and the x-ray burst. A typical timing trace is shown in Figure 4 along with a radiograph showing a fragment 110 μ sec after impact. The two vertical strips on either side of the radiograph correspond to aluminum and steel wedges attached to the film cassette; these wedges assist in identifying the material revealed in the radiographs. The individual results of this series of tests are presented in Table I. The spread in the data obtained under a given set of experimental conditions is greater than anticipated on the basis of variation in impacting fragment mass or velocity. This probably can be attributed to either minor variations in fragment orientation at impact or to small differences in the physical properties of the target materials.

THEORY AND DISCUSSION

At an impact velocity of 3170 m/sec the initial dynamic pressure far exceeds the ordinary yield strength of the target materials used in this study and is, in fact, several times the yield strength of the impacting fragment. However, the impact phenomena described here cannot be entirely ascribed to fluid impact where both the target and impacting body are treated as fluids.[1,2] The mass recovery experiments and the radiographic investigation support this contention. In addition, the craters produced in semi-infinite targets of the various alloys investigated, unlike the hemispherical craters which are characteristic of pure fluid impact, were deep and narrow and in many instances the fragment remains were found embedded in the crater bottom. If it is assumed that the perforation

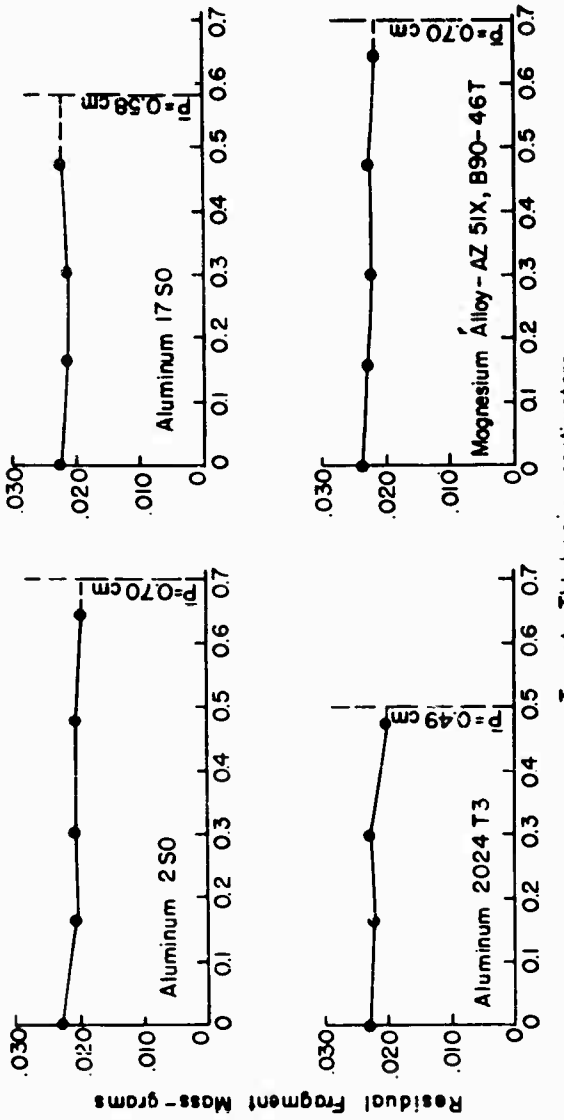

Fig. 2 Residual fragment mass as a function of target thickness for alloys of aluminum and magnesium.

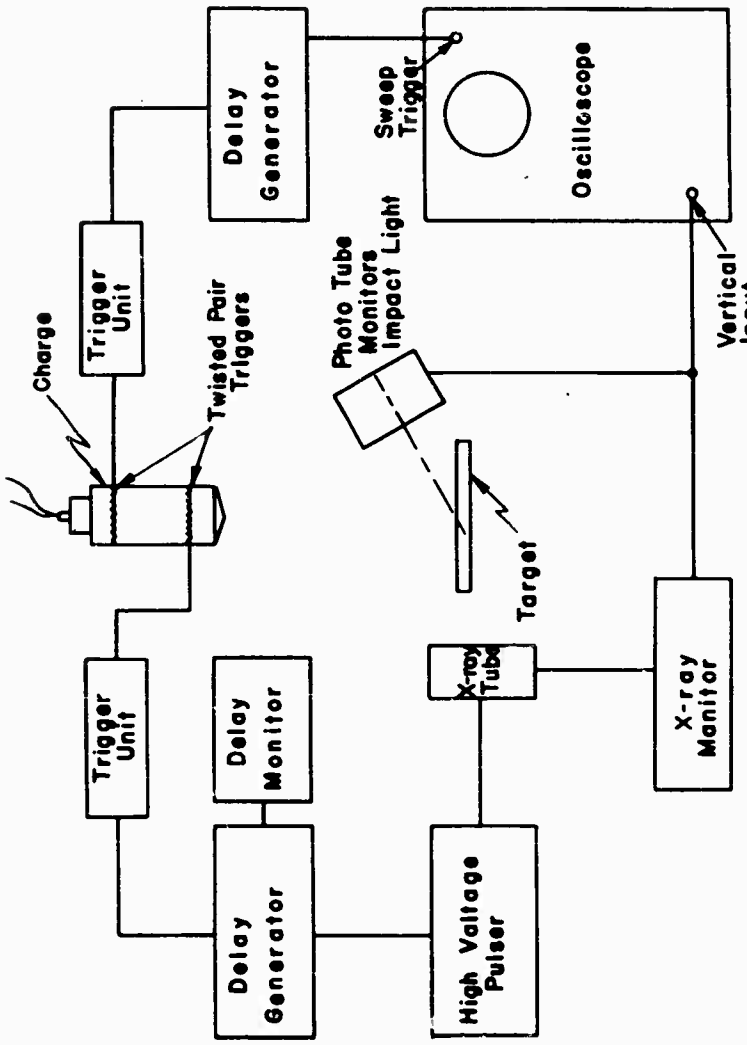

Fig. 3 Apparatus used in measuring the residual velocity of 3170 m/sec fragments after perforating various thicknesses of lightweight alloys.

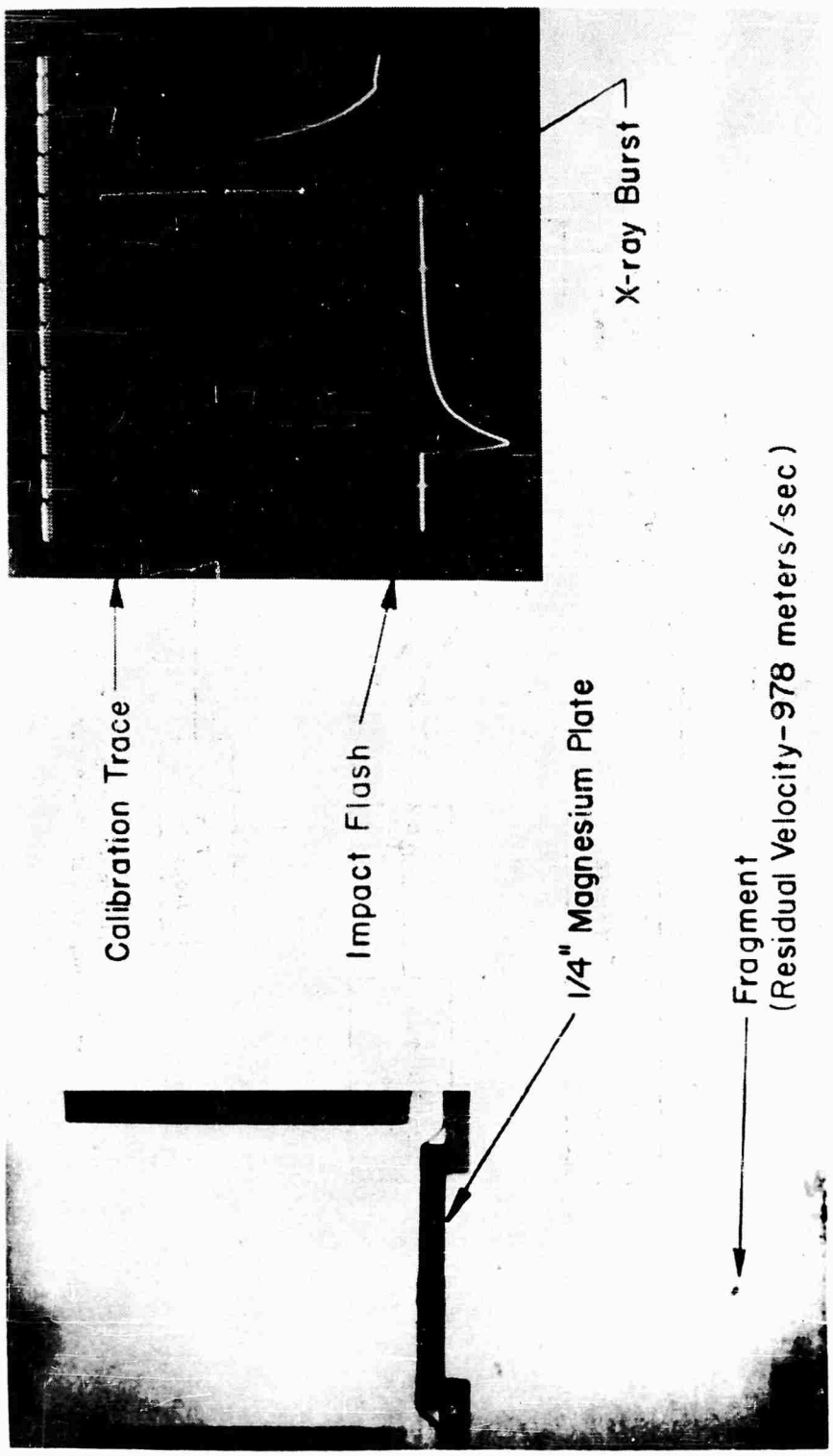

Fig. 4 Typical radiograph and timing trace used in determining residual fragment velocity.

process is completed before any marked radial expansion of the impacting fragment can take place the following simple analysis can be made.

Table I. Residual fragment velocity as a function of target thickness for a 3170 m/sec, 0.023 gm steel fragment perforating various light weight alloys.

Target Thickness (in.)		Residual Velocity (m/sec)			
		2S-O (Aluminum)	17S-O (Aluminum)	2024-T3 (Aluminum)	AZ51X, B90-46T (Magnesium)
1/16		2566	2540	2358	2688
		2469	2525	2185	2728
		2566	2568	2545	2725
		2400	2654	2388	2704
		2640	2567	2487	2783
	Average	2528	2569	2392	2725
1/8		1935	1810	1579	2185
		2056	1828	1800	1935
		1558	1570	1794	2150
		1917	1757	1366	2060
		2000	1648	1609	--
	Average	1893	1722	1629	2082
3/16		1220	856	602	1985
		1114	999	795	1541
		1275	1010	723	1672
		981	1433	634	1371
		1070	1102	573	1624
		--	--	-	1660
	Average	1132	1080	665	1642
1/4		916	--	-	978
		622	--	-	966
		507	--	-	972
		350	--	-	1073
		405	--	-	920
	Average	560	--	-	981

Treating the target as an incompressible fluid, its resistance to penetration can be expressed as

$$p = 1/2\ \rho_t \dot{z}^2 + k \qquad (1)$$

where ρ_t is the target density and $\dot{z}$ is the instantaneous fragment velocity.

This expression and variations of it have been used in a variety of penetration

theories.[3,4] The term $1/2\,\rho_t\,\dot{z}^2$ is the stagnation pressure and represents the inertial resistance of the target; the factor k accounts for the strength effects of the target in resisting deformation. The equation of motion of the fragment then becomes

$$m_f\,\ddot{z} = -(1/2\,\rho_t\,A_f\,\dot{z}^2 + k\,A_f) \tag{2}$$

where

m_f = fragment mass = .0234 gm
ρ_t = target density = 2.7 gm/cm^3
A_f = fragment cross section (assumed constant) = initial fragment area = $2.0 \cdot 10^{-2}$ cm^2
z = instantaneous depth in target measured from the surface of the target

Since the radiographic data give $\dot{z}$ as a function of z the substitution $\ddot{z} = \dot{z}\,\frac{d\dot{z}}{dz}$ considerably simplifies the treatment of Equation (2). On making this substitution the equation of motion is integrated once to give

$$1/2\,\frac{\rho_t A_f}{m_f}\,\dot{z}^2 + \frac{k\,A_f}{m_f} = \text{Constant} \cdot e^{-\frac{\rho_t A_f\, z}{m_f}} \tag{3}$$

The constant of integration can be evaluated from the condition that when $z = 0$, $\dot{z} = v_o$, the initial fragment velocity. Equation (3) then reduces to

$$\dot{z}^2 = v_o^2\,e^{-\frac{\rho_t A_f\, z}{m_f}} + \frac{2k}{\rho_t}\left(e^{-\frac{\rho_t A_f\, z}{m_f}} - 1\right) \tag{4}$$

The strength term k can be evaluated from the final condition that when $\dot{z} = 0$, $z = \overline{P}$, the maximum value of penetration observed in semi-infinite targets of the material under consideration. This method was used to calculate residual fragment velocity as a function of target thickness for the various materials tested. The results of the calculations, represented by smooth curves, are shown in Figure 5 along with the measured values given in Table I. As can be seen, agreement between theory and experiment is quite good. It should be pointed out, however, that the method of evaluating the strength factor, coupled with the form of Equation (4) assures a reasonably good fit. Nevertheless, the model described here does have some salient features of considerable interest. They can be summarized briefly as follows:

(a) The values of the strength factor, k, calculated from Equation (4) are considerably in excess of the handbook values of static strength for all of the materials tested. The calculated values were 3.37, 4.86, 6.50, and 4.92 all times 10^{10} dynes/cm^2 respectively for the 2S-0, the 17S-0, and the 2024-T3 aluminum alloys, and for the ASTM-AZ51X, B90-46T magnesium alloy. The static yield strength of each of these materials is of the order of $1 - 2 \cdot 10^9$ dynes/cm^2. If the strength factor, k, has any real physical significance, the high values

observed here are probably due to an in increase strength associated with a high strain rate. It is well known that the strength of most material increases markedly with increasing strain rate. Rough estimates indicate that the strain rate involved here is in excess of 10^5 inches per inch per sec. There are no data available in this region for direct comparison purposes but dynamic tests at strain rates of 10^4 - 10^5 inches per inch per sec show increases in strength of from 2 to 10 times the static strength for a variety of materials.[5,6,7,8]

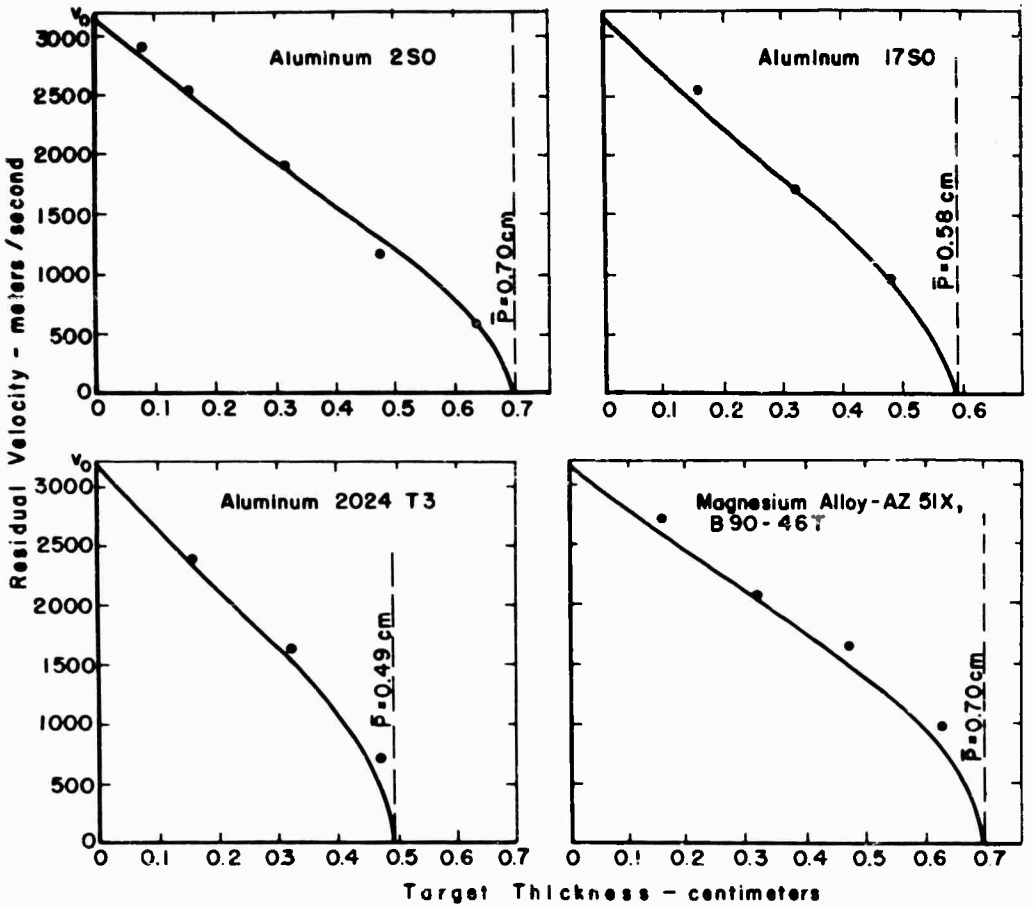

Fig. 5 Residual fragment velocity as a function of target thickness for a 0.023 gram fragment having an initial velocity of 3170 m/sec The data points represent the average of five individual measurements. The smooth curves were calculated from theory.

(11) The appearance of the target density term in Equation (4) seems to be essentially correct. While the strengths of magnesium and aluminum are comparable, their densities are considerably different, and yet, there is equally good agreement between theory and experiment for both materials.

(iii) Since the fragment used in these studies had a fixed geometry and initial velocity a rigorous test of the general validity of Equation (4) could not be made. However, this equation can be rearranged to express $\bar{P}$, the maximum penetration, in terms of the target and fragment parameters. In this form comparison with the work of other authors can be made. The penetration formula is

$$\bar{P} = \frac{m_f}{\rho_t A_f} \ln \left(1 + \frac{\rho_t}{2k} v_o^2\right) \tag{5}$$

A series of experiments described by W. Atkins at the Fourth Symposium on Hypervelocity Impact affords a particularly interesting comparison. In his impact experiments the total depth of penetration in a variety of metals was determined as a function of impact velocity. The projectiles used were 1/4-inch-diameter tungsten carbide spheres having a mass of 2.09 grams. Among the target materials investigated was 1100F aluminum, a material having physical properties closely resembling those of 2S-0 aluminum. The results of the penetration tests with this material are reproduced in Figure 6 along with a set of theoretical curves computed from Equation (5) using various values of the strength factor, k, along with the parameter involved in the NRL experiments. The lower curve was computed using the value of k determined from our results with 2S-0 aluminum. As can be seen agreement between theory and experiment is very good at the higher impact velocities. The upper curve was computed using the handbook value of the yield strength of aluminum. The central curve was fitted to the data in the low velocity region by using a value of k computed from the data point at 1500 m/sec. Taken together, the results shown in Figure 6 indicate the value of k is not truly constant for a given material but may represent a strength averaged over the entire penetration velocity spectrum. This observation, coupled with the current theories on the strength of metals, suggests that the model described here might be useful in determining the propagation rate of defects in various materials.[5] Experiments in this general area are currently in progress.

(iiii) For historical accuracy, it should be pointed out that Equation (5) is identical to a penetration formula derived by J. V. Poncelet in 1829.[5,10] His formula, originally tested at impact velocities of the order of 1000 ft/sec, expresses the penetration in a given material as

$$s = \frac{m}{2bA} \ln \left(1 + \frac{b}{a} v_o^2\right) \tag{6}$$

where

m = mass of projectile
A = cross-sectioned area of the projectile
v_o = initial velocity of the projectile

The constants a and b, empirically determined from penetration studies, can be identified with the target strength and density terms appearing in Equation (5). To date, this formula has been applied

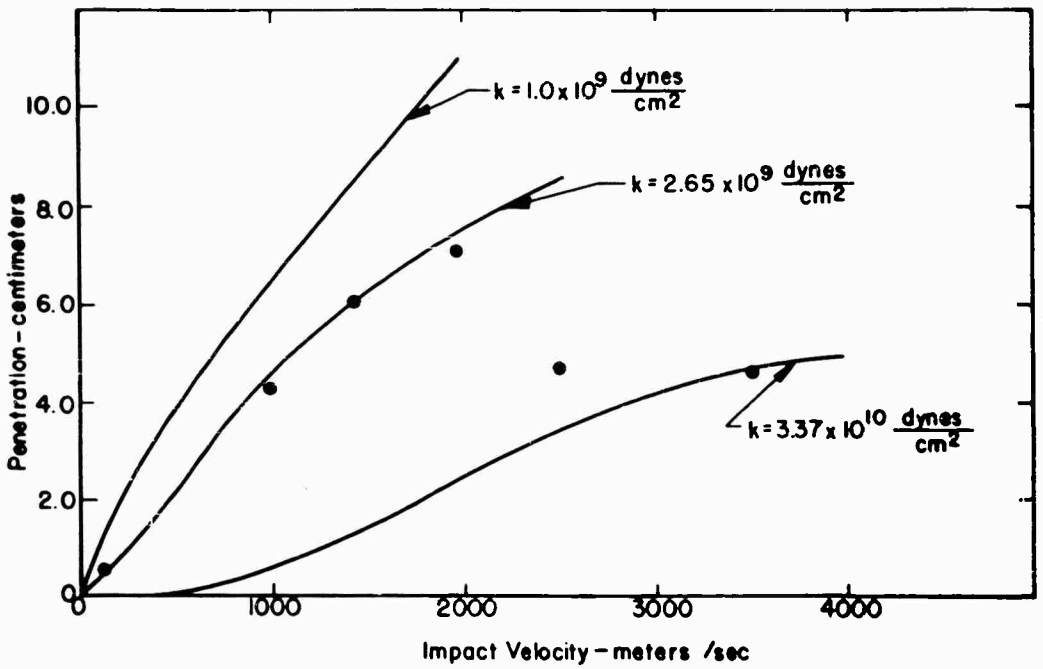

Fig. 6 Penetration depth as a function of impact velocity for a 1/4 in. diameter tungsten carbide sphere weighing 2.09 grams. The data points represent results obtained at NRL. The smooth curves were calculated from theory using various values of the strength constant.

with some success to the case of armor penetration.[10]

ACKNOWLEDGMENTS

In conclusion, I wish to express my appreciation to Dr. E. M. Pugh for his invaluable suggestions regarding the work described here. I wish also to express my thanks to K. R. Becker and R. Vitali for assisting in carrying out the experimental program.

REFERENCES

1. H. G. Hopkins and H. Kolsky, "Mechanics of Hypervelocity Impact of Solids," Fourth Symposium on Hypervelocity Impact.

2. A. C. Charters, "High Speed Impact," Scientific American, October, 1960, Volume 203, No. 4.

3. R. J. Eichelberger, Jour. Appl. Phys., Volume 27, No. 1, January, 1956.

4. Ernst Öpik, "Researches on the Physical Theory of Meteor Phenomena: 1. Theory of the Formation of Meteor Craters," Acta et Comm. Univ. Tartuensis, 1936.

5. John S. Rinehart and John Pearson, "Behavior of Metals Under Impulsive Loads," 1954, The American Society for Metals.

6. G. I. Taylor, "Scientific Papers," Volume 1, 1958, Cambridge Univ. Press.

7. H. Kolsky, Proceedings of the Physical Society, Volume 62, 1949.

8. Nelson W. Taylor, Jour. Appl. Phys., Volume 18, November, 1947.

9. N. J. Petch, "Progress in Metal Physics," 1954, Pergamon Press Ltd.

10. H. E. Wessman and W. A. Rose, "Aerial Bombardment Protection," 1942, John Wiley and Sons.

PERFORATION OF FINITE TARGETS BY HIGH VELOCITY PROJECTILES

R. Vitali

Ballistic Research Laboratories
Aberdeen Proving Ground, Maryland

K. R. Becker

U.S. Bureau of Mines
Bruceton, Pennsylvania

R. W. Watson

Carnegie Institute of Technology
Pittsburgh, Pennsylvania

INTRODUCTION

The increasing demand for information pertaining to the effects of hypervelocity impact on targets of finite thickness has led to the following investigation of target perforation by a small, high velocity projectile. The behavior of five different target materials, lead, aluminum 2SO, 2024SO and 2024T-3, and magnesium AZ51X, B90-46T, has been investigated at two angles of attack, 0 degrees and 60 degrees. The projectile employed throughout is a 0.024 gram steel cylinder, projected at a velocity of 3.2 km/sec. The target materials varied in thickness, ranging from 0.031 inch to 1.0 inch. Graphs are presented which illustrate the following: hole dimensions as functions of target thickness, mass of spall as a function of target thickness, and the spatial distribution of the spall fragments.

EXPERIMENTAL PROCEDURE

Throughout this experiment, 1 5/8-inch by 5-inch cylinders of composition B (60 RDX/40TNT) were used to project the high velocity fragments. The charges were initiated by 1 5/8-inch by 1/2-inch tetryl boosters, used in conjunction with number 8 electric detonators. A conical steel surround, which had a 1 5/8-inch diameter and 1/16-inch thickness with an apex angle of 175 degrees, was fixed to the end of each charge. A cylindrical ketos steel projectile, 1/16 inch by 1/16 inch was imbedded in the apex of the surround. This yielded a projectile velocity of 3.17 ± 0.05 km/sec and a mass of 0.024 ± 0.0005 grams.

A typical shooting arrangement is shown in Figure 1. The spall mass measurements were made by replacing the stand in Figure 1 with an aluminum

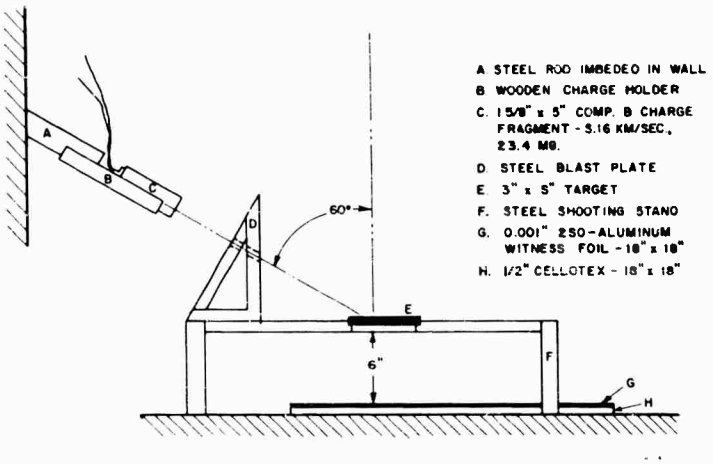

FIG 1 - SKETCH OF SHOOTING APPARATUS EMPLOYED WHEN SHOOTING AT 60° OBLIQUITY FOR DISPERSION DATA. WHEN SHOOTING FOR RECOVERY DATA, THE STEEL STAND F WAS REPLACED BY A WATER TANK CONSTRUCTED OF ALUMINUM.

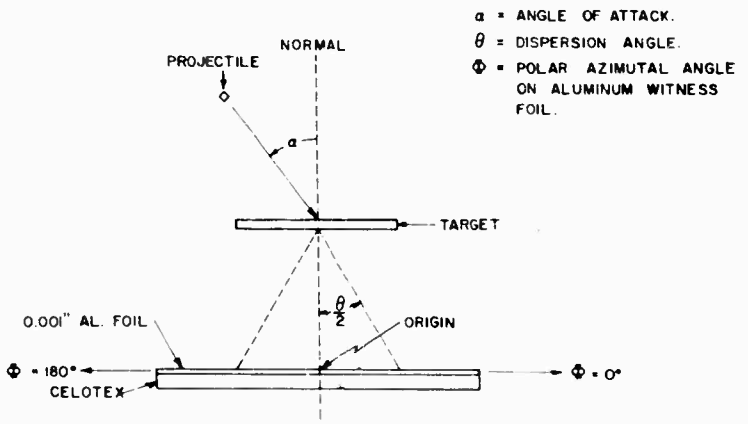

FIG. 2 - ILLUSTRATION OF SHOOTING SETUP

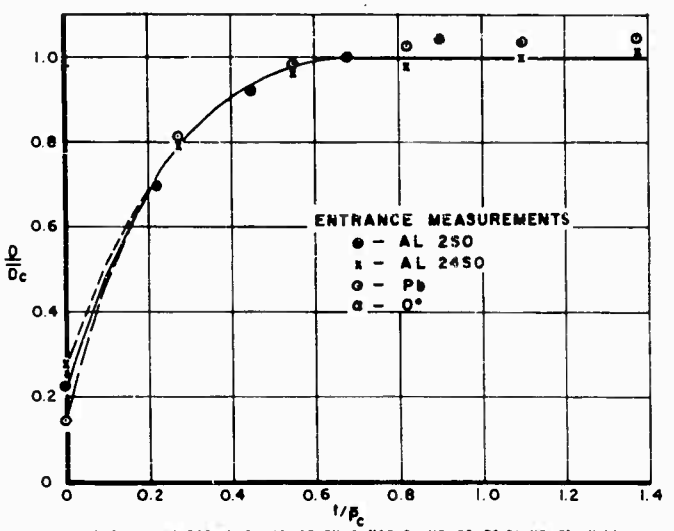

FIG. 3-GRAPH ILLUSTRATING RATIO OF ENTRANCE DIAMETER TO DIAMETER IN AN INFINITE TARGET AS A FUNCTION OF THE RATIO OF TARGET THICKNESS TO PENETRATION IN AN INFINITE TARGET AT 0° OBLIQUITY

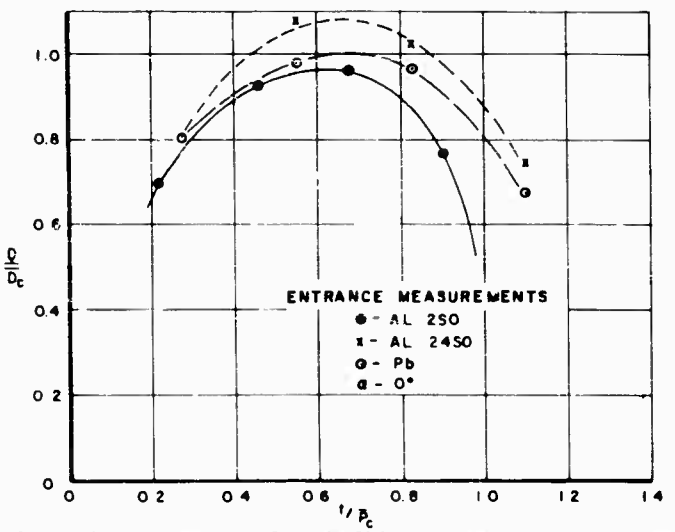

FIG 4-GRAPH ILLUSTRATING RATIO OF EXIT DIA TO DIA IN AN INFINITE TARGET, AS A FUNCTION OF THE RATIO OF TARGET THICKNESS TO PENETRATION IN AN INFINITE TARGET AT 0°

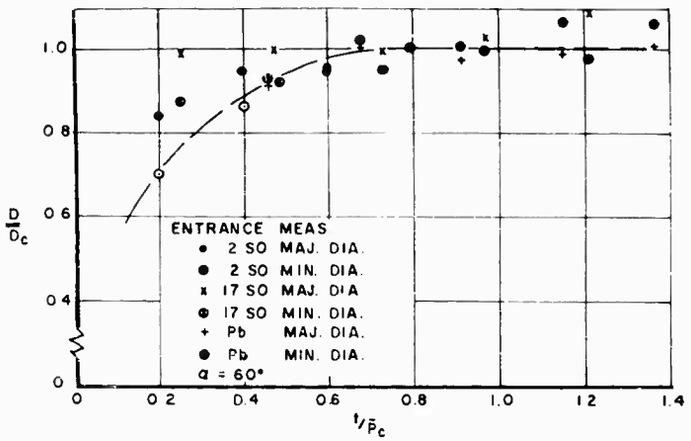

FIG 5- GRAPH ILLUSTRATING RATIO OF ENTRANCE DIA. TO DIA. IN AN INFINITE TARGET AS A FUNCTION OF RATIO OF TARGET THICKNESS TO PENETRATION IN AN INFINITE TARGET AT 60° OBLIQUITY

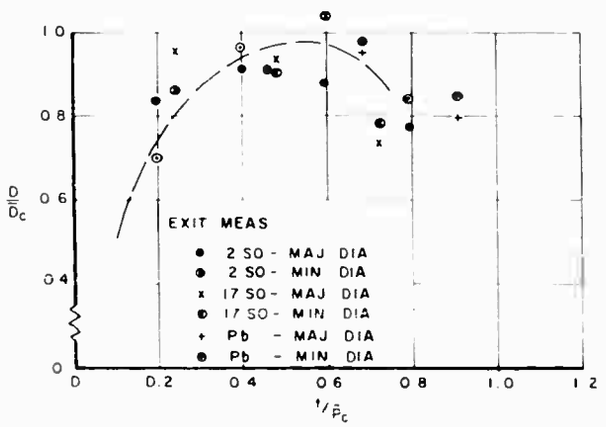

FIG 6- GRAPH ILLUSTRATING RATIO OF EXIT DIAMETERS TO DIAMETERS IN AN INFINITE TARGET AS A FUNCTION OF RATIO OF TARGET THICKNESS TO PENETRATION IN AN INFINITE TARGET AT 60° OBLIQUITY

tank. The target was rigidly fixed to the tank, which was filled with water. The recovered material was weighed on an analytical balance, and the amount of projectile material present was determined by a chemical quantitative analysis.

The spall distribution data are all based on fragments penetrating a 0.001 inch 2SO aluminum witness foil. The foil was situated behind the target as shown in Figure 1. After firing, the foil was marked in polar coordinates r and ϕ, and the number of perforations on each polar element of area was counted. In all cases, the origin of the polar coordinate system, was taken directly below the point of impact; i.e., on the normal to the target, through the point of impact. The areas described were projected back to the point of impact, and the corresponding solid angles were determined. The symbols used throughout, are shown in Figure 2.

EXPERIMENTAL RESULTS

The hole characteristics of aluminum 2SO, aluminum 24SO and lead at 0 degrees obliquity can be seen graphically in Figures 3 and 4. In Figure 3, the ratio of the entrance diameter to diameter in an infinite target is plotted as a function of the ratio of the target thickness to penetration in an infinite target. The graph illustrates, that within experimental error, the curve emanates from a point corresponding to the dimensions of the projectile and rises to that of an infinite target, when the target thickness is approximately $0.6\,\overline{P}_C$, where $\overline{P}_C$ represents the penetration in an infinite target. Figure 4 is a similar graph, but for the exit diameters. The curve is similar to that for the entrance diameters, until $0.6\,\overline{P}_C$, after which it diminishes to zero.

Figures 5 and 6 are similar curves, but for an angle of attack of 60 degrees. The results are essentially the same as those at 0 degrees.

Associated with lead is a spall phenomenon which does not occur in the stranger materials. Figure 7 shows the spall diameter minus the exit diameter as a function of target thickness, at 0 and 60 degrees obliquity.

The mass of the target spall as a function of target thickness for two obliquities are shown in Figures 8-12. All of the materials seem to maximize at $0.6\,\overline{P}_C$.

The total number of spall particles emerging from the back surface of the target as a function of target thickness is shown graphically in Figures 13-17.

Figure 18 is a graphical representation of the per cent change in number of spall fragments per change in solid angle, as a function of solid angle, for 0 degrees obliquity. The data have been reduced to this state, by assuming that the spall distribution is independent of target thickness or material. The assumption is based on previous investigations with shaped charge jets. This seems to be a valid assumption. At 0 degrees obliquity, the pattern of spall has circular symmetry about an axis normal to the target, and through the perforation.

In order to determine the center of the dispersion pattern at 60 degrees

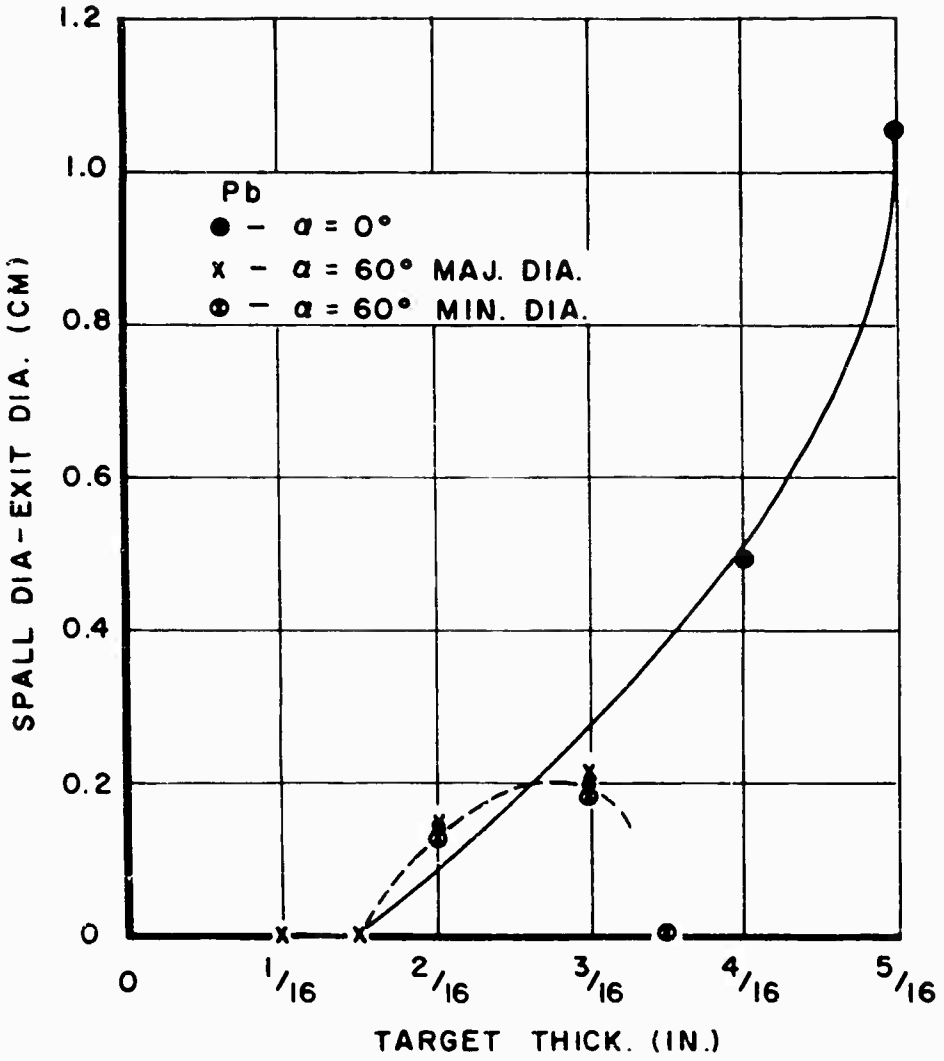

FIG. 7 – GRAPH ILLUSTRATING SPALL DIAMETER MINUS EXIT DIAMETER IN LEAD

obliquity, graphs of the per cent change in the number of spall fragments per change in azimuthal angle on the witness foil, as a function of the azimuthal angle, have been drawn. Assuming independence of thickness, a reduced plot for aluminum 2SO, aluminum 2024SO and aluminum 2024 T-3 is shown in Figure 19. It should be noted that ♦ = 0 degrees is in the direction of the projectile trajectory. A similar plot for lead is shown in Figure 20. It can be seen that, once again,

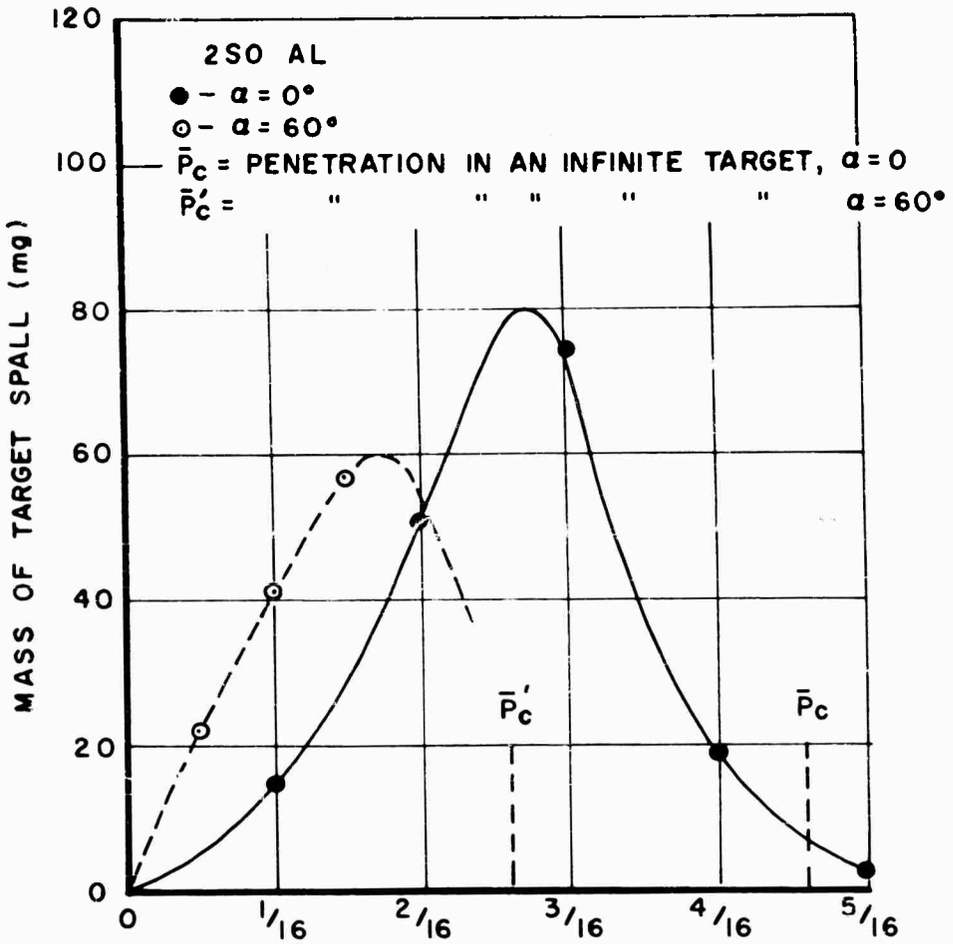

Fig. 8–Graph illustrating mass of target spall as a function of target thickness for 2-SO Al at 0 and 60° obliquity.

lead differs, in that the areal density of spall hits is essentially constant, or if any maximum occurs, it is at $\phi = 180$ degrees. Employing the results of these graphs, plots were made of the per cent of the number of spall fragments per solid angle as a function of solid angle, within a given increment of the azimuthal angle. For the three aluminum alloys, the increment was $-10^{\circ} \geq \phi \geq 10^{\circ}$,

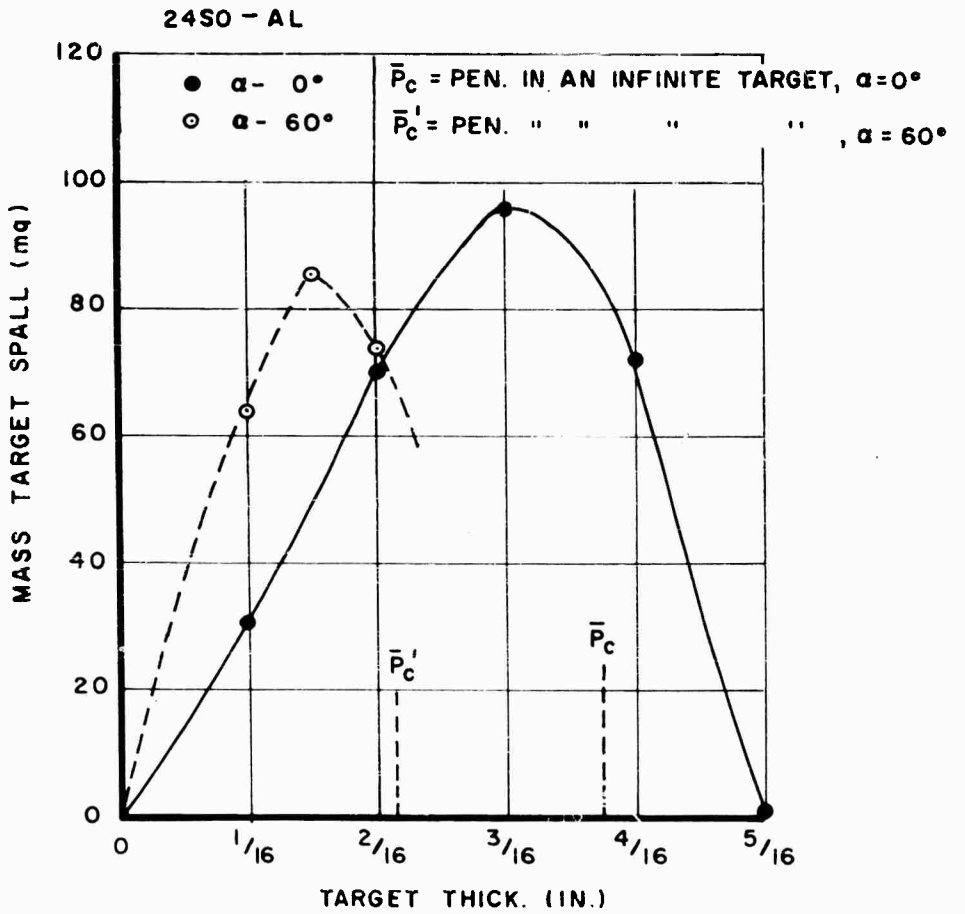

FIG. 9 - GRAPH ILLUSTRATING MASS OF TARGET SPALL AT A FUNCTION OF TARGET THICKNESS FOR 24SO AL AT 0° AND 60° OBLIQUITY

and they are shown in Figures 21 through 24. This determines the angle about which circular symmetry of the spall occurs. For the three aluminum alloys, this axis makes an angle of 50 to 55 degrees with the normal to the target and has the azimuthal direction $\phi = 0$. Lead, shown in Figure 26 is within an increment $-60^{\circ} \geq \phi \geq 60^{\circ}$. The maximum for lead occurs very near the origin, and is very similar to the results at 0 degrees obliquity.

CONCLUSION

The spall and target damage data obtained from finite targets impacted

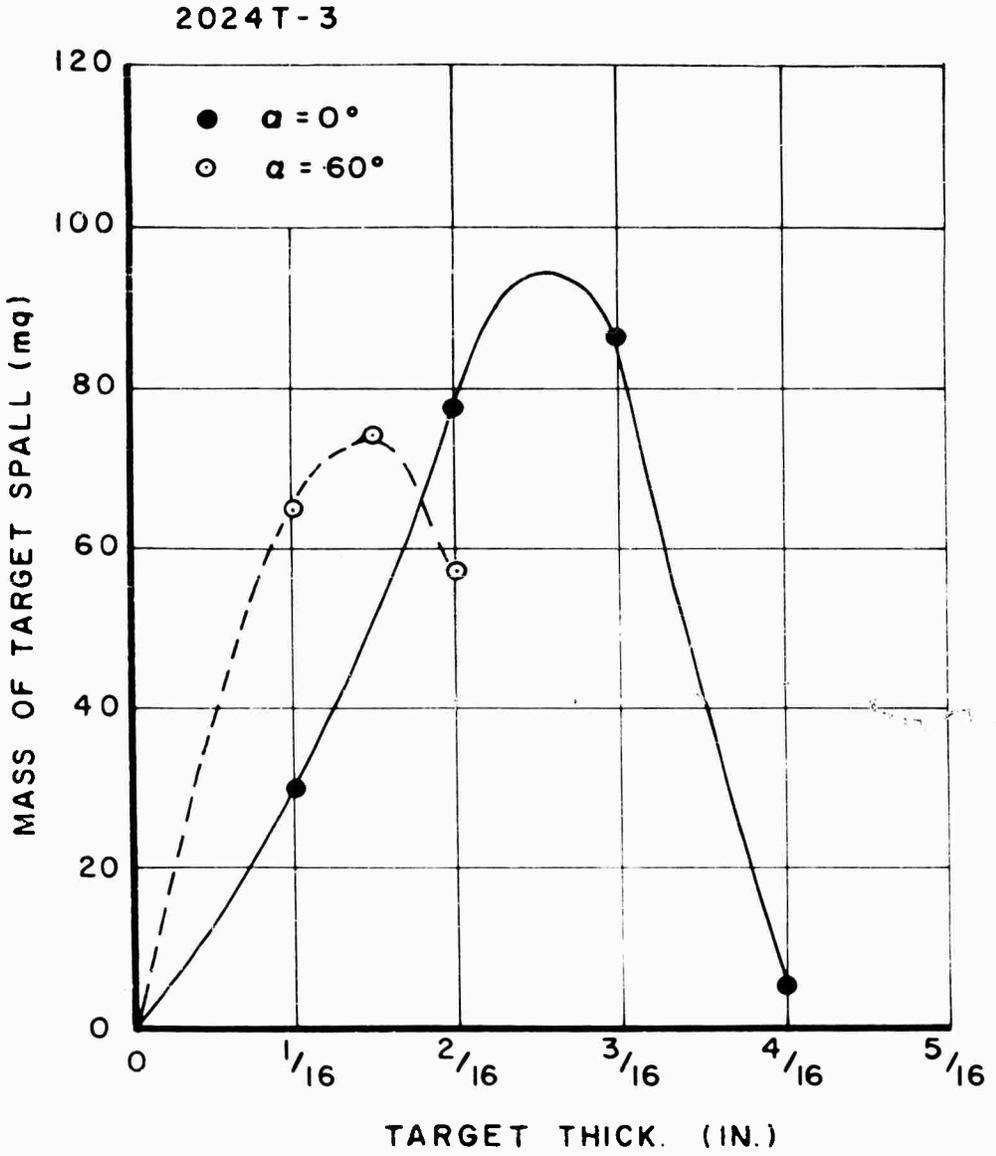

FIG. 10 - GRAPH ILLUSTRATING MASS OF TARGET SPALL AS A FUNCTION OF TARGET THICKNESS FOR 2024T-3 ALUMINUM AT 0° AND 60° OBLIQUITY

with a high velocity projectile indicates a similarity to that occurring with shaped charge jets. It is not yet conclusive however, and depends heavily on the results of further investigations. The investigations are continuing, and will be completed in the near future, at which time they will be reported.

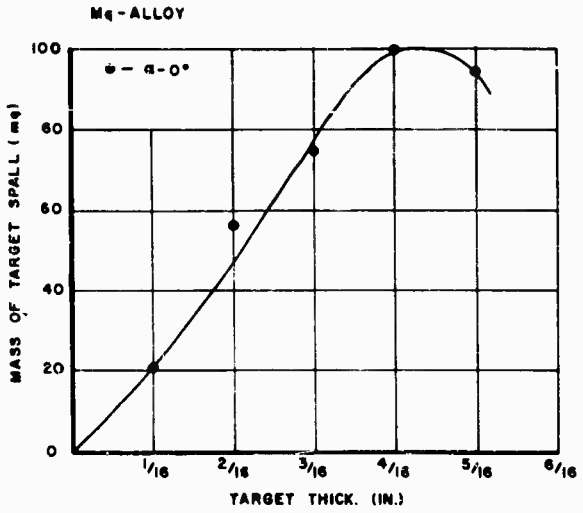

FIG. 11 - GRAPH ILLUSTRATING MASS OF TARGET SPALL AS A FUNCTION OF TARGET THICKNESS FOR Mg (AZ51X, Rεo-46T) AT 0° OBLIQUITY

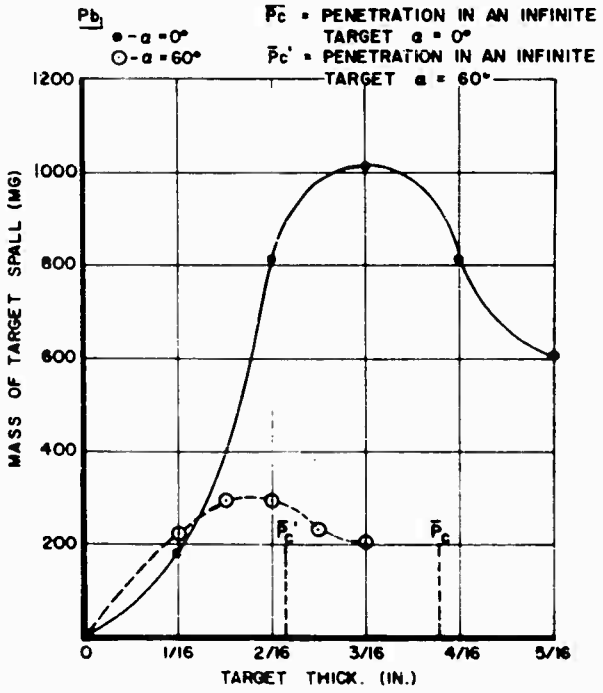

FIG. 12 - GRAPH ILLUSTRATING MASS OF TARGET SPALL AS A FUNCTION OF TARGET THICKNESS FOR LEAD AT 0° AND 60° OBLIQUITY.

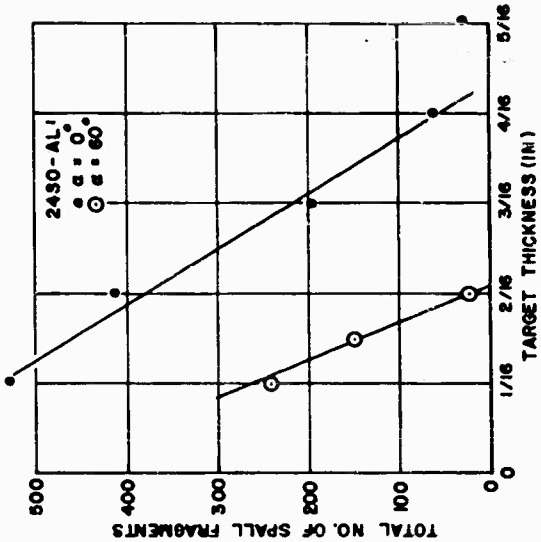

FIG. 14 — GRAPH ILLUSTRATING TOTAL NUMBER OF SPALL FRAGMENT AS A FUNCTION OF TARGET THICKNESS FOR 24 SO AT 0° AND 60° OBLIQUITY.

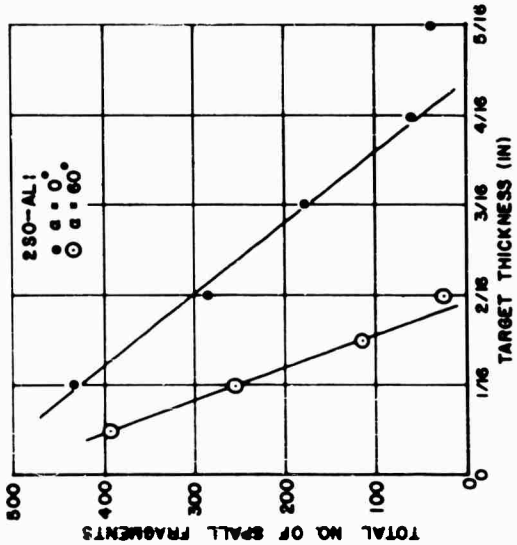

FIG. 13 — GRAPH ILLUSTRATING TOTAL NUMBER OF SPALL FRAGMENTS AS A FUNCTION OF TARGET THICKNESS FOR 2S0 AL AT 0° AND 60° OBLIQUITY.

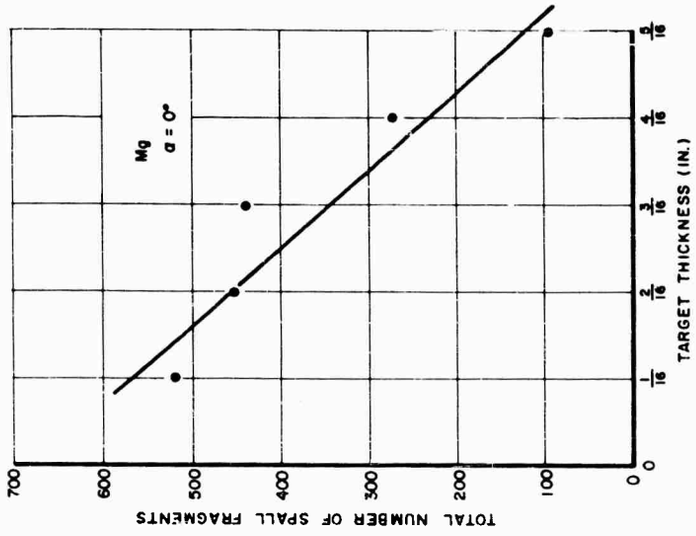

FIG. 16 - SAME AS 13 FOR Mg (AZ51X, B90-46T)

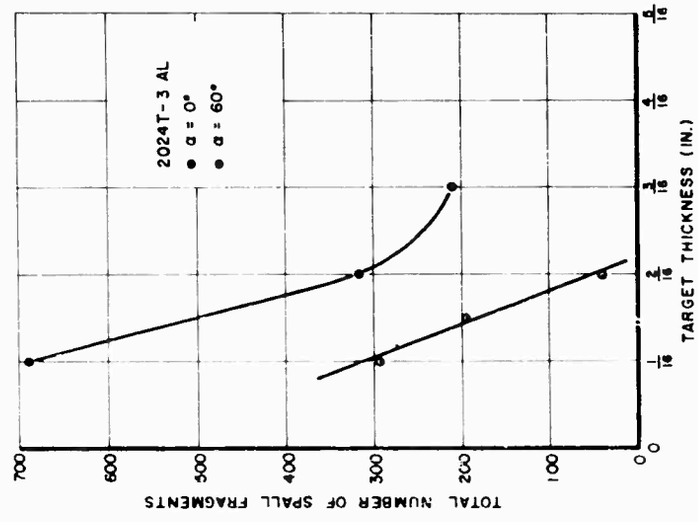

FIG. 15 - SAME AS 13 FOR 2024-3

FIG. 17 – GRAPH ILLUSTRATING TOTAL NUMBER OF SPALL FRAGMENTS AS A FUNCTION OF TARGET THICKNESS FOR LEAD AT 0° AND 60° OBLIQUITY.

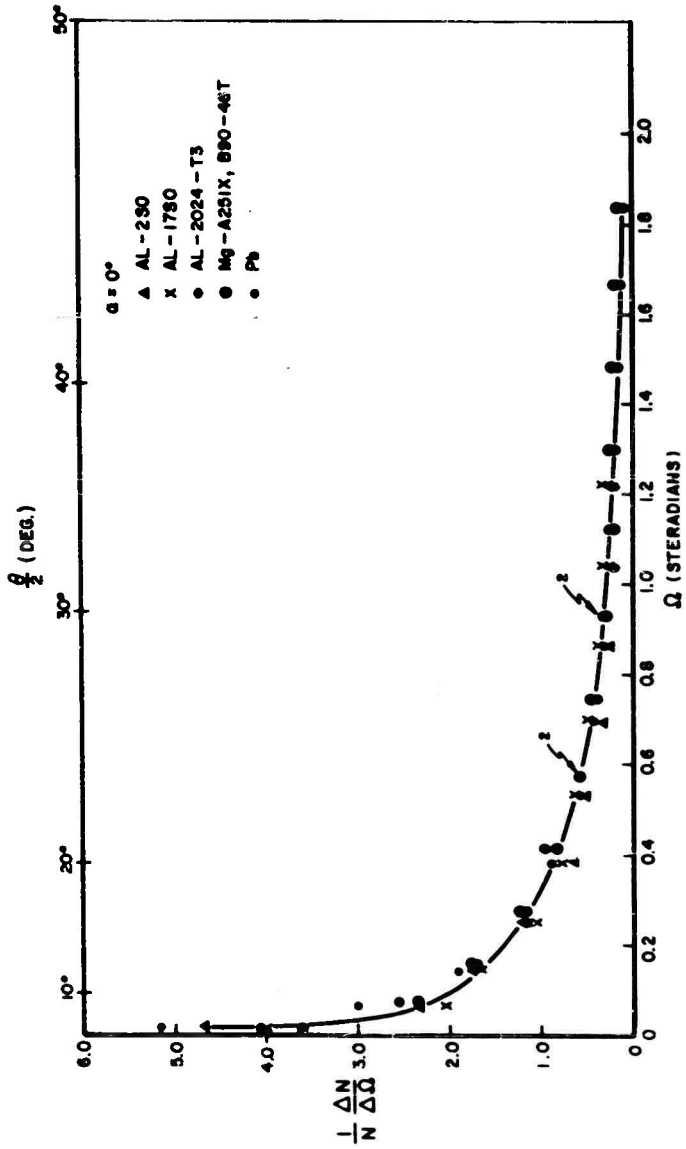

FIG. 18 – GRAPHICAL REPRESENTATION OF PERCENT OF SPALL FRAGMENTS PER CHANGE IN SOLID ANGLE AS A FUNCTION OF SOLID ANGLE. DATA REDUCED ON THE ASSUMPTION THAT THE SPALL CONFIGURATION IS INDEPENDENT OF TARGET THICKNESS.

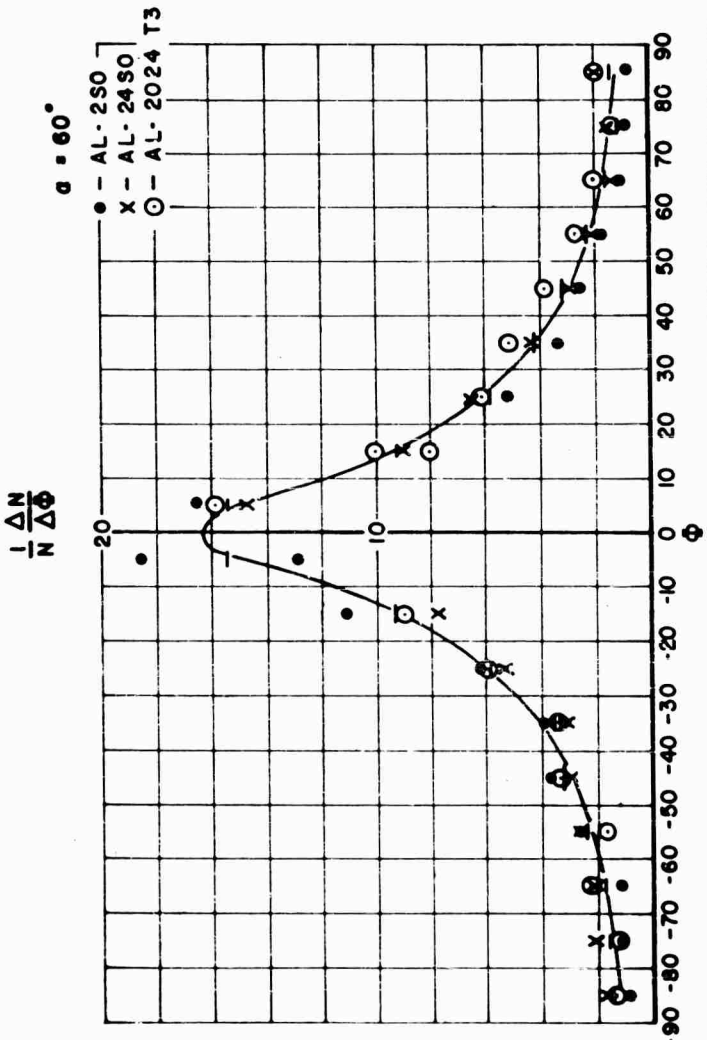

FIG. 19 – GRAPH ILLUSTRATING PERCENT OF SPALL FRAGMENTS PER CHANGE IN AZIMUTHAL ANGLE AS A FUNCTION OF AZIMUTHAL ANGLE AT 60° OBLIQUITY. THE AZIMUTHAL ANGLE IS ZERO IN THE DIRECTION OF THE FLIGHT OF THE PROJECTILE. SHOWN ARE AL 2SO, AL 24SO AND AL 2024 T3.

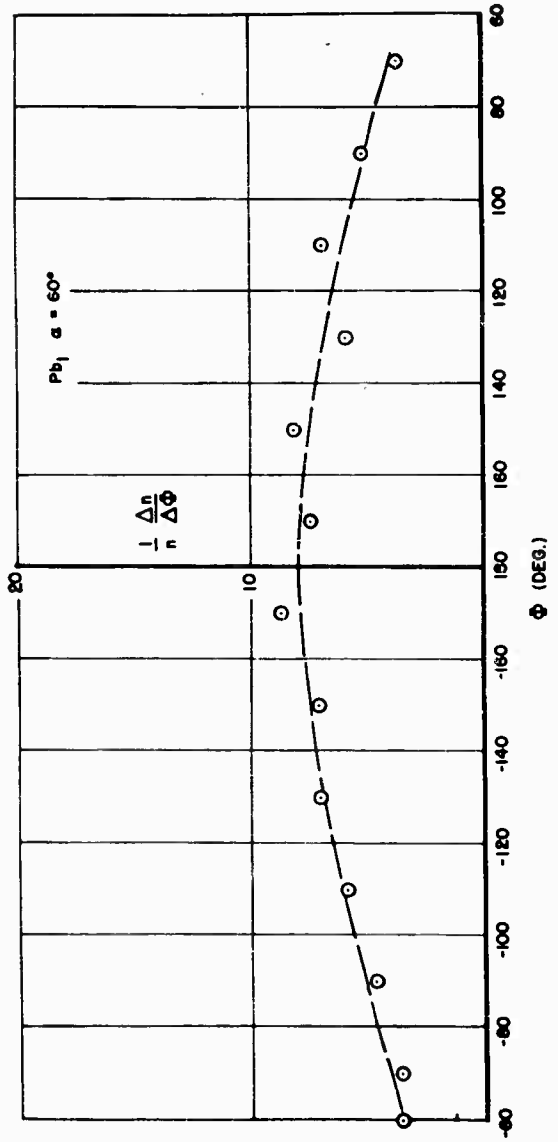

FIG. 20 – GRAPH ILLUSTRATING PERCENT OF SPALL FRAGMENTS PER CHANGE IN AZIMUTHAL ANGLE AS A FUNCTION OF AZIMUTHAL ANGLE AT 60° OBLIQUITY. THE AZIMUTHAL ANGLE IS ZERO IN IN THE DIRECTION OF THE FLIGHT OF THE PROJECTILE.

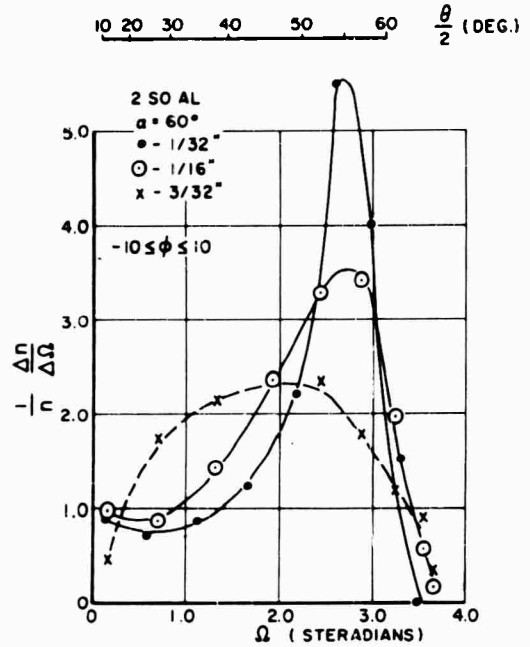

FIG. 21 – GRAPH ILLUSTRATING PERCENT OF SPALL FRAGMENTS PER CHANGE IN SOLID ANGLE AS A FUNCTION OF SOLID ANGLE FOR VARIOUS TARGET THICKNESSES OF 2 SO AL AT 60° OBLIQUITY.

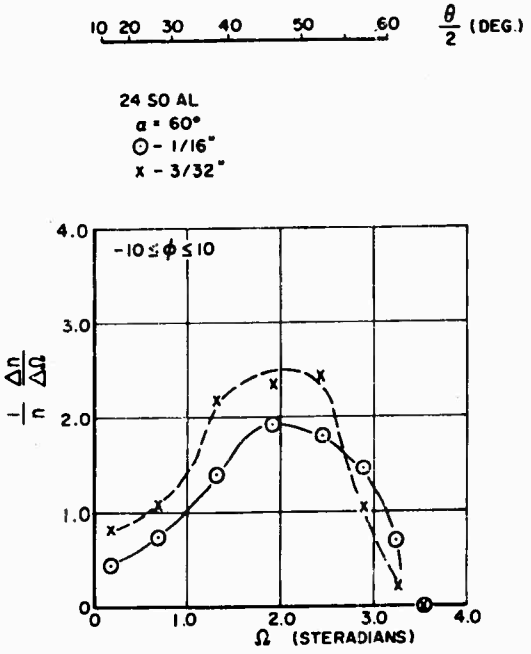

FIG. 22 – GRAPH ILLUSTRATING PERCENT OF SPALL FRAGMENTS PER CHANGE IN SOLID ANGLE AS A FUNCTION OF SOLID ANGLE FOR VARIOUS TARGET THICKNESSES OF 24 SO AL AT 60° OBLIQUITY.

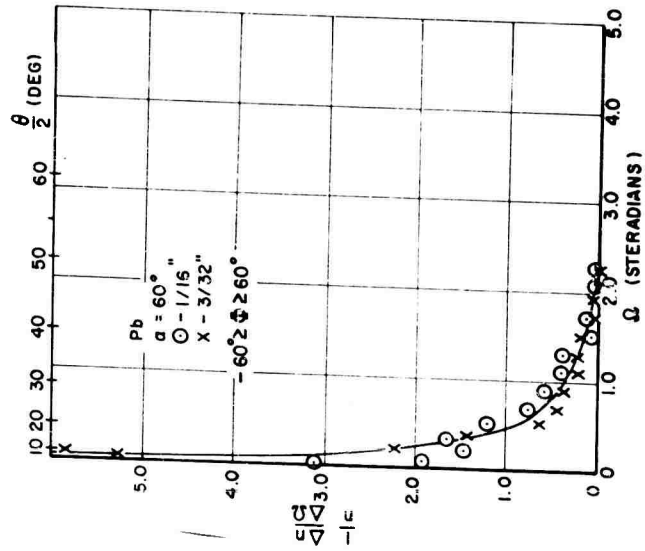

FIG. 24 GRAPH ILLUSTRATING PER CENT OF SPALL FRAGMENTS PER CHANGE IN SOLID ANGLE AS A FUNCTION OF SOLID ANGLE FOR VARIOUS TARGET THICKNESSES OF LEAD AT 60° OBLIQUITY.

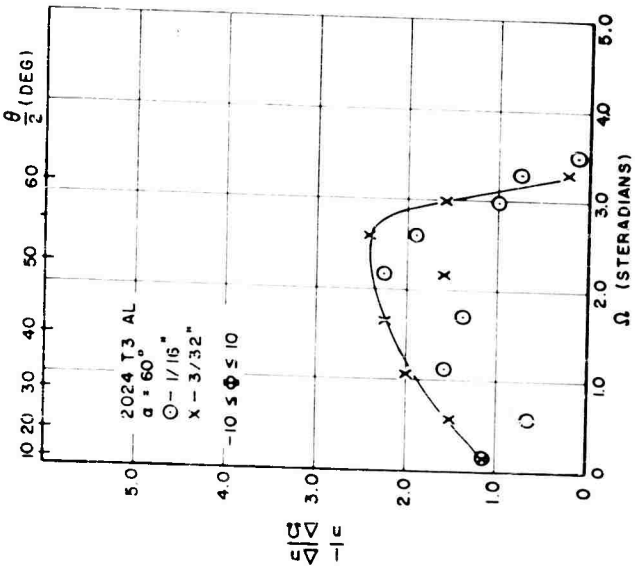

FIG. 23 GRAPH ILLUSTRATING PER CENT OF SPALL FRAGMENTS PER CHANGE IN SOLID ANGLE AS A FUNCTION OF SOLID ANGLE FOR VARIOUS TARGET THICKNESSES OF 2024 T3 AL AT 60° OBLIQUITY.

PENETRATION OF THIN PLATES

K. N. Kreyenhagen and L. Zernow

Aerojet-General Corporation
Downey, California

1. INTRODUCTION

This paper discusses the process of penetration of thin plates by hypervelocity projectiles. In the experiments which will be described, aluminum alloy plates of 0.100-in. thickness are impacted by one gram titanium projectiles at velocities of the order of 5 km/sec. These conditions are in a regime where complete penetration easily occurs. The results of these experiments suggest a general model for such impact and penetration phenomena.

2. IMPACT AT NORMAL OBLIQUITY

Figure 1 is a series of photographs made by a rotating mirror framing camera showing the impact of a 3/8-in. dia by 1/8-in. titanium disc of one gram mass at 5.0 km/sec on a 0.100-in. thick plate of 2024-T6 aluminum alloy in air at approximately 1/50 atmosphere. The camera was run at low speed to extend the time coverage -- hence the impacting projectile is smeared. (The projectiles in all experiments which will be described were accelerated by an explosive cavity charge.) As the disc penetrates, a diverging pattern, which might be called a penetration envelope, is seen to emerge from the back side of the target plate. A luminous phenomenon occurs on the front surface of the plate.

These processes are more easily understood by the use of flash radiography. In Figure 2, a series of x-rays is shown of the same general impact situation as was described for the framing camera test. This series was made by repetition of essentially identical tests. In the second view, taken shortly after impact, a "splash" of very small particles from the face of the target plate is seen. This splash, which involves considerable less material than is found with semi-infinite targets, is apparently due at least partially to some form of jetting originating as the surfaces come in contact. The specific configuration of the initial portions of the splash is probably a function of the geometry of the impacting surfaces. The velocity of the fastest visible splash particles in Figure 2 is about the same as the impact velocity.

During penetration, the projectile was fractured rather completely by the interactions of the impact-induced stress pulse with the free surfaces of the disc. At 4.6 km/sec impact of titanium and aluminum, this pressure is initially 640

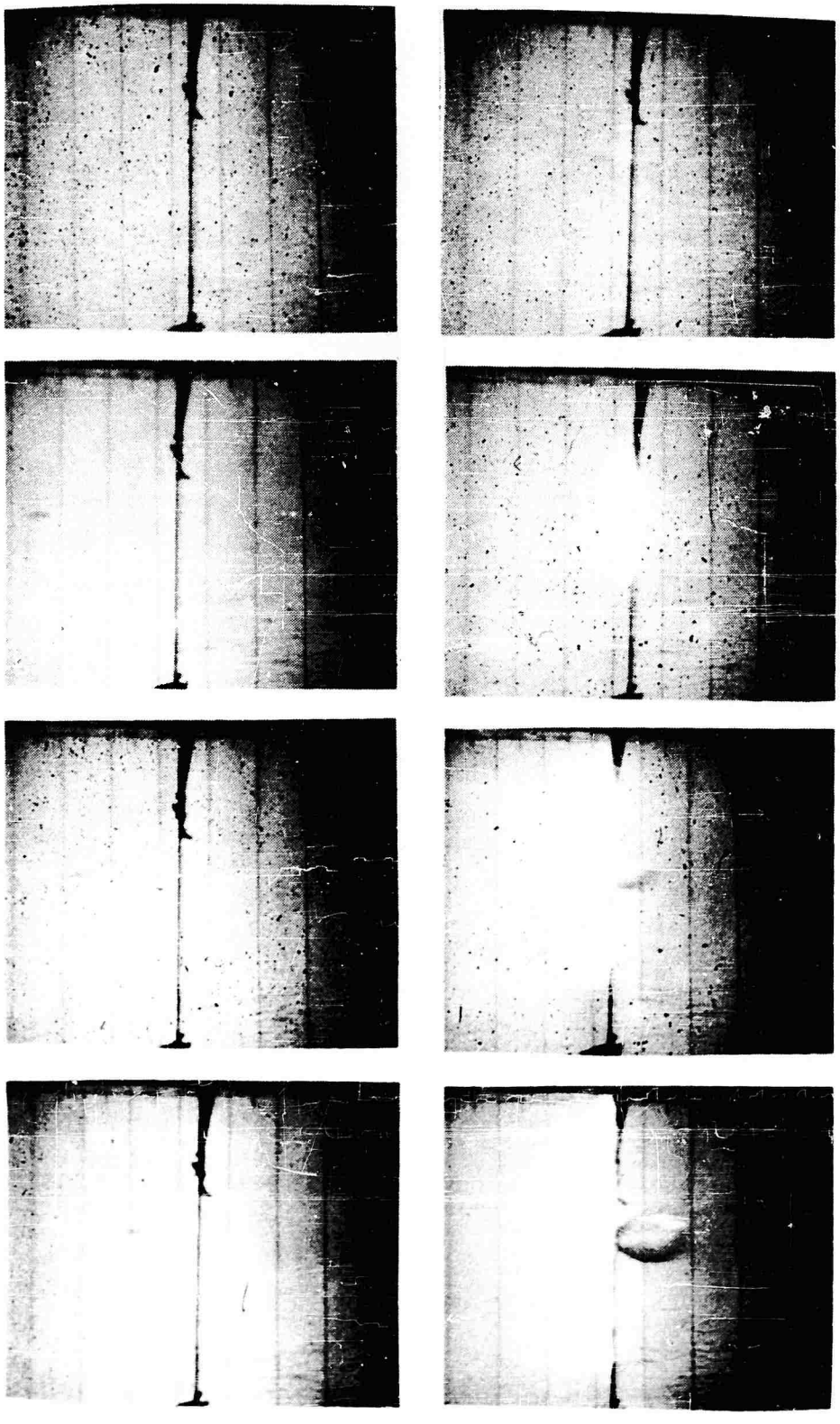

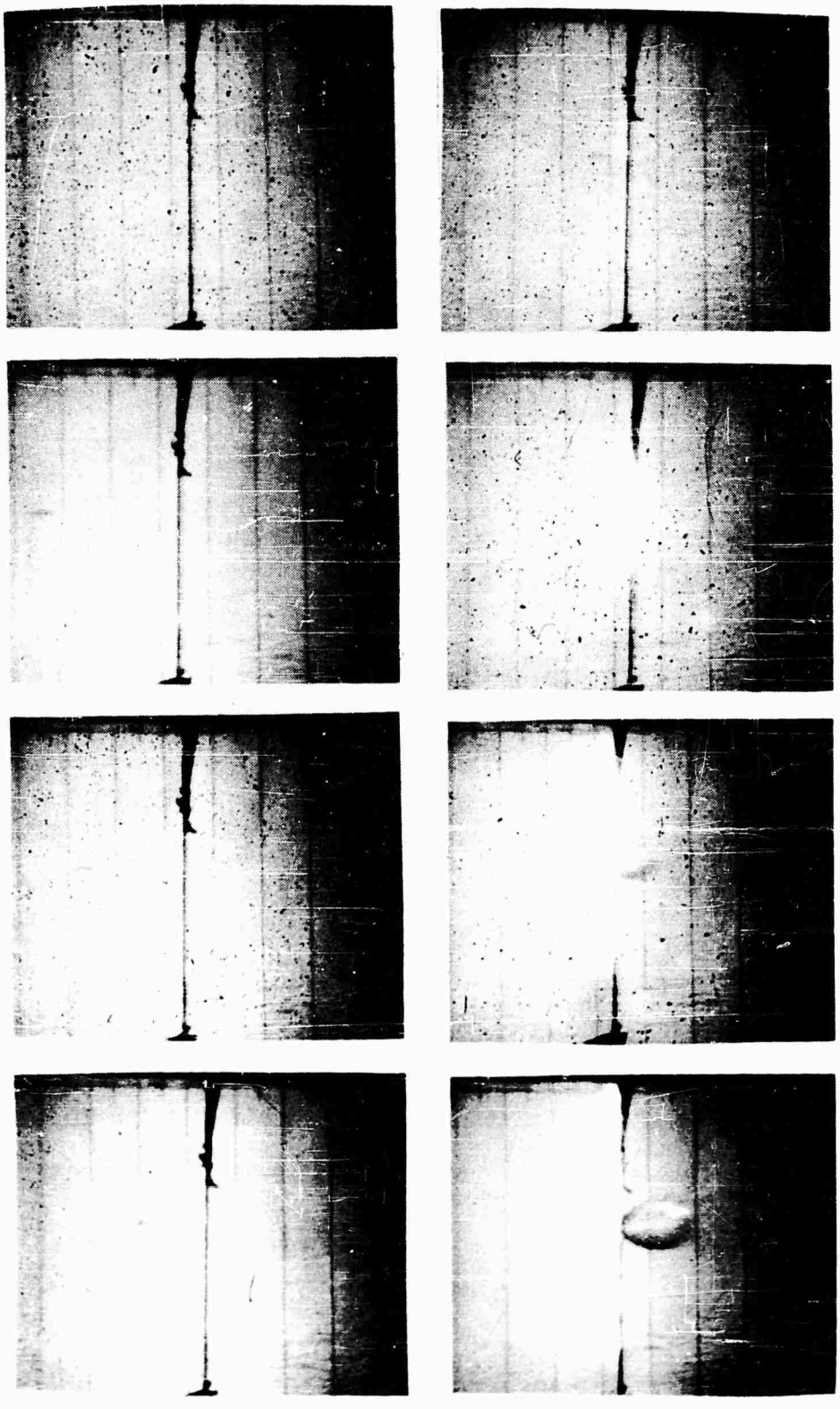

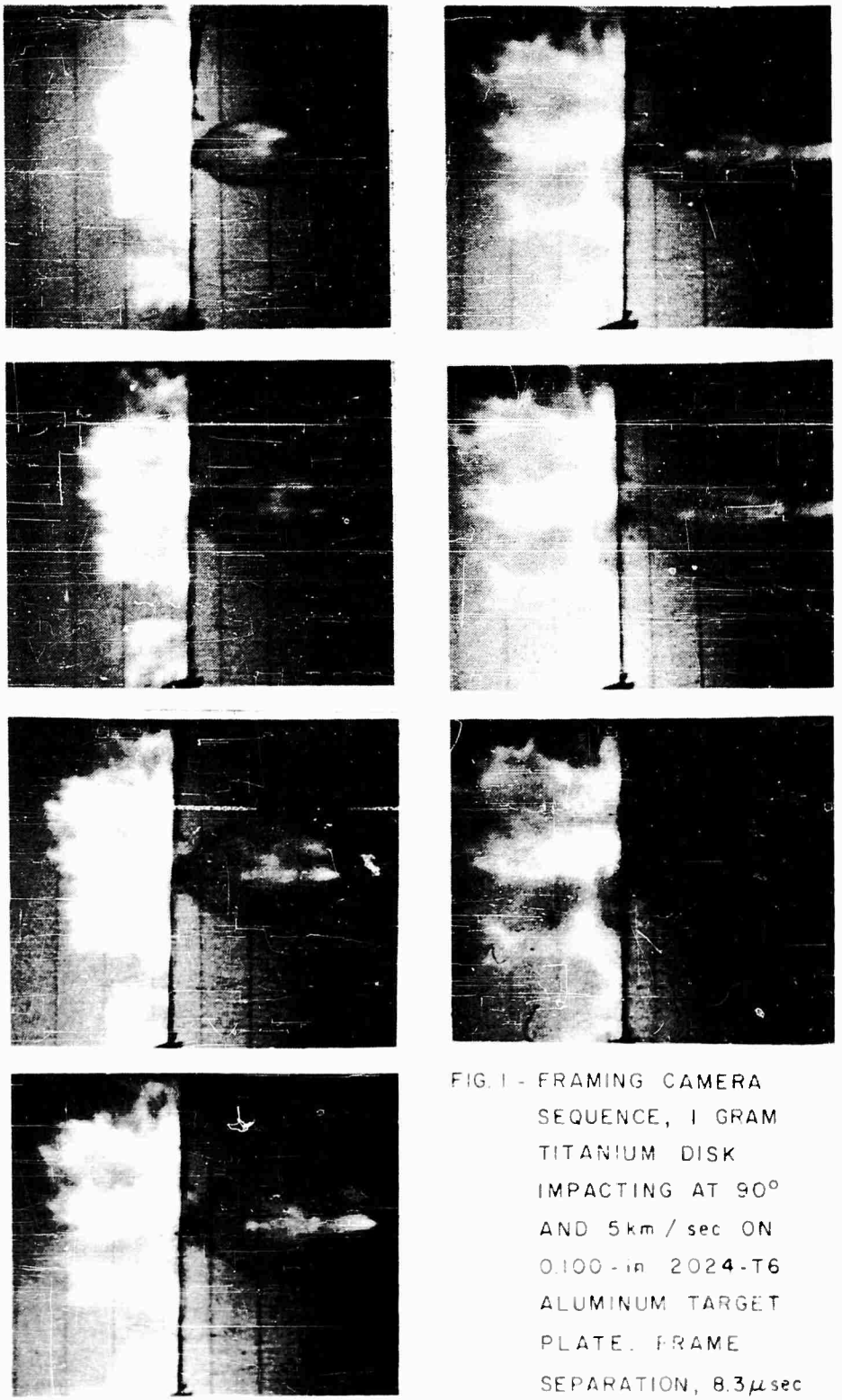

FIG. 1 - FRAMING CAMERA SEQUENCE, 1 GRAM TITANIUM DISK IMPACTING AT 90° AND 5 km / sec ON 0.100 - in 2024-T6 ALUMINUM TARGET PLATE. FRAME SEPARATION, 8.3 μsec

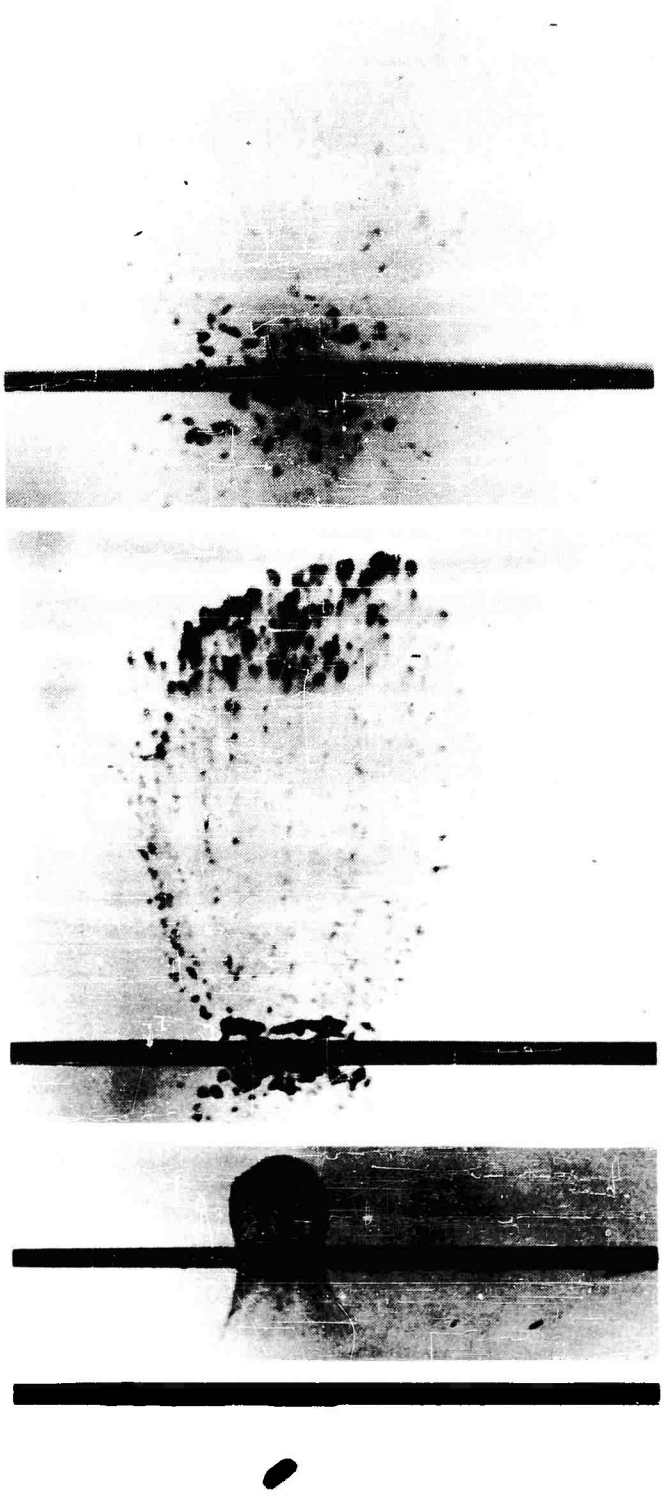

FIGURE 2 - FLASH X-RAY SERIES, 1-GRAM TITANIUM DISC IMPACTING AT APPROX. 4.6 km/sec ON 0.100-in. 2014-T6 ALUMINUM TARGET PLATE

kilobars. The target material is also fractured. From the back side of the plate emerges the envelope of these projectile and target fragments. The heaviest visible fragments are seen grouped near the leading edge of this pattern. The velocities diverge, hence the pattern disperses -- in this case with an angle of about 30°. Looking back at the target plate itself, we can see chips of target material spalling or breaking off the edge of the new hole at relatively low velocities on both sides of the target. It is apparent by comparing the second and third views that the formation of the final dimensions of the hole is taking place long after the initial penetration has occurred.

3. IMPACT AT 45° OBLIQUITY

Figures 3 and 4 are framing camera and flash radiograph series showing the same impact situations as were considered above, except that the impact angle is now 45°. The general process of penetrating is the same as for normal (90°) impact-high velocity splash, projectile and target breakup from impact, emergence of a diverging fragment pattern, and fracture of the edges of the new hole. For 45° impact, however, both the splash and fragment envelope patterns are strongly skewed, rather than symmetrical as in perpendicular impact. The major portion of the splashing particles travel normal to the impact velocity. The fragment pattern on the back of the plate is deflected, or refracted, approximately 25°.

The radiographs in this slide again represent four separate replicate shots. It is of interest to note that one large fragment of the projectile -- or perhaps of the target -- survived the impact and penetration processes in every test.

4. IMPACT AT 25° OBLIQUITY

Again impacting one gram titanium discs at approximately 5 km/sec on 0.100-in. aluminum, Figures 5 and 6 show the effects of 25° obliquity. The framing camera series in Figure 5 illustrates rather well the nature of the deflected pattern of fragments emerging from the back of the target. In the x-rays of 25° impact in Figure 6, the same general mode of penetration as was noted previously is retained, but with very pronounced effects due to the severe obliquity being evident. The splash particles now travel along the target surface. One barely visible particle is moving at nearly 7 km/sec.

5. A PROCESS FOR THIN-PLATE PENETRATION

Three separate phenomena are observed in the experiments which are illustrated above. The first is splashing from the target surface, which consists of tiny particles jetting out of the contact zone during the initial phase of impact. The second phenomenon is the breakup of the projectile and a portion of the target plate, with the resulting group of fragments emerging from the back of the target plate in a diverging pattern. The third phenomenon, which appears (as in the third view of Figure 2) to be distinct from the other two, is the breaking off of the edges of the newly formed hole into chips or small fragments which travel

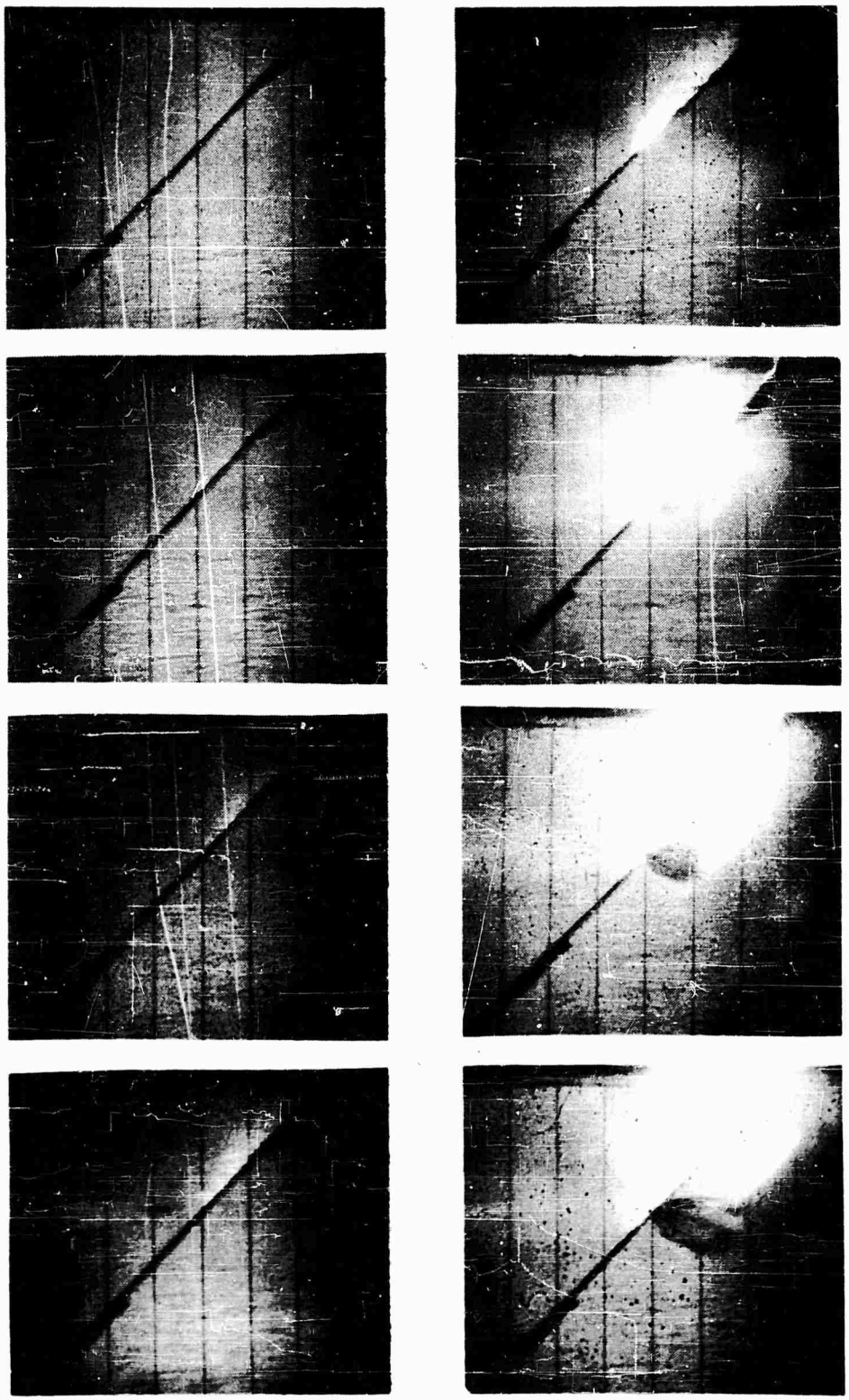

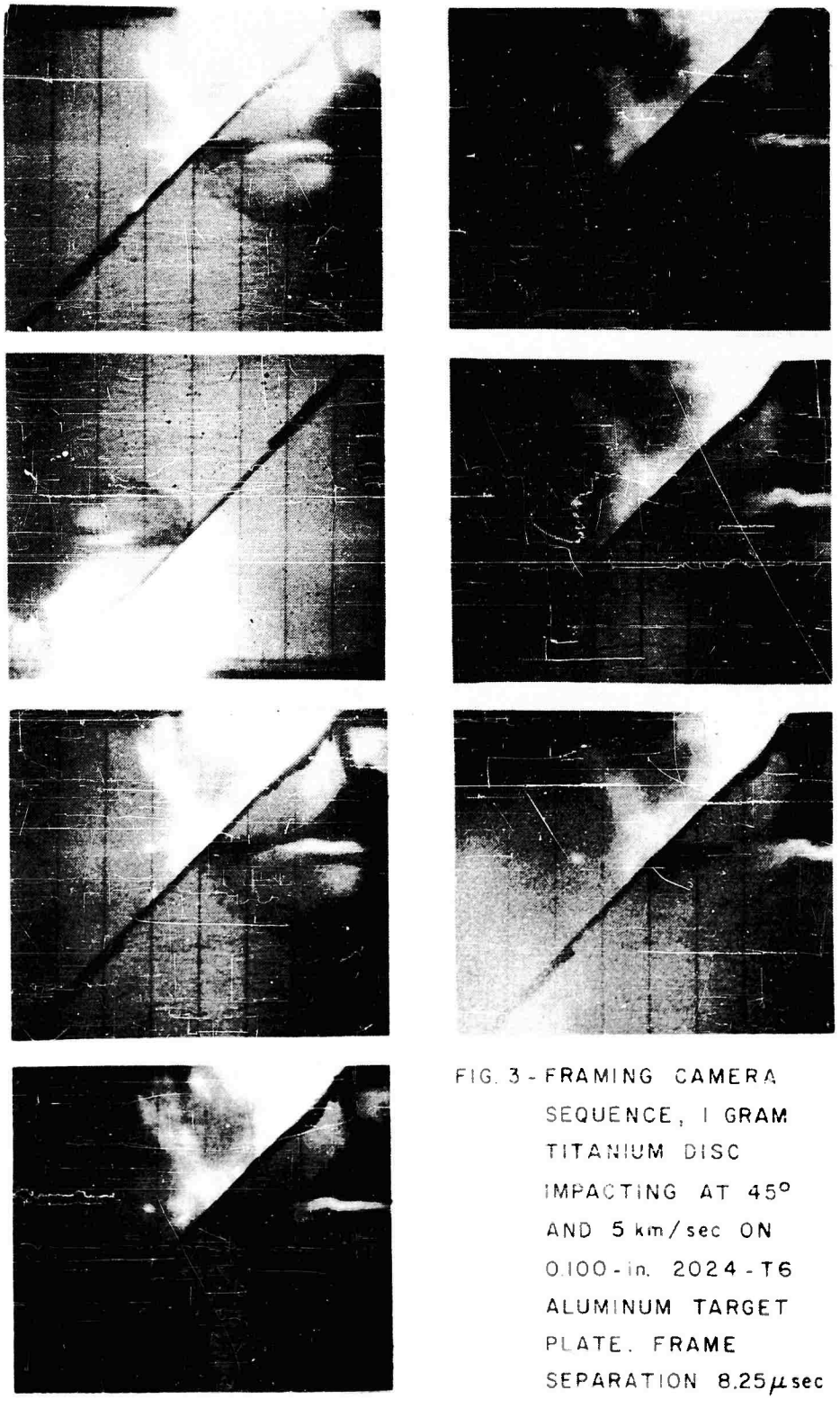

FIG. 3 - FRAMING CAMERA SEQUENCE, 1 GRAM TITANIUM DISC IMPACTING AT 45° AND 5 km/sec ON 0.100-in. 2024-T6 ALUMINUM TARGET PLATE. FRAME SEPARATION 8.25 μsec

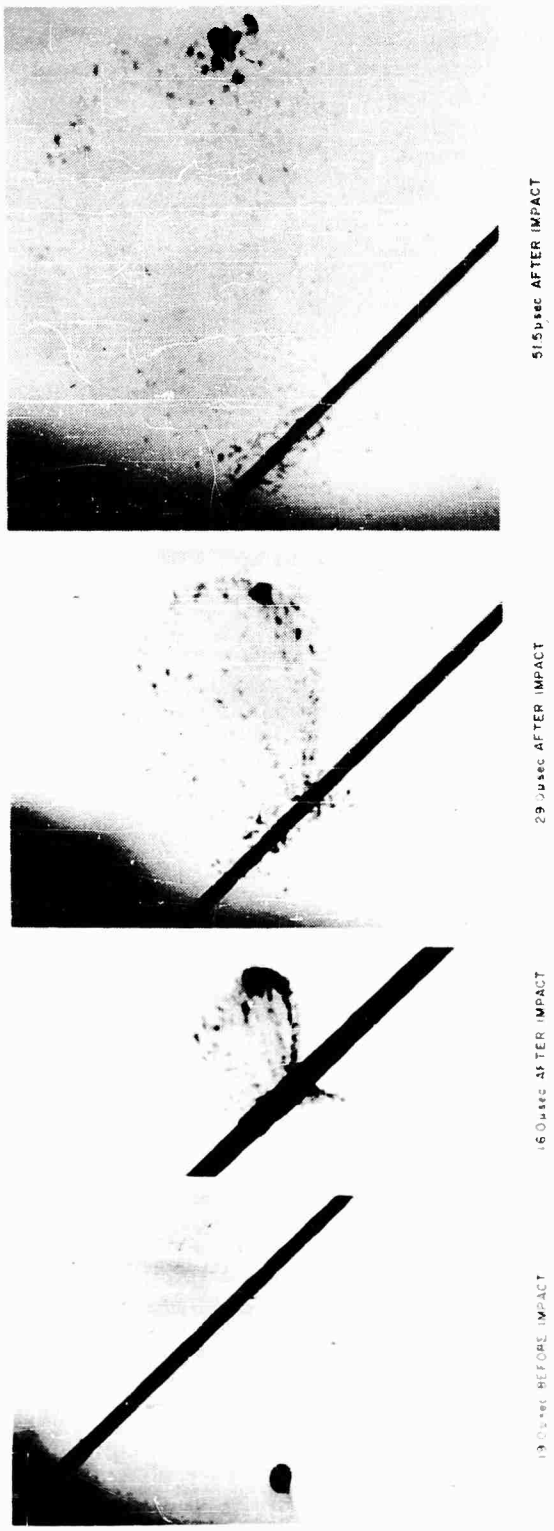

FIGURE 4 - FRAGMENT DISPERSION RESULTING FROM A 45° IMPACT OF A 1-GRAM TITANIUM PELLET (VELOCITY APPROXIMATELY 4.6 km/sec) WITH A .100-inch THICK 2014-T6 ALUMINUM ALLOY TARGET PLATE

outward slowly from both sides of the target plate. Because of this edge fracture, the final dimensions of the hole are not established until many microseconds after the initial penetration has been completed.

Since shearing action would be expected to eject these edge fragments towards the back of the target plate, the symmetry of the slow moving group of fragments on both sides of the target plate suggests that a compression, or shock wave, rather than a shear wave, is responsible for the enlargement of the hole to its final dimensions.

With the exception of the early splashing phenomenon(which is probably due to non-ideal geometry during early impact) the penetration model suggested here for 5 km/sec impact conforms to the general pattern of the 20 km/sec case proposed during this Symposium in the numerical solution of Bjork and Olshaker.

6. MULTIPLE PLATE PENETRATION

In the regime of target plate, projectile, and impact characteristics where the plate is easily penetrated and the projectile is fractured, any subsequent target behind the initial plate will be impacted by a large number of small, high velocity fragments. The effect of these many fragments on the second target plate may be greater than that of the original projectile on the initial target.

Figure 7 is a series of radiographs taken of one test with a four-channel, sequential x-ray system. The first two views are of a one gram titanium disc before it impacts a 0.100-in. thick 2014-T6 aluminum alloy plate at 4.1 km/sec. The third view shows fragments of the projectile and target about ten inches behind the initial target. The fourth view shows the same group of major fragments just prior to impacting a second, similar target, or witness plate.

In the photos above the radiograph prints, the two target plates are shown. Simple penetration has occurred in the initial plate. Of the fragments which emerged from the back of this plate, eleven penetrated the second plate which was spaced 40 in. away. The three major holes can be correlated with corresponding fragments in the third, and perhaps in the fourth radiograph. The total area of the holes in this second plate is greater than the area of the single hole in the first plate. This last observation is of some interest in designing "meteor bumpers" for space vehicles. Under many impact conditions, thin plate armoring may actually enhance damage to the defended thin plate structure.

For example, Figure 8 shows the damage to a series of thin plates which had been arranged in a parallel array, with one-inch separation. Note that the penetration hole in each succeeding plate gets larger. This is not to say that spaced armor or meteor bumpers are useless or harmful -- but rather that such devices should be applied with caution to the defense of soft targets.

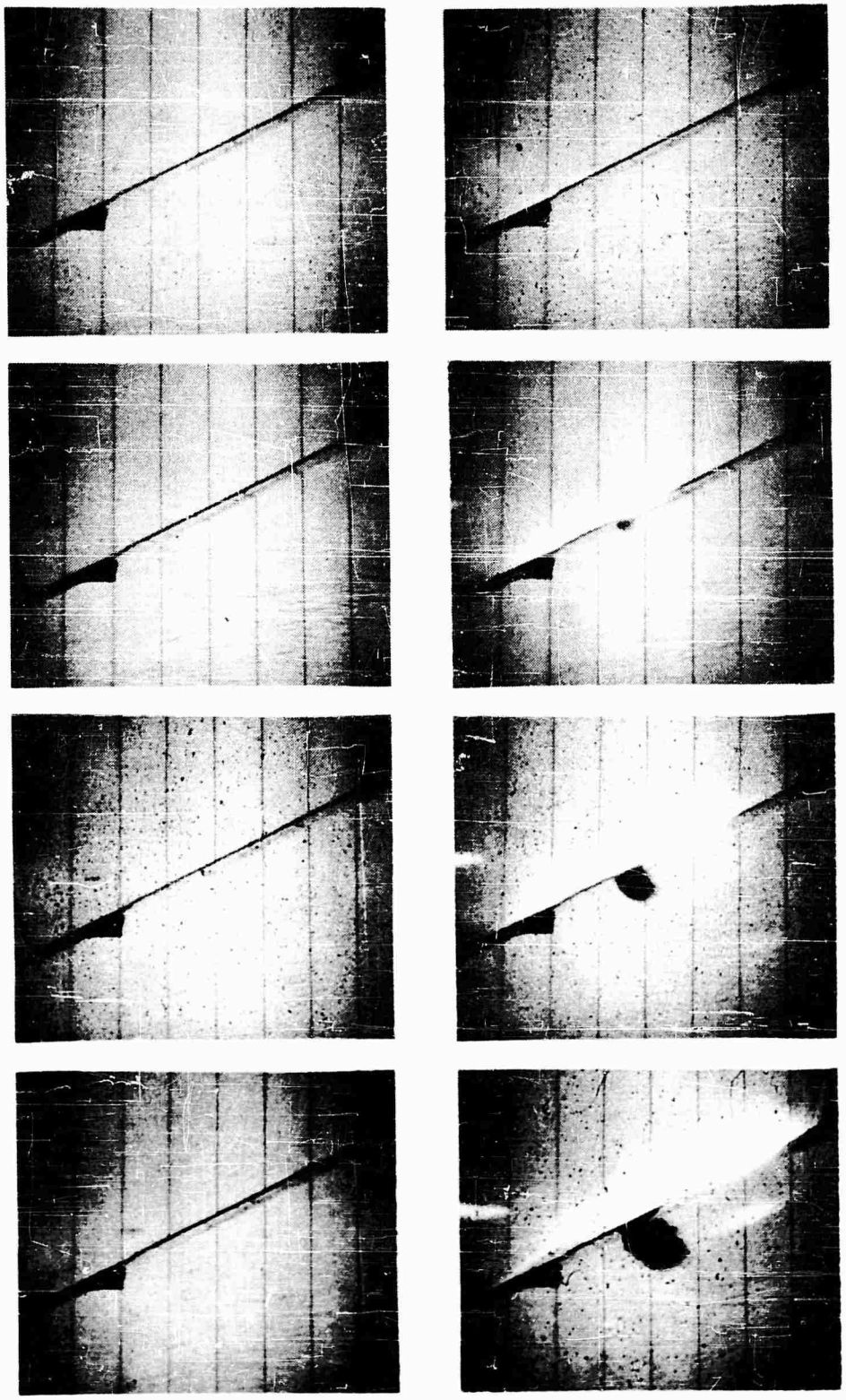

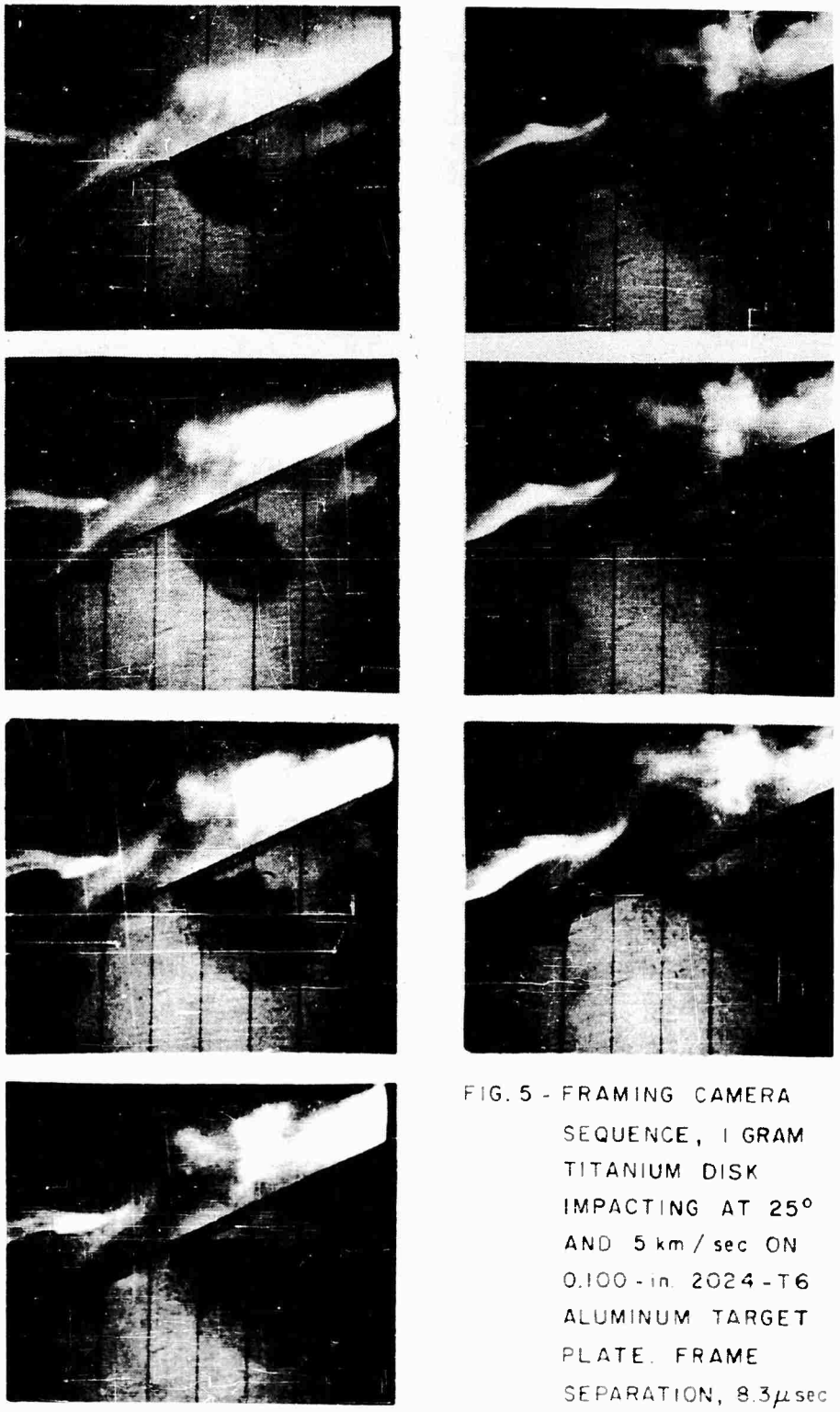

FIG. 5 - FRAMING CAMERA SEQUENCE, 1 GRAM TITANIUM DISK IMPACTING AT 25° AND 5 km / sec ON 0.100 - in. 2024 - T6 ALUMINUM TARGET PLATE. FRAME SEPARATION, 8.3 μsec

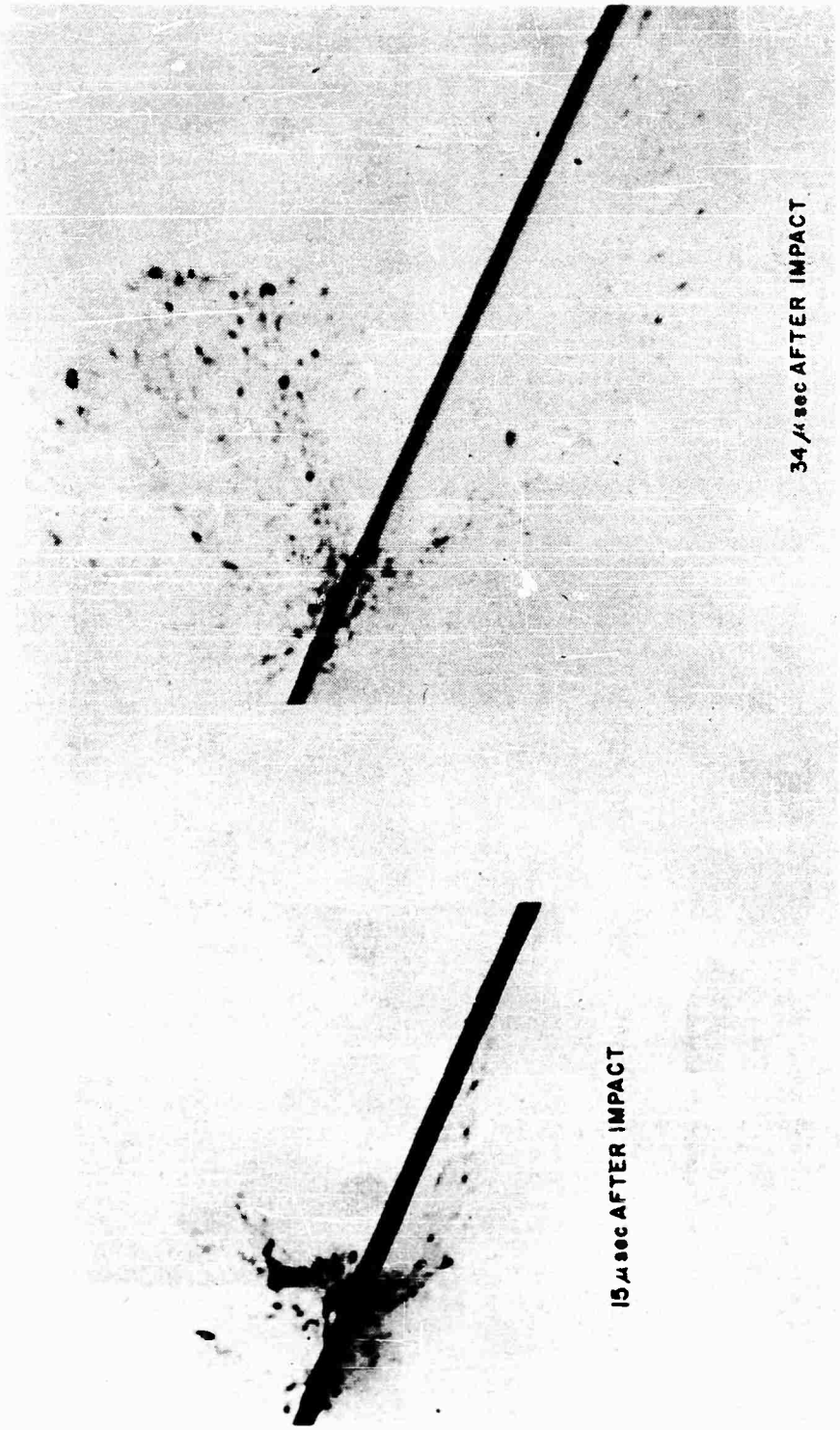

Figure 6 - Fragment dispersion resulting from a 25° impact of a 1-gram titanium disc (velocity approximately 4.6 km/sec) with a 0.100-in. thick 2014-T6 aluminum alloy target plate

FIGURE 7 - FLASH X-RAY SEQUENCE,
1-GRAM TITANIUM DISC AT 90°
ON .100-in. 2014-T6 AL. PLATES
SPACED 40 in. APART.
APPROACH VELOCITY 4.1km/sec
RESIDUAL VELOCITY 3.3km/sec
FOR MAJOR FRAGMENTS
FIRST PLATE DAMAGE
SECOND PLATE DAMAGE
207 μsec BEFORE IMPACT
77 μsec BEFORE IMPACT
63 μ sec AFTER IMPACT
213 μ sec AFTER IMPACT

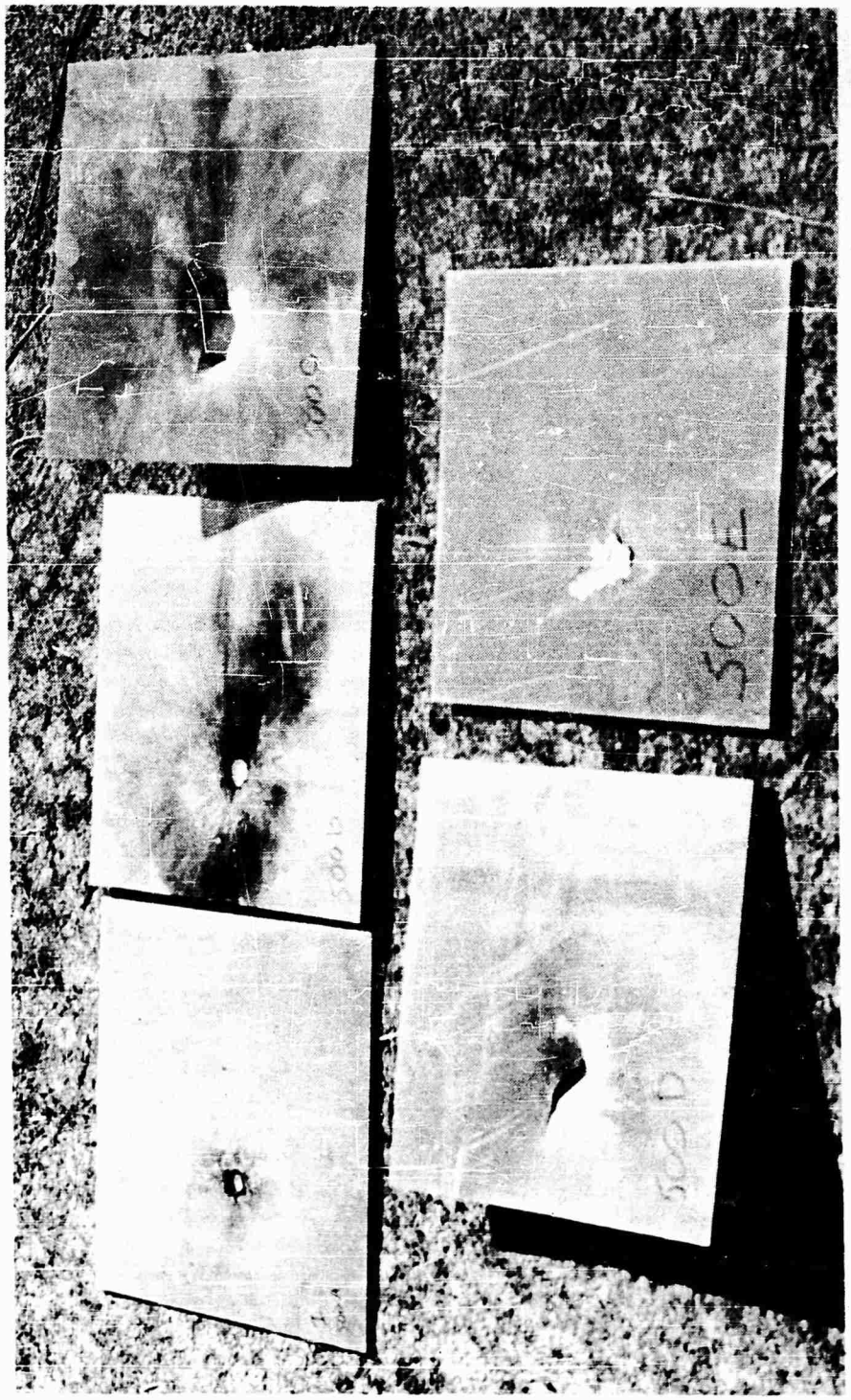

FIGURE 8 - PENETRATION OF PARALLEL ARRAY OF .100-in. 2024-T6 PLATES SPACED 1-in. APART BY 1gm. TITANIUM DISC AT 5 km/sec, IMPACT ANGLE 90°

EXPERIMENTAL HYPERVELOCITY IMPACT CRATERS IN ROCK

H. J. Moore and R. V. Lugn

U.S. Geological Survey
Menlo Park, California

D. E. Gault

National Space and Aeronautics Administration
Moffett Field, California

INTRODUCTION

An experimental investigation of hypervelocity impact on rock is being conducted jointly by the Ames Research Center of the National Aeronautics and Space Administration and the U. S. Geological Survey. Projectiles are launched with light-gas guns at the Ballistics Range at Ames Research Center. The craters and ejecta produced in these experiments are being studied by the U. S. Geological Survey.

The phenomena of impact on basalt, sandstone, dolomite, and nephrite have been investigated. Projectiles weighing from 0.02 to 0.4 grams were accelerated to velocities of 4.27×10^5 cm/sec (14,000 fps) to 7.28×10^5 cm/sec (23,900 fps) with a light-gas gun using hydrogen as the propellant medium (Charters, Denardo, and Rossow, 1957). Steel, aluminum, pyrex, polyethylene, and some complex projectiles were launched and impacted the targets normal and obliquely to plane rock surfaces in an atmosphere of air with a nominal pressure of 25mm of mercury. The metal and pyrex projectiles were mounted in supporting four-piece nylon sabots which guided the projectiles down the launching tube. After launch, aerodynamic drag acted to separate the sabots from the projectiles. Impact velocities were determined with time measurements and spark photographs of the projectiles in flight.

Impact of projectiles of the size employed produced craters in the rock targets chiefly by ejection of fragments (Fig. 1). Craters produced by about 20 shots have been examined in detail. The craters are small roughly conical depressions with crushed and intensely fractured rock at the bottoms of the depressions. The ejecta are composed of pieces of the projectiles and rock fragments ranging in size from a few microns or less to several centimeters in maximum dimension. In this paper the structural features of the craters are described and the mechanisms by which they are formed are inferred.

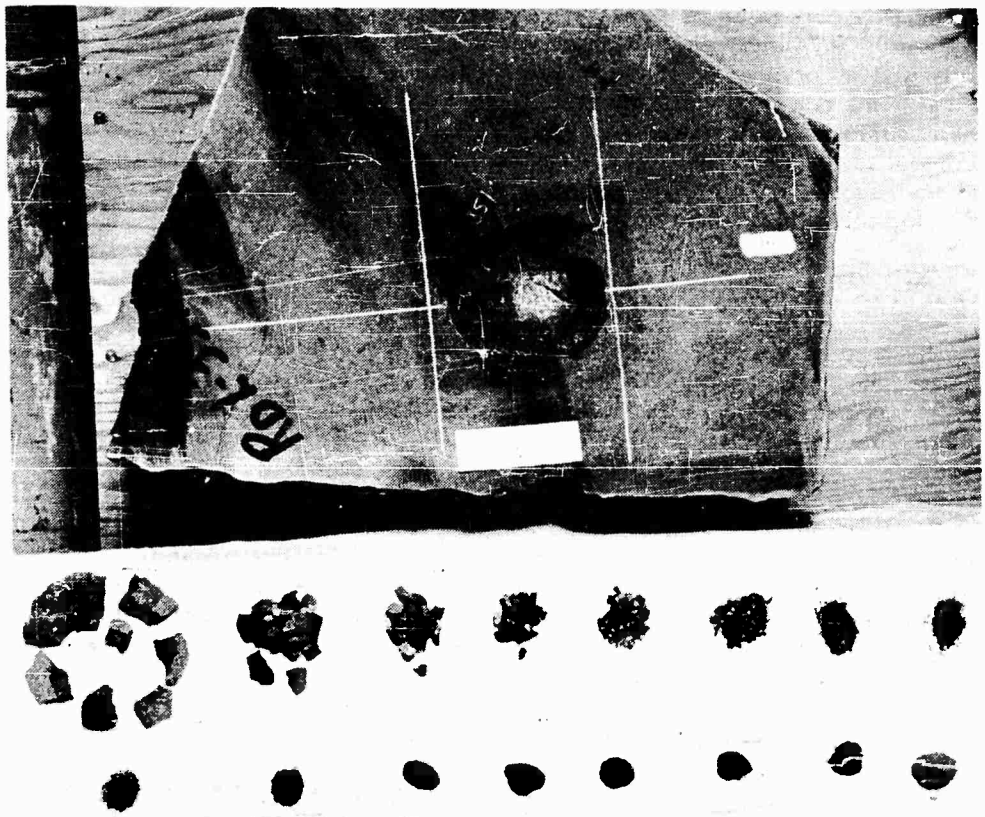

Figure 1. Photograph of crater and ejecta produced by impact of 0.588 diameter polyethylene sphere at 5.08 km/sec in basalt. Ejecta classified in logarithmic size intervals.

CRATER MORPHOLOGY

The typical craters produced are shallow inverted wide base cones approximately 0.6 to 2.4 cm deep and 4 to 12 cm across (Fig. 2) The outer margins of the craters are irregular in plan-view, whereas the lower parts of the craters are generally more symmetrical. In most cases, gently sloping crater walls join smoothly with a concave floor near the center of the crater. The crater walls are rough and hummocky in detail, and local reversals of slope are commonly present. Rises and depressions and, in some cases, cone-shaped protuberances occur on the floors of the craters (Fig. 2). Atypical crater shapes are occasionally produced, such as one crater in sandstone which has a stem-like extension and resembles a thick-stemmed sherbet glass (Fig. 3).

CRATER STRUCTURE

Crushed rock and a variety of fractures are produced in the target blocks by impact. Fractures formed in response to several different conditions of stress can be recognized and, for convenience of discussion, may be classified as follows: (1) shear fractures, (2) radial fractures, (3) spall fractures, and (4) concentric fractures.

Crushed rock. Crushed rock occurs on the floors of all craters Figs 1, 2, and 3). In the crushed rock, individual mineral grains are broken and displaced and some are pulverized. The separation between microscopic fractures increases and the number of pulverized grains decreases rapidly from the crater floor into the target block. In porous granular rocks, such as sandstone, the pore spaces are closed up and the many grains are pulverized, whereas, in dense non-porous rocks with interlocking crystals, unbroken polyhedra are formed which are enclosed in a matrix of crushed rock.

Shear fractures. Shear fractures occur in the floors of some craters (Fig. 2). The surfaces formed by shear fractures are smooth and may be identified by the presence of grooves and striae. The grooves and striae are oriented parallel to the direction of slip. Grooves and striae on individual shear surfaces converge toward the axis of symmetry of the crater (Fig. 2). In some craters, the shear surfaces intersect to form narrow truncated pyramids (Fig. 4). In craters in dolomite, some of the shear surfaces are cone-shaped with the grooves and striations radiating outward from the apex of the cones (Fig. 5). Similar cone-shaped shear surfaces found in nature at probable sites of meteorite or comet impact have been called shatter cones. Shear fractures in craters in basalt are marked by intensely pulverized rock; weakly developed grooves and striae are rarely present.

The shear fractures are slip surfaces which have formed in response to shear components of stress probably resulting from differences in the principal stresses in the diverging shockwave. Differences between the principal stresses behind the shock front will occur under conditions of plastic flow whenever the ratio of the shear strength of the rock to the peak shock pressure is not negligible. Cone-shaped shear surfaces are probably propagated from relatively incompressible small regions or grains as the shock advances. The shear failure in such a dynamic system may be somewhat analogous to that which occurs under static uniaxial compression of rock.

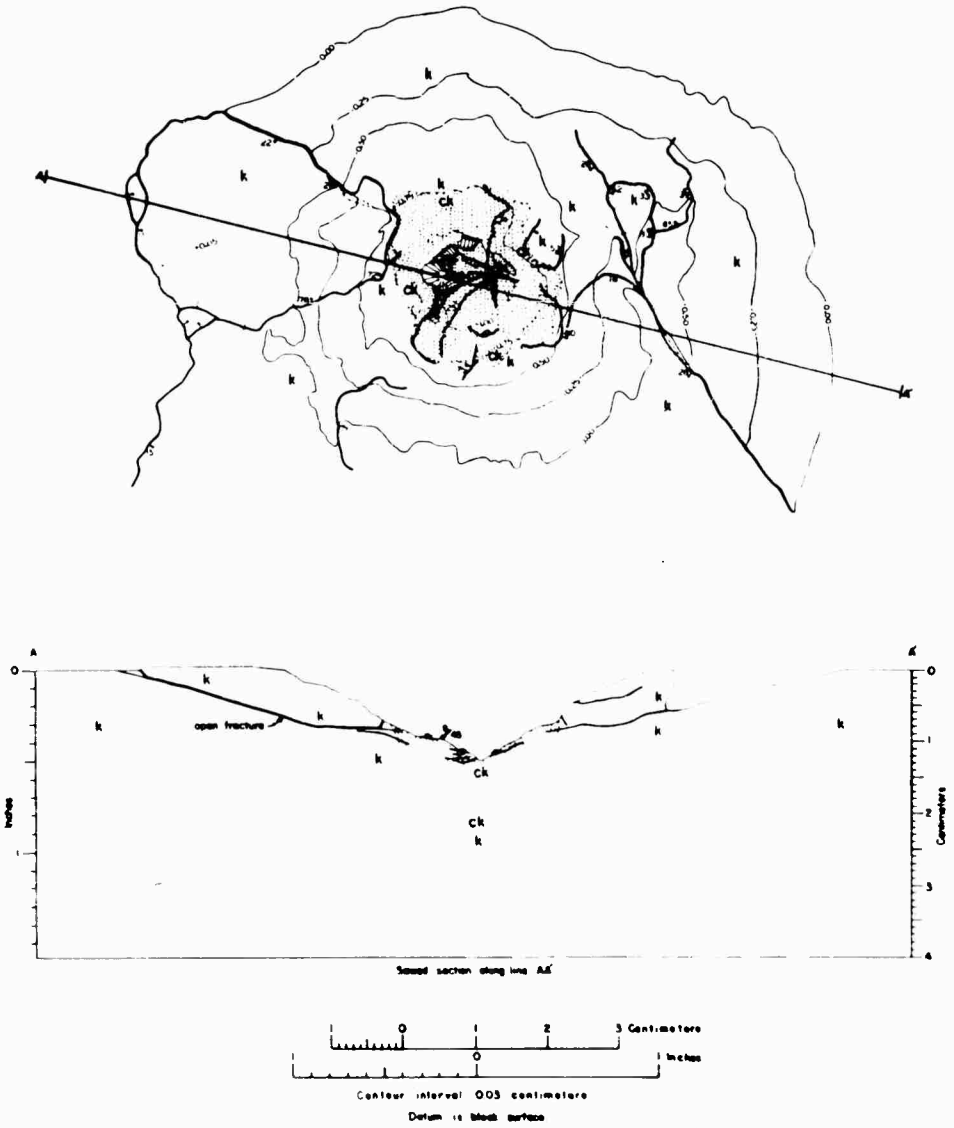

Figure 2. Topographic and Structural Map of Hypervelocity Impact Crater in Dolomite.

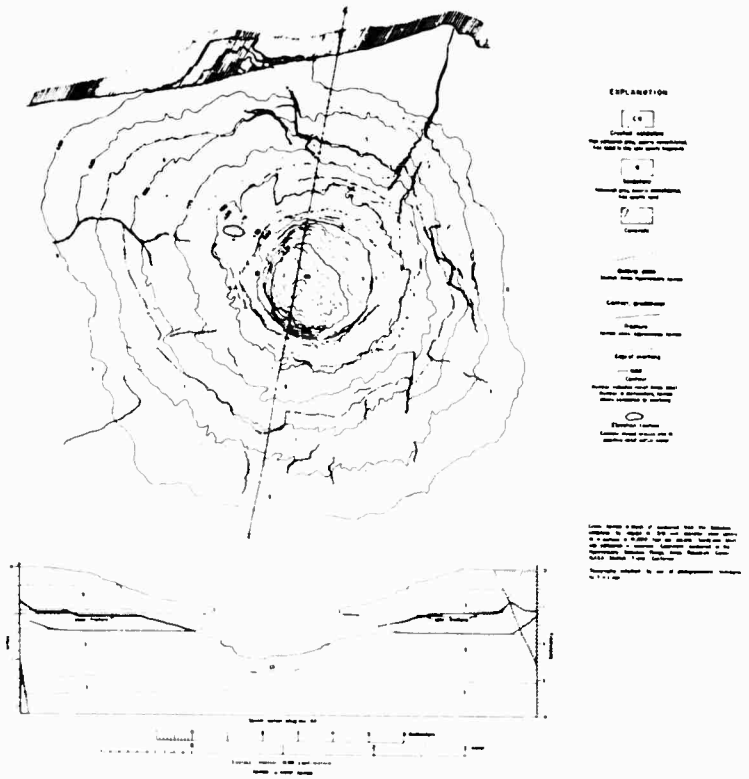

Figure 3. Topographic and Structural Map of Hypervelocity Impact Crater in Sandstone.

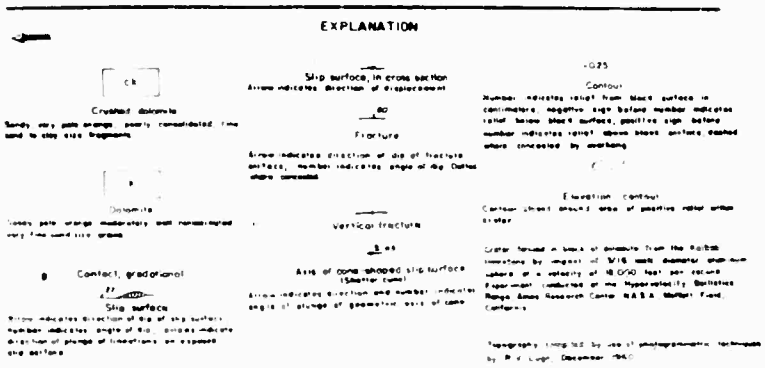

Figure 4. Photograph of Crater Formed in Nephrite by Impact of 0.300 g Cooper-Faced Cylinder at 4.85 km/sec.

Shear fractures and conical surfaces are systematically distributed with respect to the axis of symmetry of the crater. The axes of two shatter cones in a crater in dolomite intersect the crater axis at a depth from the original surface between one-third and one-half of the depth of the crater (Fig. 2). In a crater in nephrite, bisectors of angles between adjacent shear fractures intersect at two points in cross-sectional planes (Fig. 6) and in three dimensions, the points of intersection of all shear fracture bisectors describe an oval centered about and perpendicular to the axis of crater symmetry. The plane of the oval lies at about one-half the depth of the crater from the block surface. A spherical projectile was used in the experiment with dolomite whereas a cylindrical projectile was used in the experiment with nephrite. The differences of the crater structures produced in these two experiments may be related partly to the differences in the projectile characteristics or to differences in the physical properties of the target or both.

Radial fractures. Fractures radiating from the crater axis are present in most craters (Figs. 7 and 8). The fractures are tensile breaks with rough surfaces and are nearly perpendicular to the surface of impact on the target-block. Many radial fractures are discontinuous; isolated radial fractures may occur several centimeters from the crater walls. In some dense nonporous rocks such as nephrite and basalt, the radial fractures are, in many cases, propagated far beyond the limits of the crater. In porous rocks such as sandstone and dolomite, the radial fractures are generally confined to the crater and die out rapidly with depth.

As shown by the rough surfaces formed, radial fracturing is produced by tensional failure of the rock. Tensile stresses may be expected to occur at right angles to the direction of propagation of expanding shock wave when the shear stresses behind the shock wave are of the same order or less than the dynamic shear strength of the rock. Discontinuous radial fractures are probably propagated through local regions of relatively low tensile strength.

Spall fractures. Spall fractures are tensile breaks formed by rarefaction waves reflected from free surfaces of the target blocks. These fractures form the outer parts of the crater walls and in addition occur beneath the crater walls. The parts of the crater walls formed by the spall fractures are the rough irregularly hummocky surfaces. The largest fragments of ejecta from a crater can be fitted snugly into their respective places of origin in the crater wall in "jig-saw" puzzle fashion (Fig. 9). Inward sloping spall fracture surfaces are present on the inward part of the largest fragments, and smaller fragments from the ejecta may also be fitted in turn into their respective positions on these surfaces. About half of the total mass of ejecta from most craters is made up of pieces that may be replaced in the crater on a concentric series of spall fracture surfaces (Fig. 9). Large fragments which are completely separated by a spall fracture from the target block but which were not ejected are present in the walls of some craters.

Spall fractures that do not intersect the rock surface in all directions occur around or intersect the walls of most craters. In general, such fractures can be traced from the crater wall upward and outward into the target block where the fracture dies out. In rare cases, spall fractures disappear when traced downward toward the crater from the original surface of the block. In still other cases, spall fractures are found which do not extend to either the crater wall or the original surface of the target block.

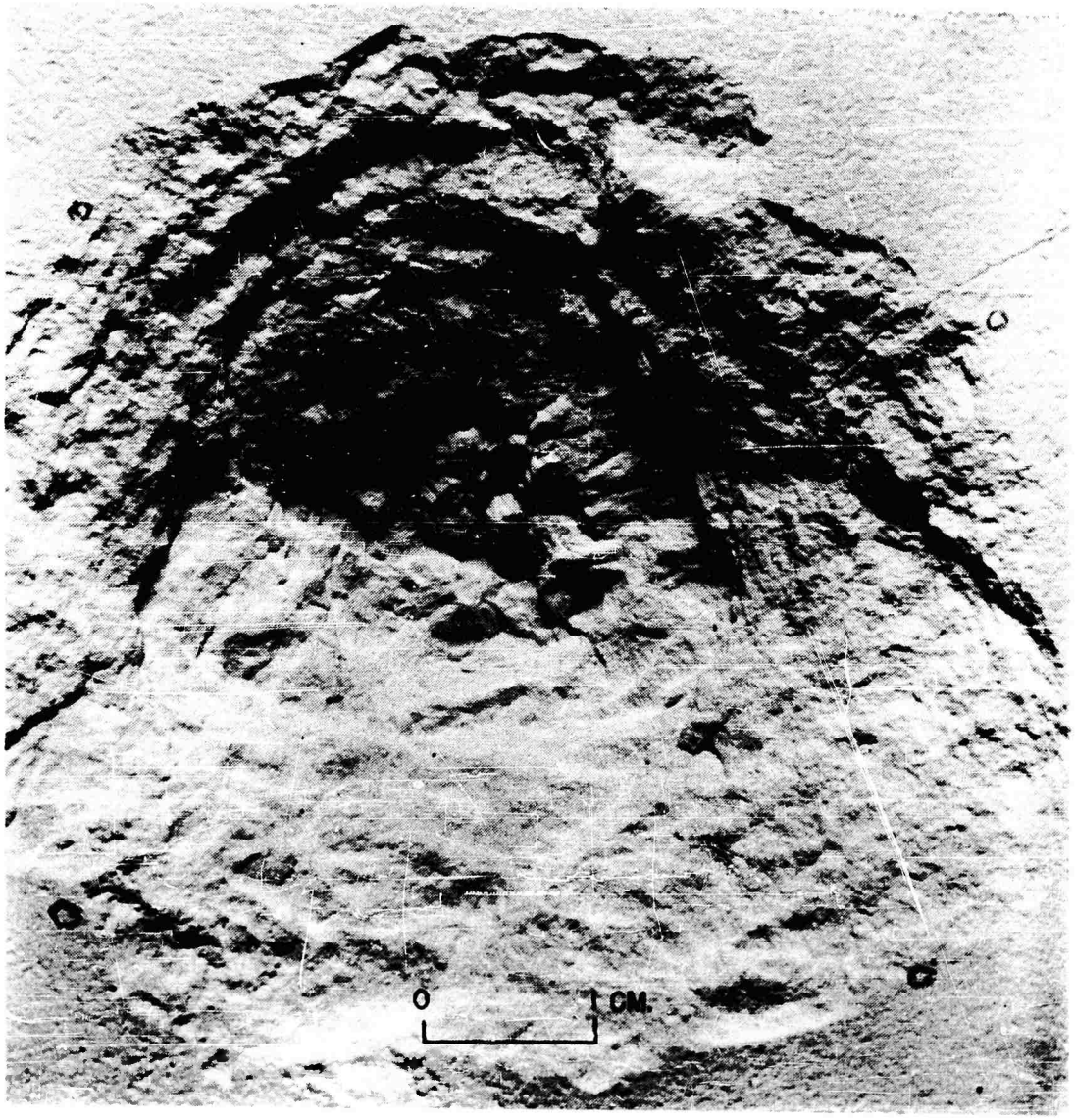

Figure 5. Photograph of Cone-Shaped Shear Surfaces on Floor of Crater in Dolomite Formed by Impact of 3/16-inch aluminum Spheres at 5.61 km/sec.

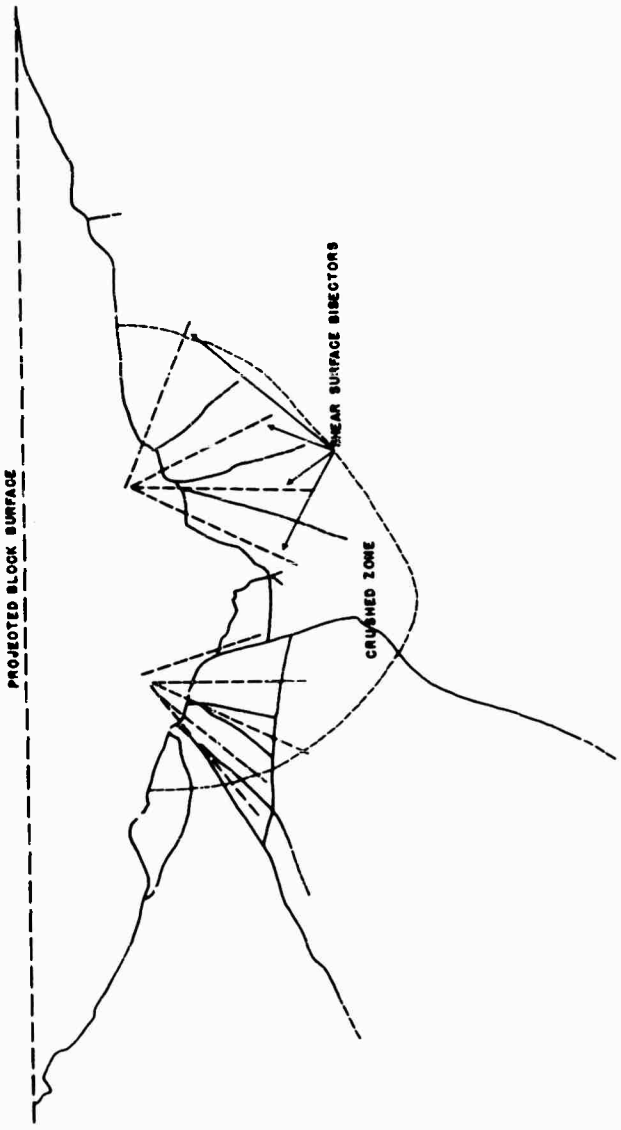

Figure 6. Cross section of crater in nephrite (see figure 4) showing intersections of bisectors of shear fractures.

Figure 7. Photograph of Crater in Basalt Showing Radial Fractures. Crater Formed by Impact of 0.588 cm Diameter Polyethylene Sphere at 5.41 km/sec.

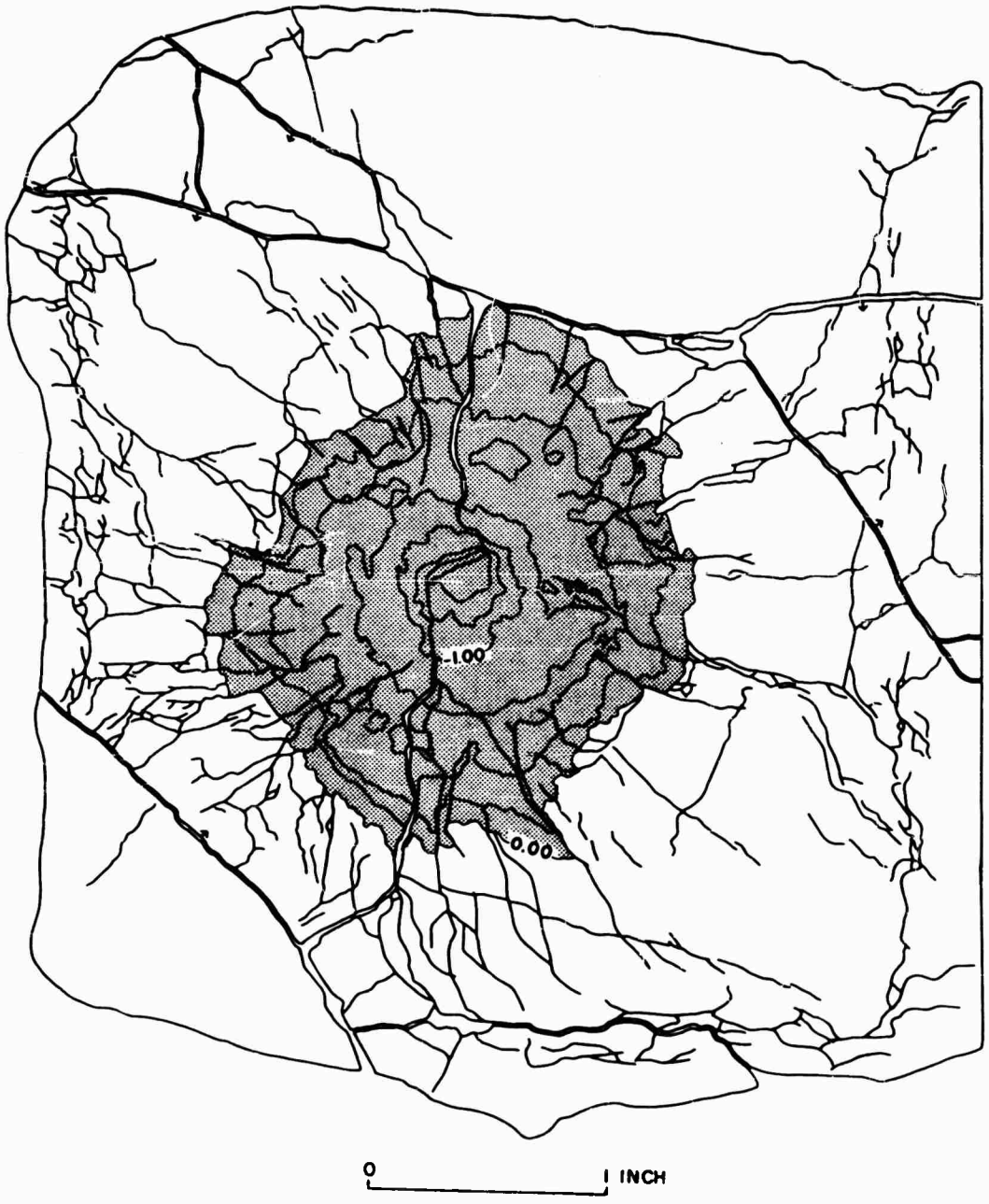

Figure 8. Topographic and structural map of crater in nephrite (see figure 4) showing radial fractures and spall fractures parallel with the sides of the target block. Crater area is shaded; contour interval is 0.25 centimeter.

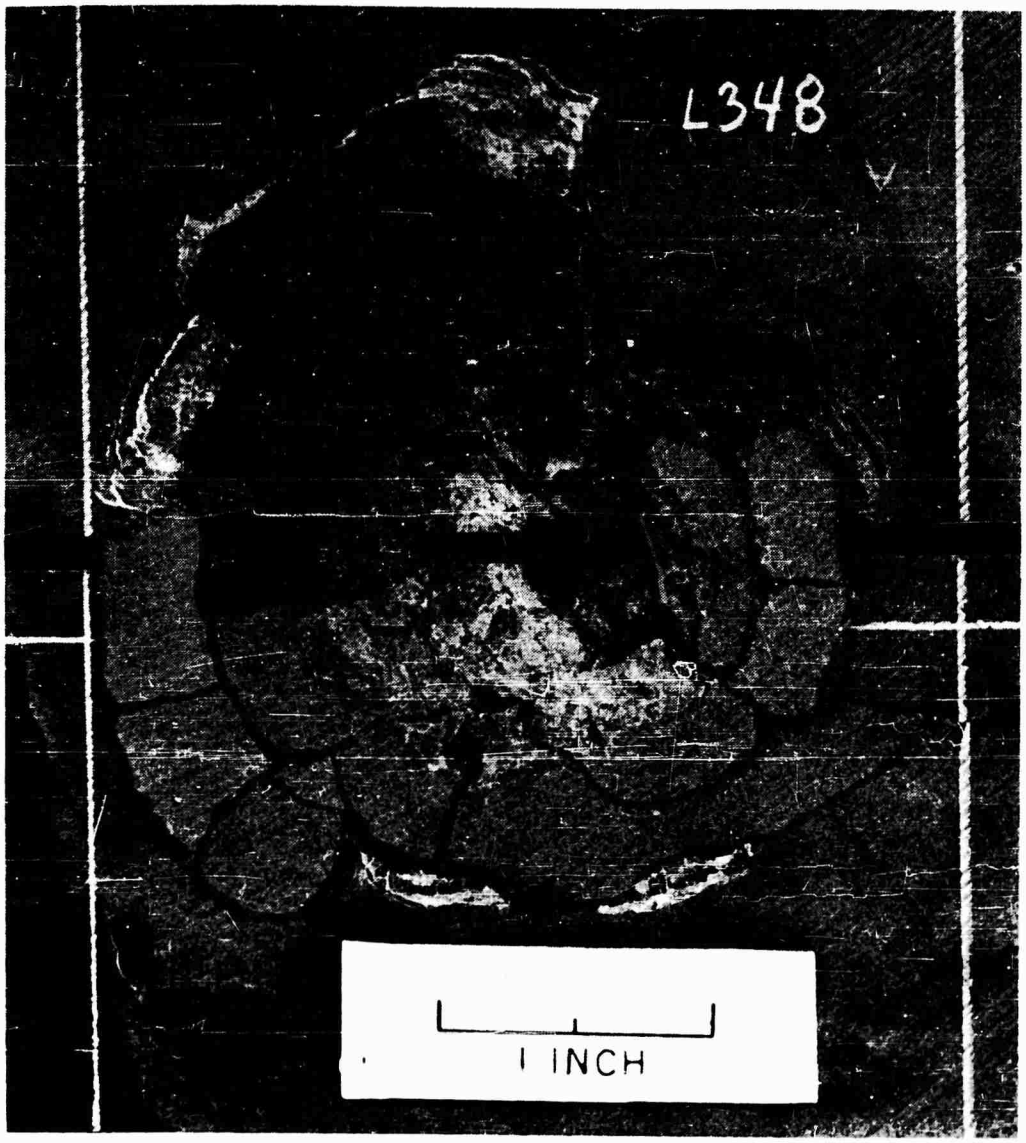

Figure 9. Photograph of Crater with Refitted Spall Fragments. Crater Formed by Impact of 0.588 cm Diameter Polyethylene Spheres at 5.96 km/sec in Basalt.

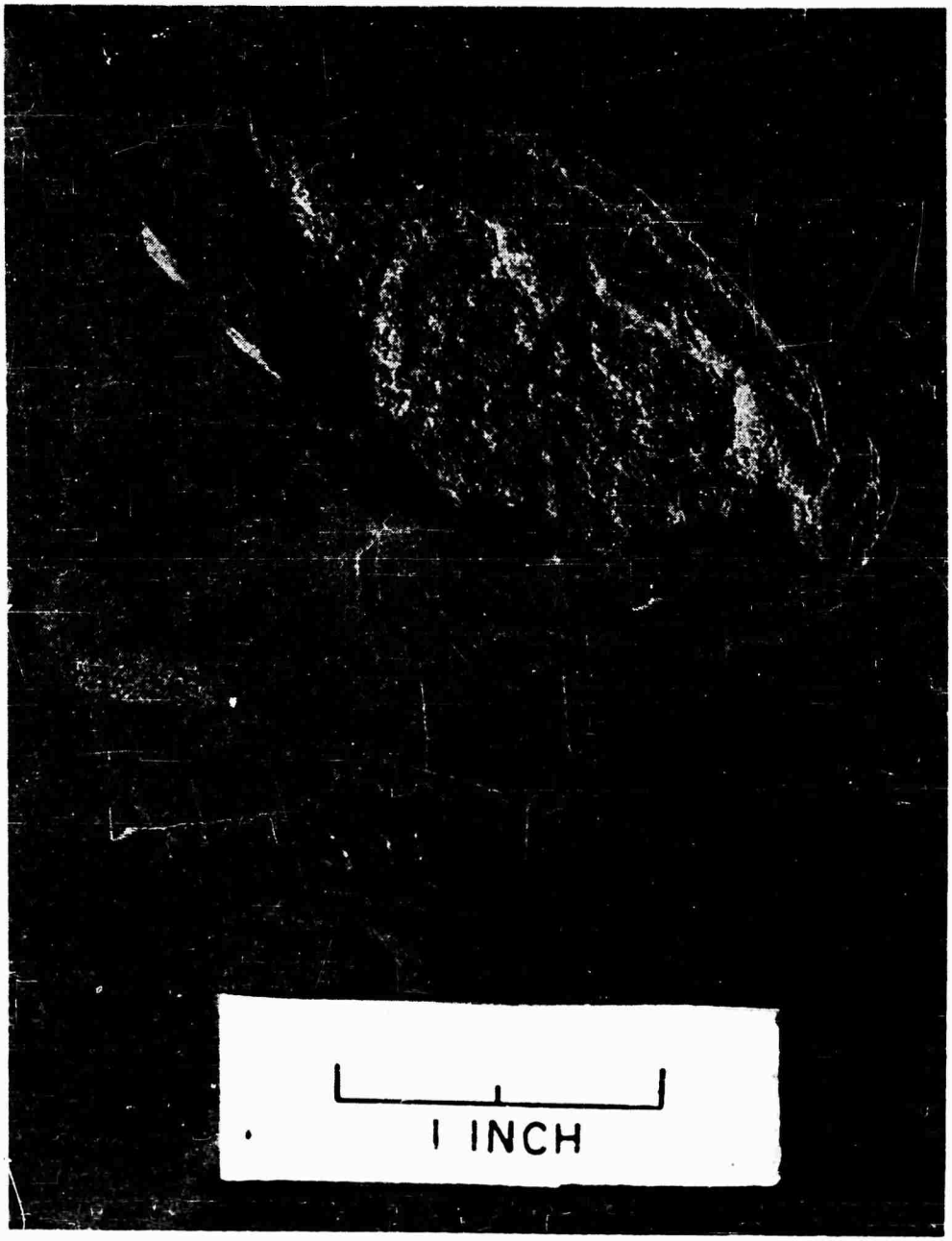

Figure 10. Photograph of spall Region on Reverse Side of the Target Block of Basalt Struck by 3/32-inch Aluminum Sphere at 7.28 kc/sec.

Spall fractures are also formed in dense nonporous rocks by rarefaction waves reflected from sides of the target blocks other than the sides struck by the projectiles. A circular region of spalling formed on the reverse side of one target block of basalt. A shallow pie-shaped crater was produced by ejection of fragments from about one-third of the circular spall region (Fig. 10). The irregular hummocky sapll fracture surface exposed is similar to the spall fracture surface in the crater (Fig. 11). formed around the path of penetration of the projectile. Where fragments were not ejected, the block surface is domed over the spall region. The limit of the dome is marked by a line of incipient fractures that may be seen as a faint light-colored trace in Figure 10. A spall fracture underlies the entire dome and separation of the two fracture surfaces increases toward the center of the dome. Because the spall fracture dies out in places at the margin of the dome, the fracture must have been propagated from the central part of the spall region outward. Spall fractures in the impact craters were also propagated outward in most cases as is shown by their tendency to die out when traced from the crater into the target block.

Certain features formed by spalling in impact craters in rock are similar to the features formed by spalling in craters produced by small charges of high explosives detonated at shallow scaled depth (see, for example, Duvall and Atchison, 1957). The shape of the outer parts of the crater walls, the shapes of the largest fragments, and the character of the spall fracture surfaces produced in the impact and high explosive experiments are closely similar. Reflection of the shock from a free surface as a rarefaction is the principal mechanism in the formation of both types of craters. Tensile fractures are initiated where the tensile stresses across the rarefaction wave are equal to the dynamic tensile strength of the rock.

The difference in shape of craters produced in rocks and the hemispherical craters produced in most metal targets by hypervelocity impact is due chiefly to spalling. Rocks have tensile strengths ($\approx$ 30-60 kg/cm^2) about two orders of magnitude less than the tensile strengths of metals ($\approx 2 \times 10^3 - 6.8 \times 10^3$ kg/cm^2) and fail in tension beyond the region of plastic flow.

Concentric fractures. Short discontinuous arcuate fracture surfaces concentric about the axis of the crater are present at the edges of some craters. These fracture surfaces are nearly perpendicular to the original surface of the target block and extend a fraction of a millimeter below the target block surface.

Concentric fractures are probably a result of tensional failure of the rock by flexing. High-speed photographs show that some spall fragments rotate outward as they leave the crater. Thus, if the spall fracture does not extend to the surface of the target block, tensional failure by flexing will occur at the outward extremities of the spall.

SEQUENCE OF EVENTS IN CRATER FORMATION

The sequence of events in the formation of hypervelocity impact craters in rock may be determined from the combined study of high speed photographs and the geometrical relations of the crater structures and ejecta. A series of photographs of oblique impact of an aluminum sphere on basalt taken with a Beckman-Whitley camera (Figs. 12a, b, c, d, and e) illustrates the phenomena

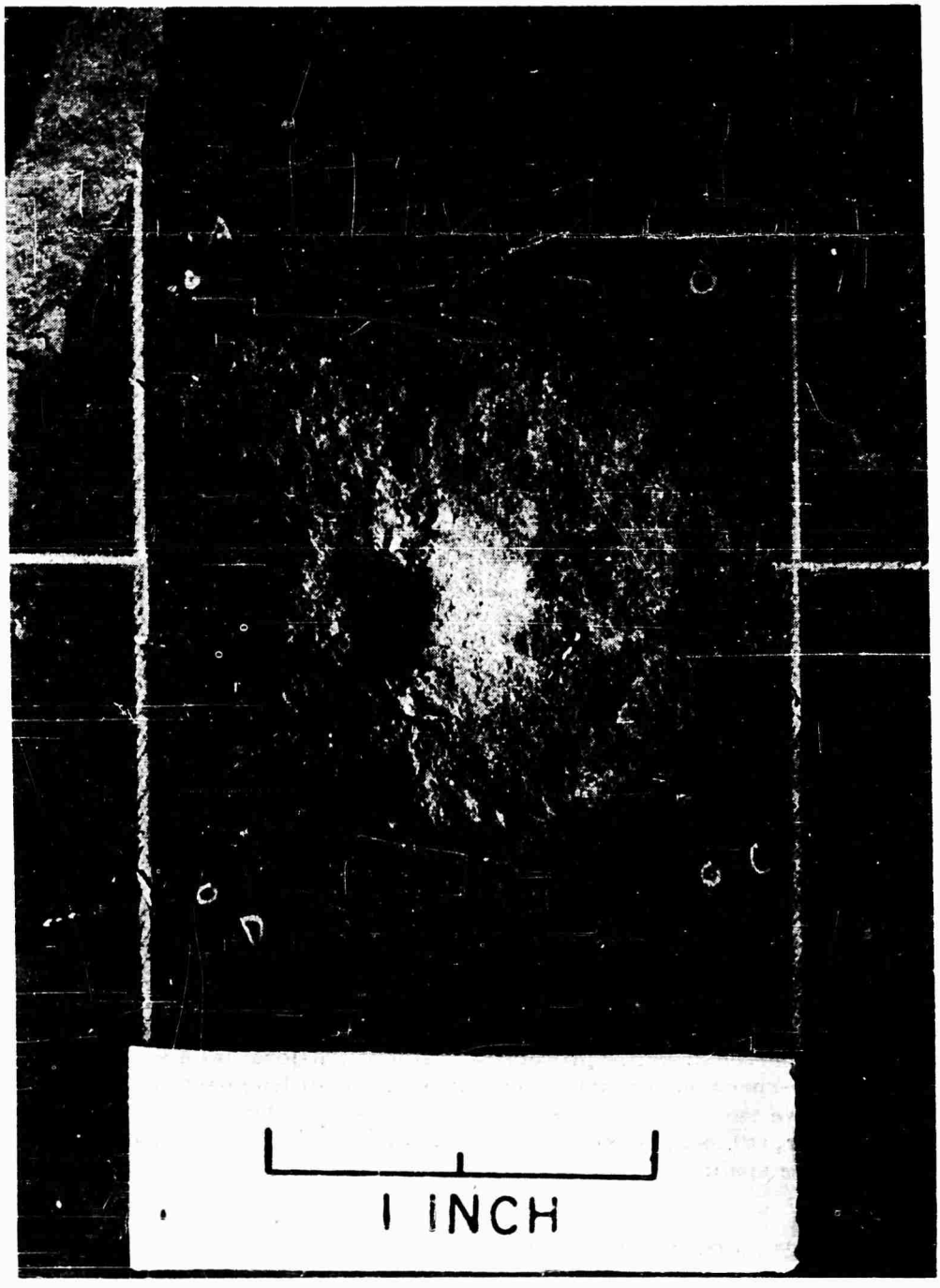

Figure 11. Photograph of Crater in Basalt Formed by Impact of 3/32-inch Aluminum Sphere at 7.28 km/sec.

a. PROJECTILE IN FLIGHT, 0.00 MICROSECONDS
b. TIME: 1.14 MICROSECONDS
c. TIME: 3.42 MICROSECONDS
SPRAY
DOME
FINAL CRATER DIAMETER
d. TIME: 11.4 MICROSECONDS
SPRAY
DOME
FINAL CRATER DIAMETER

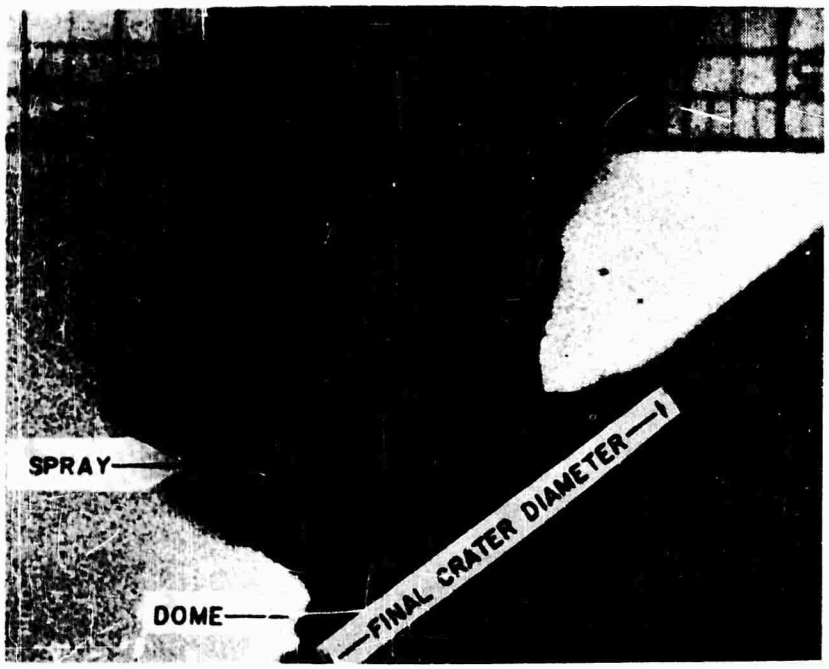

e. TIME: 28.5 MICROSECONDS

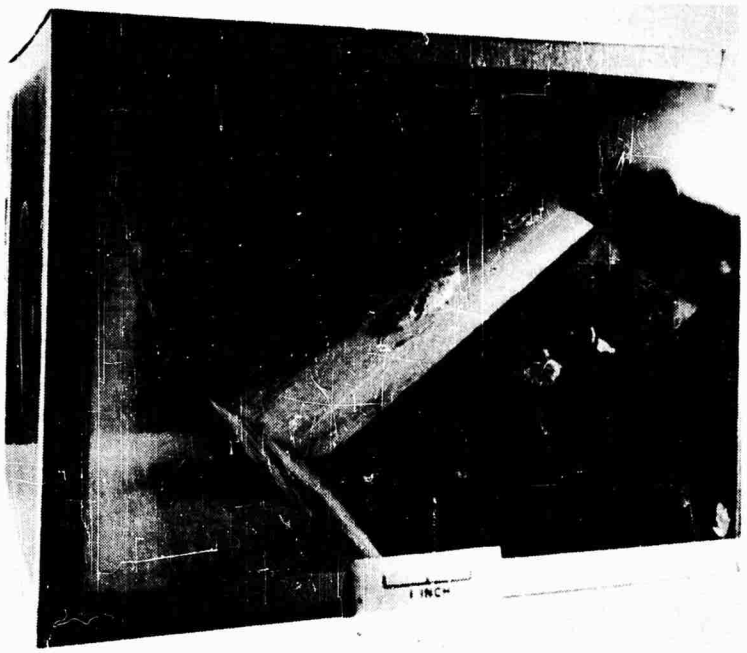

f. CRATER IN TARGET BLOCK AFTER IMPACT

Figure 12. Sequence of photographs illustrating phenomena produced by oblique impact of a 1/8-inch aluminum sphere traveling at 6.10 km/sec.

of fragment ejection. Except for asymmetry of the spray of ejecta, similar phenomena are observed in cases of impact at normal incidence.

In all experiments a luminescent front is generated at the moment of impact (Fig. 12b) which is propagated away from the projectile trajectory at speeds nearly twice the speeds of the projectile at small angles to the target block surface (Fig. 12c).

As the projectile penetrates the rock, a bowl-shaped spray or column of fine-grained ejecta is produced which grows rapidly in height and basal diameter (Figs. 12c, d, and e). The expanding column of spray grows upward at a rate that is the same order of magnitude as the speed of the projectile. The luminescent front and initial ejecta column are similar to the impact flash and initial column of ejecta produced by hypervelocity impact on metals (Gehring, 1960; and Charters, 1960). The initial column of ejecta produced by impact in rock is probably formed by flow of strongly shocked material along the wall of an expanding hemispherical cavity in the rock as illustrated for impact in metals by Gehring (1960). Because the initial shock pressures greatly exceed the dynamic shear strengths of the rocks, the conditions of flow during the initial stages of cavity growth can be approximately described as hydrodynamic (Bjork, 1958).

The base of the column of high speed ejecta expands to a radius equal to the depth of the final crater within a few microseconds. During the same interval of time a low dome is formed on the surface of the target (Fig. 12c). The visible radius of the dome increases at a rate equal to one-half to three-quarters the acoustic velocity of the rock out to the radius of the final crater (Fig. 12d). The surface of the dome rises and the base of the high speed ejecta column continues to expand at rates very much slower than the upward rate of growth of the column (Fig. 12c). Upward growth of the dome is fastest near the base of the column.

The dome exhibits irregularities which may be correlated with the margins of large spall fragments in the ejecta. For example, the bump about midway on the right slope of the dome illustrated in Figure 12d is the edge of an inner spall fragment separating from the rotating outer spall fragment; and, the flat-topped bump on the left side of the dome is another spall fragment.

The inner part of the dome and thus the inner spall fragments of which it is composed start to rise first and continue to rise at a more rapid rate than the outer part of the dome. Individual spall fragments are therefore set in motion successively in order of their distance from the center of the crater. This successive order of ejection is also illustrated by the fact the outermost spall fragments in some cases fail to be ejected from the crater (Fig. 2).

SUMMARY

Hypervelocity impact craters in rock are formed by a combination of plastic flow accompanied by crushing and shearing of the rock target and by ejection of the strongly shocked debris and of relatively undeformed fragments torn loose along tensile fractures. The formation of the crater begins with penetration of the projectile, probably under nearly hydrodynamic conditions, and the propagation of a strong shock into the rock target. Crushing and shearing of the rock

occurs in the region of plastic flow behind the shock front out to the distance at which the stress differences near the shock front drop below the dynamic shear strength of the rock. Tensile fractures are propagated beyond this distance in the direction of propagation of the shock front. Other tensile fractures are initiated by tensile stress across a rarefaction wave produced by reflection of the shock wave from the free surface of the target block. The outer part of the crater is formed by ejection of relatively coarse fragments torn loose by tensile fracturing. Individual pieces derived from the peripheral parts of the crater are bounded by parts of the initial target surface, and a combination of radial spall and concentric fracture surfaces.

Many of the features observed in craters produced by hypervelocity impact in rock, such as the crushed rock, shear fractures, radial fractures, spall fractures and concentric fractures, are also present in craters produced by high explosives in rock and soil (see, for example, Allsman, 1960).

REFERENCES

Allsman, P. L. 1960, Analysis of explosive action in breaking rock: Am. Inst. Mining Metall. Petroleum Engineers Trans., v. 217, p. 469-478.

Bjork, R. J., 1958, Effects of a meteoroid impact on steel and aluminum in space: Internat. Astronaut. Cong., 10th, London, 1958, preprint, 24 p.

Charters, A. C., 1960, High speed impact: Sci. American, v. 203, no. 4, p. 128-140.

Charters, A. C., Denardo, B. P., and Rossow, V. V., 1957, Development of a piston-compressor type light-gas gun for the launching of free-flight models of high velocity: Natl. Advisory Comm. Aeronautics Tech. Note 4143, 95 p.

Duvall, W. I., and Atchison, T. C., 1957, Rock breakage by explosives: U.S. Bur. Mines Rept. Inv., 5356, 52 p.

Gehring, J. W., 1960, Observations of the phenomena of hypervelocity impact: Proceedings of the Fourth Hypervelocity Impact Symposium, Eglin Air Force Base, Florida, April 1960, APGC-TR-60-39(I).

MICROPARTICLE HYPERVELOCITY IMPACTS FROM RANGER I

W. M. Alexander and O. E. Berg

National Aeronautics and Space Administration
Greenbelt, Maryland

ABSTRACT

An experiment to study cosmic dust was flown on Ranger I, launched August 23, 1961. The instrumentation provided simultaneous measurements of the momentum and energy of a microparticle impacting on acoustical and light flash detectors.

Recent hypervelocity laboratory studies using microparticles ($\sim$ 8 gm/cc) with velocities of 3.5×10^5 cm/sec $\lesssim v \lesssim 1.1 \times 10^6$ cm/sec indicate that the Ranger I Cosmic Dust Experiment detected particles having momentum and energy greater than $\sim 3 \times 10^{-6}$ dyne-seconds and $\sim .5$ ergs, respectively. The threshold mass sensitivity for the energy detector is also a function of the particle density. Preliminary data from Ranger I indicate that ten to fifteen percent of the particles detected had densities less than 2 gm/cc.

INTRODUCTION

In recent years a number of experiments designed to measure various physical parameters of interplanetary dust particles have been flown on rockets, satellites, and deep space probes. To date, the acoustical detector has provided the most statistically significant data, Figure 1 (McCracken and Alexander, 1962). Additional measurements of dust particle parameters have been made with the light flash detectors. Prior to March, 1961, laboratory calibration of sensors in dust particle experiments using microparticles with masses less than 10^{-9} gms and velocities in excess of 4×10^5 cm/sec did not exist. At that time, laboratory impact studies began using acoustical, light flash, and ionization detectors (Friichtenicht, 1961). The laboratory particles had the following dynamic properties.

density, $\sim$ 8 gm/cc;
mass, $5 \times 10^{-13} \lesssim m \lesssim 7 \times 10^{-11}$ gm; and
velocity, 3.5×10^5 cm/sec $\lesssim v \lesssim 1.1 \times 10^6$ cm/sec.

From the results of these studies and the use of present hypervelocity penetration theories, it is apparent that the dust particle experiment on Ranger I, launched on August 23, 1961, detected particles of different densities.

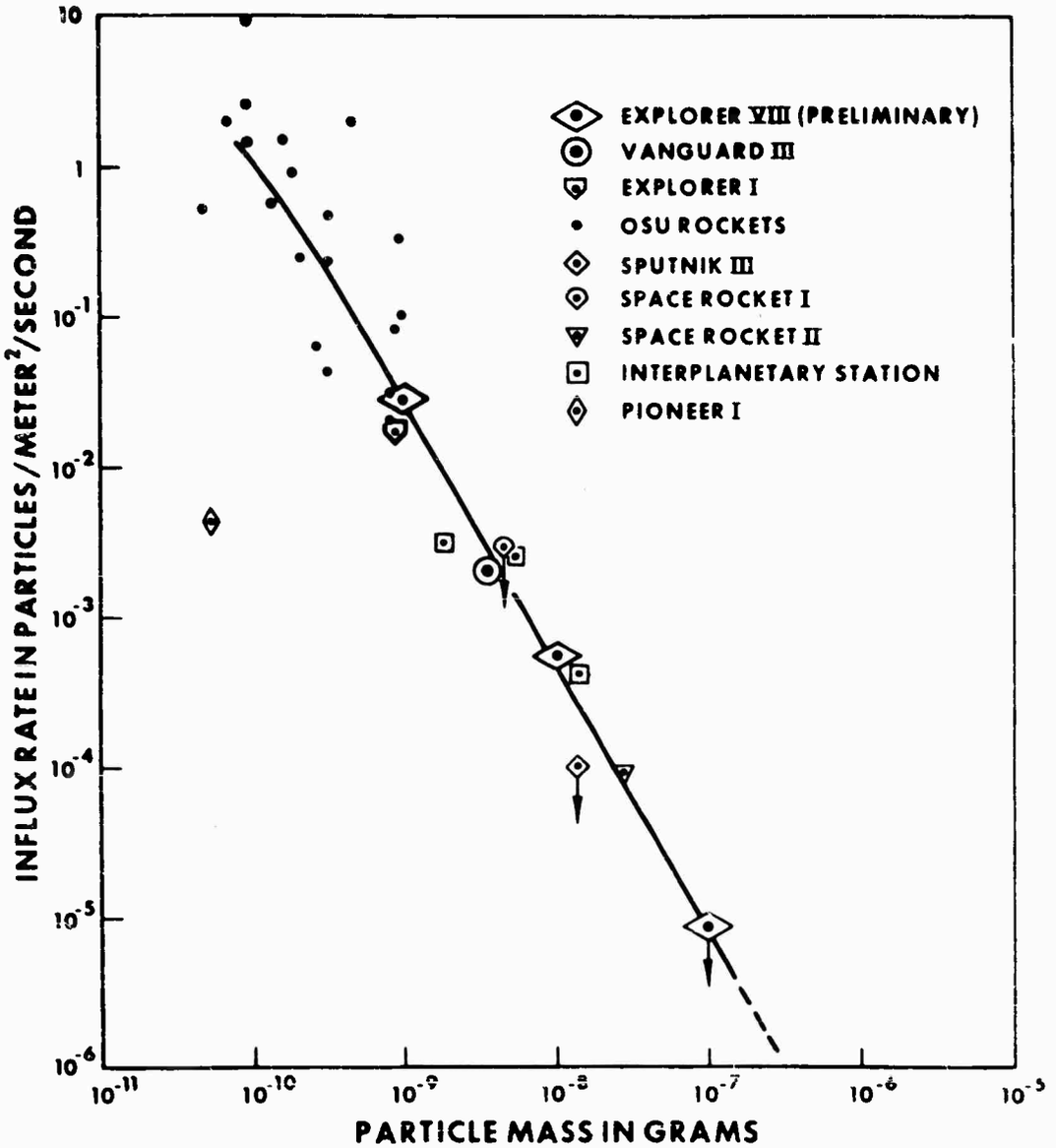

Figure 1. The average distribution curve established by direct measurements from microphone systems for interplanetary dust particles in the vicinity of Earth

EXPERIMENT INSTRUMENTATION

Figure 2 shows the functional block diagram of the cosmic dust experiment which was a part of the scientific instrumentation of Ranger I. The experiment contained two sensors, light flash and acoustical, which detected impacts of dust

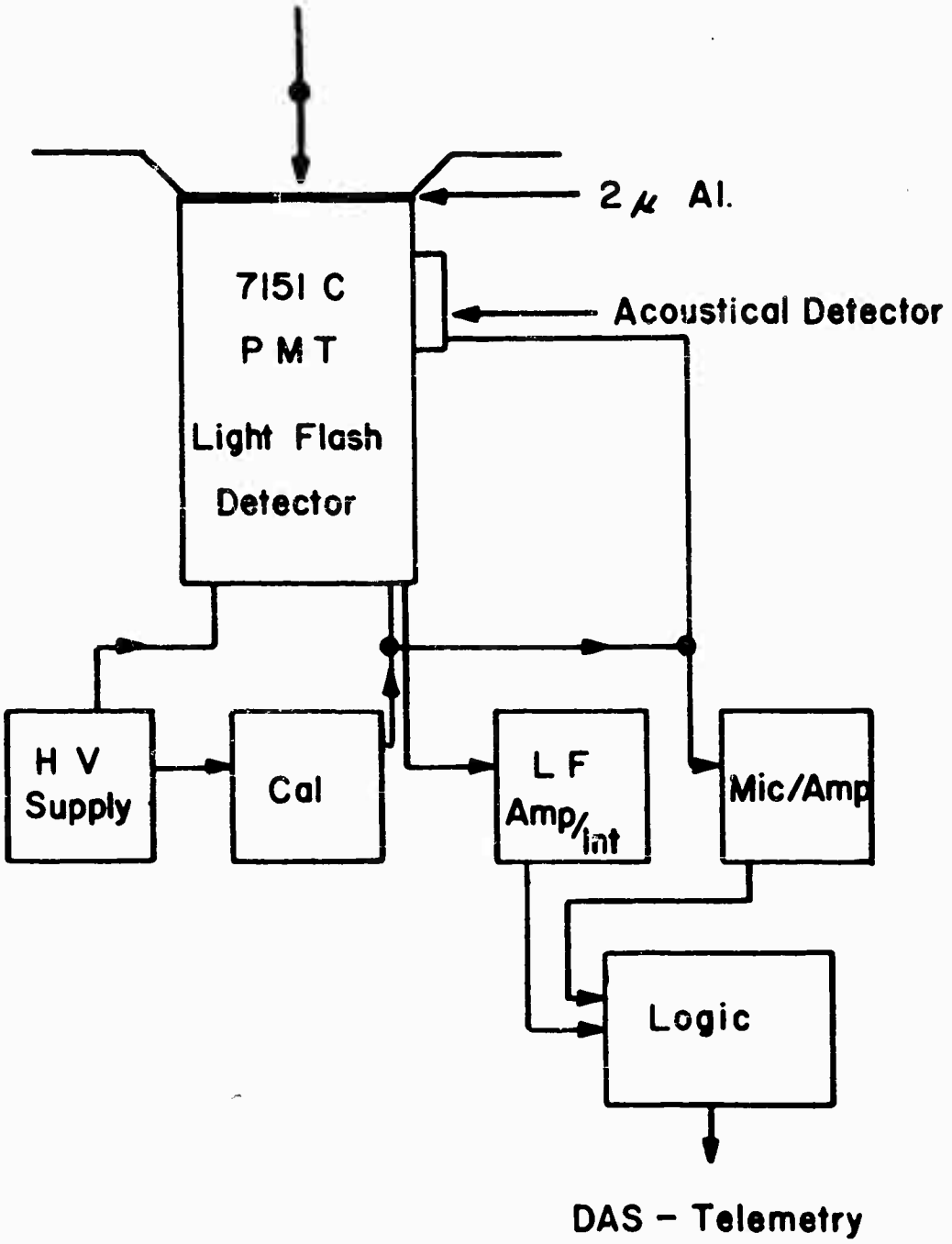

Figure 2. Block diagram – RANGER I. Cosmic dust experiment.

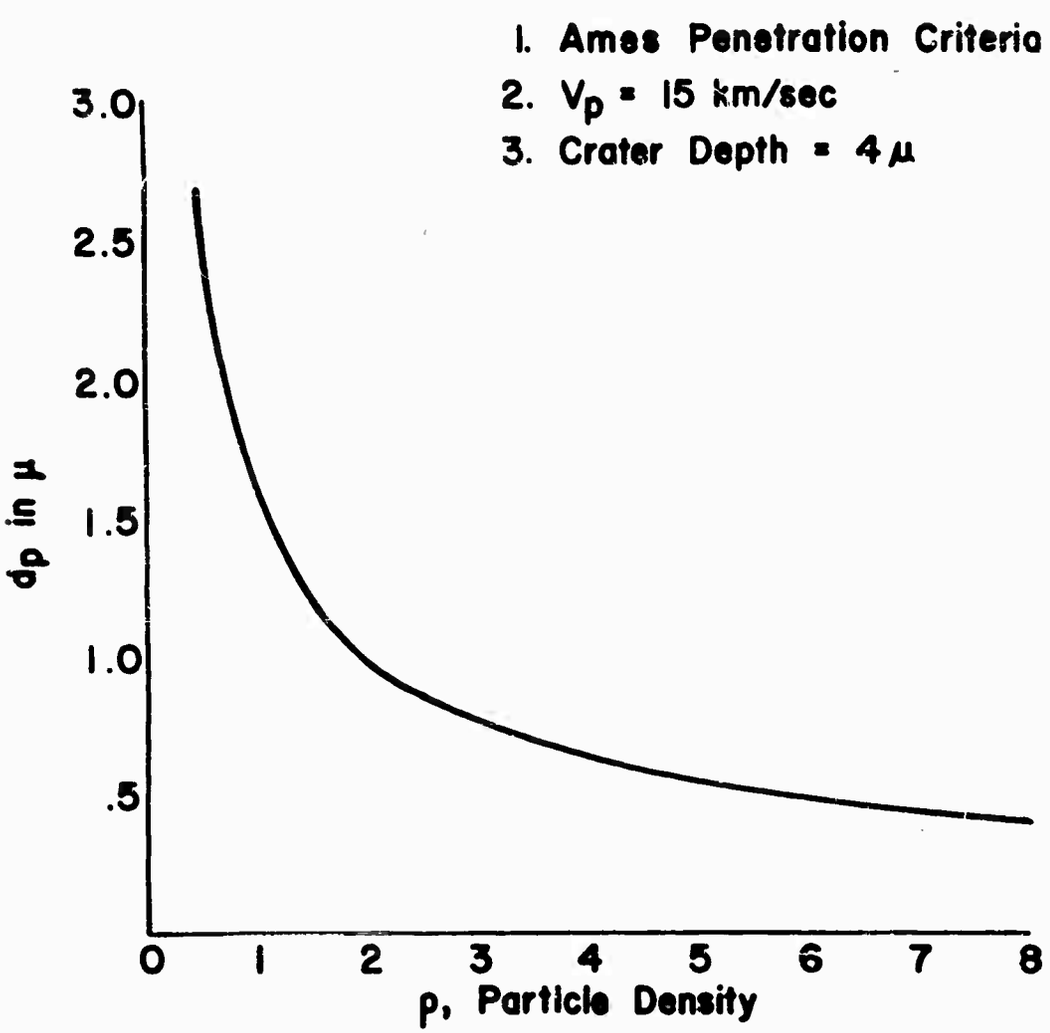

Figure 3. Threshold crater cirteria for detection of light flash

particles on a single surface. The impact surface was the face of the photomultiplier tube. The acoustical detector was attached to the glass envelope of the PMT; therefore, simultaneous detection of the impact of a single particle with both sensors was possible.

The previously mentioned impact studies indicate that the sensitivity threshold for the Ranger I acoustical detector was $3 \pm 1.5 \times 10^{-6}$ dyne-secs for velocities up to $\sim 1.5 \times 10^{6}$ cm/sec.

The PMT, Figure 2, had an evaporative coating of aluminum on the face of the tube. This coating had to be penetrated before the light flash sensor would detect an impacting particle. Numerous equations have been derived for the depth of impact surface penetration of a hypervelocity particle as a function of the dynamics and composition of the particles and the impact surfaces (Charters and Locke, 1958; Summers, 1959; Collins and Kinard, 1960; Bjork, 1960). For the purpose of an initial interpretation of the Ranger 1 dust particle experiment data, the approach outlined below is taken in order to develop a mass sensitivity threshold for the light flash detector.

Most of the presently used criteria show penetration to be a function of particle diameter and particle velocity to the 2/3 or 1/3 power. The criteria developed at the Ames Research Laboratories in recent years also includes physical parameters of the impact surface and of the particle (such as particle density). The equations of the Ames group (called the Ames criteria) are used at this time since they were evolved from experiments where the particle density was varied over an order of magnitude ($\sim$ 1.5 to $\sim$ 17 gm/cc). The Ames velocity was above the point of fluid flow, though not as high as low meteor velocities. In the Ames criteria the penetration is a function of the following particle variables: (1) particle diameter, (2) particle density to the 2/3 power, and (3) particle velocity to the 2/3 power. To establish a threshold mass sensitivity, an impact velocity and depth of penetration necessary for light detection were assumed. Using the Ames criteria, a penetration depth of 4 microns and a velocity of 1.5×10^5 cm/sec, the diameter of the threshold particle as a function of particle density was determined and shown in Figure 3. Figure 4 shows the light flash threshold sensitivity in terms of particle mass as a function of density. The acoustical sensitivity threshold (expressed in terms of mass assuming the velocity stated above) is also shown in Figure 4.

The curves in Figure 4 demonstrate that the experiment could measure three different types of events: An impact detected by the light flash sensor alone; a simultaneous detection of a single impact by both sensors; and an impact detected only by the acoustical sensor. The latter event would only be a particle of low density.

RESULTS

Ranger I was launched on August 23, 1961. Due to a vehicle system malfunction, the spacecraft was placed in a near earth orbit resulting in a spacecraft lifetime of only a few days. However, the dust particle experiment functioned properly for this period, and data was obtained from several telemetry stations. A small sampling of the dust particle distribution near the earth for a short period of time was obtained from the experiment. However, the unique contribution of this data appears to be an initial satellite measurement of particle density.

Data from sixty-six minutes of the Ranger I dust particle experiment showed the following types of impacts:

Light flash only	42 events
Both detectors	9 events
Acoustical only	6 events
	57 events

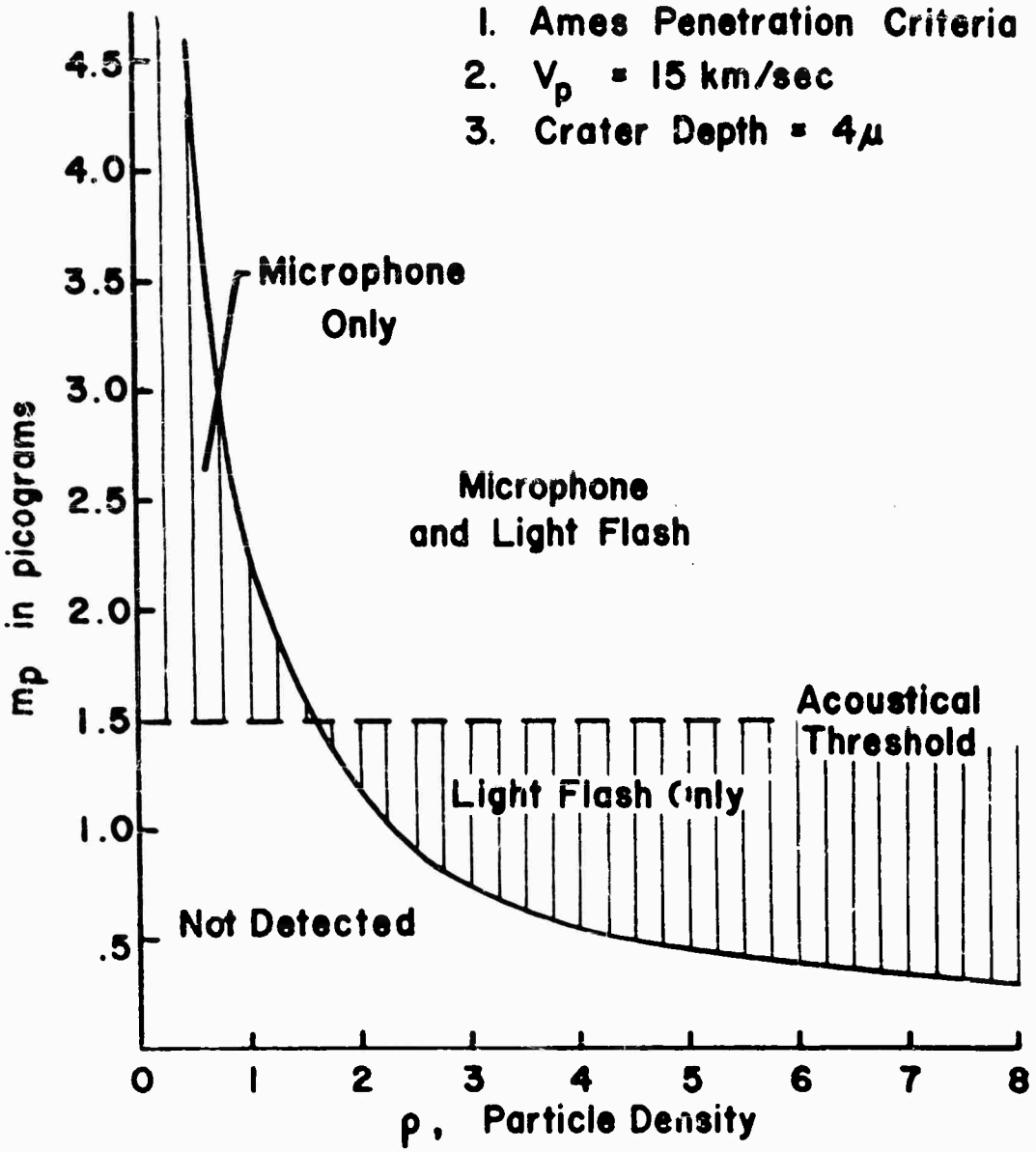

Figure 4. Mass threshold for acoustical and light flash sensors

The above information indicates that between ten and fifteen percent of the impacting particles had a density probably less than 2 gm/cc. A density greater than 2 gm/cc is indicated for sixty to seventy-five percent of the particles. It is interesting to note that these percents are quite similar to those reported recently by Hemenway from rocket collection experiments.

Other approaches concerning selection of penetration criteria could have been used. However, until a considerable advance has been made in penetration criteria, it appears reasonable to use the Ames criteria. One of the impact studies previously mentioned was an investigation of the penetration of aluminum on glass. The dimensions of the hole opening on the glass side of the Al for impacts approaching 1×10^6 cm/sec were within a factor of 1.2 of that predicted by the Ames criteria (density constant). Impact studies where the density of the particle will vary by a factor of 4 from those in use at the present time will be forthcoming in the near future.

Another question can be raised concerning the use of a constant velocity in the computations. For particles of micron dimensions that are very near the earth, the velocities should be near earth's escape velocity. Other factors could cause velocity variation, but it is felt that this variation is less than the density parameter variation. The velocity problem may be resolved if the analysis of velocity modulation due to orbital spacecraft position becomes possible.

REFERENCES

Bjork, R. L., Rand Corporation Report, P-1963, 1960.

Charters, A. C., and Locke, G. S., Jr., NACA RM A58B26, 1958.

Collins, R. D., Jr., and Kinard, W. H., NASA TN D-238, 1960.

Friichtenicht, J. F., Paper presented at Fifth Hypervelocity Symposium, 30 October - 1 November, Denver Colorado, 1961.

McCracken, C. W., and Alexander, W. M., To be published in Smithsonian Contributions to Astrophysics, 1962.

Summers, J. L., NASA TN D-94, 1959.

SUMMARY -- EXPERIMENTAL STUDIES *

R. J. Eichelberger

Ballistic Research Laboratories
Abderdeen Proving Ground, Maryland

The Fifth Symposium has been the recipient of a number of very interesting experimental papers. It is necessary to examine critically, however, their contributions to the state of knowledge, in the light of the situation existing previously.

To consider the more specialized papers first, that by Moore, Lugn, and Gault on impact in rock was especially interesting. It comprises a tour de force of the complex phenomena in brittle materials resulting from the passage and interaction of the various stress waves ensuing from hypervelocity impact. They have also shown evidence supporting the concept that the fracture phenomena are superposed upon a cratering process which is not different at least qualitatively, from that observed in ductile materials. Thus, their results are in agreement with earlier observations on brittle materials, but have materially advanced the state of detailed knowledge of the variety of effects to be studied by a careful investigator.

Kineke's observations of shock velocity in lucite have brought to light another important characteristic of at least one class of brittle materials, the polymer plastics. He has demonstrated what appears to be a relatively large strength effect (as compared with metals) that is of very great interest with respect to high speed deformation of solids, and may be of considerable practical importance, also. It clearly illustrates that a hydrodynamic approximation, neglecting strength effects, cannot be properly applied to all materials; it is important to learn whether the resistance to deformation is dependent upon deformation rate.

In the work reported on thin target perforation, that of Watson is very interesting, especially with respect to the very precise agreement between predicted and observed results. It must be always kept in mind, however, that the physical model used and consequently, the results, are applicable only at intermediate velocities; they are not representative of hypervelocity impact. The work of Humes, Hopko, and Kinard represents a beginning to the accumulation of engineering data pertinent to protection of space vehicles from meteoroid impact. The paper of Vitali, Becker, and Watson (published herewith, although not presented at the symposium) provides even greater detail and quantitative descriptions of the effects of plate perforation.

Caution must be observed, however, in applying any of the conclusions. The velocities attained in the experiments have not been sufficiently high, and the

* Remarks are confined to the unclassified papers presented in the experiment sessions of the symposium.

theoretical treatments are not sufficiently complete (and are as yet untested), to permit confident prediction of behavior under hypervelocity conditions. For example, the type of "bumper" experiments that have been conducted by a number of laboratories, in the range of impact velocities from 3 to 5 km/sec, indicate that bumpers can be very effective. On the other hand, it is known that the considerable amounts of material ejected from the crater produce an "amplification" of forward momentum. Even at moderate impact velocities, the momentum absorbed by a target is more than double that of the impacting projectile; Soviet workers have estimated that at meteoroid velocities an amplification of an order of magnitude would be experienced. If such an increase in momentum were transmitted to the surface of a vehicle by means of the spall projected from a bumper plate, more damage might be done to the vehicle than would have been done by the projectile itself. While there is no evidence to show that such would be the case, the possibility suggests caution in the interpretation of the experimental observations.

With respect to the more general aspects of crater formation, the most promising investigations reported were those pertaining to transient phenomena, reported by Kineke and by Frazier and Karpov. Kineke, in particular, has presented the initial results of a comprehensive analysis of the conditions existing during crater formation, which has already yielded significant results in terms of duration of the stages of cratering, pressures produced, and influence of material properties. Combination of these techniques with the newer, more potent acceleration techniques currently available should be very fruitful and should produce information on truly hypervelocity impact. Supplemented by techniques that are in final stages of development, which will provide observations of pressure pulse shape and of particle velocity, they should yield data entirely adequate for a detailed test of theory or for use as a foundation for theoretical efforts.

While these techniques are extremely promising, they have as yet provided only preliminary observations. Their intensive exploitation still lies in the future.

The purely empirical approach has remained relatively unproductive. The symposium has received two major contributions in the form of surveys and analyses of all the available impact data, by Herrmann and by Bruce (the latter published but not presented orally). These papers can be extremely useful, provided Herrmann's comments are given appropriate attention: the results represent a purely empirical analysis, without foundation in theory, and consequently cannot be trusted for extrapolation. More specifically, no account has been taken in either case of the multiple-stage character of the process under study; the influence of parameters that are important in only one stage is averaged over all, in effect neglecting the changes in relative importance of the several stages with varying velocity. It is perhaps regrettable that a more precarious but potentially more useful analysis, based upon the phenomenological model, was not attempted.

The impact of the new empirical work presented can perhaps be best summarized by considering each physical parameter, as was done in the introduction, and noting any changes in opinion occasioned by work during the past eighteen months.

a. Velocity - The general impression that crater volume is directly proportional to V^2 has been considerably reinforced, but still applied only to velocities less than 12 km/sec (see below, under Strength).

b. Mass - Scaling laws have been further supported. However, the conclusion of Cannon, Clark, and Lee that the validity of linear modeling laws implies viscous forces are negligible must not be carelessly extended to include strength parameters that are independent of deformation rate. Consequently, the scaling results cannot be accepted as vindication of a hydrodynamic treatment of the phenomenon.

c. Shape - No change.

d. Density - No essential improvement in the situation is evident. Superficial analysis of data still yields the result that density of both projectile and target play a role, but does not separate contributions to primary penetration and to cavitation.

e. Wave propagation velocity - No change. Again some reservations must be held, though wave propagation properties certainly are important in determining at what impact velocities changes in cratering mechanism will occur, even though they do not appear in empirical correlations.

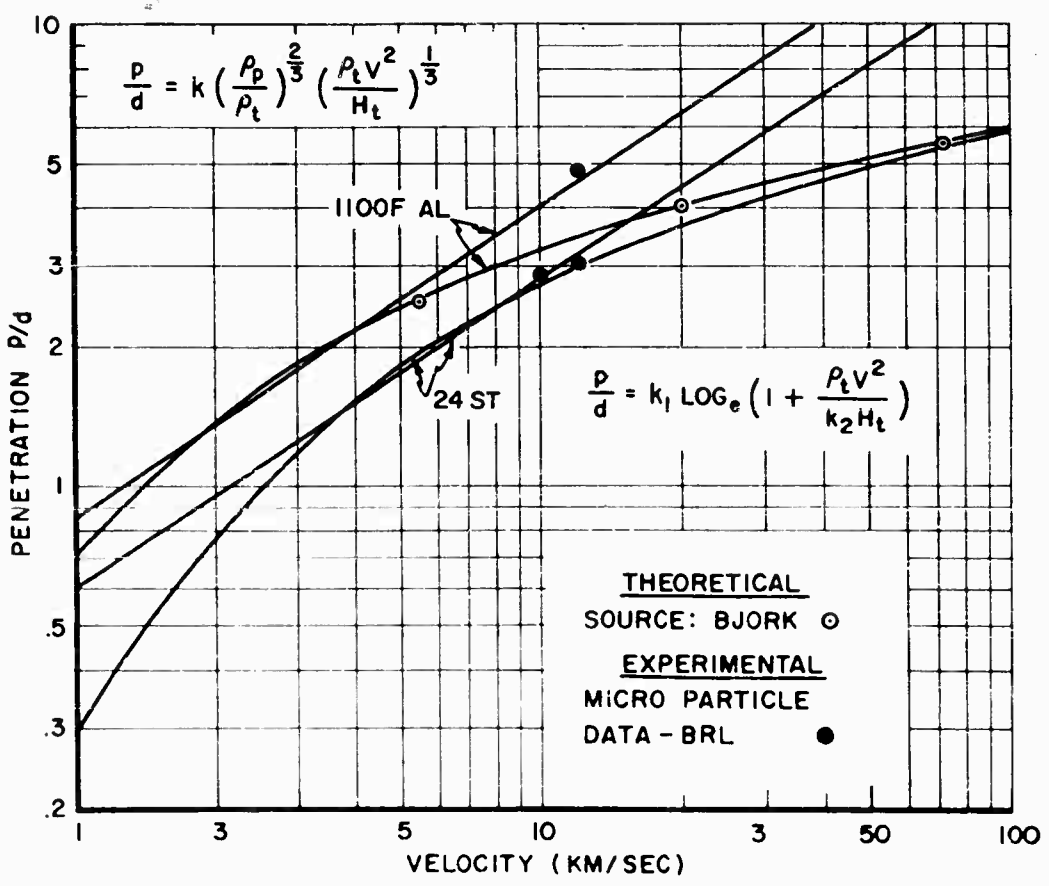

Figure 1. Comparison of micro-particle data at 10 and 12 km/sec with extrapolations of Herrmann's empirical formulae and with Bjork's theoretical results.

f. Compressibility - Still no attempt at correlation.

g. Strength - It is unanimously accepted that the resistance to deformation of the target material is important in the tests reported but, on the basis of very dubious extrapolations (Herrmann, and Rockowitz, Carey and Dignam) the inference has been drawn that the strength effects would diminish at higher impact velocities. In Figure 1 is presented an adaptation of one of Herrmann's correlation plots, with data obtained from micro-particle impacts at 10 and 12 km/sec on 1100F and 24ST aluminum targets. Since the particles were iron rather than aluminum, their close agreement with Herrmann's correlations cannot be attributed any great significance. The important point is that the ratio of penetrations into the two alloys is the same at 12 km/sec as at much lower velocities. Furthermore, tests conducted at the Ballistic Research Laboratories just prior to the symposium, using 17 km/sec jet-pellets fired into the same two alloys, showed that the influence of strength was still unabated at that velocity.

h. Obliquity - The work reported by Smith, Clayden, Wall, and Winter and the paper by Bryan (published, but not included in the symposium presentations) arrive at different conclusions concerning the quantitative correlation between crater dimensions and angle of obliquity. While the relationship proposed by Smith is more plausible, physically, it falls outside the range of uncertainty of Bryan's and Kineke's experimental data. In Figure 2, Bryan's correlation is shown with the U. K. data included for comparison. There appears to be no significant discrepancy.

In more general terms, it appears that the purely empirical approach to the hypervelocity impact problem has been singularly unproductive. Inability to achieve sufficiently high impact velocities to adopt a straight-forward engineering procedure, together with a regrettable lack of perception in analysis of the data obtained, have essentially prevented any significant progress. The latter failing is particularly lamentable because there is no justification for it. Procedures for analyzing crater data, with a view to extracting all possible information pertinent to the cavitation part of the process, were demonstrated at the Rand Symposium in 1955. Since then, a phenomenological model has been established which lends further support to the methods outlined. Yet, not a single paper has shown any inclination to follow the methods that have already been provided. Detailed inspection of crater profiles is completely neglected, and the techniques for determining flow patterns (Smith, et al., and Frazier and Karpov) are used as one-time demonstrations rather than as a means of accumulating useful quantitative information. The difficulties are likely to be circumvented in the immediate future by use of the new projection techniques described earlier in the symposium; it is nonetheless discomforting to realize the amount of effort that has been expended for so little gain.

The future, on the other hand, appears to hold particularly bright promise. Combination of the new projection techniques with the methods described for observing transient conditions should finally provide a definitive test of the theoretical results as well as the urgently needed empirical data.

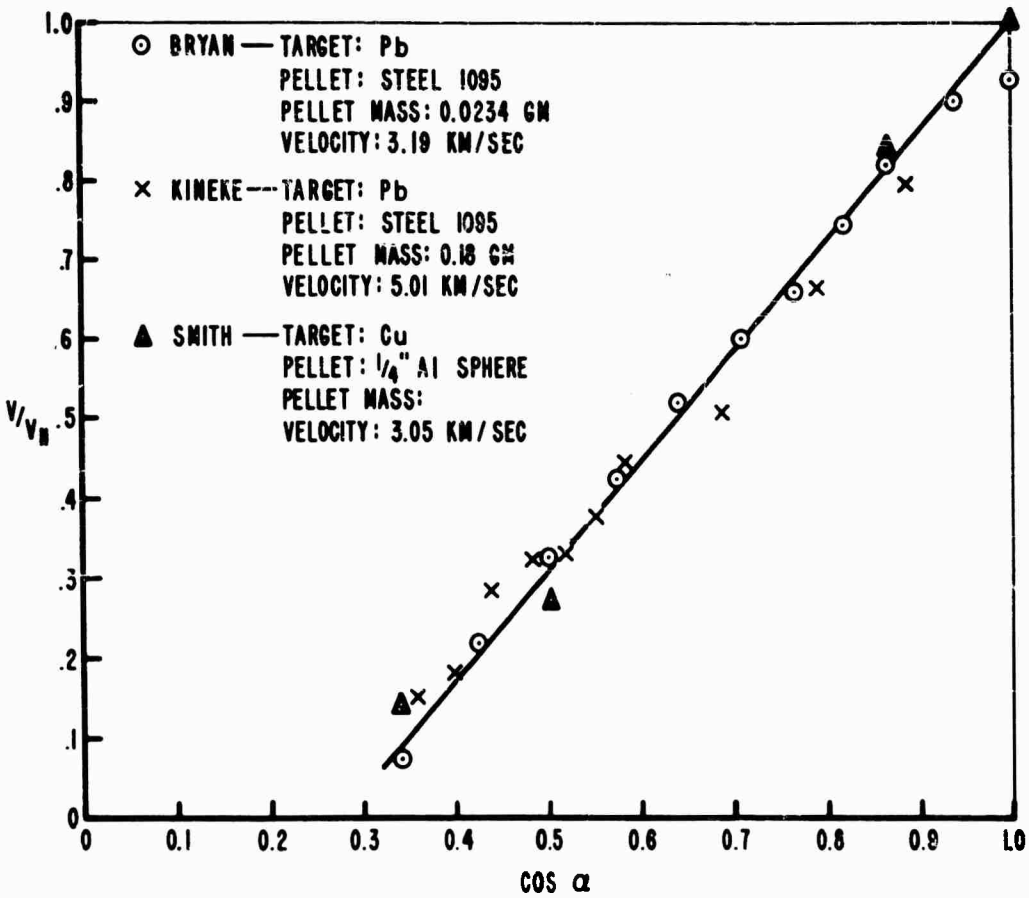

Figure 2. Comparison of data pertaining to effect of oblique incidence.

William F. Adler	The Martin Company, Denver Division
Anthony Alesi	Hq. Quartermaster R & E Company, U. S. Army
Ahmin Ali	Astronautics Division, General Dynamics Corporation
F. E. Allison	Abderdeen Proving Ground
A. L. Anderson	Eng. R & D Laboratories, U.S. Army
J. W. Armstrong	NORAD, Ent A. F. B.
Charles M. Askey	The Hayes Corporation
W. W. Atkins	U. S. Naval Research Laboratory
J. A. Backman, Jr.	Minneapolis-Honeywell Regulator Company
R. F. Badertscher	Battelle Memorial Institute
P. G. Baer	Ballistic Research Laboratories
E. T. Benedikt	Northrop Corporation
H. M. Berkowitz	The Martin Company, Denver Division
R. G. Bernier	Ballistics Research Laboratories
A. G. Bilek	Air Proving Ground Center, Eglin A. F. B.
R. E. Bisque	Weapons Systems Evaluation Group
R. L. Bjork	The Rand Corporation
J. L. Bohn	Temple University
R. B. Bowersox	The Martin Company, Denver Division
R. J. Brun	NASA, Lewis Research Center
G. D. Budris	Douglas Aircraft Company, Inc.
W. C. Burkitt	The Martin Company, Denver Division
M. W. Burnham	Denver Research Institute, University of Denver
J. J. Burns	The Martin Company, Denver Division
R. E. Carpenter	U. S. Army Chemical Center
H. L. Carter	U. S. Naval Ordnance Laboratories
Pei C. Chou	Drexel Institute of Technology
E. N. Clark	Picatinny Arsenal
W. N. Clark	Utah Research & Development Company
W. G. Clay	Lincoln Laboratory, Massachusetts Institute of Technology
E. H. J. Comfort	AFSC, for Aerospace Corporation
Hans Conrad	Aerospace Corporation
P. L. Cowan	CARDE
Charles M. Cox	Firestone Tire & Rubber Company
G. C. Crews	Ballistics Research Laboratories
J. F. Cullinane	Aerojet-General
J. J. Dailey	Ballistics Research Laboratories
J. G. Dante	Ballistics Research Laboratories
N. Davids	Pennsylvania State University
H. L. Davis	Hq. Air Proving Ground Center, Eglin A.F. B.
E. H. Davison	NASA, Lewis Research Center
C. Demuth	M. B. Associates
B. P. Denardo	NASA, Ames Research Center
E. H. Dingman	The Martin Company, Denver Division
W. H. Dittrich	Det. 4, ASD (ASQWR), Eglin AFB
H. H. Dixon	Douglas Aircraft Company
B. E. Drimmer	U. S. Naval Ordnance Laboratories
M. Dryer	The Martin Company, Denver Division
Maurice Dubin	NASA, Goddard Space Flight Center

D. R. Dudas	Det. 4, ASD (ASQWR), Eglin A. F. B.
R. G. Dunn	Aeronautical Research Laboratories, Wright-Patterson A. F. B.
R. J. Eichelberger	Ballistics Research Laboratories
R. M. Elam	Boening Aircraft Company
Frank Fahland	U. S. Naval Research Laboratories
C. W. Fleischer	Frankford Arsenal
H. W. Fletcher	Colorado School of Mines
J. T. Frasier	Brown University
J. F. Friichtenicht	Space Technology Laboratories, Inc.
Charles O. Frush	Colorado School of Mines
L. E. Fugelso	American Machine & Foundry Company
I. M. Fyfe	University of Washington
D. E. Gault	NASA, Ames Research Center
G. M. Gaydos	Picatinny Arsenal
John W. Gehring	General Motors Corporation, Defense Systems
F. Genevese	Westinghouse Electric Corporation, Defense Products
C. M. Gillespie	A. F. Special Weapons Center, Kirtland A. F. B.
R. I. Glasser	Aerospace Corporation
E. H. Goodman	ARO, Inc., Arnold A. F. Station
R. B. Greene	Douglas Aircraft Company
Charles L. Greer	Redstone Arsenal
D. Grossman	Hq. U. S. Army Chemical Center
Charles Haas	Colorado School of Mines
D. A. Hall	U. S. Naval Research Laboratory
S. M. Halperson	U. S. Naval Research Laboratory
J. B. Harkin	American Machine & Foundry Company
J. B. Hatcher	Minneapolis-Honeywell Regulator Company
J. F. Hawk	The Hayes Corporation
W. D. Henderson	Douglas Aircraft Company
M. A. Herlin	Lincoln Laboratory, Massachusetts Institute of Technology
W. Herrmann	Aeroelastic & Structures Lab., Massachusetts Institute of Technology
J. E. Himes	Analytic Services, Inc.
H. E. Hoercher	AVCO Corporation
R. F. Hofer	National Forge Company
L. S. Holloway	Ballistics Research Laboratory
H. G. Hopkins	Defense Research Staff, British Embassy
R. N. Hopko	NASA, Langley Research Center
G. D. Hopson	General Dynamics Corporation
F. E. Howard, Jr.	Det. 4, ASD (ASQP), Eglin A. F. B.
W. G. Howell	Denver Research Institute, University of Denver
N. J. Huffington, Jr.	The Martin Company, Baltimore
D. H. Humes,	NASA, Langley Research Center
W. A. Hurd	Raytheon Company, Missile and Space Division
T. W. Ipson	Denver Research Institute, University of Denver
A. H. Jazwinski	General Dynamics/ Astronautics
E. G. Johnson	Aeronautical Research Laboratories
F. C. Jonah	Chance-Vought Corp, Astronautics Division
A. H. Jones	Aeroelastic & Structures Lab. Massachusetts Institute of Technology
B. G. Karpov	Ballistics Research Laboratories

F. J. Kendell	Utah Research & Development Company
W. H. Kinard	NASA, Langley Research Center
J. H. Kineke	Ballistics Research Laboratories
H. Kostiak	Ballistics Research Laboratories
K. N. Kreyenhagen	Aerojet-General Corporation
Arthur Krill	Denver Research Institute, University of Denver
S. Kronman	Ballistics Research Laboratories
E. T. Kruskewski	NASA, Langley Research Center
E. J. H Lane	United Aircraft Corporation
A. A. Lavine	Astropower, Inc.
G. H. Lee	U.S. Army, Research & Development Division
Y. H. Lee	Astropower, Inc.
L. B. Lennon	U.S. Army Air Defense School
R. J. Lew	The Rand Corporation
W. Levin	Air Force Systems Command, SSD
J. A. Lewis	Bell Telephone Laboratories
H. Liebowitz	Naval Research, T-3
D. B. Lull	A. D. Little, Inc.
J. F. Lundeberg	The Boeing Company
Frederick T. Main	Grumman Aircraft Engineering Corporation
Donald Malick	Institute for Cooperative Research
Richard E. Manelis	A. F. Special Weapons Center, Kirtland A. F. B.
Charles B. Martell	Office of Director of Defense
Charles K. Maxey	Yuma Test Station
Thomas S. May	The Martin Company
Joseph M. McCaughey	Frankford Arsenal
John P. McDonough	Watertown Arsenal
Ralph L. McQuire	ASD (ASRMDS-21), Wright Patterson A. F. B.
Robert R. McMath	Technical Operations, Inc.
A. R. McMillan	Picatinny Arsenal
John M Meshejian	The Hayes Corporation
M. C. Miller	R & D Division, ORD-TB
Henry J. Moore	U.S. Geological Survey
Rene B. Mortensen	Aerojet-General Corporation
P. E. Mullowney	Army Rocket & Guided Missile Agency, Redstone Arsenal
William D. Murphree	U.S. Army Ordnance Missile Command, Redstone Arsenal
D. I. Myers	Raytheon Company
E. B. Nassengill	U.S. Naval Weapons Evaluation Facility
Donald E. Nestler	General Electric Company, MSVD
George R. Nice	Defense Research Staff, British Embassy
Charles R. Nysmith	NASA, Ames Research Center
D. L. Oberg	Beech Aircraft Corporation
Arnold E. Olshaker	The Rand Corporation
Hubert W. Ottenstroer	Naval Research Laboratory
Edward P. Palmer	University of Utah, High Velocity Laboratory
Bob Papetti	The Rand Corporation
Daniel K. Parks	Denver Research Institute, University of Denver
Ransom B. Parlin	Operations Research, Inc.
David D. Parrish	Northrop Corporation
James C. Pearson	Picatinny Arsenal
Francis A. Penning	The Martin Company, Denver Division

John F. Pereira	Republic Aviation Corporation
Mario A. Persechino	U. S. Naval Research Laboratories
William R. Peters	Colorado School of Mines
Dante Piacesi, Jr.	U. S. Naval Ordnance Laboratories
Eugene W. Pike	Lincoln Laboratory, Massachusetts Institute of Technology
John A. Pike	Beech Aircraft Corporation
Carroll D. Porter	U. S. Naval Research Laboratories
Darrell Porter	Colorado School of Mines
William R. Porter	The Martin Company, Orlando Florida
George L. Pratt	Arnold Engineering, Arnold A. F. B.
William E. Preston	U. S. Naval Ordnance Laboratories
Emerson M. Pugh	Carnegie Institute of Technology
Ellsworth H. Quinnell	Hq. Ordnance Weapons Command, ORDOW-TD
R. F. Recht	Denver Research Institute, University of Denver
Robert E. Reed	California Institute of Technology
Thomas D. Reisert	The Martin Company, Baltimore
Lynn G. Richards	Aberdeen Proving Ground
W. M. Richtmann	Colorado School of Mines
John S. Rinehart	Colorado School of Mines
T. D. Riney	General Electric Company, MSVD
Murray A. Rockowitz	AVCO Corporation
James W. Rogers	U. S. Naval Ordnance Test Station
R. F. Rolsten	General Dynamics Corporation
P. L. Roney	CARDE
George C. Sakai	The Martin Company, Denver Division
W. B. Sander	Boeing Airplane Company
James L. Schad	A. D. Little, Inc.
Morris F. Scharff	General Dynamics Corporation
George P. Scheliebiein	Grumman Aircraft Engineering Corporation
C. N. Scully	North American Aviation, Inc.
Howard W. Semon	General Electric Company, MSVD
David B. Singer	Aerospace Corporation
Richard E. Slattery	Lincoln Laboratory, Massachusetts Institute of Technology
N. E. Slaven	U. S. Army Rocket & Guided Missile Agency, Redstone Arsenal
Frank Smith	Defense Research Staff, British Embassy
G. B. Smith	Boeing Airplane Company
Horace C. Smith	Aberdeen Proving Ground
Louis E. Smith	Denver Research Institute, University of Denver
Matthew Smith	AVCO Corporation
J. V. Sober	Picatinny Arsenal
Richard E. Soloski	General Electric Company, MSVD
Robert A. Stein	Battelle Memorial Institute
Francis S. Stepka	NASA, Lewis Research Center
William H. Sternbentz	Aerospace Corporation
Hyman M. Sternberg	U. S. Naval Ordnance Laboratories
Clifton D. Stevens	Goodyear Aircraft Corporation
James L. Summers	NASA, Ames Research Center
Hallock F. Swift	U. S. Naval Research Laboratories
James C. Talley	U. S. Naval Weapons Laboratory
Henri P. Tardif	CARDE
James Tasi	The Martin Company, Denver Division